SAND2018-12044R

Evaluation of Used Fuel Disposition in Clay-Bearing Rock

Spent Fuel and Waste Disposition

Prepared for
U.S. Department of Energy
Spent Fuel and Waste Science and Technology

Carlos F. Jové Colón, Clay Payne, Andrew Knight, Tuan Ho (SNL)

Jonny Rutqvist, Kunhwi Kim, Hao Xu, Yves Guglielmi, Jens Birkholzer (LBNL)

Florie A. Caporuscio, Kirsten B. Sauer, M. J. Rock, L. M. Houser (LANL)

James Jerden, Vineeth K. Gattu, William Ebert (ANL)

September 24^{h}, 2018

M2SF-18SN010301051

DISCLAIMER

This information was prepared as an account of work sponsored by an agency of the U.S. Government. Neither the U.S. Government nor any agency thereof, nor any of their employees, makes any warranty, expressed or implied, or assumes any legal liability or responsibility for the accuracy, completeness, or usefulness, of any information, apparatus, product, or process disclosed, or represents that its use would not infringe privately owned rights. References herein to any specific commercial product, process, or service by trade name, trade mark, manufacturer, or otherwise, does not necessarily constitute or imply its endorsement, recommendation, or favoring by the U.S. Government or any agency thereof. The views and opinions of authors expressed herein do not necessarily state or reflect those of the U.S. Government or any agency thereof.



Sandia National Laboratories is a multimission laboratory managed and operated by National Technology & Engineering Solutions of Sandia LLC, a wholly owned subsidiary of Honeywell International Inc. for the U.S. Department of Energy's National Nuclear Security Administration under contract DE-NA0003525.



SUMMARY

The DOE R&D program under the Spent Fuel Waste Science Technology (SFWST) campaign has made key progress in modeling and experimental approaches towards the characterization of chemical and physical phenomena that could impact the long-term safety assessment of nuclear waste disposition in deep clay/shale/argillaceous rock. Interactional collaboration activities such as heater tests, particularly *postmortem* sample recovery and analysis, have elucidated important information regarding changes in engineered barrier system (EBS) material exposed to years of thermal loads. Chemical and structural analyses of bentonite material from such tests has been key to the characterization of thermal effects affecting clay composition, sorption behavior, and swelling. These are crucial to evaluating the nature and extent of bentonite barrier *sacrificial zones* in the EBS during the thermal period. Thermal, hydrologic, and chemical data collected from heater tests and laboratory experiments has been used in the development and validation of THMC simulators to model near-field coupled processes affecting engineered and natural barrier materials, particularly during the thermal period. This information leads to the development of simulation approaches (e.g., continuum vs. discrete) to tackle issues related to flow and transport depending on the nature of the host-rock and EBS design concept. This report describes R&D efforts on disposal in argillaceous geologic media through developments of coupled THMC process models, hydrothermal experiments and characterization of clay/metal barrier material interactions, and spent fuel and canister material degradation. Currently, the THM modeling focus is on heater test experiments in argillite rock and gas migration in bentonite as part of international collaboration activities at underground research laboratories (URLs). In addition, field testing at an URL involves probing of fault movement and characterization of fault permeability changes. Analyses of barrier samples (bentonite) from heater tests at URLs provide compositional and structural data to evaluate changes in clay swelling and thermal behavior with distance from the heater surface. Development of a spent fuel degradation model coupled with canister corrosion effects has been centered towards its integration with Generic Disposal System Analysis (GDSA) to describe source term behavior.

As in previous milestone deliverables, this report is structured according to various national laboratory contributions describing R&D activities applicable to clay/shale/argillite media. These activities are summarized as follows:

- **International Collaboration & Disposal in Argillite R&D Activities – SNL (Part I)**
  - International Collaborations:
    - FEBEX-DP:
      - Analysis of a FEBEX-DP bentonite samples from Section 49 using X-ray Fluorescence (XRF), X-ray diffraction (XRD), and thermogravimetric analysis (TGA/DSC) analytical techniques. These analytical approaches are conducted on samples collected as a function of distance from the gallery center or heater surface.
      - XRF analyses revealed Mg enrichment in samples closest to the heater. This observation is corroborated with other FEBEX-DP studies in other sampled sections surrounding the heater. Estimated relative extent of swelling based on XRD data for air-dried and

glycolated bentonite samples shows a reduction in variability for samples closest to the heater. TGA/DSC thermal analyses indicate that measured water content falls within the data bounds of other FEBEX-DP studies from other sampled sections.

- DECOVALEX Task C:
  - PFLOTRAN 3D Reactive transport modeling of the closure test drift (CTD) focusing on shotcrete – ground water interactions of the cement liner in the water-filled tunnel. This simulation effort is part of an inter-comparison exercise between different modeling teams (SNL, JAEA, TUL) participating in this task.
  - pH predictions at the midpoint length of the CTD overestimates the measured data at later times whereas the predicted Cl- concentration prediction underestimates its decrease with time. However, pH predictions in at a monitoring borehole adjacent to the CTD show overall consistency with measured data suggesting a strong influence of the granitic host-rock on the groundwater chemistry.

- **Investigation of Coupled Processes in Argillite Rock – LBNL (Part II)**
  - TOUGH-FLAC and Modeling of Heater experiments at Mont Terri and Bure URLs
    - Mont Terri FE full-scale heater test experiment:
      - In a scoping calculation, thermal pressurization in the host rock could be reasonably well modeled, though local heterogeneities close to monitoring points probably affect the field data. Future modeling of thermal pressurization will focus at a mechanistic modeling of the anisotropic coupled THM responses and their impact on fluid pressure.
      - There is good agreement between modeled and measured evolutions in buffer temperature and relative humidity. There were based properties of bentonite and Opalinus Clay associated from the previous Mont Terri HE-E experiment.
      - Values for effective vapor diffusion coefficient and the tortuosity factors for the bentonite block were determined based on calibration of model parameters. These values are much larger than those for granular bentonite.
      - After 3.5 years of heating and water infiltration from the surrounding rock, no significant swelling stress has developed in the bentonite buffer.

- TED Experiment at Bure URL (DECOVALEX-2019 Project):
  - For step 1, as previously reported, correction of the analytical solution results of stress for the 3D THM modeling benchmark problem yield a good agreement between our model simulation and theoretical solutions.
  - For step 2, as previously reported, THM parameters of claystone from TED experiment have been determined with god agreement to experimental data: calibration on thermal conductivities to match the temperature evolution during heating, analysis of the simulation results to correct permeabilities.
  - For Step 3, we predicted THM behavior of COx clay stone during the ALC experiment by utilizing parameters of claystone calibrated from the modeling of the TED experiment.
  - Next step for the rest of FY2018 and FY2019 will be to model Step 4 of DECOVALEX-2019 Task E; to conduct model predictions at the repository scale of an area with several high-level waste cells.

- Modeling of Gas Migration in Clay Using TOUGH-FLAC and TOUGH-RBSN (DECOVALEX-2019):
  - TOUGH-FLAC modeling for a homogeneous material with model representations for a simple linear poro-elastic representation, moisture swelling, stress-dependent gas permeability, and an effective gas entry pressure could capture the main features of the experiment – including pressure, stress, and flow evolution. Still, the largest model deviations are towards the end of the experiment where gas flow shuts down.
  - For the 1D gas flow simulation using the TOUGH-RBSN simulator, the DFN approach with enhanced fracture permeability demonstrated the gas breakthrough where the pore pressure evolutions were matched well to the experimental data. However, the simulated outflow rate deviates from the experiment in terms of the flow activation time and the overall shape of the evolution curve.

- Fault Activation Monitoring Using the SIMFIP Tool
  - The SIMFIP borehole probe allows for measuring simultaneously fluid pressure and three-dimensional displacements at high frequency. SIMFIP is used to probe fault movements and estimate fault permeability variations during *in situ* fault activation experiments at depths relevant to nuclear repository sites.
  - Data gathered by SIMFIP shows that large fault permeability variations correlate with periods of large fault slip rate events. However, these permeability changes do not correlate well with the imposed pressure.

This suggest fault displacement rate might cause the effect of stress on fault reactivation and leakage.

- Field observations and numerical results show that the initial stress on a fault, affecting the permeability change and friction during fluid pressurization, has an important effect on fluid pressure diffusion and slip growth.

- **Disposal in Argillite R&D and International Collaborations (FY18) – LANL (Part III)**
  - Hydrothermal experiments (200°C and 300°C) involved Opalinus Clay (wall rock), Wyoming bentonite, Portland cement, and (low-carbon, stainless) steel. Characterization studies involved SEM-EMPA XRD, and aqueous solution compositional data of hydrothermal experiments.
  - SEM-EMPA and XRD analyses for a set of FEBEX-DP bentonite samples from Section 49.
  - Opalinus Clay experiments appears to have an increase in the illite-smectite distribution. However, there was negligible illitization in the bentonite fraction for the mixed experiment. The overall high silica saturation appears to inhibit illite formation and favoring precipitation of high-silica zeolites such as analcime/wairakite.
  - Mixture of Opalinus Clay plus bentonite produces higher corrosion rates for low-carbon steel relative to bentonite alone experiments. The higher corrosion rates are attributed to the high pyrite content in the Opalinus Clay fraction.
  - The addition of cement to a clay favors the formation of an analcime-wairakite phase at lower temperatures (200°C). This is most probably due to the high concentration of Si and Ca liberated into the groundwater from the cement.
  - FEBEX-DP bentonite clay sample characterization indicate feldspar compositions (both plagioclase and K-feldspar) vary in the outer and middle location, but more homogeneous compositions in the region closer to the heater surface. MgO and SiO_2 in smectite generally varies from the different sample block locations with distance from the heater surface.

- **Progress on the Development of the Spent Fuel Degradation and Waste Package Degradation Models – ANL (Part IV)**
  - The parameter database for the FMD (Fuel Matrix Degradation) model was updated based on comparisons between model results and existing spent fuel, and UO_2 dissolution rate data. An electro-kinetic mixed potential model for the corrosion of steels was coupled with the spent fuel dissolution reactions through the H_2 generation reactions.

- Sensitivity analyses with the new FMD model reiterate the need for experimental data to parameterize and validate the steel corrosion module added to the FMD model.
- Results from scoping experiments demonstrated a straightforward electrochemical method that provides the electrokinetic information needed for model parameterization and validation.
- Model simulations using the new FMD model agree with previous model results showing that the presence of metals that corrode at different rates can extend the time over which H_2 generation will attenuate the fuel degradation rate.

Overall Status and Future Perspectives in Disposal in Argillite R&D:

- **Experimental and thermodynamic modeling studies of barrier material interactions**
  - **Goal**: Conduct experimental and thermodynamic modeling investigations of barrier material interactions from ambient conditions up to elevated pressures and temperatures. Study degradation mechanisms of clay, cement, and metal barriers with implications to in-package chemistry and spent fuel degradation. This may also involve coupling the spent fuel degradation model (source term) with reactive transport modeling of the EBS. Developments of thermodynamic databases to be used as input feeds to coupled-process models and (geo)chemical simulators.
  - **Status & Accomplishments**: Progress on experimental and thermodynamic modeling activities:
    - A comprehensive suite of experiments focused on hydrothermal interactions of bentonite clay, steel materials, and argillaceous wall rock. This also involves and mechanistic characterization of steel corrosion in the presence of bentonite and host rock material.
    - Extensive characterization studies (compositional, structural, geochemical) of run products integrated with thermodynamic modeling to evaluate the occurrence secondary mineralization and clay phase stability at elevated pressures and temperatures.
    - Characterization studies of bentonite samples and argillaceous rock from international repository programs (FEBEX-DP) achieved through international collaborations.
    - Thermodynamic database development for the re-analysis of thermodynamic properties of aqueous, solids, and gas species.

Representation of SFWST campaign within the NEA-TDB project. Revisiting the equation of state (EoS) for H_2O. Sorption database development and modeling strategies using PhreeqC-PEST fitting routine using various surface complexation models.

- 1D-3D reactive transport modeling under non-isothermal conditions using the PFLOTRAN THC simulator. The focus is on multiphase multicomponent description of barrier interactions at a wide range of pressures and temperatures using HPC platforms.

- **Perpespectives**: Future outlooks in experimental and thermodynamic modeling studies:

  - Expand experimental work towards interactions between bentonite clay, cementitious materials, steel material, and argillaceous host rock. Investigate these interactions at various temperatures and pressures to evaluate the alteration mineralogy at the interfaces of these barrier materials.

  - Conduct hydrothermal treatment of FEBEX-DP bentonite samples and post-experiment characterization.

  - Continue expansion of thermodynamic database development towards testing and applications to geochemical and reactive transport modeling at elevated pressures and temperatures.

  - PFLOTRAN simulator for 3D non-isothermal reactive transport (THC) modeling of bentonite barrier – fluid interactions under variably saturated conditions. Also, expand analysis and validation of reactive transport simulations dealing with interactions of cementitious barrier material with fluids.

  - Thermodynamic modeling to describe barrier material interactions focusing on interactions between cementitious and other barrier materials. Expand these evaluations towards the effect on clay phase transformation and the role of zeolite formation.

  - Investigate the chemical behavior bentonite under partially saturated conditions.

  - Extend the thermodynamic analysis used in the evaluation of engineered barrier material interactions towards the description of in-package chemistry.

- **Coupled-process model development for simulation of near-field thermal, chemical, mechanical, and transport (THMC) interactions.**
    - **Goal**: Development, testing, and validation of coupled-process models for simulation of near-field thermal, chemical, mechanical, and transport (THMC) interactions in the evaluation of barrier material performance. Programmatic engagements and collaborations with international R&D activities (e.g., URL heater tests) in repository sciences.
    - **Status & Accomplishments**: Progress on THMC model development, implementation, and validation:
        - TOUGH-FLAC THM simulator with applications to disposal in argillite R&D. Simulation of bentonite swelling behavior using the BBM (Barcelona Basic Model) and BExM (Barcelona Expansive Model) constitutive model implementations.
        - Application of a TOUGH-FLAC shale / clay rock constitutive model that captures rock anisotropic properties of elasticity, strength, thermal conductivity, permeability and thermal expansion.
        - Development of TOUGH-FLAC models to simulate permeability and damage behavior in the EDZ.
        - TOUGH-RBSN simulator for coupled fracturing processes and gas migration.
        - International collaborations (Mont Terri, DECOVALEX2019): (FE Experiment – Mont Terri; COx Clay Stone – Bure, France; Closure Test Drift (CTD) experiment, Mizunami site, Japan)
        - Fault activation monitoring using the SIMFIP tool.
    - **Perspectives**: Future outlooks in THMC model development:
        - Continue engagements with international collaborations activities involving heater tests design and process model and validation.
        - In addition to the above, utilize recovered samples from heater tests and sensor data for EBS material behavior and sample characterization.
        - Expand development of continuum and discrete modeling approaches to evaluate transport phenomena.

- Reactive transport modeling under isothermal and non-isothermal conditions focusing on barrier material interactions (clay, steel, cement).
- Model development for GDSA Integration.
- Application of the SIMFIP tool for *in situ* characterization of a fracture induced by thermal pressurization (ANDRA, Bure URL site).
- Model testing and development for large-scale gas driven fracturing using 3D models for large scale problems gas-driven fracturing. Looking forward to leverage for high-performance computing (HPC).
- Coupled microbial-abiotic processes in EBS and host rocks.

- **Development of source term models for (spent nuclear) fuel matrix degradation (FMD) and integration with GDSA**
  - **Goal**: Development and implementation of an electrochemical process model for the degradation rate of spent nuclear fuel capturing the effects of steel degradation, and the presence of aqueous components affecting H_2 concentrations. Integration of these efforts with GDSA-PA and the development of an in-package chemistry model.
  - **Status & Accomplishments**: The FMD model development and implementation accounts for:
    - Effect of hydrogen generated from steel corrosion within a breached waste package
    - Alpha radiolysis and the generation of radiolytic oxidants as a function of fuel burn-up
    - Growth a porous layer of uranyl oxyhydroxide and/or uranyl peroxide corrosion phases
    - Complexation of dissolved uranium by carbonate
    - Temperature variations of reaction rates (by Arrhenius equations)
    - One-dimensional diffusion of all chemical species to and from the fuel and steel surfaces.
    - Integrated with GDSA through a PFLOTRAN code implementation
  - **Perspectives**: Future outlooks in the development of the FMD model:
    - Model enhancement through the generation of experimental data for model parameter validation and analysis in the representation of steel corrosion effects and H_2 generation

- Experimental and modeling studies investigating the corrosion rates of different alloys and EBS components that may go into the waste package design and waste form degradation
- Extend model towards development and application of an in-package chemistry model

Revision 5
01/15/2018

APPENDIX E
NTRD DOCUMENT COVER SHEET[1]

Name/Title of Deliverable/Milestone/Revision No. Evaluation of Spent Nuclear Fuel Disposition in Clay-Bearing Rocks, M2SF-18SN010301051/ Rev.0

Work Package Title and Number Argillite Disposal R&D – SNL / SF-18SN01030105

Work Package WBS Number 1.08.01.03.01

Responsible Work Package Manager Carlos F. Jove Colon (Name/Signature)

Date Submitted

Quality Rigor Level for Deliverable/Milestone[2]	☐ QRL-1 ☐ Nuclear Data	☐ QRL-2	☒ QRL-3	☐ QRL-4 Lab QA Program[3]

This deliverable was prepared in accordance with Sandia National Laboratory
(Participant/National Laboratory Name)

QA program which meets the requirements of
☐ DOE Order 414.1 ☐ NQA-1 ☐ Other

This Deliverable was subjected to:

☒ Technical Review ☐ Peer Review

Technical Review (TR)
Review Documentation Provided
☐ Signed TR Report or,
☐ Signed TR Concurrence Sheet or,
☒ Signature of TR Reviewer(s) below

Peer Review (PR)
Review Documentation Provided
☐ Signed PR Report or,
☐ Signed PR Concurrence Sheet or,
☐ Signature of PR Reviewer(s) below

Name and Signature of Reviewers

Ed Matteo

NOTE 1: *Appendix E should be filled out and submitted with the deliverable. Or, if the PICS:NE system permits, completely enter all applicable information in the PICS:NE Deliverable Form. The requirement is to ensure that all applicable information is entered either in the PICS:NE system or by using the NTRD Document Cover Sheet.*

- *In some cases there may be a milestone where an item is being fabricated, maintenance is being performed on a facility, or a document is being issued through a formal document control process where it specifically calls out a formal review of the document. In these cases, documentation (e.g., inspection report, maintenance request, work planning package documentation or the documented review of the issued document through the document control process) of the completion of the activity, along with the Document Cover Sheet, is sufficient to demonstrate achieving the milestone.*

NOTE 2: *If QRL 1, 2, or 3 is not assigned, then the QRL 4 box must be checked, and the work is understood to be performed using laboratory QA requirements. This includes any deliverable developed in conformance with the respective National Laboratory / Participant, DOE or NNSA-approved QA Program.*

NOTE 3: *If the lab has an NQA-1 program and the work to be conducted requires an NQA-1 program, then the QRL-1 box must be checked in the work Package and on the Appendix E cover sheet and the work must be performed in accordance with the Lab's NQA-1 program. The QRL-4 box should not be checked.*

AKNOWLEDGEMENTS

The authors acknowledge our gratitude to Ed Matteo (SNL), Kristopher Kuhlman (SNL), Kevin McMahon (SNL), Geoff Freeze (SNL), Emily Stein (SNL), William Spezialetti (DOE NE), Prasad Nair (DOE NE), Mark Tynan (DOE NE), and Tim Gunther (DOE NE) for their helpful discussions and contributions on various topics covered in this report.

TABLE OF CONTENTS

SUMMARY iii

AKNOWLEDGEMENTS xiii

REVISION HISTORY xxxii

ACRONYMS xxxiii

International Collaboration & Disposal in Argillite R&D Activities – SNL (Part I)

1. Introduction 2
   1.1 International Collaboration Activities: 2
2. FEBEX-DP: X-ray Fluorescence (XRF) and X-ray diffraction (XRD) Studies of Bentonite from Section 49 3
3. Methodology: XRF, XRD, and Thermal Analyses (TGA/DSC) 6
   XRF and TGA/DSC Analyses 7
   XRD Methodology 8
4. Results and Discussion: FEBEX-DP Section 49 8
   TGA/DSC Analyses 13
   XRD Data 15
5. DECOVALEX-2019 Task C: GREET (Groundwater REcovery Experiment in Tunnel), Mizunami URL, Japan 20
   Closure Test Drift (CTD): 3D H-C Model of Shotcrete Liner Interactions and 12MI33 Monitoring Borehole 20
6. 3D Reactive Transport (THC) Simulations for a Single Heat-Generating Waste Package with a Layered EBS 28
7. Conclusions 31
8. References 34

Investigation of Coupled Processes in Argillite Rock – LBNL (Part II)

1. Introduction 37
2. Status of TOUGH-FLAC Simulator 40
   2.1 TOUGH-FLAC Framework 41
   2.2 Bentonite Constitutive THM Models in TOUGH-FLAC 42

2.3 Shale Constitutive THM Models in TOUGH-FLAC 44
2.4 EDZ Models in TOUGH-FLAC 45
2.4.1 Empirical stress-permeability model 46
2.4.2 Non-linear elastic and brittle failure model 48
2.4.3 Anisotropic continuum damage model 49

3. Status of TOUGH-RBSN Simulator for Coupled Fracturing Processes 50
3.1 TOUGH-RBSN Coupling Procedure 50
3.2 Model Discretization and Discrete Fracture Representation 52
3.3 Stress Calculation and Fracture Determination in the RBSN Approach 54
3.4 Status of TOUGH-RBSN Verification and Validation 57

4. FE Experiment at the Mont Terri Site (Mont Terri Project) 57
4.1 Description and Status of the Mont Terri FE experiment 57
4.2 Progress of LBNL Modeling of FE Experiment 60
4.3 TOUGH-FLAC Model of the Mont Terri FE Experiment 61
4.4 Simulation Results with Comparison to Monitored Data 63
4.5 Summary and Status the FE Experiment Modeling 74

5. Heater Experiments at Bure in COx Clay Stone (DECOVALEX-2019) 74
5.1 DECOVALEX-2019 Task E and International Modeling Teams 75
5.2 TOUGH-FLAC Simulation Results with Comparison to Experimental Data 76
5.2.1 Step 1: 3D THM modeling benchmark 76
5.2.2 Step 2: TED experiment 80
5.2.3 Step 3 – ALC experiment 87
5.3 Summary and Status of the Bure Heater Experiment Modeling 91

6. Modeling of Gas Migration in Clay Using TOUGH-FLAC and TOUGH-RBSN (DECOVALEX-2019) 92
6.1 Gas Migration in Clay 92
6.2 DECOVALEX-2019 Task A and International Modeling Teams 93
6.3 Laboratory Experiments of Gas Migration in Bentonite 95
6.4 LBNL Model Approaches for Gas Migration 100
6.5 TOUGH-FLAC Modeling of Gas Migration Experiments 101
6.6 TOUGH-RBSN Modeling of Gas Migration Experiments 109
6.6.1 1D flow through saturated bentonite under constant volume boundary conditions 109

6.6.2 Spherical flow through saturated bentonite under constant volume boundary conditions 117
6.6.3 Summary of TOUGH-RBSN simulations for gas migration 120

7. Fault Activation Monitoring Using SIMFIP Tool 122
7.1 Introduction 122
7.2 Development of a New SIMFIP Sensor 122
7.3 Observations of fault permeability variations induced by pore pressure increase 126
7.4 Numerical analysis of key parameters conditioning fault activation induced by pore pressure increase 128
7.5 Summary and future work on fault activation monitoring and SIMFIP tool 132
7.5.1 Upgrading the SIMFIP to detect nanoscale fault movements 132
7.5.2 Future in situ testing at Mt Terri (Switzerland) and Improvements in fault permeability constitutive laws in argillite 133

8. Summary of FY2018 Progress and Future Work 133
8.1 Progress and Plans of Ongoing FY2018 Activities 134
8.2 Expanded FY2018 Argillite Research Activities 135

9. Acknowledgements 137

10. References 138

Disposal in Argillite R&D and International Collaborations (FY18) – LANL (Part III)

1. Introduction 145
1.1 Background 145
1.2 Methods 152

2. Results 153
2.1 Starting Material Characteristics 153
2.2 Results from EBS-14 to EBS-23 156
2.2.1 Aqueous Geochemistry 156
2.2.2 Clay Mineralogy 159
2.2.3 Electron Microprobe Analyses (EMPA) 164
2.2.4 SEM/EDS Results 167
2.3 FEBEX Results 169
2.3.1 Bentonite Mineralogy 169
2.3.2 Microprobe 171

2.3.3 Scanning Electron Microscopy 172
3. Discussion 174
3.1 Opalinus clay interactions with EBS backfill 174
3.2 Summary of Steel Corrosion Rates 182
3.2.1 Steel Corrosion Rates 184
3.3 Summary of Steel-Bentonite Interface Mineralogy 187
4. Conclusion 201
5. Acknowledgements 205
6. References 206

Progress on the Development of the Spent Fuel Degradation and Waste Package Degradation Models – ANL (Part IV)

1. Introduction 215
2. Update on Validation of Fuel Matrix Degradation Model Version 4 217
3. Electrochemical Experiments To Parameterize The FMDM Steel Corrosion Module 228
3.1 Background 228
3.2 Method and Results 232
4. Conclusions and Future Work 240
5. References 242

Appendices

Appendix A 245
Methods and mineral characterization 245
Appendix B 249
Water Chemistry Samples EBS-14 to EBS-23 249
Appendix C 268
X-Ray Powder Diffraction Data: EBS-14 to EBS-23 268
Appendix D 275
Electron Microprobe data 275
Appendix E 311

XRF and XRD Data (FEBEX SAMPLES) 311

Appendix F 325

SEM Images (EBS-14 to EBS-23) and (FEBEX SAMPLES) 325

TABLE OF FIGURES

International Collaboration & Disposal in Argillite R&D Activities – SNL (Part I)

Figure 1. Schematic layout of the FEBEX "in-situ" field test after the first partial dismantling showing the configuration of heater #2 at the GTS URL 4

Figure 2. Schematic configuration of sampling zones (indicated by vertical light blue bars) for the FEBEX-DP project.. 5

Figure 3. Schematic diagram of sampling locations for the FEBEX-DP dismantling of section 49. See Fig. 2 for section location relative to the heater zone.. 5

Figure 4. Bulk bentonite XRF analyses of SiO_2 (upper) and Al_2O_3 (lower) contents for Section 49 samples as a function of distance from the gallery axis 9

Figure 5. Bulk bentonite XRF analyses of MgO (upper) and CaO (lower) contents for Section 49 samples as a function of distance from the gallery axis 10

Figure 6. Bulk bentonite XRF analyses of Na_2O (upper) and K_2O (lower) contents for Section 49 samples as a function of distance from the gallery axis 11

Figure 7. Bulk bentonite XRF analyses of Ti_2O (upper panel) and Fe_2O_3 (lower panel) content for Section 49 samples as a function of distance from the gallery axis 12

Figure 8. Thermogravimetric analysis (TGA) and differential scanning calorimetry (DSC) measurements of bentonite samples for Section 49 as a function of distance from gallery axis..... 14

Figure 9. Water content measurements of bentonite samples for Section 49 as a function of distance from gallery axis..... 15

Figure 10. XRD spectra for various positions of BM-D-49 samples in the same blocks along with d-spacings 16

Figure 11. XRD spectra for various locations of B-D-49 block samples along with d-spacings 17

Figure 12. XRD spectra for various locations of B-C-49 block samples along with d-spacings..... 17

Figure 13. XRD spectra for various locations of BG-C-49 block samples along with d-spacings..... 18

Figure 14. XRD spectra for various locations of BG-D-49 block samples along with d-spacings..... 18

Figure 15. Distribution of d-spacing (d_{001}) (Å) values with distance from the heater for air-dried and glycolated bentonite samples 19

Figure 16. Distribution of d-spacing (d_{110}) (Å) values with distance from the heater for air-dried bentonite samples. 19

Figure 17. Distribution of estimated percent swelling with distance from the heater based in d-spacing measurements on air-dried and glycolated bentonite samples 20

Figure 23. Schematic figure showing the 3D single waste package model (unstructured mesh) domain in the PFLOTRAN reactive transport simulation. 29

Figure 24. Predicted temperature profile vs. time across the multi-layered EBS for PFLOTRAN simulations in TH mode (full saturation).. 29

Figure 25. Predicted temperature profile vs. time across the multi-layered EBS for PFLOTRAN simulations in GENERAL mode (variably saturated) without reactive transport. 30

Investigation of Coupled Processes in Argillite Rock – LBNL (Part II)

Figure 1-1. Schematic illustration of coupled THM processes driven by heat released from the waste package 38

Figure 1-2. TOUGH-FLAC and TOUGH-RBSN models developed for coupled THM process analysis. 39

Figure 2-1. Schematic of linking of TOUGH2 and FLAC3D in a coupled TOUGH-FLAC simulation. 42

Figure 2-2. Numerical procedure of a linked TOUGH2 and FLAC3D simulation with subscript k signifying time step. 42

Figure 2-3. BBM constitutive model showing the yield surface in q-p-s space. 43

Figure 2-4. Pore size distribution and schematic representation of the two structural levels considered in the dual structure model 44

Figure 2-5. Volumetric strain contour and extent of failure zones related to horizontal bedding planes and rock matrix. 45

Figure 2-6. Simulated and measured permeability changes around the TSX tunnel. 47

Figure 2-7. Calculated permeability distribution for generic repository emplacement tunnel in crystalline rocks using the empirical stress-permeability relation. 48

Figure 2-8. Calculated brittle failure and permeability changes around an excavation in argillite 49

Figure 2-9. The simulation result of damage distribution at TSX experiment. 50

Figure 3-1. Coupling procedure of the TOUGH-RBSN simulator 51

Figure 3-2. Fracture mapping and discretization within an unstructured Voronoi grid 53

Figure 3-3. Transformation of the grid structure for enhanced flow through discrete fractures 54

Figure 3-4. Typical RBSN lattice element ij 55

Figure 3-5. Mohr-Coulomb fracture surface with tension cut-off. 56

Figure 3-6. Stress tensor measurement at a Voronoi cell node 57

Figure 4-1. Plan view of FE experiment setup and borehole layout. 59

Figure 4-2. Heat power applied to H1, 2 and 3 during heater start-up at the Mont Terri FE experiment. 59

Figure 4-3. TOUGH-FLAC 3D numerical grid of the FE experiment 62

Figure 4-4. Conceptual model of the evolution of moisture in the heated bentonite buffer and equations for vapor diffusion in the gas phase and for liquid Darcy flow along the gradient of liquid pressure (capillary driven) 64

Figure 4-5. Comparison of modeled and measured evolutions of temperature and relative humidity at monitoring point located in granular bentonite at H2 for over two years of monitoring data. 66

Figure 4-6. Comparison of modeled (lines) and measured (symbols) evolutions of temperature and relative humidity at monitoring point located in bentonite blocks at H2 for over two years of monitoring data. 67

Figure 4-7. Comparison of modeled (lines) and measured (symbols) evolutions of temperature and relative humidity at monitoring point located in granular bentonite at H1 for over two years of monitoring data. 68

Figure 4-8. Comparison of modeled (lines) and measured (symbols) evolutions of temperature and relative humidity at monitoring point located in bentonite blocks at H1 for over two years of monitoring data. 69

Figure 4-9. Comparison of modeled (lines) and measured (symbols) evolutions of temperature and relative humidity at monitoring point located in granular bentonite at H3 for over two years of monitoring data. 70

Figure 4-10. Comparison of modeled (lines) and measured (symbols) evolutions of temperature and relative humidity at monitoring point located in bentonite blocks at H1 for over two years of monitoring data. 71

Figure 4-11. Comparison of the actual zigzag-shape cross-section of the tunnel from the laser scan with the circular shape of tunnel used in numerical modeling. 72

Figure 4-12. Results of scoping calculation for thermal pressurization effects in the host rock for pressure monitoring points located from the tunnel perpendicular to bedding and parallel to bedding. 73

Figure 5-1. Overview of DECOVALEX-2019 Task E with steps of increasing scale. 76

Figure 5-2. Geometry of the simulation domain and heater source (green elements) is a 1/8 cylinder with 2.5cm radius. 77

Figure 5-3. Simulation results of temperature at different points. 78

Figure 5-4. Simulation results of pore pressure at different points. 79

Figure 5-5. Simulation results of displacements at point P4. 79

Figure 5-6. Simulation results of stresses at point P4 80

Figure 5-7. The schematic of the TED experiment at Bure 81

Figure 5-8. The model setup the position of heater boreholes (Heater 1201~1203), extensometer boreholes (TED 1230 and TED 1231), GED tunnel surrounded by 1m EDZ, and temperature distribution at 1509 days. 82

Table 5-3. THM boundary conditions of TED experiment modeling for Step 2. 83

Figure 5-9. Heat power used for Heater 1, 2 and 3. 83

Table 5-4. THM parameters of Step 2 used for THM simulations. 84

Figure 5-10. Temperature evolution simulated with calibrated thermal conductivities at measuring points. 85

Figure 5-11. Pore pressure evolution at Boreholes 1253,1258, and 1240. 86

Figure 5-12. The ALC experiment at Bure with various monitor boreholes and microtunnel ALC1604 that are used by modeling teams in DEOVALEX-2019, Task E 87

Figure 5-13. Geometry of the model with boundary conditions: a) Observed and simulated temperature evolution at GRD tunnel; b) Observed and simulated temperature evolution at GAN tunnel; and c) Geometry of the simulation domain and boundary conditions on each surface. 88

Figure 5-14. Mesh generation in simulated domain. 89

Figure 5-15. Simulated and observed temperature evolution at measuring points. 90

Figure 5-16. Simulated pore pressure evolution at sensor points. 91

Figure 6-1. Conceptual models of gas flow 93

Figure 6-2. Above: Cut-away diagram of the pressure vessel showing the apparatus components and instrumentation 95

Figure 6-3. Observed (a) pressure evolution and (b) outflow rate 97

Figure 6-4. Schematic drawings of gas injection location and gas flow direction for 1D gas flow test (Stage 1) and spherical gas flow test (Stage 2). 98

Figure 6-5. Observed 3D spherical gas flow test results: (a) pressure/stress evolutions and (b) inflow/outflow rates. 99

Figure 6-6. Schematic of modeling approaches employed by LBNL for modeling gas migration through clay associated with DECOVALEX-2019 Task A. 100

Figure 6-7. Conceptual model for dilatant gas flow through aggregate boundaries considered in a continuum model simulation with TOUGH-FLAC. 102

Figure 6-8. 3D TOUGH-FLAC model of cylindrical sample. 103

Table 6-1. Material parameters for TOUGH-FLAC modeling of Stage 1 experiment. 104

Figure 6-9. The concept of effective gas entry pressure used for the evaluation of the initial pressure response. 105

Figure 6-10. Relation between min effective stress and permeability used in numerical modeling. 106

Figure 6-11. 3D TOUGH-FLAC model of cylindrical sample and the results of simulations of pressure. 107

Figure 6-12. Simulated and measured gas flow rate out of the sample. 107

Figure 6-13. Simulated and measured total radial stress at load cells 1, 2 and 3. 108

Figure 6-14. Simulated and measured total axial stress at injection and back ends of the sample. 108

Figure 6-15. 2D rectangular model geometry of an MX-80 bentonite sample. 110

Figure 6-16. Comparison of simulated pressure with experimental data 113

Figure 6-17. Comparisons of simulated axial stresses and radial stresses with experimental data. 114

Figure 6-18. Comparison of simulated gas flow rate with experimental data 115

Figure 6-19. Snapshots of the mesh geometry, showing fracture patterns, and pressure contours around the breakthrough. 116

Figure 6-20. 3D Voronoi mesh generation 117

Figure 6-21. Non-uniform fracturing process development during gas injection. 118

Figure 6-22. Comparison of simulated and experimental injection pressure evolutions. 119

Figure 6-23. Comparison of simulated and experimental flow rate evolutions. 120

Figure 6-24. Comparison of simulated stress evolutions and experimental stress data. 121

Figure 7-1. SIMFIP probe currently used for the fracture stimulation experiment in the SURF underground research laboratory (fracture pressure applied by the SIMFIP will be about 40 MPa) 123

Figure 7-2. SIMFIP probe currently designed at LBNL 124

Figure 7-3. Schematic of the Mt Terri Main Fault activation experiment setting 127

Figure 7-4. Upper graph – pressure and fault displacement rate monitored during pressurization tests in the interval 40.2 m. 128

Figure 7-5. Model geometry and graph of the simulated step-by-step pressure increase into the fault 129

Figure 7-6. Influence of stress conditions and fault-related frictional and hydraulic parameters on the evolution of fault slip. 131

Figure 7-7. Graphs of the maximum slip length over maximum hydraulic length as a function of permeability enhancement 132

Figure 8-1. Schematic of coupled THM responses in a repository in the near field and at the repository scale caused by heating, thermal pressurization and potential gas generation. 137

Disposal in Argillite R&D and International Collaborations (FY18) – LANL (Part III)

Figure 1. FEBEX sampling locations of section 49. Green symbols indicate granodiorite samples and yellow symbols are bentonite locations 147

Figure 2. Bounding backfill temperature histories at the waste package surface, for in-drift emplacement in crystalline rock (2.5 W/m-K) with a compacted bentonite backfill (0.6 W/m-K) 150

Figure 3. XRD patterns of bulk samples from starting Opalinus Clay and EBS-14 and EBS-15 reaction products. 154

Figure 4. SEM images of Opalinus Clay. 155

Figure 5. Solution pH from fluid collected throughout each EBS experiment 157

Table 5. Quantitative X-Ray Diffraction (QXRD) analyses of the buffer clay (Wyoming Bentonite) the wall rock (Opalinus Clay) and product results of experiments EBS-14 to EBS-23. 161

Figure 6. XRD patterns from the ethylene glycol saturated, oriented < 2 μm fractions from original Opalinus Clay and EBS-14 reactions products showing the effects of heating Opalinus Clay to 300°C for six weeks 162

Figure 7. XRD patterns from the ethylene glycol saturated, oriented fraction from original Opalinus Clay, WY bentonite, EBS-15 Opalinus fragments, and various size fractions from EBS-15 reaction products. 163

Figure 8. XRD patterns for EBS-23 and the EBS-23 cement. The peak labels correspond to the identified minerals and unmarked peaks belong to the corundum standard. 164

Figure 10. Variation in wt. % FeO and MgO vs. SiO_2 for minerals found on the steel interface 166

Figure 11. Smectite compositions for FEBEX bentonite determined by electron microprobe. 171

Figure 12. Ternary diagrams for FEBEX bentonite plagioclase and K-feldspar. 172

Figure 14. Example of intergrown quartz (qtz) and K-Feldspar (kfs) in a smectite matrix in FEBEX bentonite sample B-C-49-10. 174

Figure 15. Example of LCS coupon image used for corrosion calculation. 185

Figure 17. Pit corrosion of low carbon steel in experiment EBS-18. 186

Figure 16. Note abundant pit corrosion in upper right region of EBS-18 (low carbon steel) sample..... 186

Figure 18. BSE image of iron metal with concentric alteration zones from EBS-15. 187

Figure 19. SEM image (plan view) of Fe-phyllosilicates (saponite and chlorite) using 304 SS as a growth substrate from both ramped (EBS-2) and isothermal, 300°C (EBS-5) heating profiles 189

Figure 20. SEM image of 304 SS cross-section showing Fe-saponite interface reaction products using steel surface as a growth substrate. 190

Figure 21. XRD patterns of the air-dried and ethylene glycol saturated corrosion products on the 304 SS plate used in the EBS-2 experiment. 191

Figure 22. SEM image (plan view) of Fe-saponite using 316 SS as a growth substrate from both ramped (EBS-3) and isothermal, 300°C (EBS-10) heating profiles. 193

Figure 23. SEM (secondary electron) image of 316 SS cross-section showing Fe-saponite/chlorite growth due to exfoliation corrosion from EBS-3. 194

Figure 24. SEM (back scatter) image of 316 SS cross-section showing Fe-saponite/chlorite growth due to exfoliation corrosion from EBS-3. 195

Figure 25. XRD patterns of the air-dried and ethylene glycol saturated interface reaction products on the 316 SS plate used in the EBS-3 experiment 195

Figure 26. SEM image (plan view) of Fe-saponite growth on low-carbon steel from the ramped (EBS-6) heating experiment. 197

Figure 27. SEM image of low-carbon steel cross-section showing Fe-saponite reaction products using steel surface as a growth substrate 198

Figure 28. XRD patterns of the air-dried and ethylene glycol saturated interface reaction products on the low-carbon steel plate used in the EBS-6 experiment. 199

Figure 29. A stylized representation of phyllosilicate mineral growth at the steel interface. 200

Progress on the Development of the Spent Fuel Degradation and Waste Package Degradation Models – ANL (Part IV)

Figure 1. Summary figure showing the context of the FMDM within the source term calculation information flow (adapted from Jerden et al., 2017a). 216

Figure 2. Schematic diagram showing the reaction scheme for the FMD model and identifying other key processes that influence in-package chemistry and radionuclide mobilization.. 217

Figure 3. Summary of results from Shoesmith, 2008 showing measured corrosion potentials for simulated spent fuel specimens with and without the fission product alloy Ru ε–phase. 218

Figure 4. Comparison of results from the updated version 4 of the FMD model to experimental results..... 223

Figure 5. Comparison of results from the updated version 4 of the FMD model to experimental results..... 224

Figure 6. Results from version 4 of the FMD model showing the degradation rate and calculated Ecorr as functions of the H_2 concentration at the spent fuel surface. 225

Figure 7. Model results using FMDM V.4 showing the fuel degradation rate as a function of time and the H_2 concentration as a function of distance from the fuel surface 226

Figure 8. Model results using steel corrosion module of the FMDM V.4 showing the calculated H_2 concentration at the fuel surface as a function of the steel corrosion rate..... 227

Figure 9. Schematic diagram of the FMD model reaction scheme highlighting the reactions that consume and produce H_2. 229

Table 3. Statistical summary of immersion-type corrosion test results compiled by Arthur, 2004 (adapted). The anaerobic carbon steel corrosion rates are from King, 2007. 231

Figure 10. Three-electrode electrochemical cell used in Argonne electrochemical experiments and an example alloy working electrode 232

Figure 11. Example data from Jerden et al., 2017(a) showing they types of results obtained from electrochemical measurements..... 233

Figure 12. SEM micrographs of the polished unreacted 4320 steel electrodes 235

Figure 13. X-ray diffraction scans of oxide corrosion phases from the potentiostatic tests on 4320 carbon steel..... 236

Appendices

Figure C-1. XRD pattern for EBS-23 and the EBS-23 cement..... 271

Figure C-2. XRD pattern from the FEBEX experiment including the FEBEX starting material, the granitic host rock and the inner ring bentonite samples. 272

Figure C-3. XRD pattern from the FEBEX experiment including the FEBEX starting material, the granitic host rock and the middle ring bentonite samples. 273

Figure C-4. XRD pattern from the FEBEX experiment including the FEBEX starting material, the granitic host rock and the outer ring bentonite samples. The peaks are labeled to their corresponding minerals and unmarked peaks belong to the corundum standard. 274

Figure E-1. Bulk bentonite XRF analyses of SiO_2 content for Section 49 samples as a function of distance from the gallery axis and particle size. 312

Figure E-2. Bulk bentonite XRF analyses of Al_2O_3 content for Section 49 samples as a function of distance from the gallery axis and particle size. 313

Figure E-3. Bulk bentonite XRF analyses of MgO contents for Section 49 samples as a function of distance from the gallery axis and particle size. 314

Figure E-4. Bulk bentonite XRF analyses of CaO contents for Section 49 samples as a function of distance from the gallery axis and particle size. 315

Figure E-5. Bulk bentonite XRF analyses of Na_2O contents for Section 49 samples as a function of distance from the gallery axis and particle size. 316

Figure E-6. Bulk bentonite XRF analyses of K_2O contents for Section 49 samples as a function of distance from the gallery axis and particle size. 317

Figure E-7. Bulk bentonite XRF analyses of Ti_2O contents for Section 49 samples as a function of distance from the gallery axis and particle size. 318

Figure E-8. Bulk bentonite XRF analyses of Fe_2O_3 contents for Section 49 samples as a function of distance from the gallery axis and particle size. 319

Figure E-9. XRD spectra (air-dried and glycolated) for various positions of BM-D-49 samples in the same blocks along with d-spacings. 320

Figure E-10. XRD spectra (air-dried and glycolated) for various positions of B-D-49 samples in the same blocks along with d-spacings. 321

Figure E-11. XRD spectra (air-dried and glycolated) for various positions of B-C-49 samples in the same blocks along with d-spacings. 322

Figure E-12. XRD spectra (air-dried and glycolated) for various positions of BG-C-49 samples in the same blocks along with d-spacings. 323

Figure E-13. XRD spectra (air-dried and glycolated) for various positions of BG-D-49 samples in the same blocks along with d-spacings 324

Figure F-1. EBS-14. Backscattered electron images of thin section. Opalinus Clay cracks filled with large wairakite (wr) crystals in voids. 326

Figure F-2. EBS-14. SEM images of smectite matrix with wairakite crystals or smectite matrix alone. 327

Figure F-3. EBS-14. SEM images of a carbonate imbedded in a smectite matrix and framboidal pyrite. 328

Figure F-4. EBS-15. Electron Microprobe backscattered images of Opalinus Clay with analcime-wairakite (an-wr). 329

Figure F-5. EBS-15. Electron microprobe backscattered images of native iron grain with zoning and outward alteration from Fe-oxide, Fe-sulfide, stilpnomelane 330

Figure F-6. EBS-15. SEM images of smectite matrix with analcime-wairakite crystals illite growth. 331

Figure F-7. EBS-15. SEM images of smectite matrix with analcime-wairakite crystals 332

Figure F-8. EBS-15. SEM images of unknown fibrous material on saponite 333

Figure F-9. EBS-17. Electron microprobe images of thin section Opalinus Clay with analcime-wairakite crystals [A, B]. 334

Figure F-10. EBS-17. SEM images of analcime-wairakite solid solution crystals 335

Figure F-11. EBS-18. SEM images of analcime-wairakite zeolite in smectite matrix 336

Figure F-12. EBS-18. Electron microprobe backscattered image of thin sections showing low carbon steel corrosion (LCS) 337

Figure F-13. EBS-19. SEM images of Fe-saponite, analcime-wairakite, with minor smectite, albite, and pentlandite crystals 338

Figure F-14. EBS-20. SEM images of chlorite sprays with analcime-wairakite solid solution zeolite 339

Figure F-15. EBS-21. SEM images of unknown Al-silicate in smectite matrix 340

Figure F-16. EBS-22. Electron Microprobe backscattered images of framboidal pyrite and Opalinus Clay fragments with replacement of fossil casts lined with calcite and carbonate crystal clusters 341

Figure F-17. EBS-22. Electron Microprobe backscattered images of secondary calcite on smectite and authigenic gypsum lath 342

Figure F-18. EBS-23. Electron Microprobe backscattered images of analcime-wairakite solid solution crystals 343

Figure F-19. EBS-23. Electron Microprobe backscattered image of calcite crystal surrounded by analcime-wairakite crystals. 344

Figure F-20. FEBEX BM-C-49-1. Electron microprobe secondary electron (SE) images of potassium feldspar/smectite mix.. 345

Figure F-21. FEBEX BM-C-49-3. Electron microprobe secondary electron (SE) images depicting clay textures. 346

Figure F-22. FEBEX B-C-49-8. Electron microprobe secondary electron (SE) images depicting clay textures and authigenic plagioclase. 347

Figure F-23. FEBEX B-C-49-10. Electron microprobe secondary electron (SE) images depicting clay textures 348

Figure F-24. FEBEX B-C-49-9. Electron microprobe BSE images. 349

Figure F-25. FEBEX B-C-49-11. Electron microprobe BSE images 350

LIST OF TABLES

International Collaboration & Disposal in Argillite R&D Activities – SNL (Part I)

Table 1. Composition of standards used for the ED-XRF calibration*. 7

Investigation of Coupled Processes in Argillite Rock – LBNL (Part II)

Table 4-1. Parameters used in the modeling of the Mont Terri FE experiment. 63

Table 5-1. Model parameters of Step 1. 77

Table 5-2. Points used for comparison of numerical results and analytical solution in for Step 1. 78

Table 5-3. THM boundary conditions of TED experiment modeling for Step 2. 83

Table 5-4. THM parameters of Step 2 used for THM simulations. 84

Table 6-1. Material parameters for TOUGH-FLAC modeling of Stage 1 experiment. 104

Table 6-2. Material parameters for TOUGH-RBSN modeling of 1D gas flow through MX-80 bentonite samples. 111

Disposal in Argillite R&D and International Collaborations (FY18) – LANL (Part III)

Table 1. Samples from Section 49 obtained from FEBEX project. Samples highlighted in green were examined for this report. 148

Table 2. Initial components and reaction conditions for EBS experiments in the presence of Opalinus Clay. All experiments include bentonite clay. 151

Table 3. Synthetic groundwater chemistry used in the Opalinus Clay experiments. 152

Table 4. Mineralogical composition of starting Opalinus Clay, Wyoming Bentonite, and reaction products from EBS-14 and EBS-15. 153

Progress on the Development of the Spent Fuel Degradation and Waste Package Degradation Models – ANL (Part IV)

Table 1. Summary of FMDM parameters and data gaps that need to be addressed in experimental work to improve the accuracy of the model 220

Table 2. Specific electrochemical parameters that are dominant in determining the rate of spent fuel degradation in the FMD model. 222

Table 3. Statistical summary of immersion-type corrosion test results compiled by Arthur, 2004 (adapted) 231

Table 4. Bentonite pore water chemistry from FEBEX bentonite water extraction tests 238

Table 5. Test matrix for electrochemical experiments. Experiments will determine corrosion rates and mechanisms using standard potentiodynamic polarization, potentiostatic holds and electrical impedance spectroscopy techniques. 239

Appendices

Table C-1. Quantitative X-Ray Diffraction (QXRD) analyses of the buffer clay (Wyoming Bentonite) the wall rock (Opalinus Clay) and product results of experiments EBS-14 to EBS-23 269

Table C-2. Quantitative X-Ray Diffraction (QXRD) analyses of product results of the FEBEX experiments 270

REVISION HISTORY

Rev0	**Draft**	**September 24, 2018**

ACRONYMS

1D, 1-D	One Dimensional
2D, 2-D	Two Dimensional
3D, 3-D	Three Dimensional
ANDRA	Agence Nationale pour la Gestion Des Déchets Radioactifs (France)
ABM	Alternative Buffer Materials
ANL	Argonne National Laboratory
BBM	Barcelona Basic Model
BGR	Bundesanstalt für Geowissenschaften und Rohstoffe (Germany)
BGS	British Geological Survey
BExM	Barcelona Expansive Model
BSE	Back-Scattered Electron
BSEI	Back-Scattered Electron Image
CDM	Continuum Damage Mechanics
CEC	Cation Exchange Capacity
CFRT	Colloid-Facilitated Radionuclide Transport
CIEMAT	Centro de Investigaciones Energéticas, Medioambientales y Tecnológicas (Spain)
CMPM	Canadian Mixed Potential Model
CNSC	Canadian Nuclear Safety Commission
COx	Callovo-Oxfordian
CT	Computerized Tomography
CTD	Closure Test Drift
DECOVALEX	DEvelopment of COupled Models and their VALidation against EXperiments
DFN	Discrete Fracture Network
DOE	Department of Energy
DOE-NE	Department of Energy, Office of Nuclear Energy
DRZ	Disturbed Rock Zone
DSC	Differential Scanning Calorimetry
DSEF	Disposal Systems Evaluation Framework
EBS	Engineered Barrier System

EDS, EDX	Energy dispersive X-ray spectroscopy
EDZ	Excavated Disturbed Zone
EMP(A), EMPA	Electron Microprobe (Analysis)
ENRESA	Empresa Nacional de Residuos Radioactivos SA
EoS or EOS	Equation of State
FBG	Fiber Bragg Gratings
FCRD	Fuel Cycle Research and Development
FCT	Fuel Cycle Technologies
FCM	Fracture Continuum Model
FIB	Focused Ion Beam
FMDM	Fuel Matrix Degradation Model
FE	Full-Scale Emplacement Experiment
FEBEX	Full-scale Engineered Barriers Experiment
FEBEX-DP	Full-scale Engineered Barriers Experiment-Dismantling Project
FEP	Features, Events, and Processes
FTG	Flow Topology Graph
FY	Fiscal Year
GDSA	Generic Disposal System Analysis
GDSA-PA	Generic Disposal System Analysis – Performance Assessment
GREET	Groundwater REcovery Experiment in Tunnel
GTS	Grimsel Test Site
GW	Gigawatt
GWd	Gigawatt days
GWd/MT	Gigawatt (thermal) - days per Metric Ton
HC	Hydrological and Chemical
HE-E	Half-Scale Heater Test (Mont Terri)
HLW	High-Level nuclear Waste
HM	Hydro Mechanical
HPC	High Performance Computing
IAEA	International Atomic Energy Association
IC	Ion Chromatography
IRSN	Institut de Radioprotection et de Sûreté Nucléaire

I-S	Illite-Smectite
JAEA	Japan Atomic Energy Agency
JNC	Japan Nuclear Cycle Development Institute
KAERI	Korea Atomic Energy Research Institute
LANL	Los Alamos National Laboratory
LBNL	Lawrence Berkeley National Laboratory
LC	Loading Collapse
LCS	Low Carbon Steel
LT	Local Thickness
LLNL	Lawrence Livermore National Laboratory
MC	Mechanical-Chemical
MT	Metric Ton
MTHM	Metric Tons Heavy Metal
Micro XR CT	Micro X-ray Computer Tomography
NAGRA	National Cooperative for the Disposal of Radioactive Waste
NBS	Natural Barrier System
NE	DOE-Nuclear Energy
NEA	Nuclear Energy Agency
NIST	National Institute of Standard and Technology
NMP	Noble Metal Particles
NS	Natural (Barrier) System
NW	Nuclear Waste
OECD	Organization for Economic Co-operation and Development
P	Pressure
PA	Performance Assessment
PNNL	Pacific Northwest National Laboratory
PWR	Pressurized Water Reactor
QXRD	Quantitative X-ray Diffraction
R&D	Research and Development
RBSN	Rigid-Body-Spring Network
REV	Representative Elementary Volume

RH	Relative Humidity
SCM	Surface complexation model
SEM	Scanning Electron Microscopy
SFWST	The Spent Fuel Waste Science and Technology
SIMFIP	Step-Rate Injection Method for Fracture *In-situ* Properties
SIT	Specific Interaction Theory
SNF	Spent Nuclear Fuel
SNL	Sandia National Laboratories
SS	Stainless Steel
SURF	Sanford Underground Research Facility
T	Temperature
t	time
TC	Thermal and Chemical
TDB	Thermodynamic Database
TEM	Transmission Electron Microscopy
TGA	Thermo-Gravimetric Analysis
TH	Thermal and Hydrological
THM	Thermal-Hydrological-Mechanical
THMC	Thermal-Hydrological-Mechanical-Chemical
TM	Thermal-Mechanical
TUL	Technical University of Liberec
UFD	Used Fuel Disposition
UFDC	Used Fuel Disposition Campaign
UOX	Uranium Oxide Fuel
UPC	Universitat Politècnica de Catalunya
URL	Underground Research Laboratory
WP	Waste Package
XRD	X-ray Diffraction
XRF	X-ray Fluorescence

International Collaboration & Disposal in Argillite R&D Activities – SNL (Part I)

1. Introduction

The DOE R&D program under the Spent Fuel Waste Science Technology (SFWST) campaign has made key progress to the advancement of modeling and experimental approaches towards the characterization of chemical and physical phenomena that could impact the long-term safety assessment of nuclear waste disposition in deep clay/shale/argillaceous rock. Clay mineral transformations (e.g., smectite-illite) and interactions with other barrier materials (metal, cement, wall rock) at elevated temperatures can impact bentonite swelling and change the phase assemblage in the clay barrier. Such changes can impact long-term bentonite barrier performance. Interactional collaboration activities such as heater tests, particularly *postmortem* sample recovery and analysis, have provided key information on the changes to engineered system (EBS) material exposed to extended periods of thermal loads. Chemical and structural analyses of bentonite material from such tests has been key to the characterization of these thermal effects on clay composition, thermal properties, sorption, and swelling. These are crucial to the evaluation of *sacrificial zones* in the EBS during the thermal period. The extent of these *sacrificial zones* appears to depend on temperature with distance from the waste package surface which can influence bentonite barrier performance and the EBS design concept. The following sections describe international collaboration efforts on the compositional and structural characterization of bentonite recovered near and far from the heater surface and the application of 3D reactive transport modeling of cement liner interactions in a flooded underground drift experiment.

One of the long-standing objectives of this campaign is the development of state-of-the-art simulation capabilities for high fidelity representation of key process models and integration with the Generic Disposal System Analysis (GDSA). This process model development makes use of high performance computing (HPC) to build a high-fidelity performance assessment (PA) computational platform to support the safety case. An application of HPC is explored in a 3D reacting transport modeling problem for a single waste package and non-isothermal heating during the thermal period.

Some of the key items in support of the safety assessment for disposal in the argillite work package covered in this report are:

• International collaboration activities with long-standing repository science programs (e.g, Underground Research Laboratory – URL experiments).

• Experimental studies on hydrothermal interactions involving natural and engineered barrier materials (clay, steel, argillite).

• Coupled Thermal-Hydrological-Mechanical-Chemical (THMC) modeling.

• Updates to the SNF fuel matrix degradation model (FMDM) and the effects of canister corrosion.

1.1 International Collaboration Activities:

International collaborations on nuclear waste disposal R&D are an integral part of the Spent Fuel Waste Science and Technology (SFWST) campaign within the DOE Fuel Cycle and Technology (FCT) program. These partnerships with international repository R&D programs provide key opportunities to participate in experiments developing laboratory/field data (underground research laboratories (URL)) of engineered barrier system (EBS) interactions (e.g., near-field) and characterization of transport phenomena in the host rock (e.g., far-field). The results of these experiments are used in the evaluation of coupled processes and their representation via state-of-the-art simulation approaches to evaluate repository performance. During the thermal heating period, increases in temperature from radionuclide decay in the spent fuel (SF) waste canisters will increase temperature in the surrounding EBS driving chemical and transport processes in the near- and far-field domains of the repository. URL heater-tests for extended periods of times (e.g., years) provide key information and data on thermal effects affecting

engineered barriers in response to temperature and water saturation levels. Groundwater interactions with cementitious barriers are also important to in-drift chemistry and EBS performance during post-closure. Descriptions of the various URL experiments for various disposal design concepts according to the host country repository program and relevance to the US program is given elsewhere (Birkholzer et al., 2016; Jové Colón et al., 2016).

This part of the report will focus on two international activities within the disposal in argillite work package: FEBEX-DP and DECOVALEX Task C. The FEBEX-DP project centers on the dismantling of heater #2 (see Fig. 1) conducted during 2015 with the goal of disassembling all the remaining sections of the FEBEX "in situ test" at the Grimsel test site (GTS) URL, Switzerland, after 18+ year of heating and collection of sensor/probe data (García-Siñeriz et al., 2016; Martinez et al., 2016). Participation in the FEBEX-DP project not only facilitates international partners to access monitoring data but also to the samples collected for *postmortem* characterization of barrier materials obtained during heater dismantling. Birkholzer et al. (2017) describes previous work on bentonite-cement interfaces for FEBEX-DP epoxied overcored samples using micro-X-ray fluorescence (μ-XRF) and Multi-SEM (mSEM) scanning probe methods. The DECOVALEX-2019 Task C involves collaboration with the GREET (Groundwater REcovery Experiment in Tunnel) at the Mizunami URL, Japan, which targets the development of monitoring methodologies of groundwater in granitic rock with applications to THMC simulations (Iwatsuki et al., 2005; Iwatsuki et al., 2015). Some of the goals of GREET is to conduct a facility-scale geochemical characterization study of short- and long-term effects of tunnel excavation activities, impacts on groundwater flow and transport, and influences on groundwater chemistry (Iwatsuki et al., 2015). The data obtained from these URL activities is then used in the development and evaluation of THC models to support post-closure safety and performance assessments of the repository environment.

The main goals of this report section in each of the international activities are:

- FEBEX-DP:
    - Analysis of a FEBEX-DP bentonite samples from Section 49 using X-ray Fluorescence (XRF), X-ray diffraction (XRD), and thermogravimetric analysis (TGA/DSC) analytical techniques. These analytical approaches are conducted on samples collected as a function of distance from the gallery center or heater surface.
- DECOVALEX Task C:
    - 3D Reactive transport modeling of the closure test drift (CTD) focusing on shotcrete – ground water interactions of the cement liner in the water-filled tunnel. This simulation effort is part of an inter-comparison exercise between different modeling teams (SNL, JAEA, TUL) participating in this task.

2. FEBEX-DP: X-ray Fluorescence (XRF) and X-ray diffraction (XRD) Studies of Bentonite from Section 49

The FEBEX-DP dismantling of heater #2 (see Fig. 1) was performed during 2015 involving the careful retrieval of barrier material samples from the remaining sections of the FEBEX "in situ test" after 18+ year of heating (García-Siñeriz et al., 2016; Martinez et al., 2016). The disassembling activity involved sampling of barrier bentonite, steel liner, sensors, embedded metallic components (e.g., metal coupons), and near-field sections with tracer components. The FEBEX bentonite is composed of ~93% smectite with 2% quartz, 3% plagioclase, and about 2% cristobalite plus minor accessory phases such as calcite and K-feldspar (Huertas et al., 2000; Missana and García-Gutiérrez, 2007). The focus of this study is to conduct XRF, XRD, and TGA/DSC studies on FEBEX-DP samples from section 49 corresponding to

spatial domains near and far from the surface of heater #2 (see Fig. 2 for sample locations). Fig. 3 shows the radial locations of samples collected in Section 49 considered in this study.

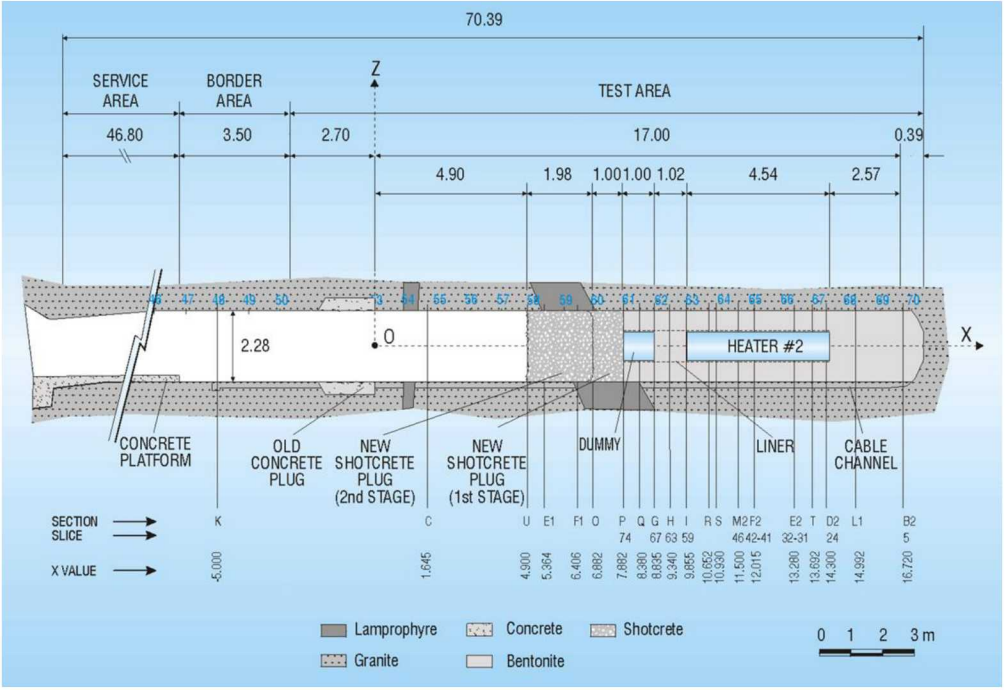


Figure 1. Schematic layout of the FEBEX "in-situ" field test after the first partial dismantling showing the configuration of heater #2 at the GTS URL (García-Siñeriz et al., 2016).

Previous studies (Birkholzer al., 2017) on Section 49 were centered on SEM/EDS characterization of samples closest to the corroded carbon steel mesh surrounding the heater. These studies revealed sparse Al-Si grains high in Fe with some K enrichment in certain cases. These grains are immersed in the clay matrix and can be identified by their different texture and morphology. The extent of the corroded region into the bentonite is rather limited which might explain the relatively low level of Fe alteration into the bentonite, particularly in the hotter zones of the heater. The main objective of this characterization study is to (1) identify bulk compositional and structural (also mineralogical) variations (XRF and XRD, respectively) of bulk bentonite samples near and far from the heater surface, (2) similarly, conduct TGA/DSC thermal analyses of these samples, and (3) compare results with those obtained by other teams for other sampled sections of the bentonite barrier as part of the FEBEX-DP project.

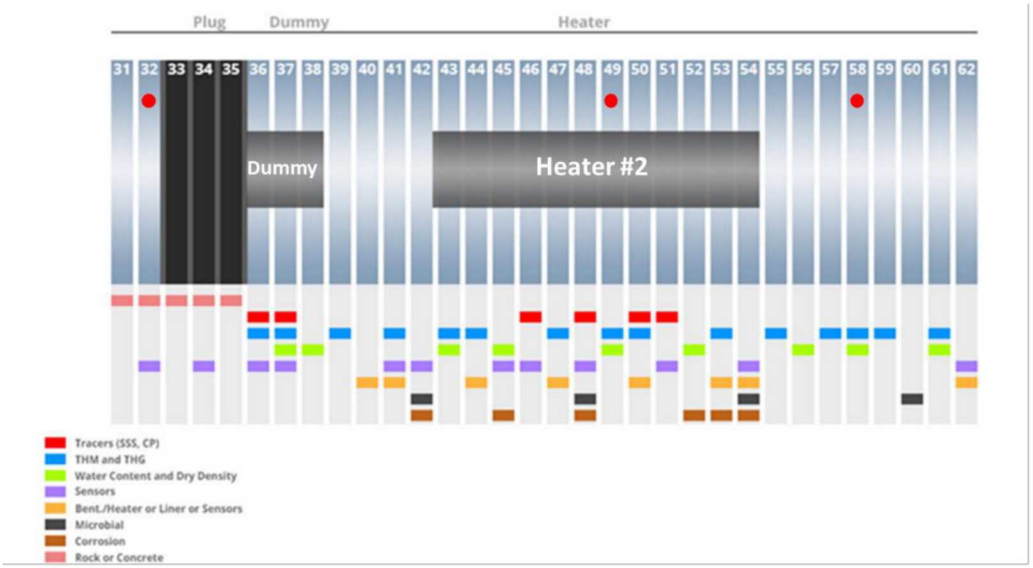


Figure 2. Schematic configuration of sampling zones (indicated by vertical light blue bars) for the FEBEX-DP project. Filled red circles indicate zones for samples obtained by Sandia National Laboratories (SNL). Source: FEBEX-DP website (members area): http://www.grimsel.com/gts-phase-vi/febex-dp/febex-dp-introduction.

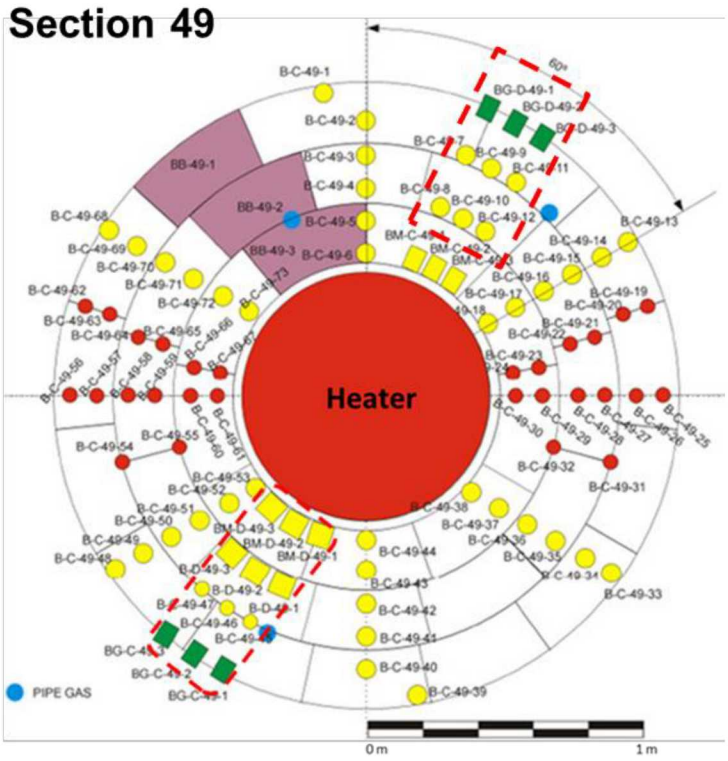


Figure 3. Schematic diagram of sampling locations for the FEBEX-DP dismantling of section 49. See Fig. 2 for section location relative to the heater zone. The red-dashed line delineates the locations of samples analyzed in this study (source: FEBEX-DP website (members area): http://www.grimsel.com/gts-phase-vi/febex-dp/febex-dp-introduction.). Note: samples BG-C-49 (1, 2, 3) were not analyzed with XRF in the current study. These analyses are planned as part of future work on these samples.

3. Methodology: XRF, XRD, and Thermal Analyses (TGA/DSC)

XRF and TGA Study

Thermal loads during the post-closure period can drive barrier alteration due to enhanced interactions with fluids, induced phase transformation, and changes in bentonite under unsaturated conditions. Jove Colon (2016) describes the 2D-3D characterization of microcracks in FEBEX-DP shotcrete-bentonite overcore outlining the importance of desiccation/shrinkage processes in bentonite and the nature of pores/voids in shotcrete. Mineral dissolution and precipitation along with transport which has been a topic of investigation particularly in the assessment of engineered barrier alteration in reactive-transport models (Marty et al., 2015; Wilson et al., 2015; Xie et al., 2015). An example is Fe-bentonite interactions which leading to mineral phase changes that could impact swelling capacity in bentonite through alteration to a non-swelling Fe-bearing phase. Also, cation exchange in the bentonite clay could also be impacted through temperature-induced drying and wetting causing variations in the cation exchange capacity (CEC) (Muurinen, 2011). Cation exchange experiments reported by Villar et al. (2017) show that FEBEX-DP bentonite samples collected from sections closest to the heater exhibit higher concentrations of exchangeable Mg and Ca and low concentrations of exchangeable Na. Moreover, aqueous extracts for bentonite samples collected in sections close to the heater exhibited higher aqueous concentrations of Mg, Ca, Na, and Cl relative to those sampled farther away from the heater. It should be noted that the aqueous extract process is influenced by ion exchange and solid phase dissolution (Villar et al., 2017). These relatively strong changes in the observed aqueous concentration behavior from these tests indicate that bentonites close to the heater were affected by thermal loads causing changes in the bentonite clay mineral and therefore their interaction with fluids. It would then be expected that such effects on bentonite sorption behavior could be manifested in the bulk clay composition.

The FEBEX-DP effort has documented bulk XRF bentonite compositional analyses with distance from the heater for various sampled sections of the EBS (Villar et al., 2017). Such compositional profiles as a function of sample radial location could provide key information of clay chemical variability, plausibly in response to thermal perturbations. Samples collected in section 49 experienced the hottest part of the heater given its location close to the center of the (cylindrical) heater longitudinal axis. XRF data of these will be analyzed and compared to data reported in Villar et al. (2017) for samples collected in other sections surrounding the heater.

Sample Preparation

Samples were prepared and analyzed as <150 μm, <75 μm, and <2μm fractions. The <150 μm and >75 μm fractions were prepared by grinding and sieving through a final sieve of 100 mesh and 200 mesh, respectively. The <2μm fraction samples were prepared by a sedimentation method as described by McKay (1992). The <75 μm fraction was transferred to a 1 L graduated cylinder. The cylinder was filled with Mili-Q H_2O (Barnstead NANOpure Diamond, resistivity of 18.2 MΩ*cm, 0.2 μm filtered and UV irradiated) up to the 30 cm mark. The top was capped and the cylinder was inverted several times to ensure adequate mixing. The contents were allowed to settle for 24 hours. After 24 hours, the remaining suspended clay was decanted into centrifuge bottles (250 mL) and centrifuged at 3000 rpm for 20 minutes. The collected liquid was decanted again and the solids were combined and place in the oven to dry at 60°C for 48+ hours.

XRF and TGA/DSC Analyses

Samples were loaded into an XRF sample cup (31 mm by 23.1 mm, double open-ended cup, Chemplex Industries, Inc., Palm City, FL) equipped with microporous film (25 μm thick, Chemplex Industries, Inc.) and analyzed with an Quant'X ARL Energy Dispersive (ED)-XRF (ThermoFisher Scientific, Waltham, MA). A method file was prepared in the Wintrace 7.2 software. In the method, the peak profiles were loaded and the analysis conditions were selected. These conditions consisted of low Z_a (4 kV, no filter), low Z_b (8 kV, cellulose filter), low Z_c (12 kV, aluminum filter), mid Z_a (16 kV, thin palladium filter), and high Z_b (50 kV, thick copper filter). Each condition was run under vacuum for 500 second live time, with an average of 50% detector dead time. A calibration was performed using fundamental parameters method and XML composition calculation. The standards used for the calibration were SARM 1, SARM 3, SARM 4, SARM 5, SARM 6 and CAMET SY-2, CANMET SY-3, and CANMET MRG-1, the composition of the major elements in each standard are shown in Table 1. Following the calibration, the bentonite samples were analyzed in triplicate and the percent composition was calculated as an average of the triplicate analyses. The water content was estimated from data obtained from thermogravimetric analysis (TGA), and the carbon content was estimated by the mass difference. The latter is just an estimate and more accurate methods are required to determine carbon in this samples.

Table 1. Composition of standards used for the ED-XRF calibration*.

	SARM-1	SARM-3	SARM-4	SARM-5	SARM-6	CANMET Sy-2	CANMET S-3	CANMET MRG-1
SiO_2	75.70 %	52.40 %	52.64 %	51.10 %	38.96 %	60.07 %	59.71 %	39.22 %
Al_2O_3	12.08 %	13.64 %	16.50 %	4.18 %	0.3 %	12.15 %	11.70%	8.51%
Total Fe	2.00 %	9.9 %	8.97 %	12.70 %	17.00 %	6.32 %	6.47 %	17.93 %
CaO	0.76 %	3.22 %	11.50 %	2.66 %	0.28 %	2.66%	2.63 %	13.49 %
Na_2O	3.36 %	8.37 %	2.46 %	0.37 %	0.04 %	8.03 %	8.30 %	14.68 %
K_2O	4.99 %	5.51 %	0.25 %	0.09 %	0.01 %	4.37 %	4.17 %	0.72 %
F	0.42 %	0.44 %	-	-	-	-	0.02 %	0.01 %
H_2O^+	0.49 %	2.31 %	0.33 %	0.26 %	0.30%	4.52 %	4.20 %	0.18 %
MgO	0.06 %	0.28 %	7.50 %	25.33 %	43.51 %	3.61 %	3.61 %	8.61 %
TiO_2	540 ppm	-	-	0.20 %	-	0.49 %	0.36 %	1.04 %
S	-	650 ppm	-	-	-	-	-	-
P_2O_5	-	-	-	90 ppm	40 ppm	0.03 %	0.04%	-

* Units in weight percent unless noted.

Thermal gravimetric analysis (TGA) and differential scanning calorimetry (DSC) analysis were conducted on all <150 μm and <2 μm bentonite fractions. The <75 μum fraction was not analyzed as it was assumed that very little changes would occur following additional sieving from 150 μm to 75 μm particle sizes. The analyses were performed using a Thermal Analyst SDT Q6000 instrument. The furnace chamber was purged with a 100 mL/min flow of ultra-pure Argon (Ar). An alumina crucible was tarred and filled with roughly 20-40 mg of bentonite. After loading the furnace with the sample, the analysis procedure consisted of (1) an isothermal step for 20 minutes at room temperature followed by (2) a ramped temperature stepping of 10°C/min from 20 to 1100 °C. The water content was estimated by the total weight loss.

XRD Methodology

X-ray diffraction (XRD) analyses were conducted on the suite of FEBEX-DP bentonite clay samples analyzed by XRF and TGA/DSC. The focus was to characterize mineral types present in the bentonite matrix and quantify d-spacings (basal d_{001}) of the smectite component. A full matrix of dried and glycol saturated samples varying in distance from the gallery axis were examined.

The powder diffraction data was collected using a Bruker D2 Phaser benchtop diffractometer with a CuKα (1.54 Å) X-ray wavelength. The analysis was conducted in a 2-theta range of 3 -70° with 0.2 s time per step with a total of 2256 steps. This resulted in XRD runs that were ~8.5 minutes in duration. Silicon wafers were chosen as the sample holders for the oriented clay mounts as it provides very low background interference and were optimal for making oriented clay slurry mounts. A desiccator was adapted into a glycolation chamber for the purposes of the project by filling the desiccator with ethylene glycol, then heating the entire desiccator. The heat caused the ethylene glycol to vaporize and create a glycol vapor saturated environment within the desiccator.

Sample preparation consisted first of crushing the clay using a mortar and pestle into small particle sizes to achieve a "powder like" consistency. XRD analysis of dried clay sample consisted of adding ~0.1 g of clay to a 25 mL scintillation vial. 1 mL of a 70-30% water-ethanol mixture was added to the scintillation vial to have a mass/liquid ratio of 0.1. The ethanol was added to the samples to decrease the cracking behavior of the oriented clay samples upon drying. The suspended clay was hand shaken vigorously until clay was sufficiently suspended. Then using a 1000 µL micropipette the slurry was pipetted in a circular motion onto the zero-background silicon wafer. The wafer was then placed in the convection oven between 60-70°C and allowed to dry. After the sample had completely dried, the wafer was placed in the Bruker sample holder to perform the XRD analysis. After completion of XRD analysis of the dried samples, this bentonite material was then placed into a desiccator over a pool of ethylene glycol. The desiccator was then placed in the oven heated at 60°C and left for 24 hours to ensure glycol saturation of the bentonite samples. The following day the sample was removed from the desiccator and the XRD analysis was conducted immediately to ensure the bentonite remained glycol saturated.

4. Results and Discussion: FEBEX-DP Section 49

XRF Analyses

Figures 4 to 7 summarize all the collected XRF elemental data along with data reported by Villar et al. (2017). For clarity, Figs. E-1 through E-8 in Appendix E show the same data as in Figs. 4 through 7 but plotted separately as a function of distance from gallery center for each size fraction. The analyzed oxides are SiO_2, Al_2O_3, MgO, CaO, Na_2O, K_2O, TiO_2, and Fe_2O_3. As shown in Fig. 4, SiO_2 content falls within the ranges of data reported by Villar et al. (2017) but tending towards lower concentration bounds below reference values for FEBEX bentonite. Similarly, Al_2O_3 content mainly falls within the range of the lower bounding data for FEBEX reference values with no apparent correlation with distance from the gallery center.

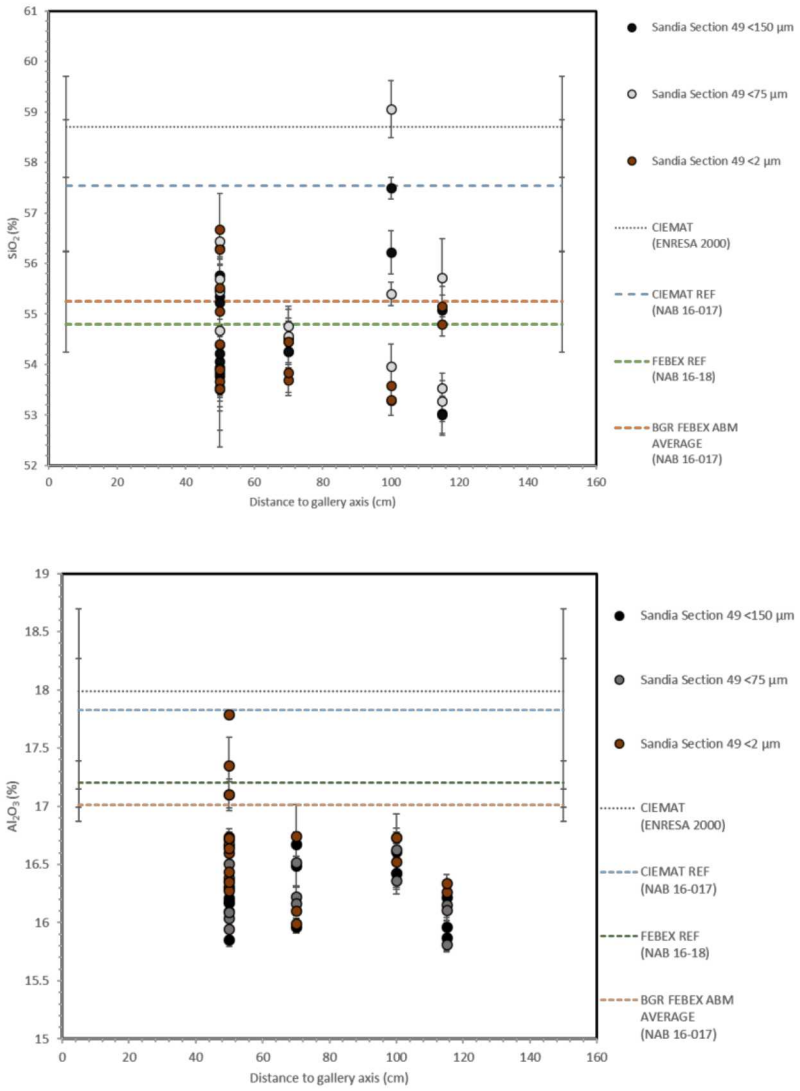


Figure 4. Bulk bentonite XRF analyses of SiO2 (upper) and Al2O3 (lower) contents for Section 49 samples as a function of distance from the gallery axis. Filled symbols denote analyses conducted in this study for size fractions of <150, <75, and <2 microns. Horizontal dashed-lines delineate the range of FEBEX bentonite compositions including reference values by different groups (Villar et al. 2017).

Fig. 5 shows a comparison of MgO and CaO contents between Section 49 samples in this study and analyses from other sections reported by Villar et al. (2017). Notice that MgO content increases with decreasing distance from the heater or towards the heater surface (~50 cm from the gallery center). The same trend is observed for other samples surrounding the heater (S45, S48, S50, S53), particularly for sample S48 which like S49 experienced the hottest location of the heater (Villar et al., 2017). Similar observations were made by Villar et al. (2017) for exchangeable Mg where its largest concentration was observed in samples close to the heater. Also, most of our MgO content data lies above the FEBEX reference values. The Mg enrichment in bentonite close to the heater could potentially affect the clay swelling and sorption behavior. CaO content data doesn't show a clear correlation with distance from the gallery center. However, Villar et al. (2017) noticed a slight overall enrichment of CaO content towards the gallery walls. Overall, measured CaO contents are spread above and below the bounds for the FEBEX reference values.

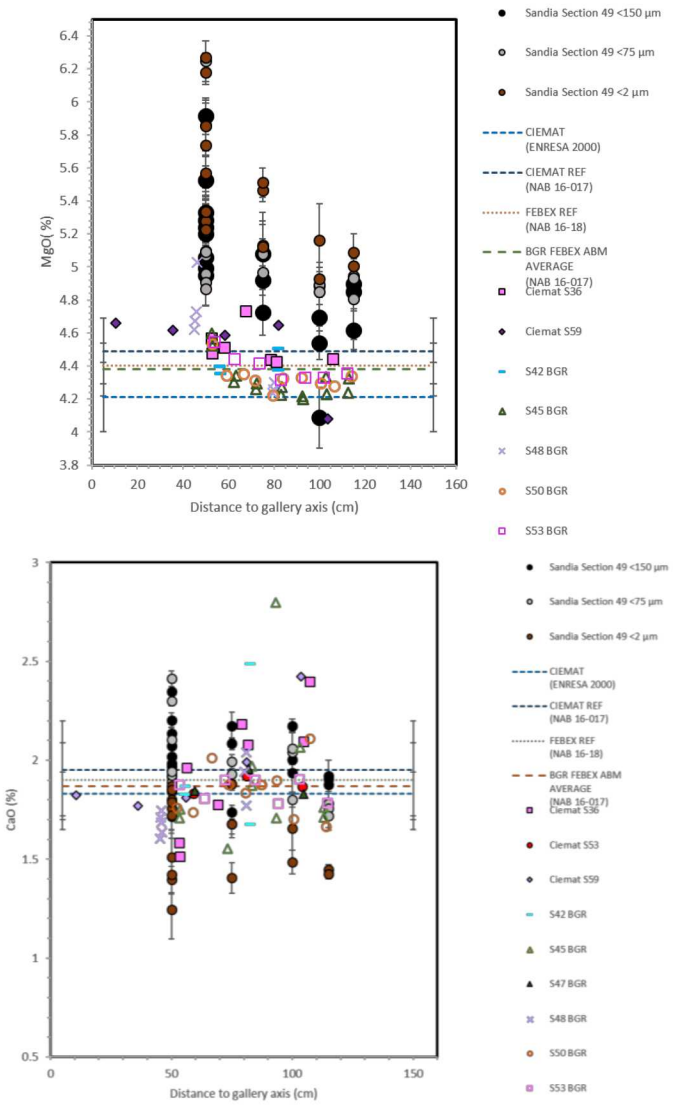


Figure 5. Bulk bentonite XRF analyses of MgO (upper) and CaO (lower) contents for Section 49 samples as a function of distance from the gallery axis. Filled circles denote analyses conducted in this study for size fractions of <150, <75, and <2 microns. Horizontal dashed-lines delineate the range of FEBEX bentonite compositions including reference values by different groups (Villar et al. 2017).

Fig. 6 shows a comparison of Na_2O and K_2O contents between Section 49 samples in this study and analyses from other sections reported by Villar et al. (2017). As in CaO, our data for Na_2O content doesn't show a clear correlation with distance from the gallery center. Limitations in Na detection in the XRF method of our study produces data with large uncertainties and therefore resolving apparent data trends with distance from the gallery center is difficult. Na_2O content reported by Villar et al. (2017) decreases towards the surface of the heater as shown in Fig. 6. Such trend is opposite to that of MgO probably suggesting ion exchange enhanced with increasing temperatures. Overall, K_2O content tends to decrease towards the heater with values within and below the ranges of the FEBEX reference data bounds.

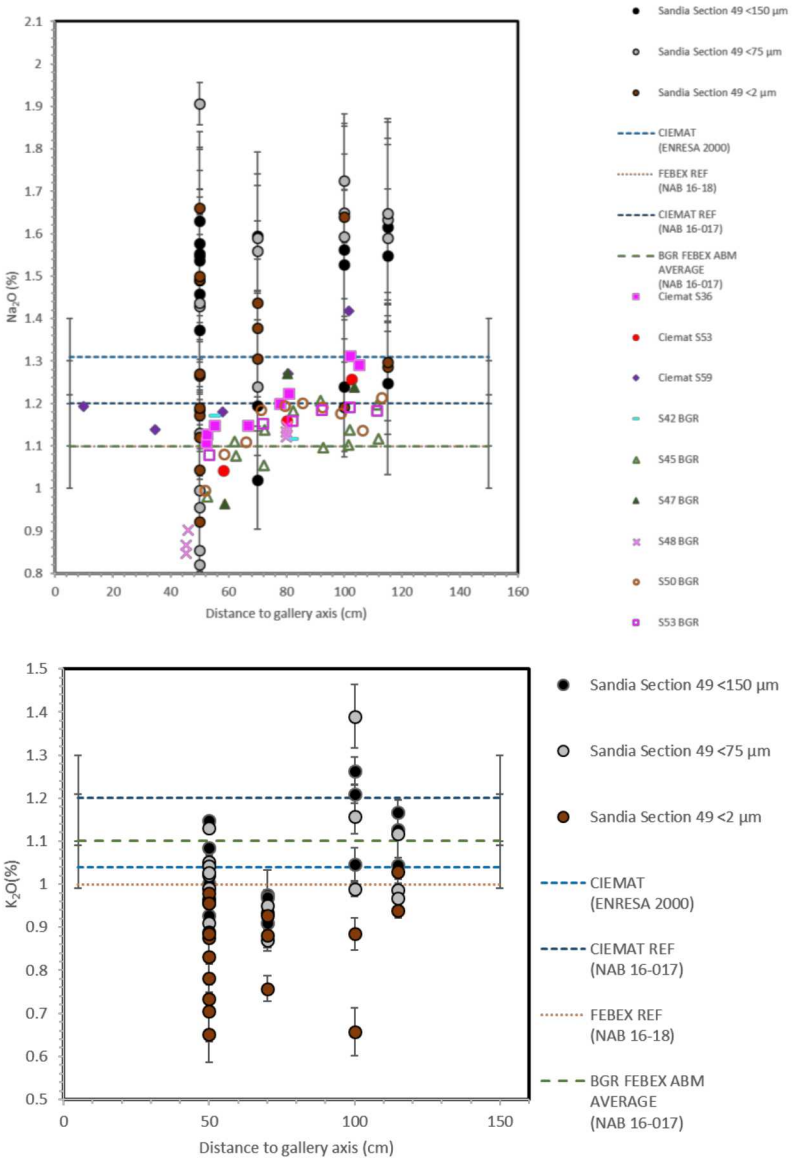


Figure 6. Bulk bentonite XRF analyses of Na_2O (upper) and K_2O (lower) contents for Section 49 samples as a function of distance from the gallery axis. Filled circles denote analyses conducted in this study for size fractions of <150, <75, and <2 microns. Horizontal dashed-lines delineate the range of FEBEX bentonite compositions including reference values by different groups (Villar et al. 2017).

The <2 microns fraction data show this decreasing K_2O content trend towards the heater and bounds data below the FEBEX reference values. The reason for the lower values in this finer fraction is probably due to the presence of K-bearing minerals (e.g., feldspar) separated during the settling procedure. Similarly, Fig. 7 shows the distribution of TiO_2 and Fe_2O_3 content generally decreasing towards the heater, particularly for the finer fraction.

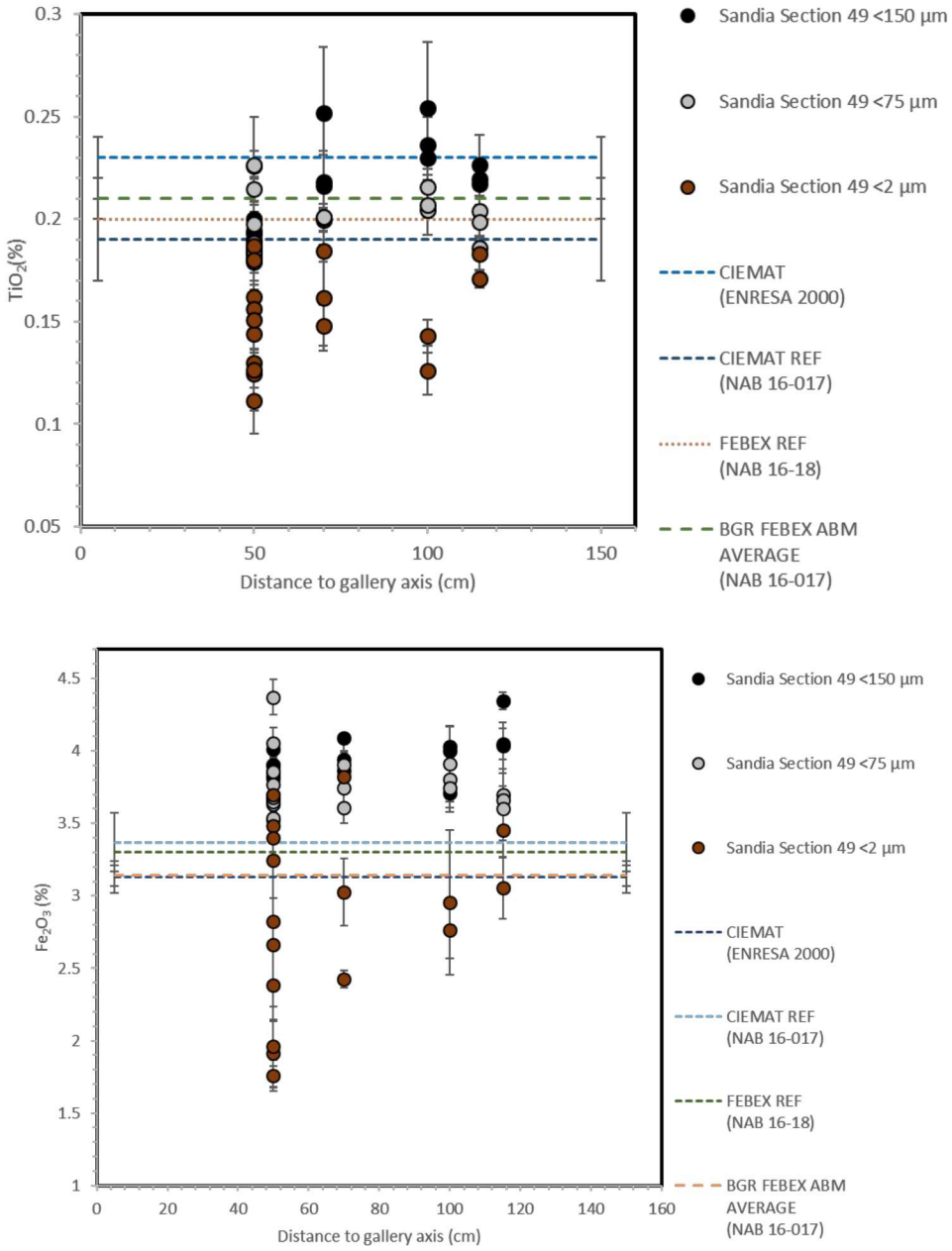


Figure 7. Bulk bentonite XRF analyses of Ti2O (upper panel) and Fe2O3 (lower panel) content for Section 49 samples as a function of distance from the gallery axis. Filled circles denote analyses conducted in this study for size fractions of <150, <75, and <2 microns. Horizontal dashed-lines delineate the range of FEBEX bentonite compositions including reference values by different groups (Villar et al. 2017).

TGA/DSC Analyses

TGA and DSC data are summarized in Fig. 8 for all the considered samples as a function of distance from the gallery axis. Fig. 9 shows the retrieved water content as a function of distance from gallery axis. The outlier sample with lowest water content (B-C-49-1; uppermost curve in the TGA mass loss and smallest water content value in Figs. 8 and 9, respectively) was located next to a gas pipe within the bentonite barrier. This may explain the much lower water content relative to the other samples.

Overall, the water content data retrieved from TGA (Figs. 8 and 9) show a spread of values with no clear dependency with distance from gallery axis or the heater surface located at ~50 cm from the gallery axis. Water content data reported by Villar et al. (2017) clearly shows an increasing trend with distance from the gallery axis. However, such a trend was not observed from our TGA data possibly due to differences in the adopted methodologies to quantify water content. In the TGA method the bentonite sample is exposed to 110°C for 10 minutes. Water content data reported in Villar et al. (2017) was obtained through heating the sample at 105-110 °C from 2 to 7 days.

DSC data shows a strong endothermic peak around 100-110 °C but also reaching temperatures of 120-125 °C in some samples. This peak corresponds to dehydration of adsorbed water at clay hydration sites (Tajeddine et al., 2015; Vieillard et al., 2016). The DSC analyses reported in Villar et al. (2017) on FEBEX bentonite samples from Section 47 have a similar profile with temperature but with slightly higher temperature values (~136°C) for this first endothermic peak. The second endothermic peak around 650°C is consistent with the range of dehydroxylation temperatures observed for smectite clays (Tajeddine et al., 2015; Vieillard et al., 2016; Villar et al. 2017).

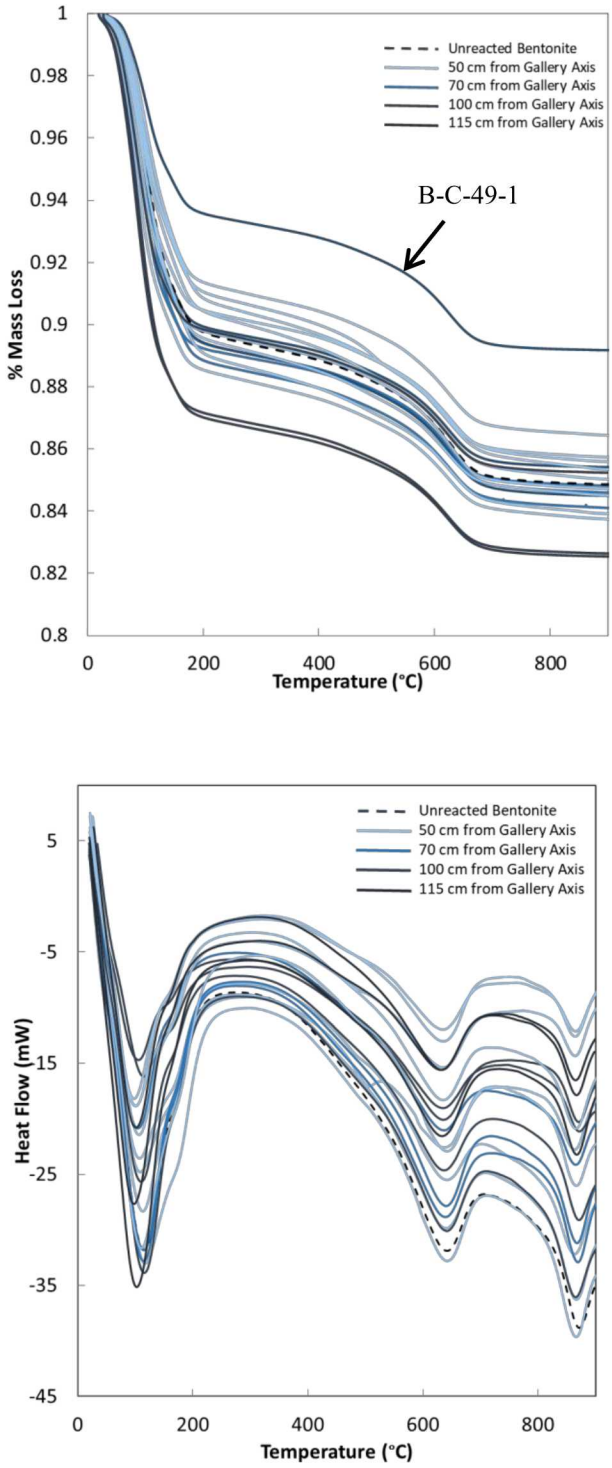


Figure 8. Thermogravimetric analysis (TGA) and differential scanning calorimetry (DSC) measurements of bentonite samples for Section 49 as a function of distance from gallery axis. Dashed-line represents the unreacted FEBEX bentonite. Outlier (uppermost) curve in TGA upper figure represents sample B-C-49-1 located next to a gas pipe within the bentonite barrier (see schematic Fig. 3 for location).

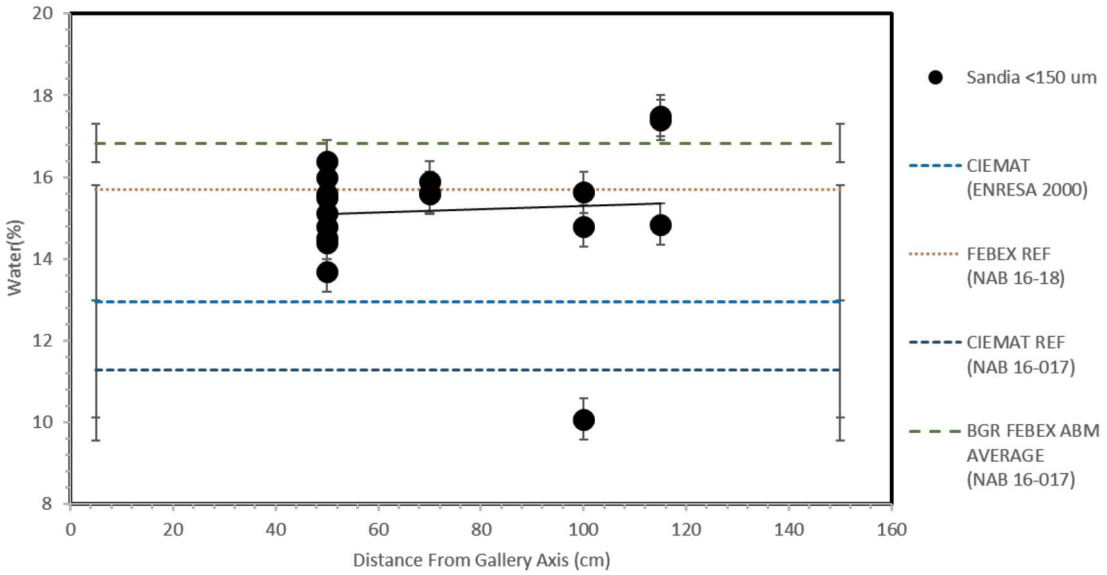


Figure 9. Water content measurements of bentonite samples for Section 49 as a function of distance from gallery axis. Solid line represents the overall trend of the data (see text). Horizontal dashed-lines delineate water content measurements of FEBEX bentonite samples from other studies shown here for comparison. Outlier (lowermost) value represents sample B-C-49-1 located next to a gas pipe within the bentonite barrier (see schematic Fig. 3 for location).

Not considering the outlier, Fig. 9 shows a rather weak tendency towards higher water content with distance from the heater surface. In general, the TGA and DSC curves have a qualitative similar form when compared to the thermal studies by Tajeddine et al. (2015) and Vieillard et al. (2016) on MX-80 montmorillonite, and by Villar et al. (2017) on FEBEX bentonite from other FEBEX-DP sampled sections. Work is planned to conduct further analysis and comparisons between the FEBEX bentonite data sets and the Tajeddine et al. (2015), and Vieillard et al. (2016) studies on MX-80 montmorillonite to evaluate differences in thermal properties between the two bentonite clay compositions.

XRD Data

Figures 10 through 14 show the representative XRD spectra collected for glycolated samples from Section 49. The spectra are presented as stacked plots with X-ray intensity (Y-axis; arbitrary units) vs. 2θ. XRD spectra for air-dried samples along with its corresponding glycolated profile are given in Figs. A-9 to A-13 in Appendix A. Quantification of bentonite mineralogical composition through XRD was not part of the current study but it is planned for future work. This compositional information can be found in Villar et al. (2017) where a divalent smectite is the main component (~92%) of the FEBEX bentonite. XRD peaks for quartz and feldspar were resolved mainly in the air-dried bentonite samples having similar 2θ ranges as reported in Villar et al. (2017). Calcite was not observed in our samples. Also, no definite evidence illite occurrence was found in these samples. XRD peaks for accessory minerals in the bentonite like quartz and feldspar were not observed in some samples, maybe indicative of the variability in their mineralogical content even within the same block or because of limited detection with the XRD method.

In general, comparisons between glycolated bentonite spectra from this study and those from Villar et al. (2017) on FEBEX-DP bentonite samples from other sections show close similarities in the peaks for smectite $d_{00\ell}$ (d_{001}, d_{002}, d_{003}, d_{004}, d_{005}) reflections. The only exception is the d_{006} peak which was not observed in our samples but it was present in the spectra reported for samples BB-53-4 by Villar et al. (2017). The range of smectite $d_{00\ell}$ values are consistent with those reported by Villar et al. (2017). The

strong basal (d_{001}) reflections around 13-14 Å is characteristic of Mg-bearing montmorillonites whereas its value of around 16.4 Å for the glycolated samples suggest a state of nearly full interlayer expansion (Teich-McGoldrick et al., 2015). Fig. 15 summarizes the distribution of d_{001} values with distance from the heater for air-dried and glycolated samples. As shown in this figure, there is no clear trend or apparent correlation between d_{001} values and sample radial location with respect to distance from the heater. Values for smectite d_{001} basal reflections are affected by the its hydration state and the interlayer cation. However, d_{110} reflections are representative of the smectite structure and are unaffected by interlayer hydration (Grim, 1968). These peaks were resolved in our air-dried samples and their distribution with distance from the heater is shown in Fig. 16. Like the d_{001} distribution in Fig. 15, there is no clear trend with distance from the heater except for the apparent reduced variability in these values for samples closest to the heater.

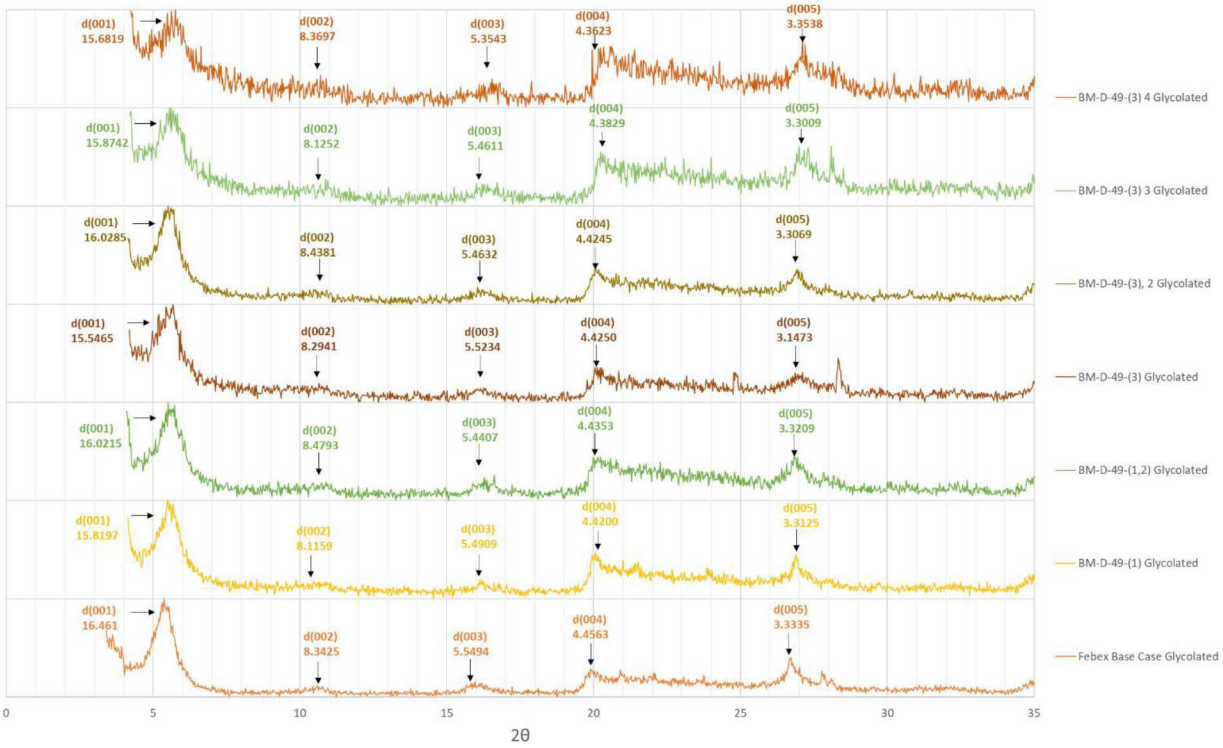


Figure 10. XRD spectra for various positions of BM-D-49 samples in the same blocks along with d-spacings (see schematic Fig. 3 for sample locations). XRD spectrum of FEBEX base case or reference material is shown at the bottom for comparison. These samples are closest to the heater.

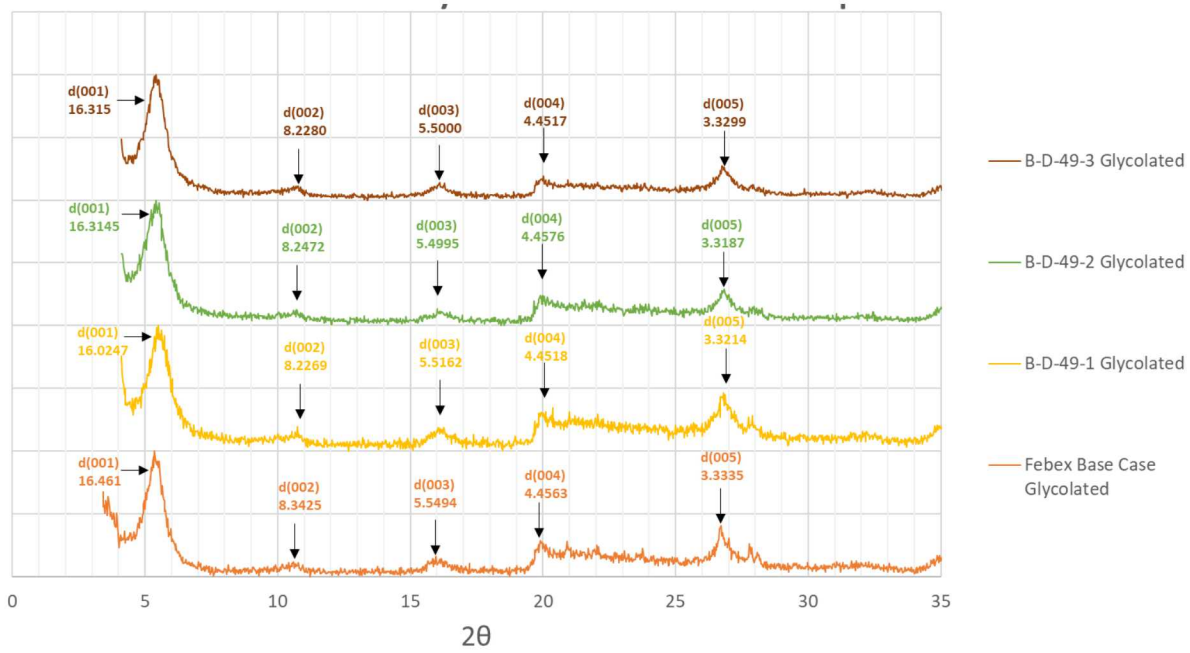


Figure 11. XRD spectra for various locations of B-D-49 block samples along with d-spacings (see schematic Fig. 3 for sample locations). XRD spectrum of FEBEX base case or reference material is shown at the bottom for comparison.

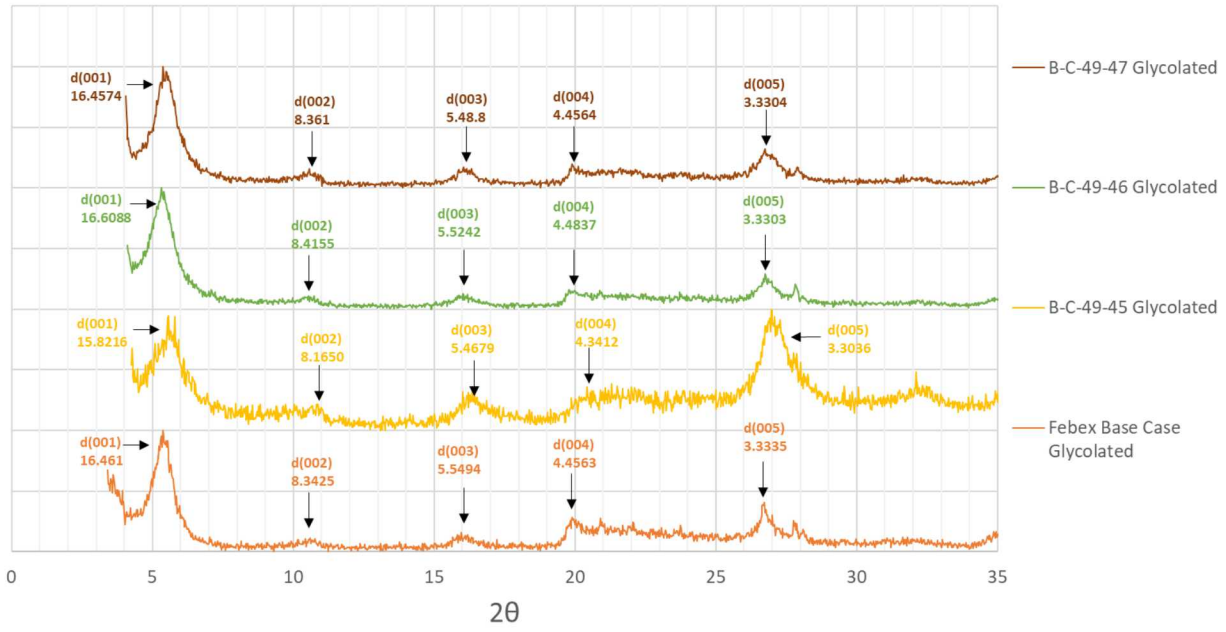


Figure 12. XRD spectra for various locations of B-C-49 block samples along with d-spacings (see schematic Fig. 3 for sample locations). XRD spectrum of FEBEX base case or reference material is shown at the bottom for comparison.

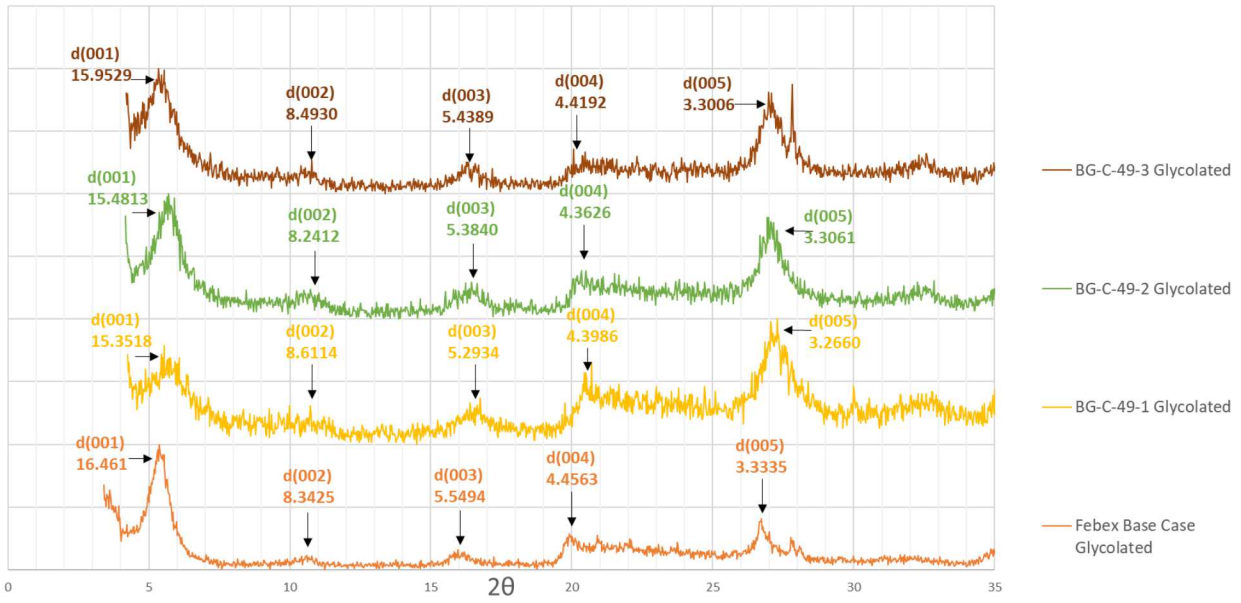


Figure 13. XRD spectra for various locations of BG-C-49 block samples along with d-spacings (see schematic Fig. 3 for sample locations). XRD spectrum of FEBEX base case or reference material is shown at the bottom for comparison. These are the most distal bentonite samples from the heater surface.

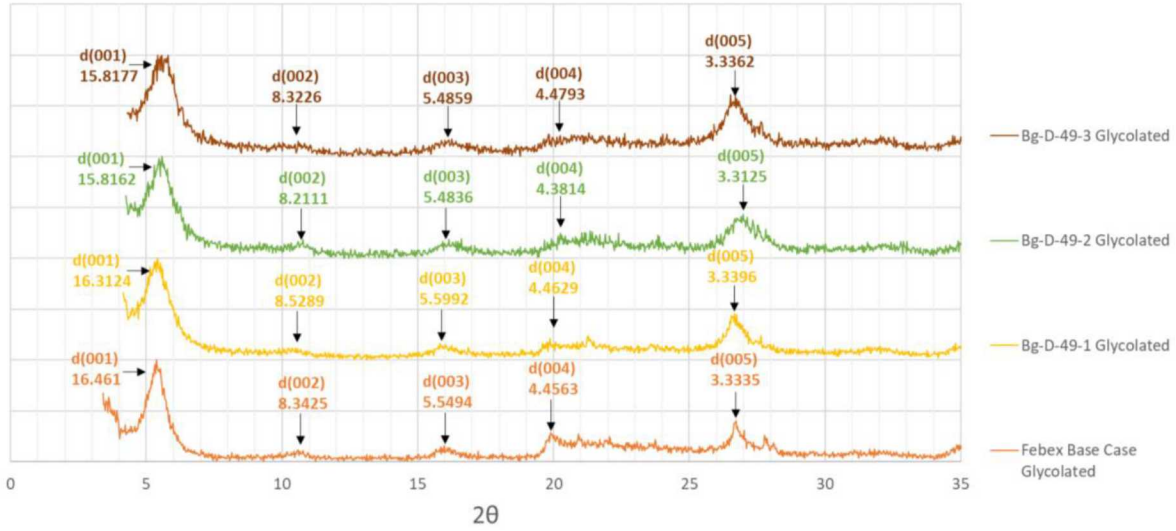


Figure 14. XRD spectra for various locations of BG-D-49 block samples along with d-spacings (see schematic Fig. 3 for sample locations). XRD spectrum of FEBEX base case or reference material is shown at the bottom for comparison. These are the most distal bentonite samples from the heater surface.

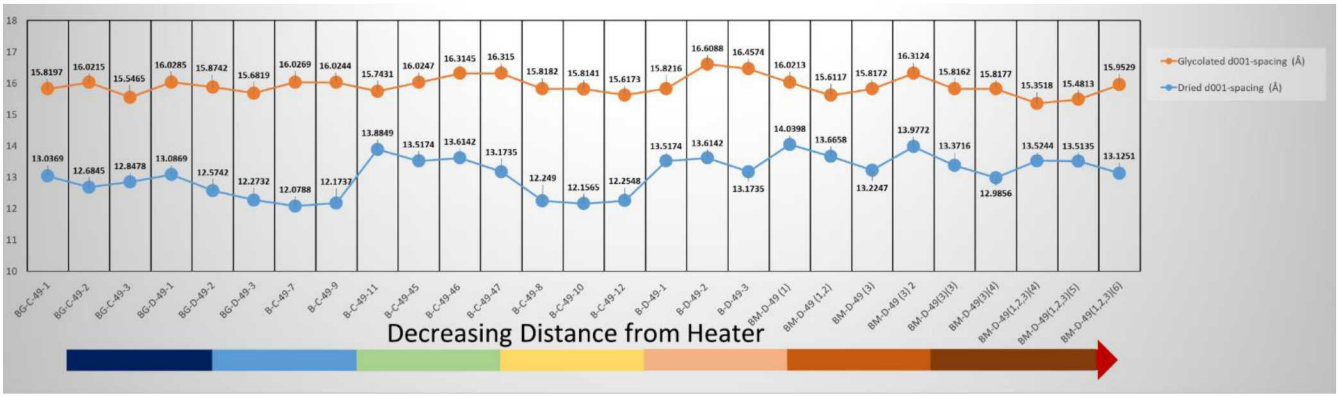


Figure 15. Distribution of d-spacing (d_{001}) (Å) values with distance from the heater for air-dried and glycolated bentonite samples (see schematic Fig. 3 for sample locations).

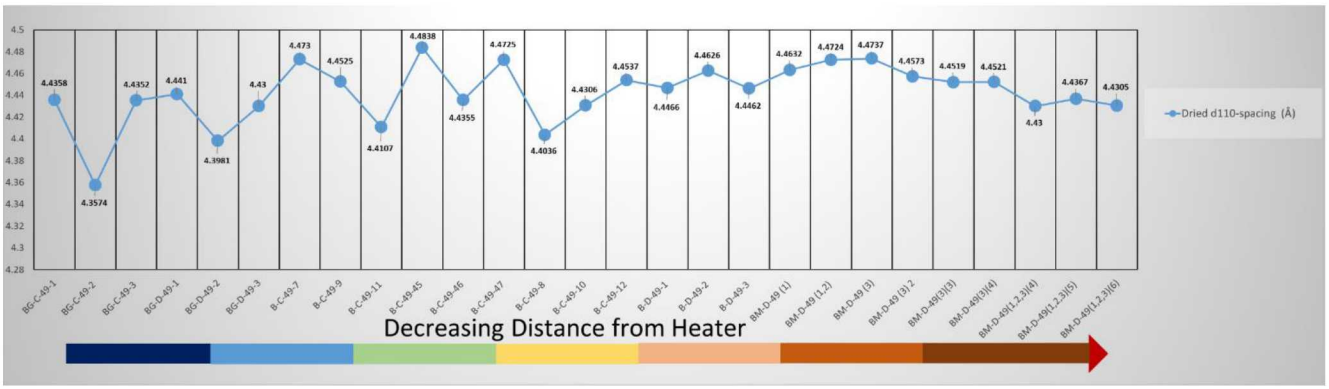


Figure 16. Distribution of d-spacing (d_{110}) (Å) values with distance from the heater for air-dried bentonite samples (see schematic Fig. 3 for sample locations). Notice the reduced variability in d_{110} values for samples closest to the heater.

Using the differences in d_{001} d-spacing data between air-dried and glycolated bentonite samples we estimated the apparent relative extent of swelling to evaluate the effect of distance from the heater. Fig. 17 illustrates the distribution of values for the relative extent of swelling for the various samples with distance from the heater. Like the distributions of d_{110} reflections, the variability in the relative extent of swelling appears to be reduced for bentonite closest to the heater where the overall variation ranges from around 15%-20% in the BM-D-49 samples. The overall variation in the relative extent of swelling for samples far from the heater was larger, in the order of ~14%-32%. The highest estimate of relative swelling extent is around 32% for samples located farther from the gallery axis whereas samples closest to the heater the value is around 20%. The value of 32% is consistent with the maximum swelling expansion measured by Friedrich et al. (2016) for untreated FEBEX bentonite using environmental SEM (ESEM). The reason for this larger variability in swelling behavior with distance from the heater is currently a matter of further study. This behavior could be related to thermal effects on bentonite and/or changes in the smectite chemistry. Moreover, such a level of variation at the scale of the sample blocks could have implications to swelling heterogeneities and thus uncertainties in the extent of swelling predicted in coupled THMC models. The XRD study is still work in progress and further analysis of these data plus additional XRD analyses are planned for future work. Increasing the number of XRD analyses in all samples is needed to advance further comparisons on variability trends between different locations.

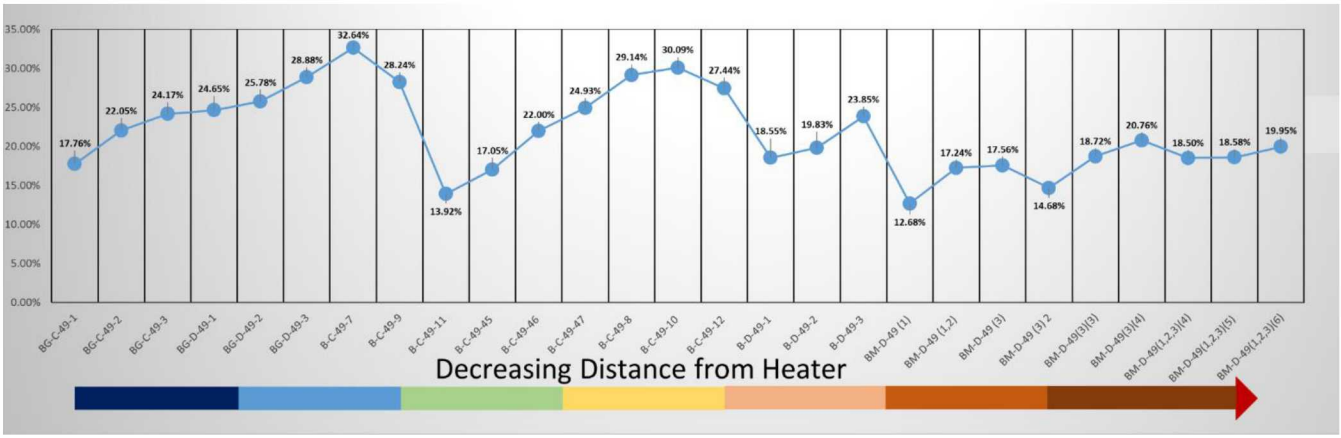


Figure 17. Distribution of estimated percent swelling with distance from the heater based in d-spacing measurements on air-dried and glycolated bentonite samples (see schematic Fig. 3 for sample locations). Notice the reduced variability in estimated swelling extent for samples closest to the heater.

5. DECOVALEX-2019 Task C: GREET (Groundwater REcovery Experiment in Tunnel), Mizunami URL, Japan

The DECOVALEX-2019 project phase started this year with seven tasks (A-G) targeting various issues relevant to coupled THMC processes driven experimental and URL field data. The Disposal in Argillite work package has expressed interest in the GREET (Groundwater REcovery Experiment in Tunnel, Mizunami URL, JAEA, Japan) URL project on the hydrochemical characterization of the site as part of the groundwater recovery activity from the closure test drift (CTD). The CTD is a tunnel section (46.5 m long × 5.0 m wide × 4.5 m high) of the URL sealed by plug and filled with groundwater. A series of boreholes allow for monitoring water pressure and chemistry during the experiment. In FY17, geochemical modeling was applied to the analysis of dilution trends observed in monitoring borehole data through simulation of groundwater mixing. Interactions with cementitious barrier materials in the CTD were evaluated through 1D reactive-transport modeling for a water-filled tunnel scenario. The current study extends the work conducted on cement interactions in the flooded CTD to evaluate shotcrete liner interactions using a 3D model representation of this domain implemented in the reactive transport simulation code PFLOTRAN (Lichtner et al., 2013). PFLOTRAN is an open source, state-of-the-art massively parallel subsurface flow and reactive transport code with extensive modeling capabilities of THC processes. PFLOTRAN is developed to run on massively parallel or high performance computing (HPC) platforms where efficient scalability becomes important. pH and Cl^- concentration data obtained recently at the site will be used as a test to the model.

The GREET project task leader has kindly provided web access to the geochemical and hydrological data, as it becomes available, to be reviewed by the task participants. Hydrochemical data from the DECOVALEX-19 (Task C) was obtained from the JAEA team and/or information at the GREET website (http://www.jaea.go.jp/04/tono/miu/dataset/greet/greet.html).

Closure Test Drift (CTD): 3D H-C Model of Shotcrete Liner Interactions and 12MI33 Monitoring Borehole

The Closure Test Drift (CTD) is a tunnel facility (Fig. 18) at 500 meters below ground level to investigate the effects of hydrological, geomechanical, and geochemical variations during drift excavation and post-closure in fractured granitic rock. The facility is equipped with monitoring probes for water sampling, hydraulic pressure, and rock displacement. Mapping of fractures was conducted

during drift excavation. The CTD tunnel is lined with Mg-bearing ordinary Portland cement (OPC) shotcrete and is sealed by using a low-heat Portland cement plug (Iwatsuki et al., 2017). After closure, the tunnel was filled with water to study environmental changes including effects on hydrochemistry due to interactions with barrier materials such as shotcrete. Like FEBEX-DP and other international repository science activities, interactions with cementitious barrier materials (e.g., shotcrete) is important given its potential for alkaline reactions with other silicates (e.g., clay barriers, host rock) and the generation of high pH pore solutions. These processes could lead to dissolution/precipitation processes at barrier interfaces that could affect solute (radionuclide) transport and clay barrier sorption properties.

A 3D reactive transport representation (Fig. 19) has been implemented on a hydrological model of the site near the CTD. The goal is to extend the hydrological model to capture the extent of high pH effects within the flooded tunnel and with distance from the cement-water interface. Such interactions in the water-filled zone may influence pore solution chemistry in the nearby monitoring borehole (12MI33) where fractures in the excavated disturbed zone (EDZ) are present throughout the length of the CTD. Currently, the hydrological model does not include fractures but their inclusion into the model is planned for future work. Water chemistry measurements in zone 6 of the 12MI33 monitoring borehole show elevated pH values suggesting the influence of the nearby cement liner material in the sampled solution.

The 3D reactive reactive-transport model implementation is done in PFLOTRAN using similar parameters (e.g., material properties) to those adopted previously in the 1D evaluation of EBS material interactions (Jové Colón et al., 2016). The PFLOTRAN simulations were conducted in TH mode (coupled thermal-hydrological flow) assuming full saturation and transport by diffusion only. Thermodynamic data for cementitious phases such as CSH(1.6), portlandite, and ettringite were obtained from the THERMODDEM database (Blanc et al., 2012; Blanc et al., 2006). The composition of the cementitious domain resembles that of ordinary Portland cement (OPC) assuming a calcite aggregate (Jové Colón et al., 2016). Dissolution rates of cementitious solids were obtained from various sources as described in Jové Colón et al. (2016). The length of water-filled domain is about 47 m with a height of 5 m closely resembling the CTD dimensions. The cement plug thickness is 2 m and the shotcrete liner is 0.1 m. The flooded CTD domain is represented by a porous medium having a porosity of almost unity and a very high permeability. The groundwater in the flooded domain is assumed to have the same chemistry as that of the host granitic rock. This groundwater also represents the starting solution chemistry of the filled CTD. The simulations were performed over a period of 400 days.

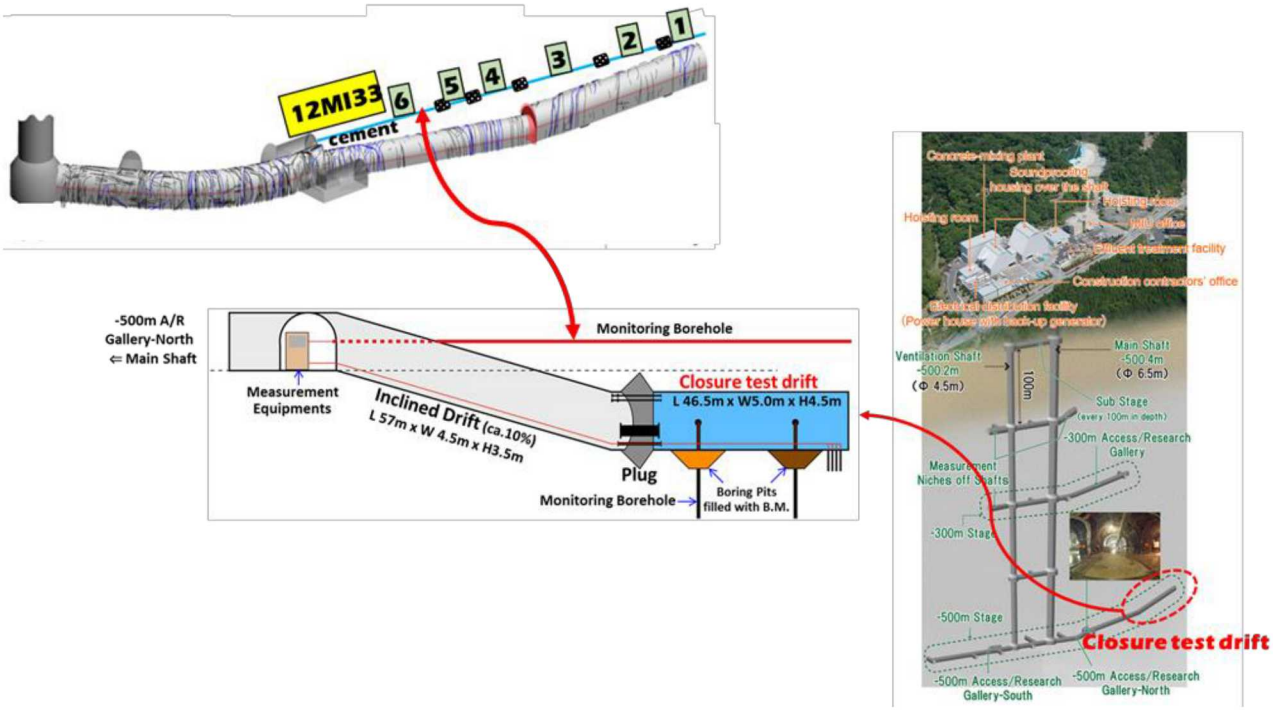


Figure 18. Diagrammatic picture of the closure test drift (CTD) at the Mizunami URL site, Japan. Upper schematic picture shows the inclined tunnel with CTD and the 12MI33 borehole with six monitoring zones. Figure content kindly provided by Dr. Teruki Iwatsuki (JAEA).

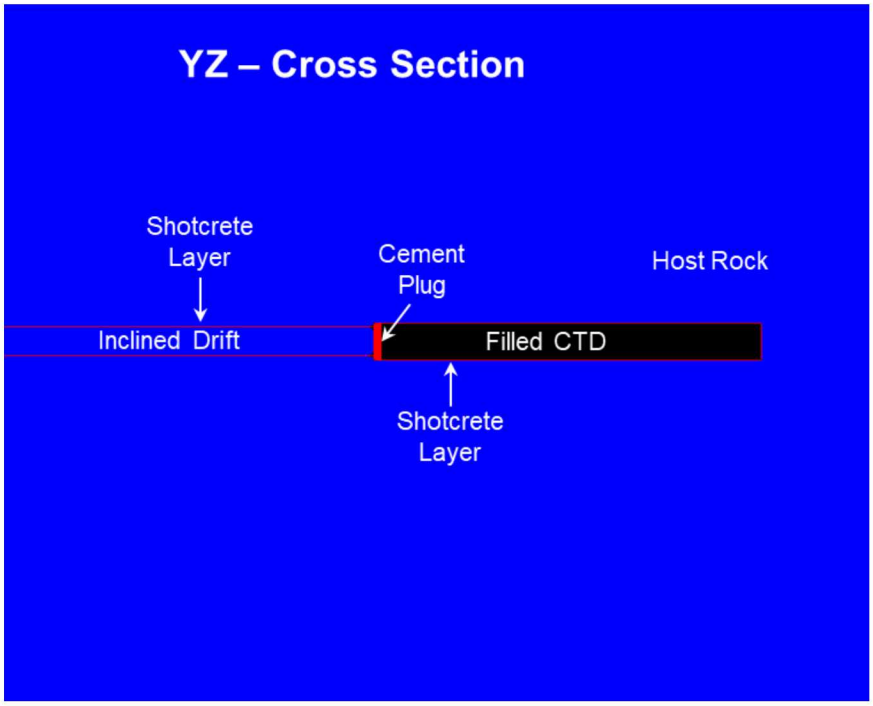


Figure 19. Schematic figure showing a YZ cross section of the model domain in the PFLOTRAN reactive transport simulation of the CTD. Red areas delineate the shotcrete liner and cement plug. Observation points (not shown) are positioned at the tunnel length midpoint starting from the shotcrete-water interface up to a meter inside the water-filled tunnel.

Fig. 20 shows four time-snapshots (0, 70, 150, 310 days) of the pH mapping to represent the evolution of the reactive front from the shotcrete liner domain. As expected, pH increases with time from the interface into the water-filled CTD region and the host rock. After ~300 days of simulation time, the increase in pH because of the advancing front reaches ~0.5 m from the shotcrete interface into flooded CTD. About 1 m into the CTD, the pH remains close to the starting pH 8.9 for remainder of the simulation.

The current stage of GREET effort involves the prediction of changes in groundwater chemistry to then be compared with data from monitoring boreholes from within the CTD and from the host rock within the excavated disturbed zone (EDZ). Fig. 21 (upper panel) shows the pH predictions from PFLOTRAN and the JAEA group along with pH and Cl^- measurements of the solution within the CTD. The measured pH data (blue dots connected by a line) show a rapid monotonic increase early in time then progressing towards a pH~10. Notice that measure pH data after 3/2016 show more variation with time (i.e., deviations from a monotonic increase) but still trending towards pH~10. The PFLOTRAN simulation results (solid curves) are shown for three observation points at a distance from the shotcrete interface (at the interface, 0.45 m, and 1 m) into the filled CTD. Notice that pH predictions at the interface overestimate the measured data progressing towards eventual equilibrium with the shotcrete cement (pH~11.3). As expected, predictions at 0.45 m show a slower pH increase due to diffusive transport from the shotcrete interface into the filled CTD. This increase reaches pH~10.3 towards the end of the simulation which is closer to the measured pH and it is also close to the JAEA Case 0 predictions. pH predictions at 1 m from the shotcrete interface show little increase with time indicating the limited effect of the reaction front on groundwater pH towards the tunnel axis. These pH predictions are also consistent with that of the JAEA Case 1.

Fig. 21 shows the measured concentration of Cl^- (lower panel) decreasing with time starting from 475 mg/L towards a steady-state value of ~403 mg/L. Although the PFLOTRAN simulation predicts a decrease in Cl^- concentration with time at the shotcrete interface, the extent of such is much smaller when compared to the measurement. It is not clear what would cause such a large decrease but possible reasons are groundwater mixing/dilution and/or Cl^- uptake by precipitation of a Cl-bearing cementitious phase. Both are possibilities that need verification through monitoring activities.

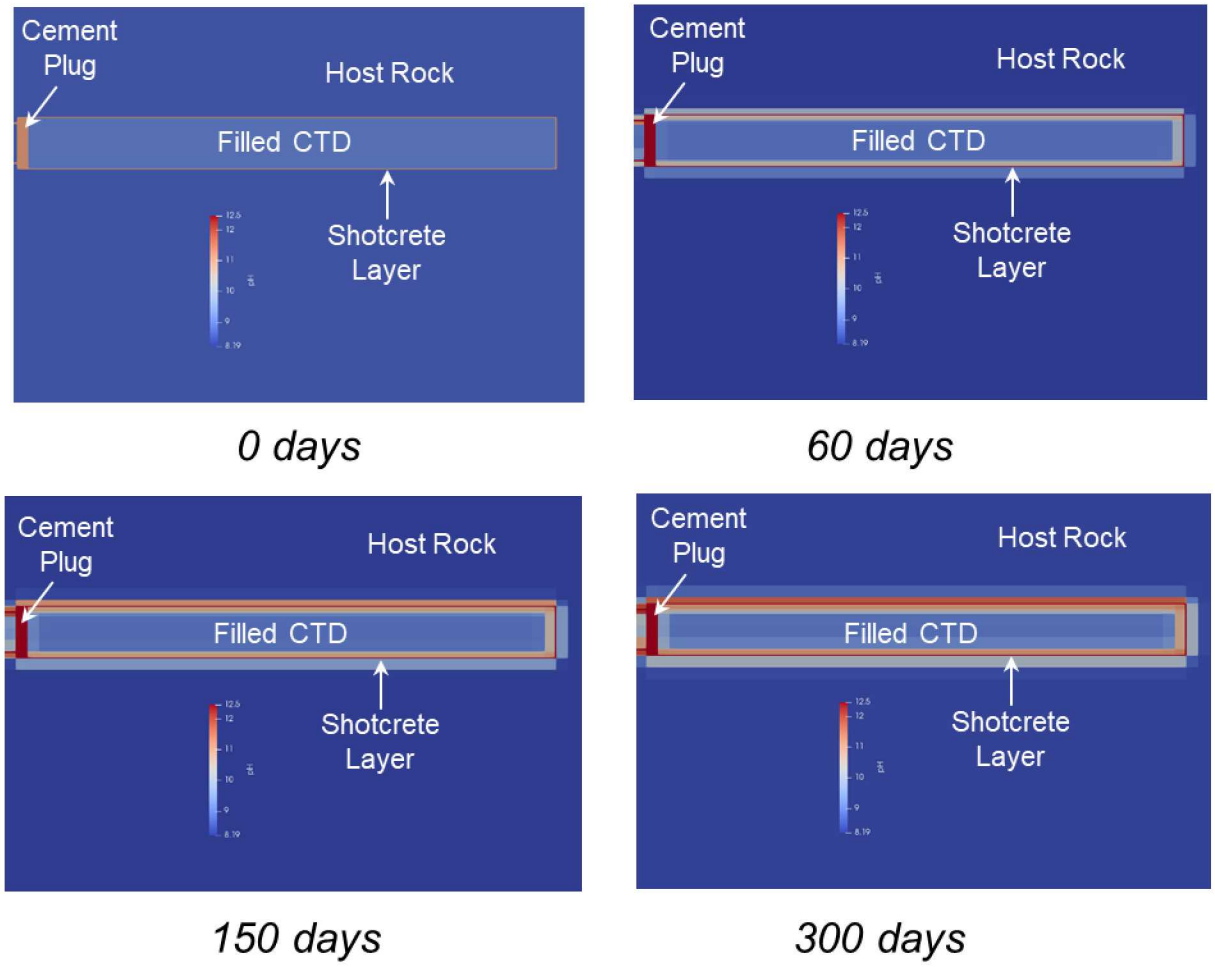


Figure 20. Predicted pH of the PFLOTRAN 3D reactive transport model of the CTD and surrounding host rock. The reaction front diffuses into the CTD and into host rock. pH color map scale ranges from 8.19 to 12.5.

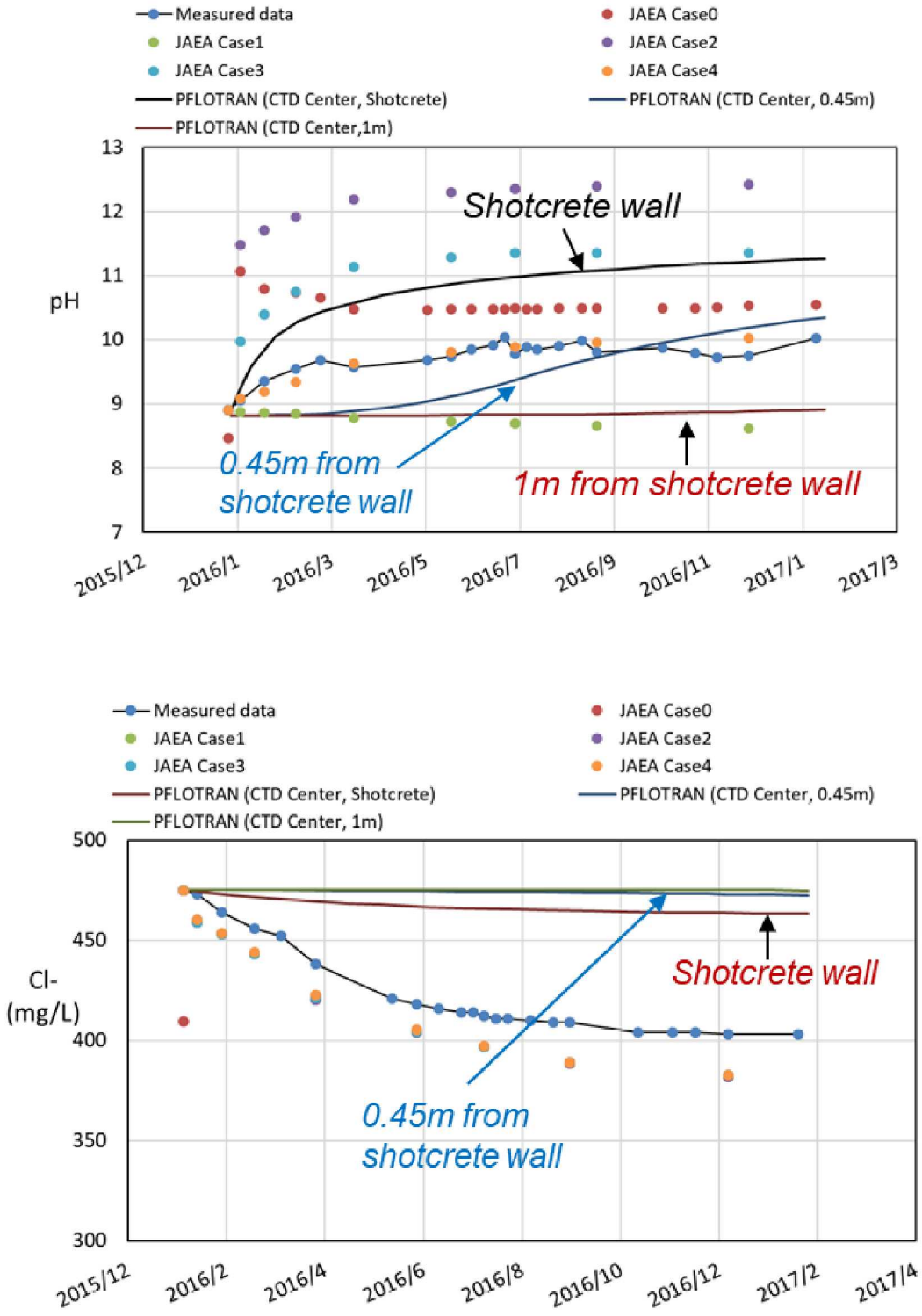


Figure 21. Measured and predicted pH (upper panel) and Cl^- concentration (lower panel) profiles at the midpoint region of the CTD.

Fig. 22 describes measured and predicted pH at the six monitoring zones in borehole 12MI33. As illustrated in this figure, the monitoring borehole lies in the host rock parallel to the CTD and next to the inclined tunnel. The groundwater in this region interacts with the granitic host rock, however, zone 6 is closer to the cement liner. This is also illustrated in Fig. 22 where sampled groundwaters in zone 6 reaches pH~11. The PFLOTRAN pH prediction is the essentially the same for all six zones where this trend is generally consistent within the scatter of the measured pH's from zones 1-5. However, the prediction for zone 6 doesn't capture the pH increase most likely because of limited interaction with the cement liner. This may be indicative of enhanced transport in this zone and the next step will to accommodate this effect in the model.

All these preliminary results provide ideas on how to improve the 3D H-C model:

- Finer mesh at the shotcrete-water interface inside the filled CTD. This would allow the placement of observation points at shorter distances to monitor chemical changes away from the shotcrete interface.
- The initial rapid increase in measured pH is difficult to simulate in scenarios where observations are far from the shotcrete interface. Therefore, changes to the kinetic rate law and transport parameterization should be considered to better represent such pH profile. Parameter analysis within the mineral dissolution kinetics formulations in PFLOTRAN will be considered for dissolution cementitious phase (e.g., portlandite).
- Addition of Cl-bearing cementitious phases (e.g., Friedel's salt) to represent Cl^- depletion through solid formation. Groundwater mixing close to the shotcrete-rock domain will be explored as well.
- Shotcrete composition will be updated to capture the effects of Mg-bearing phases present in the liner material.
- Extending the 3D H-C model to accommodate fracture effects on flow and transport.

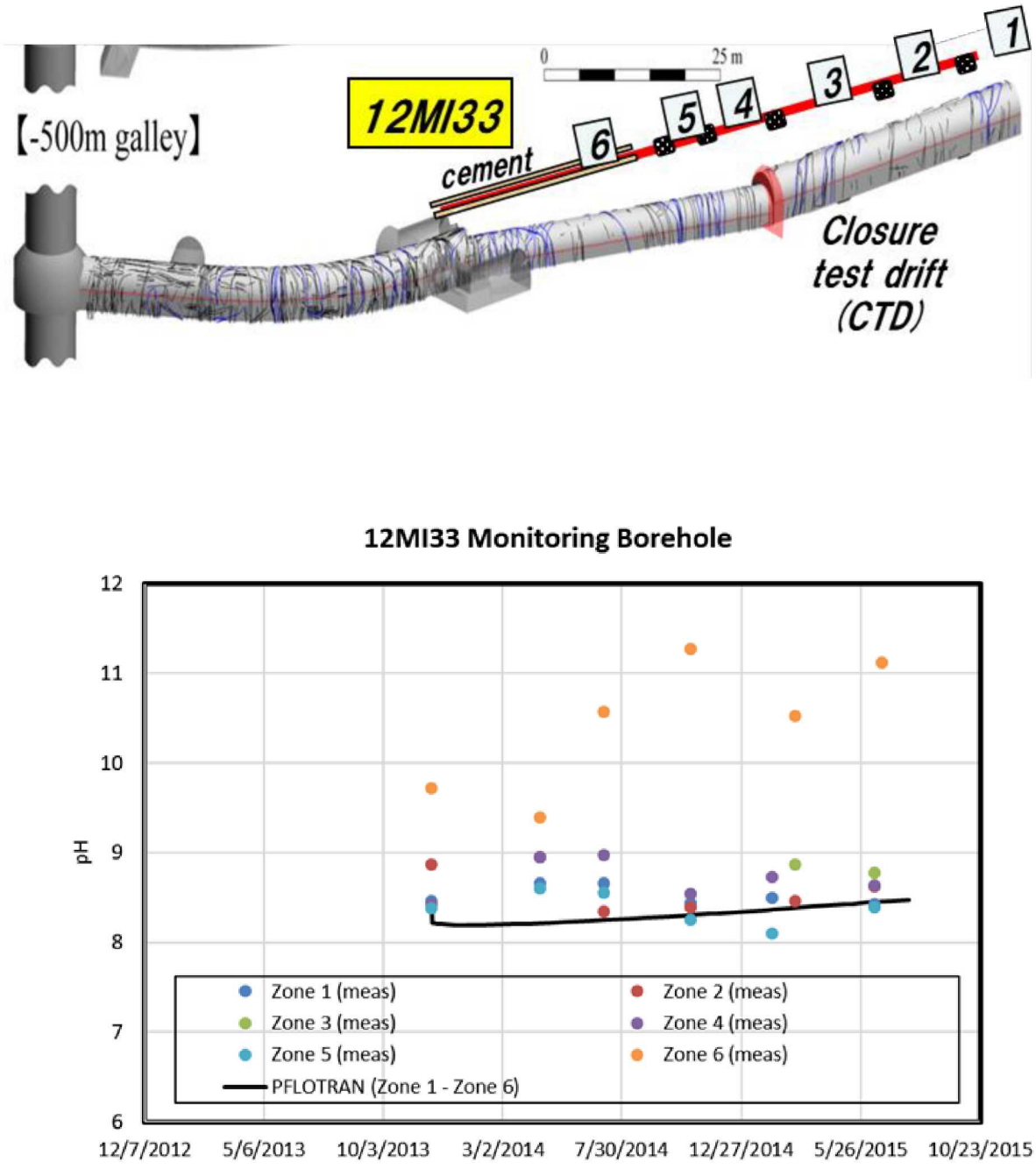


Figure 22. Schematic diagram of borehole 12MI33 (upper panel) with six monitoring zones. Measured and predicted pH (lower panel) profiles at monitoring zones 1 through 6.

6. 3D Reactive Transport (THC) Simulations for a Single Heat-Generating Waste Package with a Layered EBS

Jové Colón et al. (2016) describes a 1D reactive transport model with a multi-layered EBS under non-isothermal conditions. Following this 1D model parameterization as a baseline, here we developed a 3D extension of such model representation using PFLOTRAN. Simulation parameters for solid materials and aqueous components are also described in Jové Colón et al. (2016). However, the 3D model domain was represented using an unstructured mesh similar to that described for the thermal model in Jové Colón et al. (2013). The mesh was constructed using the Cubit software (Blacker et al., 2016) and then converted to a format readable by PFLOTRAN. The dimensions of the EBS domain components are:

- Waste canister length and diameter: 4.7 m and 1.15 m, respectively
- Steel overpack thickness: 0.1 m
- Inner and outer bentonite layer thickness: 1.24 m
- Cement (OPC) liner thickness: 0.75 m
- Cement (OPC) spacer length: 5.3 m

Figure 23 depicts the 3D model domain with the EBS components along with a 2D projection of the EBS meshed domain. The inner bentonite layer contains some quartz to slightly enhance the thermal conductivity whereas the outer bentonite layer has none. The THERMODDEM thermodynamic database (Blanc et al., 2012; Blanc et al., 2006) is used for all solid and aqueous components. The non-isothermal simulations were conducted using SNF decay heat data based on the thermal analysis by Greenberg et al. (2013). The decay heat load is based on 12 UOX PWR assemblies with a 40 GWd per SNF assembly and 50-year storage time. As described in Jové Colón et al. (2016), three types of initial pore water chemistries for the cement liner, clay barrier, and clay-rock zones were considered: (a) dilute alkaline pH water (cement liner), (b) “FEBEX-like” pore water (Fernandez et al., 2004; Fernandez et al., 2001) (inner- and outer-clay), and (c) clay-rock pore water chemistry based on the work by Turrero et al. (2006) on Opalinus Clay. Some minor changes to the water chemistry were considered to evaluate issues with code run stability during the heating. Interactions with waste form and waste package internals are not considered in this simulations for simplicity.

The simulations were conducted in PFLOTRAN TH mode (full saturation) and GENERAL mode (variably saturated). Figure 24 shows the preliminary results for the temperature profile with time of the fully saturated case focusing on the thermal period. Peak temperatures at the waste package center and at the center of the inner bentonite layer are ~163°C and ~103°C, respectively. Peak temperatures farther out from the inner bentonite layer are below 100°C. The most reactive regions in the bentonite layers are those near the cement liner and spacers. The predicted volume fractions of illite are extremely small and spatially tracks high temperatures mainly accros the inner bentonite layer. Similar results from the LBNL modeling group also predict very amounts of illite in their simulations. Longer simulations are needed to conduct sensitivity analysis by varying pore solution chemistry to better evaluate this result. The significance of this is the spatio-temporal prediction of secondary mineral formation during bentonite alteration under non-isothermal conditions. Such prediction would be crucial to the assessment of *sacrificial zones* in the bentonite domain. The code runs are computationally intensive and require many processing nodes to achieve simulation times in the order of hundreds of years. Work is planned along these lines to scale the simulations to longer times. Still, focusing on simulations during the thermal peak period is a very important aspect to the highest level of bentonite alteration.

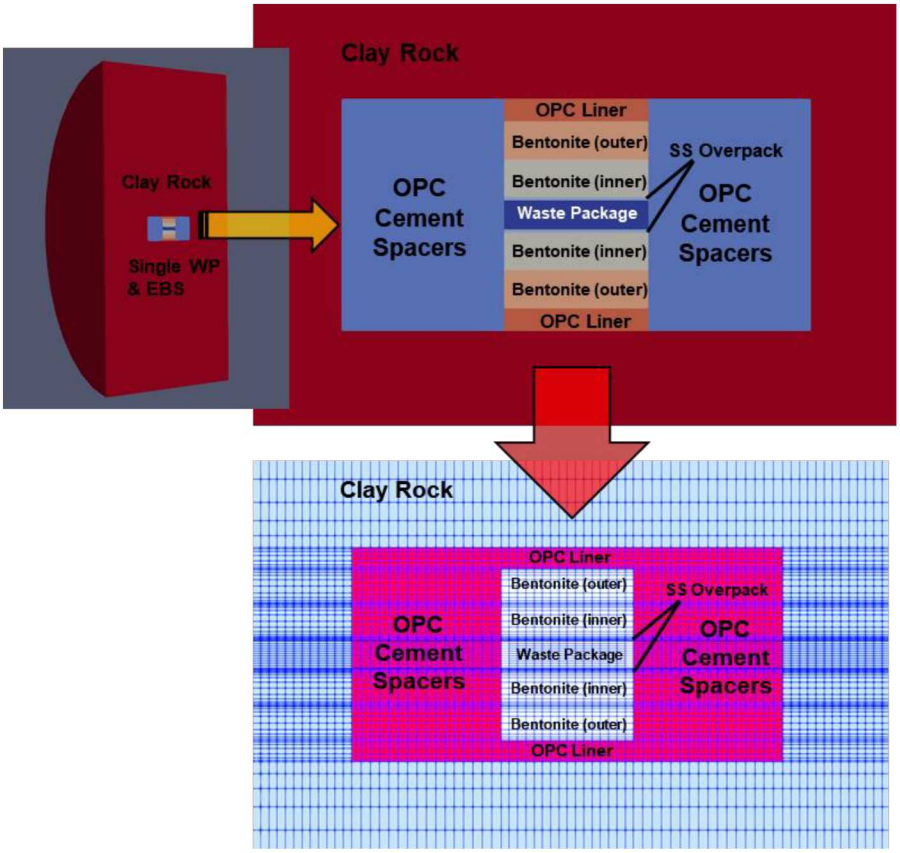


Figure 23. Schematic figure showing the 3D single waste package model (unstructured mesh) domain in the PFLOTRAN reactive transport simulation.

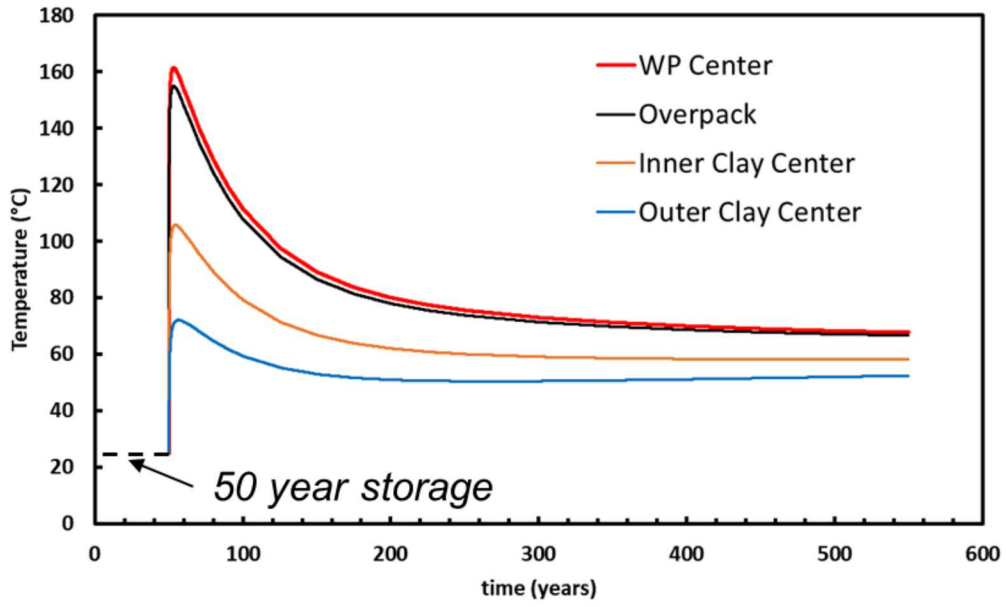


Figure 24. Predicted temperature profile vs. time across the multi-layered EBS for PFLOTRAN simulations in TH mode (full saturation). Thermal load based on decay heat for 12 UOX PWR assemblies with a 40 GWd per SNF assembly and 50-year storage time.

PFLOTRAN simulations in GENERAL mode (variably saturated or multiphase) were more computationally intensive than TH mode and resulted in much shorter simulation times. In addition, canister heating caused dryout at the center of the waste package generating extreme solution concentrations at this cell location. This causes convergence issues in the reactive transport part of the simulation leading to code run termination. Salt solid precipitation in dryout cells and "forcing" the simulation to a specified saturation level resulted in slight code run stability improvements. Simulations were conducted with and without chemistry to evaluate code run stability issues. Only preliminary results from simulations without chemistry will be shown. Comparison of preliminary results from simulations using different approaches to improve stability yield similar predictions for temperature, liquid/gas pressure, and liquid/gas saturation at observations points (excluding the waste package center) in the bentonite layers, cement liner, and clay rock. These regions did not experience cell dryout issues. Figure 25 shows the resulting temperature profile with time ~14 years through the thermal period for the variably saturated case with no chemistry. As expected for the unsaturated case, the predicted peak temperatures at the observation points are slightly lower than in the saturated case. Work is planned to improve code stability in multiphase simulations with and without reactive transport.

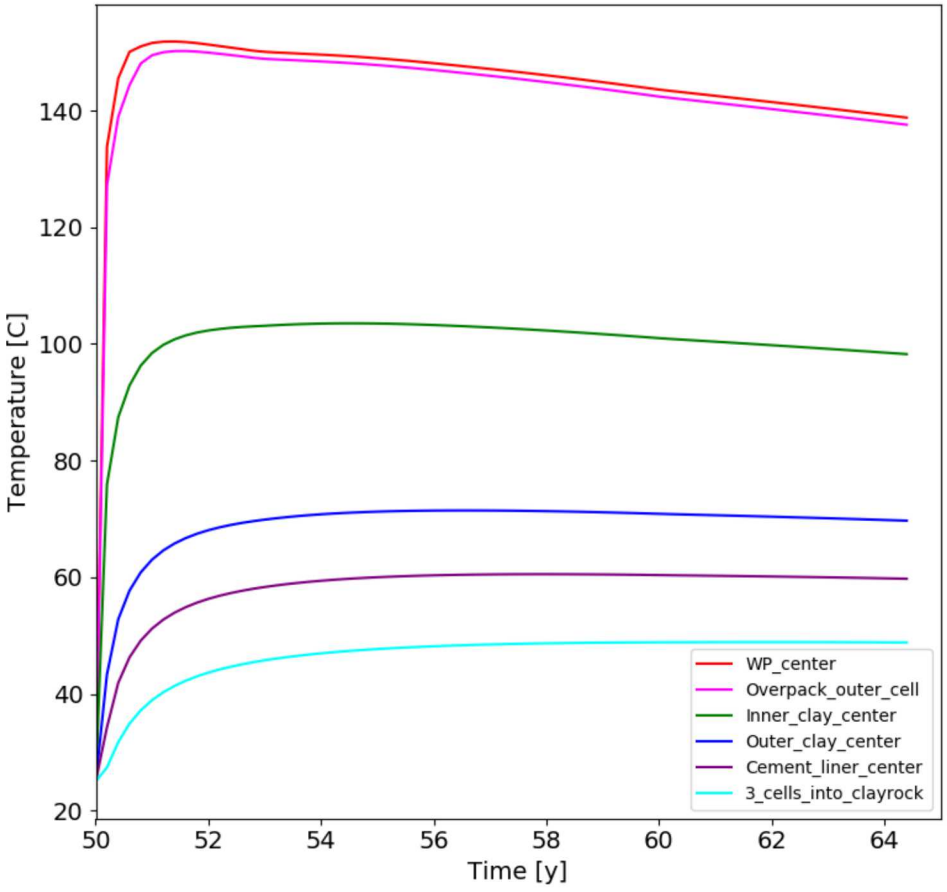


Figure 25. Predicted temperature profile vs. time across the multi-layered EBS for PFLOTRAN simulations in GENERAL mode (variably saturated) without reactive transport.

7. Conclusions

- **FEBEX-DP:** Compositional (XRF), structural (XRD), and thermal (TGA/DSC) characterization studies on FEBEX-DP bentonite samples from Section 49 were conducted to evaluate the effects thermal loads with distance from the heater. The most salient features of this characterization study can be summarized as follows:
  - XRF analyses revealed Mg enrichment in samples closest to the heater. This observation is corroborated with other FEBEX-DP studies in other sampled sections surrounding the heater. This Mg enrichment is distinctly sharp for samples adjacent to the heater surface and may indicate thermally-induced effects of bentonite interactions driven by elevated temperatures. Such a change in smectite composition could potentially affect swelling behavior and sorption properties. Based on the change in Mg enrichment with distance from the heater surface, a rough estimate of the extent of the sacrificial zone could be in the order of ~20 – ~25 cm at the location of Section 49. Given the anticipation of higher temperatures generated by large canisters, the influence on barrier performance under thermal loads needs further investigation.
  - TGA/DSC thermal analyses indicate that measured water content falls within the data bounds of other FEBEX-DP studies from other sampled sections. There is a rather weak tendency towards higher water content with distance from the heater surface. Overall, TGA and DSC profiles with temperature are similar to those from other FEBEX-DP bentonite samples and literature studies on montmorillonite.
  - XRD spectra and d-spacing values for samples close and far from the heater are similar to others in the FEBEX-DP project. There is no clear trend or apparent correlation between d_{001} values and distance from the heater. Similarly, d_{110} values show no clear trend with distance from the heater. However, there is an apparent reduction in variability for d_{110} values for samples closest to the heater. Similarly, estimates of relative extent of swelling between air-dried and glycolated bentonite samples indicate a similar reduction in variability for samples closest to the heater. The swelling extent variability with distance from the heater appears to be significant and could have implications to the uncertainty in the prediction of swelling in response to thermal effects on bentonite. More XRD and TGA/DSC analyses are needed to further evaluate these trends.
- **DECOVALEX-2019 Task C of GREET Experiment** – 3D reactive transport modeling of the CTD and monitoring borehole 12MI33:
  - 3D reactive transport modeling of shotcrete liner interactions was implemented on a hydrological model of the site domain comprising the CTD. PFLOTRAN predictions of pH and Cl^- from groundwaters sampled at the midpoint length of the CTD showed deviations from the measurements. The predicted pH overestimates the measured data at later times whereas the predicted Cl^- concentration prediction underestimates its decrease with time. Future work to assess the nature of these deviations will include exploring kinetic rate law and transport parameterizations to better represent the pH profile. Groundwater mixing/dilution and/or Cl^- uptake by precipitation of a Cl-bearing phase (e.g., Friedel's salt) will be explored to evaluate the observed decrease in Cl^- concentration with time.
  - The 3D reactive transport model was also used to model groundwater interactions in six zones of the monitoring borehole 12MI33. This borehole lies parallel to the CTD and near the inclined drift. PFLOTRAN pH predictions of zones 1-5 in the monitoring borehole show overall consistency with the measured data suggesting the control of the

granitic host-rock on the groundwater chemistry. The high pH observed in zone 6 appears to be influenced by interactions with the nearby cement liner and could not be predicted by the current model. This probably suggest enhanced mixing at this zone.

- **3D PFLOTRAN non-isothermal single waste package reactive transport simulations using under saturated and unsaturated conditions:**
  - Fully saturated simulations: PFLOTRAN simulations predict peak temperatures at the waste package center and at the center of the inner bentonite layer are ~163°C and ~103°C, respectively. This result is for a canister enclosing 12 UOX PWR assemblies with a 40 GWd per SNF assembly and 50-year storage time. Peak temperatures farther out from the inner bentonite layer are below 100°C. The most reactive regions in the bentonite layers are those near the cement liner and spacers. The predicted volume fractions of illite are extremely small and spatially tracks high temperatures mainly accros the inner bentonite layer. Although simulations at longer times are needed, the significance of this is the spatio-temporal prediction of secondary mineral formation during bentonite alteration under non-isothermal conditions. This is key to the evaluation of *sacrificial zones* in the bentonite domain.
  - Unsaturated simulations: As expected, PFLOTRAN predictions of peak temperatures are slightly lower than those under saturated conditions. These simulations are much more computationally intensive and resulted in much shorter simulation times. There were also convergence issues due to cell dryout at the center of the waste package. This is work in progress and work is planned to assess these issues.

VII. FY19 Work

Planned work on **FEBEX-DP** samples for FY19 (and the remainder of FY18):

- Continue assessment of compositional (XRF), structural (XRD), and thermal (TGS/DSC) data plus additional analyses of bentonite samples from Section 49. Focus will be on further evaluation of thermal analysis and XRD data with the observed compositional changes, and comparison with other studies on bentonite clay.
- Conduct compositional, structural, and thermal characterization of the FEBEX-DP bentonite samples from Section 58. This suite of samples is located far from the heater (in contrast with those of Section 49) and were not exposed to thermal loads.
- Experimental investigations on illitization using FEBEX-DP samples instead of treated clays as starting material. This work will be conducted in concert with the SFWST crystalline work package.

Planned work on **DECOVALEX Task C** for FY19 (and the remainder of FY18):

- Continue 3D reactive-transport modeling work on DECOVALEX-2019 Task C (GREET) emphasizing on modeling the CTD chemical data. The effects of shotcrete liner interactions in the CTD will be the focus of this work to evaluate predictions of measured pH and Cl^- data. Shotcrete chemistry will be expanded to have Mg-bearing components instead of generic OPC.
- Extend the 3D reactive transport modeling to be integrated with hydrological simulations in fractured rock conducted with the SFWST crystalline work package team. Investigate the effect of fractures adjacent to monitoring boreholes in the CTD on groundwater pH and other aqueous constituents.

Planned work on Disposal in Argillite R&D for FY19 (and the remainder of FY18):

- Continue evaluation of 3D single waste package reactive simulations with PFLOTRAN under saturated and unsaturated conditions. The assessment of convergence issues mainly for reactive transport simulations at unsaturated conditions. Extend simulations times far beyond the peak thermal period.
- Thermodynamic description of barrier material interactions focusing on reaction with cementitious materials. This activity is linked to experiments conducted at LANL for chemical interactions of cement with other barrier materials under hydrothermal conditions.
- Thermodynamic database development work conducted in parallel with LLNL. This work will analyze the effect of updates of thermodynamic data to key species.
- In-package chemistry: Extend the thermodynamic analysis used in the evaluation of engineered barrier material interactions towards the description of in-package chemistry. This work will leverage the use of thermodynamic modeling and first principles calculations to assess the stability of phases resulting from in-package/fluid interactions.

8. References

Birkholzer, J., Faybishenko, B., Zheng, L., Rutqvist, J., Dobson, P., Fox, P. M., Reimus, P., Viswanathan, H., Jove-Colon, C. F., Wang, Y., Kuhlman, K., McMahon, K., and Zavarin, M., 2017, International Collaboration Activities in Different Geologic Disposal Environments (SFWD-SFWST-2017-000013), Prepared for US Department of Energy, Spent Fuel and Waste Disposition Campaign (SFWD-SFWST-2017-000013): Berkeley, California, (National Laboratory Report No. LBNL-2001063), p. 236 pp.

Birkholzer, J., Faybishenko, B., Zheng, L., Rutqvist, J., Reimus, P., Viswanathan, H., Jove Colon, C. F., Wang, Y., and Zavarin, M., 2016, International Collaboration Activities in Different Geologic Disposal Environments (FCRD-UFD-2016-000077): Lawrence Berkeley National Laboratory (LBNL-1006321).

Blacker, T. D., Owen, S. J., Staten, M. L., Quadros, W. R., Hanks, B., Clark, B. W., Meyers, R. J., Ernst, C., Merkley, K., and Morris, R., 2016, CUBIT geometry and mesh generation toolkit 15.1 user documentation: Sandia National Lab.(SNL-NM), Albuquerque, NM (United States).

Blanc, P., Lassin, A., Piantone, P., Azaroual, M., Jacquemet, N., Fabbri, A., and Gaucher, A., 2012, Thermoddem: A geochemical database focused on low temperature water/rock interactions and waste materials: Applied Geochemistry, v. 27, p. 2107-2116.

Blanc, P., Piantone, P., Lassin, A., and Burnol, A., 2006, Thermochimie : Sélection de constantes thermodynamiques pour les éléments majeurs, le plomb et le cadmium, Rapport final BRGM/RP-54902-FR: France, BRGM, p. 157.

Fernandez, A. M., Baeyens, B., Bradbury, M., and Rivas, P., 2004, Analysis of the porewater chemical composition of a Spanish compacted bentonite used in an engineered barrier: Physics and Chemistry of the Earth, v. 29, no. 1, p. 105-118.

Fernandez, A. M., Cuevas, J., and Rivas, P., 2001, Pore water chemistry of the Febex bentonite: Scientific Basis for Nuclear Waste Management XXIV, v. 663, p. 573-588.

Friedrich, F., Schild, D., Weidler, P. G., and Schäfer, T., 2016, Hydration of FEBEX Bentonite as Observed by Environmental Scanning Electron Microscopy (ESEM), Filling the Gaps - From Microscopic Pore Structures to Transport Properties in Shales: Virginia, USA, The Clay Minerals Society, p. 199-210.

García-Siñeriz, J. L., Abós, H., Martínez, V., De la Rosa, C., Mäder, U., and Kober, F., 2016, FEBEX DP: Dismantling of heater 2 at the FEBEX "in situ" test: Description of operations - Arbeitsbericht NAB 16-11: National Cooperative for the Disposal of Radioactive Waste (NAGRA).

Greenberg, H. R., Wen, J., and Buscheck, T., 2013, Scoping Thermal Analysis of Alternative Dual-Purpose Canister Disposal Concepts (LLNL-TR-639869): Livermore, CA, Lawrence Livermore National Laboratory, p. 54.

Grim, R. E., 1968, Clay mineralogy. International series in the earth and planetary sciences: McGraw-Hill, New York.

Huertas, F., Fuentes-Cantillana, J. L., Jullien, F., Rivas, P., Linares, J., Fariña, P., Ghoreychi, M., Jockwer, N., Kickmaier, W., Martínez, M. A., Samper, J., Alonso, E., and Elorza, F. J., 2000, Full-scale engineered barriers experiment for a deep geological repository for high-level radioactive waste in crystalline host rock (FEBEX project): Final report. EUR 19147.

Iwatsuki, T., Furue, R., Mie, H., Ioka, S., and Mizuno, T., 2005, Hydrochemical baseline condition of groundwater at the Mizunami underground research laboratory (MIU): Applied geochemistry, v. 20, no. 12, p. 2283-2302.

Iwatsuki, T., Hagiwara, H., Ohmori, K., Munemoto, T., and Onoe, H., 2015, Hydrochemical disturbances measured in groundwater during the construction and operation of a large-scale underground facility in deep crystalline rock in Japan: Environmental Earth Sciences, v. 74, no. 4, p. 3041-3057.

Iwatsuki, T., Munemoto, T., Kubota, M., Hayashida, K., and Kato, T., 2017, Characterization of rare earth elements (REEs) associated with suspended particles in deep granitic groundwater and their post-closure behavior from a simulated underground facility: Applied Geochemistry, v. 82, p. 134-145.

Jové Colón, C. F., Greathouse, J. A., Teich-McGoldrick, S., Cygan, R. T., Weck, P. F., Hansen, G. A., Criscenti, L. J., Caporuscio, F. A., Cheshire, M., Rearick, M. S., McCarney, M. K., Greenberg, H. R., Wolery, T.

J., Sutton, M., Zavarin, M., Kersting, A. B., Begg, J. B., Blink, J. A., Buscheck, T., Benedicto-Cordoba, A., Zhao, P., Rutqvist, J., Steefel, C. I., Birkholzer, J., Liu, H.-H., Davis, J. A., Tinnacher, R., Bourg, I., Zheng, L., and Vilarrasa, V., 2013, EBS Model Development and Evaluation Report (FCRD-UFD-2013-000312): Albuquerque, NM, Sandia National Laboratories, SAND2013-8512 P, p. 508.

Jové Colón, C. F., Hammond, G. E., Kuhlman, K., Zheng, L., Kim, K., Xu, H., Rutqvist, J., Caporuscio, F. A., Norskog, K. E., Maner, J., Palaich, S., Cheshire, M., Zavarin, M., Wolery, T. J., Atkins-Duffin, C., Jerden, J. L., Copple, J. M., Cruse, T., and Ebert, W. L., 2016, Evaluation of Used Fuel Disposition in Clay-Bearing Rock (FCRD-UFD-2016-000074): Sandia National Laboratories.

Lichtner, P. C., Hammond, G. E., Lu, C., Karra, S., Bisht, G., Andre, B., Mills, R. T., and Kumar, J., 2013, PFLOTRAN User Manual: http://www.pflotran.org.

Martinez, V., Abós, H., and García-Siñeriz, J. L., 2016, FEBEXe: Final Sensor Data Report (FEBEX "in situ" Experiment) - Arbeitsbericht NAB 16-19: National Cooperative for the Disposal of Radioactive Waste (NAGRA).

Marty, N. C. M., Bildstein, O., Blanc, P., Claret, F., Cochepin, B., Gaucher, E. C., Jacques, D., Lartigue, J. E., Liu, S. H., Mayer, K. U., Meeussen, J. C. L., Munier, I., Pointeau, I., Su, D. Y., and Steefel, C. I., 2015, Benchmarks for multicomponent reactive transport across a cement/clay interface: Computational Geosciences, v. 19, no. 3, p. 635-653.

McKay, J., 1992, Clay Separation, University of Western Ohio, LSIS Technical Memorandum #92-1.

Missana, T., and García-Gutiérrez, M., 2007, Adsorption of bivalent ions (Ca (II), Sr (II) and Co (II)) onto FEBEX bentonite: Physics and Chemistry of the Earth, Parts A/B/C, v. 32, no. 8, p. 559-567.

Muurinen, A., 2011, Measurements on Cation Exchange Capacity of Bentonite in the Long-Term Test of Buffer Material (LOT), Working Report 2011-10: Eurajoki, Finland, POSIVA, p. 30.

Tajeddine, L., Gailhanou, H., Blanc, P., Lassin, A., Gaboreau, S., and Vieillard, P., 2015, Hydration–dehydration behavior and thermodynamics of MX-80 montmorillonite studied using thermal analysis: Thermochimica Acta, v. 604, p. 83-93.

Teich-McGoldrick, S. L., Greathouse, J. A., Jové-Colón, C. F., and Cygan, R. T., 2015, Swelling Properties of Montmorillonite and Beidellite Clay Minerals from Molecular Simulation: Comparison of Temperature, Interlayer Cation, and Charge Location Effects: The Journal of Physical Chemistry C, v. 119, no. 36, p. 20880-20891.

Turrero, M., Fernández, A., Peña, J., Sánchez, M., Wersin, P., Bossart, P., Sánchez, M., Melón, A., Garralón, A., and Yllera, A., 2006, Pore water chemistry of a Paleogene continental mudrock in Spain and a Jurassic marine mudrock in Switzerland: Sampling methods and geochemical interpretation: Journal of Iberian Geology, v. 32, no. 2, p. 233-258.

Vieillard, P., Tajeddine, L., Gailhanou, H., Blanc, P., and Lassin, A., 2016, Thermo-Analytical Techniques on MX-80 Montmorillonite: A Way to Know the Behavior of Water and its Thermodynamic Properties during Hydration–Dehydration Processes: Pharm Anal Acta, v. 7, p. 462.

Villar, M. V., Fernandez, A. M., Romero, E., Dueck, A., Cuevas, J., Plotze, M., Kaufhold, S., Dohrmann, R., Iglesias, R. J., Sakaki, T., Voltolini, M., Zheng, L., Kawamoto, K., and Kober, F., 2017, FEBEX-DP Post-mortem THM/THG Analysis Report, NAGRA Arbeitsbericht NAB 16-17: Wettingen, Switzerland, NAGRA, p. 187 pp.

Wilson, J. C., Benbow, S., Sasamoto, H., Savage, D., and Watson, C., 2015, Thermodynamic and fully-coupled reactive transport models of a steel-bentonite interface: Applied Geochemistry.

Xie, M. L., Mayer, K. U., Claret, F., Alt-Epping, P., Jacques, D., Steefel, C., Chiaberge, C., and Simunek, J., 2015, Implementation and evaluation of permeability-porosity and tortuosity-porosity relationships linked to mineral dissolution-precipitation: Computational Geosciences, v. 19, no. 3, p. 655-671.

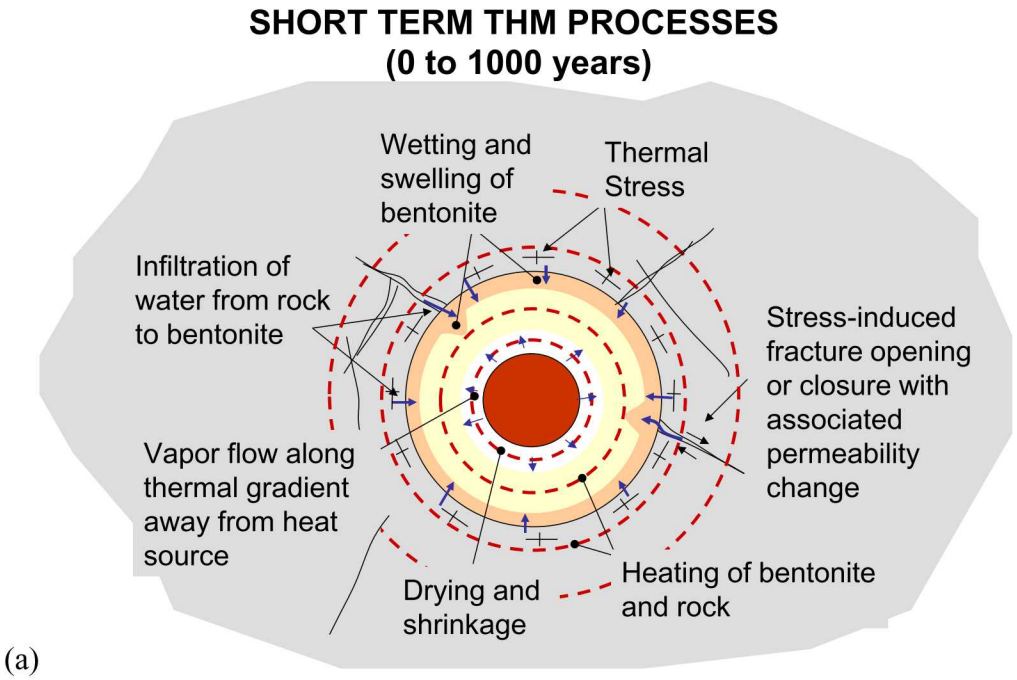
Investigation of Coupled Processes in Argillite Rock – LBNL (Part II)

1. Introduction

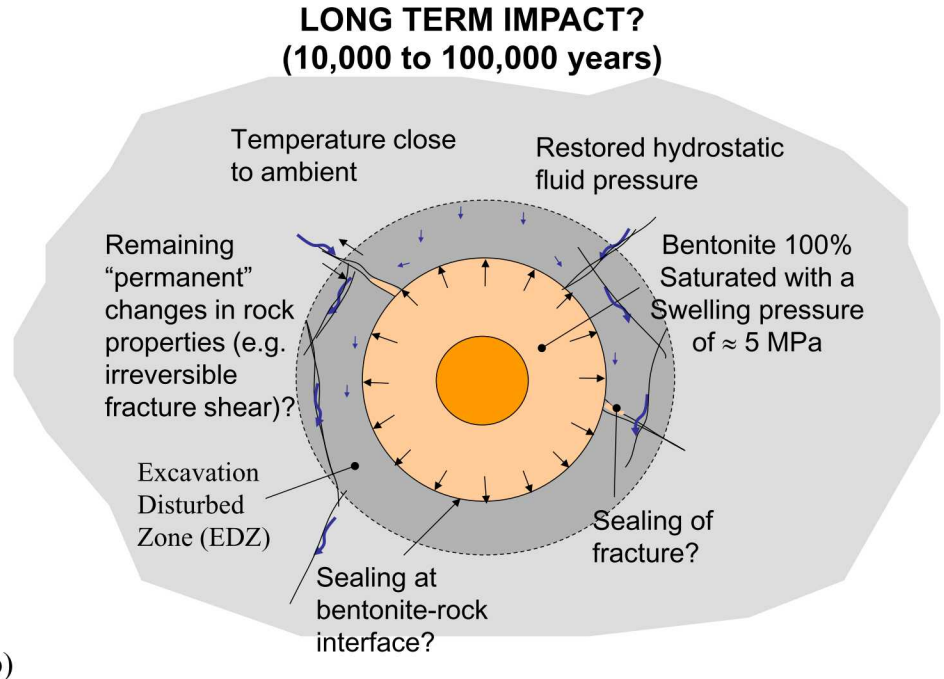
Shale and argillite geological formations have been considered as potential host rock for geological disposal of high-level radioactive waste (HLW) throughout the world because of their low permeability, low diffusion coefficient, high retention capacity for radionuclides, and capability to self-seal fractures. The low permeability of clay and shale rock are well-known in the hydrogeology community where these rock types represent aquitards that severely limit groundwater movement, and in petroleum industry, where they act as caprocks limiting the rise of buoyant petroleum fluids. While fractures can occur in such formations, argillite and shale often demonstrate the tendency to self-seal fractures, which reduces the effects of fractures on bulk permeability. Other favorable characteristics of argillite/shale are the strong sorptive behavior for many radionuclides, reducing conditions because of the lack of oxygen transport from the surface, and chemical buffering the effects of materials introduced through repository construction, operation, and emplaced materials.

The focus of research within the Spent Fuel and Waste Science and Technology (SFWST), formerly called Used Fuel Disposal (UFD), Campaign is on repository-induced interactions that may affect the key safety characteristics of engineered barrier system (EBS) bentonite and host rock. These include thermal-hydrological-mechanical-chemical (THMC) processes that occur because of repository construction and waste emplacement. Some of the key questions addressed in this part of the report include the formation of an excavation damaged zone (EDZ) near tunnels and the evolution of near field coupled thermo-hydro-mechanical (THM) processes after waste emplacement. In particular, this part of the report describes our efforts to model these processes with confidence.

Within the SFWST program, LBNL's work on argillite disposal research & development (R&D) started in 2010 by leveraging on previous experience on coupled THM processes modeling within domestic and international nuclear waste programs (Rutqvist et al., 2001; 2002; 2011). Much of this work has been dedicated to develop and validate coupled THM simulators for the modeling of near-field coupled processes. Such near-field coupled processes are relatively short-lived from a safety assessment perspective, but could give rise to permanent changes, such as the formation of a thermally altered or damaged zone around excavations that could provide a path for transport of radionuclides if released from a waste package (Figure 1-1). For a repository hosted in clay-rock, the mechanical evolution and swelling of the protective buffer surrounding the waste package (often bentonite) are imperative to its functions, such as to provide long-term mechanical support to seal the EDZ. At the same time, the mechanical evolution of the buffer is governed by complex coupled interactions with temperature and hydraulics, between micro and macro clay structures, as well as with the host rock. Currently, more advanced constitutive mechanical models are being applied, but those require a large number of input parameters for describing processes at the different structural levels. It is therefore important to test and validate these models at a relevant field scale, in addition to verification and validation against independent analytical and numerical solutions and well-controlled laboratory experiments.



(a)



(b)

Figure 1-1. Schematic illustration of coupled THM processes driven by heat released from the waste package: (a) short-term THM processes, and (b) long-term impact of early time coupled THM processes.

LBNL is developing two complementary coupled simulation approaches to model THM processes (Figure 1-2). TOUGH-FLAC, based on linking LBNL's TOUGH2 multiphase fluid flow simulator with the FLAC3D geomechanics code, provides an efficient continuum modeling approach with state-of-the-art constitutive models for bentonite and host rock (Rutqvist et al., 2002; Rutqvist 2011; 2017). The complementary TOUGH-RBSN simulator, based on linking the TOUGH2 simulator with the Rigid-Body-Spring Network (RBSN) model, enables explicit modeling of discrete fractures and fracturing (Asahina et al. 2014; Kim et al., 2017). The TOUGH-RBSN is most suitable for detailed analysis of fracturing in laboratory samples as well as within the EDZ, whereas TOUGH-FLAC enables modeling of the evolution of the EBS, EDZ and surround host rock at a larger scale (Figure 1-2). TOUGH-FLAC with appropriated constitutive models is also used to calculate the evolution of the permeability and transport properties in the EDZ that can then be provided as input to future safety assessment models and Generic Disposal Systems Analysis (GDSA).

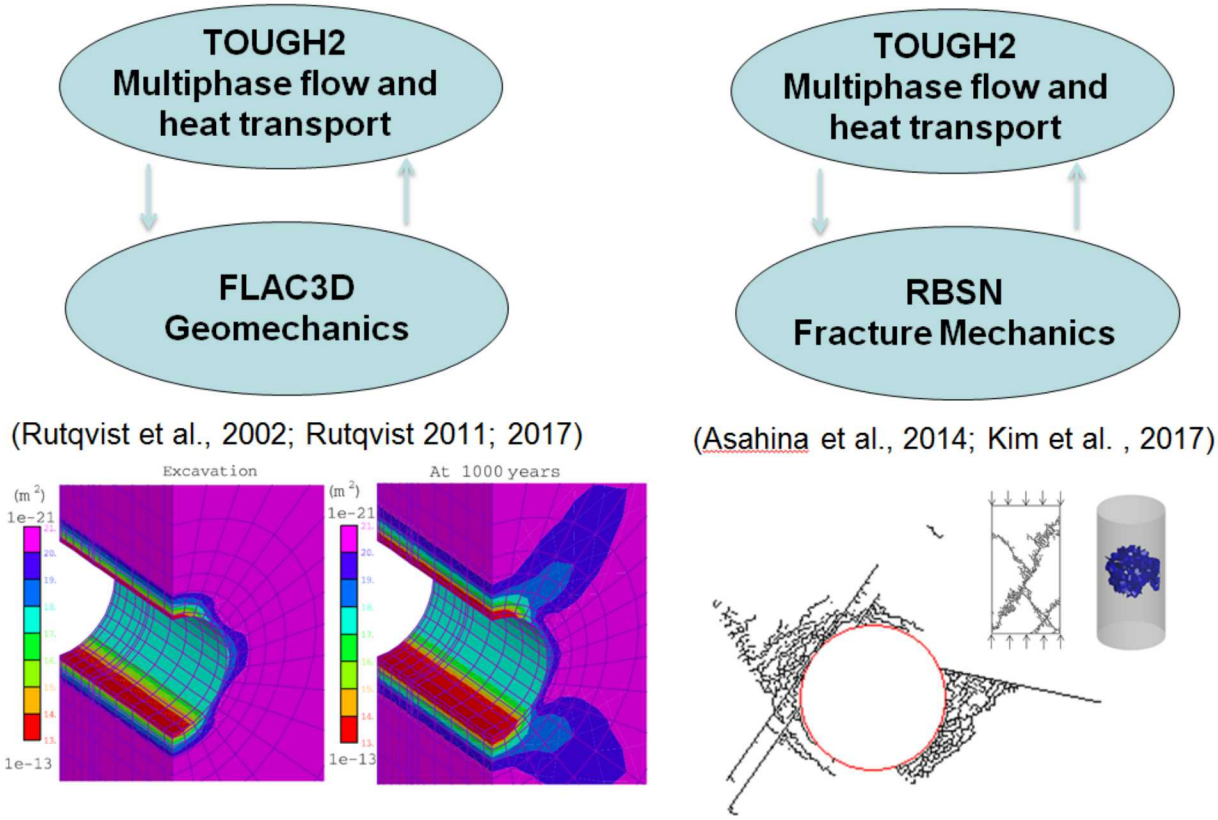


Figure 1-2. TOUGH-FLAC (left) and TOUGH-RBSN (right) models developed for coupled THM process analysis.

In this part of the report, we present our FY2018 progress on these activities. The document delivers milestone M3SF-18LB010301031 "Investigation of Coupled Processes in Argillite Rock" in the LBNL Argillite R&D Work Package (SF-18LB01030103) with input from Activity SF-18LB010301071 "LBNL FY18 Argillite International Collaboration" in the LBNL Argillite International Collaboration Work Package (SF-18LB01030107). These activities address key Features, Events, and Processes (FEPs), which have been ranked in importance from medium to high, as listed in Table 7 of the Used Fuel Disposition Campaign Disposal Research and Development Roadmap (FCR&D-USED-2011-000065 REV 1) (Nutt, 2012). Specifically, they address FEP 2.2.01, Excavation Disturbed Zone, for clay/shale, by investigating how coupled processes affect EDZ evolution; FEP 2.2.05, Flow and Transport Pathways; and FEP 2.2.08, Hydrologic Processes, and FEP 2.2.07, Mechanical Processes, as well as FEP 2.2.12, Gas Sources and Effects.

The activities documented in this part of the report also address a number of research topics identified in Research & Development (R&D) Plan for Used Fuel Disposition Campaign (UFDC) Natural System Evaluation and Tool Development (Wang 2011), including Topics S3, Disposal System Modeling – Natural System; P1, Development of Discrete Fracture Network (DFN) Model; P14, Technical Basis for Thermal Loading Limits; and P15, Modeling of Disturbed Rock Zone (DRZ) Evolution (Clay Repository).

In the following Sections 2 and 3 we present the current status of the TOUGH-FLAC and TOUGH-RBSN simulators for modeling coupled THM processes in argillite, including fracturing. This is followed in Sections 4 and 5 by validation of the TOUGH-FLAC model against major *in situ* heater experiments at the Mont Terri Underground Research Laboratory (URL) in Switzerland and at the URL in Bure, France. The heater experiments modeled are the Mont Terri FE (Full-scale Emplacement) Experiment, conducted as part of the Mont Terri Project, and the TED and ALC experiments conducted in Callovo-Oxfordian claystone (COx) at the Meuse/Haute-Marne (MHM) URL in Bure, France. The modeling of the TED and ALC heater experiments is part of a modeling task (Task E) of the international DECOVALEX-2019 project. DECOVALEX, which stands for DEvelopment of COupled Models and their VALidation against EXperiments, is an international collaborative activity, in which DOE and LBNL gain access to unique laboratory and field data defined as modeling test cases. DECOVALEX tasks are studied collectively among several international groups to better understand the processes and to improve numerical models that could eventually be applied in the performance assessment for nuclear waste disposal in clay host rocks and bentonite backfill. Section 6 presents LBNL's activities for modeling gas migration in bentonite related to another task (Task A) of the international DECOVALEX project. In Section 7, we present new FY2018 work related to monitoring and characterization of faults using a unique borehole tool. Finally, in Section 8, we conclude with a summary of achievements in FY2018, planned work for the rest of FY2018, and proposed work for FY2019.

2. Status of TOUGH-FLAC Simulator

The TOUGH-FLAC simulator (Rutqvist et al., 2002; Rutqvist, 2011), used within the SFWST Argillite R&D work package, has been adapted for modeling coupled THM processes associated with bentonite backfilled repositories in argillite host rocks. For rigorous modeling of the THM behavior of bentonite-based (swelling) buffer and back-fill materials, the BBM (Barcelona Basic Model) and BExM (Barcelona Expansive Model) have been implemented into TOUGH-FLAC

(Rutqvist et al., 2011; 2014b; Vilarrasa et al., 2016). Constitutive models to describe anisotropic THM behavior of shale rocks have also been adapted. This model development has been accompanied by extensive testing, verification and validation, including participation within international collaborative projects such as DECOVALEX. In the following subsections we present more details on the status of the TOUGH-FLAC, including the status of the numerical framework for coupled THM modeling and geomechanical constitutive models, followed by a list of completed verification and validation examples, as well as new verifications against analytical solutions.

2.1 TOUGH-FLAC Framework

As mentioned in the introduction, the TOUGH-FLAC simulator (Rutqvist 2011; 2017), is based on linking the TOUGH2 multiphase flow and heat transport simulator (Pruess et al., 2012) with the FLAC3D geomechanical simulator (Itasca 2011). In this approach, TOUGH2 (Pruess et al., 2012) is used for solving multiphase flow and heat transport equations, whereas FLAC3D (Itasca, 2011) is used for solving geomechanical stress-strain equations.

For analysis of coupled THM problems, TOUGH2 and FLAC3D are executed on compatible numerical grids and linked through a coupled THM model (Figure 2-1) with coupling functions to pass relevant information between the field equations, which are solved in the respective codes. In the coupling scheme between TOUGH2 and FLAC3D, the TOUGH2 multiphase pressures, saturation, and temperature are provided to update temperature, and pore pressure to FLAC3D (Figure 2-1). After data transfer, FLAC3D internally calculates thermal expansion, swelling, and effective stress. Conversely, element stress or deformation from FLAC3D is supplied to TOUGH2 to correct element porosity, permeability, and capillary pressure for the fluid-flow simulation in TOUGH2. The corrections of hydraulic properties are based on material-specific functions.

In a TOUGH-FLAC simulation, the calculation is stepped forward in time with the transient multiphase fluid flow analysis in TOUGH2, and at each time step or at the TOUGH2 Newton iteration level, a quasi-static mechanical analysis is conducted with FLAC3D to calculate stress-induced changes in porosity and intrinsic permeability (Figure 2-2). In this scheme, the fluid-flow sequence is solved first under fixed stress with a porosity correction $\Delta\Phi_c$ derived from the constitutive equations of solid:

$$\mathrm{d}\Phi = \left(\frac{b^2}{K} + \frac{b-\phi}{K_s}\right)\mathrm{d}p + \phi\alpha_s \mathrm{d}T - \Delta\Phi_c \tag{2.1}$$

$$\Delta\Phi_c = -\frac{b}{K}\mathrm{d}\sigma_v = -\frac{b}{K}(K\mathrm{d}\epsilon_v - b\mathrm{d}p - K\alpha\mathrm{d}T) \tag{2.2}$$

where K is the bulk modulus of porous medium, K_s is the bulk modulus of solid skeleton, b is the Biot's coefficient, p is the pore pressure, ϕ is the porosity, α_s is the volumetric thermal expansion coefficient of solid grains, T is the absolute temperature, σ_v is the mean stress, and ϵ_v is the volumetric strain. The resulting pressure and temperature are prescribed in the mechanical sequence. This corresponds to so-called stress-fixed iterations in the sequential scheme, in which the solution becomes unconditionally stable. The resulting THM analysis may be explicit sequential, meaning that the porosity and permeability is evaluated only at the beginning of each time step, or the analysis may be implicit sequential, with permeability and porosity updated on the Newton iteration level toward the end of the time step using an iterative process.

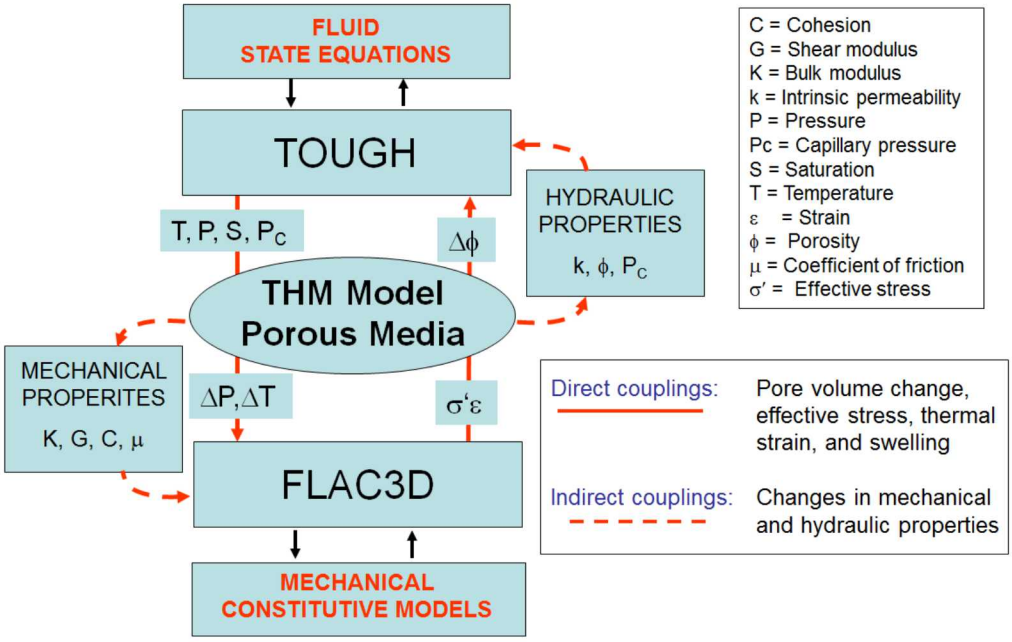


Figure 2-1. Schematic of linking of TOUGH2 and FLAC3D in a coupled TOUGH-FLAC simulation.

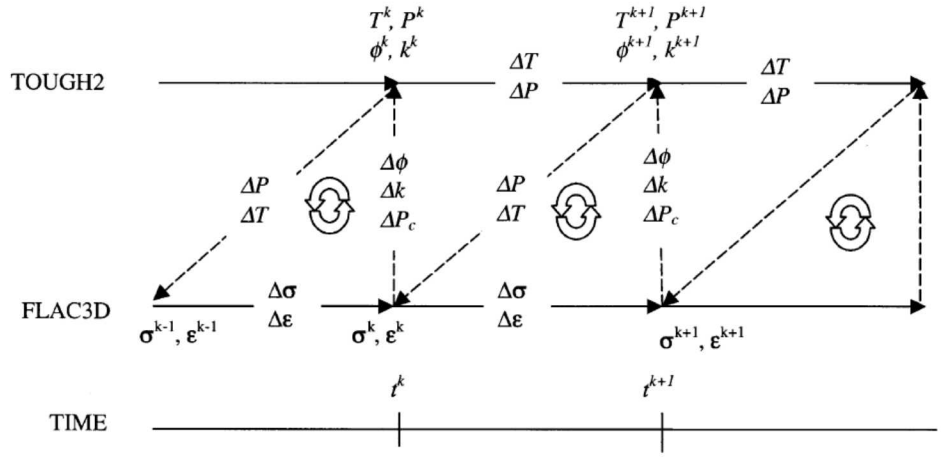


Figure 2-2. Numerical procedure of a linked TOUGH2 and FLAC3D simulation with subscript k signifying time step.

2.2 Bentonite Constitutive THM Models in TOUGH-FLAC

Since 2010, the TOUGH-FLAC simulator has been adapted and applied to issues related to nuclear waste disposal with bentonite backfilled tunnels (Rutqvist et al., 2011; 2014b). This includes implementation of the BBM (Alonso et al., 1990) for the mechanical behavior of unsaturated soils, which has been applied for modeling of bentonite backfill behavior (Rutqvist et al., 2011). The model can describe many typical features of unsaturated soil mechanical behavior, including wetting-induced swelling or collapse strains, depending on the magnitude of applied stress, as well

as the increase in shear strength and apparent preconsolidation stress with suction (Gens et al., 2006). Figure 2-3 presents the yield surface of the BBM model in *q-p-s* space. The shaded surface corresponds to the elastic region at fully water-saturated conditions. The figure also shows how the yield surface expands at unsaturated and dryer conditions when suction increases. There is an increase in both the apparent pre-consolidation pressure along the load collapse (LC) yield surface and by the increasing tensile strength, which in turn leads to an increased cohesion and shear strength.

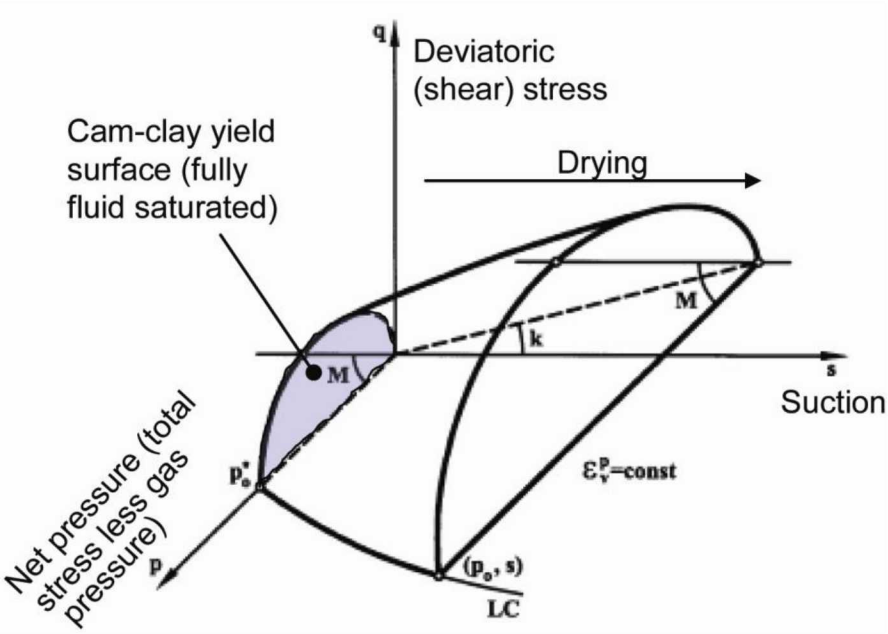
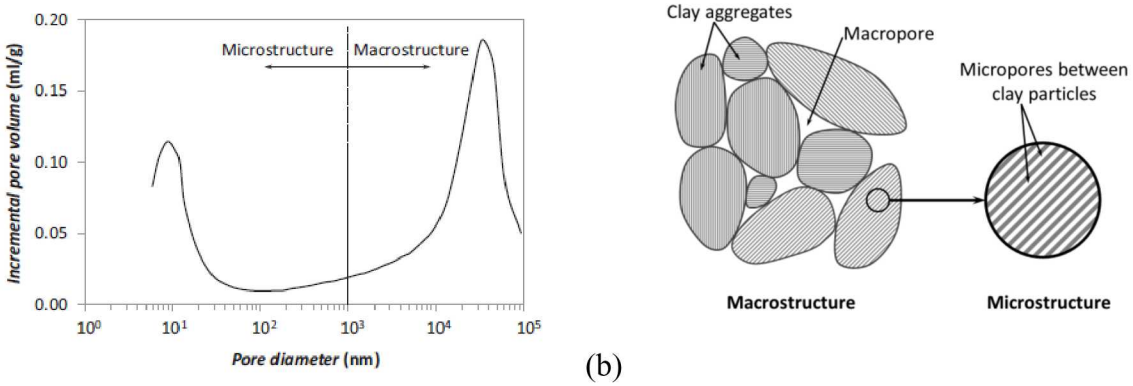


Figure 2-3. BBM constitutive model showing the yield surface in q-p-s space.

The BBM has been used for modeling bentonite-buffer behavior in various national nuclear waste programs in Europe and Japan. For example, the BBM was successfully applied to model the coupled THM behavior of unsaturated bentonite clay associated with the full-scale engineered barrier experiment (FEBEX) *in situ* heater test at the Grimsel Test Site, Switzerland (Gens et al., 2009). The BBM has also been applied to other types of bentonite-sand mixtures based on MX-80, considered as an option for an isolating buffer in the Swedish KBS-3 repository concept (Kristensson and Åkesson 2008). As part of the Used Fuel Disposition (UFD) program, the BBM was also used by Rutqvist et al. (2014b) for modeling of coupled THM processes around a generic repository in a clay host formation. In the last few years, as part of the UFD and current SFWST program, the BBM has been extended to a dual-structure model, corresponding to the Barcelona Expansive Model (BExM). In a dual-structure model, the material consists of two structural levels: a microstructure in which the interactions occur at the particle level, and a macrostructure that accounts for the overall fabric arrangement of the material comprising aggregates and macropores (Figure 2-3) (Gens et al., 2006, Sánchez et al., 2005, Gens and Alonso 1992). A dual-structure model has important features for modeling the mechanical behavior of a bentonite buffer, such as irreversible strain during suction cycles. Moreover, a dual-structure model provides the necessary

link between chemistry and mechanics, enabling us to develop a coupled THMC model for the analysis of long-term EBS behavior. This approach enables mechanistic modeling of processes important for long-term buffer stability, including effects of pore-water salinity on swelling (loss of swelling), conversion of smectite to nonexpansive mineral forms (loss of swelling), and swelling pressure versus exchangeable cations. Details of the development, testing and applications of the dual-structure model, were first presented in the FY2014 UFD milestone report titled "Investigation of Coupled THMC Processes and Reactive Transport: FY14 Progress" (Rutqvist et al. 2014a) and have also been published in a journal paper (Vilarrasa et al., 2016).



(a) (b)

Figure 2-4. (a) Pore size distribution, and (b) schematic representation of the two structural levels considered in the dual structure model. Clay particles are represented by the gray lines (Vilarrasa et al., 2016).

The model implementation of BExM was further tested and validated as documented in the FY2016 milestone report titled "DR Argillite Disposal R&D at LBNL" (Zheng et al., 2016) by modeling (1) one swelling pressure test on Boom clay pellets, (2) two cyclic wetting-drying tests on one type of expansive clay, and (3) two tests with combination of loading paths on compacted bentonite samples. Based on the simulation results, the model is capable to reproduce the observed behavior of expansive clays during experiments associated with suction changes. The computation results we obtained with BExM agree well with the experiment data, and also follow the same tendency of results presented by BExM developers. However, considerable uncertainties still exists in the use of the BExM model, because of complexities in the underlying processes and the large number of parameters needed to define the constitutive dual-structure behavior of clays.

2.3 Shale Constitutive THM Models in TOUGH-FLAC

Through modeling of a number of *in situ* experiments at Mont Terri and Bure underground research laboratories (URL's), constitutive models for coupled THM behavior of clay stone (or shale) have been developed and adapted. Modeling of these *in situ* experiments and other field studies have shown that it is important to consider anisotropic properties of shale elasticity, strength, thermal conductivity, permeability and thermal expansion.

The FLAC3D ubiquitous joint model can handle anisotropic strength properties of shale, and this model has been commonly used for geomechanical modeling of Opalinus Clay at Mont Terri (Corcum and Martin, 2007). The theory and implementation of this model in FLAC3D is described

in the FLAC3D manual (Itasca, 2011). The model accounts for the presence of an orientation of weakness (weak plane) in a Mohr-Coulomb constitutive model. The criterion for failure on the planes, of a given orientation is based on the escalation of a composite Mohr-Coulomb envelope with tension cutoff. The rock-strength input parameters includes fiction angle and tension cutoff with weaker properties for the weak (joint) planes compared to that of the intermediate intact rock. Figure 2-5 shows the results of a simulation involving a horizontal emplacement tunnel in Opalinus Clay with horizontal bedding (Rutqvist et al., 2014). On top and bottom of the emplacement tunnel we can see shear failure that occurred along bedding planes.

The results of modeling of heater experiments at Mont Terri and Bure showed the need to take into account anisotropic thermal conductivity to match temperature measurements at the experiments (Garitte et al., 2017). Anisotropic thermal conductivity is not standard in TOUGH2 and TOUGH-FLAC and was implemented into the TOUGH2 source code. Anisotropic permeability can be considered in the standard TOUGH2 code for rectilinear grid.

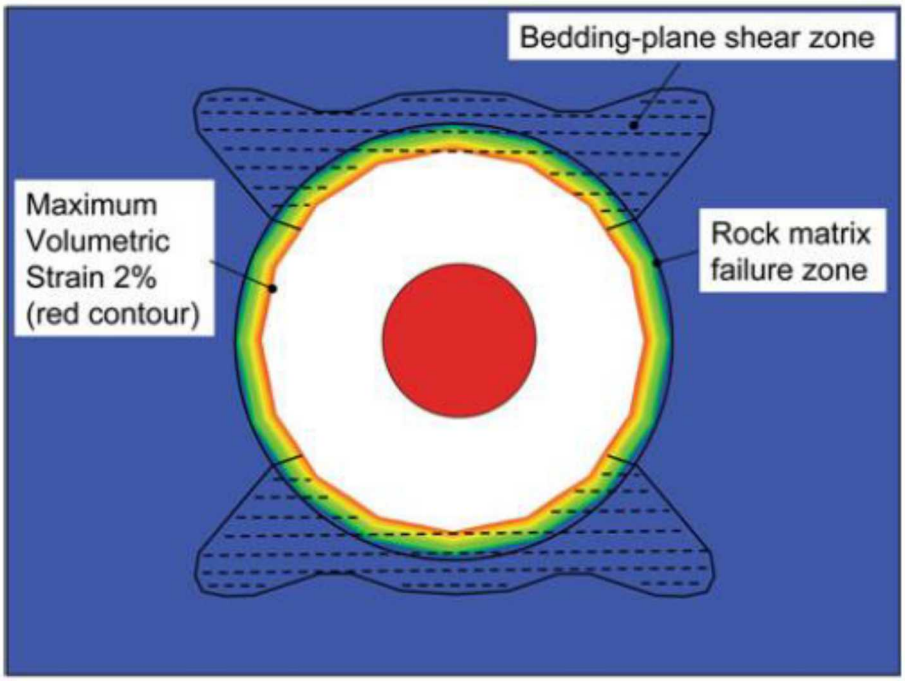


Figure 2-5. Volumetric strain contour and extent of failure zones related to horizontal bedding planes and rock matrix (Rutqvist et al., 2014).

2.4 EDZ Models in TOUGH-FLAC

The EDZ is one of the most important features taken into account in the performance assessment of repositories in argillite, and was assigned the highest research priority ranking in the 2012 UFD Road Map (Nutt, 2012). Models of different sophistications have been developed and applied to model the EDZ using TOUGH-FLAC, including

1) Empirical stress-permeability model;

2) Non-linear elastic and brittle failure model; and

3) Anisotropic continuum damage model.

The three models are summarized in the following subsections.

2.4.1 Empirical stress-permeability model

An empirical stress-permeability model calibrated against *in situ* EDZ data is described in Rutqvist (2015). The empirical EDZ model was applied in a previous phase of the DECOVALEX project related to nuclear waste disposal in crystalline rock (Rutqvist et al., 2009). The empirical EDZ model was calibrated against EDZ data from the TSX experiment conducted at the underground research laboratory in Manitoba, Canada (Martino et al., 2004).

The permeability around the tunnel was simulated using the empirical stress-permeability relationship in which permeability is a function of the effective mean stress, σ'_m, and deviatoric stress, σ_d, according to (Rutqvist et al., 2009):

$$k = [k_r + \Delta k_{\max} \exp(\beta_1 \sigma'_m)] \cdot \exp(\gamma \Delta \sigma_d) \tag{2.3}$$

where k_r is residual (or irreducible) permeability at high compressive mean stress, Δk_{max}, β_1 and γ are fitting constants, and $\Delta\sigma_d$ is the change in deviatoric stress relative to a critical deviatoric stress for onset of shear-induced permeability.

Figure 2-6 compares simulated and measured permeability changes for $\beta_1 = 4\times10^{-7}$ Pa^{-1}, $k_r = 2\times10^{-21}$ m^2, $\Delta k_{max} = 8\times10^{-17}$ m^2, $\gamma = 3\times10^{-7}$ Pa^{-1}, and with the critical deviatoric stress for onset of shear-induced permeability set to 55 MPa. The 55 MPa critical deviatoric stress roughly coincides with the extent of a cluster of microseismic events at the top of the tunnel and to about 0.3 of the instantaneous uniaxial compressive stress of small-scale core samples, which is consistent with the stress level at which crack initiation has been observed in studies of Lac du Bonnet granitic samples (Martin and Chandler, 1994).

Based on the relationship calibrated against field measurements of EDZ during excavation, a model prediction of the longer term EDZ evolution of a nuclear waste emplacement tunnel was conducted (Ngyuen et al., 2009). Figure 2-7 present the EDZ permeability distribution after excavation and at 1000 years after emplacement when the thermal-mechanical stress might be the highest. Figure 2-7 shows that there is some increase in EDZ permeability at 1000 years compared to that after excavation, though the changes are small.

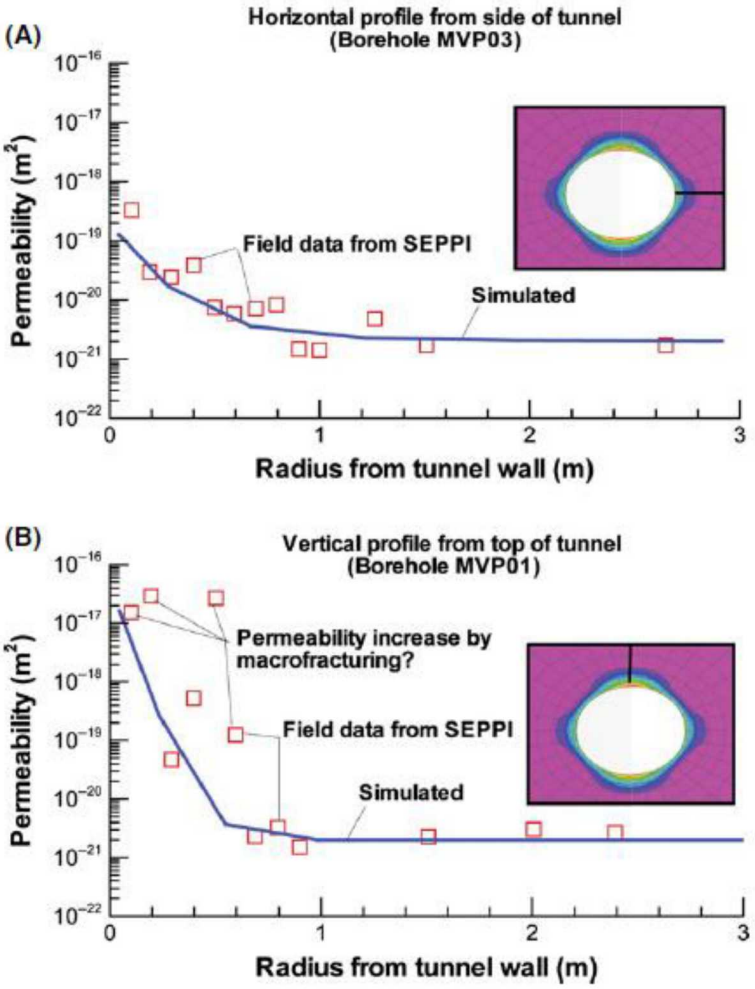


Figure 2-6. Simulated and measured permeability changes around the TSX tunnel (Rutqvist et al. 2009). Permeability versus radius along (A) a horizontal profile from the side of the tunnel, and (B) a vertical profile from the top of the tunnel.

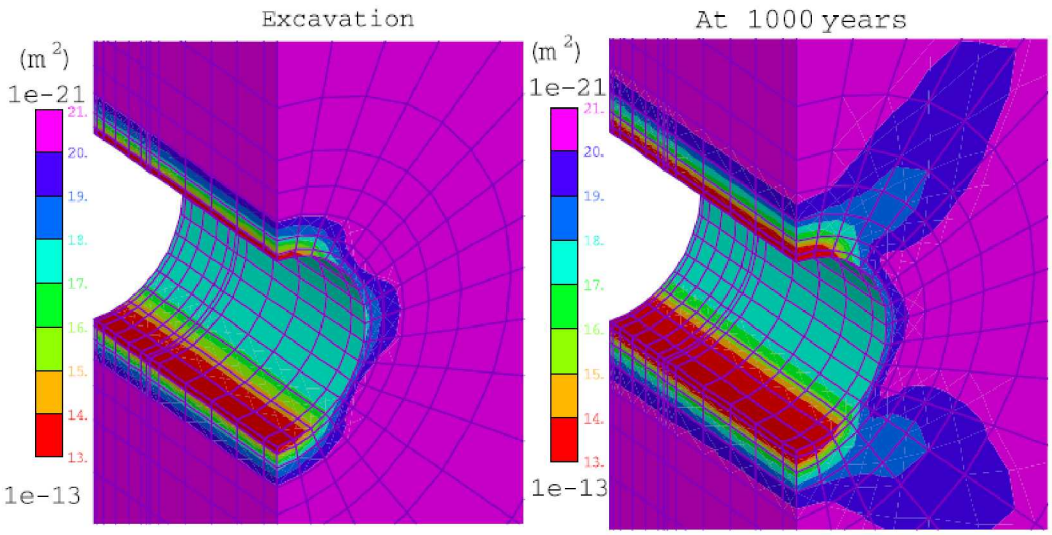
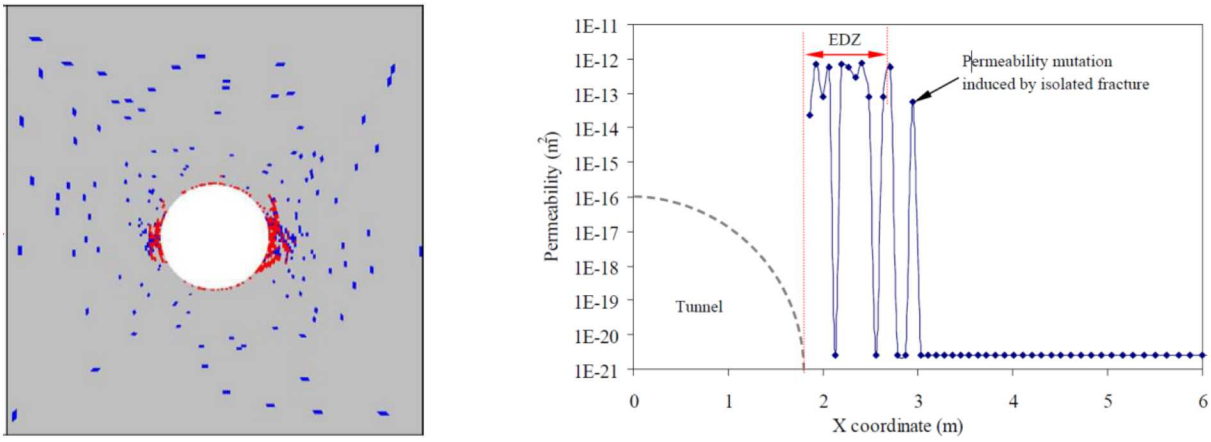


Figure 2-7. Calculated permeability distribution for generic repository emplacement tunnel in crystalline rocks using the empirical stress-permeability relation (Nguyen et al., 2009).

2.4.2 Non-linear elastic and brittle failure model

A non-linear elastic and brittle failure model was implemented in TOUGH-FLAC and demonstrated in the FY2012 Milestone Report titled "Report on Modeling Coupled Processes in the Near Field of a Clay Repository" (Liu et al., 2012). The non-linear elastic model, denoted the two-part Hooke's model (TPHM), provided a new constitutive relationship, and associated formulations regarding rock hydraulic/mechanical properties. The usefulness and validity of the TPHM were demonstrated by the consistence between simulation results and field observations at the Mont Terri URL. The brittle failure model was applied using a fine-grid numerical approach, based on the explicit incorporation of small-scale heterogeneity of mechanical properties. Using the combination of the TPHM and the fine-grid numerical approach of the results of investigations were compared with field results at Mont Terri.

Figure 2-8 shows the example of calculated brittle failure and permeability changes around a tunnel in a host rock representing Oplalinus Clay. The model simulation captured both the observed displacements and the size of the damage zone. Moreover, the fine-grid numerical approach, together with an explicit incorporation of the small-scale heterogeneity of mechanical properties, was able to capture the overall behavior of the EDZ, as demonstrated by the consistency between the simulated and the observed EDZ size, which was about 1 m on the side of the tunnel. The calculated hydraulic conductivity values are especially high in the EDZ within the tunnel sidewalls, varying between 2.39×10^{-14} m^2 and 7.45×10^{-13} m^2, is consistent with measured data at the Mont Terri Laboratory (Bossart et al., 2002; Bossart et al., 2004). Such a model validated against field data could also be used to calculate EDZ evolution over the longer term. However, while the current model addresses permeability changes induced during excavation, it does not address sealing and healing processes that might be important over the long term.



(a) (b)

Figure 2-8. (a) Calculated brittle failure and (b) permeability changes around an excavation in argillite (Liu et al., 2012).

2.4.3 Anisotropic continuum damage model

In FY2017, an anisotropic damage model named Deviatoric Stress Induced Damage (DSID) was implemented into the simulator to account for crack propagation due to microstructure changes (Zheng et al., 2017). This new damage model is hyper-elastic, i.e., the stress-strain relationship was derived from the expression of a thermodynamic potential, and was derived based on Continuum Damage Mechanics (CDM), which avoids to model cracks at the micro-scale, as opposed to micro-mechanics. Damage effects are analyzed at the scale of Representative Elementary Volume (REV) with the concept of effective stress to account for the reduction of undamaged areas (Chaboche, 1992). REV is the smallest volume over which a measurement can be made that will yield a value representative of the whole, and it ranges from 10^{-3} m to 0.1 m, depending on the material and the focused problem. The model implementation has been validated by comparison with modeling several laboratory experiments on granite and by comparing computation results with different codes. The agreements on simulation results proved the damage model was implemented correctly in our simulator and was capable to reproduce the same non-linear mechanical behavior due to damage propagation. For instance, the damage model was utilized to predict the evolution of the disturbed rock zone (DRZ) around emplacement tunnels, where the model enabled to capture the micro-crack propagation induced by the excavation (Figure 2-9).

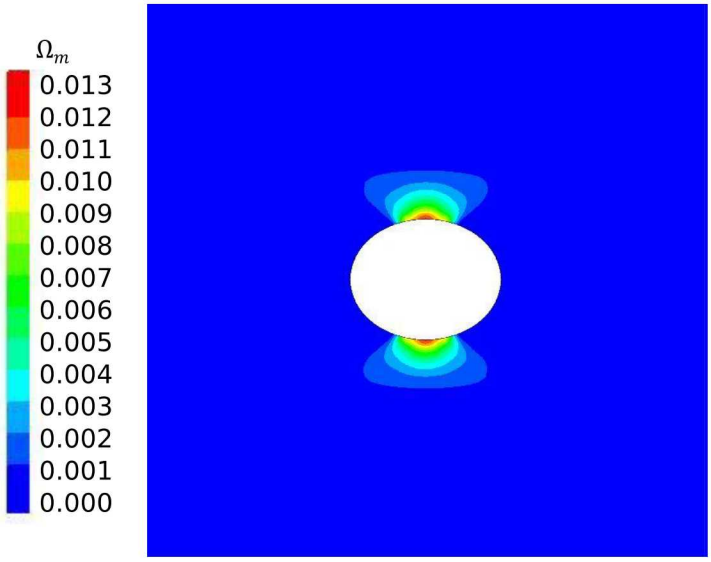


Figure 2-9. The simulation result of damage distribution at TSX experiment.

3. Status of TOUGH-RBSN Simulator for Coupled Fracturing Processes

The TOUGH-RBSN simulator (Asahina et al., 2014; Kim et al., 2017) has been used for modeling coupled THM processes related with fracture/damage behavior. The individual physical processes related to fracture propagation are represented by separate program modules: the TOUGH2 code for multiphase flow and mass transport based on the finite volume approach; and the rigid-body-spring network (RBSN) model for mechanical and fracture-damage behavior, which are sequentially coupled with each other. The discrete fracture network (DFN) approach is adopted in the coupling procedure, where fractures have enhanced flow properties as well as degraded mechanical properties in a discrete manner. This section presents more details on the TOUGH-RBSN simulator, including the status of the numerical framework for THM coupling procedure, modeling of discrete fractures for enhanced flow in the TOUGH2 code, and fracture determination in the RBSN approach.

3.1 TOUGH-RBSN Coupling Procedure

Figure 3-1 shows a schematic flow diagram of the coupling procedure between the TOUGH2 and RBSN codes. Coupling modules are implemented in each side of the modeling codes, by which material properties and mechanical boundary conditions are updated with the outputs of primary variables of physical quantities. Pore pressure and degree of saturation are primary variables of the TOUGH2 analysis, which are involved in the RBSN simulation to determine the effective stress and swelling/shrinkage strain. In return, the primary variables of the RBSN model, stress/strain states, damage index, and fracture aperture, are used to evaluate hydrological properties and conditions for the TOUGH2 simulation.

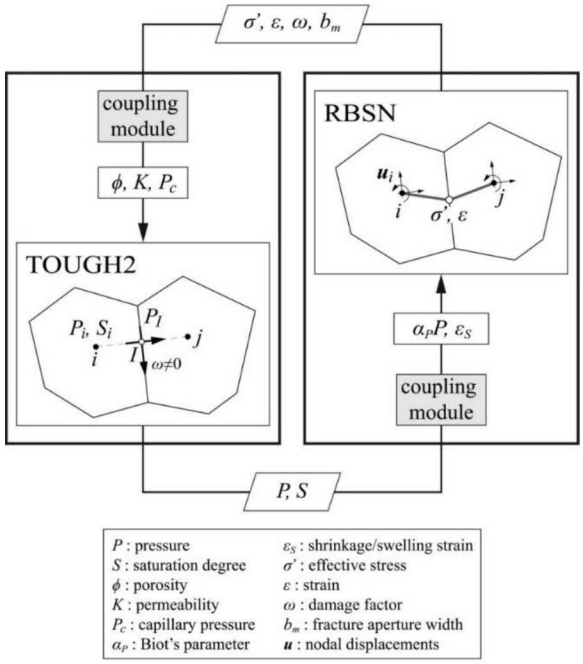


Figure 3-1. Coupling procedure of the TOUGH-RBSN simulator (adapted from Kim et al., 2017).

First, the TOUGH2 to RBSN link supplies pressure and degree of saturation to update the mechanical quantities. Based on the linear poro-elasticity theory, the effective (grain-to-grain) stress $\sigma_n{}'$ is calculated from the pore pressure P (Biot and Willis, 1957):

$$\sigma_n{}' = \sigma_n + \alpha_p P \tag{3.1}$$

where σ_n is the total normal stress obtained from overall loading, including external loads; α_p is Biot's effective stress parameter. Note that tensile stress is taken to be positive for the sign convention. Also, the shrinkage/swelling effect due to the local changes of liquid saturations ΔS can be taken into account:

$$\Delta\varepsilon_s = \alpha_s \Delta S \tag{3.2}$$

where ε_s is shrinkage/swelling strain; and α_s is the moisture swelling coefficient. If a poro-elastic geomaterial is subjected to confinement conditions, the stress due to swelling/shrinkage can be calculated as

$$\Delta\sigma' = \Delta\varepsilon_s E \tag{3.3}$$

where E is the Young's modulus.

The fracture process of a local rigid-body-spring element is realized by degrading the springs. A fracture event entails a reduction of spring stiffnesses and a release of the associated elemental forces. For the degraded spring set, the modified stiffness matrix $\mathbf{D}'$ is

$$\mathbf{D}' = (1 - \omega)\mathbf{D} \tag{3.4}$$

where ω is a scalar damage index with a range from zero (undamaged) to 1 (completely damaged). For brittle fracturing, which is applied to the cases presented in this part of the report, ω is directly switched from 0 to 1 once a fracture event occurs (i.e., the stress state of an element violate the failure criteria).

Next, the RBSN to TOUGH2 link supplies the effective stress and the strain calculated in the lattice element to update the hydrological properties of the corresponding TOUGH2 grid blocks *i* and *j* on the left side of Figure 3-1. Porosity, permeability, and capillary pressure are generally related with the effective stress and strain values (Rutqvist and Tsang, 2002).

If fracturing occurs at element *ij* (i.e., $\omega \neq 0$), the associated fracture node *I* and additional connections are activated in the TOUGH2 model. The permeability of an individual fracture depends on the hydraulic aperture b_h (Witherspoon et al., 1980). According to a parallel-plate model, the fracture permeability is defined as $b^2/12$. The hydraulic aperture is coupled to the mechanical aperture b_m (Rutqvist et al., 1998, 2000):

$$b_h = f(b_r + \langle b_m - b_r \rangle) \tag{3.5}$$

where $\langle x \rangle = 1/2(x + |x|)$ represents Macaulay brackets, and b_r is the residual hydraulic aperture. $f \leq 1.0$ is a dimensionless factor that accounts for the slowdown of flow in a natural rough fracture in comparison to the ideal case of parallel smooth fracture surfaces.

In the TOUGH-RBSN sequential coupling, TOUGH2 is a main driver of analysis, which controls the time stepping during the coupling procedure, while the RBSN approach solves the mechanical response as a quasi-static process at each time step. The selection of small time steps is important to find stable solutions of the mechanical response, so the TOUGH2 input defines the upper limit for time step size with a small value to avoid any abrupt change of hydrological conditions over time steps.

3.2 Model Discretization and Discrete Fracture Representation

The computational domain for both the TOUGH2 and RBSN calculations is tessellated using a Voronoi diagram (Okabe et al.,2000). The discretization process is carried out basically in three Steps: 1) nodal point insertion, 2) Delaunay tessellation, and 3) Voronoi discretization. Within the domain, nodal points are positioned in regular or irregular formation. Introducing a parameter for minimum allowable distance can define the desired nodal density of the unstructured grid. The Delaunay tessellation is conducted based on the nodal positions, where each Delaunay edge defines the nodal connection of the corresponding lattice element. Through the dual Voronoi tessellation, the spatial domain is collectively filled with discrete polyhedral cells that render the elemental volumes. More detailed procedure of the domain partitioning is presented elsewhere (Yip et al., 2005; Asahina and Bolander, 2011).

For the discrete fracture network (DFN) approach, fractures and such discontinuities are explicitly modeled within the Voronoi grid. Voronoi cells generally represent the matrix component in a geomaterial constitution, and pre-existing or newly generated fractures are placed on the Voronoi cell boundaries. The geometry of fracture networks (e.g., orientation, length, curvature) can be obtained by observational mapping data, computer-generated statistical reproductions, or

mechanical simulation results. An example of the discretization procedure in 2D modeling involving a straight fracture is as follows:

1. Generate a Voronoi unstructured grid for the spatial domain,
2. Overlay the reference fracture trajectory onto the grid,
3. Test all connections of natural neighboring nodes to check if they cross the fracture. For example, compare connections *ij* and *jk* in Figure 3-2, and
4. Collect the Voronoi cell boundaries corresponding to the nodal connections that cross the reference fracture (such as *ij*) and form discretized fractures.

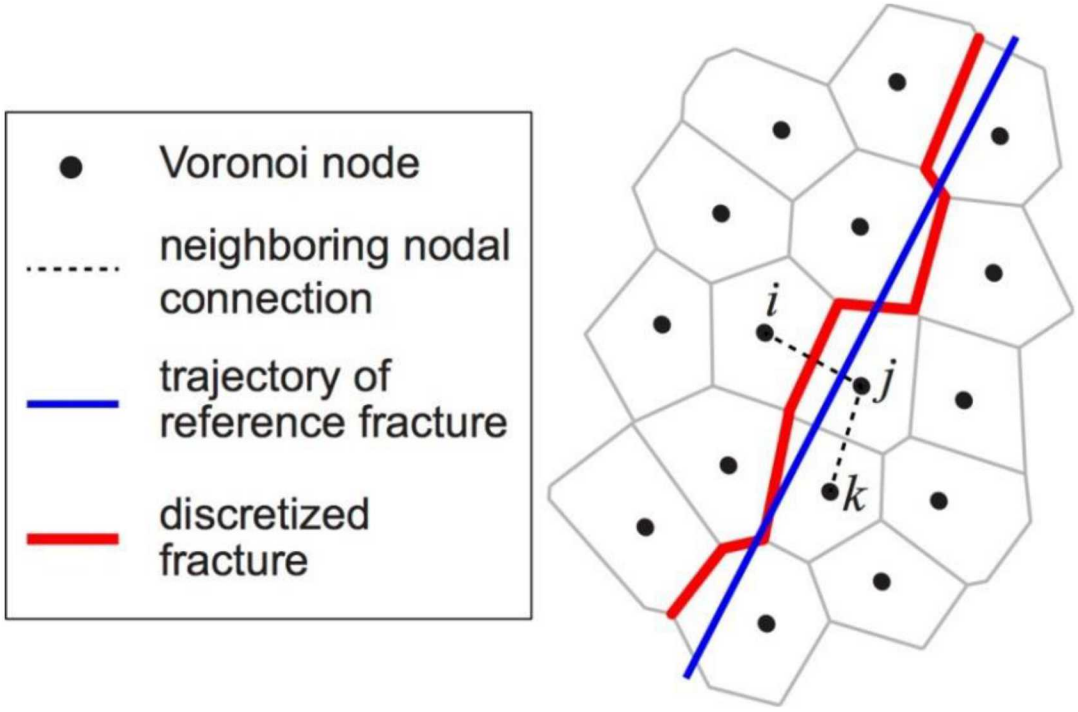


Figure 3-2. Fracture mapping and discretization within an unstructured Voronoi grid (adapted from Asahina et al., 2014).

By repeating the above process for multiple fractures, a network of discrete fractures can be generated. This fracture discretization process is completely automated and can be easily extended to more complicated geometries in 3D modeling. However, the grid size should be carefully chosen to obtain a sufficiently precise representation of the reference fracture. A finer grid can accommodate the discretized fractures that conform more closely to the reference fracture.

In the simulations using a grid structure of the ordinary Voronoi discretization, flow and mass transfer are enacted only through the connections of the neighboring Voronoi nodes (called cell-cell connections in Figure 3-3a. However, if fracturing occurs within the matrix, substantially enhanced flow may arise through the fracture path. In order to demonstrate the accelerate flow in the DFN approach, the grid structure is modified, for which additional interface nodes and the

associated connections are introduced. As shown in Figure 3-3b, an interface node with increased permeability is inserted where the cell-cell connection intersects the Voronoi cell boundary. The original cell-cell connection is divided into two cell-interface (and vice versa) connections by the interface node. In addition, the connections between the interface nodes are established to activate flow channels in discrete fractures.

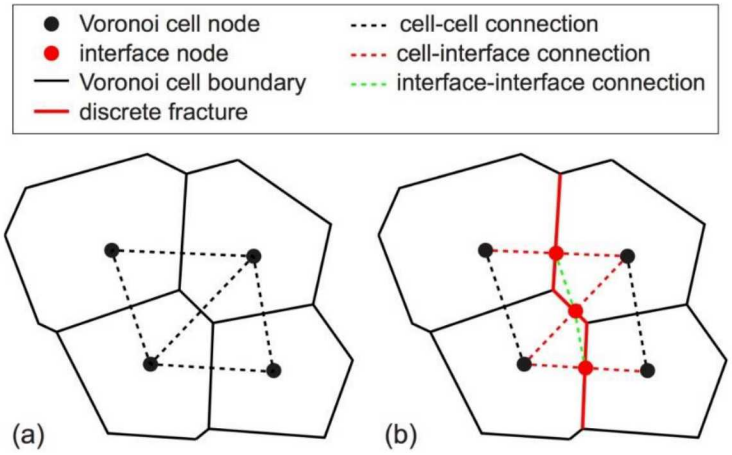


Figure 3-3. Transformation of the grid structure for enhanced flow through discrete fractures: (a) original Voronoi cell nodes and connections; and (b) insertion of interface nodes and connections.

3.3 Stress Calculation and Fracture Determination in the RBSN Approach

Elasticity and fracture-damage of geomaterials are modeled using the rigid-body-spring network (RBSN) approach. As a discrete modeling approach, the RBSN represents the mechanical system by a collection of simple lattice (two-node) elements. The lattice topology is defined by the Delaunay tessellation, and the dual Voronoi diagram is used to render the volume of a discretized domain (Figure 3-4a). The elemental formulations are based on the rigid-body-spring concept (Kawai, 1978; Bolander and Saito, 1998). A lattice element consists of a zero-size spring set located at the centroid of the common Voronoi cell boundary and two rigid arm constraints that relate the spring set to the nodes (Figure 3-4b). For 3D modeling, a spring set is formed from three axial springs and three rotational springs in local $n - s - t$ coordinates (Figure 3-4c). The $n-$axis is normal, and the $s - t$ plane is parallel to the Voronoi cell boundary.

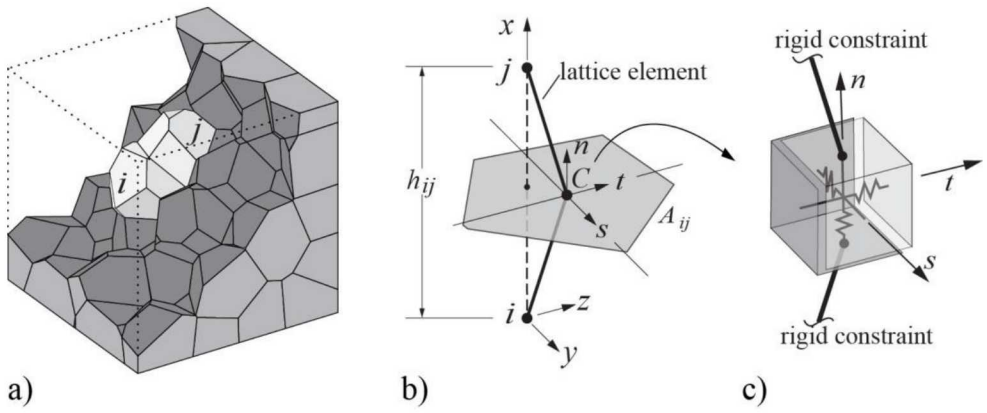


Figure 3-4. Typical RBSN lattice element *ij*: (a) within a Voronoi grid; (b) isolated from the network; and (c) a zero-size spring set located at centroid *C* of Voronoi cell boundary area A_{ij}.

A diagonal matrix $\mathbf{D} = \mathrm{diag}[k_s, k_t, k_n, k_{\phi n}, k_{\phi s}, k_{\phi t}]$ consists of the six spring coefficients which are defined according to the geometrical properties of Voronoi diagram:

$$k_s = k_t = \alpha_1 k_n = \alpha_1 \alpha_2 E \frac{A_{ij}}{h_{ij}}, \quad k_{\phi n} = E \frac{J_p}{h_{ij}}, \quad k_{\phi s} = E \frac{I_{ss}}{h_{ij}}, \quad k_{\phi t} = E \frac{I_{tt}}{h_{ij}} \tag{3.6}$$

where *E* is the elastic modulus, J_p, I_{ss}, and I_{tt} are the polar and two principal moments of inertia of the Voronoi cell boundary with respect to the centroid, respectively. The spring coefficients are scaled by the element length h_{ij} and the area of the Voronoi cell boundary A_{ij}. Effective Poisson ratio can be represented by adjusting α_1 and α_2. By setting $\alpha_1 = \alpha_2 = 1$, the models behave with elastic homogeneity under uniform straining, albeit with zero effective Poisson ratio (Asahina and Bolander, 2011; Kim and Lim, 2011).

Fracture may initiate within a lattice element when the stress state exceeds the given material strength. To determine the criticality of the stress state, a stress ratio is calculated for each lattice element:

$$R_f = \sigma_e / \hat{\sigma} \tag{3.7}$$

where σ_e is the element stress state and $\hat{\sigma}$ is the critical stress defined by fracture criteria. During iterative calculations, only one element, with the most critical stress state (i.e., the largest $R_f \geq 1$), is allowed to break per iteration, and the fracture event entails a reduction of spring stiffnesses and a release of the associated elemental forces. Various user-defined fracture models can be applied to evaluate stress of lattice elements and set the critical stress related to the material strength parameters. Strength properties of each element are determined as critical stress components on a Mohr-Coulomb surface. Figure 3-5 shows the fracture surface with a tension cut-off, where the envelop is defined by three parameters: the angle of internal friction ψ (surface inclination with respect to σ_n-axis); cohesive strength *c* (surface intersection with the shear axes); and the tensile strength f_n. Herein, two different types of stress evaluation are described within the Mohr-Coulomb based failure criteria.

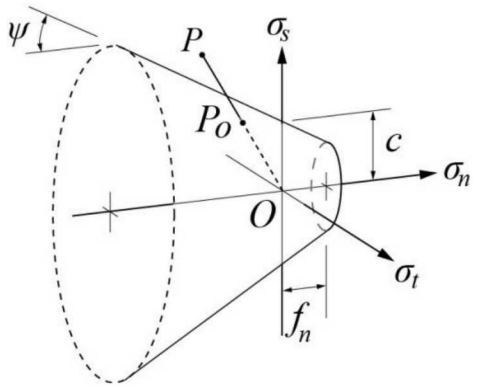


Figure 3-5. Mohr-Coulomb fracture surface with tension cut-off.

The first type is so-called the vectorial stress measurement, which uses the spring force vector for normal and shear stress components. Measures of stress $P(\sigma_n, \sigma_s, \sigma_t)$ are derived by averaging the axial spring forces F_n, F_s, and F_t over the cell boundary area A_{ij}. The criticality of the stress state is assessed as $R_f = \overline{OP}/\overline{OP_O}$, where P_O is the point at which $\overline{OP}$ intersects the fracture surface (see Figure 3-5). At the present stage of model development, there is no option to gradually damage the springs (e.g., with softening behavior) for fracture softening. However, other studies have indicated the possibility of modeling damage process by shrinking the Mohr-Coulomb surface (Shen and Shen, 2002; Kim and Lim, 2011).

The second type is to calculate the stress tensor for each nodal point, so-called the tensorial stress measurement. Stress tensors at Voronoi cell nodes are possible by considering the equilibrium conditions of the spring forces. Sets of the spring forces are applied at the boundaries surrounding a Voronoi cell (Figure 3-6 a), and nodal force components F_{nn}, F_{ns}, and F_{nt} can be calculated for an arbitrary section passing through the Voronoi cell node with its corresponding local $n - s - t$ coordinates, which satisfy the equilibrium condition with all the forces acting on the remaining cell boundaries (Figure 3-6b). Moment contributions to equilibrium are not considered here. By dividing these force components by the cut-face area, the corresponding stress components σ_n, σ_s, and σ_t can be obtained. By repeating this process for three mutually perpendicular sections, the full stress tensor is obtained (Figure 3-6c). Details are given elsewhere (Yip et al., 2005). From the stress tensors at two neighboring nodes, the stress tensor of the inter-element is calculated according to

$$\overline{\boldsymbol{\sigma}} = (\boldsymbol{\sigma}_i + \boldsymbol{\sigma}_j)/2 \tag{3.8}$$

where $\boldsymbol{\sigma}_i$ and $\boldsymbol{\sigma}_j$ are the stress tensors at the neighboring nodes i and j, respectively. The maximum principal tensile stress of $\overline{\boldsymbol{\sigma}}$ serves as σ_e in Equation (3.8). In this way, fracture under multiaxial stress conditions can be simulated. Note that the gas migration simulations using TOUGH-RBSN, presented in Section 6, have adopted this tensorial stress measurement for fracture determination.

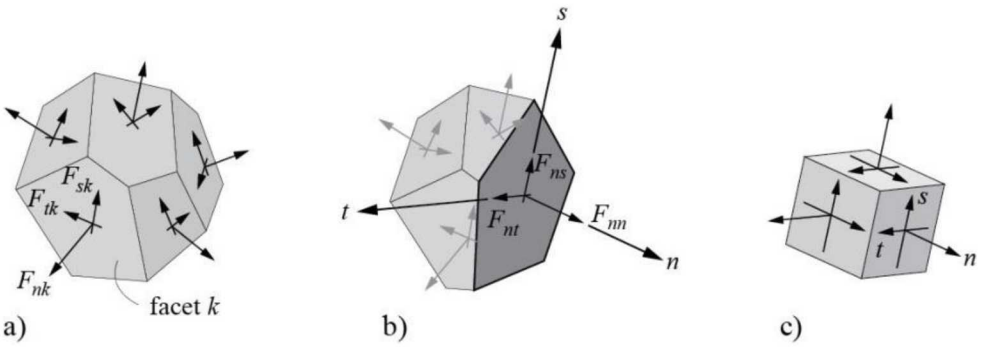


Figure 3-6. Stress tensor measurement at a Voronoi cell node: (a) components of spring force local coordinates; (b) a set of nodal forces satisfying the equilibrium; and (c) complete stress tensor at Voronoi cell node (adapted from Yip et al., 2005).

3.4 Status of TOUGH-RBSN Verification and Validation

Coupled THM processes, including fracture propagation, within argillaceous rocks and clay rich geomaterials have been simulated using the TOUGH-RBSN code with adequate constitutive models, which are verified and validated against laboratory tests and analytic solutions. In the following, completed verifications and validations of TOUGH-RBSN are listed with the references in which those activities are documented.

- Simulations of swelling stress development and desiccation cracking in geomaterials validated against independent laboratory test data (Asahina et al., 2014)
- Hydraulic fracture propagation in rock-analogue samples made of soda-lime glass with a designed fracture geometry (Kim et al., 2017)

In addition, LBNL is currently involved in DECOVALEX-2019, an international collaborative activity for validating various modeling approaches against unique laboratory and field data. TOUGH-RBSN has been used to model two-phase liquid and gas flow in saturated bentonite sample with dilatant flow path and fracture generation. Intermediate results have been presented in Tamayo-Mas et al. (2018), where extensive comparisons of simulation results using 11 different modeling approaches are made with laboratory test data. The TOUGH-RBSN models with relevant conceptual models exhibit key responses such as pressure/stress evolutions in a plausible match with the experimental data, which will be presented in Section 6.

4. FE Experiment at the Mont Terri Site (Mont Terri Project)

In this section, we present the current status of the FE Experiment at Mont Terri and updated TOUGH-FLAC modeling of the experiment. In particular, in FY2018 we have extended the modeling for comparison with up to 3.5 years of field data from the experiment at additional monitoring points within the bentonite buffer and surrounding host rock. In the following, we first provide a description and status of the FE Experiment and then present the results of current THM modeling.

4.1 Description and Status of the Mont Terri FE experiment

The Mont Terri FE experiment is undertaken by NAGRA, Switzerland, as an ultimate test for the performance of geologic disposal in Opalinus Clay, with focus on both the EBS components and the host-rock behavior. It will be one of the largest and longest-duration heater tests worldwide,

with focus on both the EBS components and the host-rock behavior. The FE experiment is conducted in a side tunnel at Mont Terri, excavated along the claystone bedding planes, extending 50 m in length and about 2.8 m in diameter (Figure 4-1). Heating from emplaced waste is simulated by three heat-producing canisters of 1500 W maximum power. The temperature is expected to exceed 100°C, with a target temperature of 125 to 135°C at the inner parts of the buffer. A sophisticated monitoring program has been implemented, including dense instrumentation of the bentonite buffer and host rock, and extensive geophysical monitoring.

The experiment will provide data useful for the validation of THM coupling effects regarding the processes in the host rock, while correctly accounting for (and examining) the conditions in the emplacement tunnel temperature, saturation, and swelling pressure. Due to the 1:1 scale of the experiment, it will be possible to achieve realistic temperature, saturation, and stress gradients. It will also be possible to test backfilling technology with granular bentonite, as well as lining technology with shotcrete, anchors, and steel ribs. Processes examined in the test cover many aspects of repository evolution, such as creation and desaturation of the EDZ during tunnel excavation and operation (including ventilation for about one year), as well as reconsolidation of the EDZ, resaturation, thermal stresses, and thermal pore-pressure increase after backfilling and heating (heating and monitoring period > 10 years).

In 2011, a niche in front of the FE tunnel was constructed, followed by a first phase of instrumentation of the rock mass surrounding the tunnel, using boreholes from the niche. The FE tunnel was then excavated by road-header in 2012; which was followed by another phase of instrumentation. The tunnel was open for a one-year ventilation period. This was followed by the emplacement of the heaters, bentonite buffer, and a concrete plug, after which the heating was gradually turned on during the fall of 2014 and early 2015, with full heat power of 1350 W at all three heaters (H1, H2, H3) from February 18, 2015 (Figure 4-2). The heating is expected to go on for at least 15 years, with continuous monitoring of THM processes in both the bentonite buffer and surrounding rock.

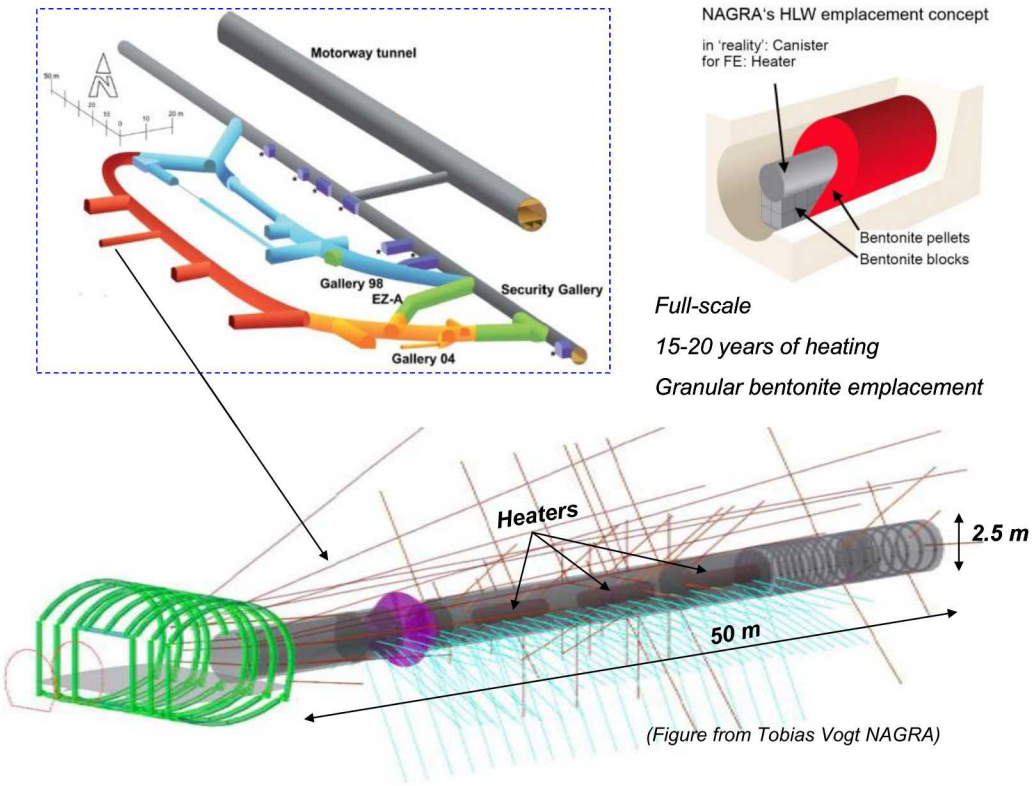


Figure 4-1. Plan view of FE experiment setup and borehole layout.

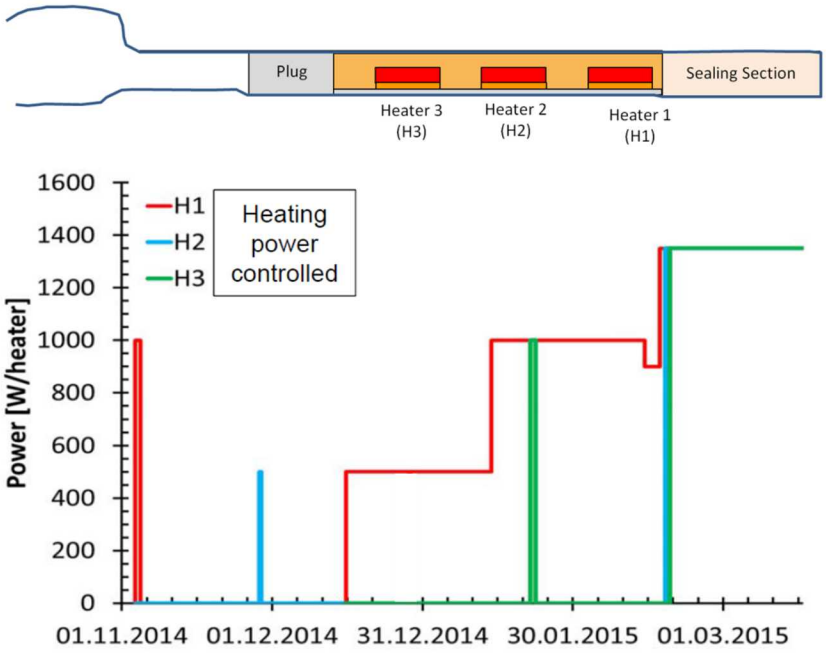


Figure 4-2. Heat power applied to H1, 2 and 3 during heater start-up at the Mont Terri FE experiment.

4.2 Progress of LBNL Modeling of FE Experiment

DOE is one of the experimental partners for the FE heater experiment, and LBNL is one of the modeling teams. In addition to LBNL, six other modeling teams are currently involved in the Mont Terri FE experiment from Germany (2 teams), U.K., Spain, Switzerland, and Canada.

Each modeling team develops its conceptual models and material properties using available literature (papers and reports) on lab experiments and previous Mont Terri *in situ* tests, etc. In the FY2013 UFD milestone report (Houseworth et al., 2013), we also made a first full THM 3D simulation of the FE heater test, including the BBM model for calculating the mechanical responses. These were scoping and preliminary predictions with the material properties available at the time, though in some cases including a different kind of bentonite.

In the FY2015 UFD milestone report (Zheng et al., 2015), we presented simulation results related to the thermal evolution for different heat power schemes. This included a staged heating during the first few months of the experiment. A staged heating schedule was also adopted in the real experiment to be able to use early data for determining the maximum heat load so that temperatures would not exceed certain limits. For example, the maximum temperature should not exceed 150°C as such high temperature could potentially damage the monitoring system. The modeling presented in the FY2015 UFD milestone report indeed showed that temperature could increase to about 150°C if the maximum heat power of 1500 W would be applied on each of the heaters. It was decided by NAGRA to limit the maximum heat power to 1350 W to maintain maximum temperature well below 150°C.

In the FY2016 UFD milestone report (Zheng et al., 2016), we presented the results of initial interpretative modeling of the FE experiment with comparison to field data for the first year of heating. The approach was to use the previously developed 3D model of the FE experiment, but with THM properties updated and determined from the modeling of the smaller scale HE-E experiment. In the modeling, we obtained a good agreement with monitored evolution of temperature and relative humidity, when using an effective diffusivity that was lowered using a tortuosity factor as low as 0.14 (Zheng et al., 2016).

In the FY2017 SFWST milestone report (Zheng et al., 2017), we updated model simulations with comparison to monitoring data extended to more than two years, including additional comparison for monitoring points located at other sections along the tunnel, i.e., comparisons made at monitoring sections located at all three heaters. The agreement between modeling and experimental data for temperature and relatively humidity was generally good, though some disagreement was found related to the relative humidity evolution in the bentonite blocks below the heaters.

In this part of the report, we present updated model simulations with comparison to monitoring data extended to about 3.5 years, including additional comparison for monitoring points located in the buffer as well as in the host rock. We have also conducted additional sensitivity analysis and obtained a better match of relative humidity evolution in the bentonite blocks below the heaters.

4.3 TOUGH-FLAC Model of the Mont Terri FE Experiment

For the modeling of the FE experiment, we have developed a conceptual model and modeling approach that were presented in previous milestone reports (Houseworth et al., 2013; Zheng et al., 2014; Zheng et al., 2015; Zheng et al., 2016). The host rock is modeled using TOUGH-FLAC with anisotropic properties considering bedding planes of the Opalinus Clay. To accurately model anisotropic thermal and hydrological behavior, we created an inclined TOUGH2 mesh. Anisotropic mechanical material behavior is simulated using the FLAC3D ubiquitous joint model, with initial material properties derived from the excavation design analysis of the experimental tunnels. In the ubiquitous joint model, weak planes are assumed along the bedding planes of the Opalinus Clay, in which the shear strength properties are different along bedding versus across bedding (Houseworth et al. 2013). For the bentonite, we started with the BBM model as applied by the CINEMAT and Universitat Politècnica de Catalunya (UPC) (Garitte and Gens, 2012), and derived specific input material parameters for the MX-80 bentonite pellets, which is used as the emplaced buffer around the heaters. With this modeling approach, we are able to simulate THM processes in both the bentonite and host rock, as well as their interactions.

Figure 4-3 presents the 3D TOUGH-FLAC numerical grid of the FE experiment. This model grid includes all vital material components for the modeling of the FE experiment, including layered Opalinus Clay host rock, excavation disturbed zone, tunnel, three heaters, bentonite buffer, concrete liner, and concrete plug. The initial conditions for the model simulation are 2 MPa pore-fluid pressure and 15°C temperature for the host rock. The 2 MPa pore pressure is not under hydrostatic conditions, and the process is affected by the existing tunnel system at the site. In our simulations, we first run a simulation with an open tunnel at atmospheric pressure for one year, creating a pressure drop and hydraulic gradient around the tunnel. Thereafter, we assume instantaneous emplacement of the heater and buffer, and start our heating simulation.

The thermal and hydraulic material properties for modeling the FE experiment are given in Table 4-1. These properties are based on the modeling studies of several other smaller scale heater experiments at the Mont Terri laboratory, including the HE-D and HE-E experiments described in previous reports (Zheng et al., 2015; 2016). The intrinsic permeability of gas flow in the bentonite is about six orders of magnitude higher than the intrinsic permeability for liquid flow, and this is simulated in TOUGH2 using a high value of the Klinkenberg parameter. The initial saturation in granular bentonite and bentonite block are different that in the previous HE-E experiment, and is for the FE experiment set to 16.5% for granular bentonite and to 75% for bentonite blocks.

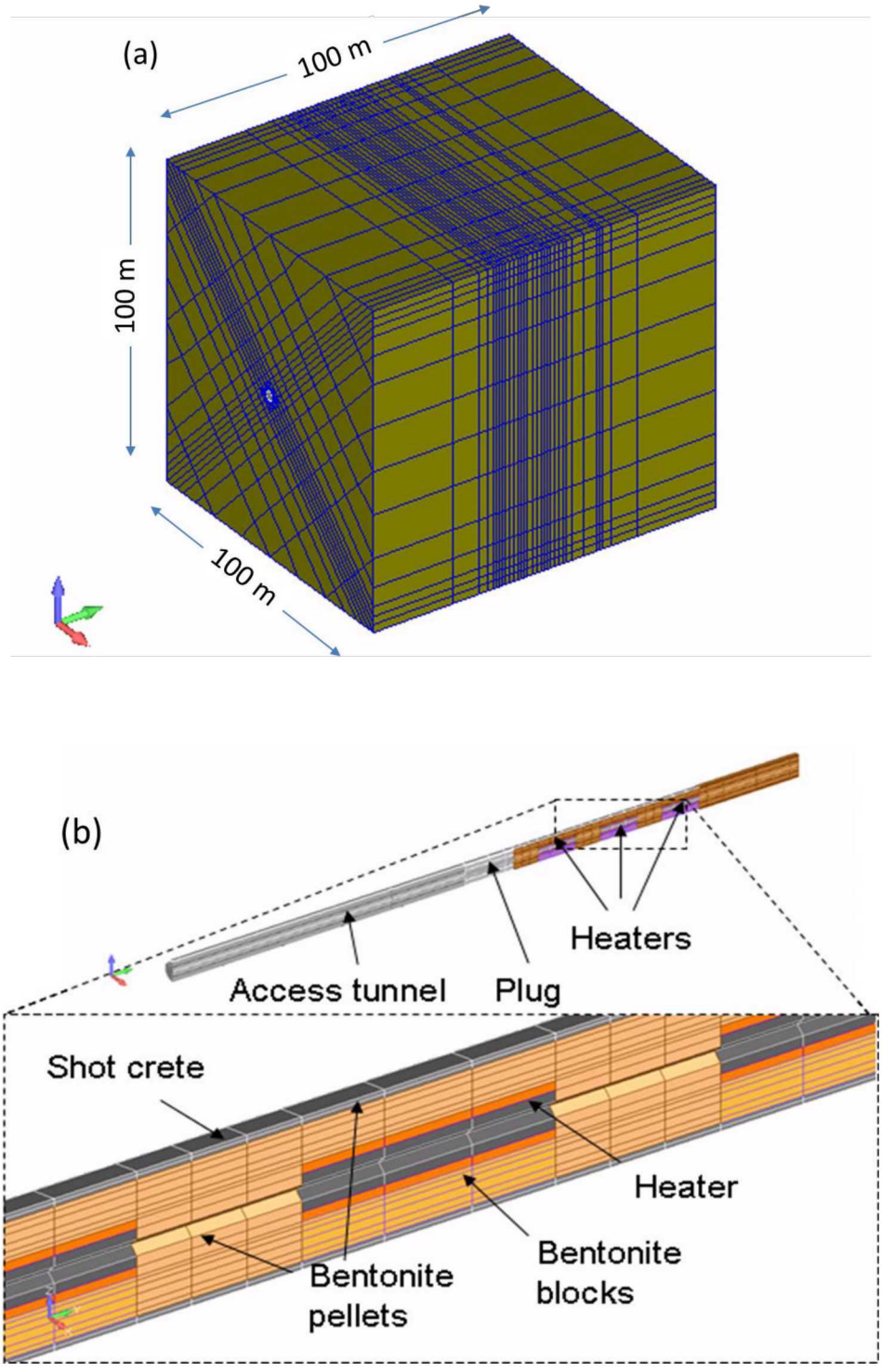


Figure 4-3. TOUGH-FLAC 3D numerical grid of the FE experiment. (a) entire model and (b) details of the materials and gridding of the EBS.

Table 4-1. Parameters used in the modeling of the Mont Terri FE experiment.

Parameters	Symbol	Opalinus Clay	Granular Bentonite	Bentonite blocks	Concrete (shotcrete and plugs)	Unit
Grain density	ρ_g	2.7×10^3	2.7×10^3	2.7×10^3	2.7×10^3	kg/m^3
Porosity	$Ø$	0.15	0.46	0.389	0.15	-
Intrinsic permeability	k	5.0×10^{-20}	5.0×10^{-21}	2.0×10^{-21}	3.5×10^{-21}	m^2
Liquid relative permeability (Corey, 1954) $k_{lr}(S_l) = \left(\frac{S_l - S_{lr}}{S_{ls} - S_{lr}}\right)^A$	A	-	5	3	-	-
Liquid relative permeability (van Genuchten, 1980) $k_{lr}(S_l) = \left(\frac{S_l - S_{lr}}{S_{ls} - S_{lr}}\right)^{1/2}\left[1-\left\{1-\left(\frac{S_l - S_{lr}}{S_{sl} - S_{lr}}\right)^{1/m}\right\}^m\right]^2$	m	0.52	-	-	0.52	-
Capillary curve (van Genuchten, 1980) $\psi(S_l) = Po\left\{\left(\frac{S_l - S_{lr}}{S_{ls} - S_{lr}}\right)^{-1/m} - 1\right\}^{1-m}$	P_0	1.09×10^7	1.0×10^7	3.0×10^7	1.09×10^7	Pa
	M	0.29	0.4	0.32	0.29	-
	S_{ls}	1.0	1.0	1.0	1.0	-
	S_{lr}	0.01	0.0	0.0	0.01	-
Thermal conductivity (wet)	λ_{sat}	1.7	1.3	1.0	1.7	W/m°K
Thermal conductivity (dry)	λ_{dry}	1.06	0.3	0.5	1.06	W/m°K
Grain specific heat	C	800	950	950	800	J/kg°K

4.4 Simulation Results with Comparison to Monitored Data

Here we first focus on the simulation and monitored data for the evolution of temperature and relative humidity in the bentonite buffer. A conceptual model of the evolution of moisture content is shown in Figure 4-4. The figure shows the creation of a thermal gradient due to the heating. Near the heater, liquid evaporates to vapor in the gas phase, which is then transported outwards by diffusion toward cooler regions where some of the vapor is condensed to liquid. At the same time, liquid water infiltrates from the rock into the bentonite buffer. The wetting of the outer parts of the buffer and the drying of the inner parts cause gradients in liquid saturation and capillary pressure, which will result in liquid fluid flow from the outer parts towards the inner dryer parts of the buffer.

The outward vapor diffusion is modeled in TOUGH2 using the following equation:

$$\mathbf{i}_g^w = -\rho_g \phi S_g \tau D_g^w \mathbf{I} \nabla X_g^w \tag{4-1}$$

where $\mathbf{i}_g^w$ is diffusion of water component in the gas phase, ρ_g is density of gas, ϕ is porosity, S_g is gas saturation, τ is flow tortuosity factor, D_g^w is water vapor diffusion coefficient, and X_g^w is mass fraction of water in the gas phase. The vapor diffusion is from areas of high mass fraction of water vapor in the gas phase (near the heater) toward outer regions of the buffer of lower mass fraction of water vapor in the gas phase. Effective vapor diffusion for the partially saturated porous media is affected by porosity, gas saturation and the flow tortuosity factor (see also Figure 4-4).

The liquid flux from the outer parts of the buffer toward the inner parts is governed by the following equation:

$$\mathbf{q}_l^w = -\rho_l X_l^w \frac{\mathbf{k} k_{rl}}{\mu_l}\left(\nabla P_l - \rho_l \mathbf{g} \nabla z\right) \tag{4-2}$$

where $\mathbf{q}_l^w$ is the liquid water mass flux, ρ_l is density of liquid, X_l^w is mass fraction of water in liquid phase, **k** is intrinsic permeability, k_{rl} is relative permeability for liquid flow, μ_l is dynamic fluid viscosity, P_l is liquid pressure, ***g*** is acceleration from gravity, and z is elevation. The liquid flux is driven by the liquid pressure gradient, which in turn is strongly dependent on the capillary pressure and the water retention functions. At emplacement, there is a strong suction (high capillary pressure) within the partially saturated buffer and this suction becomes higher near the heater due to drying by evaporation. The flux also depends on the liquid flow mobility, including effects of intrinsic permeability and relative permeability for liquid flow.

The key parameters affecting the early time evolution of the moisture content are the water retention, absolute permeability and relative permeability, and the effective vapor diffusion coefficient for the partially saturated porous media. These parameters are usually determined from various laboratory experiments. The material parameters for the bentonite at the FE heater experiment have been determined by a number of experiments, both on granular bentonite samples and compacted bentonite blocks. Another key parameter is the saturation dependent thermal conductivity of the bentonite. The thermal conductivity impacts the temperature evolution and the thermal gradient and will therefore also impact the evolution of the moisture in the bentonite buffer.

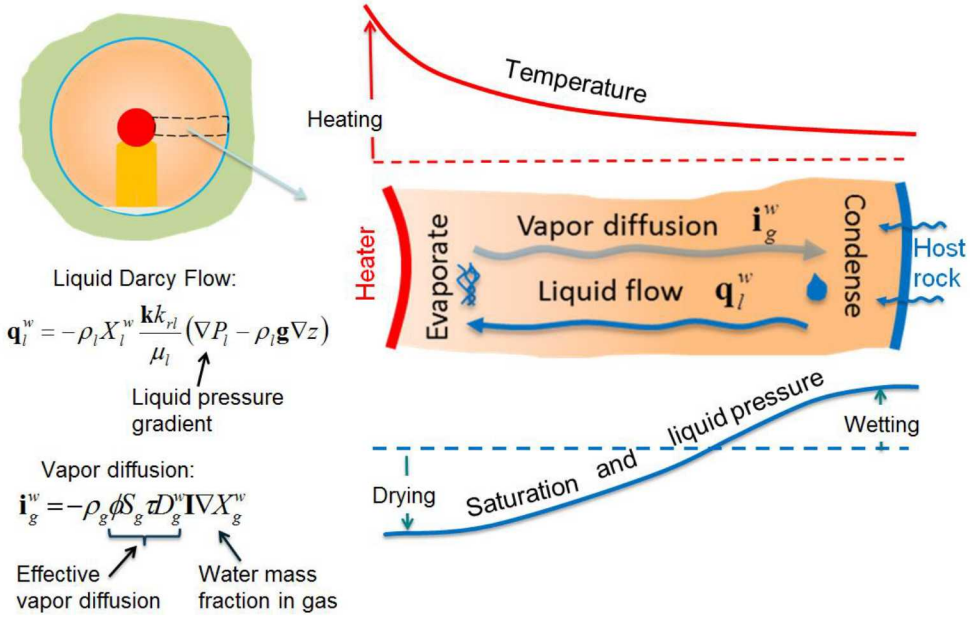


Figure 4-4. Conceptual model of the evolution of moisture in the heated bentonite buffer and equations for vapor diffusion in the gas phase and for liquid Darcy flow along the gradient of liquid pressure (capillary driven)

In the FY2016 milestone report (Zheng et al., 2016), the simulation results with comparison to the one year experimental data were presented. One of the main results reported was the fact that a tortuosity parameter as low as $\tau = 0.14$ was applied in order to obtain good match for the evolution of relative humidity in the buffer. In the FY2017 milestone report (Zheng et al., 2017), we found that this value of tortuosity ($\tau = 0.14$) still holds true for up to two years of heating and for a number of monitoring points at all three heaters.

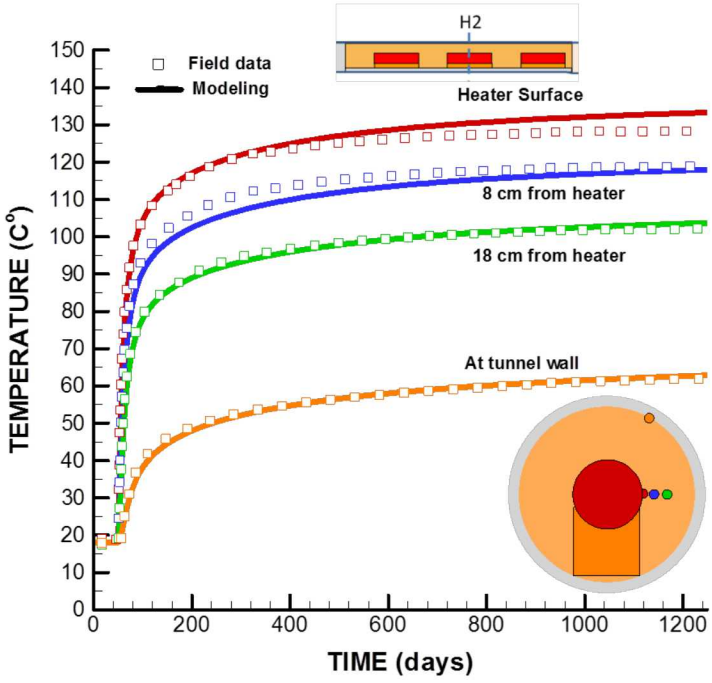
In FY2018, we have expanded the analysis with comparison to about 3.5 years of field data with detailed comparison at all three heaters. The FY2018 updated numerical results were compared to measured data at monitoring points within the bentonite buffer, which are shown in Figures 4-5 to 4-10. The time zero in these figures are at 12/28/2014, which is just after the start of the heating at H1. The material parameters used in the modeling are almost the same as those in the FY2017 milestone report. For example, we still apply a tortuosity factor of 0.14 for the granular bentonite, but we have updated the tortuosity factor for the bentonite blocks, which is now 0.33.

Overall the results shown in Figures 4-5 to 4-10 confirm an excellent agreement in buffer temperature evolution and a good agreement in the evolution of relative humidity. An improvement in FY2018 was the match of the relative humidity evolution in the bentonite blocks below the heater (Figures 4-6b, 4-8b, and 4-10b). This was achieved by calibrating the tortuosity coefficient for the bentonite blocks, which is now set to 0.33 instead of 0.14. The simulated evolution of relative humidity near the tunnel wall is also in good agreement with measurements, but some disagreement can be observed for the results at H3 (Figure 4-9b), where the measurements show a more rapid increase of relative humidity. However, the rate of wetting is very sensitive to how far from the rock wall the monitoring point is located. In the modeling, the tunnel is simulated as a perfect circle, while in the field the shape of the tunnel is not perfectly circular (Figure 4-11). Also in the modeling the shotcrete is modeled with a certain uniform thickness, which might be different from the heterogeneous shotcrete thickness in the field. Overall though, the rate of inflow from the rock and the relative humidity evolution is captured very well. In general, the rate of inflow to saturate the buffer is small due to the low permeability of the host rock.

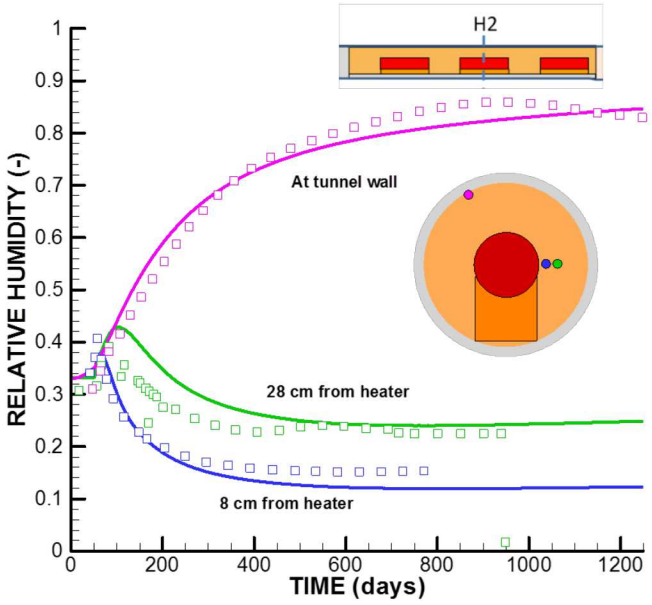
Some minor discrepancies in the temperature evolution can be noted close to H1. The calculated temperature at H1 is generally smaller than the measured. In fact, the calculations show that the heater in the middle (H2) has about 2°C higher maximum temperature than at H1 and H3. In the field on the other hand, H1 has a slightly higher maximum temperature than H2 and H3. The higher temperature at H1 could be due to a heterogeneous buffer, in which the buffer density affects the local thermal conductivity. Another factor that can impact the temperature in the buffer close to the heater is the fact that the heater is not exactly centered at the tunnel axis, but shifted slightly to the right as shown in Figure 4-11.

In FY2018 we have also conducted scoping calculations related to thermal pressurization in the host rock as measured at several monitoring points near H2. The scoping calculations were conducted to understand the different pressure responses at monitoring points located in a direction perpendicular to bedding and parallel to bedding. Thermal pressurization occurs because of thermal expansion of pore fluid in a medium of low permeability. The thermal expansion coefficient of water is much higher than that of Opalinus Clay and therefore a temperature increase will cause the pore water pressure to increase. Important parameters for pressure responses during

thermal pressurization are pore compressibility (which is related to bulk modulus and porosity) and permeability (Rutqvist et al., 2014).

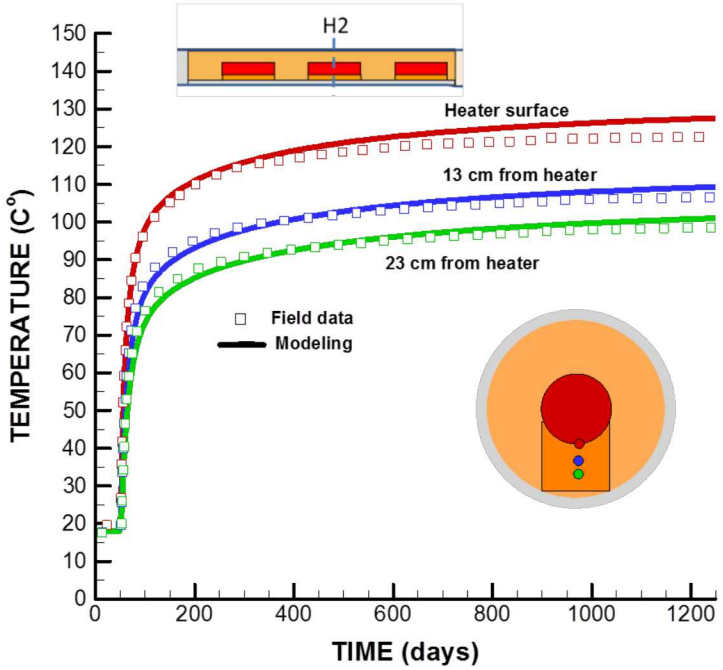


(a)

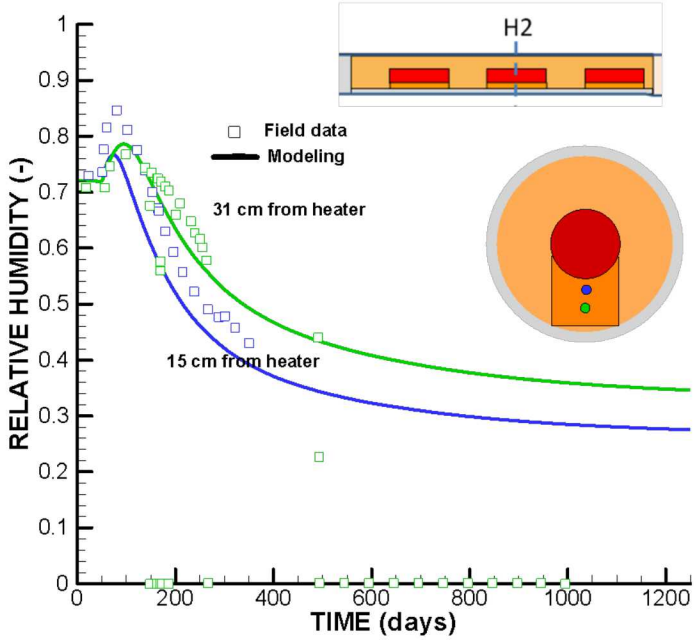


(b)

Figure 4-5. Comparison of modeled (lines) and measured (symbols) evolutions of (a) temperature and (b) relative humidity at monitoring point located in granular bentonite at H2 for over two years of monitoring data.

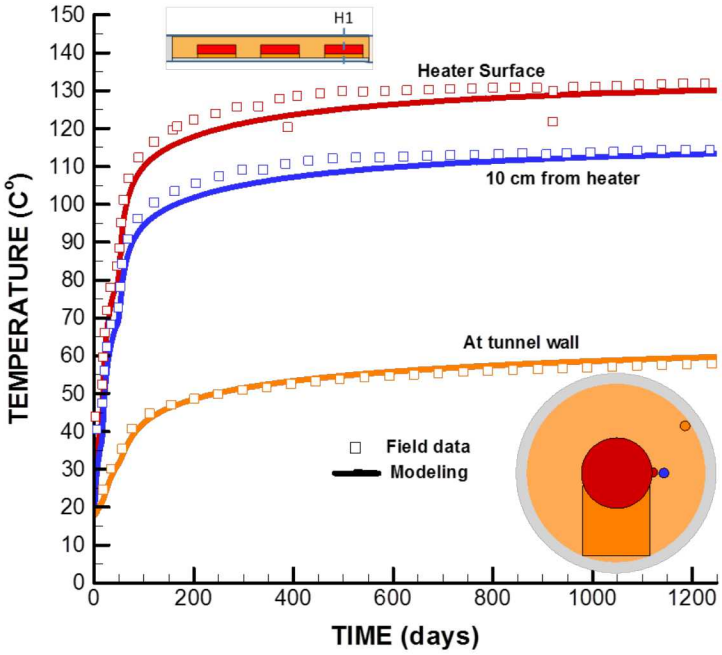


(a)

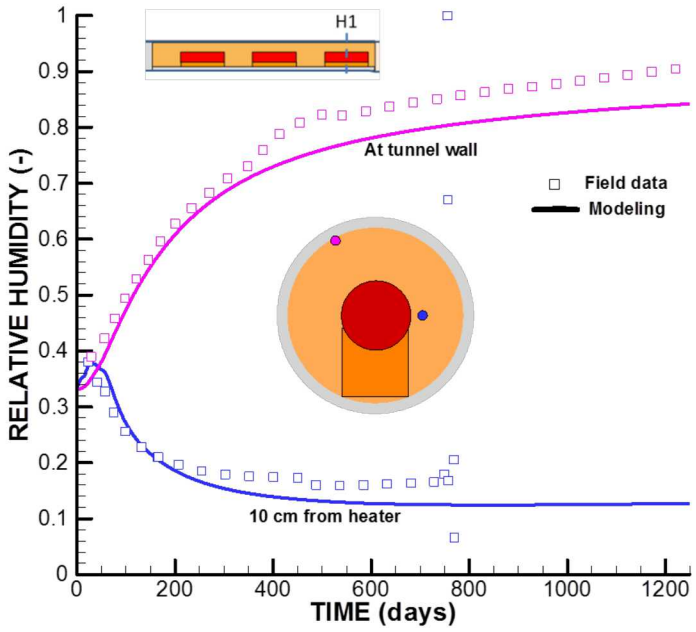


(b)

Figure 4-6. Comparison of modeled (lines) and measured (symbols) evolutions of (a) temperature and (b) relative humidity at monitoring point located in bentonite blocks at H2 for over two years of monitoring data.

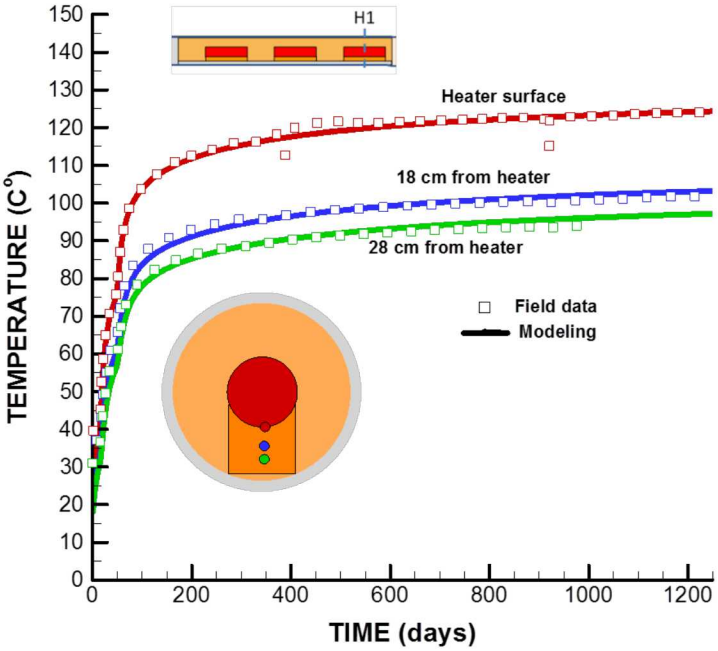


(a)

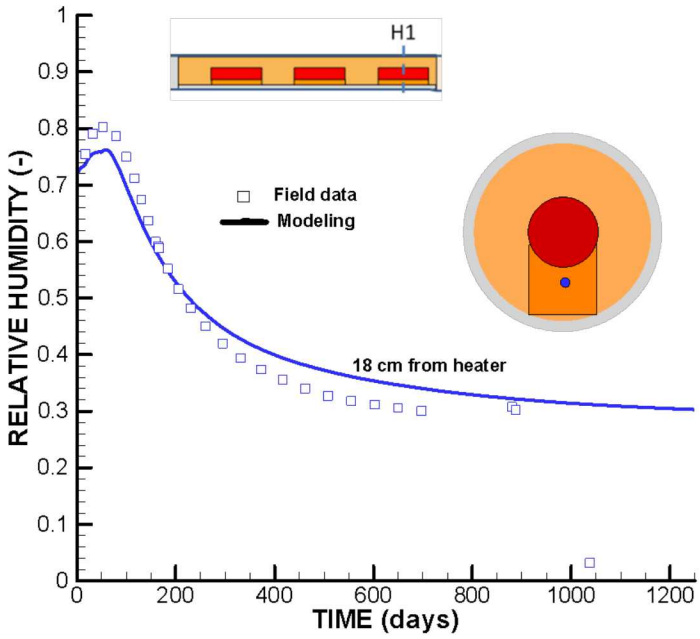


(b)

Figure 4-7. Comparison of modeled (lines) and measured (symbols) evolutions of (a) temperature and (b) relative humidity at monitoring point located in granular bentonite at H1 for over two years of monitoring data.

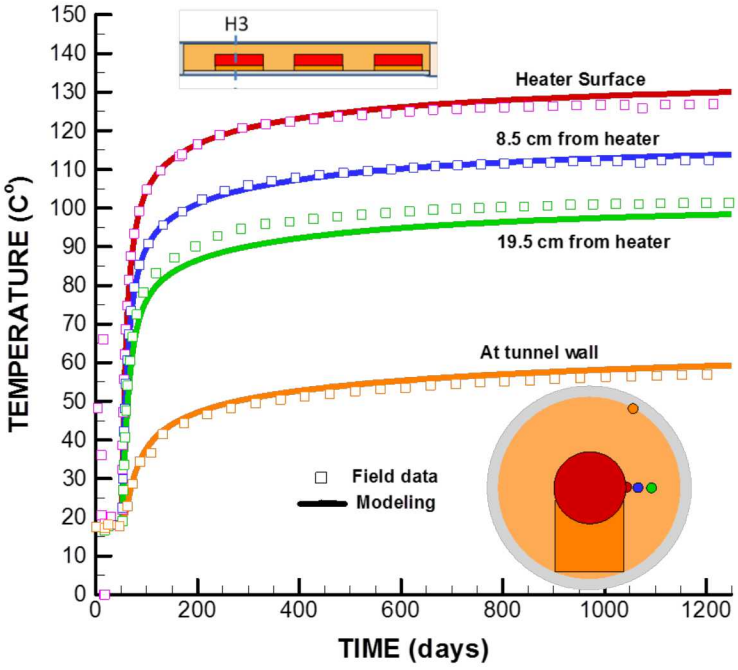


(a)

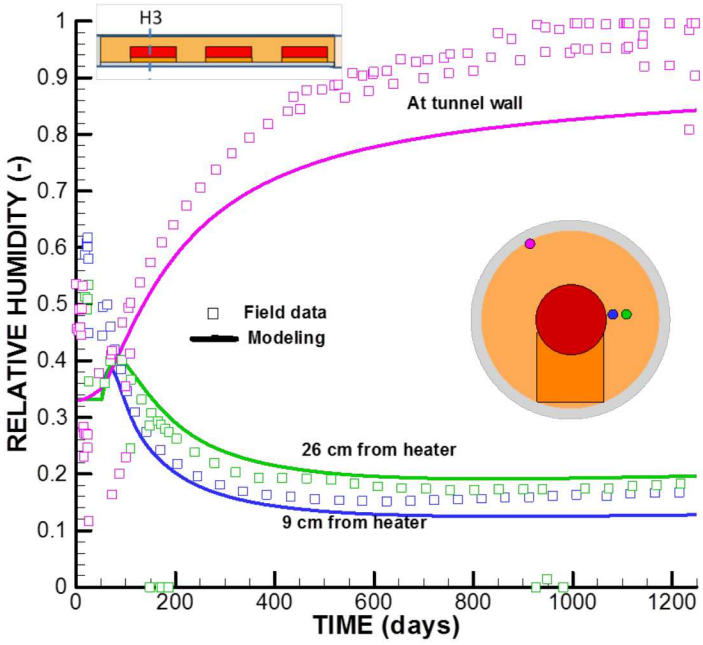


(b)

Figure 4-8. Comparison of modeled (lines) and measured (symbols) evolutions of (a) temperature and (b) relative humidity at monitoring point located in bentonite blocks at H1 for over two years of monitoring data.

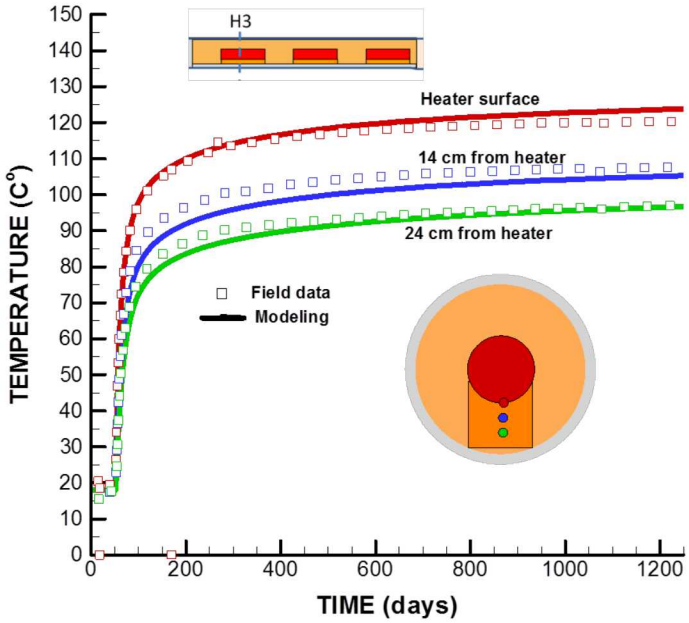


(a)

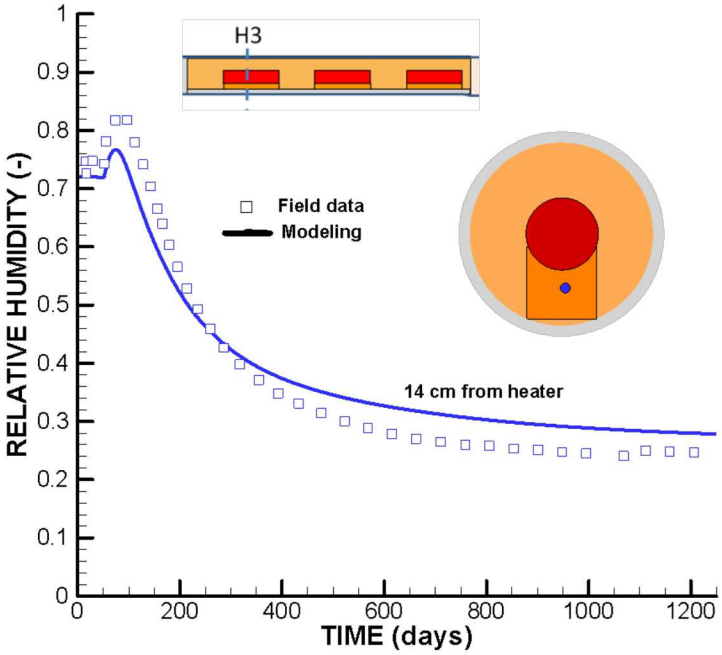


(b)

Figure 4-9. Comparison of modeled (lines) and measured (symbols) evolutions of (a) temperature and (b) relative humidity at monitoring point located in granular bentonite at H3 for over two years of monitoring data.



(a)



(b)

Figure 4-10. Comparison of modeled (lines) and measured (symbols) evolutions of (a) temperature and (b) relative humidity at monitoring point located in bentonite blocks at H1 for over two years of monitoring data.

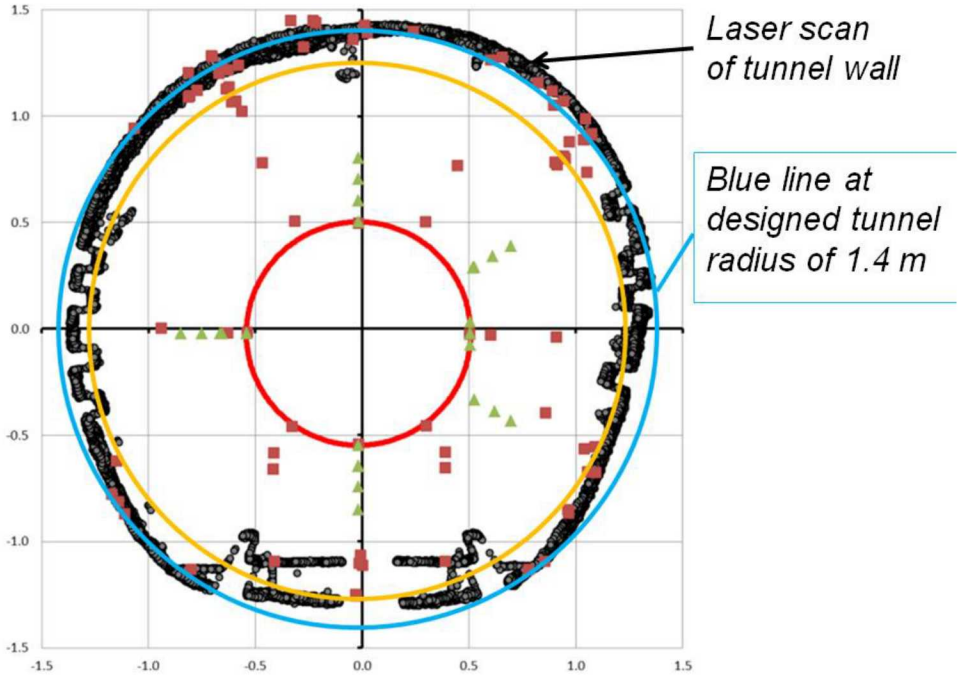
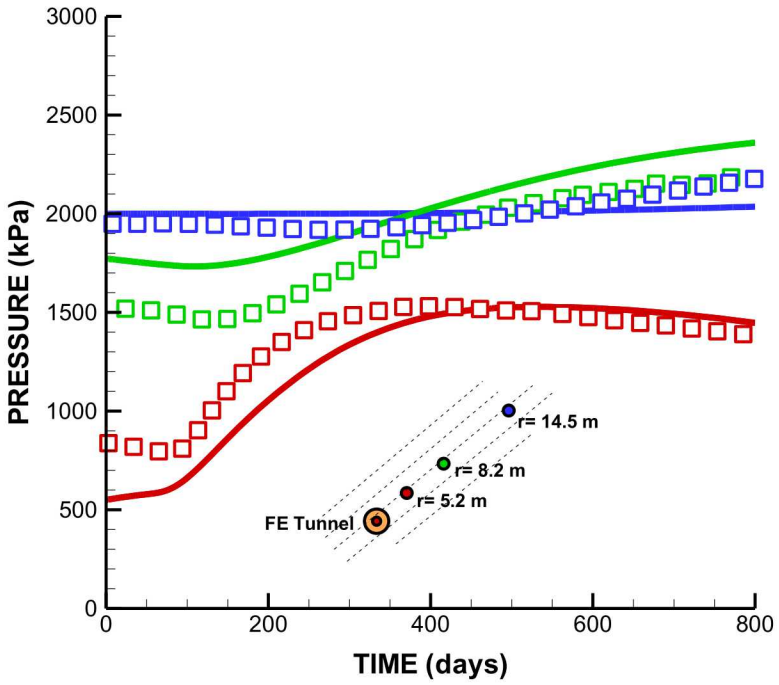
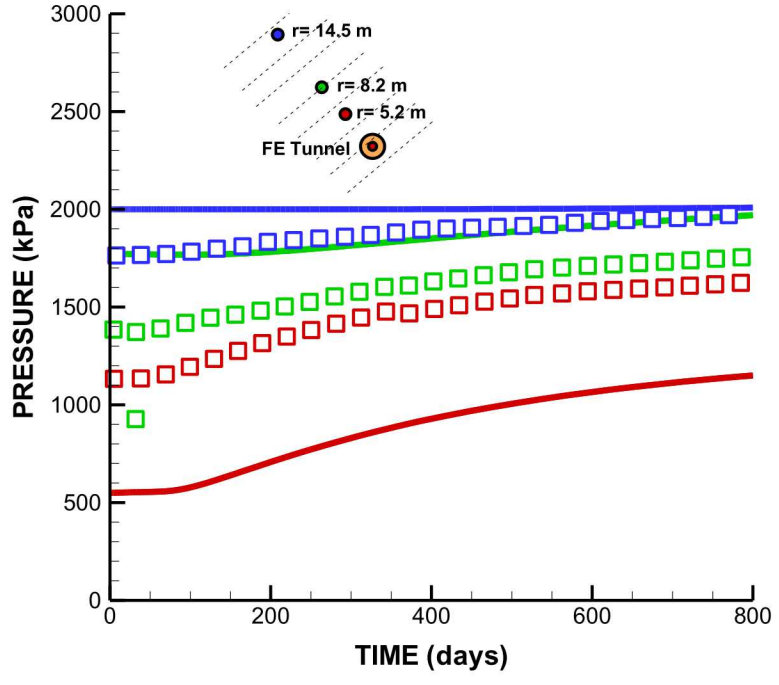


Figure 4-11. Comparison of the actual zigzag-shape cross-section of the tunnel from the laser scan with the circular shape of tunnel used in numerical modeling. The red circle in the middle is the heater. Squares and triangles indicate locations of some of monitoring sensors. Axis units are in meters.

In our base simulations for studying the evolution of temperature and relative humidly in the buffer we used the value of a permeability k = 5e-20 m^2, which is based on previous analysis of field experiments at Mont Terri. However, for better matching the thermal pressurization at the FE heater test we had to reduce the rock permeability to 1e-20 m^2 (for monitoring points located along a borehole perpendicular to bedding) and 2e-20 m^2 (for monitoring points located along a borehole parallel to bedding). Moreover, considering the average bulk modulus and porosity in Opalinus Clay at Mont Terri, the pore compressibility would be about 1e-9 Pa^{-1}. By setting permeability to 2e-20 m^2 and pore compressibility to 1e-9 Pa^{-1} we obtained a reasonably good match between simulated and monitoring pressure evolution for monitoring points located along a borehole parallel to bedding (Figure 4-12 a). For monitoring points located perpendicular to bedding, permeability was set to 2e-20 m^2 with a pore compressibility of 5e-9 Pa^{-1} (Figure 4-12b) This indicates that the difference between coupled THM responses are mainly due to a difference in fluid storage. In future modeling, we will study this in detail and will try to apply and explain these differences using anisotropic material models.



(a)



(b)

Figure 4-12. Results of scoping calculation for thermal pressurization effects in the host rock for pressure monitoring points located from the tunnel (a) perpendicular to bedding and (b) parallel to bedding.

4.5 Summary and Status the FE Experiment Modeling

As a modeling team in the Mont Terri FE experiment, we have conducted various types of modeling over the past few years, including benchmarking, heating design modeling, model predictions and interpretative modeling. Currently, we have interpreted data for up to 3.5 years of heating, including data on temperature and relatively humidity in the bentonite buffer and pressure in the host rock. Some finding and lessons learned are as follows:

- A good agreement between modeled and measured evolutions in buffer temperature and relative humidity was achieved at the FE experiment based on a model prediction using properties of bentonite and Opalinus Clay determined associated with the previous Mont Terri HE-E experiment.
- A value of the effective vapor diffusion coefficient (and medium tortuosity factor) could be precisely calibrated against measured relative humidity evolution in the granular bentonite, but the value was much lower than used for previous modeling of the HE-E experiment. This difference and the potential role of enhanced thermal diffusion of the early-time TH response in the buffer are open questions that warrant further studies.
- The values of the effective vapor diffusivity coefficient and the tortuosity factors for the bentonite block were determined based on the calibration of model parameters, and these values are much higher than for the granular bentonite.
- In a scoping calculation, thermal pressurization in the host rock could be reasonably well modeled, though local heterogeneities close to monitoring points probably affect the field data. Future modeling of thermal pressurization will focus at a mechanistic modeling of the anisotropic coupled THM responses and their impact on fluid pressure.

Still after 3.5 years of heating and water infiltration from the surrounding rock, no significant swelling stress has developed in the bentonite buffer. Measurements show the highest total pressure in the buffer is less than 0.5 MPa, but with a trend of accelerated stress increase in FY2019. We will continue modeling of the FE experiment along with new monitoring data, focusing more on the mechanical evolution of the buffer and host rock.

5. Heater Experiments at Bure in COx Clay Stone (DECOVALEX-2019)

In this section, we present recent TOUGH-FLAC modeling results related to the *in situ* heater experiment, conducted in Callovo-Oxfordian claystone (COx) at the Underground Research Laboratory (MHM URL) in Bure, France. The modeling of heater tests is one of the Tasks of the DECOVALEX-2019 project. In the following, we first provide a description of the DECOVALEX-2019 Task E and international modeling teams associated with this task; then provide a description of the *in situ* experiment and updated TOUGH-FLAC simulation results with comparison to experimental data.

5.1 DECOVALEX-2019 Task E and International Modeling Teams

DECOVALEX-2019 Task E is a study addressing important issues related to the repository design and safety calculation: how to go from a sample scale to a repository scale? Thermally induced pore pressure build-up and stress changes around a repository are important issues studied in this task, which is coordinated by ANDRA (French National Radioactive Waste Management Agency), and involves modeling of two *in situ* tests performed at the URL in Bure (France):

- The TED experiment, a small-scale heating experiment focused on the claystone THM behavior of the undisturbed rock mass in the far field; and
- The ALC experiment, a one-to-one scale heating experiment especially focused on the interaction between the surrounding rock and the support (steel casing in this case) in the near field.

Following the modeling of the two *in situ* tests, the impact of the behavior at the repository scale (considering several parallel cells) will be modeled. This application should address some key technical challenges, such as the variability of the THM parameters and the determination of appropriate boundary conditions when modeling is used to represent a series of parallel cells.

DECOVALEX-2019 Task E is conducted by a step-by-step approach, from small-scale to full-scale studies (Figure 5-1). It is structured into four main steps:

- Step 1: Simple 3D THM modeling benchmark;
- Step 2: Interpretative modeling of the TED experiment (back analysis);
- Step 3: Modeling of the ALC experiment
    - Step 3a: Predictive modeling of the ALC experiment using the reference values for the rock mass parameters determined in Step 2;
    - Step 3b: Interpretative modeling of the ALC experiment;
- Step 4: Prediction at the repository scale of an area with several high level waste cells.

The participating groups in the DECOVALEX-2019, Task E are:

- Canada: NWMO
- France: ANDRA, University of Lille
- Germany: BGR (UFZ Leipzig)
- UK: RWM (Quintessa Ltd)
- USA: DOE, LBNL

Currently, Step 1 related to 3D THM modeling benchmark, has been completed, Step 2 related to interpretative modeling of the TED experiment at Bure has been completed, and Step 3 related to blind prediction and interpretative modeling of the ALC experiment is ongoing. The prediction at the repository scale for Step 4 should be started before the next DECOVALEX-2019 workshop, which will be held in October 2018.

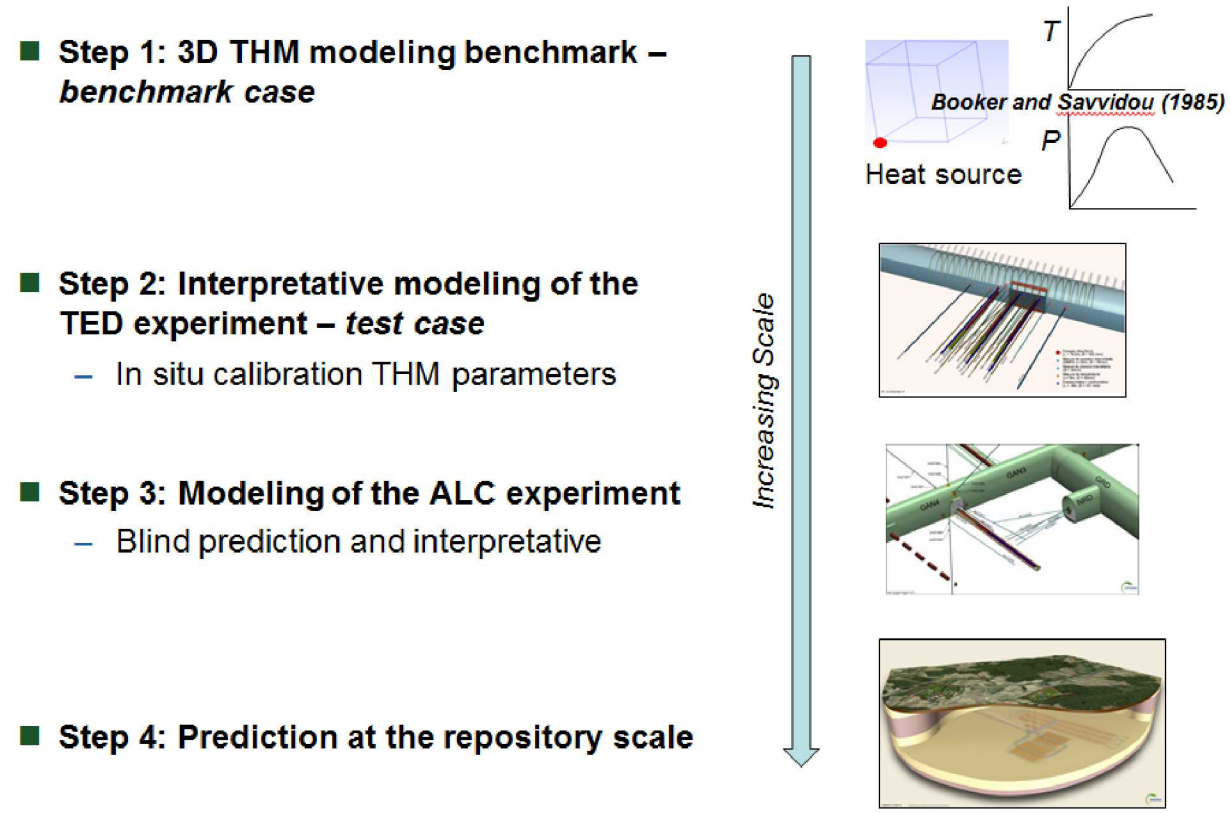


Figure 5-1. Overview of DECOVALEX-2019 Task E with steps of increasing scale.

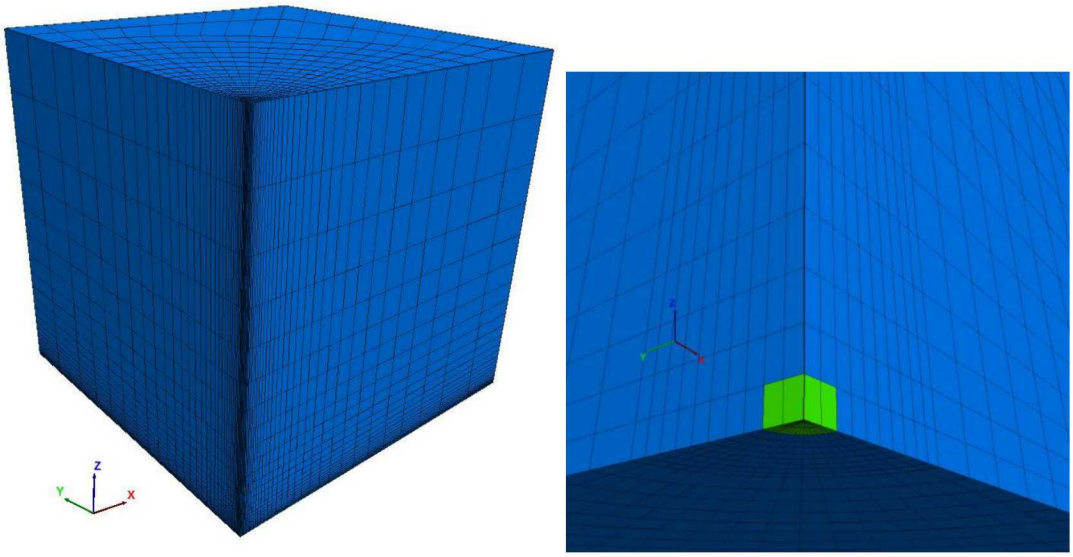
5.2 TOUGH-FLAC Simulation Results with Comparison to Experimental Data

5.2.1 Step 1: 3D THM modeling benchmark

Step 1 of Task E is a basic benchmark test considering the consolidation of an infinite homogeneous saturated porous medium around a constant point heat input. Booker and Savvidou (1985) provided the analytical solution for this problem based on the hypothesis that the pore water and the solid grains are incompressible. The 3D model is a cube of 15m×15m×15m, which is generated with FLAC3D, shown in Figure 5-2. Considering the symmetric planes, only one eighth of the model is simulated. Due to the limitation of the temperature in the module EOS1 (equation of state) in TOUGH2, we need to assign a larger size for the heat source with high thermal conductivity to lower the temperature inside heat source. Therefore, the heat source is represented by a 1/8 cylinder with 2.5 cm radius centered at the origin point and is refined with smaller meshes. The initial temperature, pore pressure and stresses are set to 0°C and

0 Pa. Regarding thermal and hydraulic conditions and considering symmetric conditions, the three symmetry planes are impermeable and adiabatic. At far field, the temperature and pore pressure are set to 0°C and 0 Pa. At the heat source, the constant heat power of Q=700 W is instantaneously

applied at time *t*=0. Regarding mechanical conditions, all domain boundaries are free except the symmetry planes, where null displacement conditions are applied normal to the boundaries.



a) b)

Figure 5-2. a) Geometry of the simulation domain, and b) Heater source (green elements) is a 1/8 cylinder with 2.5cm radius.

A homogenous and isotropic material is considered. The model parameters are listed in Table 5-1. The table includes the THM parameters of the two components, solid phase and pore water.

Table 5-1. Model parameters of Step 1.

Parameters	Values
Porosity	$\phi = 0.15$
Equivalent thermal conductivity [W/m/K]	$\lambda = 1.7$
Equivalent density [kg/m^3]	$\rho = 2400$
Equivalent heat capacity [J/kg/K]	$C_p = 1000$
Permeability [m^2]	$k = 4.5 \times 10^{-20}$
Young modulus [MPa]	$E = 4500$
Poisson's ratio	$\nu = 0.3$
Density of solid grains [kg/m^3]	$\rho_s = 2700$
Heat capacity of solid grains [J/kg/K]	$C_{ps} = 773$
Volumetric coefficient of thermal expansion of solid grains [1/K]	$\alpha_s = 4.2 \times 10^{-5}$
Density of water [kg/m^3]	$\rho_w = 1000$
Compressibility of water [1/Pa]	$c_w = 0^*$
Heat capacity of water [J/kg/K]	$C_{pw} = 4180$
Dynamic viscosity of water [Pa×s]	$\mu_w = 1 \times 10^{-3}$
Volumetric coefficient of thermal expansion of water [1/K]	$\alpha_w = 4 \times 10^{-4}$

*Note: the analytical solution in (Booker and Savvidou, 1985) assumes the water is incompressible, indicating $c_w = 0$.

Comparison between modeling results and analytical solution for, temperature, pressure, displacements (u_x, u_y, u_z), and stresses evolution up to 365 days is provided at the points given in Table 5-2.

Table 5-2. Points used for comparison of numerical results and analytical solution in for Step 1.

Points	(x, y, z) coordinates	Quantity
P1	(0.35, 0, 0)	Temperature, pressure
P2	(0.5, 0, 0)	Temperature, pressure
P3	(1.5, 0, 0)	Temperature, pressure
P4	(0.35, 0.5, 0.6)	Temperature, pressure, displacements, stresses

In FY2017, we have computed the evolution of temperature, pressure, and displacements at point P1, P2, P3 and P4 as listed in Table 5-2. Comparison between numerical results with analytical solution is shown in Figures 5-3 to 5-5. An overall good agreement is obtained related to the temperature, pore pressure and displacement evolution between numerical simulations and analytical solutions, except the displacement in x-direction at P4 is 0.02 mm smaller than analytical solution. The reason for that could be that the position of P4 is slightly inaccurate when interpolation is used in the numerical method.

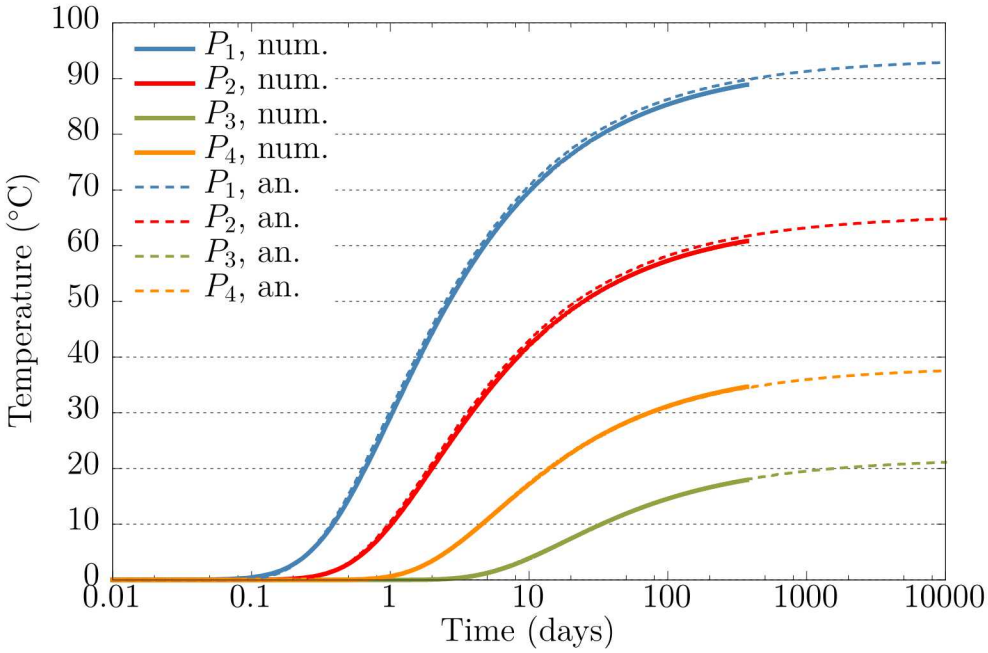


Figure 5-3. Simulation results of temperature at different points.

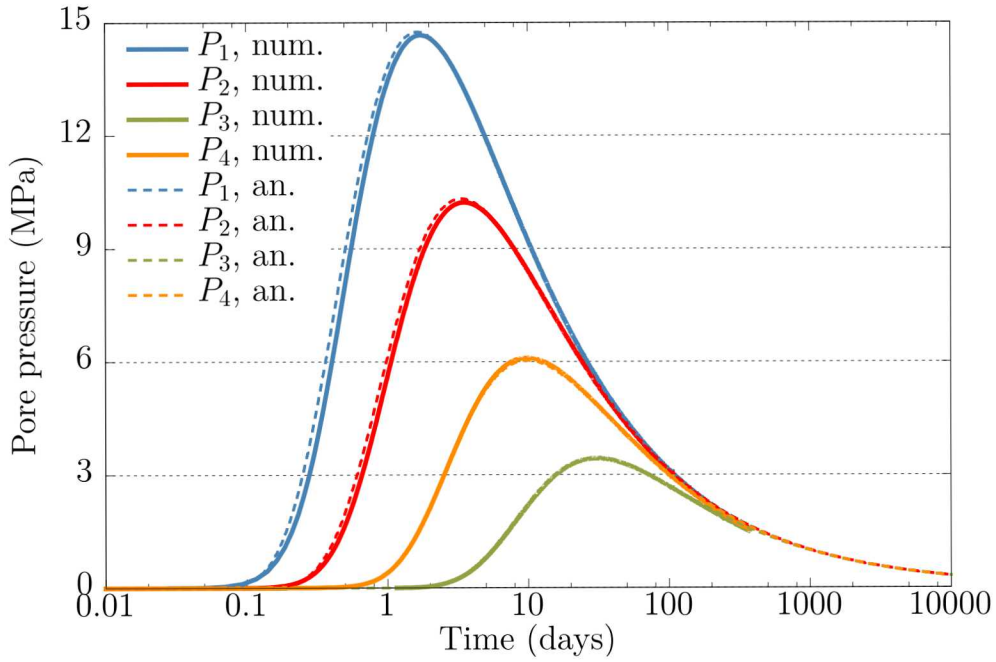


Figure 5-4. Simulation results of pore pressure at different points.

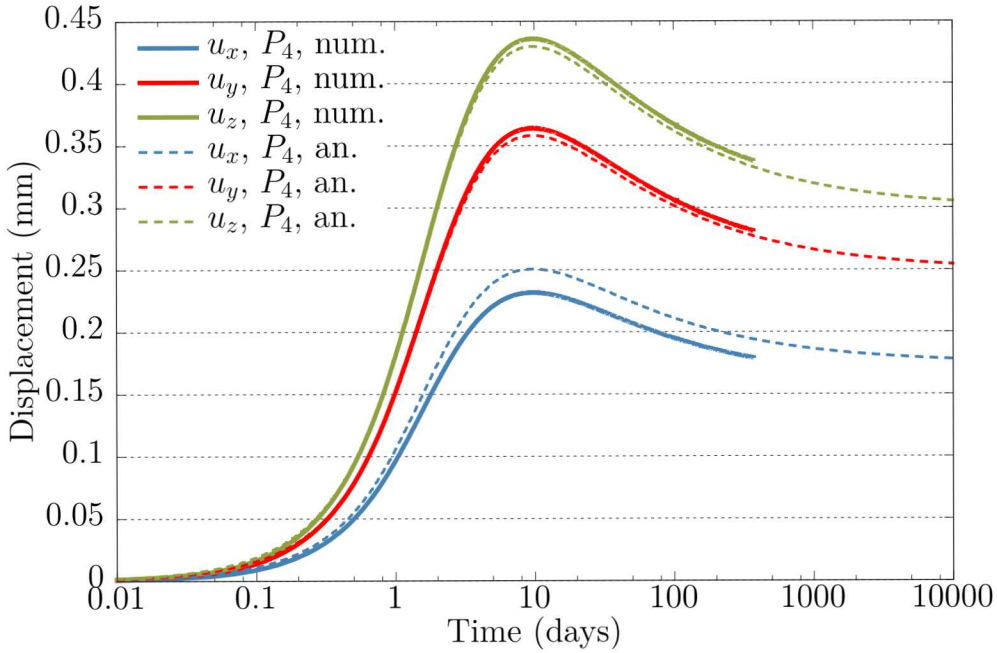
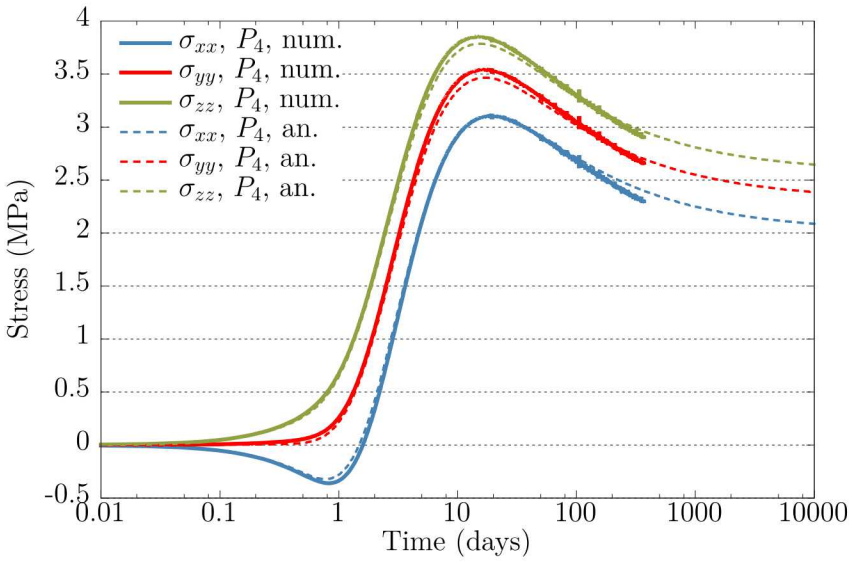
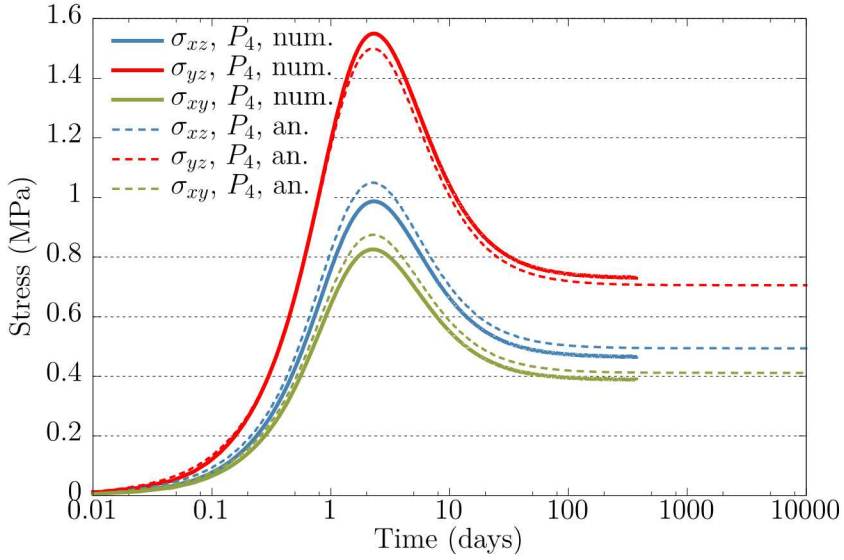


Figure 5-5. Simulation results of displacements at point P4.

Because the analytical solution of stresses in Booker and Savvidou (1985) is not correct, the stress results were not displayed in our FY2017 milestone report (Zheng et al., 2017). In FY2018, the analytical solution for stresses has been derived based on the methodology in Booker and Savvidou's paper. The simulated stress results are as presented in Figures 5-6a and b, are now in a good agreement with the analytical solution, which verifies the correctness of the TOUGH-FLAC code as well as the results of modeling of temperature, pore pressure and displacements.



a)



b)

Figure 5-6. Simulation results of stresses at point P4: a) Normal stresses, b) Shear stresses.

5.2.2 Step 2: TED experiment

The TED experiment lasted three years from 2010 to 2013. It involved three heaters at a depth of 490 m, in three parallel boreholes at a separation of about 2.7 m (Figure 5-7). The three heaters were 4 m long and were installed at the end of 160 mm diameter and 16 m long boreholes, drilled from a main drift and parallel to the maximum horizontal stress. This arrangement represented a similar configuration to high-level nuclear waste cells with parallel microtunnels, but at a smaller scale. The TED experiment was heavily instrumented with 108 temperature sensors in the rock mass, 69 temperature sensors in the 3 heater boreholes, 18 piezometers, 2 extensometers and

inclinometers, and 10 temperature sensors recording the temperature at the level of the main drift. The temperature measurements made during the TED experiment showed that the rock has an anisotropic thermal conductivity, because at the same distance from the heater, the temperature increase is higher in the bedding plane than that in the perpendicular direction. Observations of pore pressure also showed that its evolution depended on the location with respect to the bedding plane; following a power law increase, the pore pressure increased faster in the direction parallel to bedding than that in perpendicular direction.

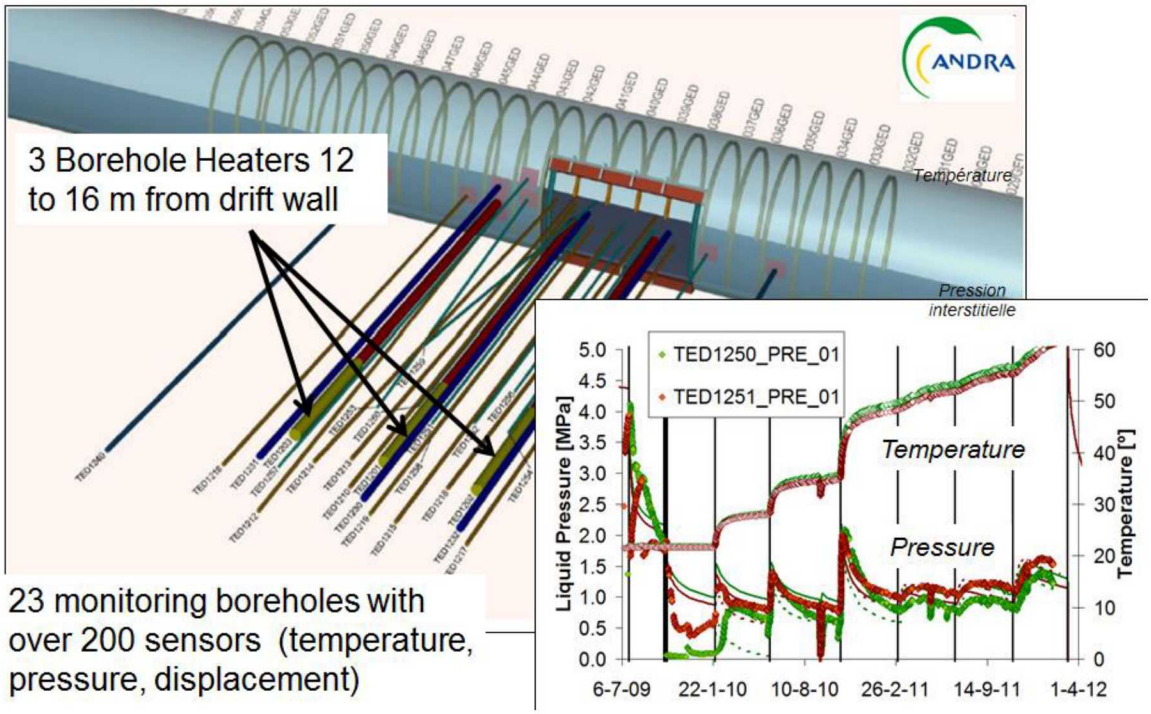


Figure 5-7. The schematic of the TED experiment at Bure. The insert on the figure is the graphs of pressure and temperature evolution, which were used by modeling teams in DECOVALEX-2019 Task E for interpretative modeling.

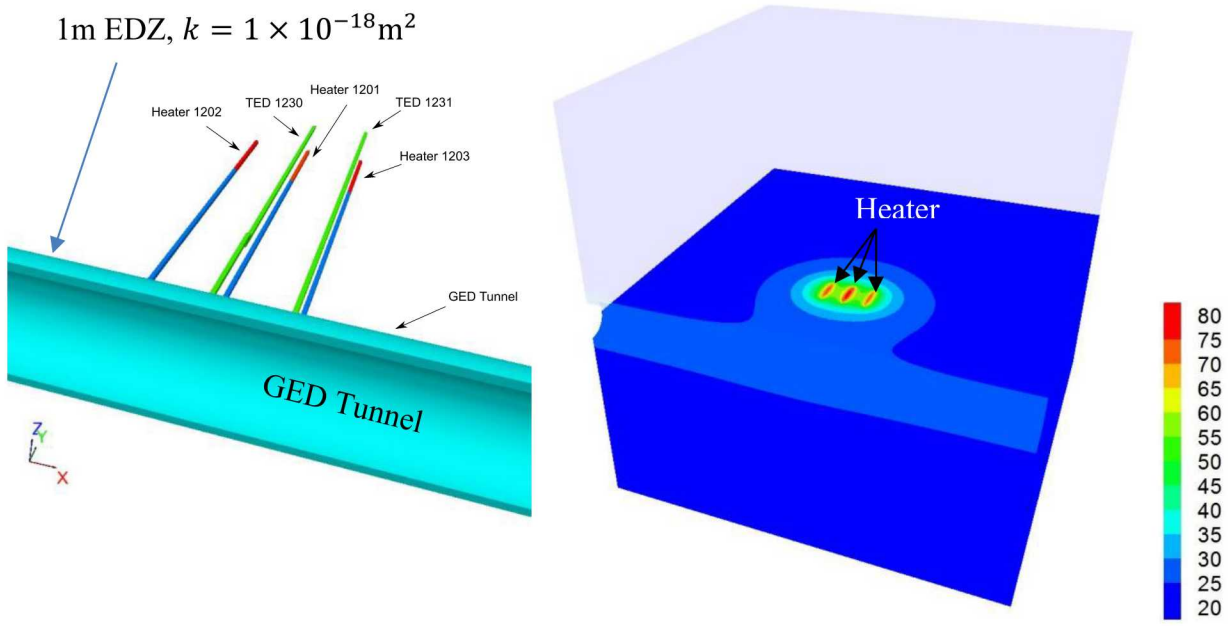
The purpose of Step 2 is to model the THM response of COx claystone in the TED experiment and to calibrate the numerical models against experimental data. This modeling of the TED experiment will also help improve understanding of physical phenomena observed.

The domain geometry simulated is a cube with a side length of 50 m centered in the height z = 0, i.e., almost exactly at the GED drift center at the depth of 490 m. The model represents only a half of the GED drift (Figure 5-8). Three heaters are embedded at the center of the domain with surrounded refined grids. For the modeling purposes, it is assumed that the whole domain is saturated and remains saturated during the experiment. The boundary conditions are summarized in Table 5-3.

In the previous FY2017 milestone report, the drilling of heater boreholes and extensometer boreholes were not explicitly modeled, indicating no water flow from the rock matrix into these boreholes. As a result, the pore pressure at the sensor in TED 1253, which is close to draining boreholes, was predicted much higher than experimental observation. Besides that, we did not account for the excavation of GED tunnel and drilling of the boreholes. Therefore, the effects

induced by excavation ware not studied, and the pore pressure prior to the heating phase was assumed distributed uniformly in the host rock. The variability of permeability in the EDZ was not considered.

In FY2018, the updated model started with instant excavation of the GED tunnel, followed by drilling of other boreholes. Then at 506 days after excavation, the heating phase started and was running for about 1251 days. The time zero corresponds to the excavation of GED tunnel at 04/21/2008. Heater 1 was turned on first, and it took three steps to reach the planned heat power (600W). After Heater 1 had been turned on for 400 days, Heaters 2 and 3 were turned on to heat the domain, including three heat power steps. The recent model computed with the raw data of heat power is shown in Figure 5-9. As suggested by other modeling teams among the DECOVALEX participants, a cylindrical EDZ was applied around GED tunnel with 1m thickness in order to include the variability of permeability due to excavation (Figure 5-8a). The pore water pressure is considered uniform at 4.7 MPa in the entire domain when excavation started. The stress values follow the anisotropic state of stress. For calculations, the stresses proposed by the task lead from ANDRA are: the major horizontal stress σ_H =16.1 MPa, and the horizontal minor stress σ_h = 12.4 MPa, and the lithostatic stress σ_v =12.7 MPa.



a) b)

Figure 5-8. a) The model setup the position of heater boreholes (Heater 1201~1203), extensometer boreholes (TED 1230 and TED 1231), and GED tunnel surrounded by 1m EDZ and b) Temperature distribution at 1509 days.

Table 5-3. THM boundary conditions of TED experiment modeling for Step 2.

Boundary	Thermal condition	Hydraulic condition	Mechanical condition
External faces (except top and bottom)	No heat flux	No water flux	No normal displacements
Top surface	*In situ* temperature T = 21°C	4.7 MPa	Vertical geostatic stress $\sigma_v = 12.7$ MPa
Bottom	*In situ* temperature T = 23°C	4.7 MPa	No normal displacements
GED drift wall	Temperature measurements in the GED drift	Draining condition: atmospheric pressure	No normal displacements
TED1230 and TED1231 Boreholes (extensometers)*	No heat flux	Draining condition: atmospheric pressure	No normal displacements
Heater Boreholes	History of applied power (Figure 5-9)	Draining condition: atmospheric pressure	

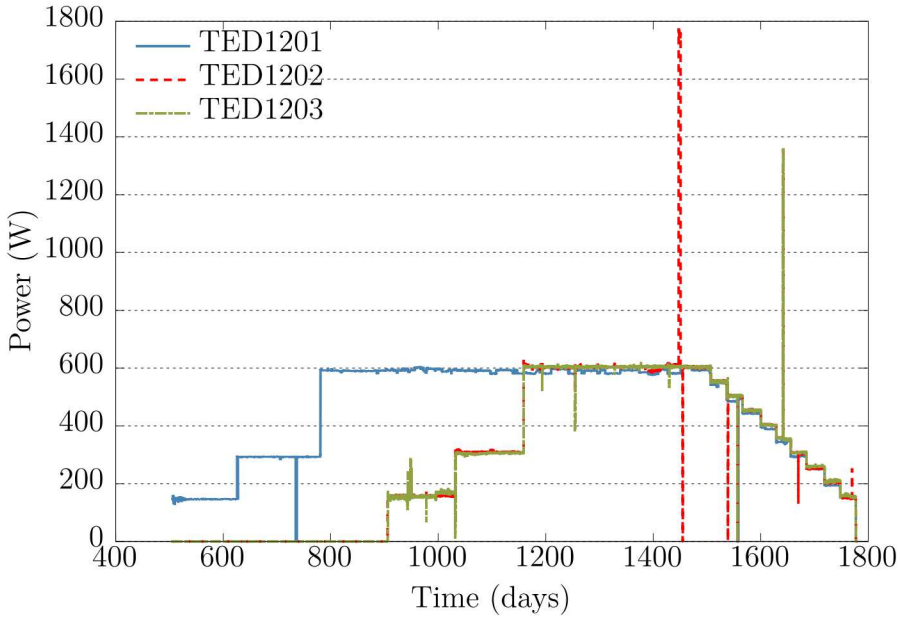


Figure 5-9. Heat power used for Heater 1, 2 and 3.

The THM computation with the simulator TOUGH-FLAC included water properties calculated from the steam table equations (IFC-1967). We have recalibrated thermal conductivity, mechanical properties and permeability of COx rock, because we applied other conditions, such as the drainage boundary. All parameters utilized in the current model are summarized in Table 5-4.

.

Table 5-4. THM parameters of Step 2 used for THM simulations.

Parameters	Values
Porosity	$\phi = 0.15$
Equivalent thermal conductivity parallel to bedding [W/m/K]	$\lambda = 2.05$
Equivalent thermal conductivity perpendicular to bedding [W/m/K]	$\lambda = 1.15$
Equivalent density [kg/m^3]	$\rho = 2400$
Density of solid grains [kg/m^3]	$\rho_s = 2600$
Heat capacity of solid grains [J/kg/K]	$C_{ps} = 800$
Permeability parallel to bedding [m^2]	$K_{\parallel} = 3 \times 10^{-20}$
Permeability perpendicular to bedding [m^2]	$K_{\perp} = 0.7 \times 10^{-20}$
Biot coefficient	$b = 0.7$
Volumetric coefficient of thermal expansion of solid grains [1/K]	$\alpha_s = 4.2 \times 10^{-5}$
Young's modulus parallel to bedding [GPa]	$E_1 = E_{\parallel} = 6$
Young's modulus perpendicular to bedding [GPa]	$E_3 = E_{\perp} = 3$
Poisson's ratio inside the bedding plane [-]	$\nu_{12} = 0.3$
Poisson's ratio between in bedding plane and out-of-plane [-]	$\nu_{13} = 0.3$
Water properties (ρ_w, c_w, C_{pw}, μ_w, α_w)	(IFC-1967)

In TED experiment, 6 sensors were placed at different boreholes near heaters to measure the temperature evolution during the heating stage. The collected data were used as a basis for calibration of thermal properties. Figure 5-10 displays the recent temperature results based on the results of simulations with calibrated parameters. As the figure shows, a good agreement at Boreholes 1210, 1219, 1250, and 1251 is achieved between the model prediction and the experimental data. Note that although the model simulation overestimated the temperature by about 3 to 5^o at the two points farthest from the heater, Boreholes 1253 and 1258, the experiment team reported that these two sensors as unreliable. So the calibration on the thermal properties based on other locations is acceptable.

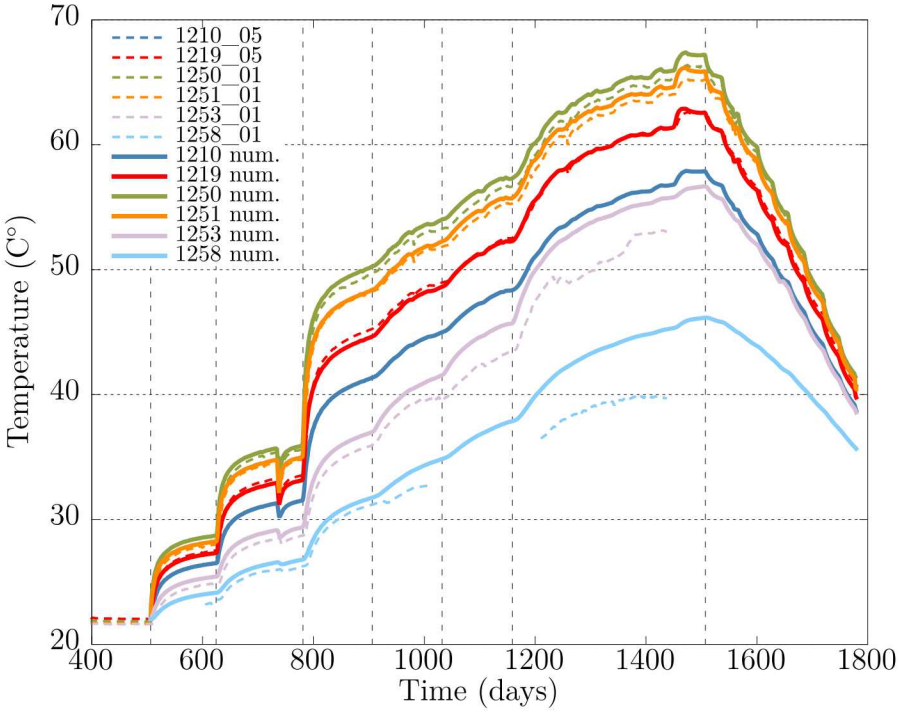
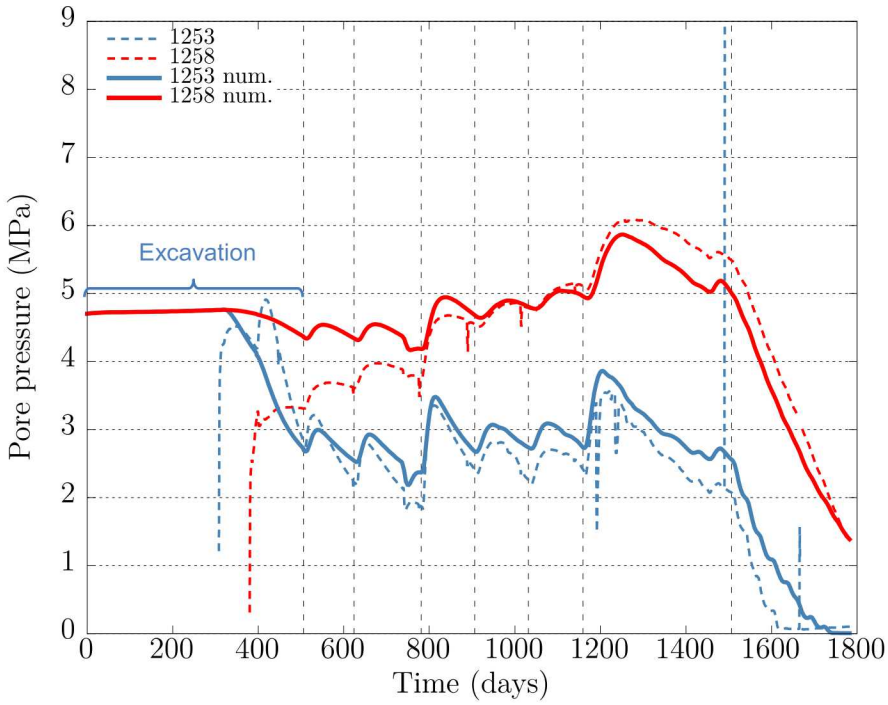
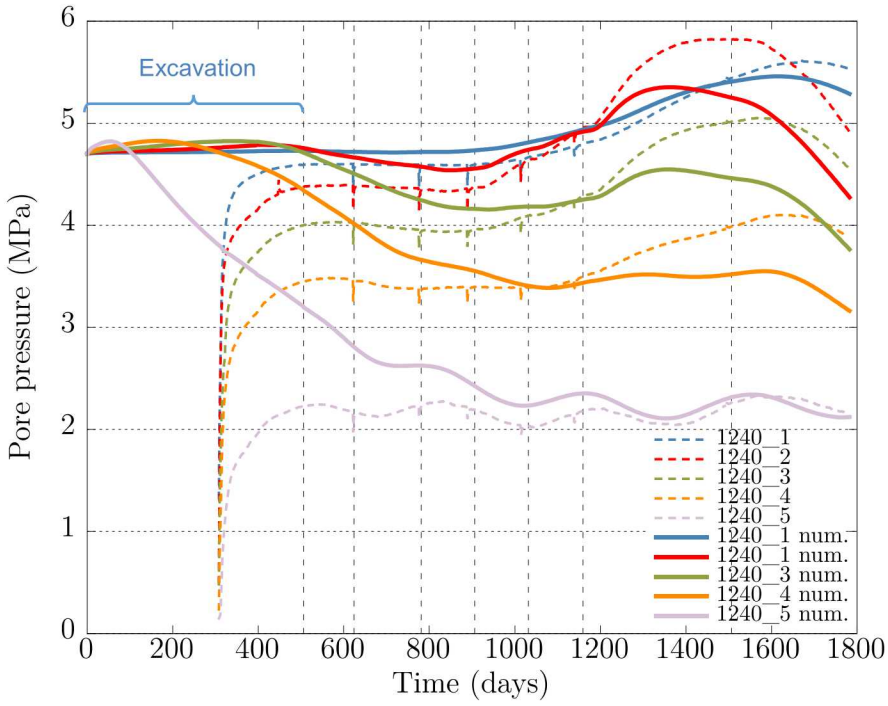


Figure 5-10. Temperature evolution simulated with calibrated thermal conductivities at measuring points.

Figure 5-11a presents the simulation results and experimental observations of pore pressure at the sensor positions in Boreholes 1253 and 1258. From the figure, the simulated pore pressure at Borehole 1253 is in good agreement with experimental data recorded by the sensor. Although some disagreements of pore pressure at Borehole 1258 are noted, especially the pore pressure at the beginning of the heating phase, but after 800 days the predicted pore pressure agrees with experimental data. The explanation is that the simulation results of pore pressure depends on the final status of the excavation phase, while the observed data were affected by the heterogeneity of rock matrix and pore pressure build-up after sensor installation. Figure 5-11b displays the simulated and observed pore pressure at five sensor positions in Borehole 1240. Compared with experimental data, the trend of pore pressure change has been captured while the magnitude of pore pressure at peak is underestimated.



a)



b)

Figure 5-11. a) Pore pressure evolution at Boreholes 1253 and 1258. b) Pore pressure evolution at Boreholes 1240.

In FY2018, more conditions are applied in the model, such as the tunnel excavation, boreholes, EDZ around the tunnel and the drainage boundary at boreholes. The new model simulated with re-calibrated parameters provides a better prediction of temperature and pore pressure compared to last year's results. However, no measured data on stresses are available.

5.2.3 Step 3 – ALC experiment

The ALC experiment started its heating phase in 2013 and is an ongoing *in situ* heating test performed in the MHM URL. The experiment is a full scale representation of a single high-level waste cell in COx claystone. The ALC1604 microtunnel was drilled from the GAN drift. It has a total length of 25 m and it includes different parts. The heated part in ALC experiment is located in the body part of ALC1604 between 10 and 25 m deep (Figure 5-12) and is made up of five heating elements. Each element is 3 meters long and has a diameter of 508 mm. The ALC experiment was heavily instrumented with temperature and relative humidity sensors, piezometers, strain gauges, and displacement sensors. The temperature measurements made during the ALC experiment showed a similar phenomenon as in the TED experiment, indicating an anisotropic thermal conductivity; because at the same distance from the heater, the temperature increase is higher in the bedding plane than that in the perpendicular direction. Observations of pore pressure showed that its evolution depended on the location with respect to the bedding, and strong hydro-mechanical (HM) coupling induces opposite pore pressure change near ALC1604 after its excavation. In the vertical direction, the volumetric strain is positive (volumetric expansion), indicating the pore pressure decrease, because in the horizontal direction, the volumetric strain is negative (the volume decreases), driving pore pressure increase.

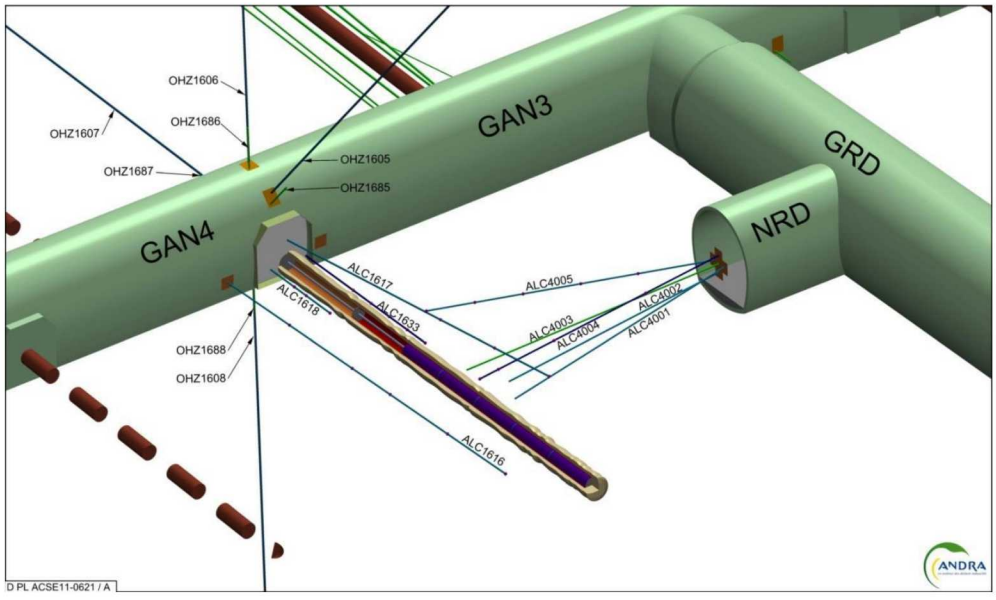


Figure 5-12. The ALC experiment at Bure with various monitor boreholes and microtunnel ALC1604 that are used by modeling teams in DEOVALEX-2019, Task E, for interpretative modeling.

The purpose of Step 3 is to predict the THM response of COx claystone in the ALC experiment with calibrated material parameters from TED experiment. Modeling of ALC experiment will help

investigate the behavior of the cell and the casing under thermal loading, and to understand the THM behavior of the COx and of the interface between the rock mass and the casing.

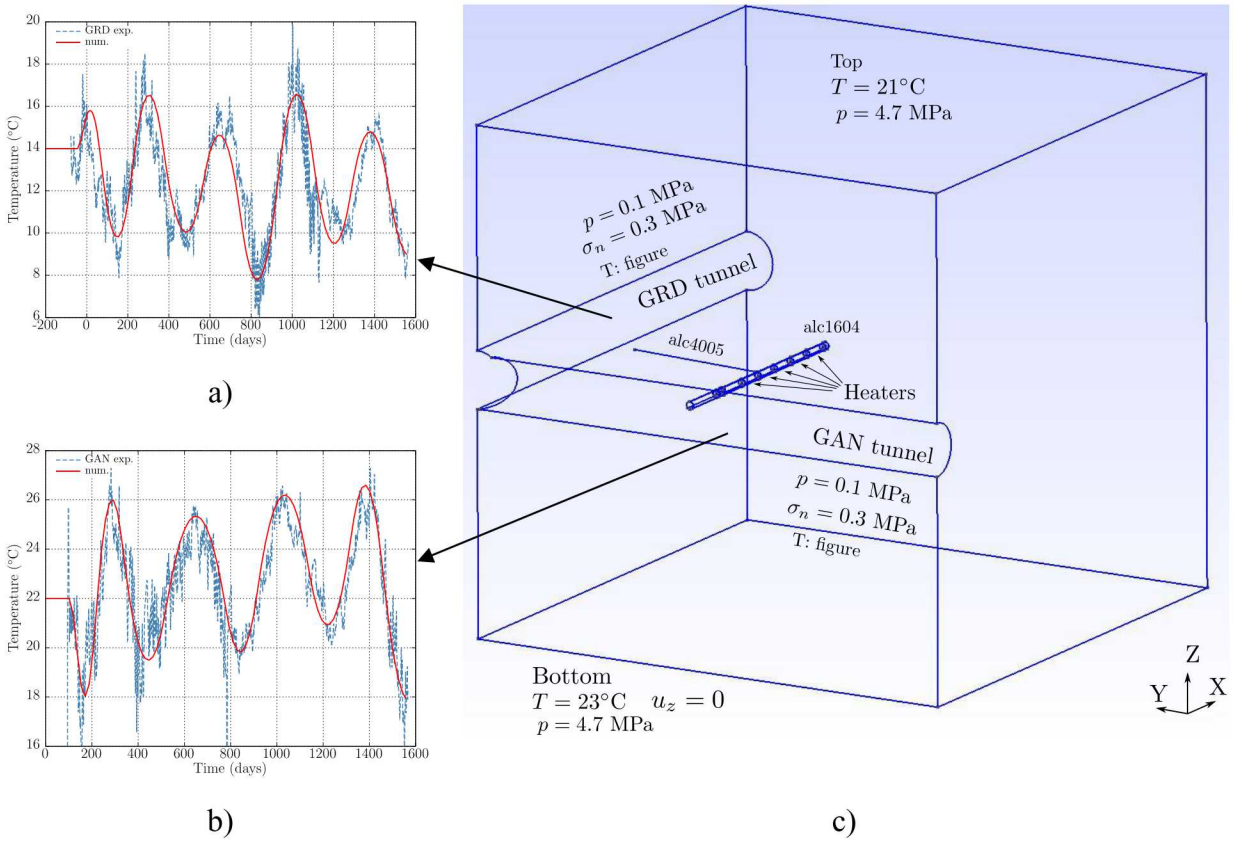


Figure 5-13. Geometry of the model with boundary conditions: a) Observed and simulated temperature evolution at GRD tunnel; b) Observed and simulated temperature evolution at GAN tunnel; and c) Geometry of the simulation domain and boundary conditions on each surface.

The geometry model domain is a cube with a side length of 50 m centered in height at z = 0, with half of the GAN tunnel excavated along the *y*-direction, and half of the GRD tunnel excavated along the *x*-direction (Figure 5-13c). Five heating elements are located in ALC1604 between 10 and 25 m along *x*-direction. The heaters are discretized with refined elements. Casing and gap inside the borehole are both explicitly discretized (Figure 5-14). For modeling purposes, it is assumed that the whole domain is saturated and remains saturated during the experiment. An additional draining borehole, ALC4005, is explicitly simulated with excavation and drainage as Figure 5-13 shows.

In the simulation, the model started with instant excavation of GAN and GRD tunnels, followed by drilling of other boreholes. Then at 458 days after the excavation, the heating phase started and was running for about 1500 days. The time zero, corresponds to the excavation of tunnels, is at 11/01/2011. A heating test at a very low power (33 W/m, 495 W in total) was conducted between January 31 and February 15, 2013. The main heating phase started on April 18, 2013, at a constant nominal power of 220 W/m (3300 W in total) for the 15 m occupied by the heater elements (i.e., 660W per element). The initial pore water pressure is considered uniform at 4.7 MPa in the entire

domain when excavation started. The stress values follow the anisotropic state of stress. For the calculation the stresses are proposed as: the major horizontal stress σ_H is set to 16.1 MPa in y-direction, and the horizontal minor stress σ_h and the lithostatic stress σ_v are set respectively to 12.4 MPa in x-direction and 12.7 MPa.

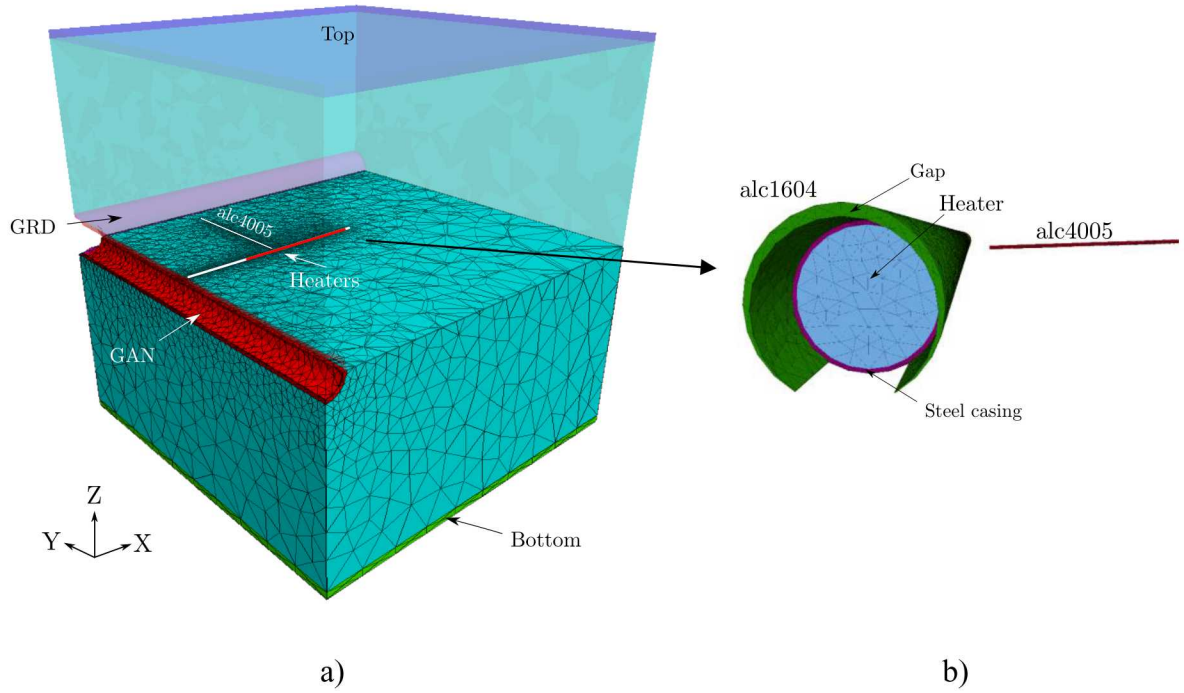


Figure 5-14. Mesh generation in simulated domain. a) Mesh in the entire domain. b) Mesh generation for heater, casing and the gap between them.

The THM computation of ALC experiment is conducted with the parameters, calibrated from TED test, which are listed in Table 5-4.

In the field, six sensors were placed at different boreholes near heaters to measure the temperature evolution during the heating stage. These collected data are used as a basis for calibration of thermal properties. Figure 5-15 displays the temperature results compared with experimental data recorded by the sensors. As the figure shows, a good agreement is achieved between the model prediction and the experimental data. However, at sensors 1617-1 and 1617-2, our model predicted higher temperature than observed data, while at sensors 1616-5 and 4005-4, the model underestimated the temperature. A possible explanation is that the simulation is based on an assumption of homogeneous host rock, while the *in situ* COx clay stone is heterogeneous.

Figure 5-16 presents simulation results of pore pressure at the sensor positions in the boreholes. From the figure, it is found that the pore pressure decreases after the initial excavation of the GAN and GRD tunnels, which is due to the drainage conditions applied on tunnel surfaces. Then, around 0 day, corresponding to the day of 10/23/2011, the drilling of the microtunnel (ALC1604) is computed, and the results indicate the relevant hydro-mechanical (HM) coupling. Volumetric expansion due to excavation of ALC1604 occur at sensors 1617-1 and 1617-2, which are above

ALC1604. As a result, pore pressure at these two positions decreases. In the horizontal direction, volumetric compression occurs at sensors 1616-2 and 1616-5, which raises the pore pressure. After the heating started, the pore pressure increased due to thermal pressurization except at sensor 1616-5, which was close to the GAN tunnel, and affected by the temperature boundary on the surface of the tunnel. Sensor 4005-4 shows similar response. Since it is far from the heaters, the temperature changes are small and the peak of pore pressure is lower than at other sensors.

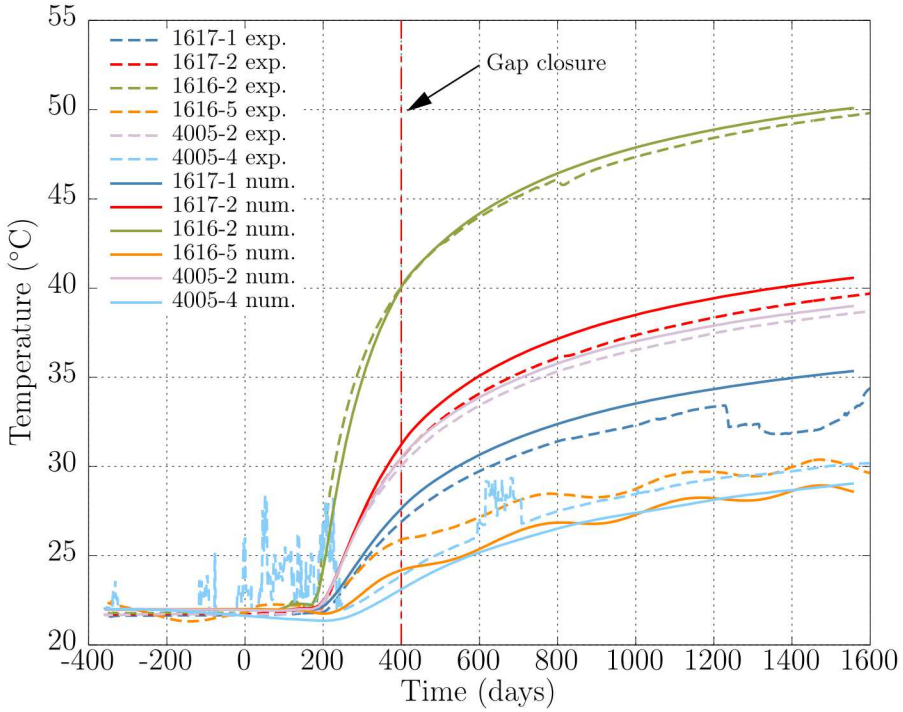


Figure 5-15. Simulated and observed temperature evolution at measuring points.

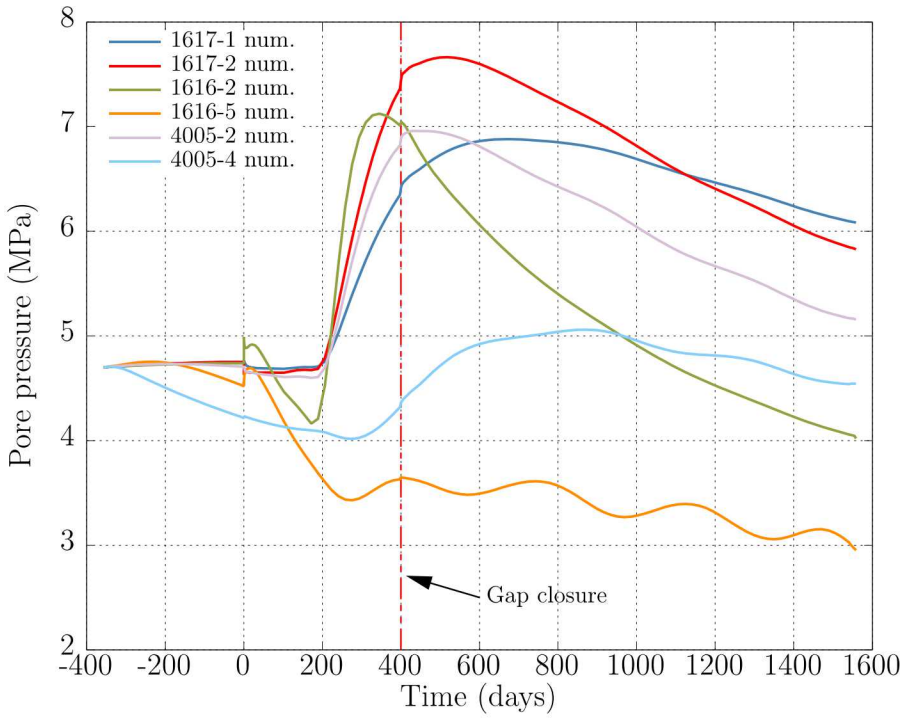


Figure 5-16. Simulated pore pressure evolution at sensor points.

In FY2018, we have investigated the THM behavior of COx rock associated with the ALC experiment with the TOUGH-FLAC simulator. In the numerical simulation, excavation of tunnels and boreholes were explicitly computed, and drainage conditions were applied at boreholes. A good agreement was achieved between numerical simulation and experimental observation of temperature. After we receive the measured data on pore pressure from the experiment team, we will compare our results with the experimental data, which will help us to understand THM processes in COx host rock.

5.3 Summary and Status of the Bure Heater Experiment Modeling

In FY2018, along with Task E of the DECOVALEX-2019 project, we have updated our model to simulate coupled THM processes associated with the TED *in situ* heating test performed in COx claystone, and completed new simulations to predict THM processes at the larger scale ALC *in situ* heating experiment. The current progress on this task is:

- For Step 1, we have corrected the analytical solution results of stress for the 3D THM modeling benchmark problem, a good agreement was achieved between our model simulation and theoretical solutions.
- For Step 2, we have determined THM parameters of claystone from the TED experiment, including calibration on thermal conductivities to match the temperature evolution during the heating phase, and back analysis on the simulation results to correct permeability. The heating phase of the TED experiment has been simulated with TOUGH-FLAC with good match to experimental data.

- For Step 3, we predicted THM behavior of COx clay stone during the ALC experiment by utilizing parameters of claystone from calibrated from the modeling of the TED experiment. The heating phase of the ALC experiment has been simulated with TOUGH-FLAC to experimental temperature data. We will compare our result on pore pressure with experimental data after we receive the measured data from the DECOVALEX-2019 Task E coordinators.

The next step for the rest of FY2018 and FY2019 will be to model Step 4 of DECOVALEX-2019 Task E; that is, we will conduct model predictions at the repository scale of an area with several high level waste cells.

6. Modeling of Gas Migration in Clay Using TOUGH-FLAC and TOUGH-RBSN (DECOVALEX-2019)

In this section, we present LBNL's activities for modeling gas migration in clay related to Task A of the DECOVALEX-2019 project. This is an international collaborative activity, in which DOE and LBNL gain access to the results of unique laboratory experiments of gas migration. These results are now used for numerical modeling to better understand the processes, to improve numerical models, and which will ultimately be applied in the performance assessment of nuclear waste disposal in clay host rocks and bentonite backfill. The Task A of DECOVALEX-2019 is coordinated by the British Geological Survey (BGS), that is also sharing their extensive data set on coupled THM responses during gas migration in bentonite and clay stone. In FY2018 LBNL has continued to participate in Task A of DECOVALEX-2019, as one of 11 international research teams (a list of research teams in given in Section 6.2), and conducted new simulations of gas flow through bentonite with comparison to the experimental data. In the following, we first introduce the issue of gas migration, the DECOVALEX-2019 tasks, experimental data and finally the LBNL modeling results.

6.1 Gas Migration in Clay

Gas migration in clay-based buffer materials has been the subject of a number of international research programmes in the field of nuclear waste disposal, including both laboratory scale and *in situ* experiment (e.g. Horseman et al., 2004; Harrington et al., 2012; Cuss et al., 2014). Substantial insight has been gained in the phenomenology of gas transport processes in bentonite and clay stone under different THM conditions. A number of model approaches have been proposed for the interpretation of the experimental results and for the analysis of gas release scenarios from geological repositories in the context of long-term safety assessment. The predictive capability of the gas transport models is yet limited, indicating that basic mechanisms of gas transport in bentonite are not understood in sufficient detail to provide the ground for robust conceptual and quantitative models.

The processes governing the movement of repository gases through bentonite and argillaceous host rocks can be split into two components: (1) molecular diffusion (governed by Fick's law), and (2) bulk advection (Harrington, 2016). In repository concepts such as the Swedish KBS-3, corrosion of metallic materials under anoxic conditions will lead to the formation of hydrogen. Radioactive decay of the waste and the radiolysis of water are additional source terms. If the rate

of gas production exceeds the rate of gas diffusion within the pores of the barrier or host rock, a discrete gas phase will form. Under these conditions, gas will continue to accumulate until its pressure becomes sufficiently large for it to enter the surrounding material.

Four primary phenomenological models describing gas flow, shown in Figure 6-1, can be defined as following: (1) gas movement by diffusion and/or solution within interstitial fluids along prevailing hydraulic gradients; (2) gas flow in the original porosity of the fabric, commonly referred to as viscocapillary (or two-phase) flow; (3) gas flow along localized dilatant pathways, which may or may not interact with the continuum stress field; and (4) gas fracturing of the rock similar to that performed during hydrocarbon stimulation exercises (Harrington, 2016).

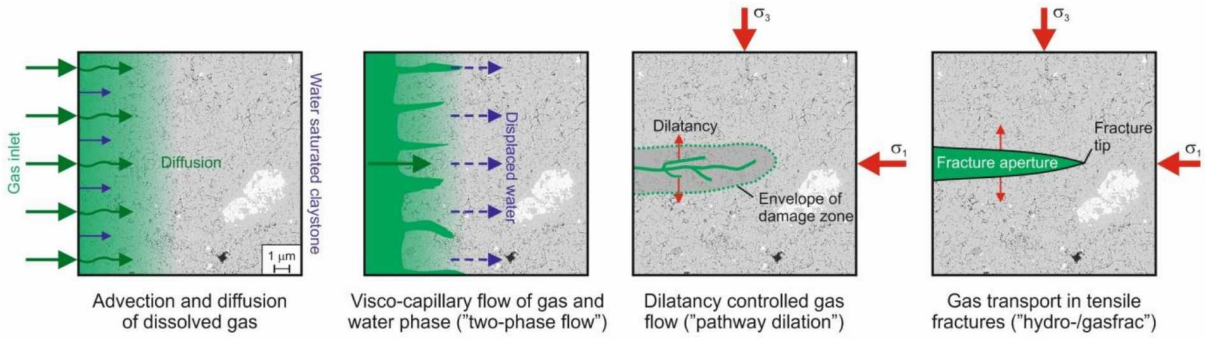


Figure 6-1. Conceptual models of gas flow (Harrington, 2016)

Studies on gas migration in clays (Horseman et al., 1999; 2004; Harrington and Horseman, 1999) indicate that classic concepts of porous medium two-phase flow are inappropriate and continuum approaches to modeling gas flow may be questionable, depending on the scale of the processes and resolution of the numerical model. However, the detail of the dilatant mechanisms controlling gas entry, flow and pathway sealing are unclear. As such, development of new and novel numerical representations for the quantitative treatment of gas in clay-based repository systems is therefore required (Harrington, 2016).

6.2 DECOVALEX-2019 Task A and International Modeling Teams

The purpose of Task A in DECOVALEX-2019 is to obtain better understanding of the processes governing the adjective movement of gas in low permeability clay barrier materials (Harrington, 2016). Special attention is given to the mechanisms controlling factors such as gas entry and flow, as well as pathway stability and sealing, which will impact barrier performance. In Task A of DECOVALEX-2019, new numerical prediction of gas fluxes will be developed by the participating international modeling teams. The models will be tested against a series of controlled laboratory tests, in a staged manner, building in complexity (both in terms of the experimental and modeling approaches). It is anticipated that the development of these models will provide a valuable tool to assess the impact of gas flow on barrier and host materials, providing information which could be used to support future repository design.

Data from a series of flow tests performed on initially saturated samples will be made available to project participants. These long-term tests, performed under carefully controlled laboratory conditions, provide detailed datasets applicable to examine gas migration behavior under steady state conditions. As such, a number of test geometries have been used, ranging in complexity from relatively simple one-dimensional flow tests on bentonite to triaxial tests performed on natural samples of COx claystone. To gain insights into the adjective movement of gas through these materials, laboratory data will be used to guide and benchmark numerical model development in an iterative process, increasing in model complexity from one test stage to the next (Harrington, 2016).

The initial plan of the task includes 4 distinct stages (Harrington, 2016):

- Stage 0: Code development:
  - Initial aim is to understand and reflect on the apparent fluctuating behavior of all experimental data. References and publications will be made available and the teams will be asked to develop one or more modeling approaches.
- Stage 1: 1D gas flow through saturated bentonite under controlled laboratory conditions
  - Data will be provided from a 1D gas flow test, performed on saturated bentonite subjected to a constant volume boundary condition.
- Stage 2: 3D spherical gas flow under controlled laboratory conditions
  - A: spherical flow through saturated bentonite, under a constant volume boundary condition.
  - B (optional): a second dataset under the same experimental boundary conditions is also offered, against which the models can be tested.
- Stage 3: Application of previous models to a natural clay-based system
  - A: triaxial test performed on a sample Callovo-Oxfordian claystone (COx). This dataset comprises a number of stages including initial hydration, hydraulic testing and gas injection.
  - B (optional): gas flow through hydrated bentonite pellets under constant volume conditions. If appropriate, data from a long-term test performed by the Commission for Atomic Energy and Alternative Energies (CEA) will be made available for Teams participating in this task.

The following international organizations and modeling teams are involved in DECOVALEX-2019, Task A (gas migration in clay):

- UK: British Geological Survey (BGS-Task Leader).
- UK: Quintessa
- Germany: Bundesanstalt für Geowissenschaften und Rohstoffe (BGR)
- Germany: Helmholtz-Centre for Environmental Research (UFZ)
- USA: Sandia National Laboratory
- USA: Lawrence Berkley National Laboratory
- France : Institut de Radioprotection et de Sûreté Nucléaire (IRSN)
- Korea: Korea Atomic Energy Research Institute (KAERI)
- Canada: Canadian Nuclear Safety Commission (CNSC)
- Spain: Universitat Politècnica de Catalunya (UPC)

- Taiwan: Taiwan Power Company (Taipower)

The research teams have completed Stage 1 (1D gas flow test) and are currently working on Stage 2 (3D spherical gas flow). Related to the initial Stage 0, initial code development was completed though the code development continues along with modeling of the various experimental data in Stages 1 through 3. In Section 6.3, we briefly present Stage 1 and Stage 2 experimental data. In FY2018 LBNL has updated simulations of Stage 1 (1D gas flow test) as well as completely new simulations of Stage 2 (3D gas flow test).

6.3 Laboratory Experiments of Gas Migration in Bentonite

Stage 1 experimental data consists of 1D gas flow test through a saturated sample of MX-80 bentonite. The experimental data is provided to the DEOCOVALEX-2019 modeling teams by the task coordinators from BGS, who is also conducting the gas-migration experiments. The experiment is conducted on a cylindrical bentonite sample, 120 mm in height and 60 mm in diameter. The sample is placed in a pressure vessel that allows for monitoring of the evolution of pressure and stress at different locations along the sample, as well as inflow and outflow rates through filters (Figure 6-2).

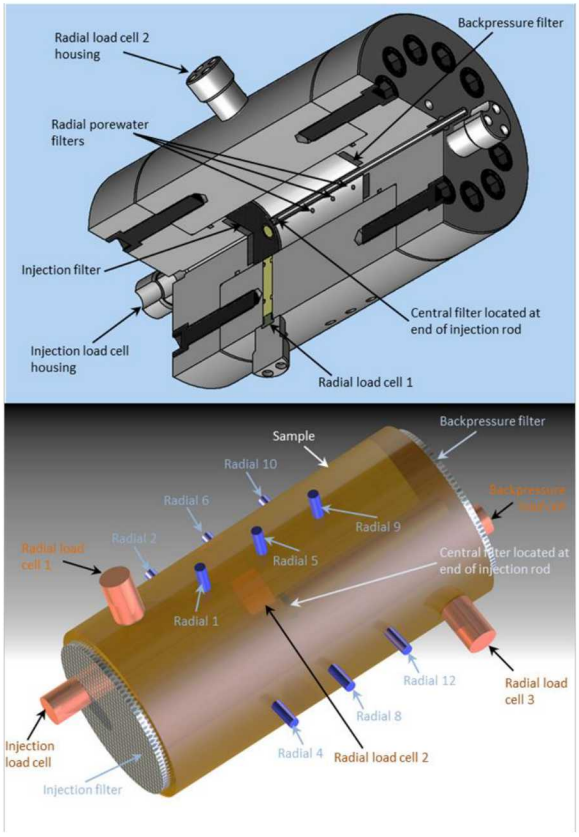
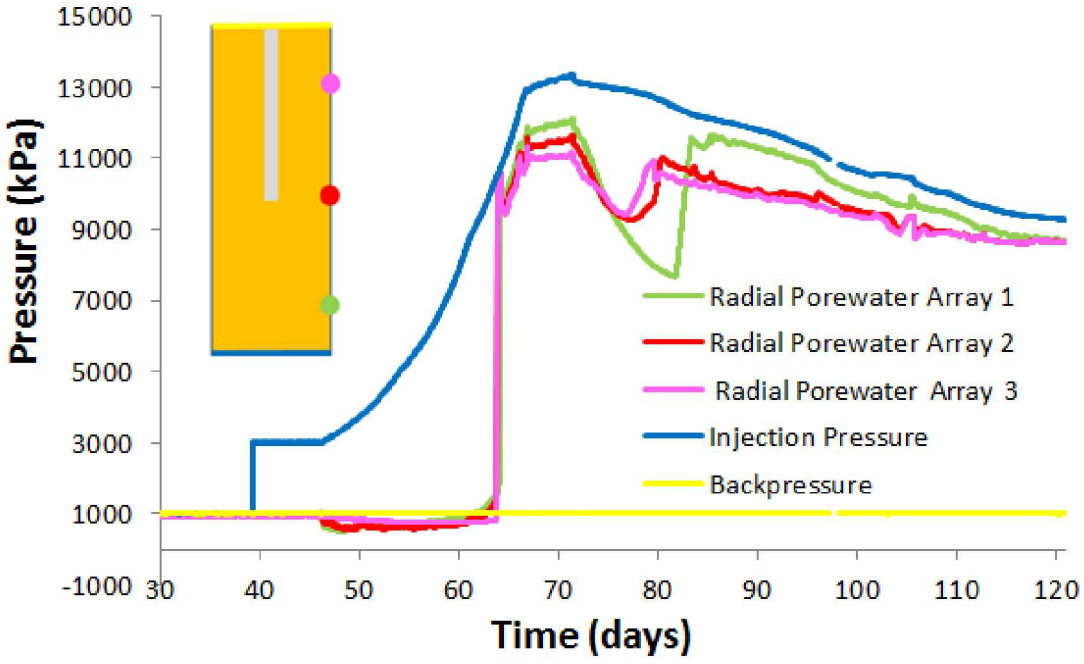
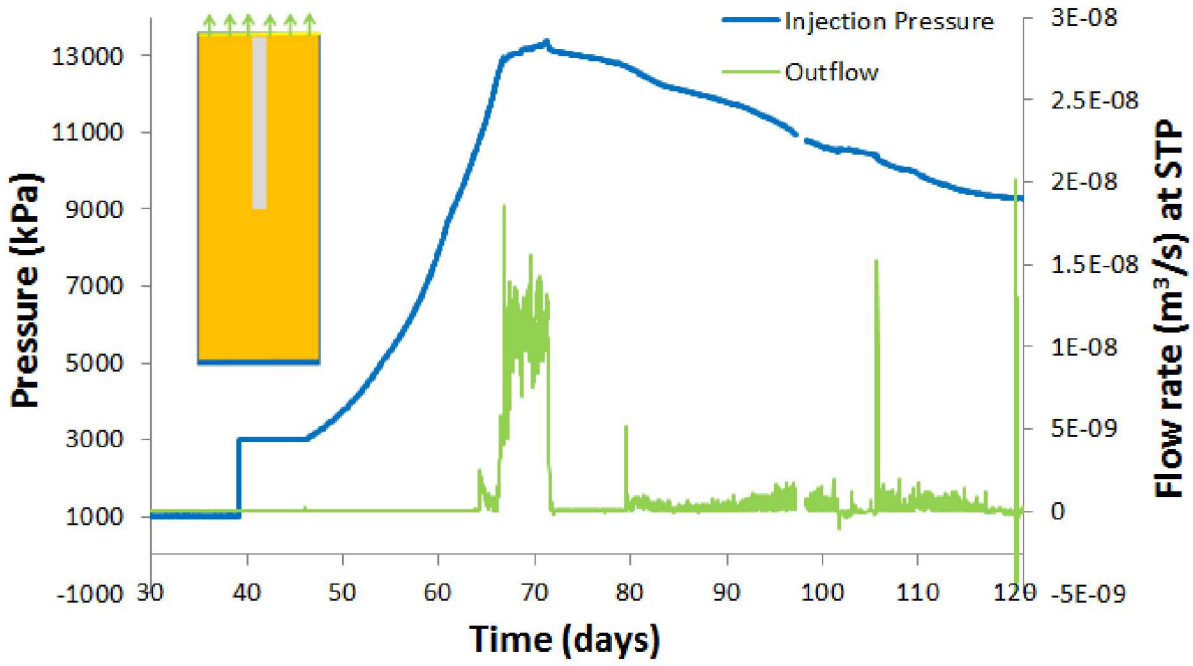


Figure 6-2. Above: Cut-away diagram of the pressure vessel showing the apparatus components and instrumentation. Below: image of the sample showing the relative positions of the load cells and pore pressure filters (Harrington, 2016).

Part of the experimental results related to pressure and outflow is shown in Figure 6-3. In the experiment, the bentonite sample was hydrated prior to gas testing through all radial and backpressure filters. The water was infiltrated and equilibrated at a pressure of 1 MPa. The hydration resulted in swelling and development of swelling stress within the sample (not shown here). Once total stress began to plateau, helium gas was introduced in to the injection filter at an initial pressure of 3 MPa (blue line in Figures 6-3a and b). This was left to equilibrate with the water in the pump for seven days. Thereafter, gas was injected into the injection chamber resulting in a gradual increase of injection gas pressure (blue line in Figures 6-3a and b), while keeping the back pressure constant at 1 MPa (yellow line in Figure 6-3a). When the injection pressure reached about 10 MPa, an abrupt increase in pressure was observed at monitoring points along the sample (green, red, purple lines in Figure 6-3a). At the same time there was a sudden temporal increase of gas outflow (green line in Figure 6-3b). The injection was then shutdown and the injection pressure went down slowly along with the pressure measured at other points along the sample.



(a)



(b)

Figure 6-3. Observed (a) pressure evolution and (b) outflow rate (Modified from Harrington, 2016).

Stage 2 experimental data were collected to describe 3D spherical gas flow through a saturated sample of MX-80 bentonite. The experiment has been conducted by BGS, who has also tested the 1D gas flow through bentonite to obtain the Stage 1 experimental data. They have adopted the same sample geometry as used in Stage 1, but varied the injection location from one side of base surface (Figure 6-4a) to the center of the sample (Figure 6-4b). Staged hydration and gas injection processes have been carefully controlled over 700 days to minimize the perturbation of the system/sample and better reflect realistic conditions of a deep geological disposal facility. The DECOVALEX teams performed numerical simulations of coupled gas pressure and stress responses for the period from 735 to 835 days, when the gas breakthrough occurred.

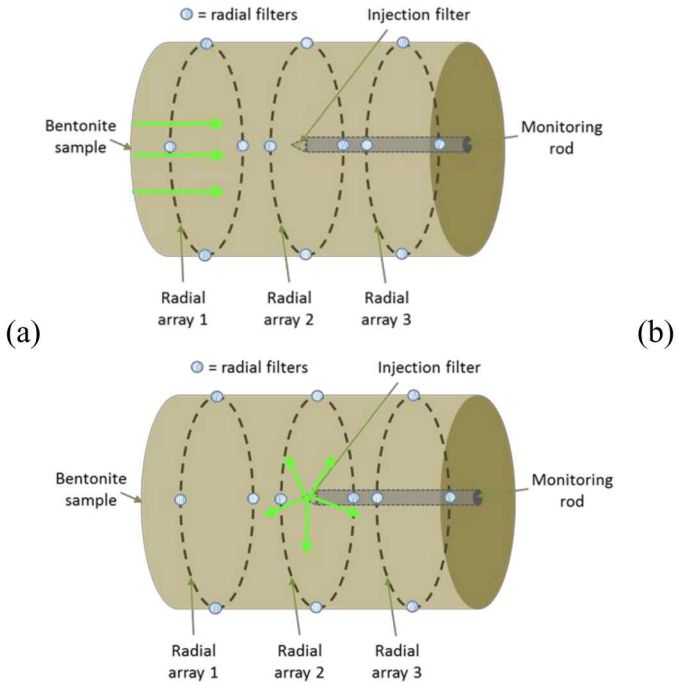
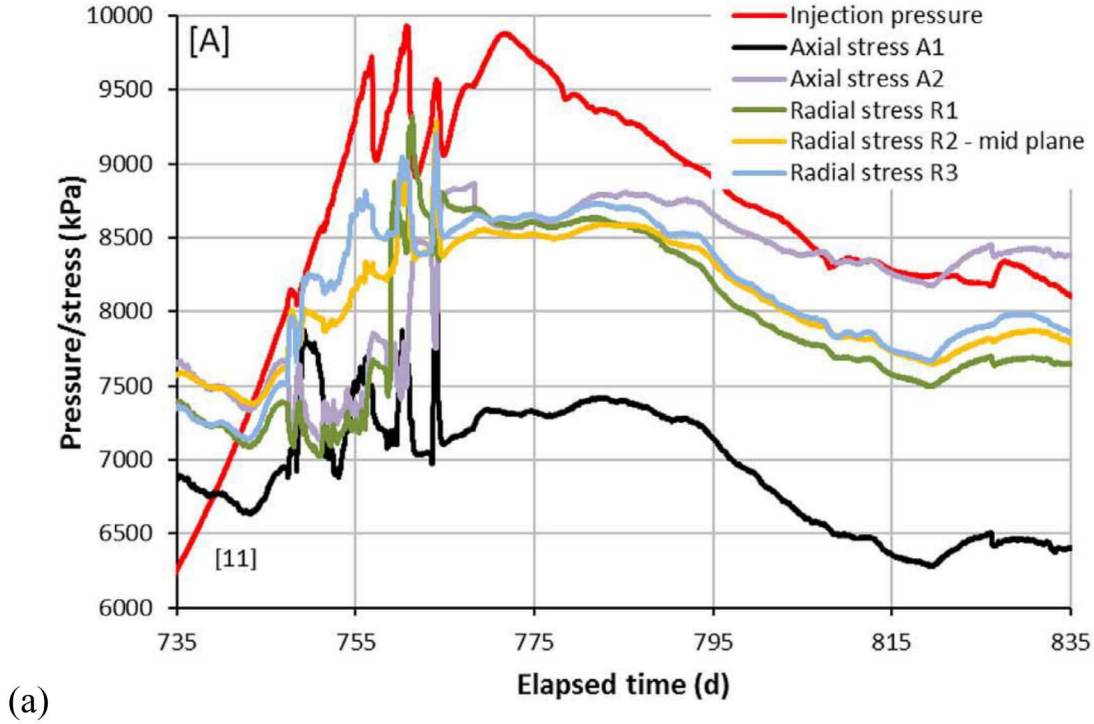
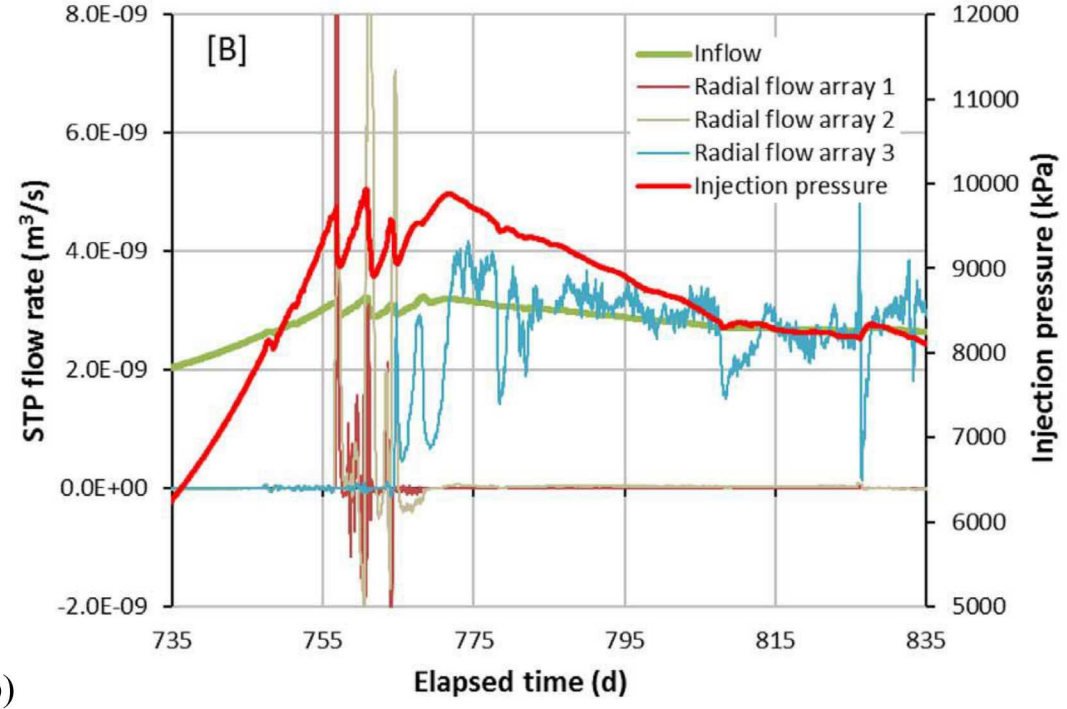


Figure 6-4. Schematic drawings of gas injection location and gas flow direction for (a) 1D gas flow test (Stage 1) and (b) spherical gas flow test (Stage 2).

Figure 6-5 shows experimental results in terms of pressure/stress evolutions and inflow/outflow rates between 735 days and 835 days of gas injection. Standard temperature and pressure (STP) are defined as 273.15 K, 101.325 kPa respectively. The peak in gas pressure (around day 767.6) is followed by a protracted negative pressure transient leading to a quasi-steady state by around day 825 (Figure 6-5a). During this period, the change in injection pressure is crudely mirrored by stress which exhibits none of the apparent chaotic patterns observed at earlier breakthrough events. The reduction in the variability of stress from day 768 onwards is accompanied by the development of stable outflow conditions, with flux localized to one drainage array (Figure 6-5b).



(a)



(b)

Figure 6-5. Observed 3D spherical gas flow test results: (a) pressure/stress evolutions and (b) inflow/outflow rates (Harrington et al., 2017).

6.4 LBNL Model Approaches for Gas Migration

LBNL is exploring two different approaches for modeling gas migration associated with DECOVALEX-2019, Task A (Figure 6-6):

1) Continuum modeling approach using TOUGH-FLAC simulator (Rutqvist, 2011), and

2) Discrete fracture modeling approach using TOUGH-RBSN simulator (Kim et al., 2017)

The two approaches are complementary. The continuum approach is based on current developments and applications of TOUGH-FLAC on bentonite and clay host rocks for the modeling of long-term THM performance of nuclear waste repositories in clay host rocks. The TOUGH2 code and other continuum models have been used in the past to model gas migration in clay considering heterogeneous clay properties with pressure dependent permeability, but without considering geomechanical coupling (e.g., Senger and Marschall, 2008; Senger et al., 2014). In this study, such a continuum approach will be extended to include full geomechanics coupling within the framework of TOUGH-FLAC. The discrete fracture modeling approach is based on current development of the TOUGH-RBSN simulator, in which the opening of grain boundaries for dilatant gas migration is modeled explicitly using a fracture mechanics approach. The TOUGH-RBSN has previously been applied for modeling fluid driven hydraulic fracturing and complex fracturing in clay host rocks (Kim et al., 2017). The TOUGH-RBSN should be suitable for modeling of complex flow paths associated with dilatant gas migration in clays.

In Sections 6.4 and 6.5, the continuum and discrete modeling results are presented, respectively. They cover the experimental works for Stage 1—1D gas migration and provide preliminary simulation results, and for Stage 2—spherical gas migration through a 120 mm long sample of water saturated MX-80 bentonite.

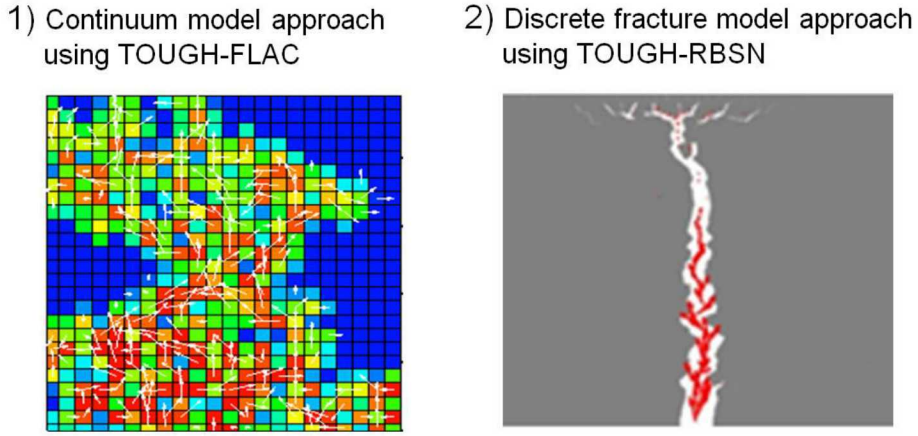


Figure 6-6. Schematic of modeling approaches employed by LBNL for modeling gas migration through clay associated with DECOVALEX-2019 Task A. To the left, the continuum approach using TOUGH-FLAC is illustrated involving heterogeneous properties with the possibility of the formation of dilatant flow paths through pressure or strain dependent permeability in individual cells. The actual color figure to the left is from TOUGH2 modeling in Senger and Marschall (2008), in which the white arrows show gas flow velocity and colors are gas saturation. To the right, the discrete fracture modeling approach using TOUGH-RBSN, involving complex fracturing to simulate the formation of dilatant flow paths. The red shows the fluid flow pathways through the fracture shown in white color.

6.5 TOUGH-FLAC Modeling of Gas Migration Experiments

In FY2018, the continuum modeling results have been updated based on the comparison to experimental data. Based on a large number of simulation tests with comparison to experimental data, we arrived at the following basic approach and material models

1) Multiphase (gas and liquid) flow;

2) Linear poro-elastic model;

3) A linear moisture swelling model;

4) A gas permeability model related to minimum effective compressive stress.

The linear poro-elastic model is based on the assumption of a linear elastic response, and we assume an effective stress law, which responds to the maximum phase pore pressure, which could be either gas pressure (for partially saturated media) or liquid pressure (for fully saturated media). That is:

$$\sigma' = \sigma - P^{\emptyset} \tag{6.1}$$

where

$$P^{\emptyset} = Max(P^{l}, P^{g}) \tag{6.2}$$

where P^{ϕ} is the pore pressure, and P^{l} *and* P^{g} are liquid and gas phase pressures, respectively.

The linear moisture swelling model implies a swelling strain as a function of liquid saturation, leading to a swelling stress according to

$$\Delta\sigma_{sw} = 3K\Delta\varepsilon_{sw} = 3K\Delta S_{l}\beta_{sw} \tag{6.3}$$

where S_l is liquid saturation, and β_{sw} is the moisture swelling coefficient. These models have been used in the past for simplified modeling of bentonite behavior, and are described in Rutqvist et al. (2011). The applied gas permeability model considers a fracture-like behavior of permeability for dilatant flow paths (Figure 6-7). In this model, permeability is a non-linear function of the effective minimum compressive stress.

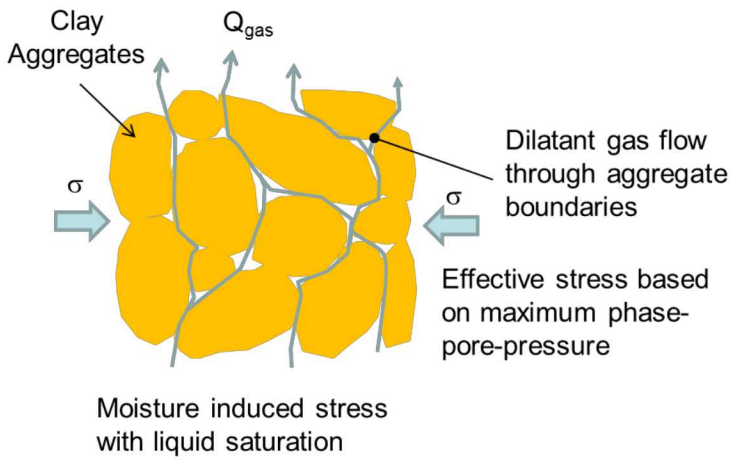


Figure 6-7. Conceptual model for dilatant gas flow through aggregate boundaries considered in a continuum model simulation with TOUGH-FLAC.

A full 3D model has been developed to model heterogeneous material properties. However, the modeling simulations conducted to date have been done assuming homogeneous properties of the MX-80. The test geometry in this case is a 3D model as shown in Figure 6-8. The sample dimensions are 120 mm long and 60 mm diameter. We included additional elements on the top and bottom in the TOUGH2 fluid flow domain to simulate the injection and back-pressure filters.

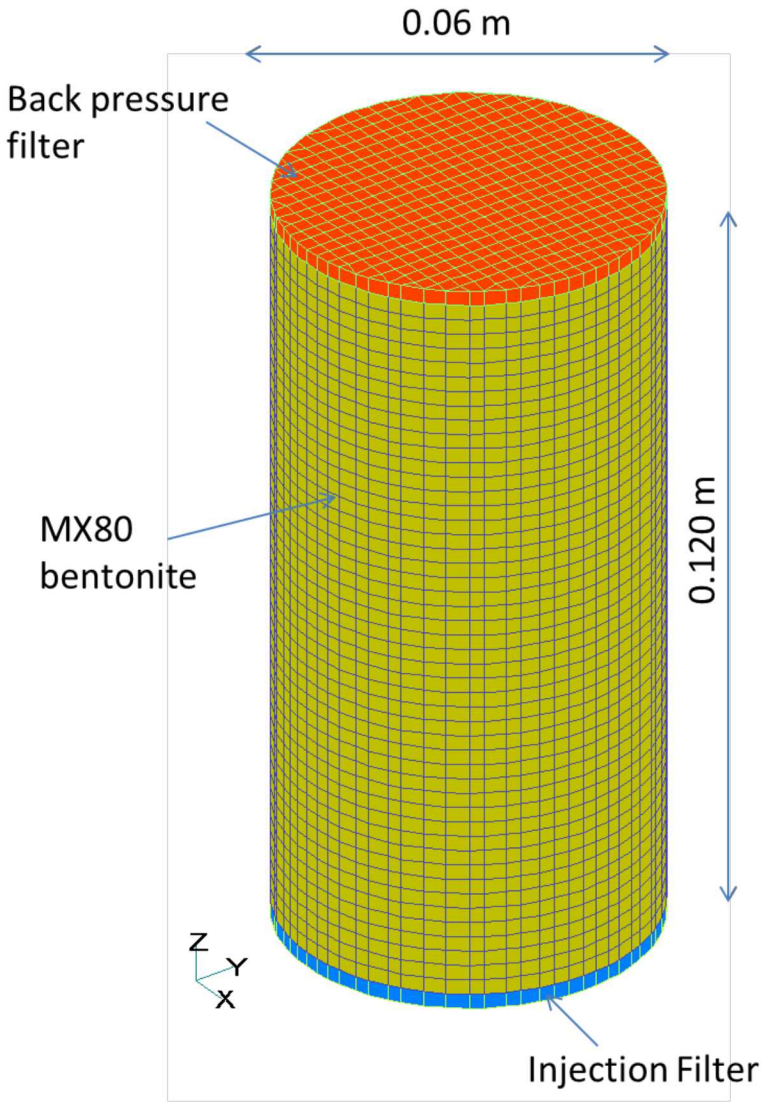


Figure 6-8. 3D TOUGH-FLAC model of cylindrical sample.

Initial conditions of 1 MPa fluid pressure and fully water saturated sample were used for modeling. In the current modeling, the injection pressure was controlled at the injection boundary elements at full gas saturation, with variable pressure ranging according to measured data. A back pressure of 1 MPa was maintained in the elements simulating the back pressure filter. The simulation starts at 20 days assuming fully saturated sample, the initial axial stress of 9.5 MPa and the radial initial stress of 6.5 MPa. In simulations, the sample was assumed to be mechanically confined.

Numerous sensitivity studies were conducted for matching the simulation results. Finally, some material properties were fixed, while others where used for final matching of simulation results. Table 6-1 lists the basic and specific material parameters that will be explained. The parameters marked in bold in Table 6-1 were calibrated. Other parameters were fixed, including those denoted as basic reference values, which are typical values for MX-80 bentonite and given by the DECOVALEX-2019 task lead.

Table 6-1. Material parameters for TOUGH-FLAC modeling of Stage 1 experiment.

	Meaning	Symbol [units]	Value
Basic reference values	Young's modulus	E [MPa]	307
	Poisson's ratio	ν [-]	0.4
	Porosity	ϕ_0 [-]	0.44
	Intrinsic permeability	k_0 [m^2]	3.4×10^{-21}
HM coupling parameters	Pore compressibility[1]	c_p [Pa^{-1}]	4.44×10^{-9}
	Biot's coefficient	α_p [-]	1
	Swelling coefficient	$\boldsymbol{\beta_{\beta sw}}$ **[-]**	**0.02**
	Max aperture for stress-k	**bho [m]**	**29×10^{-6}**
	Reference stress for stress-k	$\boldsymbol{\sigma_{n,ref}}$ **[MPa]**	**0.2**
van Genuchten capillary pressure model	Apparent gas entry pressure	P_0 [MPa]	18
	Residual liquid saturation	S_{lr} [-]	0.01
	Shape factor	λ [-]	0.45
Corey relative permeability	Residual liquid saturation	S_{lr} [-]	0.1
	Residual gas saturation	$\boldsymbol{S_{gr}}$ **[-]**	**0.11**
	Enhancement factor for k_{rg}	$\boldsymbol{m_g}$ **[-]**	**375**

Based on the results of matching the stress evolution from experimental data and modeling, it is required to consider both the poro-elastic stress changes and the moisture swelling effect. During gas injection, the poro-elastic stress change will tend to increase the compressive stresses, because the sample is confined mechanically. The poro-elastic stress increase is roughly proportional to the pressure changes, which far exceeds the observed stress changes. However, considering the effect of moisture swelling, or in this case shrinkage due to reduced water saturation as gas is injected, some of the poro-elastic stress changes will be offset and the observed stress evolution can be matched reasonable well. In the simulations the Young's modulus was fixed to 307 MPa, which is a reasonable approximation for saturated or near saturated bentonite, taking into account the dry density and a confining stress. To match the observed stress magnitude as moisture swelling parameter of 0.02 was determined through sensitivity analysis. Poisson's ratio was set to 0.4.

The van Genuchten (1980) capillary pressure model is used to define the water retention curve given by

$$P_c(S) = P_0\left([S^*]^{-1/\lambda} - 1\right)^{1-\lambda} \tag{6.4}$$

with $S^* = (S - S_{lr})/(1 - S_{lr})$. The relevant capillary pressure parameters are adopted for bentonite (Senger and Marschall, 2008): apparent gas entry pressure P_0=18 MPa, shape factor λ=0.45, and residual liquid saturation S_{lr}=0.01.

The relative permeability-saturation relationships of liquid and gaseous phases are parameterized using Corey's model as

$$k_{rl}(S) = \hat{S}^4$$
$$k_{rg}(S) = m_g\left(1 - \hat{S}\right)^2\left(1 - \hat{S}^2\right) \quad (6.5)$$

where $\hat{S} = (S - S_{lr})/\left(1 - S_{lr} - S_{gr}\right)$, and m_g is a multiplying factor for the enhanced gas permeability (Corey, 1954). The residual saturations S_{lr} and S_{gr} are provided to limit the mobility of the respective phase, i.e., both liquid and gaseous phases mobility can vary only in the range of $S = \left[S_{lr}, 1 - S_{gr}\right]$.

For matching the abrupt gas breakthrough occurred at a gas pressure of about 10 MPa in the gas injection chamber, the concept of an effective gas entry pressure, P_{ge}, was applied according to Senger and Marschall (2008). The concept is illustrated in Figure 6-9, where a residual gas saturation of S_{gr} = 0.11, which is a parameter of the gas relative permeability function) corresponds to the effective gas entry pressure P_{ge} = 10 MPa.

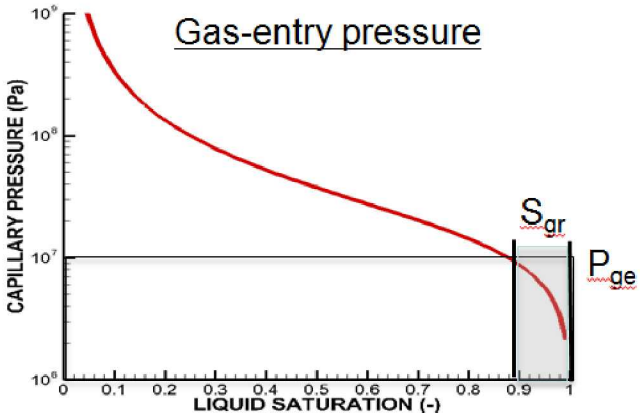


Figure 6-9. The concept of effective gas entry pressure used for the evaluation of the initial pressure response.

In the current simulations, the intrinsic permeability was set to a fixed value of $k = 3.4\times10^{-21}$ m^2 based on other independent laboratory tests. The gas entry pressure was necessary to prevent any gas migration and pressure changes to occur in the sample until about 60 days, when abrupt increases of sample pressure occurred. The gas permeability can increase more strongly with the

gas saturation as well as a result of changes in effective stress. A relation between permeability and effective minimum compressive stress is shown in Figure 6-10. The two parameters, bh0 = 2.9×10^{-6} m, and $\sigma_{n,ref} = 0.2\times10^{6}$ Pa were determined by trial simulations to obtain the best possible match with experimental data.

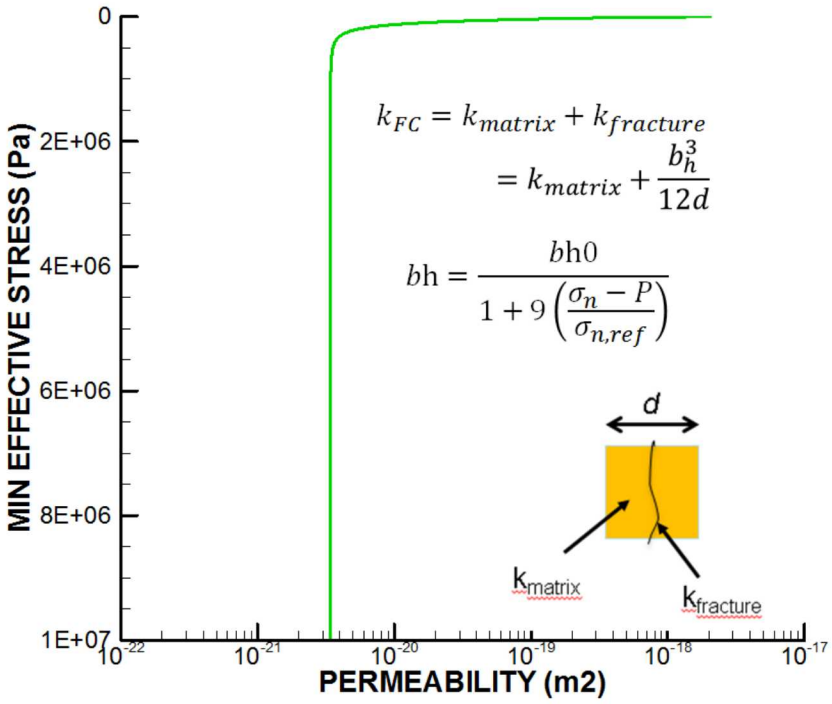


Figure 6-10. Relation between min effective stress and permeability used in numerical modeling.

The simulation results with comparison to measured data are shown in Figures 6-11 to 6-14. The measured abrupt pressure increase within the sample after about 67 days was captured very well in the modeling (Figure 6-11). The subsequent general pressure decline is also captured, though some of the pressure fluctuations at around 80 days are not captured in the modeling. .

The abrupt increase in outflow rate and the maximum magnitude is also accurately captured in the modeling (Figure 6-12). The observed subsequent complete shut-down of gas flow is not captured in the modeling, which shows a more gradual decline in gas flow rate.

The general evolution and magnitudes in radial and axial stresses are also modelled quite accurately (Figures 6-13 and 6-14). The modeling shows a bit more uniform stress compared to the data, and the stress decline toward the end is not captured in the modeling.

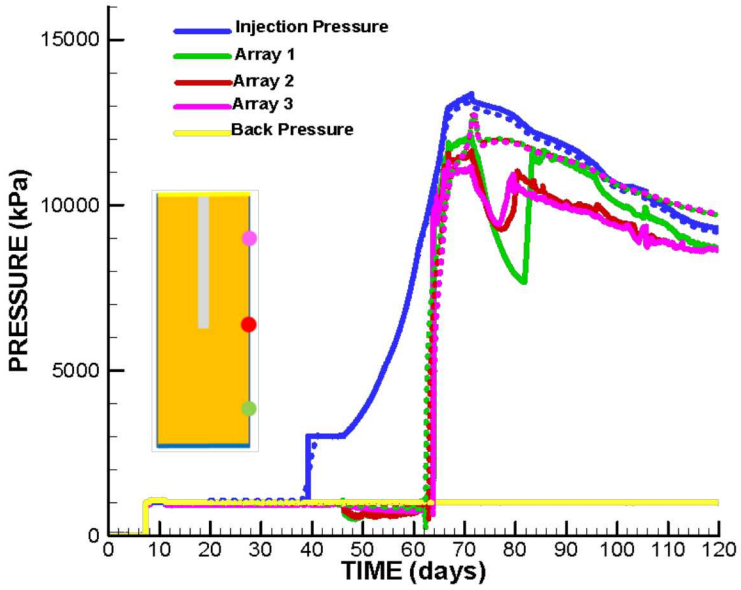


Figure 6-11. 3D TOUGH-FLAC model of cylindrical sample and the results of simulations of pressure.

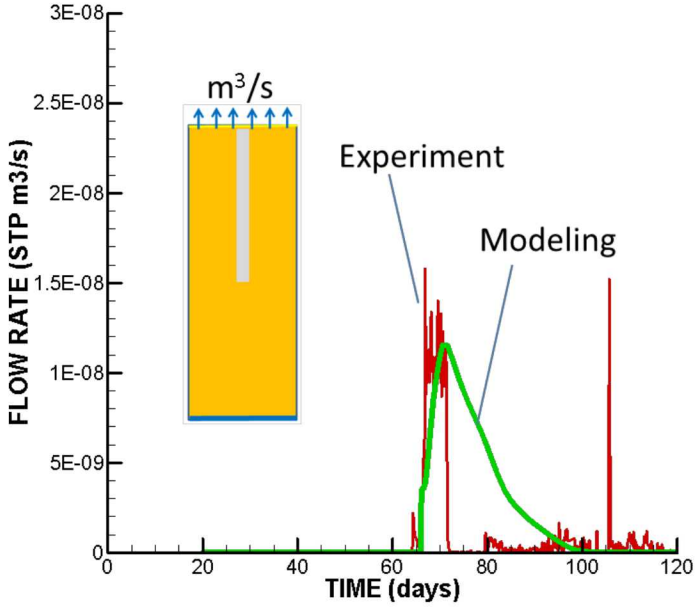


Figure 6-12. Simulated (green line) and measured (red line) gas flow rate out of the sample.

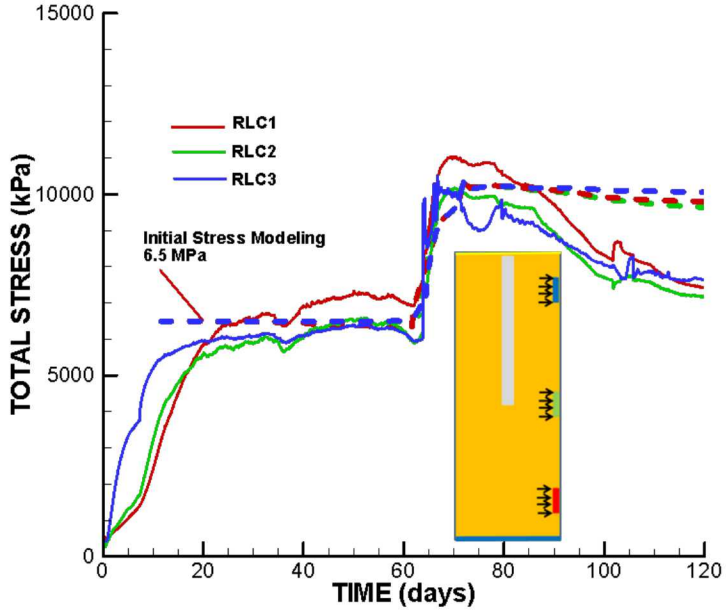


Figure 6-13. Simulated (dashed lines) and measured (solid lines) total radial stress at load cells 1, 2 and 3.

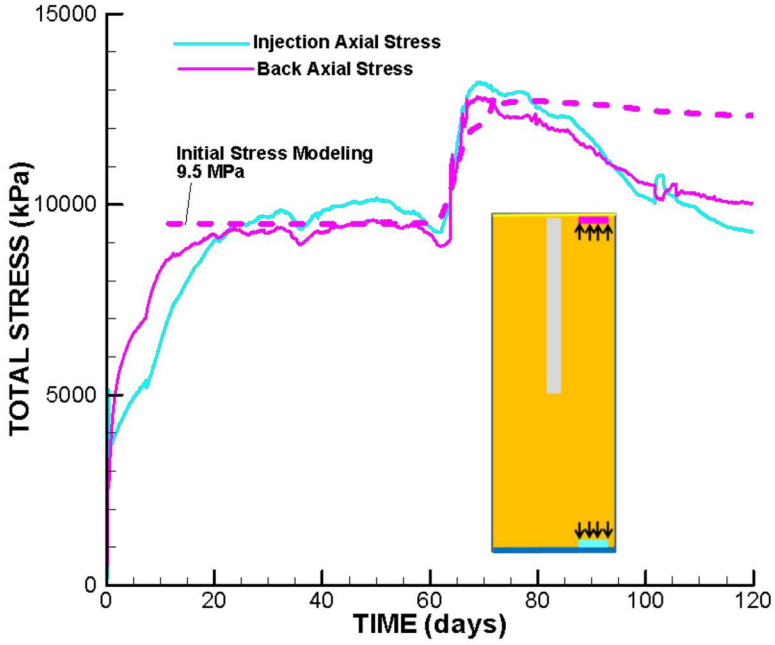


Figure 6-14. Simulated (dashed lines) and measured (solid lines) total axial stress at injection and back ends of the sample.

In summary, the homogeneous material model with simple linear poro-elastic and moisture swelling model and model for stress-dependent gas permeability, and an effective gas entry pressure, could capture the main features of the experiment, including pressure, stress and flow evolution. The biggest deviation from the data occurred just after 70 days, when the experimental gas flow appears to shut-down completely.

Future improvements to this model could include:

1. Application of the BBM for matching stress evolution;
2. Modeling of the injection system and imposed flow rate rather than imposing the injection pressure;
3. Modeling of the initial stage of loading and saturation of the sample; and
4. Utilizing heterogeneous properties of media in the model development.

The BBM is used to simulate the non-linear elastic (rather than linear elastic) mechanical behavior, and, therefore, it might be possible to better match the stress evolution post 70 days. Taking into account heterogeneous properties will help simulate the formation of localized flow paths, which would be especially important for modeling the Stage 2A, 3D spherical flow experiment.

6.6 TOUGH-RBSN Modeling of Gas Migration Experiments

We have used the TOUGH-RBSN simulator for modeling two-phase flow with mechanical deformation and fracture/damage processes. The TOUGH-RBSN simulator is distinguished from continuum-based approaches (e.g., TOUGH-FLAC) by its capability of the discrete representation of fracture formations affected by coupled THM processes. The general coupling procedure of TOUGH-RBSN is similar to the sequential coupling in TOUGH-FLAC (Rutqvist et al., 2002; Rutqvist, 2011), but the TOUGH-RBSN coupling modules have been substantially modified to account for the fluid flow through discrete fractures (Asahina et al., 2014; Kim et al., 2017).

This section presents simulations of two types of gas flow experiments: (1) 1D flow through a saturated bentonite (MX-80) sample, and (2) spherical flow in a saturated bentonite sample. The 2D rectangular and 3D cylindrical models for numerical simulations were generated based on the Voronoi discretization. The discrete fracture network (DFN) approach was used to demonstrate enhanced gas flow through discrete fracture paths. Simulated porewater pressure, total stress, and flow rate were compared with the laboratory test results for model validation. Comparison of fracture patterns and pressure distributions during fracturing processes were used for the qualitative analysis of gas pressure-induced fracture propagation and fracture-assisted flow.

6.6.1 1D flow through saturated bentonite under constant volume boundary conditions

A 120×60 mm rectangular 2D mesh was constructed, comprising of 1401 Voronoi cells and 3840 lattice elements. An additional 2 mm-thick layer of elements was padded on each side of the domain boundaries to provide a uniform mechanical confinement (i.e., fixed displacement boundary conditions). Figure 6-15 shows the resulting mesh geometry, where colored marks indicate the measuring points of pressure evolutions during simulations.

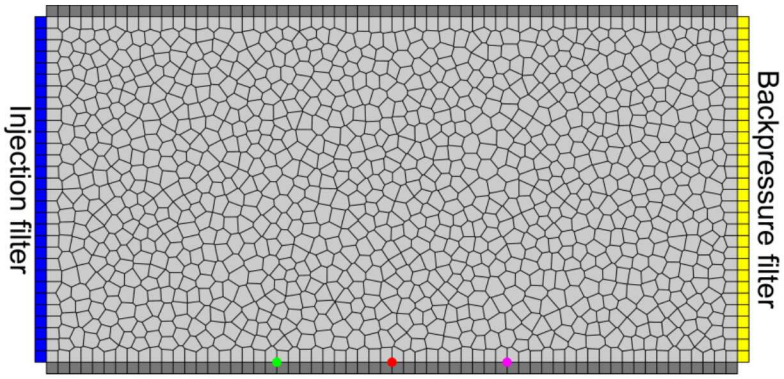


Figure 6-15. 2D rectangular model geometry of an MX-80 bentonite sample.

The initial confining stress values are given from the measurements of load cells in the experimental program, which reads 9 MPa in the axial direction and 6 MPa in the radial direction. The initial pore pressure was 1 MPa, and the initial saturation of the domain was 0.999 to represent fully saturated conditions. While the padding elements surrounding the specimen were fixed with the initial stress loaded, gas injection at the left boundary was controlled to match the injection pressure measured from the experiment. 1 MPa backpressure at the right boundary was upheld during simulations. Hydrologically, the left and right padding elements are highly permeable as for the filter boundaries, whereas the top and bottom elements have zero permeability representing insulation.

Table 6-2 lists the parameters for mechanical and hydrological model assumptions adopted in this study. The current TOUGH-RBSN model observes all the baseline parameters conforming to the values suggested from the DECOVALEX Task A coordinator from BGS. The Poisson's ratio of 0.4 is used for deriving the pore compressibility of the bentonite material. The RBSN models adopt the zero Poisson's ratio to avoid an unwilled artificial heterogeneity, which aggravates the elastic homogeneous representation in the mechanics of the lattice network. Pre-calibration processes have been performed to match the experimental data, and the calibrated parameters are given in the notes of Table 6-2.

Because of the granular texture of the bentonite sample, the grain-to-grain strength is considered to be very low. Herein, a Mohr-Coulomb failure criterion is adopted, for which the tensile strength f_t = 0.1 MPa, cohesive strength c = 0.1 MPa, and the internal friction angle β = 18°. Due to the fully confined boundary conditions with the initial pressure and stress conditions, the fracture surfaces are more likely to be in contact during simulations, and, thus, the mechanical resistance may exist between the fracture surfaces. In that sense, it is simply assumed that a fractured element regain the mechanical properties of intact material when the crack displacement indicates the fracture closure.

In the TOUGH-RBSN simulations, the TOUGH2 model configuration comprises of two types of elements. The first element type is the cell elements, whose geometry is associated to the Voronoi cells. The cell elements represent the matrix/grain bulk, for which the porosity-dependent permeability is defined as

$$k = k_0 \frac{\phi^3}{(1-\phi)^2} \frac{(1-\phi_0)^2}{{\phi_0}^3} \tag{6.6}$$

where k_0 is the intrinsic permeability, and ϕ_0 is the initial porosity.

Table 6-2. Material parameters for TOUGH-RBSN modeling of 1D gas flow through MX-80 bentonite samples.

	Meaning	Symbol [units]	Value
Basic reference values	Young's modulus	E [MPa]	307
	Poisson's ratio	ν [-]	0.4
	Porosity	ϕ_0 [-]	0.44
	Intrinsic permeability	k_0 [m^2]	3.4×10^{-21}
HM coupling parameters	Pore compressibility[1]	c_p [Pa^{-1}]	4.44×10^{-9}
	Biot's coefficient	α_p [-]	1
	Swelling coefficient[2]	α_s [-]	0.1
Mohr-Coulomb failure criterion	Tensile strength	f_t [MPa]	0.1
	Cohesive strength	c [MPa]	0.1
	Internal friction angle	β [deg.]	18
van Genuchten capillary pressure	Apparent gas entry pressure	P_0 [MPa]	18
	Residual liquid saturation	S_{lr} [-]	0.01
	Shape factor	λ [-]	0.45
Corey relative permeability	Residual liquid saturation	S_{lr} [-]	0.8
	Residual gas saturation[4]	S_{gr} [-]	0.0877
	Enhancement factor for k_{rg}	m_g [-]	1

Note:

[1] The pore compressibility is analytically derived from the bulk modulus K: $c_p = \frac{1}{K\phi} = \frac{3(1-2\nu)}{E\phi}$.

[2] The swelling coefficient is calibrated to match the peak values of total stress responses.

[3] The parameters are adopted from Senger and Marchall (2008).

[4] S_{gr}= 0.0877 corresponds to the air-entry pressure P_{ae}= 8 MPa, which is the pressure difference between injection and backpressure points at the breakthrough.

The other element type is the interface elements, which represent potential fractures or pre-existing fractures embedded in a portion of the matrix volume. It is assumed that the interface element is positioned at the common boundary of two adjacent cell elements, and one fracture plane cut the element into two parallel plates. The permeability is calculated as the sum of two components:

$$k = k_{matrix} + k_{fracture} \tag{6.7}$$

where each component is conditionally calculated based on the fracture activation. If an interface element is yet to be fractured, k_{matrix} is calculated based on Equation (6.6) and $k_{fracture}$ is simply assumed to be zero. On the other hand, if the interface element is fractured, $k_{fracture}$ will be predominant to enhance the total permeability, and k_{matrix} is assumed to revert to the initial intrinsic permeability k_0. This conditional expression of the permeability is written as

$$k = \begin{cases} k_0 \frac{\phi^3}{(1-\phi)^2} \frac{(1-\phi_0)^2}{{\phi_0}^3}, & \text{if unfractured} \\ k_0 + \frac{b^3}{12a}, & \text{if fractured} \end{cases} \tag{6.8}$$

where a is the element width, and b is the aperture.

The van Genuchten capillary pressure Eq. (6.4) is used to define the water retention curve. The relevant capillary pressure parameters are adopted for MX80 bentonite (Senger and Marschall, 2008): apparent gas entry pressure P_0=18 MPa, shape factor λ=0.45, and residual liquid saturation S_{lr}=0.01.

The relative permeability-saturation relationships of liquid and gaseous phases are parameterized using Corey model as

The relative permeability-saturation relationships of liquid and gaseous phases are parameterized using Corey model as

$$\begin{aligned} k_{rl}(S) &= \hat{S}^4 \\ k_{rg}(S) &= m_g\left(1-\hat{S}\right)^2\left(1-\hat{S}^2\right) \end{aligned} \tag{6.9}$$

where $\hat{S} = (S - S_{lr})/\left(1 - S_{lr} - S_{gr}\right)$ and m_g is a multiplying factor for the enhanced gas permeability. The residual saturations S_{lr} and S_{gr} are provided to limit the mobility of the respective phase, i.e., both liquid and gaseous phases can vary their mobilities only in the range of $S = \left[S_{lr}, 1 - S_{gr}\right]$. Note that S_{lr}=0.8 in this equation is different from that in Equation (6.4) for the capillary pressure. To avoid unphysical situation with $P_c = \infty$, larger S_{lr} for the relative permeability is usually chosen as compared to S_{lr} for the capillary pressure (Pruess et al., 2012). Residual gas saturation, S_{gr}, can be used to define the air entry pressure in relationship with the capillary pressure function. S_{gr}=0.0877 corresponds to the air entry pressure of 8 MPa.

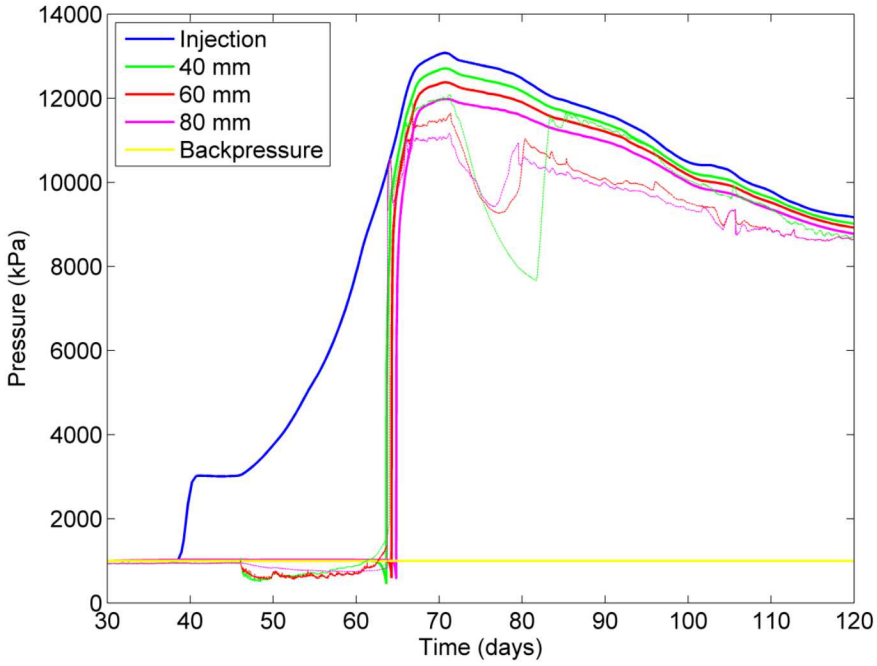


Figure 6-16. Comparison of simulated pressure (solid thick lines) with experimental data (dotted thin lines).

Figures 6-16 to 6-18 compare simulation results with the experimental data for pore pressure, axial and radial stress, and outflow rate over time, respectively. As shown in Figure 6-16, the simulated pore pressures exhibit an abrupt increase after around 65 days of injection, which are in a good agreement with the experimental data. In the post-peak region, the uniform pressure evolutions along the length indicate that permeability of the sample has increased after the gas breakthrough.

Figure 6-17 presents axial and radial total stress evolutions, which accord quite well with the experimental data. The initial stress configuration (σ_x: σ_y = 9 MPa:6 MPa) is maintained until the gas entry around 60 days due to the 8 MPa air entry pressure corresponding to the assigned residual gas saturation. The axial stresses measured at the injection boundary and the backpressure boundary both well agree with the experimental data (Figure 6-17a), and the radial stress evolution curves indicate the gas breakthrough with abrupt pressure increase (Figure 6-17b). Note that the linear swelling/shrinkage model with a calibrated coefficient α_s=0.1 is used to match the peak stress levels.

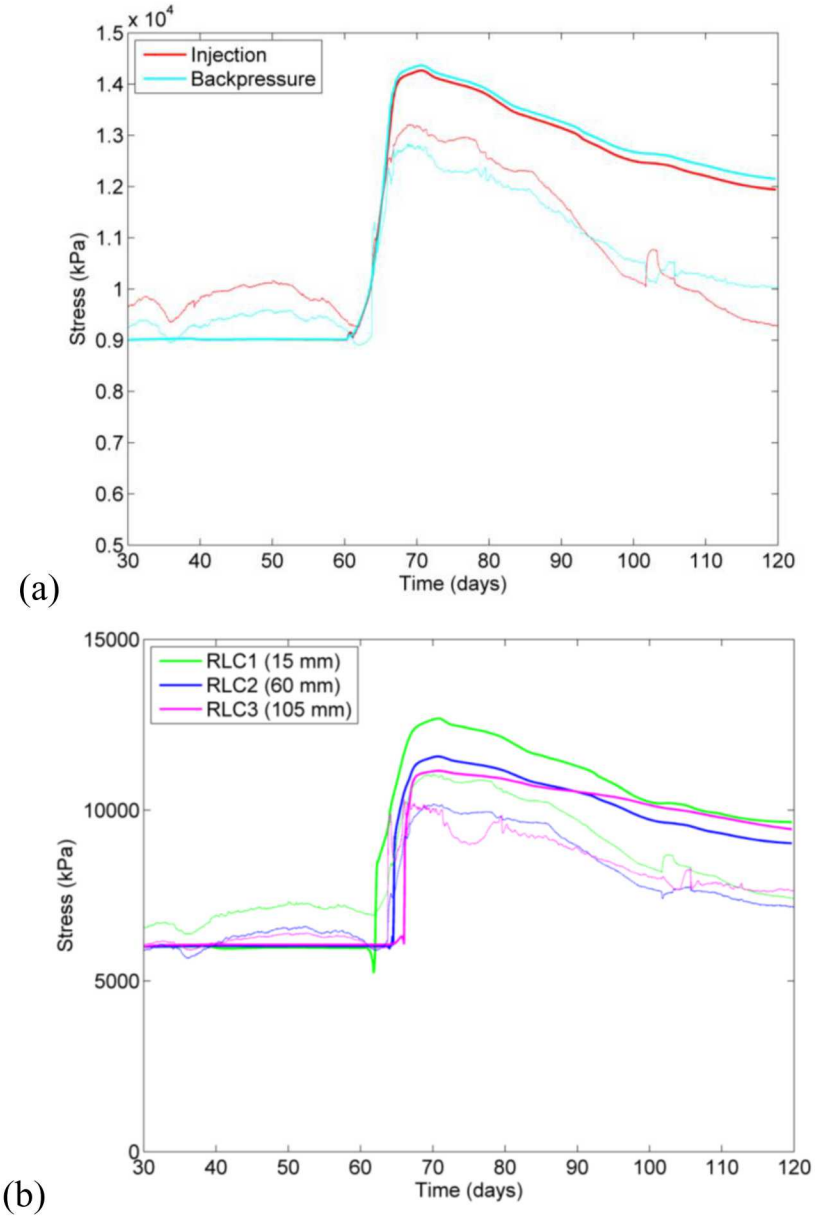


Figure 6-17. Comparisons of simulated (a) axial stresses and (b) radial stresses with experimental data.

In Figure 6-18, the simulated outflow rate could match the level of peak flow rate. However, the activation of outflow is delayed by about five days compared to the experimental result. We hypothesize that the simulations of the gas breakthrough process would be improved by changing the relative permeability function. Also, the complete cut-down of flow after 72 days is not captured since the injection boundary condition is not physically controlled by the flow rate.

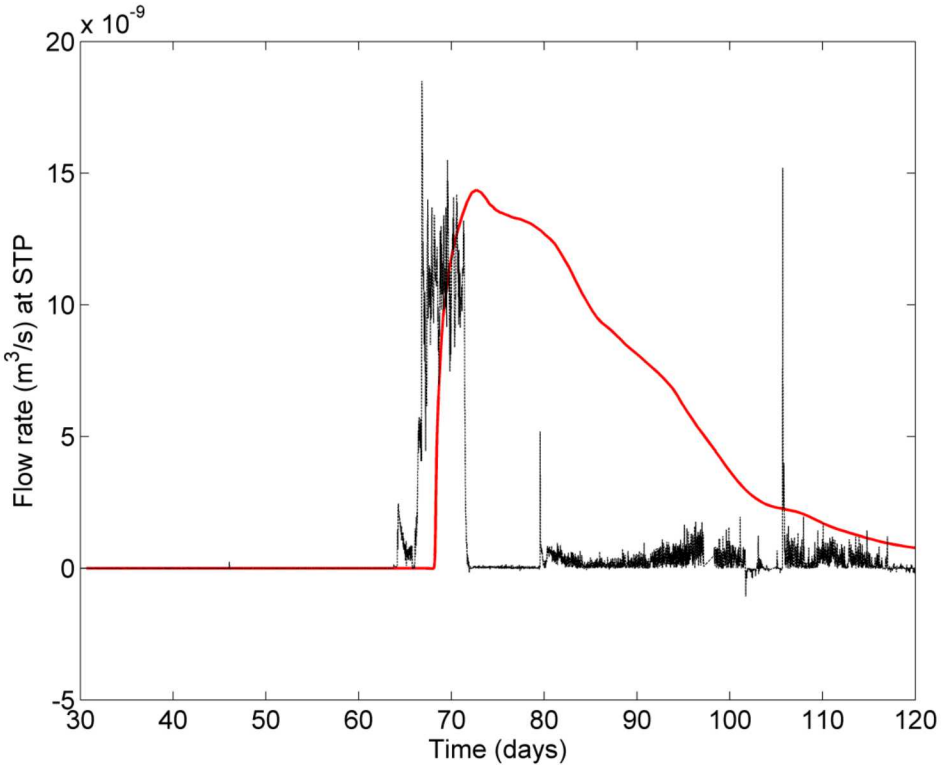


Figure 6-18. Comparison of simulated gas flow rate (red line) with experimental data (black line).

Figure 6-19 presents snapshots of the fracture pattern and the pore pressure contour during the breakthrough. The fractures initiate from the injection boundary and propagate into the sample. In the early stage with relatively low injection pressure, Figure 6-19a presents the fracture paths selectively activated to make distinct flow pathways. As shown in Figures 6-19b and c, with higher injection pressure, the whole cross section is somewhat uniformly fractured to enhance the gas flow (i.e., 1D flow). Figure 6-19d shows the fracturing is accelerated on the upper side of the sample when the fractures reach the backpressure boundary. However, the pressurized zone does not closely follow the fractured zone until the whole cross section is fractured, shown in Figure 6-19e.

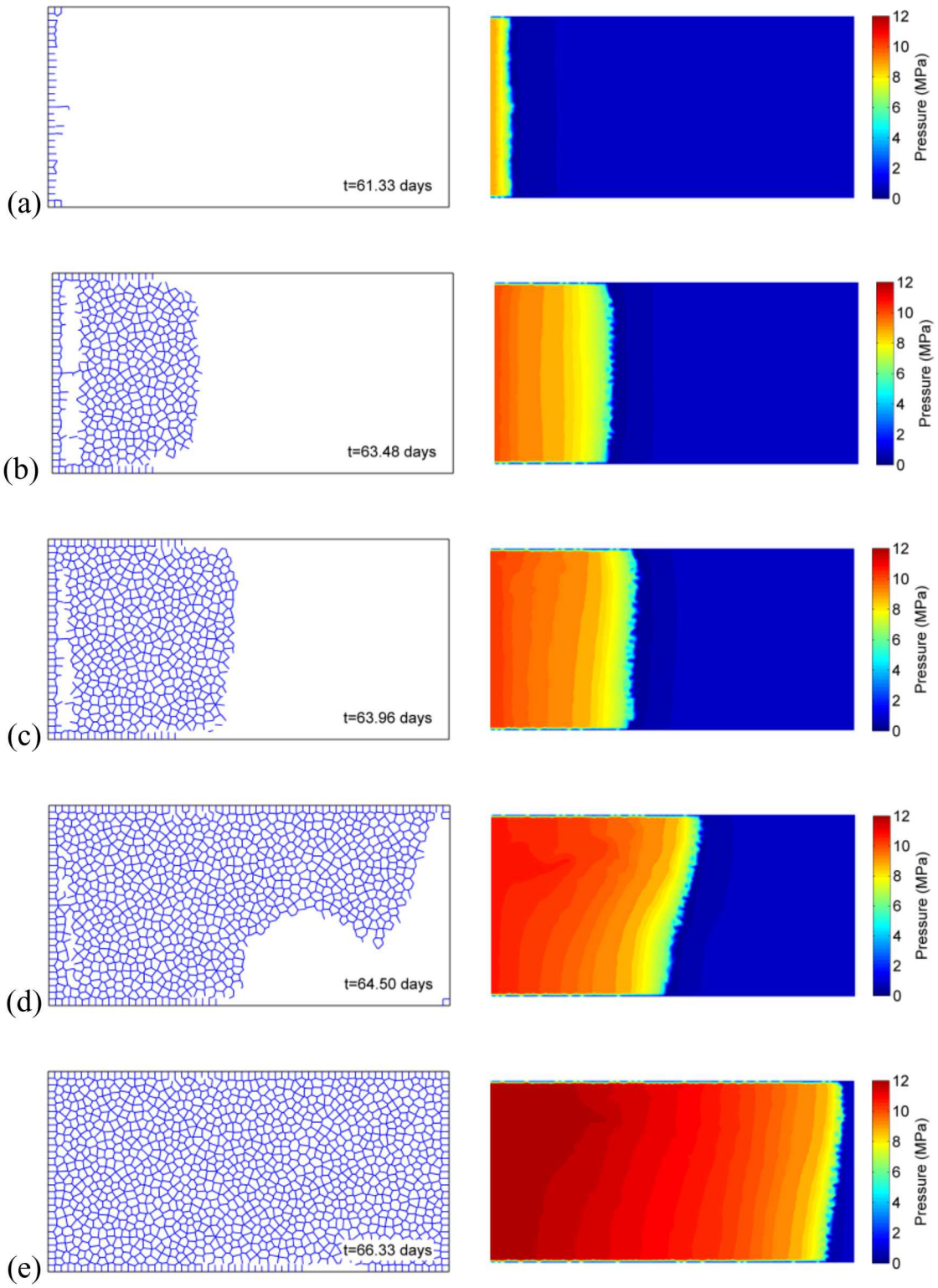


Figure 6-19. Snapshots of the mesh geometry, showing fracture patterns (left), and pressure contours (right) around the breakthrough.

6.6.2 Spherical flow through saturated bentonite under constant volume boundary conditions

For spherical flow modeling, we generated 3D Voronoi mesh of a cylinder with 120 mm height and 60 mm diameter (Figure 6-20), which is composed of 7,856 Voronoi cells and 33,316 lattice elements. Additional elements are added on the axial and circumferential surfaces to provide a constant volume boundary condition (zero-displacement constraints). Initial confinement with isotropic stress of 7.5 MPa is assumed in the sample as a mechanical condition, and the initial pore pressure of 1 MPa is given with fully saturated hydrological condition. While the padding elements surrounding the sample domain are constrained, 168 ml of gas (air) is injected into a boundary element with full gas saturation. A constant injection rate of 2.75×10^{-9} m^3/s at STP is maintained throughout the simulation. Elements at 12 locations on the circumferential surface of the sample, indicated by green marks in Figure 6-20a, are connected to the backpressure boundary element with a constant 1 MPa pressure. Outflow values are measured at the connections between those circumferential elements and the backpressure boundary element. Reactions are measured at the constrained padding elements to derive stress values at the load cells, which are colored in red in Figure 6-20b.

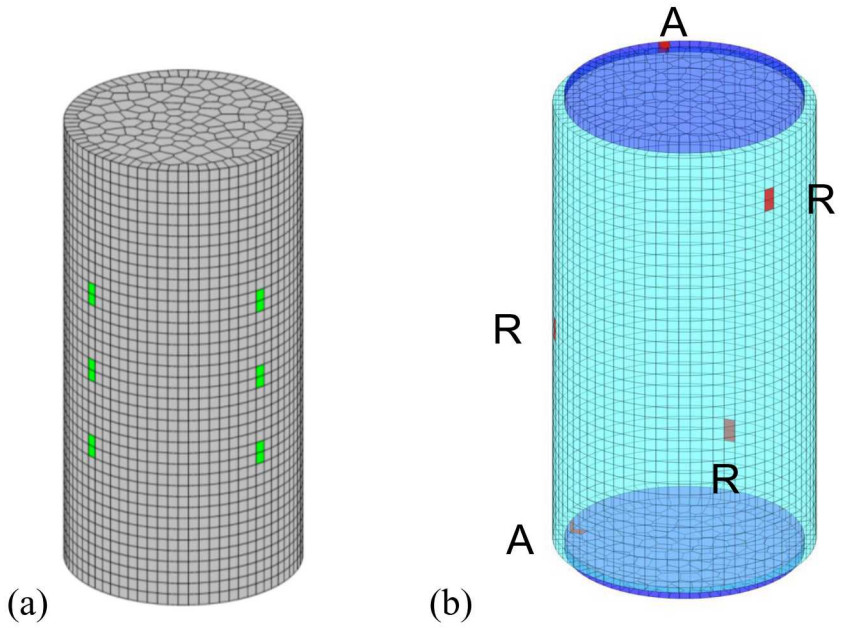


Figure 6-20. 3D Voronoi mesh generation: (a) Mesh discretization of bentonite domain. six Green marks (and six hidden on the other side) indicate the locations of porewater sensors for outflow measurement; and (b) Outer elements are padded for zero-displacement constraints. Red marks indicate the location of load cells, where the local stress values are measured.

The conceptual model is basically identical to the 1D gas flow model described in Section 6.5.1, except the scaling of the fracture capillary pressure. The fracture capillary pressure tends to decrease as the fracture aperture increases, so the water retention and air entry pressure in the fracture can be reduced. The water retention curve is defined using Equation (6.4). For a fracture

element, the apparent gas entry pressure P'_0 of the element will be scaled by the permeability function given by

$$P'_0 = P_0 \left(\frac{k_0}{k}\right)^{1/3} \tag{6.10}$$

where k_0 is the intrinsic permeability (before fracturing), and k is the permeability of the fracture element.

Fundamental model parameters are kept as those given in Table 6-2. However, the residual gas saturation has changed to 0.0709, which corresponds to the air-entry pressure of 7 MPa. Pre-calibration for the compressibility of the injection boundary element has been performed to match the initial injection pressure development.

Figure 6-21 shows snapshots of fracture development during gas injection. Fractures are initiated at the center of the sample, where the gas injection occurs. Then, the main fracture cluster grows into a spherical shape toward the lateral surface of the sample. After the fracture cluster reaches the lateral surface, near-surface fractures propagate in the longitudinal direction. These non-uniform fracture patterns form heterogeneous enhanced permeability domain within the sample, where preferential flow paths would be generated.

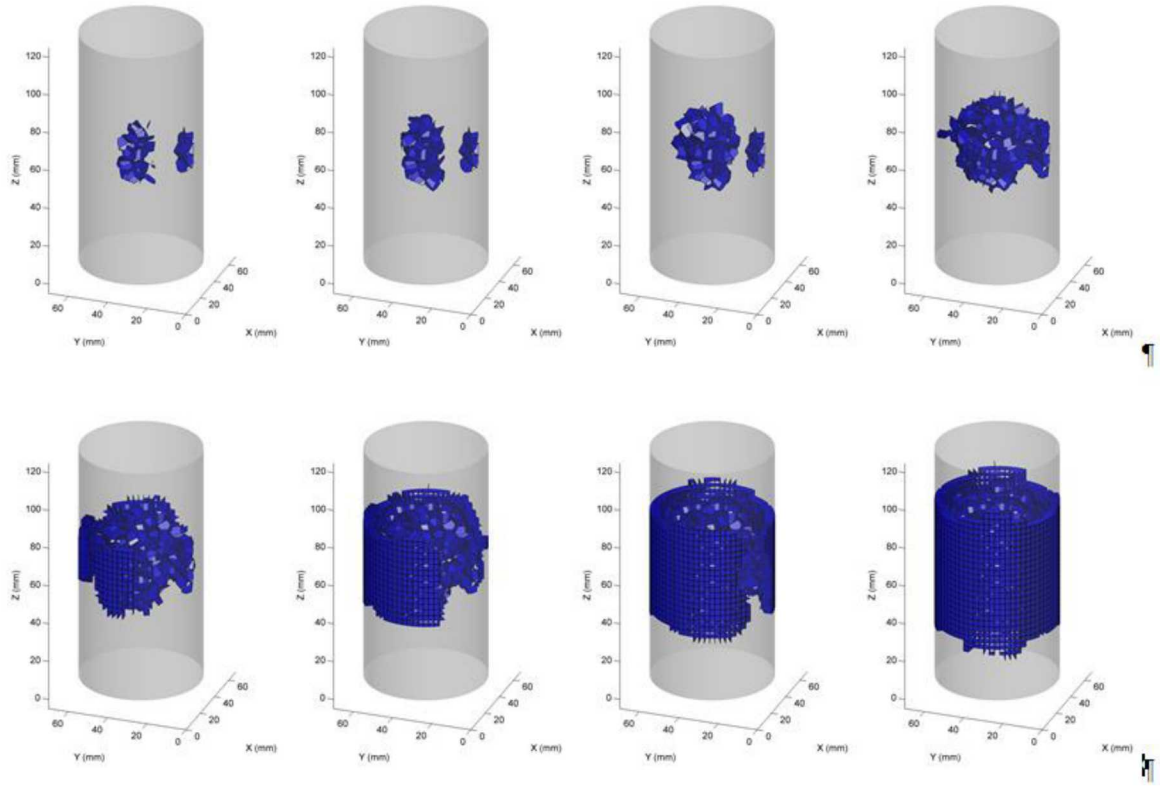


Figure 6-21. Non-uniform fracturing process development during gas injection.

Figure 6-22 presents the injection pressure evolution compared to the experimental result. With a constant injection rate, the pressure of the injection boundary element develops with a decent agreement with the experimental curve up to the peak, and the timing and the level of the peak pressure are comparable to the experimental results. However, the simulation does not

demonstrate the recursive recovery and the pressure drop, which were observed in the experiment. Simulated pressure in the post-peak region shows similar trend of diminution and final pressure level compared to the pressure evolution in the experiment.

Figure 6-23 shows inflow rate to the sample and outflow rates through radial pore water arrays. Inflow rate was gradually increasing starting from about 744 days, when the initial gas entry occurred, and then around 758 days jumped to match the level of injection rate setting, which implies the gas breakthrough. About one day after the inflow rate jumped, the gas breakthrough affected the flow responses through radial pore water arrays. In the experiment, only one radial array took a dominant outflow in concordance with the inflow rate. However, contrary to the experimental observation, the simulation exhibits lower outflow rates for all three radial arrays. Multiple lower outflow rates with no dominant flow direction indicate that the inflow diverges to multiple outflows connected through the fractures.

Figure 6-24 shows the stress evolutions measured at the locations of load cells. Unlike the experimental results shown in Figure 6-24b, the simulated stresses in Figure 6-24a are maintained until the initial gas penetrated into the sample. The largest stress increase occurred at the radial load cell R2 placed in the middle of the sample, which is attributed to the closest distance from the injection location. The axial load cells, with the eccentric location from the center of the sample, do not gain as much stress increase as the load cell R2. Later, around 760 days, load cells R1 and R3 gain stress values as the fractures reach out to axial direction and the corresponding gas flow and pressure increase occurred.

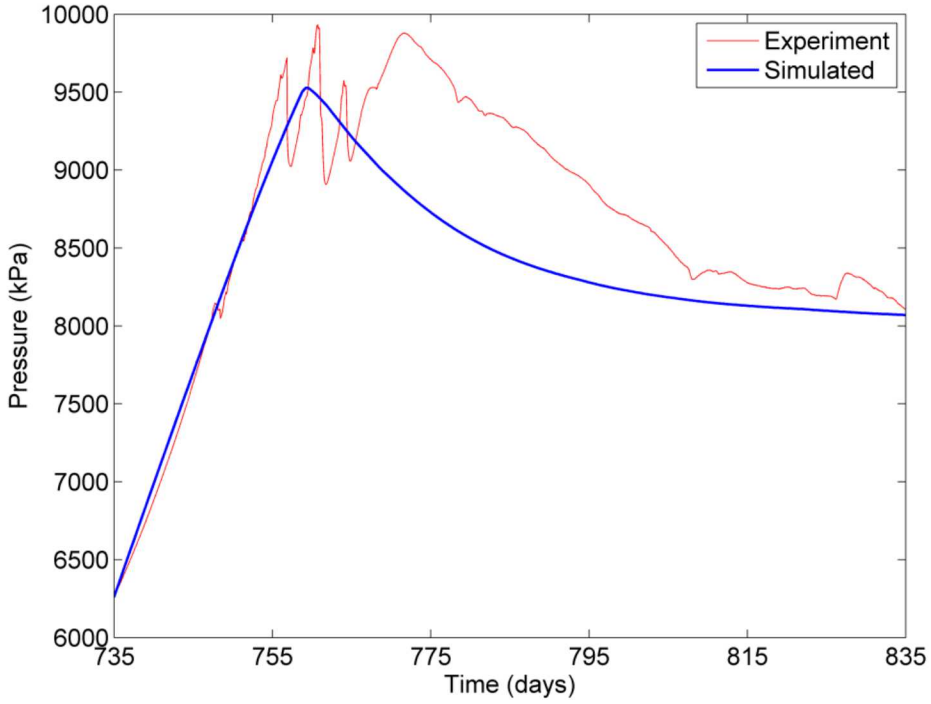


Figure 6-22. Comparison of simulated and experimental injection pressure evolutions.

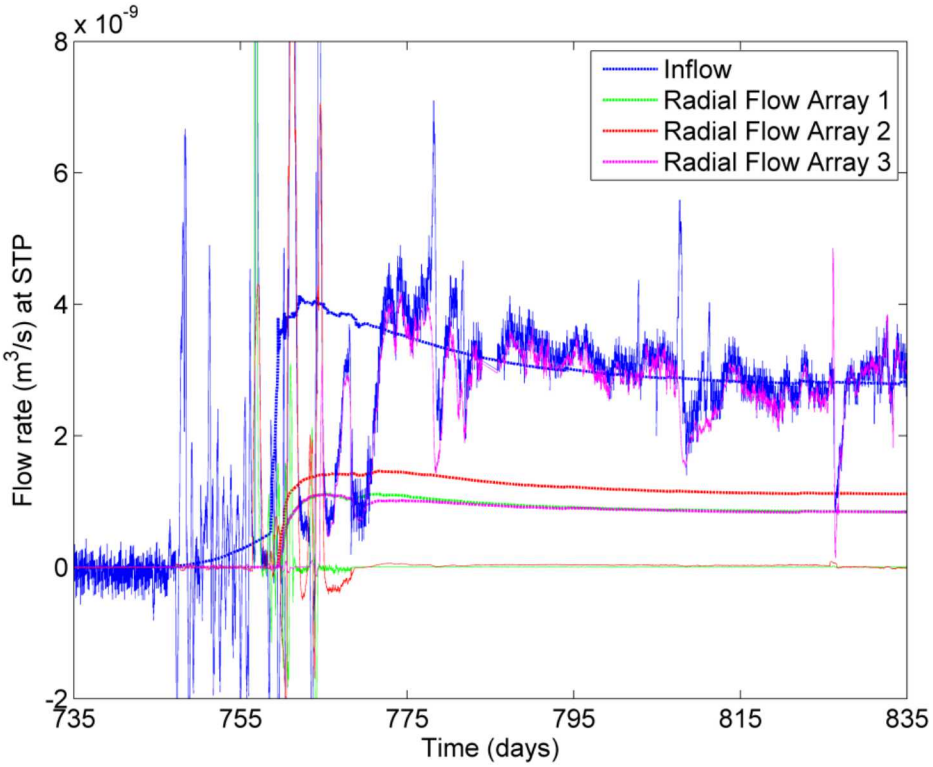


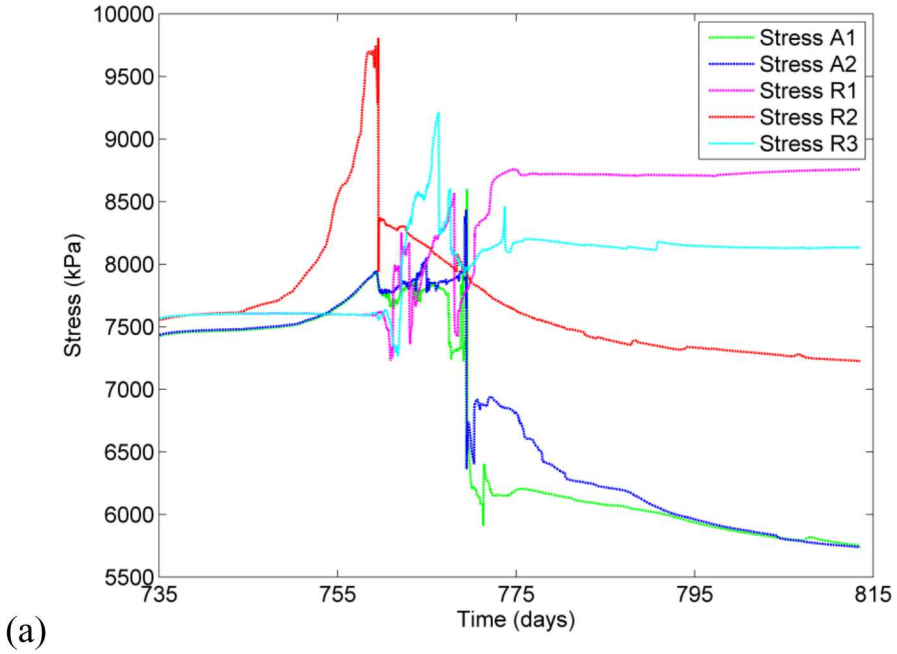
Figure 6-23. Comparison of simulated and experimental flow rate evolutions.

6.6.3 Summary of TOUGH-RBSN simulations for gas migration

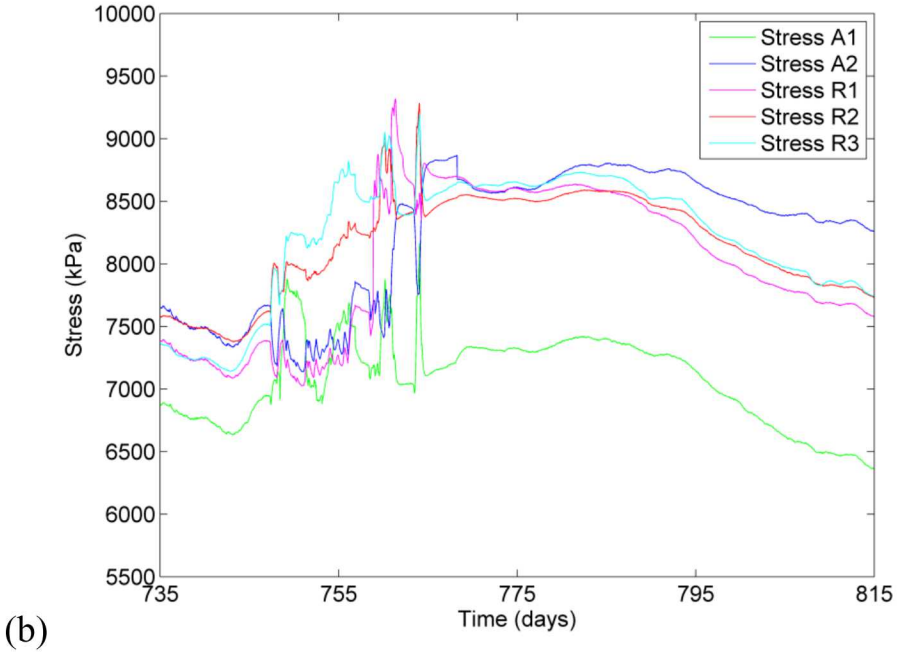
For the 1D gas flow simulation, the DFN approach with enhanced fracture permeability demonstrated the gas breakthrough, where the pore pressure evolutions were matched well to the experimental data. The adoption of air entry pressure and swelling/shrinkage concepts helped simulate total stress evolutions in a decent accordance with the experimental results. However, the simulated outflow rate deviates from the experiment in terms of the flow activation time and the overall shape of the evolution curve.

The results of simulations of 3D spherical gas flow show the developed model captured some of key responses in gas pressure-induced fracturing processes. However, the current simulations are computationally very demanding, because the time step size becomes very small, especially during the fracturing stage. The capillary pressure values of fracture elements are varying depending on the fracture permeability (calculated using the cubic law based on the fracture aperture) for every time step, so some nonlinearity in the flow calculation hinders time marching with big strides. We expect to be able to retain the time step size using a constant scaling of capillary pressure values for the fractur elements.

For FY2019, we plan to continue to participate in the DECOVALEX-2019 Task A, with access to additional laboratory data for different types of geologic barrier materials. We will strive to resolve the convergence rate issues in the coupled multiphase flow simulations and find better and more efficient concepts and model parameters to demonstrate more realistic gas breakthrough features.



(a)



(b)

Figure 6-24. Comparison of (a) simulated stress evolutions, and (b) experimental stress data.

7. Fault Activation Monitoring Using SIMFIP Tool

7.1 Introduction

Faults of various sizes may be reactivated by thermal, hydraulic and mechanical disturbances during operational or post-closure periods. Observations suggest that remote earthquake waves can enhance basin-wide fluid transport extending to depths of a few kilometers. Understanding these phenomena has great importance for the design of geologic disposal of radioactive wastes, because the performance depends on the integrity of the natural system and barriers to contain radionuclides for tens of thousands of years. It is thus crucial that the permeability changes in response to earthquakes, specifically those occurring in fault zones and other preferential subsurface pathways such as the EDZ, can be better understood and eventually be predicted with confidence. LBNL has been developing a new instrument called Step-Rate Injection Method for Fracture *In-situ* Properties (SIMFIP) that may allow for probing the physical processes affecting fault reactivation in low permeability host rock layers at field scale. In parallel to instrument development, LBNL is being conducting *in situ* fault activation experiments at depths relevant to nuclear repository sites, using the SIMFIP to probe fault movements and to estimate fault permeability variations.

In this chapter, we first describe the current SIMFIP sensor developments that are conducted within the frame of this project. Second, through preliminary field test observations and numerical analyses, we explore how fault permeability can vary with slip and/or slip rate under pressurization in the range that could be expected in a host rock. Our results indicate that a good knowledge of the initial state of stress, permeability and friction parameters are key constituents to explore the hydraulic and mechanical response of a fault to a fluid pressurization. They also show that fault displacement rate might play a larger role than fault displacements in fault permeability variations, highlighting the importance of developing a sensor such as the SIMFIP sensor to track minor fault displacements, but at eventual high slip rate and their repeated effects on fault potential leakage in low permeable argillite host rock. Finally, we describe the perspectives to improve the SIMFIP ability to capture the fault displacements and pore pressure variations over a broad band of frequencies from 1 to 500Hz and in very low permeability rocks and to implement the physics of short-to-long term fault pressure and strain/strain rate evolution in numerical model(s) to predict fault permeability evolution in response to weak loadings by passing seismic waves.

7.2 Development of a New SIMFIP Sensor

The SIMFIP (Guglielmi et al., 2015a) technique combines the advantages of a stress relief method (because it allows constraining the full components of the stress tensor using a 6-component displacement sensor) with the advantages of a hydraulic or sleeve fracturing method (because the sensor is integrated in a straddle packer system which is easy to move downhole). Figure 7-1 shows a photograph of the SIMFIP tool just prior to deployment in a deep mine setting. Figure 7-2 shows a schematic representation of the SIMFIP tool, as well as a representative dataset from a real-world test.

The first SIMFIP instrument developed by Y. Guglielmi has been used for several research experiments in mine-based environments (Guglielmi et al., 2015b). In 2015, the SIMFIP allowed for the first direct in-situ continuous measurement of a field-scale fault transitioning from aseismic to seismic slip. Since 2017, further engineering of the SIMFIP performed at LBNL allowed for

increasing the pressure conditions under which the SIMFIP can operate, and it is currently being tested in the deep Sanford Underground Research Facility (SURF), which is an underground research laboratory, within the framework of the EGS Collab SIGMA-V project (see Figure 7-1). The current state of development of the SIMFIP is at a TRL of 3-to-4. It has been tested in field boreholes in more than 20 tests at depths relevant to host rock depository sites. Some tests were performed in argillite underground laboratory at Mont Terri (Switzerland) and Tournemire (France).

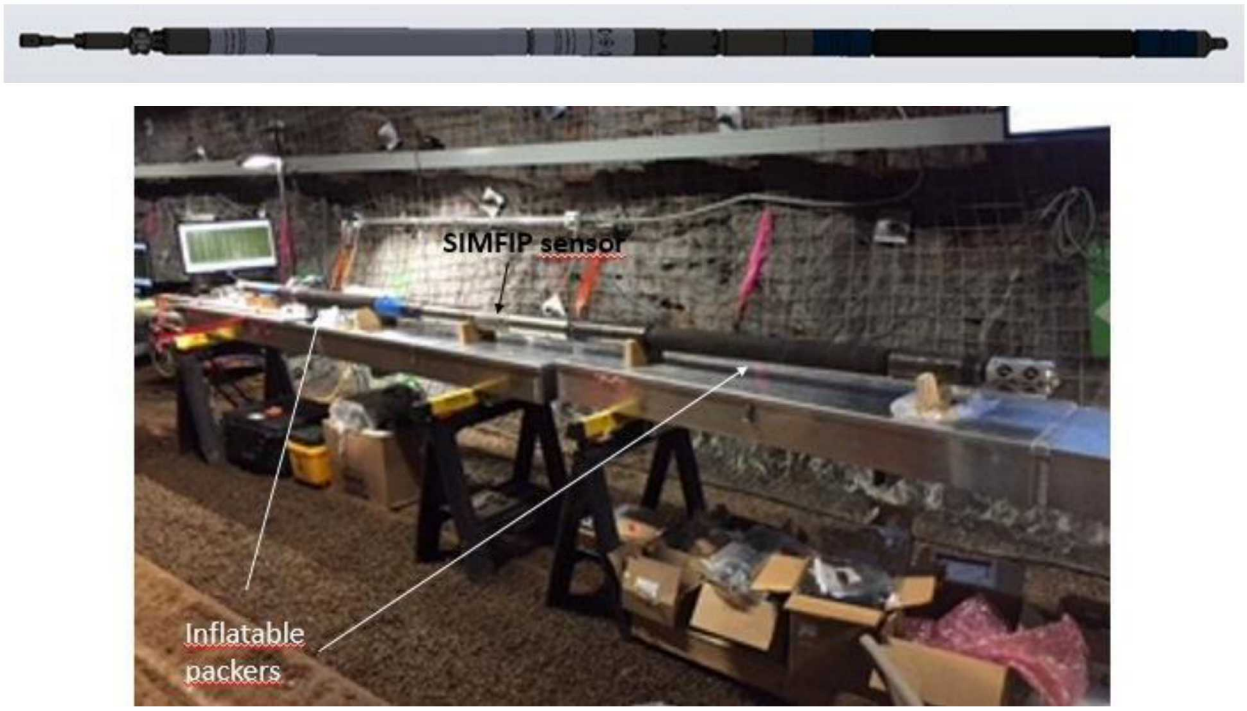


Figure 7-1. SIMFIP probe currently used for the fracture stimulation experiment in the SURF underground research laboratory (fracture pressure applied by the SIMFIP will be about 40MPa). Upper figure shows a Solid Works design of the SIMFIP and the photo shows the current SIMFIP probe.

The SIMFIP borehole probe allows for measuring simultaneously fluid pressure and three-dimensional displacements at high frequency (Figure 7-2). The injection interval is isolated in an open borehole using two inflatable rubber packers. The sealed interval length is currently of length 1.6 m, but can be varied to >20 m long by setting a chain of SIMFIP cages (Figure 7-3). Each SIMFIP cage is 0.2 m long and 0.1 m diameter pre-calibrated aluminum cage that can either: (Case 1) be connected to two 0.25 m long elements to allow for clamping both ends of the cage on borehole wall, or (Case 2) be directly connected to the packers. Dimensions of the SIMFIP cage can be varied depending on the target borehole conditions. In Case 1, when it is clamped, the cage is disconnected from the straddle packer system. In Case 2, the SIMFIP replaces the mandrel that connects the packers. When packers are inflated, they play two roles: (a) sealing the test interval,

and (b) anchoring the SIMFIP cage. Case 2 is the simplest and easiest to set the SIMFIP probe, but the SIMFIP signal must be calibrated to account for the packers' effect during the test (this results in a relatively lower resolution of the SIMFIP signal in Case 2 compared to Case 1). Case 1 allows for a very high-resolution measurement.

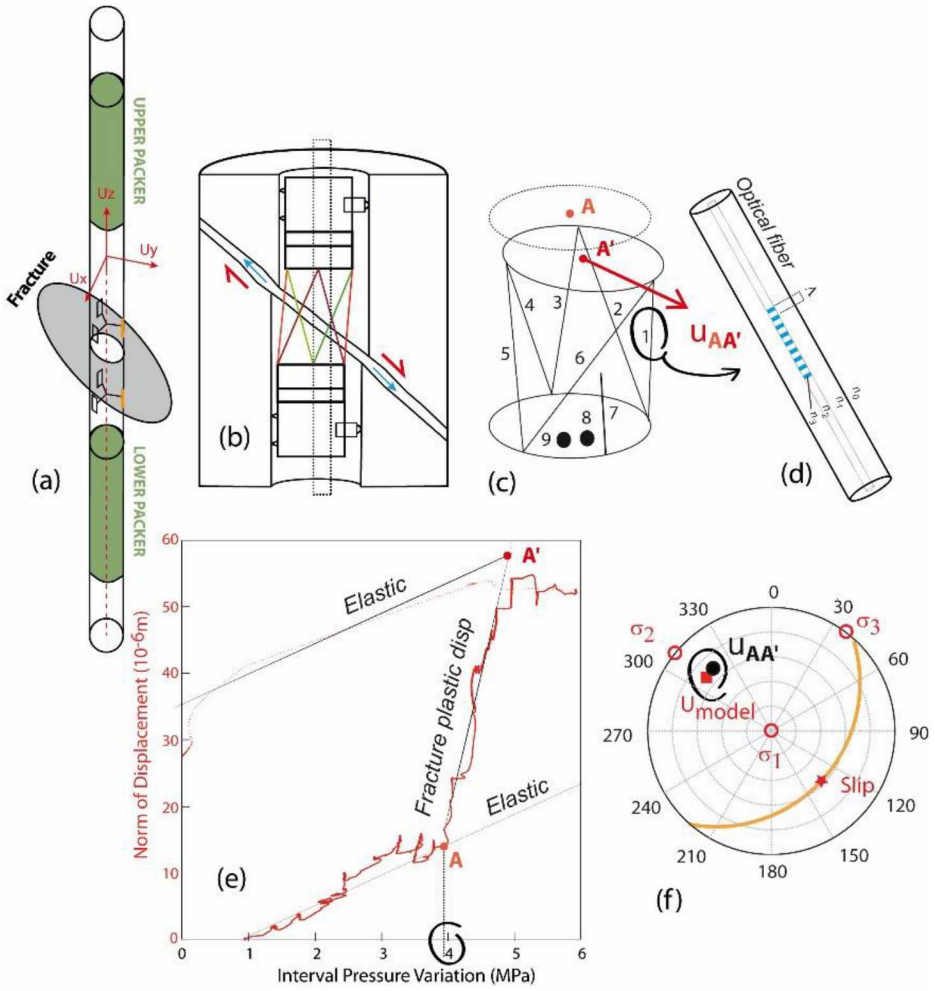


Figure 7-2. SIMFIP probe currently designed at LBNL: (a) Schematic typical SIMFIP setting across a natural fracture; (b) Details of the SIMFIP anchoring across the fracture; (c) Principles of the sensor which is a deforming cage in 6 different directions + 1 reference (7) + one pore pressure (8) + one temperature (9); (d) We build all our sensors using Bragg gages all connected on the same optical fiber; (e) Example of a fracture response to a pressure variation in the straddle packer interval, here showing the fracture plastic movement from A to A'; (f) Plastic displacement of the fracture's walls UAA' is plotted in a stereographic projection with the fracture plane orientation. Knowing both the fracture activation pressure and the three-dimensional plastic displacement allows a refined estimation of the absolute values of all the stress tensor components (including SH) by fitting a calculated vector with the measured one.

The SIMFIP is designed to capture micrometer to nanometer displacements of fractures affecting the borehole. In the case of a preexisting natural fracture the SIMFIP will be set across the fracture,

anchored on either side of the fracture. A logging OPTV-type tool can be coupled to the SIMFIP probe to target the tested fracture interval in real-time. In the case of an induced fracture, the Case 2 configuration will be used to capture the orientation and the pressure at which the fracture grows from the borehole interval. In both cases, when the fracture is deforming according to the water pressure increase in the interval, the cage allows for obtaining angle dependent strain measurements, which are used to constrain the full three-dimensional strain tensor and the three rotations. The raw data are 6 strain measurements performed with optical fiber Bragg gratings (FBG) that are mechanically clamped on the 6 wings of the deforming cage. In addition, there is a reference FBG that is subject to ambient pressure and temperature, and which remains unstressed. It is used to correct linearly the strain measurements from temperature and pressure variations in the chamber. The 6+1 FBG are distributed along one single fiber that brings the sensor signals to an FBG interrogator set at the surface. A MicronOptics Si155 acquisition system is currently used. This interrogator allows picking shifts in the FBG wavelength that relate to FBG deformation over a large spectrum of FBG wavelengths.

The 6 components of the tensor describing the relative displacement and rotation between the upper and lower rings are calculated as a linear function of the 6 strain components (named A to F in Equation 7-1). The transfer matrix is calculated as the product of two 6 × 6 matrices calibrated in the laboratory: **A** converts strain data to efforts, i.e., forces and moments applied on the deforming body, and $\mathbf{C_0}$ converts these efforts to the translation and rotation components of the tensor, given by the following equation

$$\begin{pmatrix} u_x \\ u_y \\ u_z \\ r_x \\ r_y \\ r_z \end{pmatrix} = \mathbf{Co} \cdot \mathbf{A} \cdot \begin{pmatrix} A \\ B \\ C \\ D \\ E \\ F \end{pmatrix} \tag{7-1}$$

By convention, u_y corresponds to the axial strain, u_x and u_z to the radial strains. The variables r_x, r_y and r_z are the counter-clockwise rotations (right-hand convention) along the corresponding axes. The displacement range is 0.7 and 3.5 mm in the axial and radial directions of the borehole, respectively; the current accuracy is $\pm$ 0.1×10^{-6} m. A compass set on the probe provides the orientation of measurements with a 0.1° accuracy. The strain data are logged together with pump parameters (pressure and flow rate); water pressure in the anchoring hydraulics and water pressure in the packer hydraulics are measured at the surface. Temperature and pressure are measured in the borehole above, between, and below the packers using specially designed pressure and temperature sensors, which are also based on FBG technology. The chamber P/T sensors are run on the same fiber as the SIMFIP strains. The upper and lower P/T sensors are run on a second independent optical fiber. Ranges can be adapted depending on the depth of tests.

During the tests, the injection pressure is imposed by the pump, while flowrate, pressure, temperature and displacement variations from the SIMFIP probe are continuously monitored at a

1000 Hz sampling frequency. Raw data are saved into one ASCII file every five minutes. Pre-processing of the SIMFIP raw data is automated in the acquisition software (written in the LabView format), including the following steps: (1) correction of fiber Bragg gauges measurements from temperature and pressure, (2) detection of the FBG spectra overlapping problems (and filtering), and (3) filtering from outliers using a medium filter (outliers can occur when the interrogator cannot calculate the FBG wavelength because of some wavelength heterogeneity in the assigned FBG spectral region).

7.3 Observations of fault permeability variations induced by pore pressure increase

Here we show observations from a controlled fault activation experiment conducted in the Mont Terri underground laboratory (Switzerland), affecting the Opalinus clay layer. One of the goals of this experiment was to apply the SIMFIP sensor to monitor a slip pulse propagation between an injection and a monitoring vertical borehole, both drilled about 5m away across the fault. The Fault "core" consists of a thrust zone about 0.8 to 3 m wide, which is bounded by two major fault planes. At the depth of the experiment, the upper fault boundary plane is oriented N050° and dipping 60°SE and the lower boundary plane is oriented N050° and dipping 40°SE (Figure 7-3). The detailed fracture structures visible on cores, and the strain intensity within the core zone of the Main Fault, are clearly heterogeneous, including zones with fault gouge, C'-type shear bands, meso-scale folds, microfolds, numerous fault planes and apparently undisturbed parts. Parts of the Main Fault comprise a 'scaly' fabric, where the rock splits progressively into smaller fish-like flakes. The different sets of faults in the Main Fault can be interpreted as Riedel P- and R-shears. The very low fault permeability determined before activation is ~10^{-17} m^2, which is close to the permeability of the host rock. State of stress estimated in and around the fault is characterized by a normal regime with the maximum principal stress σ_1 = 5.3±0.2 MPa sub-vertical, σ_2 = 4.5±0.2 MPa sub-horizontal, and striking N310±10° and σ_3 = 3.8±0.2 MPa sub-horizontal and striking N040±10°E (Figure 7-3).

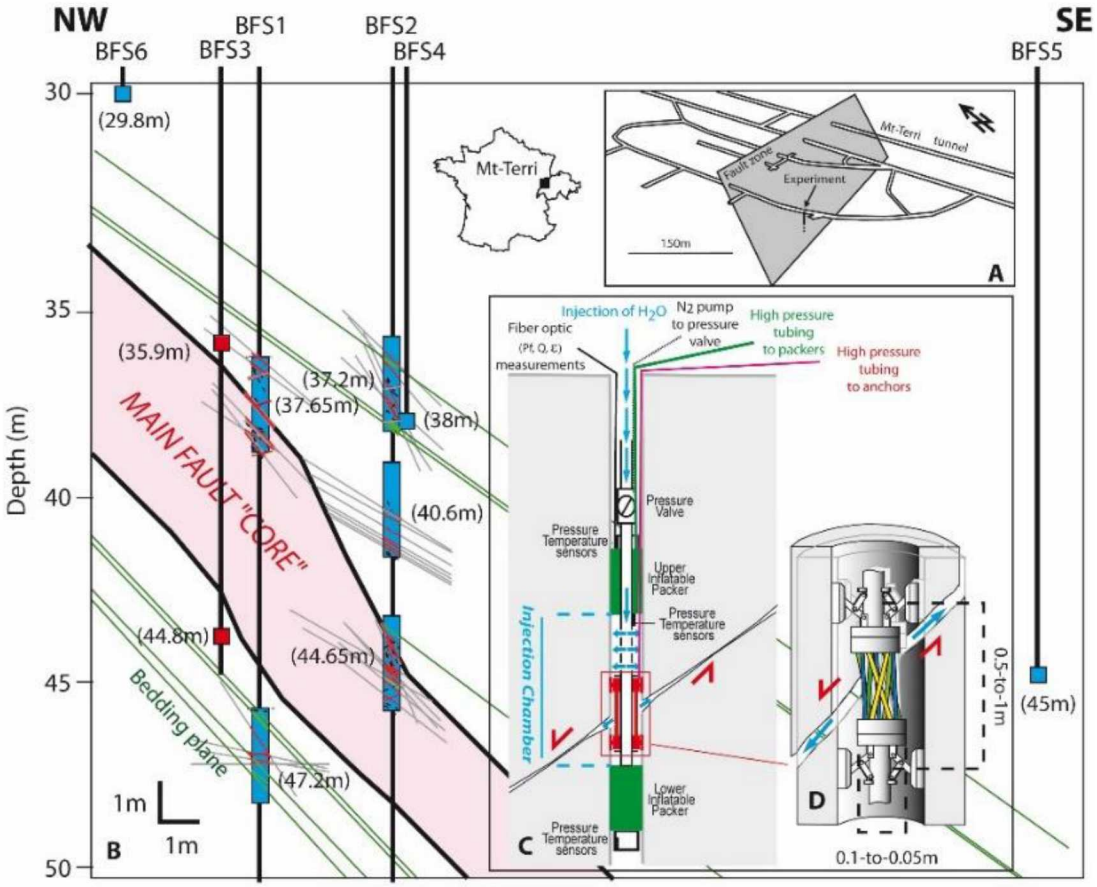


Figure 7-3. Schematic of the Mt Terri Main Fault activation experiment setting. A – Location of the experiment in vertical boreholes intersecting the Main Fault Zone, which is shown as a grey plane cross-cutting the Mt-Terri galleries. B – Vertical cross section perpendicular to the fault, showing the SIMFIP pressurization intervals as blue rectangles. C and D – Schematic of the SIMFIP probe and sensor used for these tests.

In Figure 7-4, we are presenting the graphs depicting the permeability change during repeated pressure pulses conducted at the interval located 40.6 m below the galleries (see Figure 7-3(A) for location). The upper red and blue curves show the imposed step-by-step pressure variations. Red segments of the pressure curve correspond to time intervals of the pressure increase in the borehole. Blue segments of the pressure curve correspond to the transient pressure evolution caused by the fault hydromechanical response after the pressure was increased in the test interval. Green segments show the fault displacement rate variations measured by the SIMFIP sensor (here it is the rate of the total displacement vector, which was continuously monitored by the SIMFIP during the test). For comparison, the lower graph shows the fault permeability variations obtained from fully coupled hydromechanical modeling with the TOUGH-FLAC simulator.

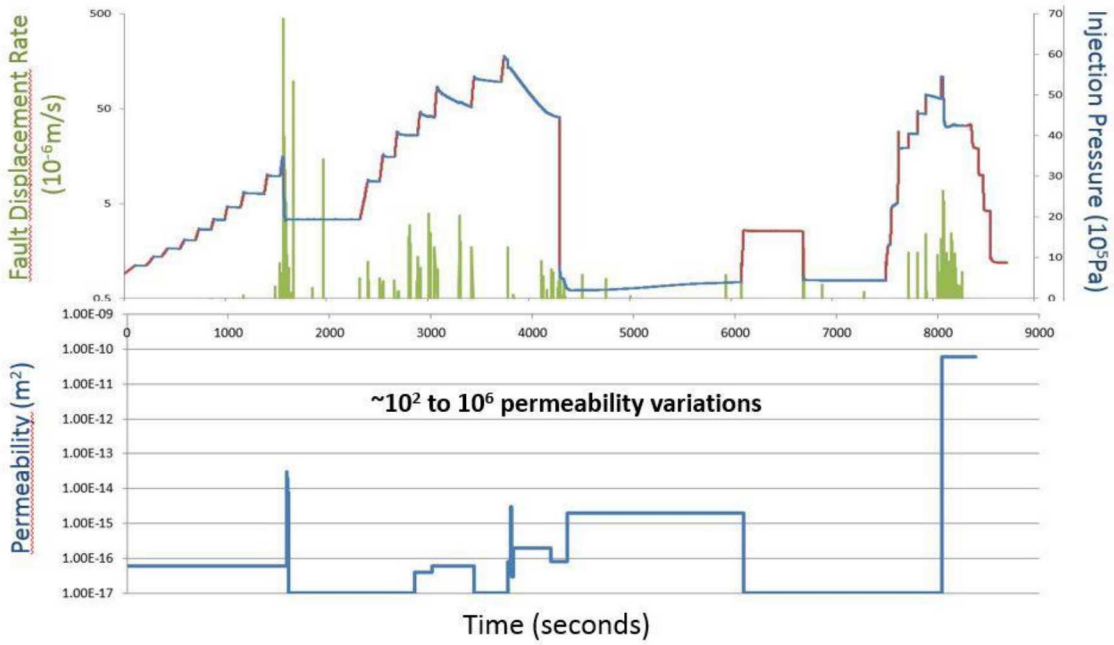


Figure 7-4. Upper graph – pressure (red and blue) and fault displacement rate (green) monitored during pressurization tests in the interval 40.2 m. Lower graph – interval permeability estimated from the fully coupled modeling of the pressure using the TOUGH-FLAC simulator.

Comparison of the upper and lower graphs shows that the large permeability variations correlate with periods of large slip rate events at 1500, 3800 and 8000 seconds, respectively. Interestingly, these permeability changes do not match well with the pressure imposed in the interval. Indeed, the 1500-second event is associated to a factor of 10 larger permeability change than the 3800-second one, although it occurs at a fault opening pressure about 2 MPa lower. This observation reveals that a relatively small pressurization associated with a high displacement rate might produce a larger permeability variation than a high pressurization associated to a small displacement rate. Thus, fault displacement rate might cause the effect of stress on fault reactivation and leakage. This observation also shows that the continuous fault displacement monitored by the SIMFIP sensor allows for tracking changes in faults displacement rates as potential precursors to "large" fault leaks (for simplicity we only show here the displacement rates, which are derived from the SIMFIP measured displacements).

7.4 Numerical analysis of key parameters conditioning fault activation induced by pore pressure increase

To investigate the coupling between fault permeability enhancement and slip or slip rate during fluid pressurization, we use the 3DEC code (Itasca Consulting Group, 2016), a distinct element method (Cundall, 1988) to simulate the interaction between fluid flow and fault slip evolution, including hydromechanical coupling, effective stress and friction. To describe the relationship between the fluid pressure diffusion and the permeability change with the fault normal displacement, the model uses the cubic law (Witherspoon et al., 1980). The method has been previously used to understand the hydromechanical behavior of fractured rock and fault zones

during fluid pressurization (Cappa et al., 2006; Guglielmi et al., 2008), and to show that the evolution of the fault hydraulic diffusivity is a fully coupled problem depending on stress and fluid pressure (Guglielmi et al., 2015b).

Our 2D model (200 m × 50 m) considers a fluid injection into a horizontal flat fault in homogeneous elastic and impervious media (Figure 7-5a). The remote normal (σ_n) and shear stress (τ) resolved on the fault plane are constant. During injection, the fluid pressure is increased into the fault step-by-step of 0.5 MPa every 150 seconds at a point-source (Figure 7-5b). The total time of injection is 1050 seconds. For numerical accuracy, we used the fine mesh size (0.15 m) along the fault, which was gradually increased to 0.5 m in the direction normal to the fault toward model boundaries.

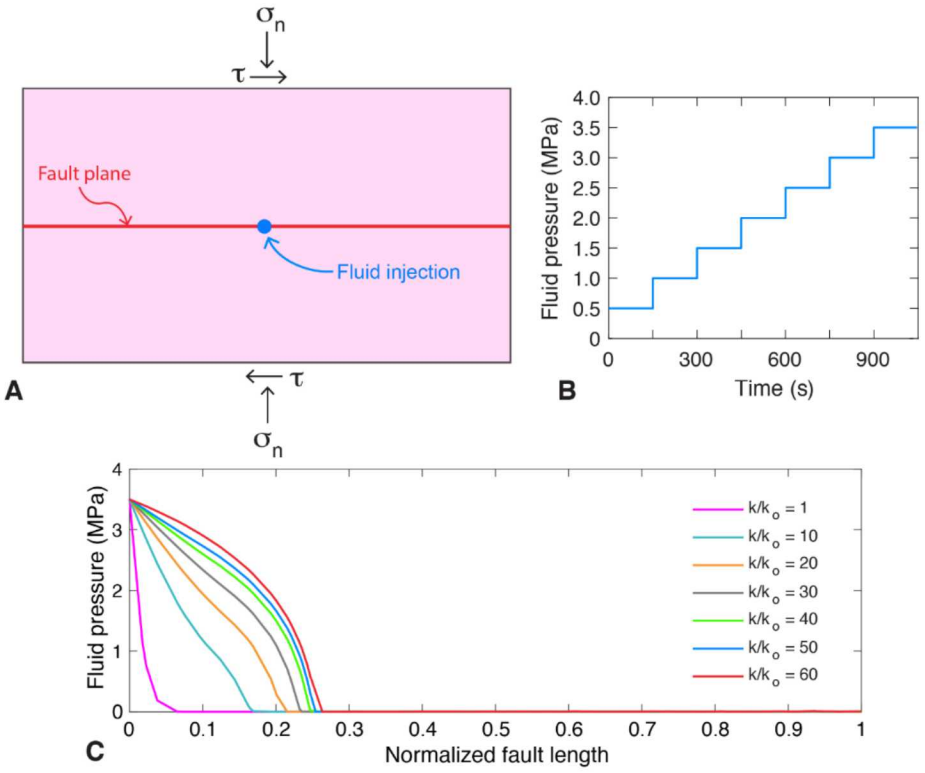


Figure 7-5. (a) Model geometry, and (b) graph of the simulated step-by-step pressure increase into the fault. The remote normal (σ_n) and shear stress (τ) resolved on the fault plane are constant, (c) half-profiles of fluid pressure calculated along the fault, assuming different permeability ratios (k/k_o). The injection point is located at $x = 0$ along the horizontal axis x representing the distance along fault. Half-profiles are plotted at the end of injection scenario (1050 seconds in Figure 7-4).

In these preliminary tests, we considered the following initial values of the normal stress and the fluid pressure into the fault: $\sigma_{no} = 4.25$ MPa and $p_o = 0$ MPa. We used two different values of shear stress $\tau_o = 1.65$ and 2 MPa to evaluate the effects of different levels of fault criticality to failure, $\sigma_{no}/\tau_o = 0.388$ and 0.47, respectively. We have tested the effects of different values of permeability changes with fault displacements $k/k_o = 1$, 10, 20, 30, 40, 50, and 60. The initial hydraulic aperture was assumed to be 9.15 microns (corresponding $k = 7 \times 10^{-12}$ m^2 calculated from the cubic law).

Rock elastic properties are K = 20 GPa for the bulk modulus and G = 9 GPa for the shear modulus (more realistic argillite properties will be considered in furter numerical simulations).

Here, we have tested constant friction and rate-and-state friction (Marone, 1998). For a rate-and-state fault, we assumed the following frictional parameters: μ_o = 0.6, (a-b) = -0.002, and d_c = 10 microns. μ_o is the friction coefficient at a reference slip velocity. The parameter a quantifies the direct effect of a change in slip velocity. The parameter b describes the effect of the state variable (here, we use the "aging law" (Dieterich, 1979)). The characteristic slip distance, d_c, governs the evolution of the state variable. For the fault model with a constant friction, we assume a static value (μ_s) of 0.6. For simplicity, shear-induced dilatancy is neglected in the simulations.

The modeling results shown in Figure 7-5c revealed that the development of the fluid pressure along the fault varies as a function of different permeability enhancement. Modeling results indicate that both the magnitude and distribution of the steady-state overpressure, as well as the size of the pressurized area, depend on the permeability change. For constant permeability, the pressure perturbation is less pronounced, and the highest pressure and sharpest pressure gradients are situated near the pressurization point. For the modeling scenario with evolving permeability, the pressurization produces a reduction in effective normal stress by increasing the fluid pressure, which leads to opening the fault and increasing its permeability. The size of the pressurized zone is growing significantly with the fault permeability enhancement. Modeling results show that higher the permeability increase, the greater the pressurized area is (Figure 7-5c).

Then, we investigated the effects of the fluid pressure development on the size of the slip zone, and its dependency on the background stress and fault parameters (Figure 7-6). During the fluid pressurization along the fault, the reduction in frictional resistance to sliding, in the presence of a background fault-resolved shear stress, drives the growth of slip. Here, we modeled an aseismic slip (i.e., slow slip without dynamic effects). In Figure 7-6, we compared the slip length as a function of the length of the pressurized zone for a representative range of stress ratio (τ_o/σ_{no}), friction laws and permeability evolution (k/k_o). We found that the slip growth is controlled by a combination of the background stress, frictional weakening and permeability enhancement. For example, a fault with higher background stress and larger enhanced permeability can produce larger slip growth. The background stress affects both the timing of the onset of rupture and the subsequent size evolution of the slip area (Figure 7-6a). Reducing the shear stress delays the onset of rupture and decreases the maximal size of the slip area, whereas the increased shear stress leads to the earlier onset and a larger slipping zone. The effect of the fault friction is also illustrated in Figure 7-6a. Fault frictional weakening using the rate-and-state friction law influences the temporal evolution of the slipping area and may produce larger ruptures. This is expected because friction weakening leads to the reduced fault strength with sequences of accelerated and increased slip, while constant friction tends to stabilize the fault strength, resulting in a less pronounced slip.

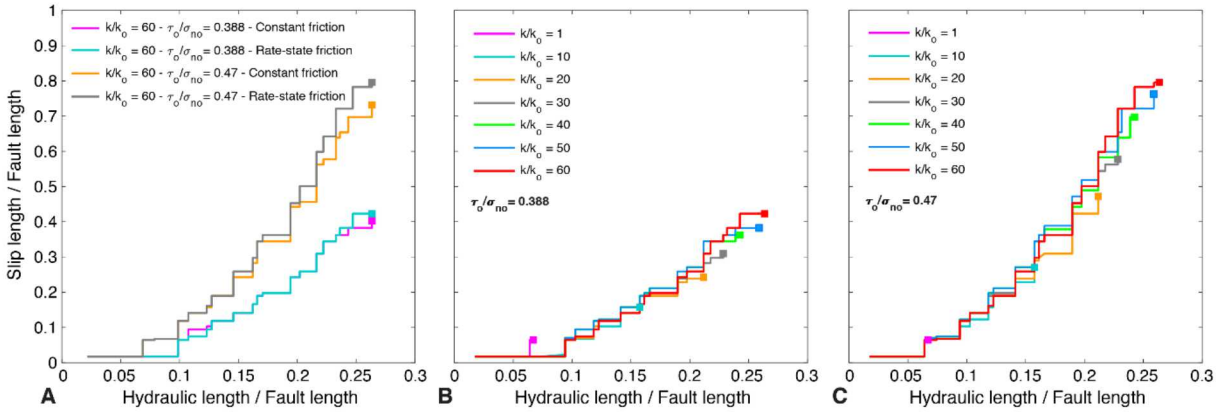


Figure 7-6. Influence of stress conditions and fault-related frictional and hydraulic parameters on the evolution of fault slip. Slip length as function of the hydraulic length for different (a) initial stress ratios and friction laws (i.e., constant friction, rate-and-state friction), and changes in fault permeability for two different stress regimes, (b) $\tau_o/\sigma_{no} = 0.388$ and (c) $\tau_o/\sigma_{no} = 0.47$, respectively.

Modeling results also indicate that the permeability evolution affects the spatial extent of the fluid overpressure on the fault, and the fault resistance to rupture; hence, it affects both the maximum diffusion length and the size of slip zone (Figures 7-6b and c). All simulation results, including permeability changes $k/k_o > 1$, show that the growth of the fault slip outpaces the growing fluid pressure front. Higher the increase in fault permeability, higher the growth of the slip front is. In addition, the most noticeable difference between the slip and pressure fronts occurs for the higher, more critical, initial stress ratio $\tau_o/\sigma_{no} = 0.47$.

In summary, the initial stress on the fault and the change in fault permeability have an important impact on fault slip, which can occur over a zone much greater than the fluid-pressurized zone. For instance, the size of the slip zone is about 1.74 and 3.23 times greater than the size of the pressurized dilatant zone, respectively, for an initial stress ratio of 0.388 and 0.47, respectively (Figure 7-7). Thus, in addition to the fault frictional weakening, the size of the slip zone is controlled by the integral effect of the spatial extent of fluid pressure on the fault. The spatial extent of the largest slip increases with the spatial extent of the largest fluid pressure.

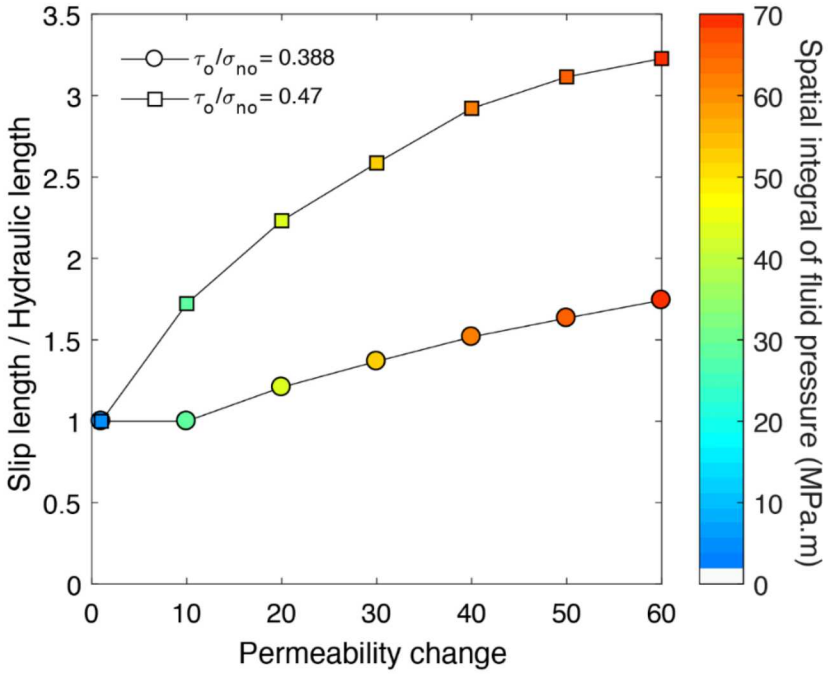


Figure 7-7. Graphs of the maximum slip length over maximum hydraulic length as a function of permeability enhancement. The color bar shows the spatial integral of fluid pressure computed at the end of injection.

7.5 Summary and future work on fault activation monitoring and SIMFIP tool

7.5.1 Upgrading the SIMFIP to detect nanoscale fault movements

In the next steps, we plan to increase the resolution of SIMFIP to nanometer accuracy over a broad band of frequencies [0 - 500Hz]. This will allow for capturing dynamic stress variations remotely from the borehole, ranging from below seismic detection to conventional seismic. Further engineering of the SIMFIP will focus on:

- Upgrading the SIMFIP resolution and accuracy to the nanostrain. This will be done by (i) engineering very high-resolution clamping systems to optimally bite the borehole wall, and (ii) testing different types of FBG sensors geometries from longer uniform FBG to more complex systems, such as Fabbry-Perot cavity based on FBG sensors, (iii) refining the SIMFIP cage design in order to make an ultra-compliant, and (iv) testing more advanced spectrometers based on the Stationary-Wave Integrated Fourier-Transform.
- Designing and testing different SIMFIP configurations including several SIMFIP cages in long intervals and configure a SIMFIP as a permanent long term monitoring sensor (instead of the current probe setting). We target testing >20 m long chains of SIMFIP that could simultaneously probe the full stress tensor at relevant host rock scales, allowing monitoring

three-dimensional displacements across a canister spacing or across a plurimeter thick fault or damage zone.

- Calibrating the SIMFIP to a broader band static to perform seismic stress monitoring. This is currently conducted by upgrading our existing calibration bench in the LBNL's laboratory that allows for applying to the SIMFIP probes both known forces and displacements in multiple directions. Current bench resolution is 0.05 mm and 100 Pa for displacements and stresses, respectively. We will (i) add more sensors to better characterize the coupling between SIMFIP and bench displacements, (ii) add accelerometers to characterize bench vibrations, and (iii) add hydraulic piston to produce computer controlled seismic waves in a [1, 10 Hz] frequency range.

7.5.2 Future *in situ* testing at Mt Terri (Switzerland) and Improvements in fault permeability constitutive laws in argillite

Our field observations and numerical results show that the initial stress on a fault, affecting the change in permeability and friction during a fluid pressurization directly into a fault, has an important effect on the fluid pressure diffusion and slip growth. Thus, our results indicate that a good knowledge of the initial state of stress, permeability and friction parameters are key requirements to explore the hydraulic and mechanical response of a fault to a fluid pressurization. In addition, we have shown that the fault deformation affects a volume largely greater than the volume pressurized by fluids. These results show that the new developments of friction with hydro-mechanical coupling made in the 3DEC code can be used for simulating the fault response to a fluid pressurization in argillite.

Next steps will include the initiation of a new fault activation experiment at Mont Terri. We plan to distribute sensors both close to the point of pressure variation and several meters apart from the pressure source to obtain a good spatial coverage of fluid pressure and deformation, and, hence, the estimation of the volume affected by the long-term permeability and stress changes. This experiment called FS-B should start in July 2018. In parallel, future numerical model improvements will include inelastic shear-induced dilatancy. We plan to use our improved numerical code to study a real dataset of fluid pressure and fault motion measurements, geology, rock properties, etc. collected during the FS-experiment at Mont Terri in order to improve our understanding of both the long-term permeability and stress changes in a fault zone in an argillite host rock.

8. Summary of FY2018 Progress and Future Work

Here we summarize FY2018 progress and provide an outlook for the rest of FY2018 and future work planned for FY2019. First, in Section 8.1, we summarize in more detail the progress and plans of the ongoing argillite R&D and international activities. Thereafter, in Section 8.2, we present a summary of new activities for an expanded work scope and activities being launched as a result of new incremental FY2018 funding.

8.1 Progress and Plans of Ongoing FY2018 Activities

In FY2018 much work has been focused on modeling of the Mont Terri FE heater experiments in Opalinus clay and two *in situ* experiments at the Bure URL in COx claystone. Participating in these two international activities improved knowledge and provided data for model validation for two different clay types host rocks and for two different repository design concepts: the emplacement in horizontal tunnels (Swiss concept), and emplacement in micro-tunnels extended from the walls of larger tunnels (French concept). A comprehensive effort has also been dedicated to modeling of gas migration in bentonite, which is important to determine the fate of gas generated from metal corrosion of the waste package in a potential repository. In addition, new research has been launched on the evaluation of activation of faults and potential creation of flow paths through otherwise impermeable clay host rocks. Along with modeling these field and laboratory experiments, necessary model developments and improvements have been conducted.

1) Modeling of FE experiment at Mont Terri in Opalinus Clay

The Mont Terri experiment is unique because it is the only full-scale experiment in argillite, which involves natural resaturation of the bentonite buffer from the host rock (without artificial wetting). The experiment has been run with heating since the beginning of 2015 and the temperature at the heaters reached approaching 130°C. Modeling using TOUGH-FLAC of the first 3.5 years of heating has resulted in obtaining an excellent agreement between experimentally measured and simulated temperature and a good agreement between measured and simulated relative humidity (and saturation) in the buffer. The pattern of the buffer drying near the heaters was matched by assuming a reduced vapor diffusivity (the latter was calibrated by changing the tortuosity factor). In general, the buffer wetting caused by flow from the surrounding argillite rock is slow, and after 3.5 years, no substantial swelling stress has developed in the buffer. It will be very important to evaluate the mechanical behavior and a swelling stress in the buffer, as these are among the key functions of the buffer. In FY2019, we will continue modeling of the FE experiment along with new monitoring data, focusing more on the mechanical evolution of the buffer and host rock.

2) Modeling of heater experiments at Bure URL

Task E of the DECOVALEX-2019 project involves the evaluation of upscaling of THM properties and processes from laboratory-scale experiments, via *in situ* experiments, to a full repository scale. We have conducted coupled THM modeling following the task schedule of DECOVALEX-2019 along with other international modeling teams. The task also provides an opportunity to validate the software, TOUGH-FLAC, at a relevant field scale, in this case in COx clay stone. This year, we have made a good progress in modeling of two experiments with good agreement of addressing thermal pressurization. It is important to be able to accurately predict thermal pressurization and its impact on the stress field and potential for fracturing of the rock. A number of verification and validation steps have been completed and THM parameters of the COx claystone have been determined and validated. The next step to be conducted in FY2019 will be to model Step 4 of DECOVALEX-2019 Task E; that is, we will conduct model predictions at the repository scale of an area with several high level waste cells.

3) Modeling gas migration in bentonite

In FY2018, LBNL, as one of 11 international research teams, has continued to participate in DECOVALEX-2019 and conducted new simulations of gas flow through bentonite, and the results

of simulations were compared with experimental data. Using two modeling approaches—continuum modeling (TOUGH-FLAC) and discrete fracture modeling (TOUGH-RBSN)—a good agreement was achieved with the results of the one-dimensional flow experiment, though not perfect regarding flow rate evolution. In FY2018, we also conducted a preliminary analysis of a spherical gas flow experiment using TOUGH-RBSN with a network for flow channels created from the injection point. Despite of a number of challenging problems involved in modeling of gas migration in bentonite, a good agreement between simulated and experimental data regarding the pressure and flow was achieved, although the internal micro-scale processes are not well known. In FY2019, we will continue modeling experiments related to the DECOVALEX-2019 tasks with comparison to experimental data and results of other modeling teams.

4) Fault activation monitoring using SIMFIP tool

We are leveraging on research and development at LBNL of a specialized borehole tool call SIMFIP. The SIMFIP tool allows for probing the physics of fault reactivation in low permeability host rock layers at the field scale. In parallel to the instrument development, LBNL is conducting *in situ* fault activation experiments at depths relevant to nuclear repository sites, using the SIMFIP to probe fault movements and to estimate fault permeability variations. Our results indicate that a good knowledge of the initial state of stress, permeability and friction parameters are key ingredients to explore the hydraulic and mechanical response of a fault to a fluid pressurization. The results also show that the fault displacement rate might play a larger role than fault displacements in fault permeability variations, highlighting the importance of developing a sensor, such as the SIMFIP sensor, to track minor fault displacements, but at an ultimate high slip rate and their repeated effects on fault leakage in low permeability argillite host rock. New international field tests are planned for investigating long-term effects of fault slip, including long term sealing and healing after initial creation of a fluid path, as well as fault reactivation caused by distant seismic events. In FY2019, we plan to upgrade the SIMFIP tool to be able to detect nanoscale fault movements and continue the development of constitutive models for fault and fracture hydromechanical evolution in argillite host rock, along with modeling of new field experiments.

8.2 Expanded FY2018 Argillite Research Activities

The expanded Argillite Disposal R&D and Argillite International at LBNL will be focused on the following activities: (1) Coupled processes model development with GDSA integration, (2) Deployment of monitoring thermal pressurization during a heater experiment at ANDRA's URL in Bure, (3) Model testing and development for large scale gas driven fracturing, (4) participation in DECOVLAEX-2019 fault slip study, (5) Coupled microbial-abiotic processes in EBS and host rocks. These activities will be carried out for the rest of FY2018 (June-September 2018) and will continue in FY2019. The relevance of these new activities, as an expansion of LBNL's existing work on coupled THM processes R&D in argillite, is illustrated in Figure 8-1. Issues related to gas generation and thermal pressurization are relevant for assessing the performance of the system, as to prevent new flow paths to form along the EDZ or across a low permeability clay host rock. Key questions include the faith of generated gas and the likelihood for creating such a flow path and the long-term evolution of such a flow path, including sealing and healing.

1) Model development and testing for GDSA Integration

This task involves a necessary model development and adaptation of TOUGH-FLAC for GDSA integration. We plan to upgrade to latest parallel version of FLAC3D and link it to TOUGH3, which is the newly released version of the TOUGH family codes. We will collaborate with Sandia National Laboratories to evaluate how to integrate our work on near field coupled THM processes into their PFLORTRAN generic disposal simulations. This will involve practical applications of EDZ constitutive models with a need to develop EDZ models that can model long-term sealing and healing.

2) *In Situ* characterization of fracturing induced by thermal pressurization

The SIMFIP tool will be used for *in situ* characterization of a fracture induced by thermal pressurization at ANDRA's URL in Bure. This will be part of an *in situ* heating experiment in COx claystone aimed at studying potential fracturing induced by high fluid pressure during thermal pressurization. A borehole will be drill through the heated volume, and the SIMFIP tool will be used to characterize any effects of fracturing. Resulting changes in the complete strain tensors via the SIMFIP 6-component deformation cage coupled to changes in pore pressure will be inverted to characterize host rock within the heated zone. Characterizations will be conducted at different temperatures and analyzed using fully coupled THM models.

3) Model testing and development for large-scale gas driven fracturing

We will test and adapt 3D models for modeling large-scale (tens to hundreds of meters) fluid and gas driven discrete fracture propagation relevant to argillite disposal. We will evaluate existing discrete fracture modeling software, and/or other in-house options to decide the best approach to be adopted for high-performance computing (HPC) and visualization of 3D discrete fracture propagation in the field. We will model examples related to large-scale (hundreds of meters) 3D discrete gas driven fracture propagation from a repository tunnel located in argillite. This is again relevant to the potential impact of gas generation and its potential for creating a new flow path through initially impermeable host rock.

4) Participate in the DECOVALEX-2019, fault slip task

Scientists from LBNL are currently the technical leads of DECOVALEX-2019, Task B, related to modeling of fault activation experiments at Mont Terri, in Opalinus Clay, funded by the Swiss. As part of the expanded international collaboration, we will increase LBNL's involvement as a modeling team in this DECOVALEX-2019 task.

5) Coupled microbial-abiotic processes in EBS and host rocks

Preliminary laboratory and modeling investigations will be conducted to evaluate the role of coupled microbial-abiotic processes in host rock materials. Particular emphasis will be on processes driven by corrosion byproducts, including H_2 gas. The goal is to understand the role that these coupled microbial-abiotic processes have on controlling the fate of the corrosion byproducts and in inducing changes in the chemical and physical properties of the bentonite and host rock, which could alter future repository performance.

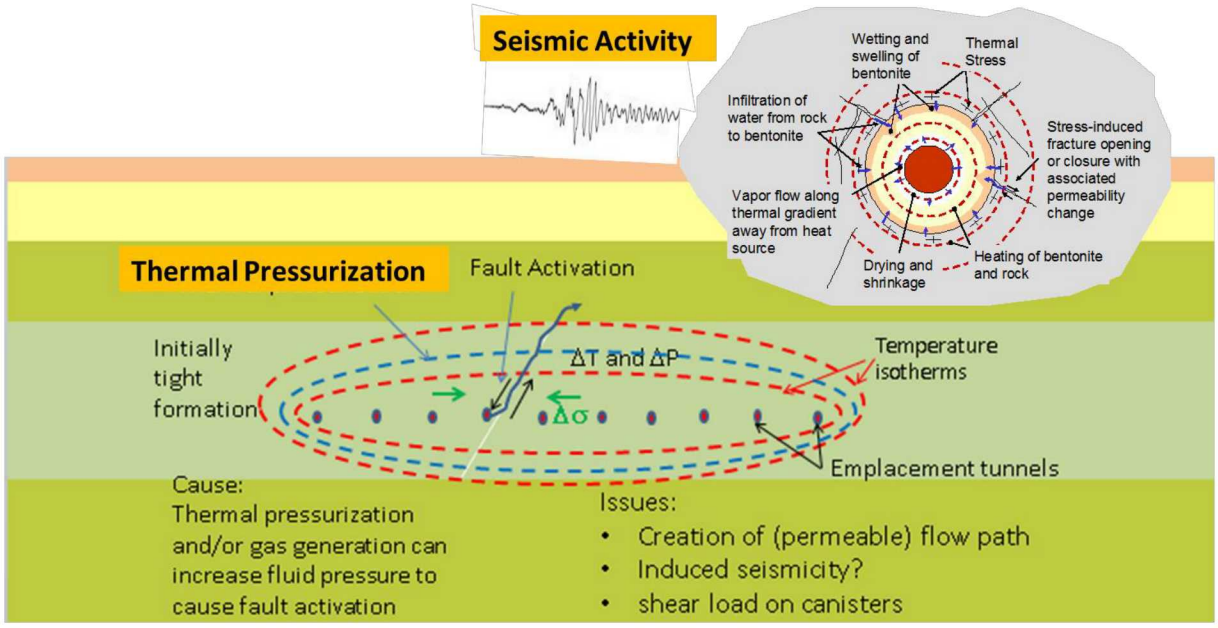


Figure 8-1. Schematic of coupled THM responses in a repository in the near field (upper right) and at the repository scale caused by heating, thermal pressurization and potential gas generation.

9. Acknowledgements

This work was supported by the Spent Fuel and Waste Science and Technology Campaign, Office of Nuclear Energy, of the U.S. Department of Energy under Contract Number DE-AC02-05CH11231 with Lawrence Berkeley National Laboratory.

10. References

Alonso, E.E., Gens, A., and Josa, A. (1990) A constitutive model for partially saturated soils. Geotechnique. 40: 405-430.

Asahina, D., and Bolander, J.E. (2011) Voronoi-based discretizations for fracture analysis of particulate materials, Powder Technology, 213, 92–99.

Asahina, D., Houseworth, J.E., Birkholzer, J.T., Rutqvist, J., and Bolander, J.E. (2014) Hydro-mechanical model for wetting/drying and fracture development in geomaterials, Computers & Geosciences, 65, 13–23.

Biot, M.A., and Willis, D.G. (1957) The elastic coefficients of the theory of consolidation, Journal of Applied Mechanics, 24, 594–601.

Bolander, J.E., and Saito, S. (1998) Fracture analyses using spring networks with random geometry, Eng. Fract. Mech., 61, 569–591.

Booker, J.R., and Savvidou, C. (1985) Consolidation around a point heat source. International Journal for Numerical and Analytical Methods in Geomechanics 9, 173–184.

Bossart, P., Meier, P.M, Moeri, A, Trick, T, and Mayor, J-C. (2002) Geological and hydraulic characterization of the excavation disturbed zone in the Opalinus Clay of the Mont Terri Rock Laboratory. Eng Geol 66, 19–38.

Bossart, P., Trick, T., Meier, P.M., and Mayor, J.-C. (2004) Structural and hydrogeological characterisation of the excavation-disturbed zone in the Opalinus Clay (Mont Terri Project, Switzerland), Applied Clay Science, 26, 429– 448.

Cappa, F., Guglielmi, Y., Rutqvist, J., Tsang, C-F., and Thoraval, A. (2006) Hydromechanical modeling of pulse tests that measure fluid pressure and fracture normal displacement at the Coaraze Laboratory site, France, Int. J. Rock Mech. Min. Sci., 43(7):1062-1082.

Chaboche, J.-L. (1992) Damage induced anisotropy: On the difficulties associated with the active/passive unilateral condition. International Journal of Damage Mechanics 1, 148–171.

Corkum, A.G., and Martin, CD. (2007) Modeling a mine-by test at the Mont Terri rock laboratory, Switzerland. International Journal of Rock Mechanics & Mining Sciences 44, 846–859.

Corey, A.T. (1954) The Interrelation Between Gas and Oil Relative Permeabilities, Producers Monthly, 38-41.

Cundall, P.A. (1988) Formulation of a three-dimensional distinct element model—Part I. A scheme to detect and represent contacts in a system composed of many polyhedral blocks. Int. J. Rock Mech. Min. Sci. Geomech. Abstr., 25:107-116.

Cuss, R.J., Harrington, J.F., Noy, D.J., Graham, C.C., and Sellin, P. (2014) Evidence of localised gas propagation pathways in a field-scale bentonite engineered barrier system; results from three gas injection tests in the Large scale gas injection test (Lasgit). Applied Clay Science, 102, pp.81-92, doi:10.1016/j.clay.2014.10.014Harrington J (2016) Specification for

DECOVALEX-2019: Task A: modElliNg Gas INjection ExpERiments (ENGINEER). Ref: BGS-DX-v3.

Dieterich, J. H. (1979) Modeling of rock friction experimental results and constitutive equations, J. Geophys. Res., 84, 2161–2168, doi:10.1029/JB084iB05p02161.

Garitte, B., and Gens, A. (2012) TH and THM Scoping computations for the definition of an optimal instrumentation layout in the Full-scale Emplacement (FE) experiment NAGRA NIB 10-34, March 2012.

Garitte B., Shao H., Wang X.R., Nguyen T.S., Li Z., Rutqvist J., Birkholzer J., Wang W.Q., Kolditz O., Pan P.Z., Feng X.T., Lee C., Graupner B.J., Maekawa K., Manepally C., Dasgupta B., Stothoff S., Ofoegbu G., Fedors R., and Barnichon J.D. (2017) Evaluation of the predictive capability of coupled thermo-hydro-mechanical models for a heated bentonite/clay system (HE-E) in the Mont Terri Rock Laboratory. Environmental Earth Sciences, 76:64.

Gens, A., and Alonso, E. (1992) A framework for the behaviour of unsaturated expansive clays. Can. Geotech. J. 29, 1013–1032.

Gens, A., Sánchez, M., and Sheng, D. (2006) On constitutive modeling of unsaturated soils. Acta Geotechnica. 1, 137-147.

Gens, A., Sánchez, M., Guimaraes, L.D.N., Alonso, E.E., Lloret, A., Olivella, S., Villar, M.V., and Huertas, F. (2009) A full-scale *in situ* heating test for high-level nuclear waste disposal: observations, analysis and interpretation. Geotechnique 59, 377–399.

Guglielmi, Y., Cappa, F., Avouac, J.-P., Henry, P., and Elsworth, D. (2015a) Seismicity triggered by fluid injections induced aseismic slip, Science, 348(6240), 1224–1226, doi:10.1126/science.aab0476.

Guglielmi, Y., Elsworth, D., Cappa, F., Henry, P., Gout, C., Dick, P., and Durand, J. (2015b) In situ observations on the coupling between hydraulic diffusivity and displacements during fault reactivation in shales, J. Geophys. Res., 120, doi:10.1002/2015JB012158.

Harrington, J.F., and Horseman, S.T. (1999) Gas transport properties of clays and mudrocks. In: Muds And Mudstones: Physical And Fluid Flow Properties (eds A.C.Aplin, A.J. Fleet, and J.H.S. Macquaker). Geological Society of London, Special Publication No. 158, 107-124.

Harrington, J.F., Milodowski, A.E., Graham, C.C., Rushton, J.C., and Cuss, R.J. (2012) Evidence for gas-induced pathways in clay using a nanoparticle injection technique. Mineralogical Magazine. December 2012, Vol. 76(8), pp.3327-3336. DOI: 10.1180/minmag.2012.076.8.45.

Harrington, J. (2016) Specification for DECOVALEX-2019: Task A: modElliNg Gas INjection ExpERiments (ENGINEER). Ref: BGS-DX-v3.

Harrington, J.F., Graham, C.C., Cuss, R.J., and Norris, S. (2017) Gas network development in a precompacted bentonite experiment: Evidence of generation and evolution, Applied Clay Science, 147, 80–89.

Horseman, S.T., Harrington, J.F., and Sellin, P. (1999) Gas migration in clay barriers. Engineering Geology, Vol. 54, 139-149.

Horseman, S.T., Harrington, J.F., and Sellin, P. (2004) Water and gas flow in Mx80 bentonite buffer clay. In: Symposium on the Scientific Basis for Nuclear Waste Management XXVII (Kalmar), Materials Research Society, Vol. 807. 715-720.

Houseworth, J., Rutqvist, J., Asahina, D., Chen, F., Vilarrasa, V., Liu, H.H., and Birkholzer, J. (2013) Report on International Collaboration Involving the FE Heater and HG-A Tests at Mont Terri. Prepared for U.S. Department of Energy, Used Fuel Disposition Campaign, FCRD-UFD-2014-000002, Lawrence Berkeley National Laboratory.

International Formulation Committee (IFC) (1967) A Formulation of the Thermodynamic Properties of Ordinary Water Substance, IFC Secretariat, Düsseldorf, Germany.

Itasca, FLAC3D V5.0 (2011) Fast Lagrangian Analysis of Continua in 3 Dimensions, User's Guide. Itasca Consulting Group, Minneapolis, Minnesota.

Kawai, T. (1978) New discrete models and their application to seismic response analysis of structures, Nucl. Eng. Des., 48, 207–229.

Kim, K., and Lim, Y.M. (2011) Simulation of rate dependent fracture in concrete using an irregular lattice model, Cement & Concrete Composites, 33, 949–955.

Kim, K., Rutqvist, J., Nakagawa, S., and Birkholzer, J. (2017) TOUGH-RBSN simulator for hydraulic fracture propagation within fractured media: Model validations against laboratory experiments, Computers & Geosciences, 108, 72–85.

Kristensson, O., and Åkesson, M. (2008) Mechanical modeling of MX-80 – Quick tools for BBM parameter analysis. Phys Chem Earth, Parts A/B/C. 33, Supplement 1: S508-S515.

Liu, H.H., Houseworth, J., Rutqvist, J., Li, L., Asahina, D., Chen, F., and Birkholzer, J. (2012) Report on Modeling Coupled Processes in the Near Field of a Clay Repository. Prepared for U.S. Department of Energy, Used Fuel Disposition Campaign, FCRD-UFD-2012-000223, Lawrence Berkeley National Laboratory.

Marone, C. (1998) Laboratory-derived friction laws and their application to seismic faulting, Ann. Rev. Earth Planet. Sci., 26, 643–696.

Martin C.D., and Chandler N.A. (1994) The progressive fracture of Lac du Bonnet Granite. International Journal of Rock Mechanics and Mining Sciences & Geomechanics Abstract, 31, 643–59.

Martino, J.B., and Chandler, N.A. (2004) Excavation-induced studies at the Underground Research Laboratory. International Journal of Rock Mechanics and Mining Sciences, 41, 1413–26.

Nguyen, T.S., Börgesson, L., Chijimatsu, M., Hernelind, J., Jing, L., Kobayashi, A., and Rutqvist, J. (2009) A case study on the influence of THM coupling on the near field safety of a spent fuel repository in sparsely fractured granite. Environmental Geology, 57, 1239–1254.

Nutt, M. (2012) Used Fuel Disposition Campaign Disposal Research and Development Roadmap (FCRD-USED-2011-000065 REV1), U.S. DOE Used Fuel Disposition Campaign.

Okabe, A., Boots, B., Sugihara, K., and Chiu, S.N. (2000) Spatial Tessellations: Concepts and Applications of Voronoi Diagrams, 2nd ed., Wiley, NYC, 696 pages.

Pruess, K., Oldenburg, C.M., and Moridis, G. (2012) TOUGH2 User's Guide, Version 2.1, LBNL-43134(revised), Lawrence Berkeley National Laboratory, Berkeley, California.

Rutqvist, J., Noorishad, J., Tsang, C.-F., and Stephansson, O. (1998) Determination of fracture storativity in hard rocks using high-pressure injection testing, Water Resources Research, 34(10), 2551–2560.

Rutqvist, J., Tsang, C.-F., and Stephansson, O. (2000) Uncertainty in the maximum principal stress estimated from hydraulic fracturing measurements due to the presence of the induced fracture, International Journal of Rock Mechanics and Mining Sciences, 37, 107–120.

Rutqvist, J., Börgesson, L., Chijimatsu, M., Kobayashi, A., Nguyen, T. S., Jing, L., Noorishad, J., and Tsang, C.-F. (2001) Thermohydromechanics of partially saturated geological media – Governing equations and formulation of four finite element models. International Journal of Rock Mechanics and Mining Sciences, 38, 105-127. Rutqvist, J., Wu, Y.-S., Tsang, C.-F., and Bodvarsson, G. (2002). A modeling approach for analysis of coupled multiphase fluid flow, heat transfer and deformation in fractured porous rock. International Journal of Rock Mechanics & Mining Sciences, 39, 429-442.

Rutqvist, J., and Tsang, C.-F. (2002) A study of caprock hydromechanical changes associated with CO2-injection into a brine formation, Environmental Geology, 42, 296–305.

Rutqvist, J., Börgesson, L., Chijimatsu, M., Hernelind, J., Jing, L., Kobayashi, A., and Nguyen, S. (2009) Modeling of damage, permeability changes and pressure responses during excavation of the TSX tunnel in granitic rock at URL, Canada. Environmental Geology, 57, 1263–1274.Rutqvist, J. (2011) Status of the TOUGH-FLAC simulator and recent applications related to coupled fluid flow and crustal deformations. Computers & Geosciences, 37, 739–750.

Rutqvist, J., Ijiri, Y, and Yamamoto, H. (2011) Implementation of the Barcelona Basic Model into TOUGH-FLAC for simulations of the geomechanical behavior of unsaturated soils. Computers & Geosciences, 37, 751–762.Rutqvist, J., Ijiri, Y., and Yamamoto, H. (2011) Implementation of the Barcelona Basic Model into TOUGH-FLAC for simulations of the geomechanical behavior of unsaturated soils. Computers &Geosciences, 37, 751-762.

Rutqvist, J., Davis, J., Zheng, L., Vilarrasa, V., Houseworth, J., and Birkholzer, J. (2014a) Investigation of Coupled THMC Processes and Reactive Transport: FY14 Progress. Prepared for U.S. Department of Energy, Used Fuel Disposition, FCRD-UFD-2014-000497, Lawrence Berkeley National Laboratory, LBNL-6720E (2014a).

Rutqvist, J., Zheng, L., Chen, F., Liu, H.-H., and Birkholzer, J. (2014b) Modeling of Coupled Thermo-Hydro-Mechanical Processes with Links to Geochemistry Associated with

Bentonite-Backfilled Repository Tunnels in Clay Formations. Rock Mechanics and Rock Engineering, 47, 167–186.

Rutqvist, J. (2015) Fractured rock stress-permeability relationships from *in situ* data and effects of temperature and chemical-mechanical couplings. Geofluids, 15, 48–66.

Rutqvist, J. (2017) An overview of TOUGH-based geomechanics models. Computers & Geosciences, 108, 56–63.

Sánchez, M., Gens, A., do Nascimento Guimarães, L., and Olivella, S. (2005) A double structure generalized plasticity model for expansive materials. Int. J. Numer. Anal. Meth. Geomech., 29, 751–787.

Senger, R., and Marschall, P. (2008) Task Force on EBS / Gas Transport in Buffer Material, Nagra Arbeitsbericht NAB 08-24.

Senger R., Romero, E., Ferrari, A., and Marschall, P. (2014) Characterization of gas flow through low-permeability claystone: laboratory experiments and two-phase flow analyses. Norris, S., Bruno, J., Cathelineau, M., Delage, P., Fairhurst, C., Gaucher, E. C., Ho¨hn, E. H., Kalinichev, A., Lalieux, P. & Sellin, P. (eds) Clays in Natural and Engineered Barriers for Radioactive Wast Confinement. Geological Society, London, Special Publications, 400, http://dx.doi.org/10.1144/SP400.15

Shen, X., and Shen, G. (2002) A fracture-energy-based elasto-softening-plastic constitutive model for joints of geomaterials, Applied Mathematics and Mechanics, 23(9), 1097–1104.

Tamayo-Mas, E., Harrington, J.F., Shao, H., Dagher, E.E., Lee, J., Kim, K., Rutqvist, J., Lai, S.H., Chittenden, N., Wang, Y., Damians, I.P., and Olivella, S. (2018) Numerical modeling of gas flow in a compact clay barrier for DECOVALEX-2019, Proceedings of ARMA/DFNE 2018 (DFNE 18-623).

van Genuchten, M.T. (1980) A closed-form equation for predicting the hydraulic conductivity of unsaturated soils. Soil. Sci. Soc. Am. J., 44, 892-898.

Vilarrasa, V., Rutqvist, J., Blanco-Martin, L., and Birkholzer, J. (2016) Use of a dual structure constitutive model for predicting the long-term behavior of an expansive clay buffer in a nuclear waste repository. *ASCE's International Journal of Geomechanics,* 16, article number D4015005.

Wang, Y. (2011) Research & Development (R&D) Plan for Used Fuel Disposition Campaign (UFDC) Natural System Evaluation and Tool Development, U.S. DOE Used Fuel Disposition Campaign.

Witherspoon, P.A., Wang, J.S.Y., Iwai, K., and Gale, J.E. (1980) Validity of cubic law for fluid flow in a deformable rock fracture, Water Resources Research, 16, 1016–1024.

Yip, M., Mohle, J., and Bolander, J. (2005) Automated modeling of three-dimensional structural components using irregular lattices, Computer-Aided Civil and Infrastructure Engineering, 20, 393–407.

Zheng, L., Rutqvist, J., Steefel, C., Kim, K., Chen, F., Vilarrasa, V., Nakagawa, S., Houseworth, J., and Birkholzer J. (2014) Investigation of Coupled Processes and Impact of High Temperature Limits in Argillite Rock. Prepared for U.S. Department of Energy, Used Fuel Disposition, FCRD-UFD-2014-000493, Lawrence Berkeley National Laboratory, LBNL-6719E.

Zheng, L., Rutqvist, J., Kim, K., and Houseworth, J. (2015) Investigation of Coupled Processes and Impact of High Temperature Limits in Argillite Rock. Prepared for U.S. Department of Energy, Used Fuel Disposition, FCRD-UFD-2015-000362. LBNL-187644, Lawrence Berkeley National Laboratory.

Zheng, L., Kim, K., Xu, H., and Rutqvist, J. (2016) DR Argillite Disposal R&D at LBNL. FCRD-UFD-2016-000437, LBNL-1006013, Lawrence Berkeley National Laboratory.

Zheng L., Kim K., Xu H., Rutqvist J., Voltolini M., and Xiaoyuan C. (2017) Investigation of Coupled Processes and Impact of High Temperature Limits in Argillite Rock: FY17 Progress. Prepared for U.S. Department of Energy, Spent Fuel and Waste Disposition. SFWD-SFWST-2017-000040, LBNL-2001014, Lawrence Berkeley National Laboratory.

Argillite R&D and International Collaborations – Los Alamos National Laboratory (FY18) (Part III)

1. Introduction

The U.S. Department of Energy designed the Spent Fuel and Waste Science and Technology program to investigate the design and safety function of generic nuclear geologic repositories in a variety of geologic settings. The evaluation of engineered barrier system (EBS) concepts and interaction with the wall rock (i.e., natural barriers), waste canisters, or other EBS interfaces are important to the long-term performance and safety of geologic repositories (Nutt et al., 2011; Jove-Colon et al., 2011). The European community, especially the French, have investigated bentonite stability in contact with steel under a variety of experimental conditions in an attempt to replicate repository conditions (Pusch, 1979; Madsen, 1998; Meunier et al., 1998; Guillaume et al., 2003; Wersin et al., 2007; Mosser-Ruck et al., 2010; Ferrage et al., 2011). The majority of their research focused on lower temperature environments and atmospheric pressures. Our experimental program for FY18 aims to 1) characterize how EBS components react and change in the presence of Opalinus Clay, 2) capture steel corrosion rates at reasonable high temperature (200–300 °C, 150 bar) in-situ repository conditions, 3) characterize mineral growth on steel interface, and 4) perform mineral characterization of select samples from the The Full Scale High-Level Waste Engineered Barrier System Experiment (FEBEX) at the Grimsel Test Site (GTS) This includes QXRD analyses, SEM images, and electron microprobe data of significant mineral phases. This will document the international portion of this report.

1.1 Background

One of the more accepted ideas for high-level nuclear waste disposal is to emplace a steel waste canister in a geological repository with a bentonite barrier between the canister and host rock (Pusch, 1979; Meunier et al., 1998). Bentonite is dominantly composed of clay minerals and provides: 1) a physical barrier that prevents the infiltration of fluid from the surrounding wall rock that may interact with the waste package and 2) a chemical barrier that attenuates actinide migration if a release occurs. Furthermore, the bentonite's swelling capacity has self-sealing capabilities if cracks develop within the bentonite due to shrink-swell phenomena. However, there remain large uncertainties regarding the long-term stability of bentonite at potential repository conditions, particularly, under prolonged periods of high thermal loads. There have been numerous investigations on the stability of bentonites under various repository conditions and in contact with various metals replicating possible canister compositions (Pusch, 1979; Madsen, 1998; Meunier

et al., 1998; Guillaume et al., 2003; Wersin et al., 2007; Mosser-Ruck et al., 2010; Ferrage et al., 2011).

The FEBEX at Grimsel is an example of a long-term experiment on bentonite stability. The site in the Swiss Alps near the Grimsel Pass (Bern Canton, Switzerland) was established in 1984 as a center for underground Research and Development (R&D) supporting the geological disposal of radioactive waste (Grimsel, 2017). The FEBEX is a 1:1 scale demonstration project for the emplacement of Spent Nuclear Fuel (SNF). The FEBEX tunnel proper is located in Grimsel granodiorite at a depth of 450 meters below the surface. This is an *in situ* migration experiment conducted between boreholes situated in sparsely fractured crystalline, Grimsel granodiorite, host rock focusing on bentonite solubility, colloidal mineral migration/formation, and colloid-associated radionuclide transport. Two heaters replicating Spent Nuclear Fuel (SNF) canisters (4.5 meters long, 12 ton each) were emplaced and surrounded by blocks of compacted bentonite clay (Figure 1). In February 1997, heaters were switched on and data acquisition began. The experiment ran from February 1997 to 2002 at a constant temperature of 180 °C at the surface of the canister (FEBEX, 2014). After the heating of the first canister was stopped and that portion (including the canister) of the experiment was excavated. After removal, a dummy canister (no heating capability) was emplaced, EBS blocks were reinserted, and a concrete plug was constructed. The second portion of the experiment ran until 2015, when full excavation of FEBEX was initiated. Our samples were extracted from the second portion of the experiment (Table 1).

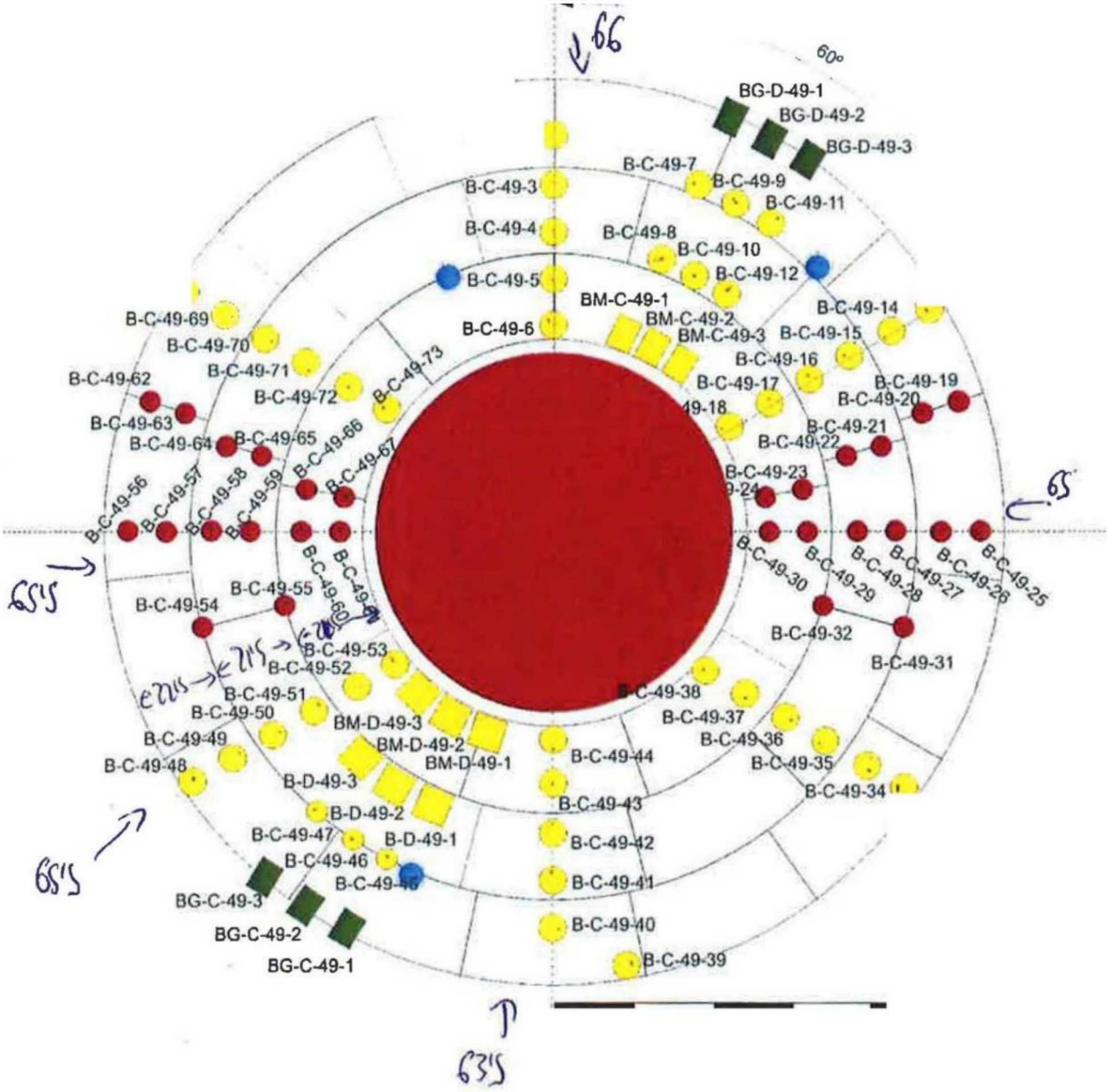


Figure 1. FEBEX sampling locations of section 49. Green symbols indicate granodiorite samples and yellow symbols are bentonite locations

Table 1. Samples from Section 49 obtained from FEBEX project. Samples highlighted in green were examined for this report.

FEBEX	Caporuscio
Box 1	BG-C-43-1
	BG-C-43-2
	BG-C-43-3
	BG-C-49-1 Granite
	BG-C-49-2 Granite
	BG-C-49-3 Granite
	B-C-49-7
	B-C-49-8
	B-C-49-9
	B-C-49-10
	B-C-49-11
	B-C-49-12
	BM-D-49-3
Box 2	BG-C-53-1-Granite
	BG-C-53-2-Granite
	BG-C-53-3-Granite
	B-C-53-7
	B-C-53-8
	B-C-53-9
	B-C-53-10
	B-C-53-11
	B-C-53-12
	BG-C-58-1 Granite
	BG-C-58-2 Granite
	BG-C-58-3 Granite
Box 3	B-C-58-67
	B-C-58-68
	B-C-58-69
	B-C-58-70
	B-C-58-71
	B-C-58-72
	B-C-58-73
	B-C-58-74
	B-C-58-75
	B-C-58-76
	B-C-58-77
	B-C-58-78
	BM-C-49-3
Block	BM-C-43-1
	BM-C-43-2
	BM-C-43-3
Liner	BM-C-43-1
	BM-C-43-2
	BM-C-43-3
Block	BG-C-43-1
	BG-C-43-2
	BG-C-43-3
Cores	B-C-43-37
	B-C-43-38
	B-C-43-39
	B-C-43-40
	B-C-43-41
	B-C-43-42
Block	BG-C-49-1
	BG-C-49-2
Block	BG-C-49-3
Block	BM-C-49-1
	BM-C-49-2
	BM-C-49-3
Liner	BM-C-49-1
	BM-C-49-2
	BM-C-49-3
Block	BM-C-53-1
	BM-C-53-2
	BM-C-53-3
Block	BG-C-53-1
	BG-C-53-2
	BG-C-53-3
Block	BG-C-58-1
	BG-C-58-2
	BG-C-58-3
Unlisted	BM-D-49-1
	BM-D-49-2

In the U.S., the exact barrier concept has yet to be determined, but may include the possible use of dual-purpose canisters for storage and subsequent disposal (Greenburg and Wen, 2013). At present, dual-purpose canister designs vary greatly, but, in most cases, canisters will be constructed from steel or stainless steel with a steel reinforced concrete overpack (IAEA, 2000). Some designs include copper cladding on the steel canister (Pusch, 2008). The proposed dual-purpose canisters for US repositories may contain up to 32 spent fuel assemblies (32 pressurized water reactors or 32-PWR), while many of the European concepts are limited to four spent fuel assemblies (4-PWR) (Pusch, 2008; Greenburg and Wen, 2013). This increased number of spent fuel assemblies within the US dual-purpose canisters will generate a greater amount of heat radiating into the host rock. For example, high-level modeling suggests a 32-PWR waste package (at 60 gigawatt-days per metric ton burnup) disposed in a clay/shale host rock, has the potential to reach 299 °C after 85 years within 1 meter from the waste package (25 years ventilation; 15 m package spacing; Greenberg and Wen, 2013). This is just one of many models/designs for canister configurations in a U.S. nuclear repository, but provides an example of a high temperature scenario (Figure 2). Further, the thermal evolution of this potential repository design demonstrates the need for high temperature experimental work on the interaction of wall rock, EBS backfill, and canister materials that have not been explored previously by the European programs.

This report summarizes results from hydrothermal experiments EBS-14 through EBS-24 that replicate a high temperature (i.e., 200 to 300°C) repository within an argillitic geologic environment. In addition, this report presents the bulk and mineral chemistry of FEBEX bentonite blocks. The FY-17 report (Caporuscio and Norskog, 2017) on FEBEX materials emphasized the petrography of clay and wall-rock samples, whereas the FY-18 efforts focused on detailed chemical analyses of FEBEX bentonite, including (Q)XRD and electron microprobe analyses. The emphasis of the report discussion is on the hydrothermal experiments, including: 1) Opalinus Clay wall rock interactions with EBS backfill, 2) steel corrosion rates, and 3) steel/bentonite interface phase reactions. Section 1 examines various reactions that include unprocessed Wyoming bentonite, Portland Cement, the clay/metal interface, and the metal/clay/host rock components. Much of the characterization and discussion on the early EBS (1-12) results have been published in Cheshire et al. (2013; 2014). Characterization of both the pre-run materials and post experiment phases of experiments EBS-1 through -17 were discussed in Caporuscio, et al. (2015) to better describe the processes that progress during the hydrothermal reactions. Section 2 summarizes steel

alteration and reaction rates and includes a description corrosion occurring on 304 SS, 316 SS, and low carbon steel. Section 3 describes the mineral interface between bentonite backfill and steel. Section 4 will summarize the mineral chemical characterization of the FEBEX-DP samples.

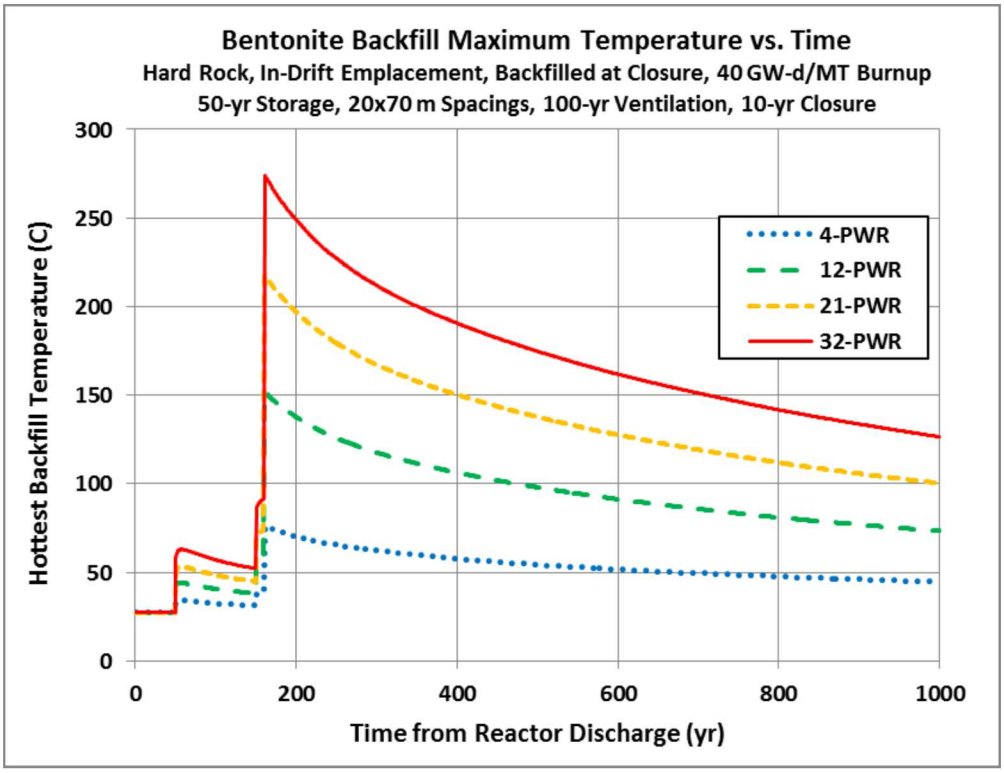


Figure 2. Bounding backfill temperature histories at the waste package surface, for in-drift emplacement in crystalline rock (2.5 W/m-K) with a compacted bentonite backfill (0.6 W/m-K). Backfill rehydration is neglected as a bounding approximation. Waste packages with various capacities are plotted, for fuel with 40 GW-d/MT burnup. For this comparative calculation all packages would be stored at the surface 50 years, then ventilated in the repository 100 years, and finally backfilled over a period of 10 years before permanent closure (personal communication from Ernest Hardin)

Table 2. Initial components and reaction conditions for EBS experiments in the presence of Opalinus Clay. All experiments include bentonite clay.

Experiment	Clay, g	Brine, g	EBS Component	Deviations	Run temp, °C	Run time
EBS-14	14.86	128.1	Opalinus clay	NA	300	6 weeks
EBS-15	14.72	158.5	Opal–316 SS	NA	300	6 weeks
EBS-17	14.44	155.2	Opal–Cu	NA	300	6 weeks
EBS-18	10.62	116.98	Opal–LCS	NA	300	6 weeks
EBS-19	14.82	120.0	Opal–304 SS	NA	300	6 weeks
EBS-20	29.08	261	Opal–316 SS	NA	300	6 month
EBS-21	13.1	126	Opal–316 SS	2 M NaCl	200	8 weeks
EBS-22-(Corr)	14.59	132	Opal–316 SS	50:50 ratio opalinus clay/ bentonite clay	200	8 weeks
EBS-23	5.95	150	Opal–cement	NA	200	8 weeks
EBS-24	6.01	150	Opal–cement–316 SS	NA	200	8 weeks

Table 3. Synthetic groundwater chemistry used in the Opalinus Clay experiments. All values were measured at 25 °C (n.m. = not measured)

	Type Solution	**Actual Solution**
Species	mg/L	mg/L
Ca^{2+}	421	426
Cl^{-}	5672	6470
CO_3^{2-}	162	n.m.
K^{+}	221	225
Na^{+}	3885	3846
Si	5	1
SO_4^{2-}	2305	998
Sr^{2+}	27	0.16
TDS	11502	12153
pH	7.24	7.50
Experiment Used		EBS-14 to -24

1.2 Methods

Analytical methods involved in the experimental setup, mineral characterization, and aqueous geochemical analyses remain unchanged from Caporuscio et al. (2014). They are listed in Appendix A for convenience.

Post-reaction steel coupons were characterized to understand steel corrosion and the mineralization of the steel-backfill interface. The post-reaction steel coupons were mounted in epoxy and next polished to expose the cross-sectioned surfaces. These mounts were then imaged using both reflected light microscopy and scanning electron microscopy (SEM). For each EBS run, ~15–40 reflected light and SEM images were taken from random locations throughout the sample to provide representative images of each sample. The thickness of the silicate interface reaction minerals (Fe-saponite, chlorite) and the depth of the corrosion were measured in Adobe Photoshop and then labeled for future analysis. Around 7–20 measurements of interface mineral thickness

and corrosion pit depth were determined from each image. Corrosion rates were determined by dividing the average corrosion depth by the number of days in the run.

2. Results

2.1 Starting Material Characteristics

Opalinus Clay. Opalinus Clay is thinly laminated, dark grey shale with dry density of 2.2–2.4 g/cm3 and water content of 6.5–8.0% (Pearson et al., 2003). This shale is dominated with 69 wt. % illite, illite-smectite mixed layers, and discrete smectite (Table 4, Figure 3).

Table 4. Mineralogical composition of starting Opalinus Clay, Wyoming Bentonite, and reaction products from EBS-14 and EBS-15. + represents material detectable but below 0.5 wt. %. b.d.l. represents material below detection limits. Illite, illite-smectite, and smectite were combined in the analyses due to difficulty quantifying each phase when a physical mixture of two or three are present.

	Switzerland	Wyoming	Opalinus	Bent-Opalinus
Illite, I-S, S	69		78	72
Smectite		72		
Chlorite	1	b.d.l.	3	+
Kaolinite	12	b.d.l.	b.d.l.	b.d.l.
Clinoptilolite	b.d.l.	13	b.d.l.	14
Analcime/Wairakite	b.d.l.	b.d.l.	3	1
Quartz	8	1	8	4
Cristobalite/Opal-C	b.d.l.	2	b.d.l.	b.d.l.
Biotite	0.5	3	0.8	0.5
Pyrite	+	0.4	0.7	b.d.l.
Plagioclase	b.d.l.	9	b.d.l.	8
K-feldspar	b.d.l.	b.d.l.	b.d.l.	+
Calcite	6	b.d.l.	5	b.d.l.
Dolomite	+	b.d.l.	b.d.l.	b.d.l.
Ankerite	2	b.d.l.	b.d.l.	b.d.l.

Illite and smectite are reported together due to the difficulty of quantifying these mineral phases when they are mixed. The illite-smectite appears to be a low expandable with a R3 illite (0.92)-smectite composition. Other clay minerals present in significant quantities include kaolinite (12 wt. %) and chlorite (1 wt. %) (Table 4, Figure 3). These clay minerals are intimately mixed and were observed to be indistinguishable in SEM images (Figure 4A and B). + is the dominant exchangeable cation in the Opalinus Clay followed by Ca^{2+}, Mg^{2+}, K^{+}, and Sr^{2+}; however, the bulk composition is dominated with CaO (7.96 wt. %), K_2O (3.05 wt. %), MgO (2.38 wt. %), and Na_2O (0.481 wt. %) (Pearson et al., 2003). These exchangeable cations should be in equilibrium with the pore water described above (synthetic Opalinus clay groundwater, Table 2). Other minerals present include calcite, ankerite, dolomite, quartz, and biotite. Well-preserved pyrite occurs primarily as < 2 µm octahedral crystals, filling fractures and/or along bedding planes. Calcite primarily occurs as pocket filling agglomerates showing layered structures with alternating calcite and clay layers (Figure 4E and F). Ankerite and dolomite were not observed in SEM analyses.

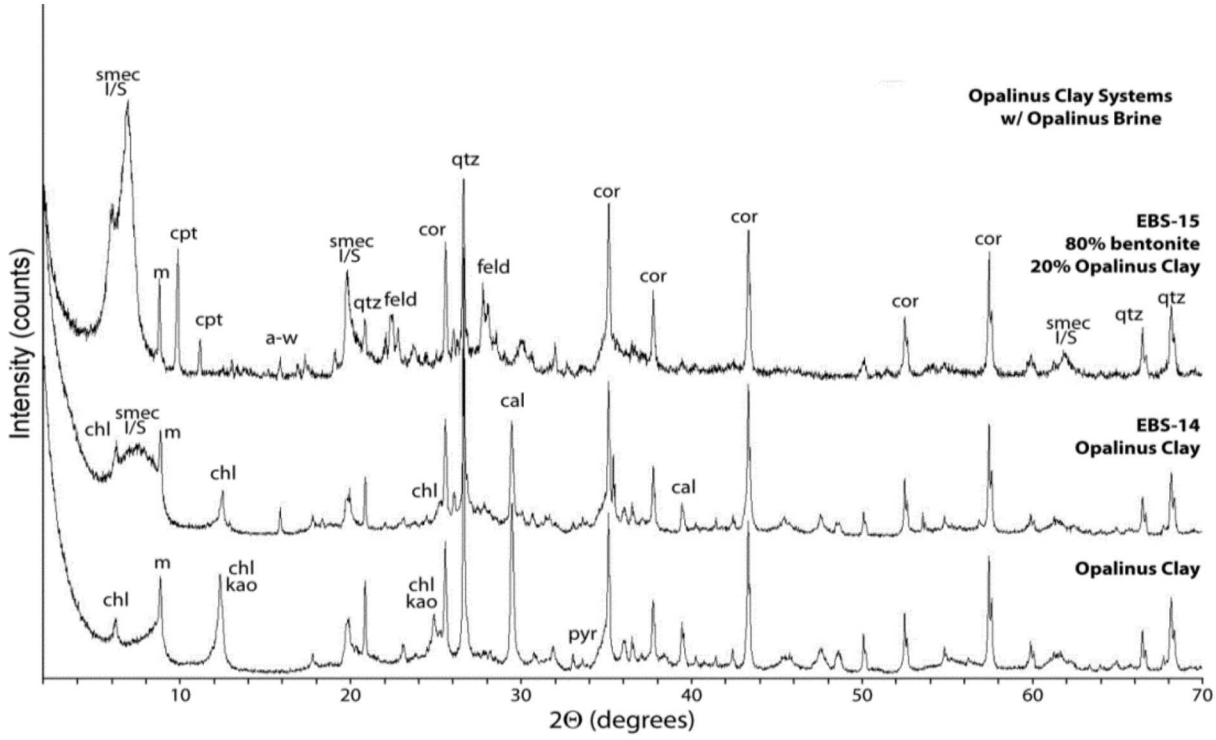


Figure 3. XRD patterns of bulk samples from starting Opalinus Clay and EBS-14 and EBS-15 reaction products.

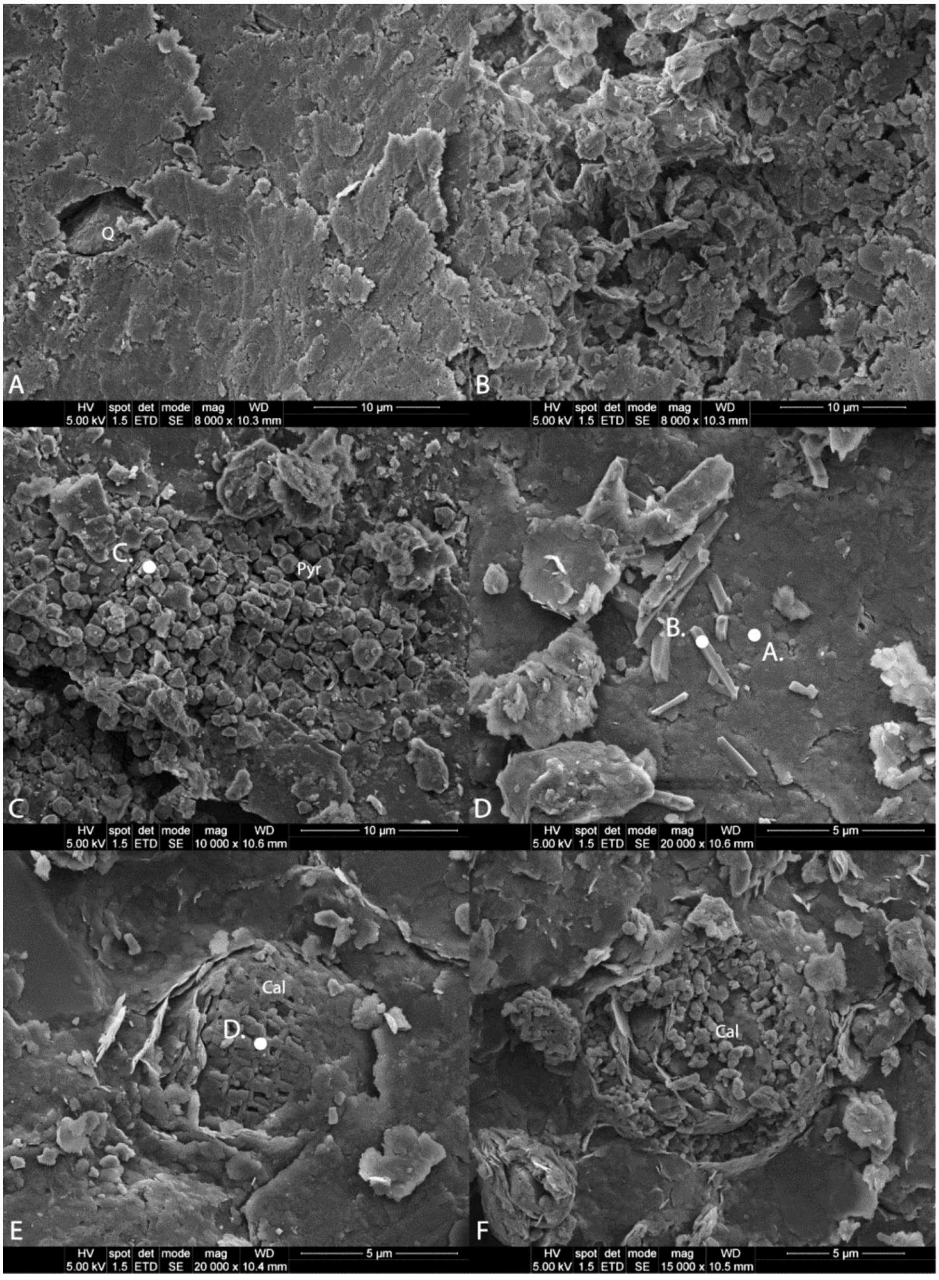


Figure 4. SEM images of Opalinus Clay. [A] Opalinus Clay bedding planes formed from the aggregation of smaller particles. Quartz (Q) particle is imbedded in the matrix. [B] Pore spaces within Opalinus Clay. [C] Cluster of < 2 µm octahedral pyrite (Pyr) fill void spaces or are disseminated throughout samples. EDX analyses at point C. are presented in Figure 19C. [D] Opalinus Clay bedding plane with platy-bladed mineral embedded in illite, illite-smectite, and chlorite matrix. EDX analyses at points A. and B. are presented in Figure 15A and B. [E] Biogenic calcite (Cal) filling a pocket with in the Opalinus Clay matrix. EDX analysis at point D is presented in Figure 19D. [F] Disturbed pocket-filling calcite showing layered structure with alternating calcite and clay layers.

Bentonite: The bentonite used in this experimental work is mined from a reducing horizon in Colony, Wyoming. Unprocessed Wyoming bentonite contains primarily montmorillonite with minor amounts of clinoptilolite and lesser plagioclase, biotite, calcite, and sulfide minerals. The QXRD results from unheated bentonite are presented in Table 1 of Appendix C.

Opalinus Clay synthetic groundwater: Synthetic groundwater was created to mimic the pore water found in the Mont Terri Opalinus Clay (Pearson et al., 2003). This solution has a pH of around 7.5 and the initial chemistry is reported in Table 2.

316 SS (NIST SRM 160b) is an iron alloy primarily with 18.37 wt. % Cr, 12.35 wt. % Ni, 2.26 wt. % Mo, 1.619 wt. % Mn, 0.5093 wt. % Si, and 0.175 wt. % Cu.

304 SS is an ion alloy which differs from 316SS in Cr/Ni ratio. Along with Fe, it contains 18 wt. % Cr, 8 wt. % Ni, <2 wt. % Mn, <1 wt. % Si, <0.045 wt. % P, and <0.03 wt. % S, and <0.08 wt. % C.

Low carbon steel (LCS) is composed of Fe along with ~0.2 wt. % C, 0.9 wt. % Mn, <0.04 wt. % P, and < 0.05% S.

Portland Cement. Portland Cement consists of ~66% of calcium silicates, (3 $CaO{\cdot}SiO_2$, and 2 $CaO{\cdot}SiO_2$), the remainder consisting of aluminum- and iron-containing silicate phases and other compounds. The ratio of CaO to SiO_2 is greater than ~2. The magnesium oxide content (MgO) is < 5 wt. %.

2.2 Results from EBS-14 to EBS-23

2.2.1 Aqueous Geochemistry

Water samples were collected periodically during the course of each experiment. The aqueous geochemistry results are reported in Appendix B and described below.

pH

All experiment solutions started with a near neutral pH; Opalinus Clay synthetic groundwater has a pH of around 7.5 (Table 2). The solution pH of experiments EBS-14 through EBS-22 generally dropped from 7.5 and stabilized about 3 weeks into the experiment to a pH of ~5–6 (Figure 5).

The pH of the EBS-23 solution, the first experiment to include Portland Cement, initially dropped to ~5–6, and then reached pH = ~8–9 around 3 weeks into the experiment (Figure 5).

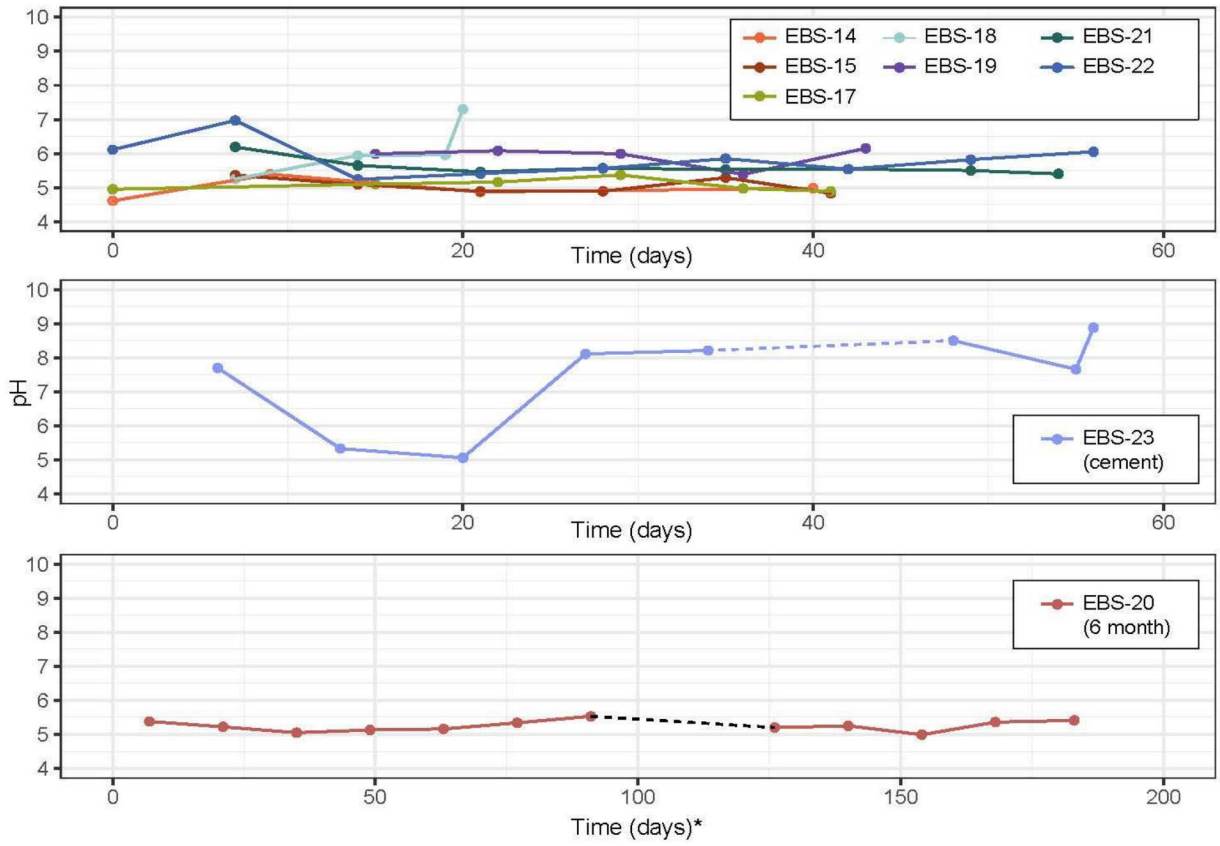


Figure 5. Solution pH from fluid collected throughout each EBS experiment**.** *Note the difference in x-axis scale for EBS-20 (6 month experiment). The dashed lines (EBS-20, EBS-23) connect periods of no meaurements beween ~90 and ~125 days.

Cations

K^+, Na^+. In all experiments, Na^+ and K^+ concentrations follow similar trends during the experiment duration. Sodium concentration ranged from ~1000 to 4000 mg/L, with the exception of EBS-21 in which a 2M NaCl was added to the starting solution resulting in [Na^+] = ~22500 mg/L during the experiment. Potassium ranged from ~50 to 300 mg/L during the experiments. Potassium and Na in solution typically follow the same trend in all experiments except EBS-21 and EBS-22: around week 2-3 of the experiment, the concentrations generally decrease, potentially as the cations are likely incorporated into zeolites. In EBS-21 and EBS-22, the Na^+ and K^+ concentrations remain relatively constant during the experiment.

Ca^{2+}. The Ca^{2+} concentration throughout each Opalinus experiment generally shows a flat or slightly increasing trend throughout the course of all the experiments. Concentrations range from ~50 to 600 mg/L during the experiment and sharply increase in the sample taken after the experiment is cooled.

SiO_2: In the EBS-14, -15, -17, -19, and -23 experiments, the $SiO_{2(aq)}$ concentration of filtered and unfiltered solutions generally remains fairly constant ~100–200 mg/L throughout the experiment. In EBS-18, the $SiO_{2(aq)}$ concentration of the filtered and unfiltered cation samples do not track together and are generally higher than the other experiments (between ~200 and 450 mg/L). In EBS-20, the 6 month experiment, silica is constant ~100 mg/L until the 49 day mark where it increases to ~200 mg/L. The $SiO_{2(aq)}$ then drops back to ~100 mg/L in the next sample (day 63) and steadily increases back to ~200 mg/L by the end of the experiment (day 168). In EBS-21, silica remained near 0 mg/L until day 49 when it increases to ~100 mg/L and reaches ~150 mg/l by the end of the experiment (day 54). Results from EBS-22 show a split between the unfiltered and filtered results: unfiltered silica reaches around 300 mg/L while filtered concentrations remain ~100 mg/L.

Fe. Iron concentrations are generally < 10 mg/L throughout the duration of the experiments. Fe goes into solution beginning at the 3 week mark (half way through the experiment) and stays in the solution. The trend of [Fe] during the experiment is generally increasing, or flat.

Mg^{2+}. In the 300 °C experiments, Mg concentration typically remains close to zero. Experiments EBS-21 and EBS-22 show much higher [Mg^{2+}] initially in comparison to the other experiments. In these two runs, Mg^{2+} concentration is shows a steady decrease from ~30–60 mg/L to <5 mg/L over the course of the 8 week experiment.

Anions

Cl^-. Chloride concentration in solution did not follow consistent trends in the experiments. In general, initial concentrations were around 3000–5000 mg/L at the beginning of the experiment, with the exception of EBS-21 (~48000 mg/L), which was doped with 2M NaCl. In EBS-15, EBS-20, and EBS-21, an increase of ~1000–2000 mg/L in [Cl^-] is observed about 3 weeks into the

experiment, followed by a decrease back to pre-spike values. In all other experiments, [Cl^-] follows a flat or slightly decreasing trend over the experiment duration.

SO_4^{2-}. Sulfate concentrations typically remained below 10 mg/L in the experiments with the exception of EBS-18, EBS-22, and EBS-23. During EBS-18, [SO_4^{2-}] increased from around 10 mg/L to 1000 mg/L. In EBS-22 and EBS-23, sulfate was initially around 100 mg/L and steadily decreased throughout the course of the experiment.

2.2.2 Clay Mineralogy

QXRD Results

Quantitative x-ray diffraction (QXRD) data were collected for all Opalinus Clay EBS experiments and are reported in Table 5 and Appendix C (Table C-1). The EBS-19 sample was analyzed twice, and both sets of results are presented. In addition, two different samples were analyzed from the EBS-23 experiment: EBS-23, which represents the EBS-components that were present at the bottom of the reaction vessel and EBS-23-Cement, which was a cement plug that formed at the top of the experiment. The mineral groups present in significant amounts in all samples include clays, feldspars, zeolites, and/or phyllosilicates, with lesser SiO2 polymorphs and/or carbonates. Other minerals identified to make up <5% in all samples include gypsum, halite, K-feldspar, magnetite, and/or pyrite. The following describes the major mineral phase abundances in each Opalinus experiment.

In experiments EBS-14 through EBS-22, clay minerals are the dominant phase present as either illite, smectite, mixed illite-smectite, and/or kaolinite. In EBS-14, EBS-15, EBS-17, and EBS-18, the relative proportions of illite vs. smectite fractions was not distinguished, and were reported together as smectite: reported values for smectite for these samples range from ~40 to 64% (Table 1 of Appendix C). Illite is reported as 0% for EBS-19 and smectite makes up ~54–57% of the sample. EBS-20 and EBS-21 have 41/21% and 54/18% for smectite/illite, respectively. In EBS-22, 2.4% smectite and 14% kaolinite is present, and the dominant clay species is illite (50%). Samples EBS-23 and EBS-23-Cement are distinct from all other samples in that no smectite or illite are reported in the QXRD results. Nontronite (~14%) and dickite (~3%) are observed in EBS-23 and no clay minerals are reported in EBS-23-Cement.

The QXRD results report plagioclase and/or K-feldspar in all experiments (Table 1 of Appendix C). As described above, K-feldspar makes up a significant portion of the precursor Opalinus Clay material (~17%). For all Opalinus EBS experiments, the reaction products have between ~0–5% K-feldspar. Plagioclase feldspar makes up between ~3 and 12% in EBS-14 through EBS-22. In EBS-23, plagioclase feldspar is identified as anorthite (Ca-end member) and is ~59% of the sample. No feldspars are identified in EBS-23-Cement.

Zeolites present in the reaction products are dominantly clinoptilolite, with lesser analcime-wairakite$_{ss}$, and rare erionite. Clinoptilolite is not observed in EBS-14, but comprises ~12–18% of EBS-15, EBS-17, EBS-18, and EBS-19 samples. Samples from EBS-20 and EBS-21 have ~8–10% clinoptilolite, whereas it is negligible in EBS-22, EBS-23, and EBS-23-Cement. Analcime-wairakite$_{ss}$ is observed in EBS-14 through EBS-20 (~0.4 to 5%) and not observed in EBS-21 and EBS-22. Samples from EBS-23 and EBS-23-Cement have ~9% and ~53% analcime, respectively, as well as ~4% erionite.

Phyllosilicates identified by QXRD in the reaction products include biotite, chlorite, and generic "mica." Biotite is observed to be ~2–12% of samples EBS-14, EBS-15, and EBS-17. Chlorite is 13% of sample EBS-14, ~0.4–4% in EBS-15 through EBS-22, and not observed in the two EBS-23 samples. Other "mica" makes up <10% in samples from EBS-18 through EBS-22.

Carbonate minerals do not make up a significant percent in any of the QXRD results, with the exception of EBS-23-cement, in which calcite (34%) and monohydrocalcite (7%) are present.

Table 5. Quantitative X-Ray Diffraction (QXRD) analyses of the buffer clay (Wyoming Bentonite) the wall rock (Opalinus Clay) and product results of experiments EBS-14 to EBS-23. Values are in weight percent. b.d.l. = below detection limit, * represents data set was normalized to 100.0, (+) represents material detectable but below 0.5 wt. %

	Wyoming Bentonite	Switzerland Opalinus Clay	EBS-14 Opalinus Clay	EBS-15 Opal -316 SS	EBS-17 Opal -Cu	EBS-18 Opalinus Clay	EBS-19 Opal -304 SS (1)	EBS-19 Opal -304 SS (2)	EBS-20 Opal -316 SS	EBS-21 Opal -316LS SS	EBS-22	EBS-23	EBS-23 Cement
	4 weeks 125 – 300 °C	6 weeks 300 °C				3 weeks 300 °C	6 weeks 300 °C		6 months 300 °C	8 weeks 200 °C			
Analcime/ Wairakite	b.d.l.		5.5	1.3	3.0	0.5	0.4	0.4	1.4			8.57	52.92
Clinoptilolite	12.0			15.0	11.7	17.8	17.1	14.8	8.2	9.6	0.1		
Erionite-Ca												4.35	4.34
Smectite	66.4	24.1	39.8	51.6	63.8	62.8	54.0	56.7	41.4	53.6	2.4	13.53	
Kaolinite	b.d.l.	16.9	1.8	0.2							14.4		
Dickite												3.14	
Plagioclase	8.3	3	3.5	11.8	11.3	6.7	10.6	9.8	14.3	4.8	1.5		
Anorthite												58.82	
K-Feldspar	b.d.l.	5.9	4.3	2.3	3.1	0.1	2.7	1.3	0.8	1.9	0.6		
Biotite	2.8	7.4	11.9	9.7	2.0								
Muscovite						7.2	9.4	8.5	5.1	1.9	0.7		
Illite									20.9	18.3	50.0		
Chlorite	b.d.l.	9.1	11.1	1.3	1.1	0.6	0.4	0.4	0.4	0.4	3.5		
Calcite	5.5	16.4	9.4						0.1	1.3	13.6		34.06
Monohydrocalcite													6.78
Dolomite	+	0.7											
Quartz	0.9	13.8	8.4	5.5	3.3	3.9	4.9	7.2	4.9	3.0	9.4	8.09	1.90
Cristobalite/ Opal-C	1.8					0.1			0.6	0.4			
Gypsum			0.5	0.3	0.1	0.4	0.2	0.5	0.3	0.2			
Halite							0.3	0.4	0.1	3.8	0.3		
Pyrite	0.4	1.1	0.7	+	0.2	+	+	+	+	+	+	+	+
Magnetite			3.1	1.1	0.5				1.4	0.6	3.6	3.50	
Siderite	1.8	0.1											
Total	**100.0***	**98.5**	**100.0**	**100.1**	**100.1**	**100.1**	**100.0**	**100.0**	**99.9**	**99.8**	**100.1**	**100.0**	**100.0**

XRD Analyses

EBS-14

As described above, the starting Opalinus Clay is dominated with illite-smectite (I-S) mixed-layers and discrete illite with minor amounts of smectite (Figure 3, 6). Reaction products from EBS-14 show three different major clay fractions: two different I-S mixed layers and one illite fraction (Figure 6). It would appear that the two different I-S fractions are R3 illite (0.9)-smectite and R1 illite (0.7)-smectite. Exact quantification of the proportion of each I-S mixed layer type is not possible, but it appears that the R3 I-S is the dominant phase in the EBS-14 reaction products.

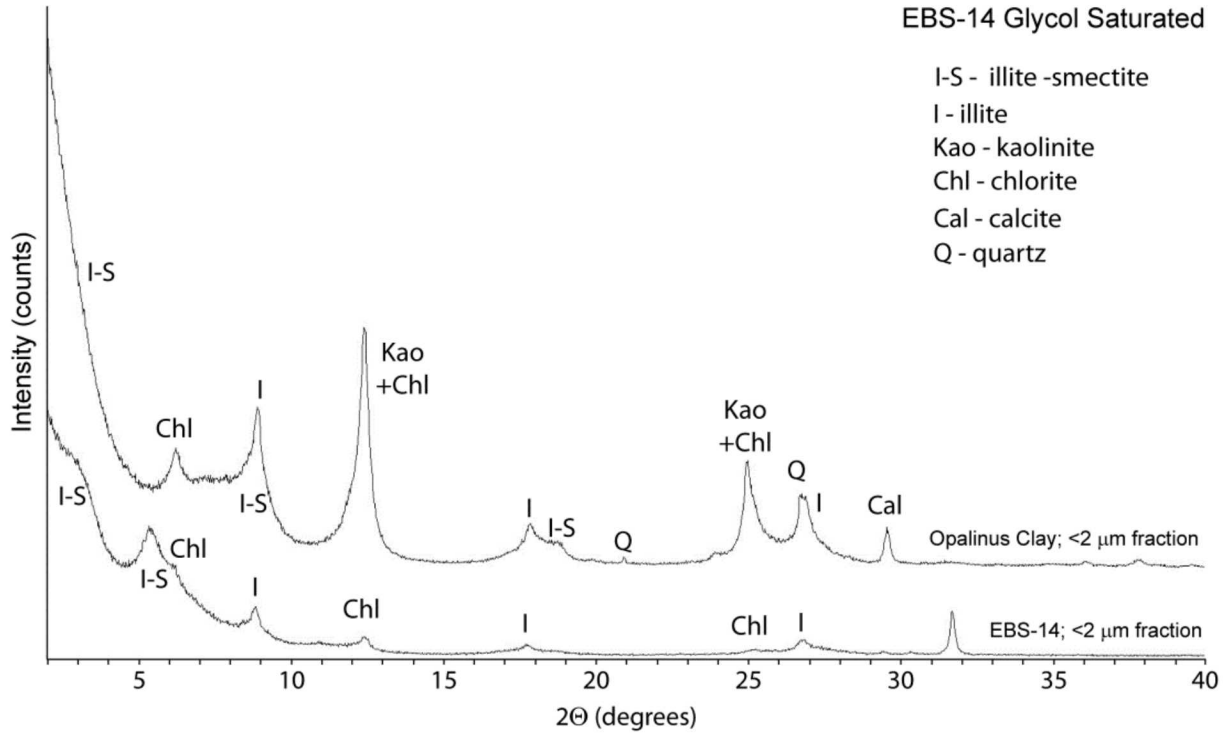


Figure 6. XRD patterns from the ethylene glycol saturated, oriented < 2 μm fractions from original Opalinus Clay and EBS-14 reactions products showing the effects of heating Opalinus Clay to 300°C for six weeks.

EBS-15

The XRD patterns from the EBS-15 reaction products vary among the type of < 2 μm fractions examined. In the bulk < 2 μm size fraction, all clay products show 100% expandability with minor occurrences of illite (Figure 7). It is evident from the bulk < 2 μm fraction, that 1) it is montmorillonite from the bentonite component that dominates this fraction and 2) this

montmorillonite has not experienced significant illitization (i.e., > illite (0.05)/smectite). Montmorillonite expands to 16.8 – 16.9 Å with a Δ2θ (002/003) values of 5.25 – 5.25°, corresponding to 100% expandability (Figure 7). Post-reacted Opalinus Clay fragments from EBS-15 showed a composition more characteristic of the starting Opalinus Clay. It was dominated with illite (possibly two), I-S, chlorite, and quartz. Illite could potentially be de-convoluted into a well-crystalline illite and a poorly-crystalline illite displaying a low, broad reflection superimposed on a sharp 10 Å illite reflection. The I-S appears to be a R0 illite (0.1)/smectite and expands to 16.8 Å with a Δ2θ (002/003) values of 5.44°, corresponding to 91% expandability. R1-3 ordered I-S were not detected.

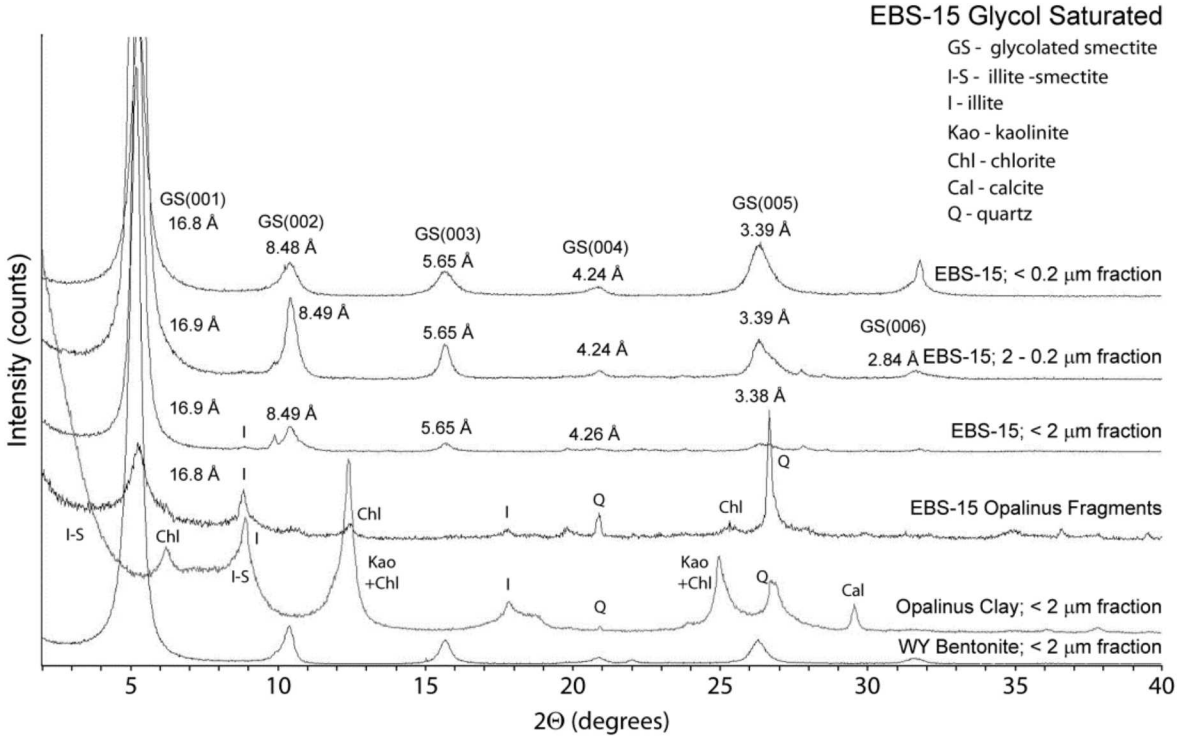


Figure 7. XRD patterns from the ethylene glycol saturated, oriented fraction from original Opalinus Clay, WY bentonite, EBS-15 Opalinus fragments, and various size fractions from EBS-15 reaction products.

EBS-23

Note that two samples were characterized for sample EBS-23. They are labeled EBS-23 (a group of crystals at the bottom of the assembly bag) and EBS-23 cement (a relatively solid gray cap of material at the top of the assembly bag). As shown in Figure 8, there are marked

differences in the mineralogy. Sample EBS-23 was dominated by K feldspar (low sanidine), smectite and lesser analcime-wairakite$_{ss}$ crystals. Dickite was also identified in EBS-23. The EBS-23 cement sample consists primarily of analcime-wairakite$_{ss}$ crystals and calcite. The calcite in EBS-23 cement was identified by QXRD, but not in the spectra peaks.

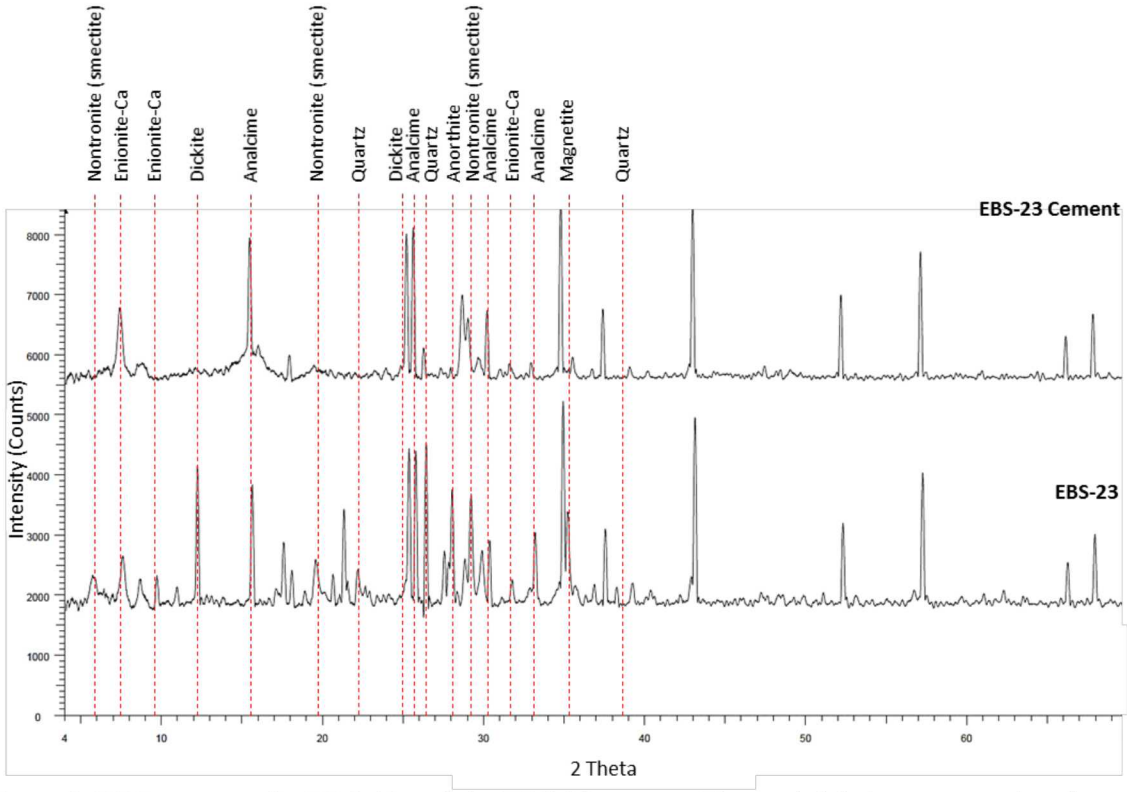


Figure 8. XRD patterns for EBS-23 and the EBS-23 cement. The peak labels correspond to the identified minerals and unmarked peaks belong to the corundum standard.

2.2.3 Electron Microprobe Analyses (EMPA)

Electron microprobe analyses primarily targeted zeolites and steel alteration products; data was also collected from some feldspars. The results of the microprobe analyses are reported in Appendix D.

Zeolites. There was significant analcime-wairakite$_{ss}$ formation with the addition of Opalinus Clay and brine in the high temperature (300 °C) experiments and in the 200 °C experiment that included Portland Cement (EBS-23). In general, the results from the zeolites show a solid solution between analcime and wairakite and these compositions are plotted in Figure 9.

Analcime-wairakite$_{ss}$ EMPA results from EBS-14, EBS-15 EBS-17, EBS-18, EBS-19, EBS-20, and EBS-23 have Si/Al ratios between ~2.2 and 3.0. The Na/(Na + Ca) ratios are between ~0.2 and 0.8, indicating an analcime–wairakite solid solution series (Figure 9). One analysis of clinoptilolite from EBS-18 has similar Si/Al and Na/(Na + Ca) ratios to analcime.

In general, analcime was not observed in EBS-21 and EBS-22, the lower temperature experiments. One analysis of a potential zeolite was collected from EBS-22, but the EMPA reveal high wt% values for FeO and MgO, indicating it is not likely a zeolite. The experiment with cement at 200°C (EBS-23) yielded abundant analcime. Two groups of analcime are observed: (1) in the fine-grained groundmass and (2) rimming grains of Opalinus Clay. The analyses of EBS-23 analcime were grouped by this textural context (Figure 9, F-17A–D). On average, analcime grains that coat Opalinus Clay fragments have higher Na/Na+Ca values (0.79) than analcime grains that are observed in the groundmass (0.68), but both groups have similar Si/Al ratios (~2.2). Further, the analcime crystals formed in EBS-23 have the highest Na/Na+Ca ratio observed in any EBS experiment with Opalinus Clay.

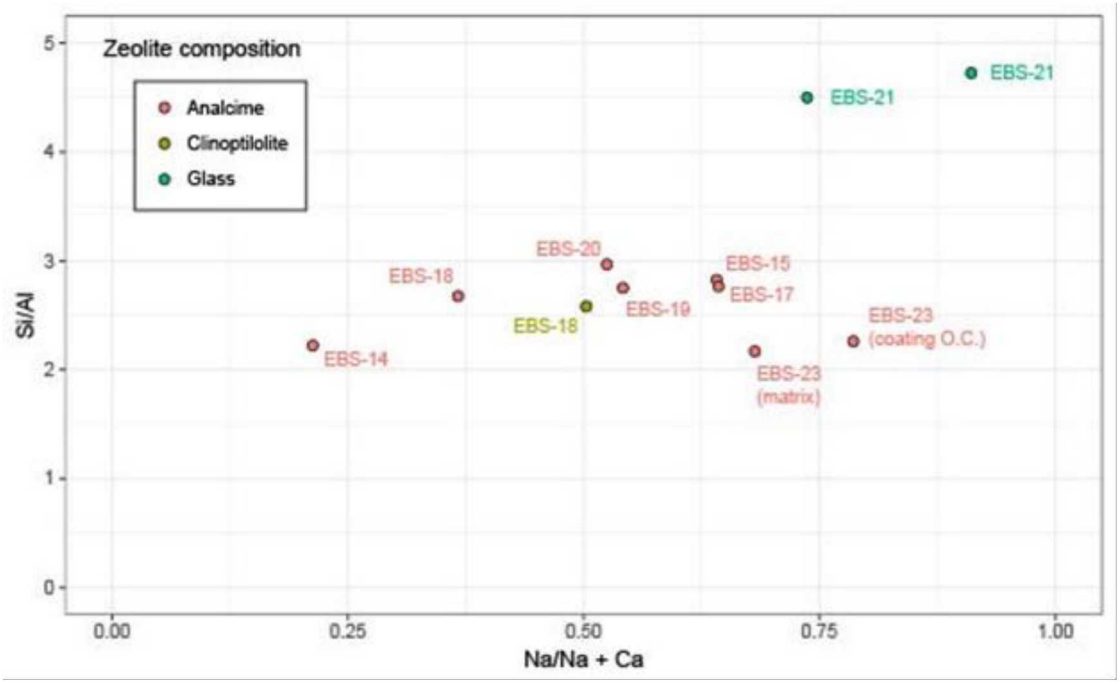


Figure 9. Variations in Na/(Na + Ca) and Si/Al ratios for zeolites and glasses. O.C. = Opalinus Clay

Steel alteration. Microprobe data was collected from authigenic minerals that formed at the steel / bentonite interface in experiments EBS-15, EBS-18, EBS-19, and EBS-22. The minerals include goethite, stilpnomelane, Fe-saponite, and chlorite (Figures 10A and 10B). Interior to the pit corrosion (Appendix F, Figures F-8, F-11F, F-12, F-13, F-14) the mineral formed is goethite, directly at the steel clay boundary are discontinuous sulfide grains (unable to analyze due to small size), and proximal to the steel layer is a layer of Fe-saponite. A mantle of phyllosilicate minerals (likely chlorite) were also observed surrounding the Fe-saponite. The FeO + MgO results from Fe-saponite, stilpnomelane, and goethite are plotted in Figure 10A. Results from the phyllosilicate mantle analyses are plotted in Figure 10B, and show a shift to higher FeO + MgO wt% and lower SiO_2 wt% values with decreased experimental temperature (Figure 10B). EMPA analyses revealed higher than accepted wt% values of $CaO + Na_2O + K_2O$ for compositionally pure chlorite. This is likely due to the fine-grained nature of the mantle and intergrowths with other phases.

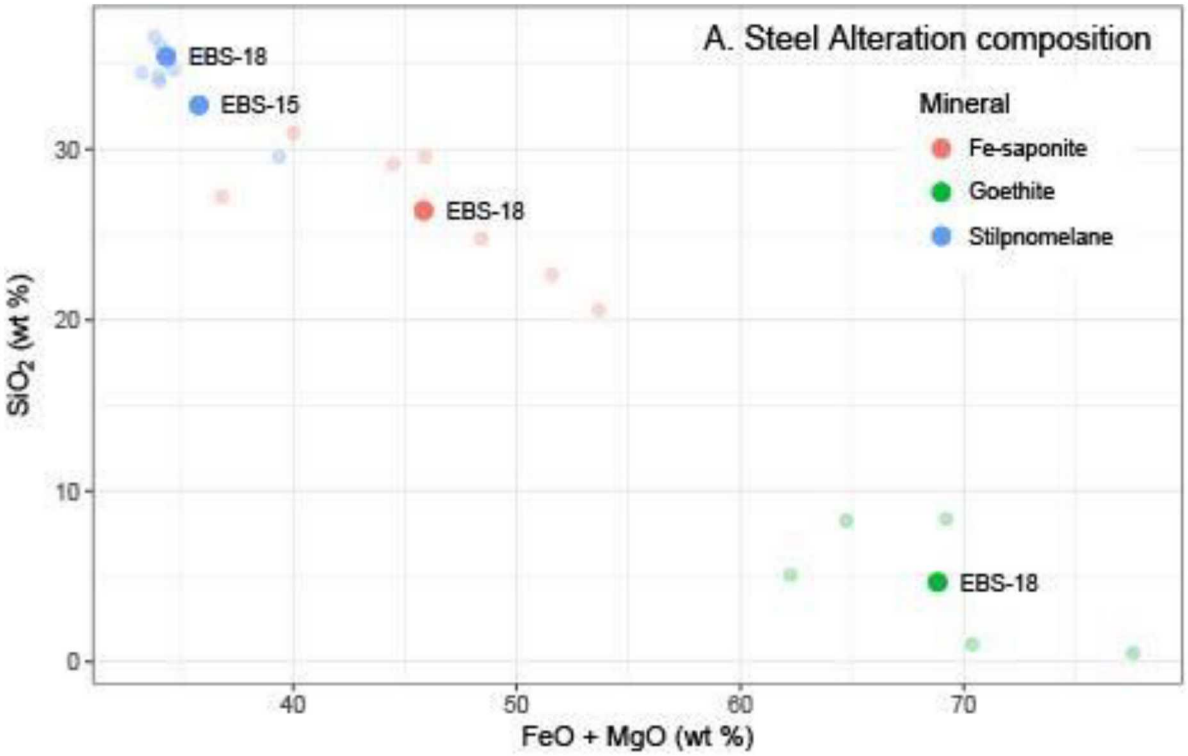


Figure 10. Variation in wt. % FeO and MgO vs. SiO_2 for minerals found on the steel interface: (A) steel alteration minerals and (B) (next page) chlorite from the outer phyllosilicate mantle. In both plots, each point corresponds to a single analysis, and the bold points correspond to averages for all data from each experiment.

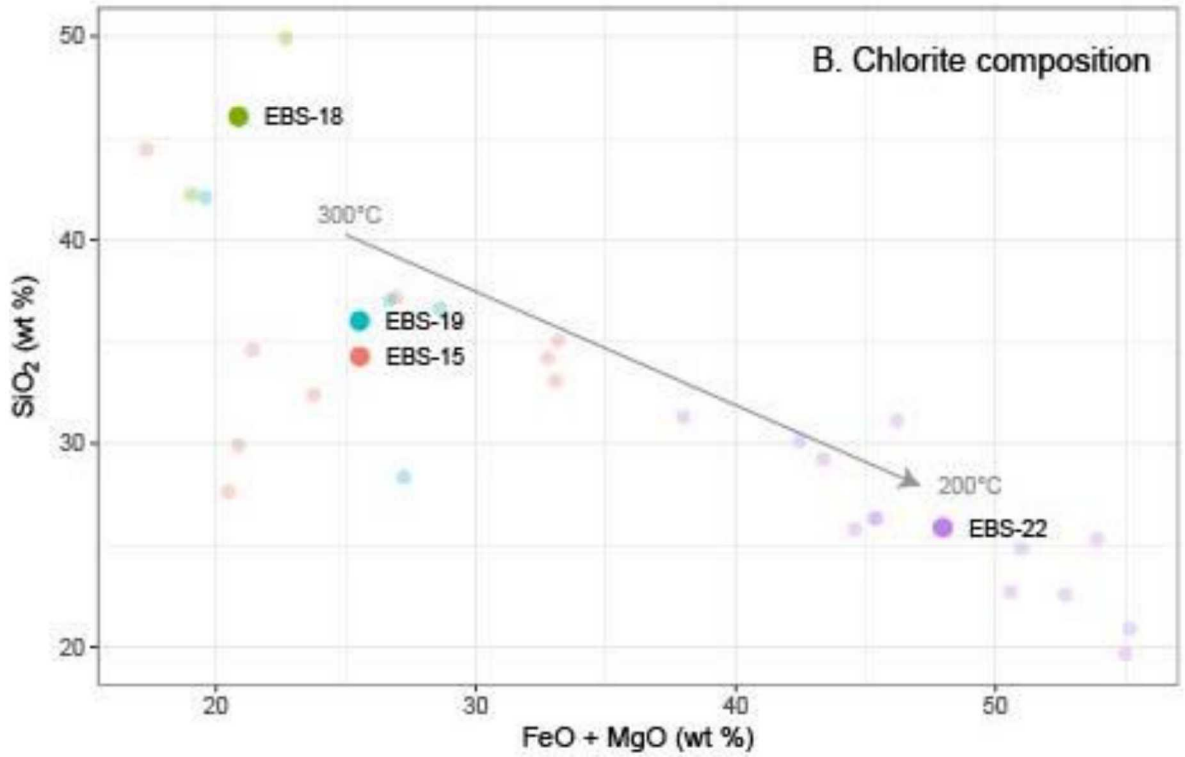


Figure 10. Variation in wt. % FeO and MgO vs. SiO2 for minerals found on the steel interface: (A) (previous page) steel alteration minerals and (B) chlorite from the outer phyllosilicate mantle. In both plots, each point corresponds to a single analysis, and the bold points correspond to averages for all data from each experiment.

2.2.4 SEM/EDS Results

Reaction products, including loose powder, epoxy mounts, and thin sections, from each experiment were characterized using the scanning electron microscope and qualitative elemental abundances were evaluated using EDX. The SEM images are presented in Appendix F and described below.

EBS-14. Backscatter electron (BSE) images of EBS-14 thin sections reveal cracks within the Opalinus Clay filled with wairakite crystals (Figure F-1). SEM images for EBS-14 show a predominately smectite matrix with calcite spheres, and feldspar and wairakite crystals (Figure F-2, F-3). SEM images from EBS-14 reveal that pyrite was unaltered during the reactions. The octahedral pyrite still occupies fractures and/or between bedding planes and displays not signs of corrosion (Figure F-3). SEM analyses show several pore-filling calcite nodules present throughout EBS-14 (Figure F-2, F-7).

EBS-15. BSE images of thin sections display zeolites, particularly analcime, within the Opalinus Clay (Figure F-4). In the EBS-15 thin sections there are zoned native iron grains and outward alteration from Fe-oxide to Fe-sulfide and stilpnomelane (Figure F-5). EBS-15 SEM images depict a smectite matrix with analcime-wairakite$_{ss}$ crystals, illite spray growth, and foliated bentonite (Figure F-6). Some SEM images also identify fossil casts and biotite within a smectite matrix (Figure F-7). Lastly, SEM images confirm the presence of analcime-wairakite$_{ss}$ crystals, saponite with fibrous millerite, and feldspars suspended in smectite on the 316 SS surface (Figure F-8). Similarly, to EBS-14, some pore-filling calcite nodules are present.

EBS-17. BSE images of EBS-17 thin sections confirm analcime crystals within the Opalinus Clay and copper pit corrosion on the Cu surface (Figure F-9). EBS-17 SEM images depict analcime-wairakite$_{ss}$ crystals, feldspar dissolution in contact with analcime-wairakite$_{ss}$, illite crystal mats, and chalcocite over-growth along the corroded copper surface (Figure F-10, F-11, and F-12). There appears to be the alignment of crystals along scratches on the copper surface (Figure F-12).

EBS-18. SEM images show pit corrosion of the low carbon steel (Figure F-14). SEM images portray euhedral isometric analcime-wairakite$_{ss}$ crystals, clinoptilolite, radial growth plagioclase, secondary smectite rose, and Fe-saponite / low carbon steel interface interactions (Figure F-13, F-14).

EBS-19. EBS-19 SEM images depict the full reaction mineral phase assemblage (e.g., Figure F-15). For example, SEM images confirm analcime-wairakite$_{ss}$ zeolites embedded in an Fe-saponite matrix with minor amounts of smectite, albite, and pentlandite crystals (Figure F-15). In EBS-19 there was an unusually high amount of zeolites present as depicted in Figure F-15, likely due to a zeolite replacement of a glass lapilli. Some of the other minerals seen were acicular clinoptilolite next to a reabsorbing K-feldspar phenocryst, and a secondary albite growth on a plagioclase phenocryst (Figure F-15).

EBS-20. For EBS-20, chlorite sprays intermix with the analcime-wairakite$_{ss}$ zeolites and Fe-saponite (Figure F-16). The analcime-wairakite$_{ss}$ zeolites, surrounded by Fe-saponite. show late stage pentlandite (white crystals) (Figure F-16). SEM images for EBS-20 indicate possible calcite spheres suspended in a smectite matrix, feldspar sprays (likely Labradorite) and feldspar dissolution (Figure F-16).

EBS-21. Images from EBS-21 include smectite matrix (Figure F-15C, D), framboidal pyrite within Opalinus Clay matrix (Fig. F-15E) and unknown Al-silicates (Fig. F-15A, B).

EBS-22. Sample EBS-22 displays images of framboidal pyrite (Fig. F-16A), Opalinus Clay fragments (Fig. F-16B, D) with replacement of fossil casts lined with calcite (Fig. F-16B) and carbonate crystal clusters (Fig. F-16C).

EBS-23. EBS-23 introduces Portland cement to the reaction and now exhibits analcime – wairakite$_{ss}$ at lower temperatures than previously encountered. Images in Appendix F include analcime-wairakite$_{ss}$ crystals (Fig. F-17 A, B, C). Note how analcime-wairakite$_{ss}$ crystals rim Opalinus Clay fragment (Fig. F-17 B). Wairakite crystals mantling Opalinus Clay fragment (Fig. F-17 D). Feldspar crystal adjacent to analcime-wairakite$_{ss}$ crystals replacing pumice lapilli (Fig. F-17 E). Bright Fe-oxide crystal next to a wairakite-rich zeolite (Fig. F-17 F). Figure F-18 shows a carbonate fragment surrounded by analcime-wairakite$_{ss}$ crystals.

2.3 FEBEX Results

(Characterization of data only, discussion will be in FY19 report due to time limitations of funding increase).

Samples from compressed bentonite blocks from the inner (BM-C-49-1, BM-C-49-2, BM-C-49-3), middle (B-C-49-8, B-C-49-10, B-C-49-12), and outer (B-C-49-7, B-C-49-9, B-C-49-11) rings of the FEBEX were characterized in order to assess any chemical or mineralogical changes with distance from the heater.

2.3.1 Bentonite Mineralogy

The QXRD and XRD peak patterns from the FEBEX bentonite samples are presented in Appendix C.

QXRD

The QXRD data (Table C-2) shows results from the starting material (unheated FEBEX bentonite), wall rock (BG-C-49-1 Granite), and three samples each from the inner, middle, and outer rings. The QXRD results indicate the presence of four main minerals in all samples: quartz, feldspar (orthoclase and albite), and smectite. The following describes the relative abundance of each mineral.

Quartz. The starting FEBEX bentonite contains 26.7% quartz and the wall rock contains 44.0%. The quartz content of post-heater bentonite samples range from 9.2–12.0% (inner ring), 10.9–12.5% (middle), and 7.1–12.8% (outer). In comparison to the starting bentonite, the quartz values for bentonite involved in the heater test are roughly half of the starting values. There are no obvious differences in %quartz in the heated bentonite samples with distance from the heater.

Feldspar. The starting FEBEX bentonite and wall rock both contain both K-feldspar (orthoclase, K end member) and plagioclase feldspar (albite, Na end member). The wall rock contains 30.8% orthoclase and 25.1% albite, whereas the FEBEX starting bentonite contains 6.5% orthoclase and 8.3% albite. The QXRD from the heated bentonite blocks from all rings dominantly indicate the presence of albite (13.0–19.0%) and %orthoclase below detection limits. One sample from the outer ring (B-C-49-11) contains 2.1% orthoclase in addition to 18.4% albite. Thus, according to the QXRD results, in comparison to the starting the bentonite, the K-feldspar in the heated bentonite has been almost completely replaced by plagioclase (Na-end member).

Smectite. The starting material (FEBEX) contains 58.6% smectite, whereas the bentonite material from all rings contain between 70.0–77.9%. There are no clear trends of smectite content in the QXRD results with distance from the heater. All heated bentonite samples show an increase of between ~12% and 20% in relative abundance of smectite in comparison to the starting FEBEX bentonite.

XRD Peak Patterns

The XRD peak patterns are divided by ring position and are compared to the patterns for pre-heater test FEBEX clay and Grimsel granodiorite wall rock (BG-C-49-1 Granite) (Figures C-2 through C-4).

The XRD results from the inner (Figure C-2), middle (Figure C-3), and outer (Figure C-4) ring samples are dominated by peaks corresponding to smectite (nontronite) with smaller feldspar (albite, orthoclase) and quartz peaks. There are no apparent differences between the XRD peak patterns with distance from the heater. The phases observed in the XRD data match with what was observed in the QXRD results. In comparison to the starting FEBEX bentonite, the ring samples have similar peaks locations and shapes.

2.3.2 Microprobe

Electron microprobe analyses primarily targeted recrystallized smectite, and feldspars. One sample each from the inner (BM-C-49-1), middle (B-C-49-10), and outer (B-C-49-9) ring was analyzed. The results of the microprobe analyses are reported in Appendix D.

Smectite. The major element oxide composition of smectite falls within the following ranges: SiO_2 49-64 wt%, Al_2O_3, 18-24%, FeO 2-7%, MgO 4-7%, 1-2% CaO, ,0.4–1% Na_2O, and 0.2–3% K_2O. The variation in weight percent Al_2O_3, CaO + K_2O + Na_2O, vs. FeO +MgO in the smectite from the three samples is compared in Figure 11A. The relative proportion of CaO + K_2O + Na_2O stays constant in the samples. The proportion of FeO + MgO and Al_2O_3 decreases

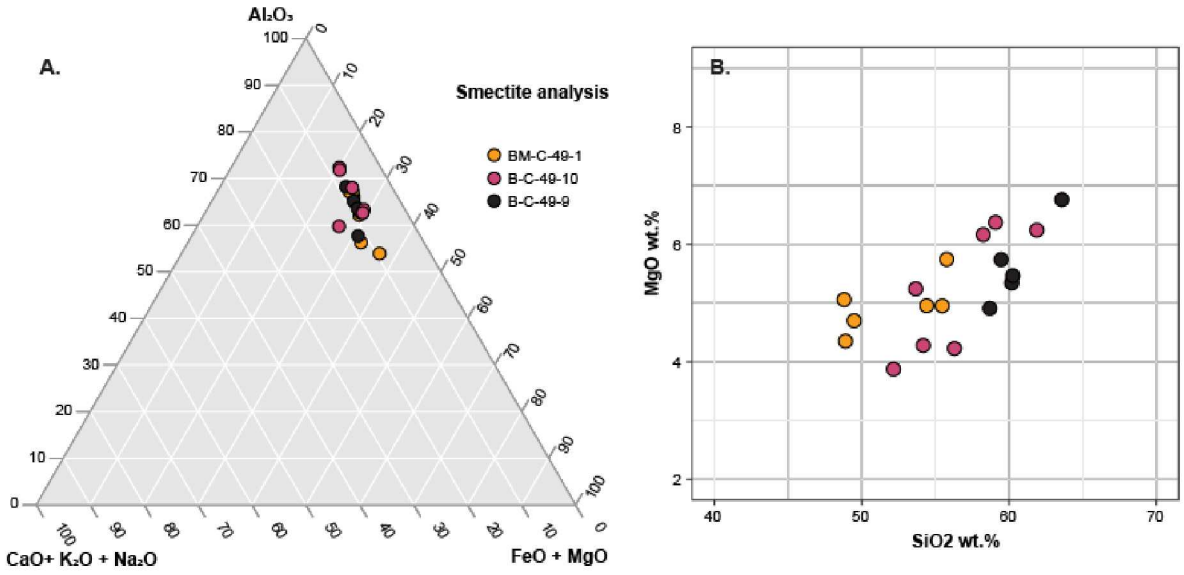


Figure 11. Smectite compositions for FEBEX bentonite determined by electron microprobe. (A) Ternary diagram of Al_2O_3 vs. CaO + Na_2O + K_2O vs. FeO + MgO and (B) variation of wt.% MgO vs. SiO_2.

with distance from the heater. Figure 11B shows the variation of wt.% MgO vs. SiO_2. The MgO and SiO_2 generally increase from the inner (BM-C-49-1) to outer (B-C-49-9) bentonite blocks (Figure 11B).

Feldspar. Compositions of both potassium and plagioclase feldspar are plotted in Figure Z. Potassium feldspar compositions are near-pure sanidine (K-end member) in the innermost bentonite block (BM-C-49-1). K-Feldspar from the middle (B-C-49-10) and outer (B-C-49-9) blocks have variable compositions that include more Na (Figure 12). Similarly, plagioclase feldspars in the inner block have uniform compositions (andesine), whereas the two other

samples have a wider range of Ca and Na values (Figure 12). One possibility is that the variation in feldspar compositions observed in the outer and middle blocks represents the original spread in feldspar compositions in the FEBEX bentonite. The compositions in the inner block may reflect homogenization due to the thermal effect of the heater.

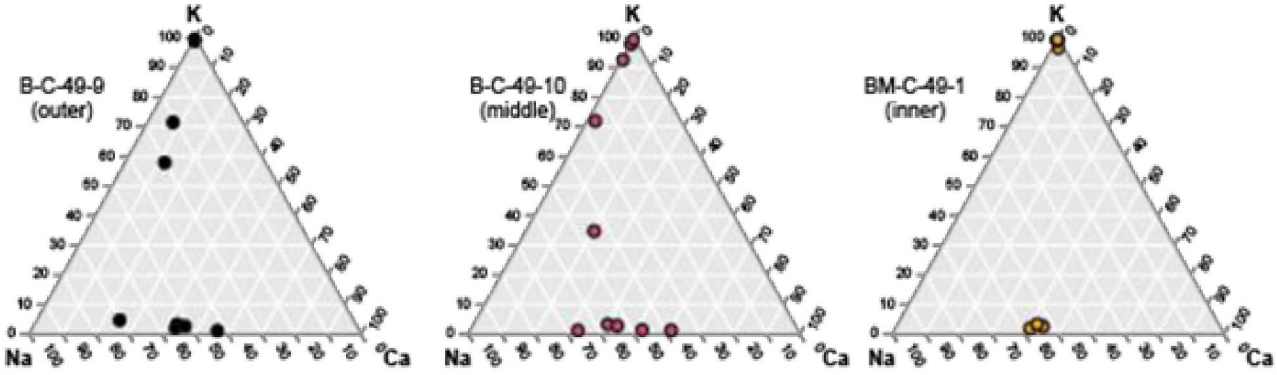


Figure 12. Ternary diagrams for FEBEX bentonite plagioclase and K-feldspar.

2.3.3 Scanning Electron Microscopy (SEM)

FEBEX bentonite samples, including loose powder and thin sections, from the inner, middle, and outer rings were characterized using scanning electron microscopes. Qualitative elemental abundances were evaluated using EDX. The SEM images are presented in Appendix F and described below.

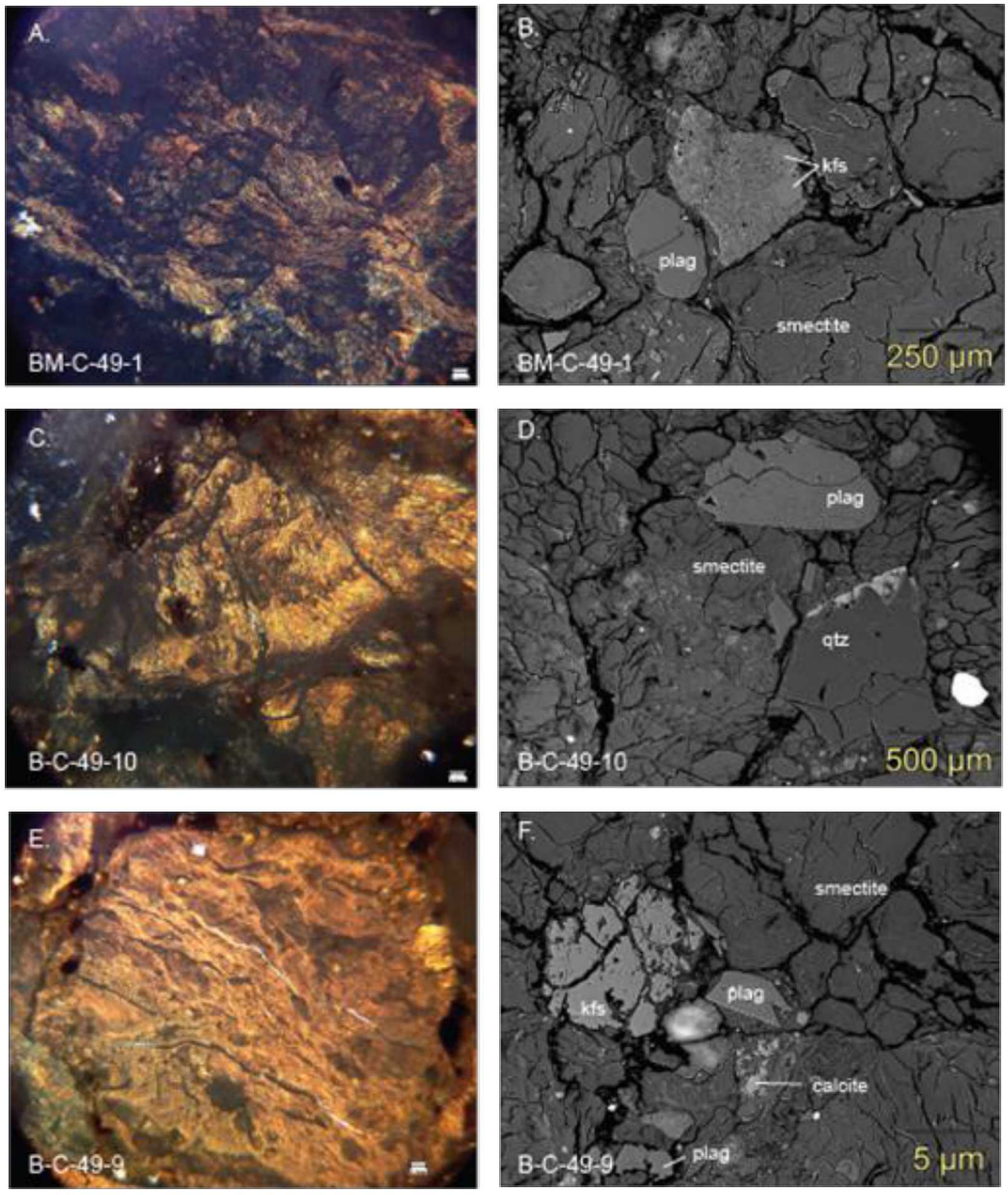


Figure 13. Crossed-polarized (A, C, E) photomicrographs and backscattered electron (BSE) images (B, D, F) of FEBEX bentonite samples. Mineral abbreviations: kfs, K-feldspar, plag, plagioclase; qtz, quartz.

The smectite chips in the FEBEX bentonite display range of textures and morphologies under crossed and plane polarized light (petrographic microscope) that likely reflect the variation in the source material for the bentonite. The variable nature of the FEBEX chips is demonstrated in Figure 13A, C, and E. In general, the clays characterized by SEM EDS indicate that these clays are Mg-rich smectites

The backscattered SEM images in Figure 13 (B, D, F) demonstrate the range of textural relationships between the smectite matrix and feldspar grains. In all samples, K-feldspar and plagioclase are rimmed by smectite (Figure 13F). Smectite is variably altered to sericite, and the largest sericite crystals are observed in the sample closest to the heater (BM-C-49-1).

Quartz and calcite are present in all samples and neither display zoning in cathodoluminescence. In addition, quartz and calcite are commonly observed to be complexly intergrown. In some cases, these minerals are also complexly intergrown with plagioclase and K-feldspar (Figure 14).

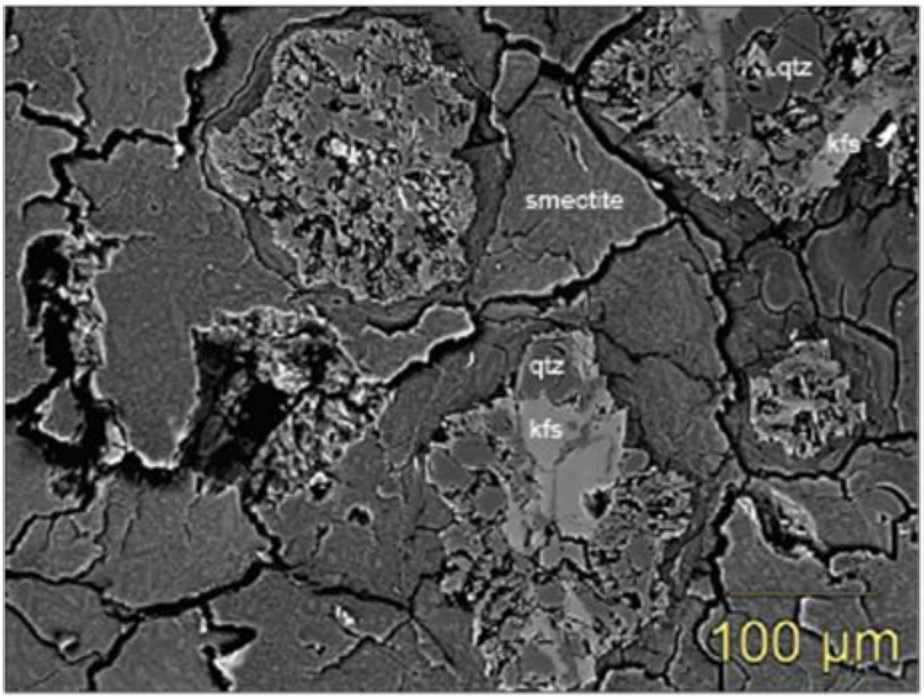


Figure 14. Example of intergrown quartz (qtz) and K-Feldspar (kfs) in a smectite matrix in FEBEX bentonite sample B-C-49-10.

3. Discussion

3.1 Opalinus clay interactions with EBS backfill

Mineral Evolution. Following the clay mineral evolution within Opalinus materials is complicated due to the variety of clay minerals present in the Opalinus experimental systems. Three systems were tested: 1) Opalinus Clay, 2) bentonite with 20 wt. % Opalinus Clay, and 3) 50% Opalinus clay and 50% bentonite. The 20% and 50% Opalinus clay experiments were setup

to represent mixing between a repository host rock with a bentonite backfill to determine what effects (if any) the host rock has on the backfill material.

After thermal processing in brine (EBS-14), the Opalinus Clay appears to have an increase in the I-S distribution. The original Opalinus material appeared to have an R3 illite (0.8-0.9)-smectite, but after 300 °C for 6 week in an Opalinus brine an R3 illite (0.9)/smectite and a R1 illite (0.7)/smectite was produced. However, illitization in the host rock may not be a major concern as Opalinus Clay is primarily a low-permeable barrier with very limited swelling capacity due to the low amounts of swelling smectite within the Opalinus Clay. The major concern is the reactivity of Opalinus Clay with the bentonite causing alteration to the bentonite constituents. There was negligible illitization within the bentonite fraction in the mixed reaction (EBS-15). This is consistent with the capsule experiments containing a bentonite with a secondary rock phase. It is important to note that these experiments do not preclude the possibility of host rock – bentonite interaction at these temperatures because kinetics may not allow the observation of mineral alterations under the current experimental duration. With any of these experiments representing repository system, kinetics is always an issue that has to be taken into account when interpreting data.

There was no evidence of illite-smectite mixed-layering during the six-month cooling experiment where montmorillonite was heated to 300 °C for four months. This is consistent with the other EBS experiments in our Na-dominated hydrothermal systems. Much of the illitization concepts related to a Na-rich systems have been previously discussed (Caporuscio et al., 2013; Cheshire et al., 2014a; 2014b), but is repeated here as it applies to the six-month system.

Smectite-to-illite transformation is not well understood and probably follows several different reaction pathways, i.e. solid-state transformation and dissolution-precipitation (Güven, 2001; Dong, 2005; Zhang et al., 2007). These different reaction mechanisms may be due to different geological or experimental conditions, including variables such as water/rock ratio, fluid composition, redox state, occurrence of microbial organisms, and presence or absence of organic matter (Small et al., 1992; Small, 1993; Güven, 2001; Dong, 2005; Zhang, et al. 2007). Solid-state transformation may be operative in closed systems with a low water/rock ratio, whereas, dissolution-precipitation may be the dominant mechanism in open systems with high water/rock

ratios (Zhang et al., 2007). In the current experiments, it appears that two major parameters are preventing smectite-to-illite alteration: alkali and silica solution compositions.

Current experimental results are consistent with other experimental data showing that a limited supply of K^+ along with a relatively high Na^+ activity significantly decreases dioctahedral smectite illitization rates (Eberl and Hower, 1977; Eberl, 1978, Eberl et al., 1978; Roberson and Lahann, 1981; Mosser-Ruck et al., 1999). Their studies also show that, in general, dioctahedral smectites with low hydration-energy interlayer-cations (e.g., K^+, Rb^+, Cs^+) are more susceptible to smectite-to-illite alteration reaction compared to dioctahedral smectites with higher hydration-energy interlayer-cations (e.g., Na^+, Ca^{2+}, Mg^{2+}). These results are consistent with capsule experiments from the current work. However, the presence of a Na-rich system does not preclude smectite illitization. There have been numerous occurrences of illite and illite/smectite occurring in natural or experimental systems that are Na-dominated (Bannister, 1943; Frey, 1969; Eberl and Hower, 1977; Eberl et al., 1978; Whitney and Velde, 1993; Mosser-Ruck et al., 1999; Środoń, 1999). But, in all these cases, either the temperatures exceeded 300°C or there was a significant potassium source from groundwater or coexisting minerals. Temperatures beyond 300°C exceed the upper temperature limits expected for a repository environment and the experimental temperature from this investigation (Greenburg and Wen, 2013). Additionally, Na-bentonites are currently the bentonite of choice for a repository backfill, thereby, providing a K-depleted and Na-enrich system. Even though the aqueous solutions in the current experiments were K-rich, the overall system (bentonite + water) was Na^+ dominant (~ 2,400 mg Na/L) and K^+ poor (~ 1,000 mg K/L). Include Ca^{2+} (~750 mg/L, bentonite + water) in the discussion, the overall $(Na^+ + Ca^{2+})/K^+$ ratio is greater than 3.0. It is evident that the dominance of Na^+ and Ca^{2+} along with the low abundance of K^+ does not facilitate illite-smectite formation after 45 days at 300°C.

Silica activities in these experiments appear to be controlled partially by silicate mineral dissolution and precipitation, in addition to clinoptilolite to analcime alteration. Solutions saturated with respect to cristobalite probably contributed to illitization retardation in these current experiments. Systems with silica concentrations higher than quartz saturation have been shown to significantly retard illitization rates (Eberl et al., 1978; Lahann and Roberson, 1980; Abercrombie et al., 1994). Abercrombie et al., (1994) has shown that a K-smectite to be the stable phase,

potentially up to 200 °C, provided silica activity is higher than ~10^{-2}. It was noted by Abercrombie et al., (1994) that as silica levels decreased, due to quartz precipitation, illitization progressed within the system. Therefore, an environment with silica concentrations saturated with respect to cristobalite at temperatures less than 300°C, such as the current experiments, smectite-to-illite alteration should further be inhibited. However, it is important to consider differences between closed, experimental systems versus geological or repository environments that open to the surrounding environment. Many processes that are observed in a closed, experimental system might be mitigated in an open system where solutes can freely move in and out of the environment.

We have shown that at higher silica activities (i.e., cristobalite saturation) clinoptilolite is altered to a high-silicon analcime under the current experimental conditions. Again, these reactions were observed in the other EBS experiments with extended periods at 300 °C. Previous studies (Smyth, 1982; Wilkin and Barnes, 1998; 2000; Cheshire et al., 2013; 2014a) have linked changes in Na, Al, and Si activities with the alteration of clinoptilolite by analcime. However, experimental work (T < 300°C) from Wilkin and Barnes (1998) indicate silica activity influences clinoptilolite alteration by affecting the reaction affinity rather than controlling the reaction equilibrium. Wilkin and Barnes (1998) also show that analcime can form in an environment saturated with respect to cristobalite provided there is a sufficient change in the Na and/or Al activities.

The effect on the repository due the changes in the system's silica phases and concentrations appears to be a significant issue regarding the repository stability and physical properties. Cementation via silica precipitation is believed to pose the greatest risks to the repository stability and isolation capability compared other mineral reaction (Pusch et al., 1998). Silica precipitation has the potential to weld the smectite lamellae together and reduce the smectite expandability (Pusch et al., 1998; Pusch, 2001). The primary mechanism for silica liberation includes smectite illitization, silica/silicate dissolution/saturation, and zeolite alteration.

As noted before, illite is precluded from forming in the bentonite only matrix experiments and is linked to silica oversaturation (Figure 2) and low K bulk content. Herbert, et al. (2016) performed experiments at low temperature (<90 ºC) on MX-80 bentonite in oxidizing conditions to investigate illitization. A main conclusion was that if the resulting reaction was silica oversaturated, illite would not form. However, smectite was created instead. Once again this agrees with our experimental results. Experiments EBS-20 to EBS-22 all contain appreciable illite. The

petrogenic origin of the illite in the run products may be due to the presence of illite in the Opalinus Clay (acting as nucleation sites) or the difference in bulk composition. This is readily reflected in that EBS-22 shows 50% illite (App. C, Figure C-1.) and the groundmass was Opalinus Clay only.

Zeolite formation. Authigenic zeolites were formed in the 300 °C experiments, EBS-14 through EBS-20, and the 200 °C experiment, EBS-23. The zeolite phases produced in experiment EBS-19 include both clinoptilolite and an analcime$_{55}$-wairakite$_{45}$ isometric zeolite (App. E, Figure F-13). When plotted on Si/Al vs percent analcime diagram (Figure 9), certain trends become obvious. There is a clear solid solution series from EBS-14 to EBS-17, with silica increasing slightly toward the analcime end-member. Sample EBS-18 was held at high pressure for 9 months, as discussed above. This co-existence of both clinoptilolite and "wairakite" within EBS-18 may also be due to long term pressurization of the reactant material. It is believed that the clinoptilolite was allowed to recrystallize from the original small grains and also transform the remnant glass shards into clinoptilolite. In addition, the samples that cluster with a Si/Al ratio between 4.5 and 5.0 were either the ramped temperature experiment (held at 300°C for only a short time) or was the starting material (MR Bentonite) from Colony, Wyoming and represent clinoptilolite or remnant glass. There is now a fairly continuous solid solution in the analcime-wairakite series from EBS-14 to EBS-17.

Cheshire et al. (2014) noted that clinoptilolite (Figure 3a) was the precursor zeolite that transformed to analcime at high temperature. The reaction was listed as:

Clinoptilolite + Na^+ + Ca^{2+} → Analcime + SiO_2 + H_2O + K^+ + Fe^{2+} + Mg^{2+}:

$(Na_{4.30},Ca_{0.39},K_{0.14},Mg_{0.20})(Si_{29.82},Al_{6.28},Fe_{0.03})O_{72}\cdot 21H_2O + 0.92Na^+ + 0.02Ca^{2+}$ →

$8.16(Na_{0.64},Ca_{0.05})(Si_{2.23},Al_{0.77})O_6\cdot 1H_2O + 0.14K^+ \; 0.20Mg^{2+} + 11.62SiO_{2(aq)} + 12.64H_2O + 0.03Fe^{2+} + 0.20H_2$

Table 6 presents data on the high temperature zeolite phase in all EBS experiments that contain Opalinus Clay as part of the mixture. Note that the experiments with bentonite only produce analcime (Na-rich, monoclinic) phases (Figure 3b). The experiment with Opalinus Clay only (EBS-14) indicates the zeolite wairakite (Ca-rich, triclinic) has grown at high temperature. Of great interest are experiments EBS-15 through EBS-20 (and EBS-23 with Portland Cement added), which contain a mixture on Wyoming bentonite as backfill and Opalinus Clay as the wall rock. The resultant zeolite produced is intermediate between analcime and wairakite in composition

(Table 6). This agrees with Seki (1971) and expands the solid solution fields that he described. The generalized reaction between the two zeolite phases with complete exchange of Na and Ca is shown below:

Wairakite → Analcime

$$\mathbf{CaAl_2Si_4O_{12}\cdot 2(H_2O) + 2Na^{+} \rightarrow Na_2Al_2Si_4O_{12}\cdot 2(H_2O) + Ca^{++}}$$

Table 6. Average compositions of post reaction zeolites

Sample	**Analcime–Wairakite solid solution**
EBS-14	An_{22}–Wrk_{78}
EBS-15	An_{64}–Wrk_{36}
EBS-17	An_{64}–Wrk_{36}
EBS-18	An_{37}–Wrk_{63}
EBS-19	An_{54}–Wrk_{46}
EBS-20	An_{52}–Wrk_{48}
EBS-21 (glass-no zeolite present)	An_{91}–Wrk_{9}
EBS-22	**None present**
EBS-23 (matrix)	An_{68}–Wrk_{32}
EBS-23 (coating Opalinus Clay)	An_{79}–Wrk_{21}

Reflected light and SEM images of the reacted Opalinus Clay show that analcime–wairakite crystals form within cracks in the wall rock material (e.g., Appendix F, Figures F-1, F-4, F-7, F-9, F-17). This is indicative of the complete sample, in that the zeolite forms only on the edges or within cracks of the Opalinus Clay. All petrographic evidence indicates that the Opalinus Clay shale has such limited porosity and permeability that the resultant wairakite crystals cannot grow in the matrix. They are relegated to leaching aluminum and silica from the wall rock and nucleating at the rock surface.

The primary authigenic zeolite in experiments with Opalinus Clay alone (EBS-14) differs from the Opalinus Clay experiments with bentonite (all other Opalinus experiments). These differences appear to be strongly related to the solution chemistry. Bentonite-bearing experiments most likely exchanged Ca into the montmorillonite interlayer producing a Ca depleted solution compared to

the Opalinus Clay experiments. Solution chemistry associated with the Opalinus clay will remain fairly unchanged unless mineral alteration occurs. The changing of solution chemistry as function of the types of clays in the system appears to indirectly control zeolite stability. The EBS-23 experiment (bentonite/Opalinus Clay/cement solids) is heavily enriched in Ca. Although the reaction conditions were at 150 bar and only 200°C abundant wairakite-rich end member zeolite was created. This was most likely due to the enhanced Ca concentration and relatively high pH of 9.1 (Wilkin and Barnes, 1998; 2000).

The analcime-wairakite$_{ss}$ series typically forms through dissolution-precipitation mechanisms through an intermediate mineral or glass phase. In the other EBS experiments, it appears that analcime formed from a direct dissolution-precipitation at the expense of precursor clinoptilolite and volcanic glass. This paragenetic sequence has been previously observed by many other researchers (Smyth, 1982; Masuda et al., 1996; Wilkin and Barnes, 1998). Natural paragenetic sequences suggest that clinoptilolite to analcime may progress at temperatures as low as 75–90 °C (Smyth 1982; Masuda et al. 1996). Alternatively, work from Wilkin and Barnes (1998; 2000) shows analcime formation kinetics are significantly increased at alkaline pH's (9–10), whereas, experiments with circum-neutral pH's showed limited to no analcime formation even at with temperatures >100°C lasting up to 26 days. It is evident that onset temperatures associated with mineral alterations that pH, along with many other solution chemistry parameters, are important to understand.

Wairakite primarily forms when excess silica is present and typically crystallizes through either an intermediate Ca-mordenite ($CaAl_2Si_{10}O_{24}\cdot 7H_2O$) or laumontite ($CaAl_2Si_4O_{12}\cdot 4H_2O$) phase (Ames and Sands, 1958; Jové and Hacker, 1997). In their experimental works, wairakite lower limit of formation is around 315 °C, with an upper limit of 450 °C. However, the inclusion of small amount of Na-substitution lowers the formational conditions for wairakite. Additionally, there are limited isomorphous substitutions between analcime and wairakite making Na- or Ca-enriched end members, as opposed of a true intermediate analcime-wairakite$_{ss}$ (Steiner, 1955; Coombs, 1955; Ames and Sands, 1958). Na-mordenite has an experimental stability range between 190 to 300°C, whereas, Ca-mordenite ranges from 340 to 380 °C (Ames and Sand, 1958).

The possible presence of mordenite and laumontite combined with information from Ames and Sand (1958) and Jové and Hacker (1997) strongly suggests that wairakite in this system is probably from the decomposition of mordenite and/or laumontite. Mordenite and laumontite, therefore,

appears to have crystallized from the decomposition of kaolinite in the silica and Na/Ca-rich fluids. This reaction would have progressed either until the reaction was quenched or when one of the reactants was depleted and in this case, kaolinite appears to be the limiting resource as it has been completely removed. The presence of Na in our system appears to have lowered the formation temperatures to below 300°C for Na-enriched wairakite.

However, when bentonite is included into Opalinus Clay experiments, the solution chemistry changes significantly forcing the formation of a high-silicon, Ca-enriched analcime. The analcime composition from this experiment is similar to analcime from EBS experiments with bentonite as the only clay. However, it is evident that the reaction mechanisms are very different. In bentonite only reactions, high-silicon analcime crystallized from clinoptilolite and unaltered glass with in the high Na and $SiO_{2(aq)}$ fluids. EBS experiments with 20 wt. % Opalinus Clay much of the original clinoptilolite is preserved, but kaolinite is completely removed. When kaolinite and clinoptilolite are present in a Na/Ca-rich fluid, kaolinite is preferentially recrystallized into either Na/Ca-mordenite and laumontite or analcime.

H_2S Generation

All experiments generated $H_2S_{(aq,g)}$, with the 300 °C isothermal reactions producing the gas faster and in greater quantities. The $H_2S_{(aq,g)}$ is most likely related to pyrite solubility in a chloride-bearing solution (Crerar et al., 1978; Ohmoto et al., 1994). The reducing nature of the experimental system easily preserved the $H_2S_{(aq,g)}$ species. Pyrite contents obtained by QXRD analyses for the Colony Wyoming bentonite (0.4 wt%) and Opalinus Clay (1.1 wt%) are listed in Table 4, Table 5, and Table C-1. Sulfide-induced corrosion of the waste canisters is the primary concern for the Swedish repository systems (Börjesson et al., 2010), therefore the Swedish Nuclear Fuel and Waste Management Company (SKB) have emplaced fairly strict sulfur specifications (sulfide content < 0.5 wt. %; total sulfur < 1 wt. %) for the bentonite buffer used in their repositories (Börjesson et al., 2010).

pH effects

Many of the reactions described above are strongly influenced by the pH of the system. Most mineral reaction rates that are of concern to a repository are increased under high pH systems. Chermak (1992) showed that under pH conditions of 11-13, Na-rectorite was formed at 150 – 200°C within 17 days. Fully formed Na-mica (paragonite) developed after 32 days. Work from Eberl and Hower (1977) and Eberl (1978) do not show illitization until 260 – 400°C at quenched

pH's ranging from 4–5. These observations are consistent with the current research. The Opalinus Clay experiment starts with a 7.5–7.8 solution pH, but during the reaction the pH drops to 4–5 (Figure 5). Experiment EBS-23 (cement) had a higher ending pH of 8–9 (Figure 5). The reactions experience significant zeolite reactions, and it appears illitization does occur under the Opalinus Clay-present environment. These high pH dependent reactions will play a major factor within the bentonite backfill near the concrete liners, especially if the concrete used contains significant K^+ concentrations. However, these same reactions should have a minor impact on the bentonite backfill near the waste package because steel and copper corrosion tend to lower the pH.

3.2 Summary of Steel Corrosion Rates

Corrosion rates (Table 7) were determined by dividing the average corrosion pit depth by the number of days in the run. Stainless steel (SS) corrosion rates from the isothermal experiments on bentonite and bentonite + Opalinus Clay are within experimental error of each other, with 304 SS exhibiting slightly higher corrosion rates than 316 SS. The corrosion rate for the four week ramped experiment (EBS-2, 304 SS) was lower than that of the isothermal experiments, 0.31 μm/day for the ramped versus ~ 0.40 μm/day for the isothermal experiments. However, for the 316 SS experiments, the corrosion rate for the ramped temperature experiment (0.27 μm/day) was roughly equivalent to that of the isothermal experiments (average of 0.26 μm/day). The six-month experiment with 316 SS had a much smaller average corrosion rate of 0.07 μm/day. This is consistent with the reduced corrosion rate being constrained by either the phyllosilicates either mantling the metal surface or lack of a reaction component (i.e., O_2, SO_4).

Table 7. Phyllosilicate (Fe-saponite / chlorite) growth and steel corrosion rates. Rates in µm are given per day. Three steel types were examined: 304 stainless steel (SS), 316 SS, and low carbon steel (LCS). The LCS corrosion mechanism was via pit corrosion, while 304 SS and 316 SS were by general corrosion. SAP stands for Phyllosilicate (Fe-saponite / chlorite) growth rates whereas CORR denotes steel corrosion rates.

Sample	Metal Type	Matrix	Temp. (°C)	SAP / Day	CORR / DAY
	304 SS				
EBS 2	304	Bentonite	125, 210, 300 °C - 4wk	0.95	0.31
EBS 5	304	Bentonite	300°C - 6wk	ND	0.43
EBS 19	304	Bent + Opal Clay	300°C - 6wk	2.66	0.38
			Average:	**1.81**	**0.37**
	316 SS				
EBS 3	316	Bentonite	125, 210, 300 °C 4wk	1.57	0.27
EBS 10	316	Bentonite	300°C - 6wk	0.61	0.29
EBS 15	316	Bent + Opal Clay	300°C - 6wk	0.98	0.23
			Average:	**1.05**	**0.26**
EBS 13	**316 SS**	**Bentonite**	**300°C - 6 Months**	**0.41**	**0.07**
	LCS				
EBS 6	LCS	Bentonite	300°C - 5wk	0.99	1.08
EBS 18	LCS	Bent + Opal Clay	300°C - 3wk	3.56	2.81
			Average:	**2.28**	**1.95**

The phyllosilicate (Fe-saponite/chlorite) growth and steel corrosion rates determinations produced the general findings as follows and the summary data for corrosion measurements are in Table 7. The low carbon steel corrosion mechanism was via pit corrosion, while 304 SS and 316 SS were by general corrosion. The low carbon steel corrosion rate (1.95 µm/day) was more rapid than the stainless steel samples. The 304 SS corrosion rate (0.37 µm/day) was slightly accelerated versus the 316 SS corrosion rate (0.26 µm/day). Note that the six month 316 SS experiment shows inhibited corrosion rates (0.07 µm/day). This may be in part due to mantling by the Fe-saponite/chlorite authigenic minerals. All phyllosilicate growth rates at the interface exhibit similar growth rate patterns to the steels (i.e., LCS>304>316> 316 six month).

The nature of corrosion pitting in the low carbon steel varied with the bulk composition of the experiments. The bentonite only matrix experiment had a lower corrosion rate (1.08 µm/day),

while the bentonite + Opalinus Clay matrix experiment corrosion rate was almost 3 times higher (2.81 μm/day). This higher corrosion rate can be attributed to the high pyrite content in the Opalinus Clay fraction. A wide variety of corrosion pit structures exist in the low carbon steel experiments (Figures 15, 16, and 17), but extremely deep corrosion pits are just as common as shallow wide ones.

3.2.1 Steel Corrosion Rates

In most of the experiments the phyllosilicates form a thick layer over a corroded/pitted layer. This layer is visible both in the SEM images of Fe corrosion (Appendix F, F-11) and the reflected light images. A notable exception to this is EBS-5, where the silicate layer was found to be absent (potentially due to removal during sample preparation for reflected light). For the ramped temperature experiments EBS-2 (304 SS) and EBS -3 (316 SS), the average phyllosilicate thicknesses were significantly different (0.95 μm vs 1.57 μm, respectively). In the isothermal experiments for stainless steel, the bentonite only (EBS-5, EBS-10) interface layer was thinner than the bentonite + Opalinus Clay (EBS-15, EBS-19) experiments, 0.61 μm/day and 1.82 μm/day, respectively. The phyllosilicate layer was thinner in the six-month long-term cooling run (EBS-13) with a depth of only 0.41 μm/day. For the nine experiments a total of 4291 measurements were made, with 1791 measurements of the phyllosilicate layer and 2500 measurements of the corrosion depth. The short-term isothermal experiments in both bentonite and Opalinus Clay yielded different average pit corrosion depths for the two steel types (304 and 316), 14.93 μm and 10.75 μm respectively. However, the six-month experiment (EBS-13) for 316 stainless developed only 13.7 μm corrosion depth, which is similar to that of EBS-15, but sustained over a much longer period of time.

Corrosion rates were determined by dividing the average corrosion pit depth by the number of days in the run. Stainless steel corrosion rates from the isothermal experiments on bentonite and bentonite + Opalinus Clay are within experimental error of each other, with 304 SS exhibiting slightly higher corrosion rates than 316 SS. The corrosion rate for the four week ramped experiment (EBS-2, 304 SS) was lower than that of the isothermal experiments, 0.31 μm/day for the ramped versus ~ 0.40 μm/day for the isothermal experiments. However, for the 316 SS experiments, the corrosion rate for the ramped temperature experiment (0.27 μm/day) was roughly equivalent to that of the isothermal experiments (average of 0.26 μm/day). The six-month

experiment with 316 SS had a much smaller average corrosion rate of 0.07 μm/day. This is consistent with the reduced corrosion rate being constrained by either the phyllosilicates either mantling the metal surface or lack of a reaction component (i.e., O_2, SO_4).

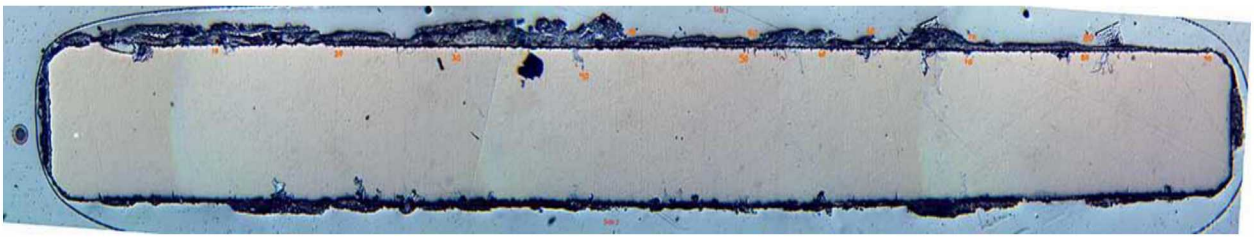


Figure 15. Example of LCS coupon image used for corrosion calculation. Sample of EBS-18 coupon used for corrosion measurement. Blue region is epoxy, dark region is phyllosilicate coating around steel, grey region is steel coupon. Orange dots are location of corrosion /silicate growth measurements.

The nature of corrosion pitting in the low carbon steel varied with the bulk composition of the experiments. The bentonite only matrix experiment had a lower corrosion rate (1.08 μm/day), while the bentonite + Opalinus Clay matrix experiment corrosion rate was almost 3 times higher (2.81 μm/day). This higher corrosion rate can be attributed to the high pyrite content in the Opalinus Clay fraction. A wide variety of corrosion pit structures exist in the low carbon steel experiments (Figures 16 and 17), but extremely deep corrosion pits are just as common as shallow wide ones.

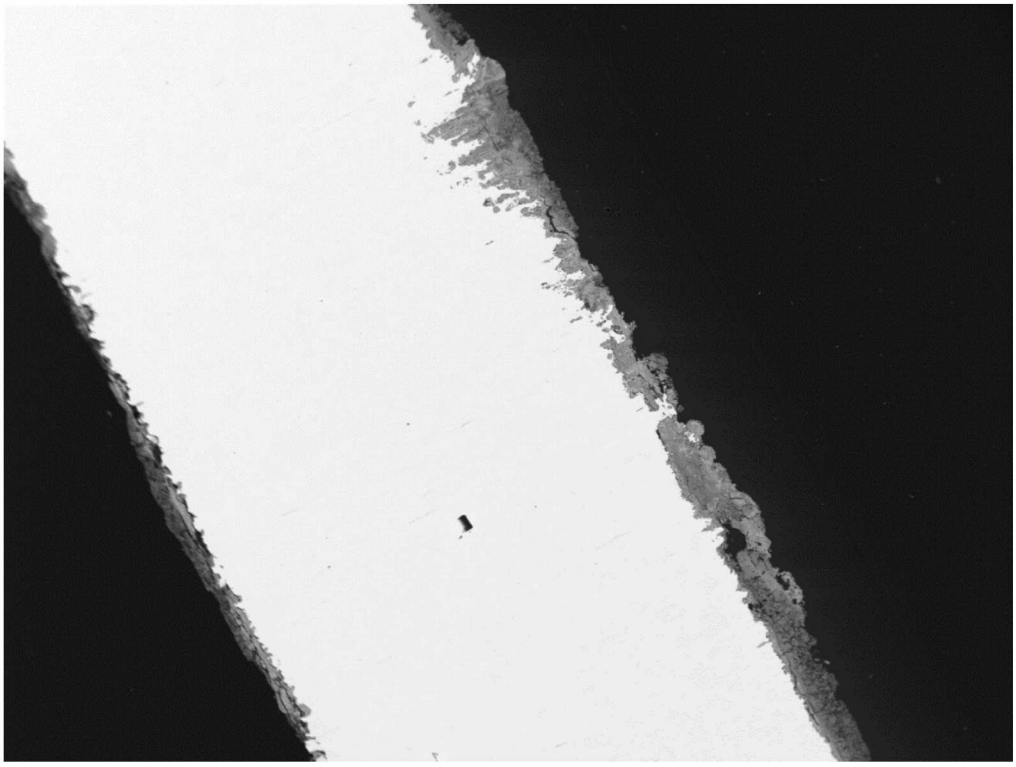


Figure 16. Note abundant pit corrosion in upper right region of EBS-18 low carbon steel (LCS) sample

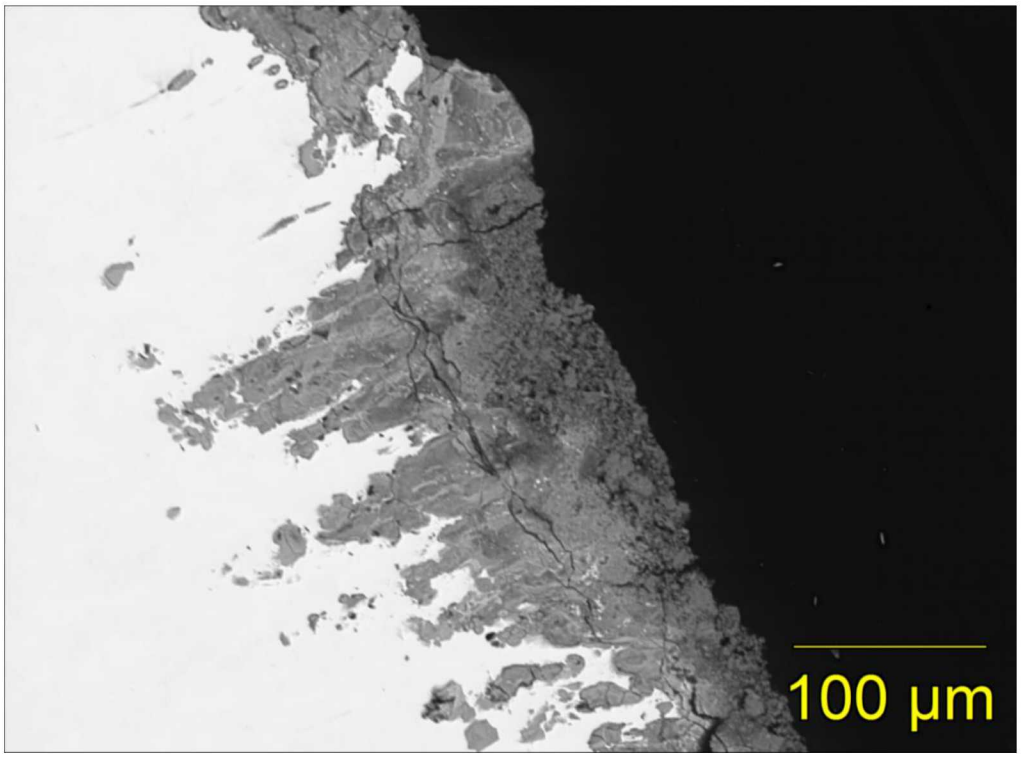


Figure 17. Pit corrosion of low carbon steel (LCS) in experiment EBS-18. The maximum depths of the pits exceed 100 microns and their width is approximately 50 microns.

3.3 Summary of Steel-Bentonite Interface Mineralogy

The following mineral phases have been previously identified (Caporuscio et al., 2014) as growing at the interface between bentonite backfill and various steels: Fe-saponite ((Ca/2,Na),3(Fe^{++})3(Si,Al)$_4O_{10}(OH)_2$, pentlandite ((Fe,Ni)$_9S_8$) (Figure 5), chromite ($Fe^{++}Cr_2O_4$), pyrrhotite (FeS) (Figure 7), millerite (NiS). We have just recently identified another interface material: stilpnomelane (Figure 18). This Fe-bearing phase seems to only occur when mantling iron metal (one of our solid buffer materials).

Although stilpnomelane is a common metamorphic mineral and occurs over a wide P, T spectra (Winkler, 1976) there is a dearth of occurrences reported in experimental literature. Similar experimental work by Ferrage (2011), Mosser-Ruck et al. (2010), Guillaume, et al. (2003) and Munier (1998) do not report this mineral phase in their reaction products. The chemical formula of stilpnomelane [K (Fe^{++},Mg, Fe^{+++})$_8$(Si,Al)$_{12}$(O,OH)$_{27}$] indicates that iron occurs in both oxidation states. Given that the iron metal in our experiments (Figure 18) is mantled first by an iron oxide (magnetite?), followed by an Fe sulfide (pyrrhotite) and finally by stilpnomelane, there is a potential that micro-domains of differing oxygen fugacity may be at play. This phenomena and mineral genesis deserves further investigation concerning iron corrosion.

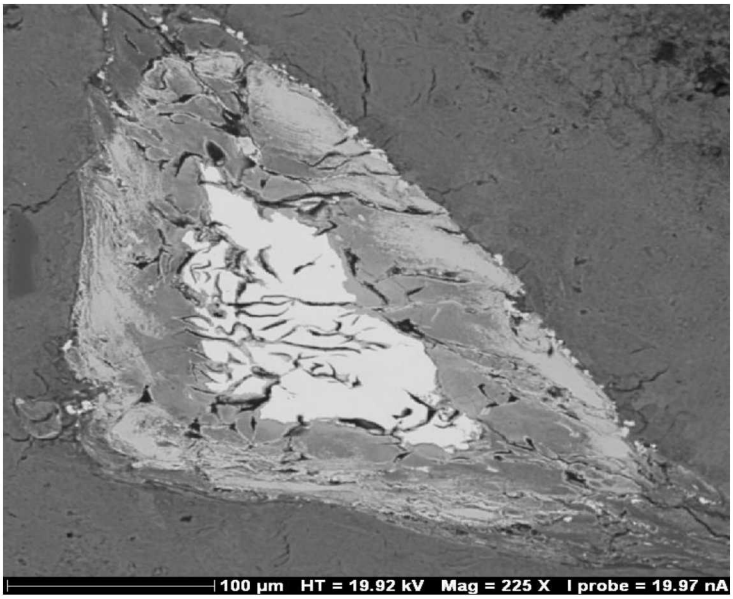


Figure 18. BSE image of iron metal with concentric alteration zones from EBS-15. Bright white core is remnant iron metal, dark grey is iron oxide, light grey is an iron sulfide (probably pyrrhotite) remaining mottled intermediate grey is stilpnomelane.

The following describes the steel interface mineralization for the three types of steel used in the Opalinus clay experiments.

304 SS. 304 stainles stee (SS) underwent uniform interface reaction during the 300 °C experiments. Post-reaction 304 SS formed a layer of smectite and chlorite covering the surface of the steel plate (Figure 19 A, B). However, smectite was the only phyllosilicate associated with the reaction site products in the six week, 300 °C reaction (Figure 19 C, D). The primary type smectite associated with the steel surface appears to be an Fe-saponite. Smectite expands upon ethylene glycol saturation to 16.8 Å (with 002 at 8.35 Å) suggesting no significant amount of mixed-layering is present. Pentlandite ((Cu, Ni, Fe)-sulfide) appears to have formed sparingly in both 304 SS experiments along with an unknown fibrous material (Figure 19 A, B). The smectite and chlorite morphologies tend to be fairly consistent producing a bladed to micaceous habit with a rose-like texture (Figure 19). The initial montmorillonite has a distinctly different morphology (foily; Figure 19C) suggesting smectite associated with the 304 SS is newly formed. The interface reaction products have thicknesses ranging from 9 to 44 μm with crystallites occurring perpendicular to 304 SS substrate (Figure 19D). There was no significant change in the interface layer thicknesses with increased reaction time at 300°C. Chemical analyses of post-reaction 304 SS and the smectite mantle indicates there was a slight Fe transfer from the 304 SS forming a Cr-enriched steel outer layer and a Fe-rich smectite and chlorite coating (Figure 20). The reaction products do include varying degrees of Cr and Ni substitutions. Accurate chemical formula for the interface reaction products are not possible due to the intimate mixing of multiple phases. The average bulk chemistry of the corrosion layer is provided in Appendix F.2. Fe-rich phyllosilicates that formed on steel plates in the ramped experiments have two 06ℓ diffraction bands 1.536 and 1.523 Å (9.138 and 9.216 Å b-parameters), corresponding to trioctahedral chlorite and smectite (Figure 21). It is uncertain which minerals species correspond to the b-parameters as there is overlap in the unit-cell parameters between the Mg, Fe-saponites (9.120 (Mg^{2+}) to 9.30 (Fe^{2+}) Å) and chlorite (9.228 to 9.294 Å) species (Kohyama et al. 1973; Moore and Reynolds 1997). The Fe-smectite produced in the six week, 300°C experiment has a 1.547 Å (9.282 Å b-parameters) 06ℓ diffraction band, consistent with Fe-saponite (Kohyama et al. 1973).

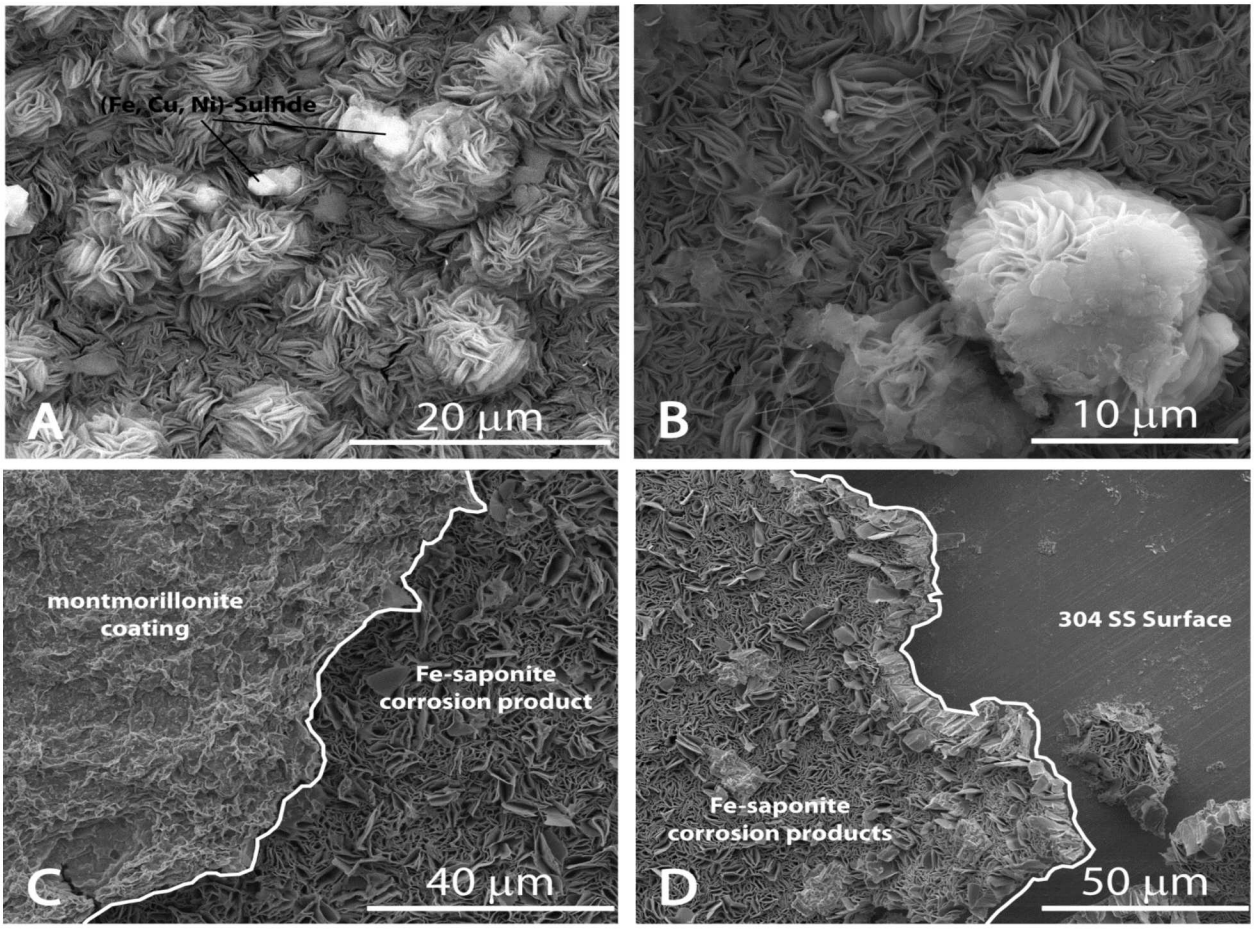


Figure 19. SEM image (plan view) of Fe-phyllosilicates (saponite and chlorite) using 304 SS as a growth substrate from both ramped (EBS-2) and isothermal, 300°C (EBS-5) heating profiles. [A] Fe-saponite and chlorite growths with later-stage pentlandite-like ((Fe, Cu, Ni)-sulfide) material from EBS-2. [B] Unknown fibers overlaying rose-like Fe-saponite and chlorite interface reaction products from EBS-2. [C] Montmorillonite coating on Fe-saponite showing the distinct morphology between the two smectites from EBS-5. [D] Boundary between the Fe-saponite interface reaction product and 304 SS surface from EBS-5.

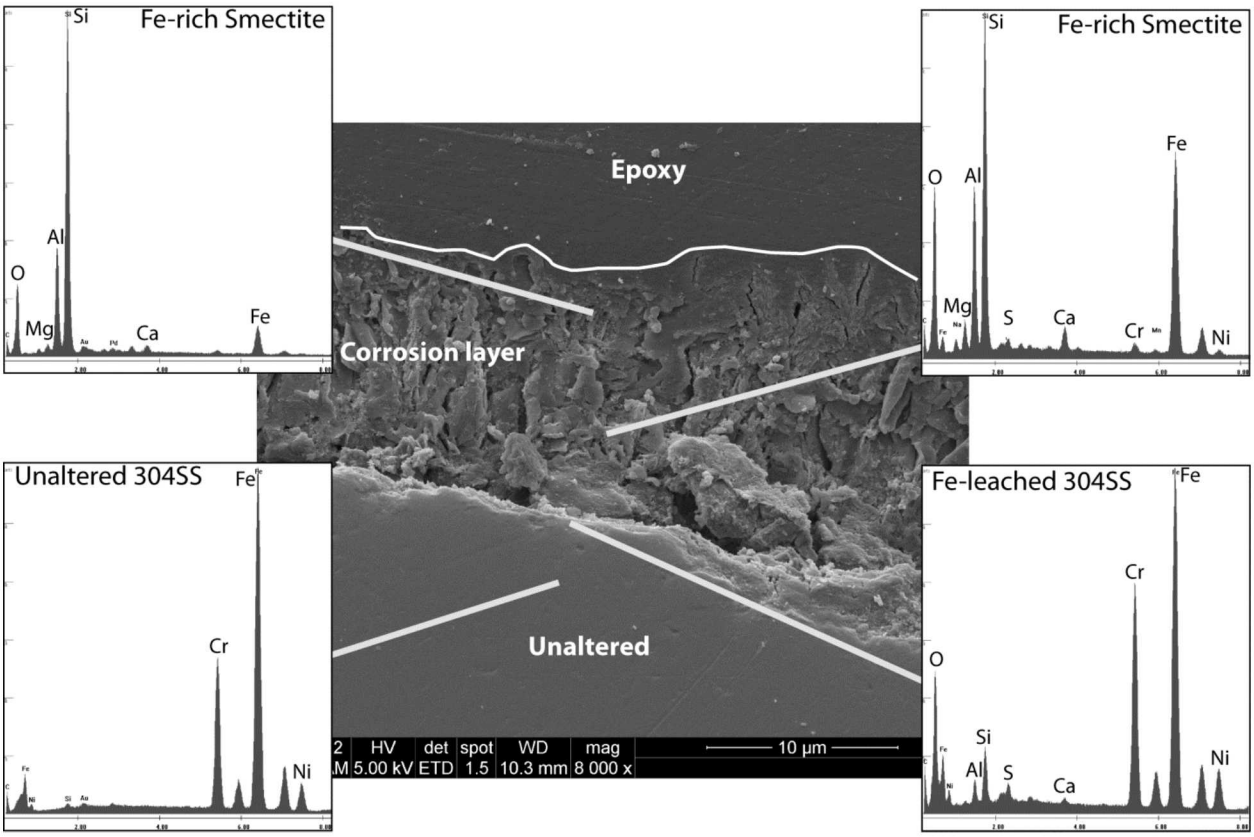


Figure 20. SEM image of 304 SS cross-section showing Fe-saponite interface reaction products using steel surface as a growth substrate. EDX analyses of post-reaction 304SS and interface reaction products indicates Fe is leached from the 304 SS forming a slightly Cr-enriched steel outer layer and an Fe-rich aluminosilicate (Fe-saponite/chlorite) coating. Uniform corrosion of the 304SS does not appear to develop significant incongruent dissolution.

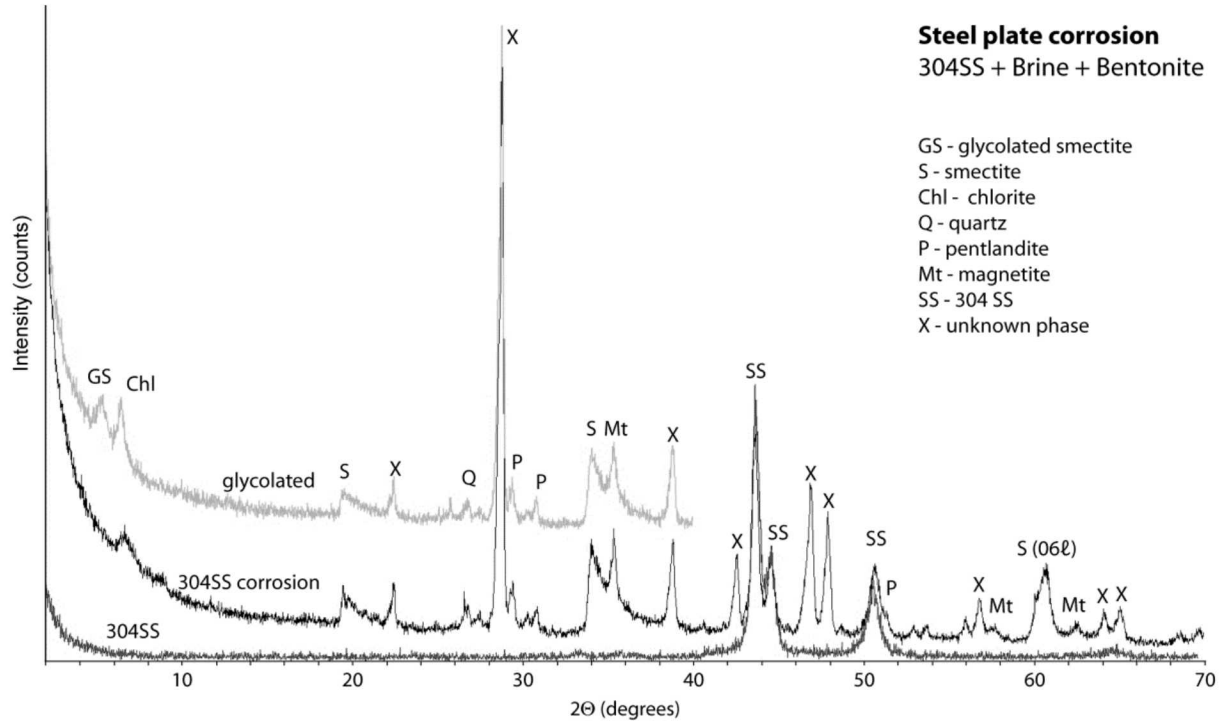


Figure 21. XRD patterns of the air-dried and ethylene glycol saturated corrosion products on the 304 SS plate used in the EBS-2 experiment. Smectite, chlorite, and pentlandite are the dominant interface reaction phases. Starting 304 SS XRD plot is also shown for comparison.

316SS. 316 stainless steel (SS) underwent exfoliation corrosion during the ramped and isothermal, 300 °C experiments. Post-reaction 316 SS formed smectite dominated interface reaction products with some chlorite covering the surface of the steel plate (Figure 22 A, B). However, smectite was the only phyllosilicate associated with interface reaction products in the six week, 300 °C reaction (Figure 22 C, D). The primary type smectite associated with the steel surface appears to be an Fe-saponite. Smectite expands to 16.8 Å (with 002 at 8.44 Å) upon ethylene glycol saturation suggesting no significant amount of mixed-layering is present. However, the six weeks, 300°C smectite product expands to 16.3 Å (002 at 8.25 Å) upon ethylene glycol saturation indicating a possible decrease in swelling capacity. A pentlandite-like ((Cu, Ni, Fe)-sulfide) material appears to have also been formed in both 316SS experiments along with what appears to be fibrous sulfides (Figure 22D). The smectite and chlorite morphologies tend to be fairly consistent producing a bladed to micaceous habit with a rose-like texture (Figure 22). The interface reaction products have thicknesses ranging from 20 to 40 μm with crystallites occurring perpendicular to 316 SS substrate (Figures 23 and 24). There was no significant change in the

interface reaction layer thicknesses with increased reaction time at 300 °C. Chemical analyses of post-reaction 316 SS and mantling products indicates there was significant Fe leaching from the 316 SS forming a Cr-enriched steel outer layer up to 4 μm thick. The Cr-enriched layer also underwent oxidation and sulfidation producing a noticeable alteration zone (Figure 23). Smectite and chlorite coatings were enriched in iron most likely from the iron leached from the 316 SS (Figure 24). Fe-rich phyllosilicates that formed on steel plates in the ramped experiments have 06ℓ diffraction bands 1.535 (9.210 Å b-parameters), corresponding to a trioctahedral phyllosilicate (Figure 25.; Kohyama et al. 1973; Moore and Reynolds 1997). It is uncertain which minerals species correspond to the b-parameters, however the b-parameter is probably related to an Fe-saponite due to a smectite dominance in the corrosion products. The Fe-smectite produced in the six week, 300 °C experiment has a fairly broad 1.54 Å (9.24 Å b-parameters) 06ℓ diffraction band, consistent with Fe-saponite (Kohyama et al. 1973).

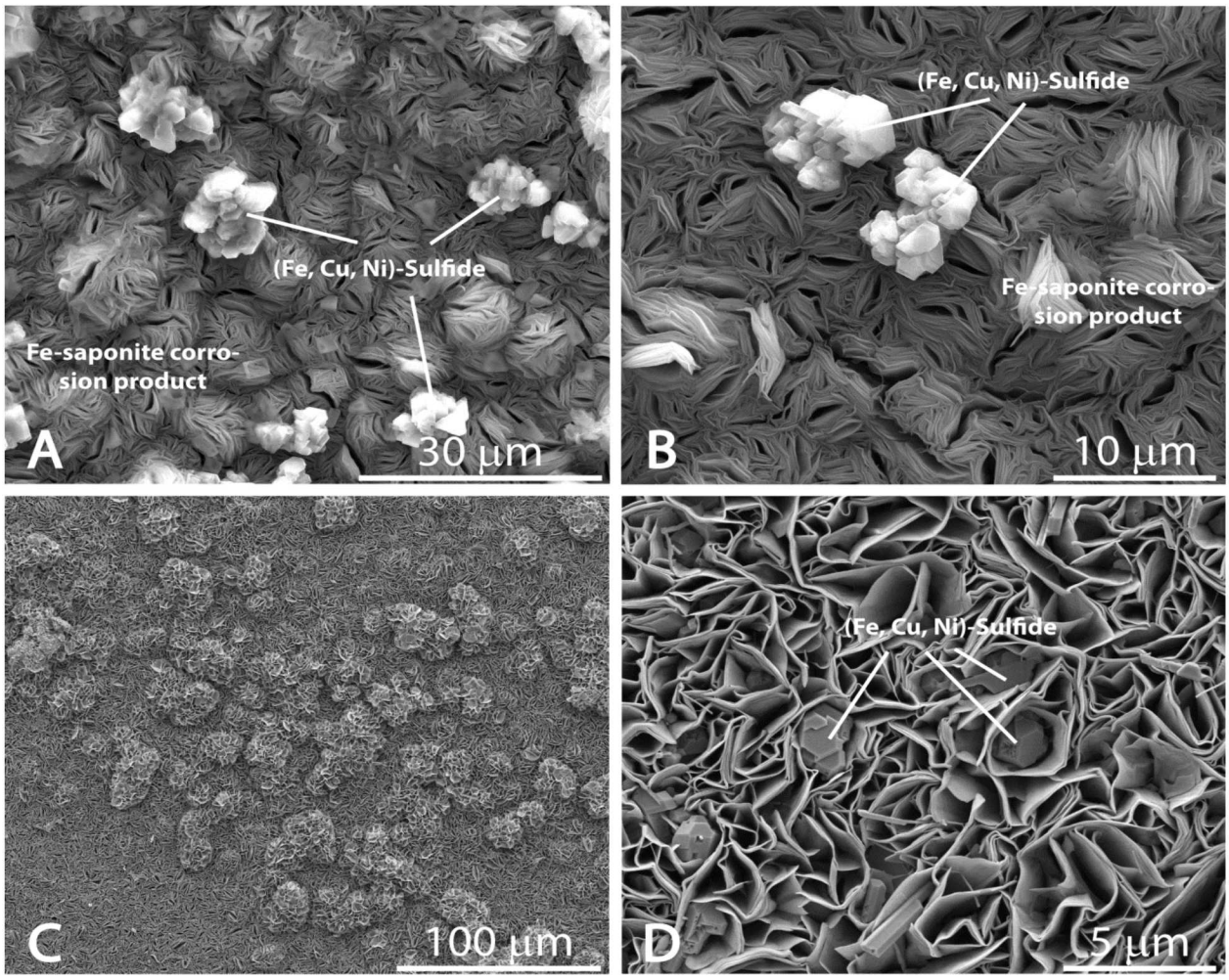


Figure 22. SEM image (plan view) of Fe-saponite using 316 SS as a growth substrate from both ramped (EBS-3) and isothermal, 300°C (EBS-10) heating profiles. [A] Dense growth of Fe-saponite and chlorite with late-stage pentlandite-like ((Fe, Cu, Ni)-sulfide) material from EBS-3. [B] Close-up of pentlandite-like ((Fe, Cu, Ni)-sulfide) material on Fe-phyllosilicates from EBS-3. [C] Honeycomb and rose-like textures associated with Fe-saponite interface reaction products from EBS-10. [D] Fe-saponite rose-like texture with pentlandite-like materials occurring between Fe-saponite foils from EBS-10.

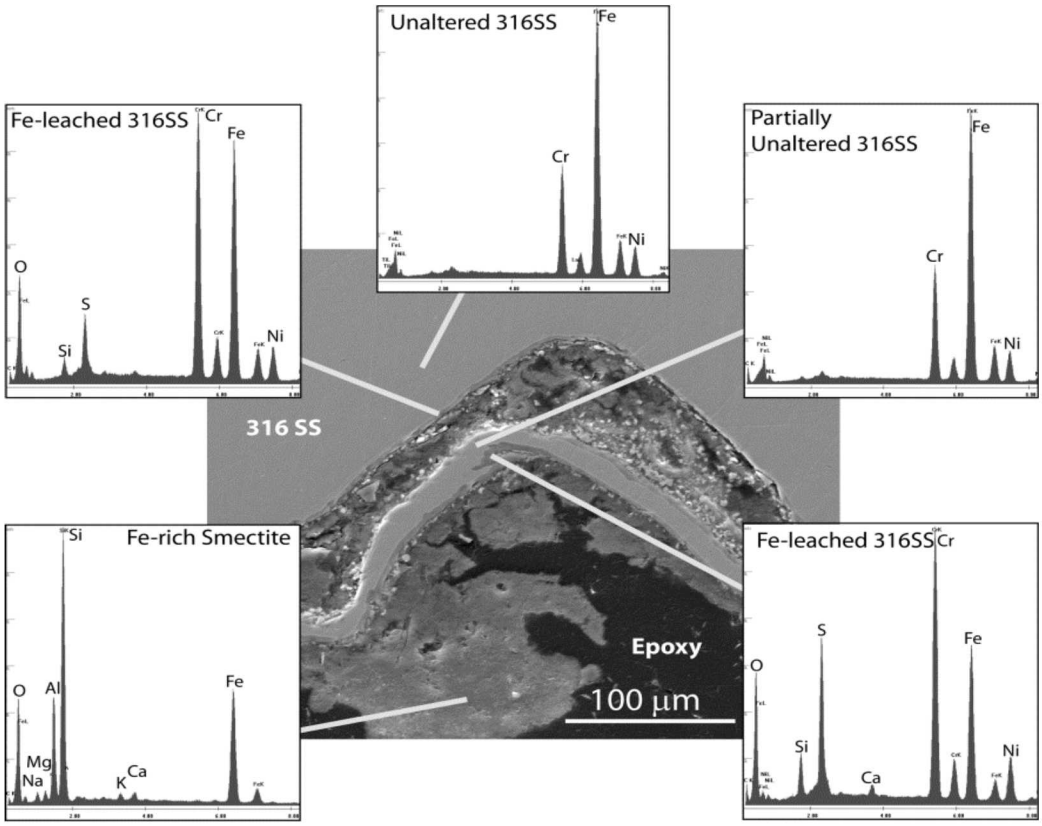


Figure 23. SEM (secondary electron) image of 316 SS cross-section showing Fe-saponite/chlorite growth due to exfoliation corrosion from EBS-3. Chemical analyses of post-reaction 316 SS and interface reaction products indicates there was significant Fe leaching from the 316 SS forming a Cr-enriched steel outer layer up to 4 µm thick.

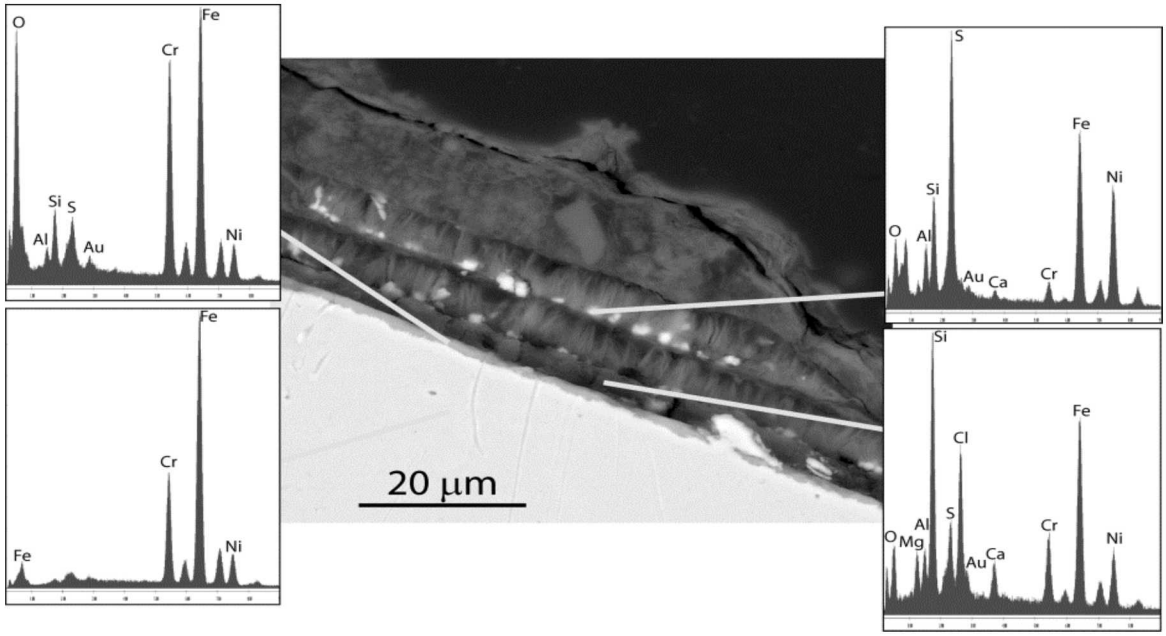


Figure 24. SEM (back scatter) image of 316 SS cross-section showing Fe-saponite/chlorite growth due to exfoliation corrosion from EBS-3. Chemical analyses of post-reaction 316 SS and interface reaction products indicates there was significant Fe leaching from the 316 SS forming a Cr-enriched steel outer layer up to 4 µm thick.

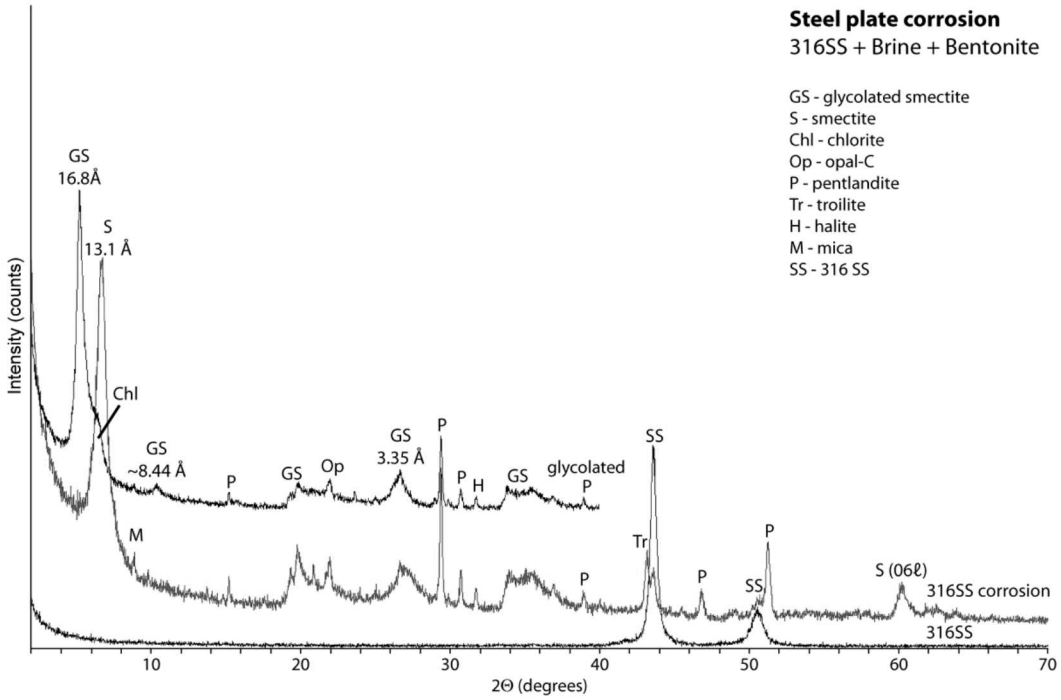


Figure 25. XRD patterns of the air-dried and ethylene glycol saturated interface reaction products on the 316 SS plate used in the EBS-3 experiment. Smectite, chlorite, and a pentlandite-like material are the dominant corrosion phases. Starting 316 SS XRD plot is also shown for comparison.

Low-carbon steel (LCS). Low-carbon steel underwent pitting corrosion during the ramped and isothermal, 300 °C experiments. Post-reaction low-carbon steel developed a smectite coating the steel plate surfaces (Figure 26). Unlike the 304 SS and 316 SS, there was no evidence of any chlorite phases present in the interface reaction product of the low-carbon steel. The primary type smectite associated with the steel surface appears to be Fe-saponite. Smectite expands to 16.6 Å (with 002 at 8.32 Å) upon ethylene glycol saturation suggesting no significant amount of mixed-layering is present. Also, pyrrhotite ($Fe_{1-x}S$) platelets formed concurrently with the smectite phases as determined their spatial distribution (Figure 26C). Smectite morphology is varied between a honeycombed texture and rose-like texture with a bladed to micaceous habit (Figure 26B, D). In addition to the small scaled textures, there is an overlying botryoidal texture with the interface reaction products (Figure 26C). These interface reaction products have thicknesses ranging from 13 to 56 μm with additional ~ 7 μm corrosion pits. The bladed to micaceous crystallites tend to occur with the longer dimensions perpendicular to the steel substrate (Figures 26 and 27). Chemical analyses of post-reaction low-carbon steel and interface reaction products indicate no chemical fractionation associated with the phase transformation process. Accurate chemical formula for the interface reaction products are not possible due to the intimate mixing of multiple phases. There does appear to be oxidation and sulfidation associated with the surface (Figure 27). Smectite is enriched in iron most likely due to the iron dissolved from the steel (Figure 27). The Fe-rich smectite has 06ℓ diffraction bands of 1.547 Å (9.264 Å b-parameters), corresponding to a trioctahedral smectite (Figure 28) (Kohyama et al. 1973; Moore and Reynolds 1997).

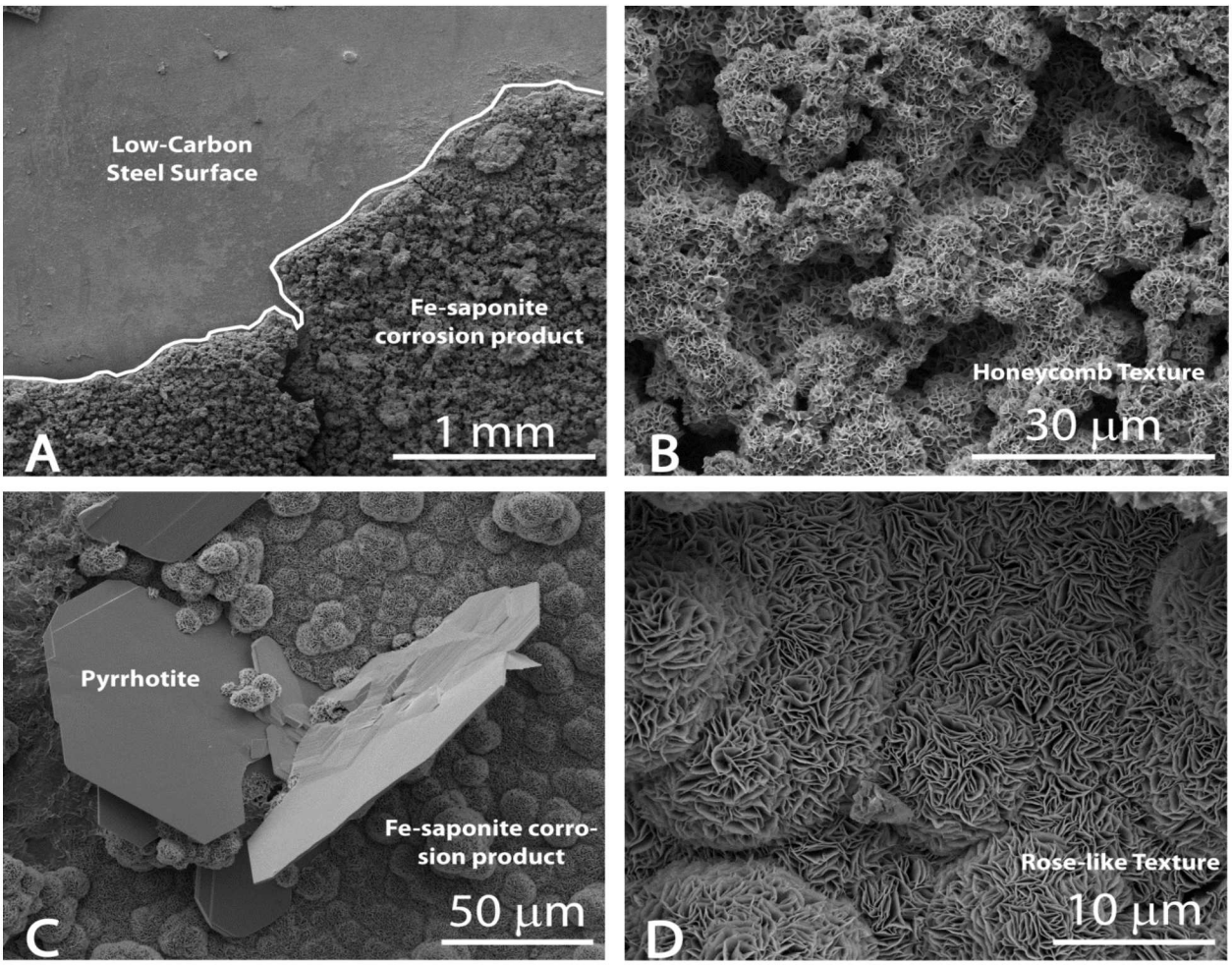


Figure 26. SEM image (plan view) of Fe-saponite growth on low-carbon steel from the ramped (EBS-6) heating experiment. [A] Boundary between the Fe-saponite interface reaction product and low-carbon steel surface. [B] Honeycombed Fe-saponite. [C] Botryoidal Fe-saponite interface reaction product with pyrrhotite platelets from EBS-6. [D] Rose-like texture of Fe-saponite.

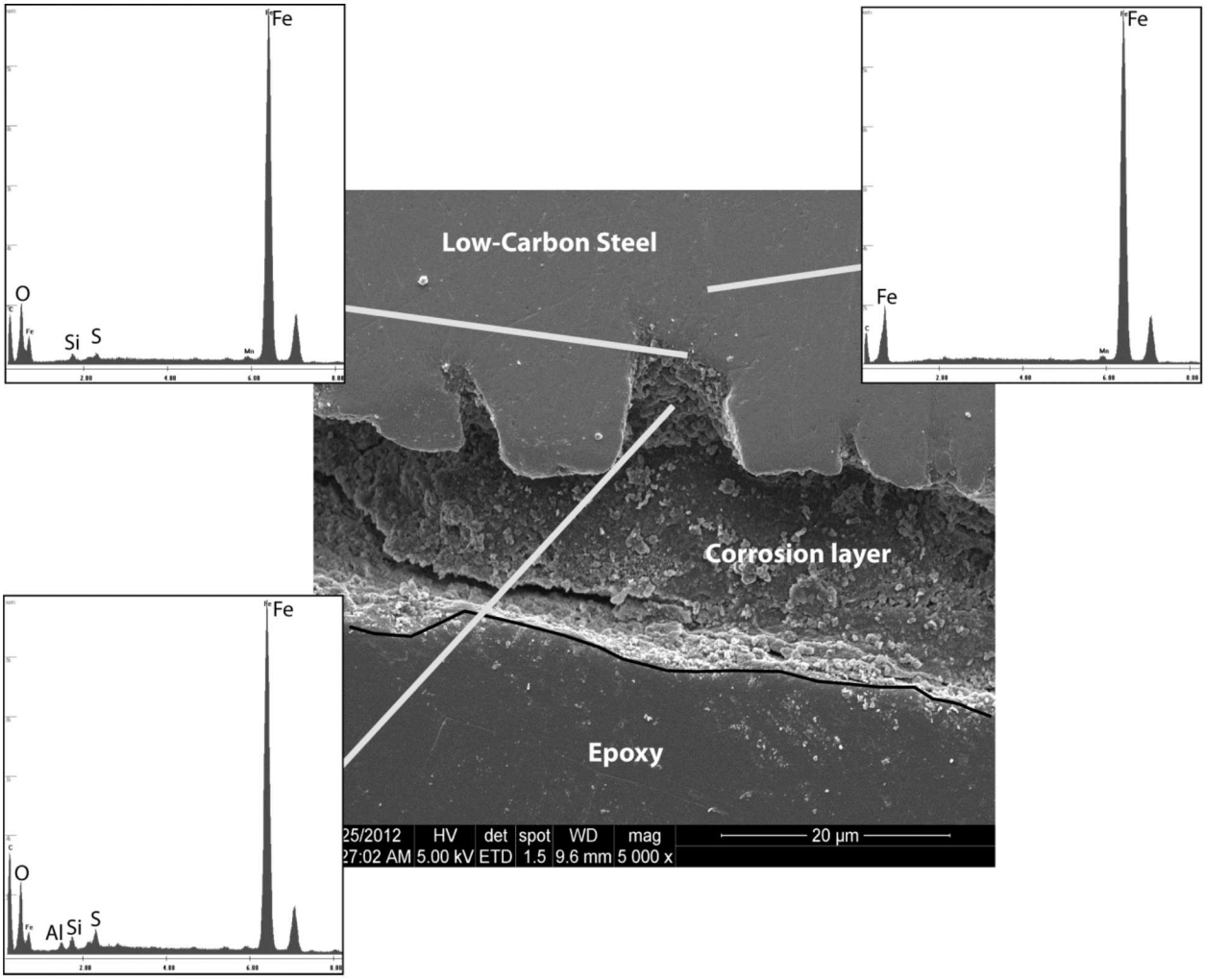


Figure 27. SEM image of low-carbon steel cross-section showing Fe-saponite reaction products using steel surface as a growth substrate. EDX analyses of post-reaction low-carbon steel and interface reaction n surfaces show a slight oxidation and sulfidation of the surface (probably due to oxide and sulfide precipitates). EDX composition of the reaction product was not collected due to erosion of Fe-saponite during sample preparation. Extensive pitting corrosion of the low-carbon steel occurs during the ramped experiments (EBS-6).

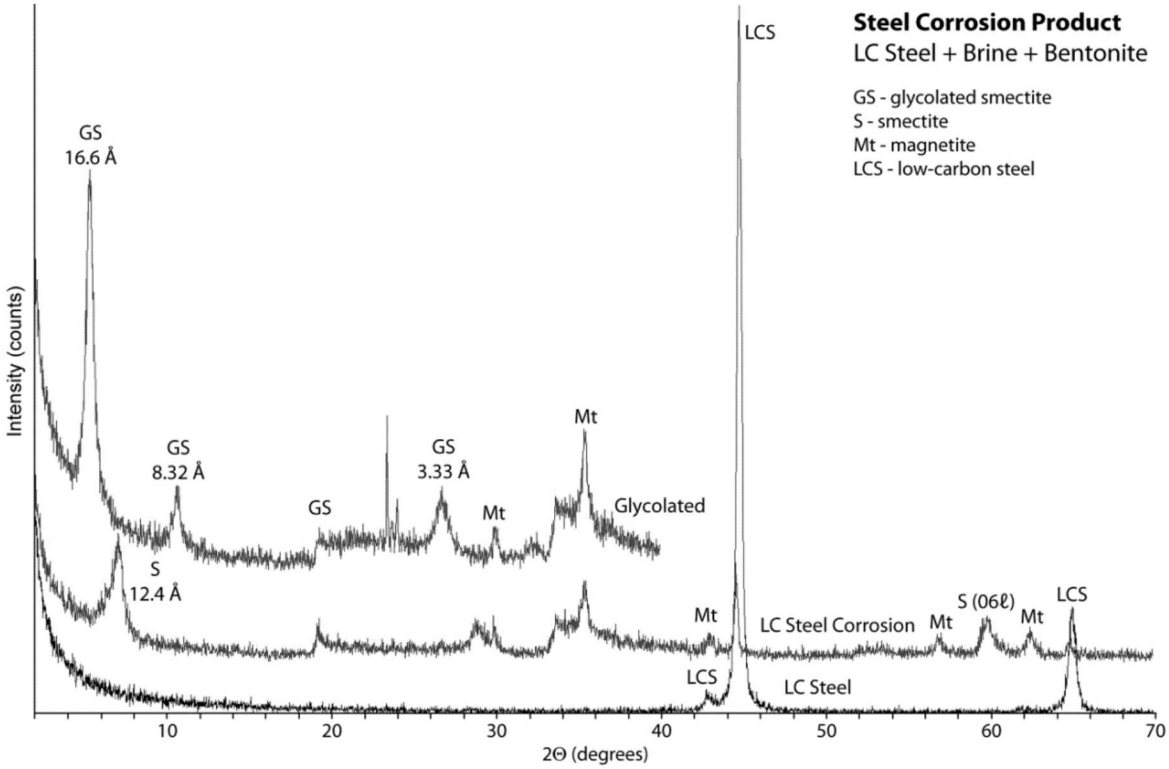


Figure 28. XRD patterns of the air-dried and ethylene glycol saturated interface reaction products on the low-carbon steel plate used in the EBS-6 experiment. Smectite is the dominant interface reaction phase. Magnetite is most likely from the starting magnetite materials used to control redox conditions. Initial low-carbon steel XRD plot is also shown for comparison.

Steel/bentonite interface reactions

Results from these experiments have shown the more dynamic environment associated with this system is at the bentonite-metal interface. Fe-rich phyllosilicates (i.e., trioctahedral, Fe-rich saponite and chlorite) are crystallized on steel surfaces forming a reactive substrate with a high surface area compared to the original steel surfaces. It is evident that the formation of these surface bound minerals is from the direct crystallization from solution in the localized environments surrounding the metal plates. The reaction is stylized in Figure 29. However, it is uncertain to what extent these authigenic minerals will have an effect on the repository system.

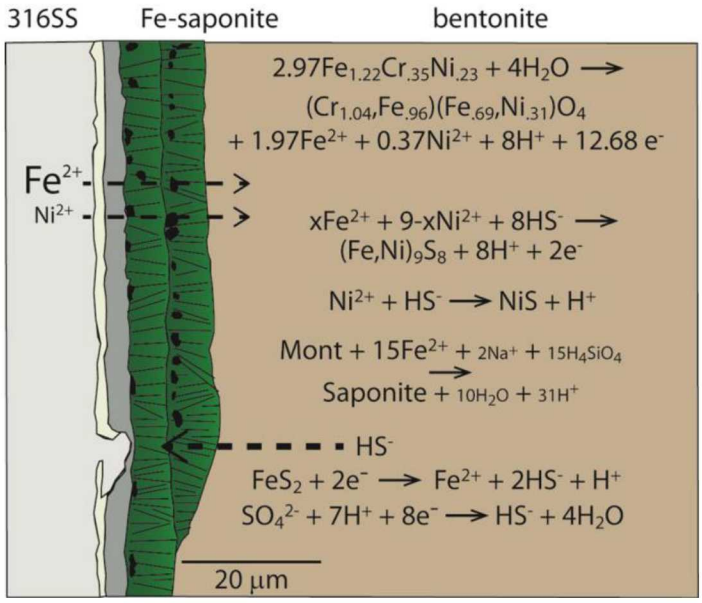


Figure 29. A stylized representation of phyllosilicate mineral growth at the steel interface. Of particular interest is the reaction Montmorillonite → Fe-saponite.

Synthetic Fe-saponites have been crystallized in dilute solutions and gels of silica, Fe-, Al-chlorides at temperatures up to 850°C and pH of 8.5 – 9.5 (Kloprogge et al., 1999). This is consistent with a partial dissolution of the steel plates contributing ferrous iron into a fluid phase with silica and aluminum, thereby facilitating Fe-saponite (smectite) crystallization with the steel surfaces acting as a growth substrate. Further, Fe-saponite alteration into chlorite has been suggested (Mosser-Ruck et al., 2010) in the presence of ferrous iron at temperatures approaching 300 °C and near-neutral pH. This was confirmed by Mosser-Ruck et al (2016) through long duration experiments (up to 9 years).The authors were able to demonstrate that smectite is consumed by dissolution to produce chlorite (chamosite) by precipitation. Mosser-Ruck et al. (2016) describes this by the generalized reaction:

3 smectite + 3 Fe +4 H_2O → 1 chlorite + 3 quartz + 2 albite +3 H_2 + zeolite

Furthermore, we were able to gather microprobe analyses (Appendix D) and images indicating chlorite grows in contact with the steel (where Si is relatively deficient) and then Fe-saponite with a higher Si content (Figure 29).

The stainless steel interaction with bentonite via congruent dissolution/oxidation can be detailed by the following reactions:

Stainless steel dissolution

$$Fe_{1.22}Cr_{0.37}Ni_{0.22} \rightarrow 1.22Fe^{2+} + 0.37Cr^{3+} + 0.22Ni^{2+} + 3.99e^{-}$$

Smectite evolution

$$Fe^{2+} + Ni^{2+} + Cr^{3+} + H_2S_{(aq)} + (Na,K,Ca)_{0.33}(Al_{1.67},Fe^{3+}_{0.20},Mg_{0.13})Si_4O_{10}(OH)_2 \rightarrow (Fe,Ni,Cr)_9S_8 +$$

smectite pentlandite

$$(Na, K, Ca)_{0.33}\,Fe_3(Si_{3.67},Al_{0.33})O_{10}(OH)_2$$

Fe-saponite

Low carbon steel interaction with clay at low temperature has been investigated by Necib et al. (2016). They determined two corrosion rates, an active (up to 200 µm/yr.) and a passive (<30 µm/yr.) behavior. They attribute the high corrosion rate to an acidic pH transient (down to 4.5 pH) common to their experiments when pyrite breaks down. Their experiments were run at 85°C and 1 atm. Although the reactants in our samples were similar, the P, T conditions were radically different. Measurement of the deepest corrosion pit for experiment EBS 18 was 125 µm (Figures 14–17), which would correlate to 1083 µm/yr. This 5-fold increase in corrosion rate for experiment EBS-18 may be due in part to the elevated P, T (150 bar, 300°C) conditions of our experiment. The other item of note is that the corrosion material inside the pit is goethite [Fe^{+3} O(OH)], an iron oxide phase indicative of highly oxidizing conditions. Perhaps this stage of corrosion is the result of microenvironments where water breaks down (hydrolysis) at the coupon surface and allows for oxidizing domains in a generally reducing environment. A second possibility is that the low carbon steel coupon began oxidizing while sitting at a pressure of 140 bar for 9 months before temperature was applied. The mechanism of pit corrosion in low carbon steel, along with corrosion rates for the three steel types (304, 326, LCS) would be a very strong focus area for continued study in EBS research.

4. Conclusion

There have been a large number of investigations on bentonite stability under various repository conditions (Madsen, 1998; Meunier et al., 1998; Guillaume et al., 2003; Guillaume et al., 2004; Mosser-Ruck et al., 2010; Ferrage et al., 2011). Yet, there remain questions regarding bentonite's overall stability and more importantly whether montmorillonite will remain relatively unaltered through the repository life-time. After initial used-fuel emplacement there will be a

pulse of heat flowing into the bentonite buffer producing an environment in which montmorillonite is typically not stable. It would be expected during the early stages of canister emplacement that silica saturation and exchange reactions will take place. However, the relatively dry environment would significantly restrict the mineral reactions due to the limited ion mobility and early saturation. As temperatures increase to peak temperature (currently unknown and will be determined during repository design), various possible zeolite reactions (mordenite, laumontite, analcime, wairakite formation) have the potential to occur if repository conditions shift to the zeolite metamorphic facies (typically starts at 50–150 °C; 100–500 bars). These zeolite reactions, along with silica saturation reactions, will control the porewater solution chemistry and determine any further mineral alteration. Illite formation can still progress, if a K-source is available, but, K-source stability with respect to the repository conditions will determine the illitization rates. It is expected that the initial heat pulse should start to decay after about 100 to 1,000 years (Wersin et al., 2007). After the high temperature pulse passes and temperatures begin to decrease, retrograde reaction have the potential to further change the high temperature mineralogy. As observed in current work, no significant retrograde reactions took place, but as with any experimental work slow kinetics of such reactions make them difficult to show experimentally. It would be expected silica saturation is maintained at continuing lower temperatures by releasing silica from solution, cementing the bentonite. Retrograde zeolite reactions are expected, but currently the extent of such reaction and types are unknown.

The repository is expected to remain “dry” during the initial 100 to 1,000 years (Wersin et al., 2007). Dry system kinetics and mineral solubility are highly restricted. Many of the chemical reactions observed in the wet system either do not take place or are restricted in the dry system. These conditions are more realistic to a repository at 300°C, because bentonite blocks or pellets typically have 10–20 wt. % H_2O and would be compressed during the repository lifetime. It is evident that reaction kinetics are accelerated under water saturation due to increased ion mobility and minerals’ saturation limits.

There have been a number of similar investigations on bentonite stability under various repository conditions and in contact with various metals replicating possible canister compositions (Guillaume et al., 2003; Guillaume et al., 2004; Wilson et al., 2006; Mosser-Ruck et al., 2010; Ferrage et al., 2011, Mosser-Ruck et al., 2016). Partial dissolution of the steel plates

contributing ferrous iron into a fluid phase with silica and aluminum facilitates Fe-saponite (smectite) crystallization. Liberated Ni is preferentially is crystallized in the sulfide phases forming pentlandite ($(Fe,Ni)_9S_8$) and millerite (NiS). Oxidative leaching of Fe and Ni forms a chromite $(Cr_{1.04},Fe_{0.96})(Fe_{0.69},Ni_{0.31})O_4$ passivation layer on the outer surface of the 316 SS plates, restricting corrosion rates (0.1 μm d^{-1} stainless steel) compared to non-alloyed metals (0.6 μm d^{-1} low-carbon steel and 0.8 μm d^{-1} copper). Bentonite not in contact with the steel waste container does not show the formation of these Fe-rich phyllosilicates. The occurrence of Fe-rich phyllosilicates most likely will not form in the bentonite away from the waste container because there is a low abundance of iron in the system. There are two possible scenarios for Fe-saponite formation: 1) direct crystallization in a Fe- and Si-rich solution as a result from bulk mineralogy influences or 2) Fe^{++} montmorillonite interactions breaking down montmorillonite and producing Fe-saponite. The latter mechanism would be a deleterious reaction to the overall repository as montmorillonite is primary mineral in the barrier.

In this work, we consider the impact host rock (i.e., Opalinus Clay from Switzerland) will have on the bentonite barrier. Several mineral alterations were observed in the heating of Opalinus clay. The primary mineral reactions are associated with zeolite formation (i.e., analcime-wairakite$_{ss}$) at the expense of remnant glass / low temperature zeolite (clinoptilolite) in the host rock. When bentonite is included into Opalinus Clay experiments, the solution chemistry changes significantly forcing the formation of a high-silicon, Ca-enriched analcime (wairakite). Interpreting clay mineral evolution within Opalinus materials is complicated due to the variety of clay minerals present in the Opalinus experimental systems. However, it does appear that illitization does occur within the bentonite fraction in the mixed reactions at the current experimental conditions. It is believed that illite growth in the bentonite – Opalinus Clay experimental system is due to precursor illite in the Opalinus Clay acting as seed sites for nucleating further illite growth. With any of these experiments representing repository system, kinetics is always an issue that has to be taken into account when interpreting data.

This document summarizes the EBS Opalinus Clay wall rock experiments EBS-14 through EBS-24 and attempts to compile pertinent 1) SEM images, 2) XRD (QXRD and clay determination) analyses, 3) electron microprobe data for major mineral phases, and 4) aqueous geochemistry data from both starting materials and the ten major experiments conducted so far

into one source. There is a discussion of more recent characterization results and interpretation of cement rich experiment (EBS-23). There is also a summary of a partial review of steel bentonite interface reactions and corrosion reactions in the steel coupons of EBS experiments.

Concepts developed so far include:

1) Illitization of smectites may be restricted due to the bulk chemistry of the overall system,

2) Pyrite within bentonite that may be used as backfill reacts readily in groundwater and the resulting H_2S(aq,g) reacts in a minor fashion with steel and aggressively with copper,

3) Bentonite heated to 300 °C in a dry environment has very restricted reactivity,

4) Experiments held at 300 °C for 4 months and then stepped down in temperature over two more months exhibit no discernable retrograde reactions. This may well be due to kinetic effects of metastable phases.

5) The interface between bentonite and steel develops a well characterized new mineral phase, Fe-saponite (especially at 300°C), that grows perpendicular to the steel surface,

6) Another Fe layered phyllosilicate, stilpnomelane, grows in the presence of native iron (one of our solid buffer materials), which alludes to the idea that oxygen fugacity may be quite variable, depending on scale,

7) Zeolites transform as temperature increases. Mine run bentonite contains clinoptilolite, and transforms to analcime at higher temperature, releasing both SiO_2 and water. Opalinus Clay upon heating develops wairakite along cracks and edges. The location of these new growth zeolites is due to the impermeable nature of the shale. Mixtures of Opalinus Clay and Colony bentonite produce an intermediate composition analcime-wairakite$_{ss}$ phase, indicating ease of cation exchange for this zeolite. The experiment EBS 18 exhibited both clinoptilolite and analcime as stable phases.

8) Addition of cement to a clay engineered barrier prompts formation of an analcime-wairakite$_{ss}$ phase at lower temperatures (200^{o}C). This is most probably due to the high concentration of Si and Ca liberated into the groundwater from the cement.

9) FEBEX clay samples were characterized briefly. Feldspar compositions (both plagioclase and K feldspar) had a range of compositions in the outer and middle rings, but very singular

compositions in the inner ring. This may indicate re-homogenization of the feldspar chemistry with increased heat. With respect to the smectite chemistry, the MgO and SiO_2 generally increase from the inner to outer bentonite blocks.

Research needs to be emphasized in the following areas for FY19:

- Continue experiments with cement component at reduced temperatures (200 ^oC)
- Perform detailed geochemical modeling of cement-rich experimental reactions.
- International FEBEX-DP – hydrothermal treatment of FEBEX samples expanding the thermal range in addition to routine mineral/geochemical interrogations.
- Perform transmission electron microscope (TEM) investigation looking at very local chemical changes within a pit corrosion metal surface.
- Corrosion of steels / interface silicate mantling effect must remain a focus of the upcoming year.
- Incorporate results into GDSA modeling codes.

This database, along with summary conclusions will be of use to other experimental teams on the DOE complex, system modeler, and the international repository science community.

5. Acknowledgements

We would like to thank George Perkins for water chemistry analyses. Scanning electron microscopy facilities were provided by Materials Science and Technology group at Los Alamos National Laboratory. Dr. Lindsey Hunt at the University of Oklahoma was instrumental in the obtaining of EMP analyses. XRD analyses were performed by Dr. Steve Chipera at Chesapeake Energy and Dr. James Maner at University Texas – Austin. Funding was through the Department of Energy's Spent Fuel and Waste Science and Technology.

6. References

Abghari, B. (2013). *Corrosion of Copper in Concentrated Aqueous Chloride under Anaerobic Conditions* (Doctoral dissertation). University of Toronto, Department of Chemical Engineering and Applied Chemistry.

Antonijevic, M.M. and Petrovic, M.B. (2008). Copper corrosion inhibitors. A review. *International Journal of Electrochemical Science*, 3, 1-28.

Abercrombie, H.J., Hutcheon, I.E., Bloch, J.D., and de Caritat, P. (1994). Silica activity and the smectite-illite reaction. *Geology*, 22, 539-542.

Ames, L.L. and Sand, L.B. (1958). Hydrothermal synthesis of wairakite and calcium-mordentite. *The American Mineralogist*, 43, 476-480.

Bannister, R.A. (1943). Brammalite (sodium-illite) a new mineral from Llandebie, South Wales. *Mineralogical Magazine*, 26, 304-307.

Betova, I., Beverskog, B., Bojinov, M., Kinnunen, P., Makela, K., Pettersson, S.-O., and Saario, T. (2003). Corrosion of copper in simulated nuclear waste repository conditions. *Electrochemical and Solid-State Letter,* 6, B19-B22.

Bojinov, M., Makela, K. (2003). Corrosion of copper in anoxic 1M NaCl solution. *Posiva Working Report* 200345, Olkiluoto, Finland.

Börjesson, L., Gunnarsson, D., Johannesson, L-E., and Jonsson, E. (2010). Design, production and initial state of the buffer. *Svensk Kärnbränslehantering Technical Report*, TR-10-15, 89.

Boulay, N., and Edwards, M. (2001). Role of temperature, chlorine, and organic matter in copper corrosion by-product release in soft water. *Water Research*, 35, 683-690.

Burgess, J. (1978). Metal ions in solution. John Wiley & Sons, Inc., p. 481.

Busenberg, E. and Clemency, C.V. (1973). Determination of the cation exchange capacity of clays and soils using an ammonia electrode. *Clays and Clay Minerals*, 21, 213-217.

Caporuscio, F.A., Cheshire, M.C., Rearick, M.S., Jove-Colon, C., and McCarney, M.K. (2013*). EBS Report - LANL experimental update of buffer/backfill at elevated P,T.* (FCRD-USED-2013-000207). Los Alamos National Lab. (LANL), Los Alamos, NM (United States).

Caporuscio, F.A., Cheshire, M.C., Rearick, M.S., and Jove-Colon, C. (2014). *LANL argillite EBS experimental program 2014*. (FCRD-USED-2014-000491). Los Alamos National Lab. (LANL), Los Alamos, NM (United States).

Caporuscio, F.A., Cheshire, M.C., Palaich, S., Norskog, K., and Jove-Colon, C. (2015). *Argillite Disposal R&D-LANL 2015. Summary of baseline experiments for generic repository engineered barriers.* (FY 2015). (FCRD-UFD-2015-000356, LA-UR-15-26110). Los Alamos National Lab. (LANL), Los Alamos, NM (United States).

Caporuscio, F.A., and Norskog, K. (2017). Disposal Overpack and Waste Package Options – LANL Petrographic descriptions of FEBEX Section 49 - Dismantlement Phase operation. (SFWD-SFWST-2017-000116, LA-UR -17-28576) Los Alamos National Lab. (LANL), Los Alamos, NM (United States).

Carlsson, T. (2008). Interactions between copper corrosion products and MX-80 bentonite. *Svensk Kärnbränslehantering Working Report*, TR-08-46, 24.

Chen, J., Qin, Z., and Shoesmith, D. (2010). Kinetics of corrosion film growth on copper in neutral chloride solutions containing small concentrations of sulfide. *Journal of the Electrochemical Society*, 157(10), C338-C345.

Chen, J., Qin, Z., and Shoesmith, D. (2011a). Long-term corrosion of copper in a dilute anaerobic sulfide solution: *Electrochimica Acta*, 56(23), 7854-7861.

Chen, J., Qin, Z., and Shoesmith, D. (2011b). Rate controlling reactions for copper corrosion in anaerobic aqueous sulphide solutions. *Corrosion Engineering, Science and Technology*, 46(2), 138-141.

Chermak, J.A. (1992). Low temperature experimental investigation of the effect of high pH NaOH solutions on the opalinus shale, Switzerland. *Clays and Clay Minerals*, 40, 650-658.

Cheshire, M.C., Caporuscio, F.A., Jové-Colón, C., and McCarney, M.K. (2013). Alteration of clinoptilolite into high-silica analcime within a bentonite barrier system under used nuclear fuel repository conditions. *Proceeding from the 14th International High-Level Radioactive Waste Management Conference,* 410-415.

Cheshire, M.C., Caporuscio, F.A., Jove-Colon, C., and McCarney, M.K. (2014). Bentonite Clay evolution at elevated pressures and temperatures: An experimental study for generic nuclear repositories. *American Mineralogist*, 99, 1662-1675.

Cheshire, M.C., Hardin, E., Caporuscio, F.A., Jove-Colon, C., and McCarney, M.K. (2014b). Geochemical investigation in an effort to increase Bentonite barrier's thermal load capacity to accommodate 32-pwr dual purpose canisters. *Proceedings from the International Conference on the Performance of Engineered Barriers*, 185-190.

Chipera, S.J. and Bish, D.L. (2002). FULLPAT: a full-pattern quantitative analysis program for X-ray powder diffraction using measured and calculated patterns. *Journal of Applied Crystallography*, 35, 744–749.

Chung, F.H. (1974). Quantitative interpretations of X-ray diffraction patterns of mixtures. I. Matrix flushing method for quantitative multicomponent analysis. *Journal of Applied Crystallography*, 7, 519-525.

Coombs, D.S. (1955). X-ray observations on wairakite and non-cubic analcime. *Mineralogical Magazine*, 30, 699-708.

Couture, R.A. (1985). Steam rapidly reduces the swelling capacity of bentonite. *Nature*, 318, 50-52.

Crerar, D.A., Susak, N.J., Borcsik, M., and Schwartz, S. (1978). Solubility of the buffer assemblage pyrite + pyrrhotite + magnetite in NaCl solution from 200 to 350°C. *Geochimica et Cosmochimica Acta*, 42, 1427-1437.

Demchenko, L.V., Zlobenko, B.P., Manichev, V.I., Kadoshnikov, V.V., and Spasova, L.V. (2004). Corrosion of archeological artefacts from the Olviya Site in Ukraine. *MRS Online Proceedings Library Archive*. 807, 1-6.

Dick, J. M. (2008). Calculation of the relative metastabilities of proteins using the CHNOSZ software package. *Geochemical Transitions*, 9, 10.

Dong, H. (2005). Interstratified illite-smectite: A review of contributions of TEM data to crystal chemical relation and reaction mechanisms. *Clay Science*, 12, Supplement 1, 6-12.

Eberl, D. and Hower, J. (1977). The hydrothermal transformation of sodium and potassium smectite into mixed-layer clay. *Clays and Clay Minerals*, 25, 215-227.

Eberl, D. (1978). Reaction series for dioctahedral smectites. *Clays and Clay Minerals*, 26, 327-340.

Eberl, D., Whitney, G., and Khourym, H. (1978). Hydrothermal reactivity of smectite. *American Mineralogist*, 63, 401-409.

Eberl, D.D., Velde, B., and McCormick, T. (1993). Synthesis of illite-smecite from smectite at Earth surface temperatures and high pH. *Clay Minerals*, 28, 49-60.

Escobar, I. S., Silva, E., Silva, C., and Ubal, A. (1999). *Proceedings from the Fourth International Conference of Copper 99-Cobre99*, 1, 371.

Ferrage, E., Vidal, O., Mosser-Ruck, R., Cathelineau, M., and Cuadros, J. (2011). A reinvestigation of smectite illitization in experimental hydrothermal conditions: Results from X-ray diffraction and transmission electron microscopy. *American Mineralogist*, 96, 207-223.

Frape, S.K., Blyth, A., Blomqvist, R., McNutt, R.H., and Gascoyne, M. (2003). Deep fluids in the continents: II. Crystalline rocks. *Treatise on Geochemistry*, 5, 541-580.

Frey, M. (1969). A mixed-layer paragonite/phengite of low-grade metamorphic origin. *Contribution to Mineralogy and Petrology*, 24, 63-65.

Greenburg, H.R. and Wen, J. (2013). Repository layout and host rock thermal gradient trade study for large waste packages in clay/shale: Using the DSEF thermal analytical model. *LLNL-TR-639869-DRAFT*, 38.

Guillaume, D., Neaman, A., Cathelineau, M., Mosser-Ruck, R., Peiffert, C., Abdelmoula, M., Dubessy, J., Villieras, F., Baronnet, A., and Michau, N. (2003). Experimental synthesis of chlorite from smectite at 300°C in the presence of metallic Fe. *Clay Minerals*, 38, 281-302.

Guillaume, D., Neaman, A., Cathelineau, M., Mosser-Ruck, R., Peiffert, C., Abdelmoula, M., Dubessy, J., Villieras, F., and Michau, N. (2004). Experimental study of the transformation of smectite at 80 to 300 °C in the presence of Fe oxides. *Clay Minerals*, 39, 17-34.

Güven, N. (2001). Mica structure and fibrous growth of illite. *Clays and Clay Minerals*, 49, 189-196.

Hallberg, R.O., Ostlund, P., and Wadsten, T. (1988). Inferences from a corrosion study of a bronze cannon, applied to high level nuclear waste disposal. *Applied Geochemistry*, 3, 273-280.

Helgeson, H. C., Delany, J. M., Nesbitt, H. W., and Bird, D. K. (1978). Summary and critique of the thermodynamic properties of rock-forming minerals. *American Journal of Science*, 278, 1-229

Herbert, H.J., Kasbohm, J., Nguyen-Thanh, L., Meyer, L., Hoang-Minh, T., Xie, M., and Mahlmann, R.F. (2016). Alteration of expandable clays by reaction with iron while being percolated by high brine solutions. *Applied Clay Science*, 121, 174-187.

International Atomic Energy Agency (IAEA). (2000). Multi-purpose container technologies for spent fuel management. *IAEA Technical Document*, IAEA-TECDOC-1192, 56.

Jové, C. and Hacker, B.R. (1997). Experimental investigation of laumontite → wairakite + H_2O: A model diagenetic reaction. *American Mineralogist*, 82, 781-789.

Jové-Colón, C. F., Caporuscio, F. A., Levy, S. S., Sutton, M., Blink, J., Greenberg, H. R., Fratoni, M., Halsey, W. G., Wolery, T. J., Rutqvist, J., et al. (2011). Disposal systems evaluations and tool development - Engineered Barrier System (EBS) Evaluation (Fuel Cycle Research and Development). Sandia National Laboratory, (FCRD-USED-2011-000132), 1-192.

Kass, J. (1990). Evaluation of copper, aluminum bronze, and copper-nickel container material for the Yucca Mountain Project. *Proceedings of a workshop on corrosion of nuclear fuel waste containers*, (IAEA-10121), (RN:23004457), 87-107.

Kim, S.S., Chun, K.S., Kang, K.C., Baik, M.H., Kwon, S.H., and Choi, J.W. (2007). Estimation of the corrosion thickness of a disposal container for high-level radioactive wastes in a wet bentonite. *Journal of Industrial and Engineering Chemistry* 13, 959-964.

King, F. (2005). Overview of the corrosion behavior of copper and steel used fuel containers in a deep geologic repository in the sedimentary rock of the Michigan Basin, Ontario. *Ontario Power Generation, Nuclear Waste Management Division Report*.

King, F. (2007). Status of the understanding of used fuel container corrosion processes – Summary of current knowledge and gap analysis (NWMO TR-2007-09): Canada, NWMO. 104.

King, F., Ahonen, L., Taxen, C., Vuorinen, U., and Werme, L. (2002). Copper corrosion under expected conditions in a deep geological repository. *POSIVA OY*, Helsinki, Finland. Report 2002-01.

King, F., Lilja, C., Pedersen, K., Pitkänen, P., and Vähänen, M. (2010). An update of the state-of-the-art report on the corrosion of copper under expected conditions in a deep geologic repository. Swedish Nuclear Fuel and Waste Management Co. (SKB), *Technical Report,* TR-10-67, 180.

King, F. and Lilja, C. (2011). Scientific basis for corrosion of copper in water and implications for canister lifetimes. *Corrosion Engineering, Science and Technology,* 46(2), 153-158.

King, F., Lilja, C., and Vähänen, M. (2013). Progress in the understanding of the long-term corrosion behavior of copper canisters. *Journal of Nuclear Materials*, 438(1), 228-237.

King, F., Litke, C.D., and Ryan, S.R. (1992). A mechanistic study on the uniform corrosion of copper in compacted Na-montmorillonite/sand mixtures. *Corrosion Science,* 33, 1979-1995.

Kloprogge J.T., Evans, R., Hickey, L., and Frost, R. (2002). Characterization and Al-pillaring of smectites from Miles, Queensland (Australia*). Applied Clay Science*, 20(4-5), 157-163.

Kohyama, N., Shimoda, S., and Sudo, T. (1973). Iron-rich saponite (ferrous and ferric forms). *Clays and Clay Minerals*, 21, 229-237.

Kumplulainen, S., Kiviranta, L., Carlsson, T., Muurinen, A., Svensson, D., Sasamoto, H., Yui, M., Wersin, P., Rosch, D. (2011). Long-term alteration of bentonite in the presence of metallic iron. *POSIVA OY*, Eurajoki, Finland, Report 2010-71.

Lahann, R.W. and Roberson, H.E. (1980). Dissolution of silica from montmorillonite: Effect of solution chemistry. *Geochimica et Cosmochimica Acta*, 44, 1937-1943.

Laird, D.A. (1996). Model for crystalline swelling of 2:1 phyllosilicates. *Clays and Clay Minerals*, 44, 553-559.

Laird, D.A. (2006). Influence of layer charge on swelling of smectites. *Applied Clay Science*, 34, 74-87.

Liuo, J.G. (1970). Synthesis and stability relations of wairakite, $CaAl_2Si_4O_{12}$ $2H_2O$. *Contributions to Mineralogy and Petrology*, 27, 259-282.

Macdonald, D.D. and Sharifi-Asl, S. (2011). Is copper immune to corrosion when in contact with water and aqueous solutions? *Swedish Radiation Safety Authority*, Report 2011-09.

Madsen, F.T. (1998). Clay mineralogical investigations related to nuclear waste disposal. *Clay Minerals*, 33, 109-129.

Masuda, H., O'Neil, J.R., Jiang, W-T, and Peacor, D.R. (1996). Relation between interlayer composition of authigenic smectite, mineral assemblages, I/S reaction rate and fluid composition in silicic ash of the Nankai Trough. *Clays and Clay Minerals*, 44, 443-459.

Meunier, A., Velde, B., and Griffault, L. (1998). The reactivity of bentonites: A Review. An application to clay barrier stability for nuclear waste storage. *Clay Minerals*, 33, 187-196.

Moore, D. M. and Reynolds, R.C. (1997). X-ray Diffraction and the identification and analysis of clay minerals. *Oxford University Press*, New York, New York, 377.

Mosser-Ruck, R., Cathelineau, M., Baronnet, A., and Trouiller, A. (1999). Hydrothermal reactivity of K-smectite at 300 °C and 100 bars: Dissolution-crystallization process and non-expandable dehydrated smectite formation. *Clay Minerals*, 34, 275-290.

Mosser-Ruck, R., Pignatelli, I., Bourdelle, F., Abdelmoula, M., Odile Barres, O., Guillaume, D., Charpentier, D., Rousset, D., Cathelineau, M., and Michau, N. (2016). Contribution of long-term hydrothermal experiments for understanding the smectite-to-chlorite conversion in geological environments. *Contributions to Mineralogy and Petrology*, 171, 97-118.

Mosser-Ruck, R., Cathelineau, M., Guillaume, D., Charpentier, D., Rousset, D., Barres, O., and Michau, N. (2010). Effects of Temperature, pH, and Iron/Clay and Liquid/Clay Ratios on Experimental Conversion of Dioctahedral Smectite to Berthierine, Chlorite, Vermiculite, or Saponite. *Clays and Clay Minerals*, 58, 280-291.

Necib, S., Linard, Y., Crusset, D., Michau, N., Daumas, S., Burger, E., Romaine, A., and Schlegel, M.L. (2016). Corrosion at the carbon steel–clay borehole water and gas interfaces at 85 ◦C under anoxic and transient acidic conditions, *Corrosion Science*, 111, 242-258.

Nunez, L., Reguera, E., Corvo, F., Gonzalez, E., and Vazquez, C. (2005). Corrosion of copper in seawater and its aerosols in a tropical island. *Corrosion Science*, 47, 461-484.

Nutt, M. Voegele, M., Jové-Colón, C.F., Wang, Y., Howard, R., Blink, J., Liu, H.H., Hardin, E., and Jenni, K. (2011). Used fuel disposition campaign disposal research and development road map (Fuel cycle research and development). Sandia National Laboratory, (FCRD-USED-2011-000065), 1-121.

Ohmoto, H., Hayashi, K-I, and Kajisa, Y. (1994). Experimental study of the solubilities of pyrite in NaCl-bearing aqueous solutions at 250-350°C. *Geochimica et Cosmochimica Acta*, 58, 2169-2185.

Pederson, K. (2010). Analysis of copper corrosion in compacted bentonite clay as a function of clay density and growth conditions for sulfate-reducing bacteria. *Journal of Applied Microbiology*, 108, 1094-1104

Pearson, F.J., Arcos, D., Bath, A., Boisson, J.-Y., Fernandez, A.M., Gabler, H.-E., Gaucher, E., Gautschi, A., Griffault, L., Hernan, P., and Waber, H.N. (2003). Mont Terri Project-geochemistry of water in the opalinus clay formation at the Mont Terri Rock Laboratory. *Reports of the Federal Office for Water and Geology* (FOWG), Geology Series No. 5.

Pouchou, J.L. and Pichoir, F. (1985) "PAP" $\phi(\rho z)$ correction procedure for improved quantitative microanalysis. *Microbeam Analysis*, Ed. Armstrong, J.T., San Francisco Press, 104-106.

Pusch, R. (1979). Highly compacted sodium bentonite for isolating rock-deposited radioactive waste products. *Nuclear Technology*, 45, 153-157.

Pusch, R. Takase, H., and Benbow,S. (1998) Chemical Processes causing cementation in heat-affected smectite- the Kinnekulle bentonite. *Svensk Kärnbränslehantering Technical Report*, TR-98-25, 62.

Pusch, R. and Kasbohm, J. (2002) Alteration of MX-80 by hydrothermal treatment under high salt content conditions. *Svensk Kärnbränslehantering Technical Report*, TR-02-06, 44.

Pusch, R. (2008). Geological Storage of Radioactive Waste. *Springer-Verlag*, Berlin, Germany, 379.

Roberson, H.E. and Lahann, R.W (1981). Smectite to illite conversion rates: Effects of solution chemistry. *Clays and Clay Minerals*, 29, 129-135.

Rosborg, B., Pan, J., and Leygraf, C. (2005). Tafel slopes used in monitoring of copper corrosion in a bentonite/groundwater environment. *Corrosion Science*, 47, 3267-3279.

Rosborg, B., Kosec, T., Kranjc, A., Pan, J., and Legat, A. (2011). Electrochemical impedance spectroscopy of pure copper exposed in bentonite under oxic conditions. *Electrochemical Acta*, 56, 7862-7870.

Sandberg, J., Wallinder, I.O., Leygraf, C., and Le Bozec, N. (2006). Corrosion-induced copper runoff from naturally and pre-patinated copper in a marine environment. *Corrosion Science*, 48, 4316-4338.

Schwartz, M. O, (2008). High-level waste disposal, ethics and thermodynamics. *Environmental Geology*, 54(7), 1485-1488.

Seki, Y. (1971). Some physical properties of analcime-wairakite solid solutions. *Journal of the Geologic Society of Japan*. 77, 1-8

Seyfried, J.R., Janecky, D.R., and Berndt, M.E. (1987). Rocking autoclaves for hydrothermal experiments II. The flexible reaction-cell system. *Hydrothermal Experimental Techniques*, Eds. Ulmer, G.C. and Barnes, H.L. John Wiley & Sons, 216-239.

Small, J.S., Hamilton, D.L., and Habesch, S. (1992). Experimental simulation of clay precipitation within reservoir sandstones 2: Mechanism of illite formation and controls on morphology. *Journal of Sedimentary Petrology*, 62, 520-529.

Small, J.S. (1993). Experimental determination of the rates of precipitation of authigenic illite and kaolinite in the presence of aqueous oxalate and comparison to the K/Ar ages of authigenic illite in reservoir sandstones. *Clays and Clay Minerals*, 41, 191-208.

Smyth, J.R. (1982). Zeolite stability constraints on radioactive waste isolation in zeolite-bearing volcanic rocks. *Journal of Geology*, 90, 195-201.

Środoń, J. (1980). Precise identification of illite/smectite interstratifications by X-ray powder diffraction. *Clays and Clay Minerals*, 28, 401-411.

Środoń, J. (1999). Nature of mixed-layer clays and mechanisms of their formation and alteration. *Annual Review of Earth and Planetary Sciences*, 27, 19-53.

Steiner, A. (1955). Wairakite, the calcium analogue of analcime, a new zeolite mineral. *Mineralogical Magazine*, 30, 691-698.

Taniguchi, N., and Kawasaki, M. (2008). Influence of sulfide concentration on the corrosion behavior of pure copper in synthetic seawater. *Journal of Nuclear Materials*, 379, 154-161.

Wersin, P., Johnson, L.H., and McKinley, I.G. (2007). Performance of the bentonite barrier at temperatures beyond 100°C: A critical review. *Physics and Chemistry of the Earth*, 32, 780-788.

Whitney, G. and Velde, B. (1993). Changes in particle morphology during illitization: An experimental study. *Clays and Clay Minerals*, 41, 209-218.

Wilkin, R.T. and Barnes, H.L. (1998). Solubility and stability of zeolites in aqueous solution: I. Analcime, Na-, and K-clinoptilolite. *American Mineralogist*, 83, 746-761.

Wilkin, R.T. and Barnes, H.L. (2000). Nucleation and growth kinetics of analcime from precursor Na-clinoptilolite. *American Mineralogist*, 85, 1329-1341.

Winkler, H.G.F. (1976) Petrogenesis of Metamorphic Rocks. Springer-Verlag, New York, 329.

Zhang G., Kim, J., Dong, H., and Sommer, A. (2007). Microbial effects in promoting the smectite to illite reaction: Role of organic matter intercalated in the interlayer. *American Mineralogist*, 92, 1401-1410.

Update on Validation and Incorporation of a New Steel Corrosion Module into Fuel Matrix Degradation Model (Part IV)

1. Introduction

The purpose of this project is to develop, test and implement a process model for the degradation rate of spent nuclear fuel that can be readily incorporated into the generic disposal system analyses (GDSA) performance assessment (PA) code to provide reliable radionuclide source terms over the service life of a deep geologic repository. The fuel matrix degradation (FMD) model (or FMDM), which is an electrochemical reactive-transport model based on fundamental redox kinetics and thermodynamics, was developed for this purpose and is currently being updated and tested. The FMD model was originally based the Canadian Mixed Potential Model (CMPM) of Shoesmith and King, 1998, and King and Kolar 2003 but has been expanded to account for key phenomena and customized for application in the ongoing spent fuel and waste science and technology (SFWS) campaign.

The continuing development and implementation of the FMD model address two high level Features, Events, and Processes (FEPs) that are recognized as high R&D priorities for the SFWST campaign (Wang et al., 2014). The FEPs addressed by this model are 2.1.02 (waste form) and 2.1.03 (waste container), which correspond to the high priority research topics P19 (Development of waste form degradation model) and P20 (Development of new waste package concepts and models for evaluation of waste package performance for long-term disposal) identified by Wang et al., 2014.

Specifically, the FMD model uses mixed potential theory to calculate the degradation rate of UO_2 by accounting for all major anodic and cathodic interfacial reactions. Other major phenomena accounted for in the FMD model include:

- Effect of hydrogen generated from steel corrosion within a breached waste package
- Alpha radiolysis and the generation of radiolytic oxidants as a function of fuel burn-up
- Growth a porous layer of uranyl oxyhydroxide and/or uranyl peroxide corrosion phases
- Complexation of dissolved uranium by carbonate
- Temperature variations of reaction rates (by Arrhenius equations)
- One-dimensional diffusion of all chemical species to and from the fuel and steel surfaces.

The most important process that the FMD model accounts for that was not addressed in the original CMPM is the oxidation of dissolved hydrogen at the spent fuel surface (Jerden et al., 2015). Leaching experiments with spent fuel and simulated spent fuel have shown that the presence of hydrogen generated during the corrosion of steel added to a test can decrease the fuel degradation rate by 4 orders of magnitude relative to tests performed with no steel present (e.g., Röllin et al., 2001, Ollila, 2008). The means by which the effect of hydrogen is accounted for in the FMD model is discussed in Section 2 below.

Jerden et al., 2017(a) and Jerden et al., 2017(b) discussed the addition of a corroding steel surface as a source of hydrogen to the FMD model (FMDM version 3). One of the main findings of that work is that the extensive coupling between the corrosion of waste package components and the spent fuel that must be taken into accounted to accurately predict radionuclide source terms. As discussed in Jerden et al., 2017(b), the Eh and pH conditions within a breached waste package will evolve with time due to coupled reactions of alloy corrosion, radiolysis, and spent fuel dissolution. The latest FMD model includes a first step towards accounting for coupled processes by linking steel corrosion kinetics and fuel degradation rates; however, more extensive experimental and

modeling work is needed to accurately model the fuel dissolution rate because the in-package solution chemistry evolves due to the corrosion of engineering materials.

The present report updates the work discussed in Jerden et al., 2017(a) and Jerden et al., 2017(b) and provides discussion of ongoing experimental validation work for the latest version of the FMD model (FMDM version 4). The electrochemical experiments that are being performed to parameterize and validate the FMD model (V.4) are discussed in Section 3 below.

As summarized in Jerden et al., 2017(b), the FMD model has been successfully integrated with the GDSA-PA code PFLOTRAN; however, there is a need to optimize the integrated code to improve computing speed. This optimization work is ongoing and will be summarized in a March 2019 milestone report. The flow of information within the integrated FMDM – GDSA-PA model is summarized in Figure 1.

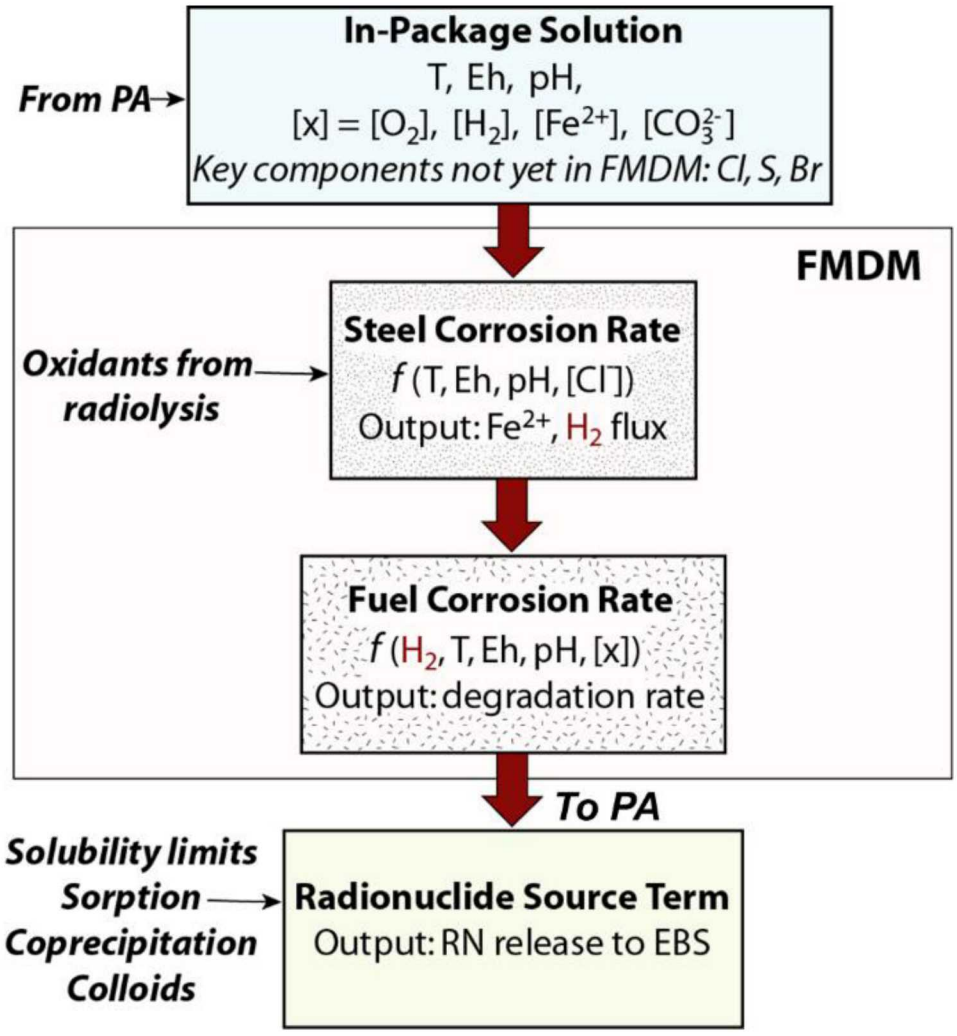


Figure 1. Summary figure showing the context of the FMDM within the source term calculation information flow (adapted from Jerden et al., 2017a).

2. Update on Validation of Fuel Matrix Degradation Model Version 4

The chemical and physical processes accounted for in the FMD model are shown schematically in Figure 2. In The model, spent fuel is exposed to an aqueous solution that has entered the waste package following a canister breaching event. The model conservatively assumes that the Zircaloy fuel cladding (not shown in Figure 2) is also breached at the time of water infiltration into the canister. The canister breaching process will be modeled separately; however, the breaching model will be coupled with the FMDM through the dependence of the spent fuel degradation rate on the concentration of hydrogen generated from the corrosion of canister steels.

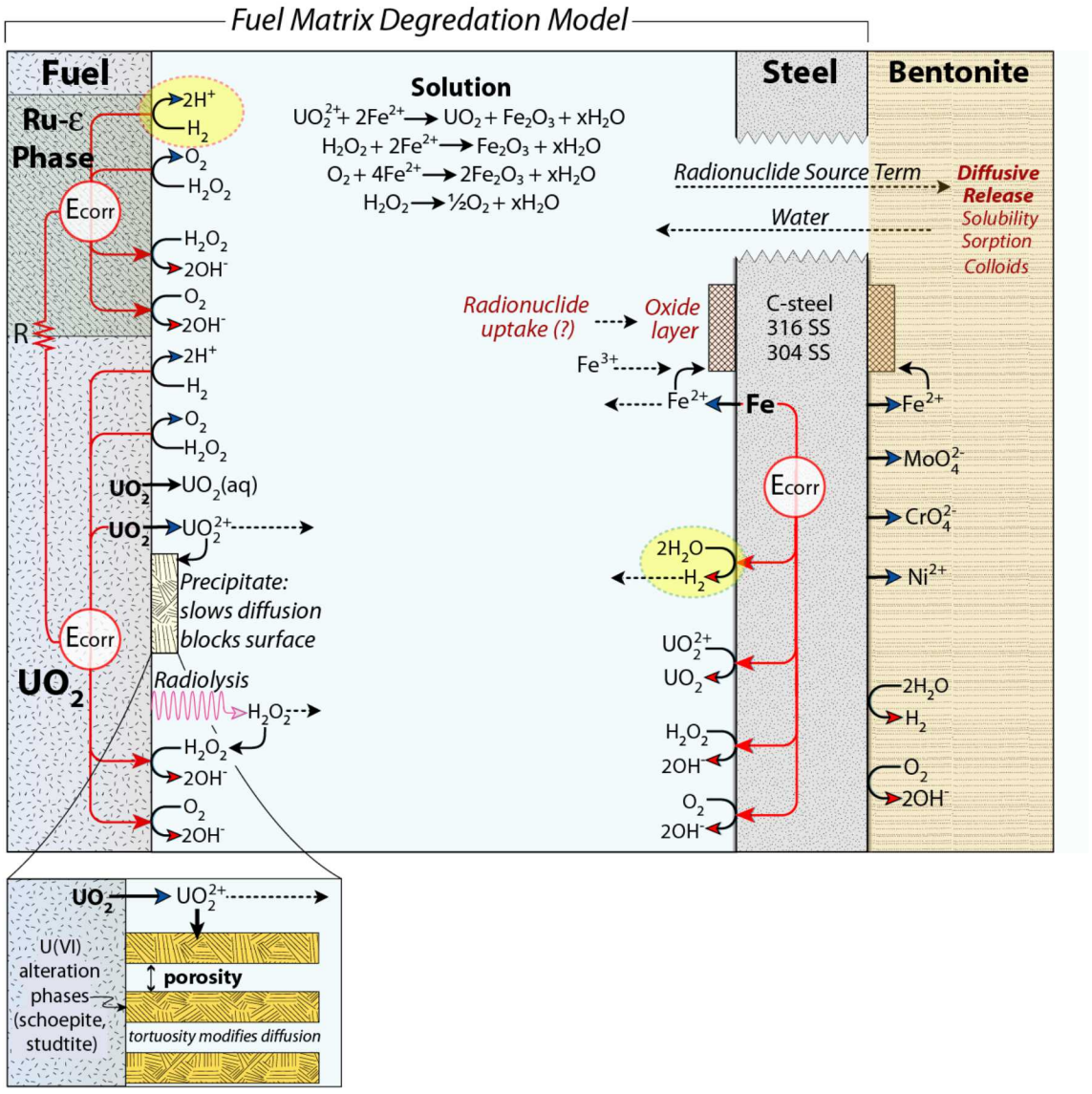


Figure 2. Schematic diagram showing the reaction scheme for the FMD model and identifying other key processes that influence in-package chemistry and radionuclide mobilization. (adapted from Jerden et al., 2017a).

Of the processes shown in Figure 2, H_2 generation and oxidation reactions (highlighted in yellow in Figure 2) have the most important impact on the fuel dissolution rate and radionuclide source term (Jerden et al. 2015). In the absence of H_2 generation, the dominant process is the oxidative dissolution of the fuel by the radiolytic oxidant H_2O_2 and its decomposition product O_2. In the FMD model, the H_2O_2 concentration is calculated using an analytical form of the radiolysis model developed at PNNL (Buck et al., 2014) and the burn-up/dose rate function that was derived from MCNPX dose rate modeling of Radulescu, 2001.

When sufficient H_2 is present, the radiolytic oxidation of the fuel is counteracted by the oxidation of H_2 at the fuel surface. As shown in Figure 2, hydrogen oxidation occurs both on the UO_2 surface and on the Ru-Mo-Pd-Rh-Tc bearing, fission product alloy commonly referred to as the ε phase. The reaction of H_2 with the ε phase is the dominant mechanism for the H_2 effect on spent fuel dissolution due to the catalytic properties of this noble metal-bearing phase. The assumption that the ε phase catalyzes H_2 oxidation at the fuel surface is supported by the electrochemical experimental work of Broczkowski et al., 2005 and Shoesmith, 2007. Their results, which are summarized in Figure 3, show that the presence of dissolved H_2 lowered the corrosion potential of simulated spent fuel specimens containing the ε-phase relative to specimens that did not contain ε phase particles. Furthermore, increasing the amount of ε-phase in the specimens (simulating higher burnup: BU 2% vs 6% in Figure 3) further decreased the measured corrosion potential for the same H_2 concentration.

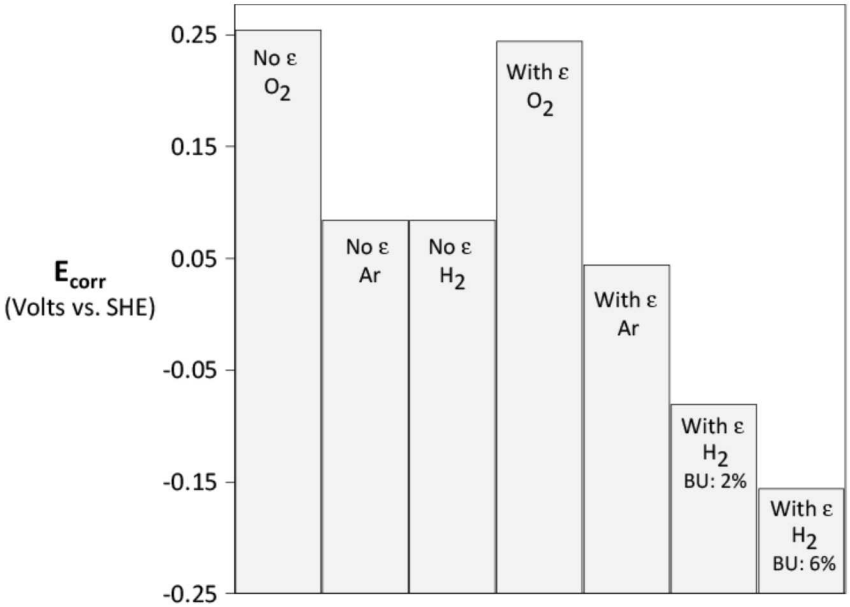


Figure 3. Summary of results from Shoesmith, 2008 showing measured corrosion potentials for simulated spent fuel specimens with and without the fission product alloy Ru □-phase. The conditions for the tests included bubbling either O2, Ar or a gas mixture of 5% H2 in Ar through the electrochemical cell solution. All tests were at 60oC. BU denotes simulated burnup, where higher burnup indicates a higher surface area coverage of the □-phase (adapted from Shoesmith, 2008).

The FMD model calculates the net effect of all redox reactions occurring in the system based on the fuel and steel corrosion potentials (E_{corr}). The corrosion potential is the voltage at which the rates of the anodic and cathodic reactions are equal, that is, at E_{corr} the anodic dissolution current density is balanced by the cathodic oxidant reduction current density (participating reactions are shown schematically in red on Figure 2). Steel corrosion rate at the E_{corr} value established by a particular environmental condition (Eh, pH, chemistry) will depend on whether it corrodes actively or passivates. Under anoxic conditions, the steel corrosion rate is directly proportional to the rate of H_2 generation at the steel surface, since the only cathodic reaction occurring under anoxic conditions is the reduction of water to form H_2. The corrosion rate can be measured electrochemically as a corrosion current, which can be converted to a surface area-normalized mass dissolution rate by using Faraday's law for implementation in the FMD model.

All of the processes shown in Figure 2 are quantified in a parameter database that is updated as new experimental results are obtained. The FMD model parameter database is summarized in Table 1 and the specific parameters updated for FMDM V.4 are shown in Table 2.

Table 1. Summary of FMDM parameters and data gaps that need to be addressed in experimental work to improve the accuracy of the model (adapted from Jerden et al., 2017b).

Parameter	Description	Data needs to improve accuracy
Dimension of fuel environment	(mm – cm)	To be updated when dimensions of waste package are known
Nodes in fuel environment	(log-space grid: fine-spacing near surface)	To be updated when dimensions of waste package are known
Fuel surface coverage by NMP	(~1%)	From literature
Dimension of steel environment	(mm – cm)	To be updated when dimensions of waste package are known
Nodes in steel environment	(log-space grid: fine-spacing near surface)	To be updated when dimensions of waste package are known
Number of FMDM time steps	(100 – 1000)	Use to optimize PA interface
Fuel alteration layer porosity	(~50%)	From literature
Fuel alteration layer tortuosity	(~0.01)	From literature
Fuel alteration layer radiolysis factor	(*not used*)	*Could be activated to account for radionuclide uptake by U secondary phases*
Alpha particle penetration depth	(35μm)	From literature
Fuel burnup	(25 – 75 GWd/MTU)	**Input from PA**
Age of fuel (time out of reactor)	30 – 100 yrs	**Input from PA**
Resistance between fuel and NMP domains	(10^{-3} Volts/Amp)	Interpretation of literature
Temperature history	function	**Input from PA**
Dose rate history	function	Based on MCNPX results of Radulescu, 2011
Spatial dose rate	function (decrease in dose rate with distance from fuel)	Based on MCNPX results of Radulescu, 2011
Rate constants for interfacial reactions in fuel and steel domains	See Figure 2 for summary of specific reactions	**Data need:** experiments needed due to lacking or inconsistent data in current literature on H_2 reactions on fuel and NMP and steel corrosion under relevant conditions
Charge transfer coefficients for interfacial half-cell reactions in fuel and steel domains	See Figure 2 for summary of specific reactions	**Data need:** experiments needed due to lacking or inconsistent data in current literature on H_2 reactions on fuel and NMP
Activation energies	T dependence: See Figure 2 for summary of specific reactions	**Data need:** experiments needed due to lacking or inconsistent data in current literature on H_2 reactions on fuel and NMP and steel corrosion under relevant conditions

Table 1. Continued.

Parameter	Description	Data needs to improve accuracy
Standard potentials for interfacial half-cell reactions: fuel and steel	See Fig. 2 for reactions	From literature
Relative area of fuel domain	Default 1:1, depends on waste package design	To be updated when dimensions of waste package are known
Relative area of steel domain	Default 1:1, depends on waste package design	To be updated when dimensions of waste package are known
Environmental leak rate (diffusion barrier factor)	Depends on waste package design, breach	Interpretation of literature
Environmental concentrations	(O_2, H_2, CO_3^{2-}, Fe^{2+}, Cl^-)	**Input from PA**
Rate constants for bulk solution reactions in fuel, steel environments	See Figure 6 for summary of specific reactions	From literature
Activation energy for bulk solution reactions	T dependence, See Figure 8 for reactions	From literature
Passivation potential of steel surface	(75 V_{SCE}) as place-holder	**Data need:** experiments needed due to lacking or inconsistent data in current literature. For example, C-steels may not passivate under repository relevant conditions. More data are needed to determine active corrosion rates and to quantify the role magnetite corrosion layers play in corrosion behavior at pH > 8.
Passivation corrosion current density	Calculated internally within FMDM	**Data need:** experiments needed due to lack of data in literature
Radiolytic oxidant (H_2O_2) generation value (G_{cond})	Analytical function for conditional G_{H2O2} value from PNNL radiolysis model	Values based on radiolysis model results, Buck et al., 2013. *Would need to be updated, expanded for brine solutions (Cl, Br)*

Table 2. Specific electrochemical parameters that are dominant in determining the rate of spent fuel degradation in the FMD model. The rate constants for the reduction of H2O2 and O2 (bold) are newly updated values for the FMDM V.4, while all others are the same as FMDM V.3. The V.3 parameters were derived from King and Kolar 2004 except for the steel corrosion parameters which are alloy specific and need to be determined experimentally.

Reactions	**Equation**	**k*** (mol m^{-2} s^{-1} or mol s^{-1})	**α**	**E^0** (V)
$UO_2 \xrightarrow{k_{UO_2}} UO_2^{2+} + 2e^-$	$i^{UO_2} = nAFk_{UO_2}\exp\left[\frac{\alpha_{UO_2}F}{RT}(E_{corr}^{UO_2} - E_{UO_2}^0)\right]$	$5.0x10^{-8}$	0.96	0.17
$H_2 + 2OH^- \xrightarrow{k_{H_2}} 2H_2O + 2e^-$	$i^{H_2} = nAFk_{H_2}\exp\left[\frac{\alpha_{H_2}F}{RT}(E_{corr}^{\varepsilon-phase} - E_{H_2}^0)\right]$	$1.0x10^{-3}$	0.5	0.58
$H_2O_2 + \xrightarrow{k_{H_2O_2}} O_2 + 2H^+ + 2e^-$	$i^{H_2O_2} = nAFk_{H_2O_2}\exp\left[\frac{\alpha_{H_2O_2}F}{RT}(E_{corr}^{UO_2} - E_{H_2O_2}^0)\right]$	$7.4x10^{-10}$	0.41	0.12
$H_2O_2 + 2e^- \xrightarrow{k_{H_2O_2}} 2OH^-$	$i^{H_2O_2} = nAFk_{H_2O_2}\exp\left[\frac{\alpha_{H_2O_2}F}{RT}(E_{corr}^{UO_2} - E_{H_2O_2}^0)\right]$	**$2.0x10^{-14}$**	-0.41	0.97
$O_2 + 2H_2O + 4e^- \xrightarrow{k_{O_2}} 4OH^-$	$i^{O_2} = nAFk_{O_2}\exp\left[\frac{\alpha_{O_2}F}{RT}(E_{corr}^{UO_2} - E_{O_2}^0)\right]$	**$1.0x10^{-12}$**	-0.50	0.43
$Fe \xrightarrow{k_{Steel}} Fe^{2+} + 2e^-$	$i^{Steel} = nAFk_{Steel}\exp\left[\frac{\alpha_{Steel}F}{RT}(E_{corr}^{Steel} - E_{Steel}^0)\right]$	*Data Need*	*Data Need*	*Data Need*
$2H_2O + 2e^- \xrightarrow{k_{H_2}} H_2 + 2OH^-$	$i^{H_2O} = nAFk_{H_2O}\exp\left[\frac{\alpha_{H_2O}F}{RT}(E_{corr}^{Steel} - E_{H_2O}^0)\right]$	$5.0x10^{-7}$	-0.48	-1.1

Where (i) is the current density for a half-call reaction (proportional to the reaction rate), (k) is the half-cell reaction rate constant, (α) is the charge transfer coefficient and (E^0) is the standard potential.

#Values shown in bold are updated constants for FMDM V.4 that were derived by comparing the FMDM results to experimental data (see Figure 4 and 5).

*The rate constant and other parameter values for steels will vary depending on the alloy composition. Electrochemical experiments with relevant alloys such as 316, 304 and low carbon steels are needed to quantify these parameter values.

As indicated in Table 2, the parameter values that were updated for FMDM V.4 are the rate constants for the reduction of H_2O_2 and O_2 on the UO_2 surface. These rate constants are used in the Butler Volmer relationships on which the FMD model is based on (see Table 2 for details).

The comparison of model results from FMDM V.4 and experimental datasets for the dissolution rate of spent fuel, simulated spent fuel and UO_2 are shown in Figures 4 and 5. The purpose of the comparison of the FMD model results to the experimental data was not to fit the data in a statistical sense, but rather to improve the accuracy of the model results while maintaining a conservative margin of safety (i.e. model

should reasonably overpredict degradation rates). As shown in Figure 3 the newer parameter value for the H_2O_2 reduction give a more accurate conservative bound to the experimental data.

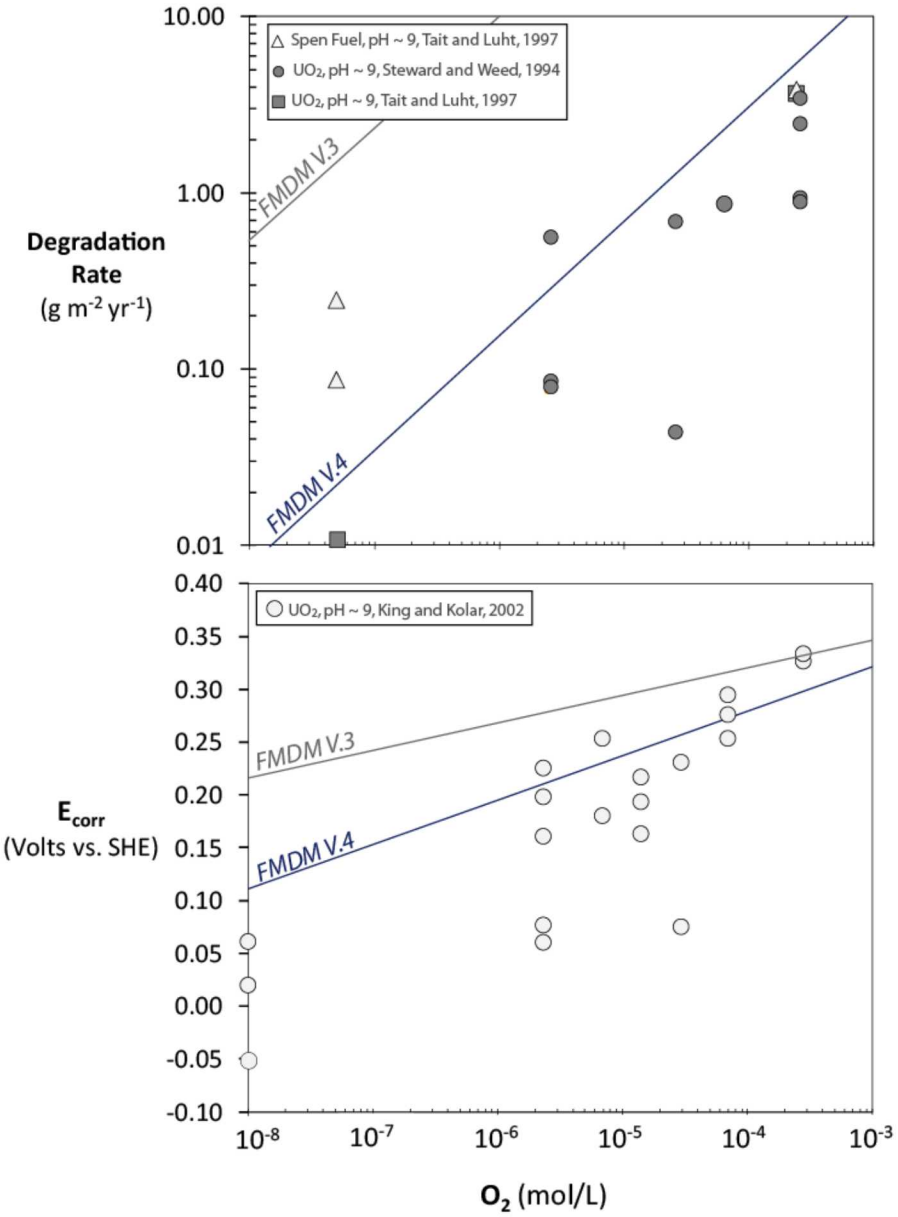


Figure 4. Comparison of results from the updated version 4 of the FMD model to experimental results. The model runs were for 25oC and no other oxidants were present.

Figure 4 shows the degradation rate (top plot) and E_{corr} (bottom plot) calculated by the FMDM V.3 and FMDM V.4 over a range of relevant dissolved concentrations of O_2 (no other oxidants present) and compares the model results to experimental data. The comparisons show that FMDM V.4 with the updated parameter value for O_2 reduction on the fuel (Table 2) is more consistent with the experimental results. The data points for spent fuel at ~$5x10^{-8}$ M O_2 in the degradation plot (top) are elevated relative to the general trend in the data due to the presence of radiolytic oxidants other than O_2 in those tests.

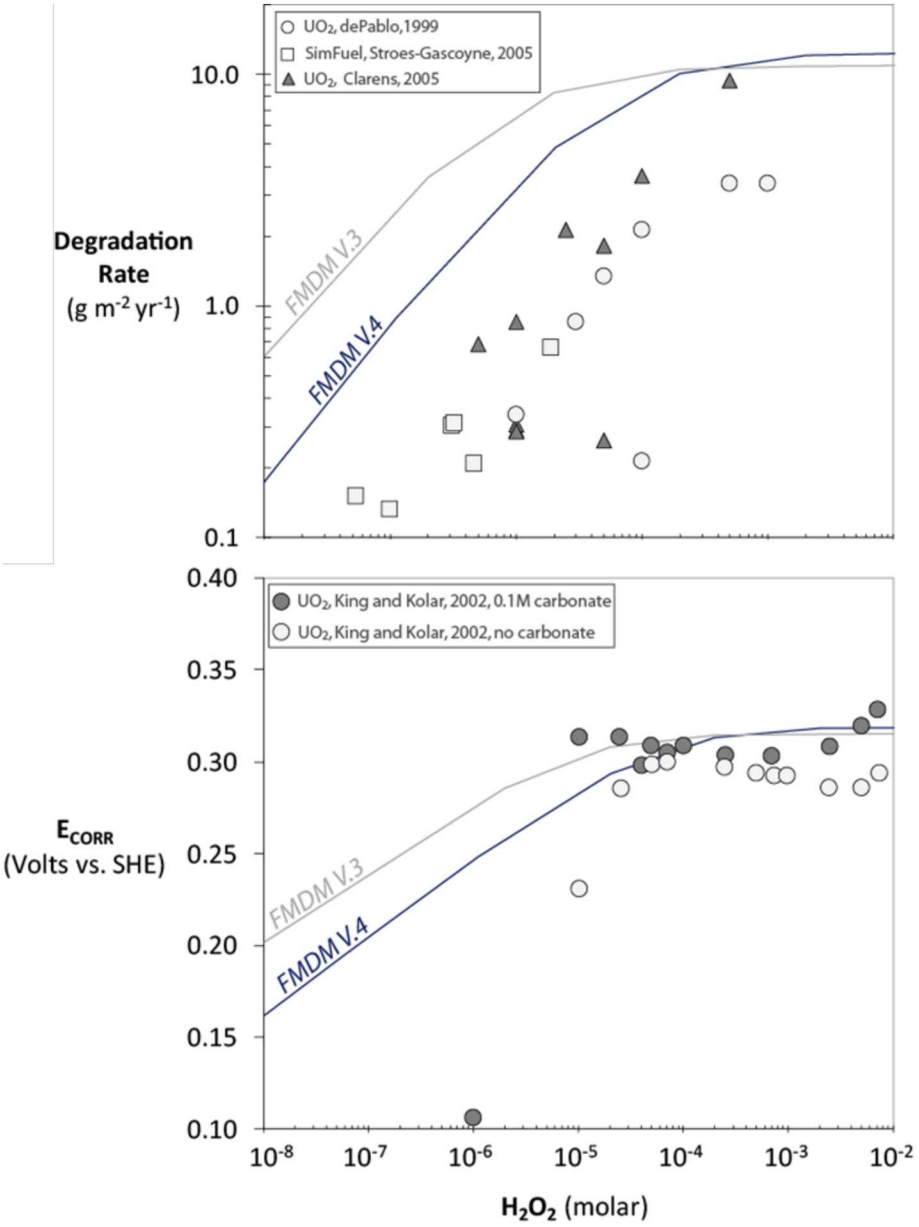


Figure 5. Comparison of results from the updated version 4 of the FMD model to experimental results. The model runs were for 25oC and an O2 concentration of 10-9 molar.

Figure 5 shows the degradation rate (top plot) and E_{corr} (bottom plot) calculated by the FMDM V.3 and FMDM V.4 over a range of relevant dissolved concentrations of H_2O_2 and compares the model results to experimental data. In general, the FMDM V.4 with the updated parameter value for H_2O_2 and O_2 reduction on the fuel (Table 2) is more consistent with the experimental results. The model results for the degradation rate (top plot) are purposefully high as the goal is for the model to provide a conservative, but realistic, upper bound for the spent fuel dissolution rate.

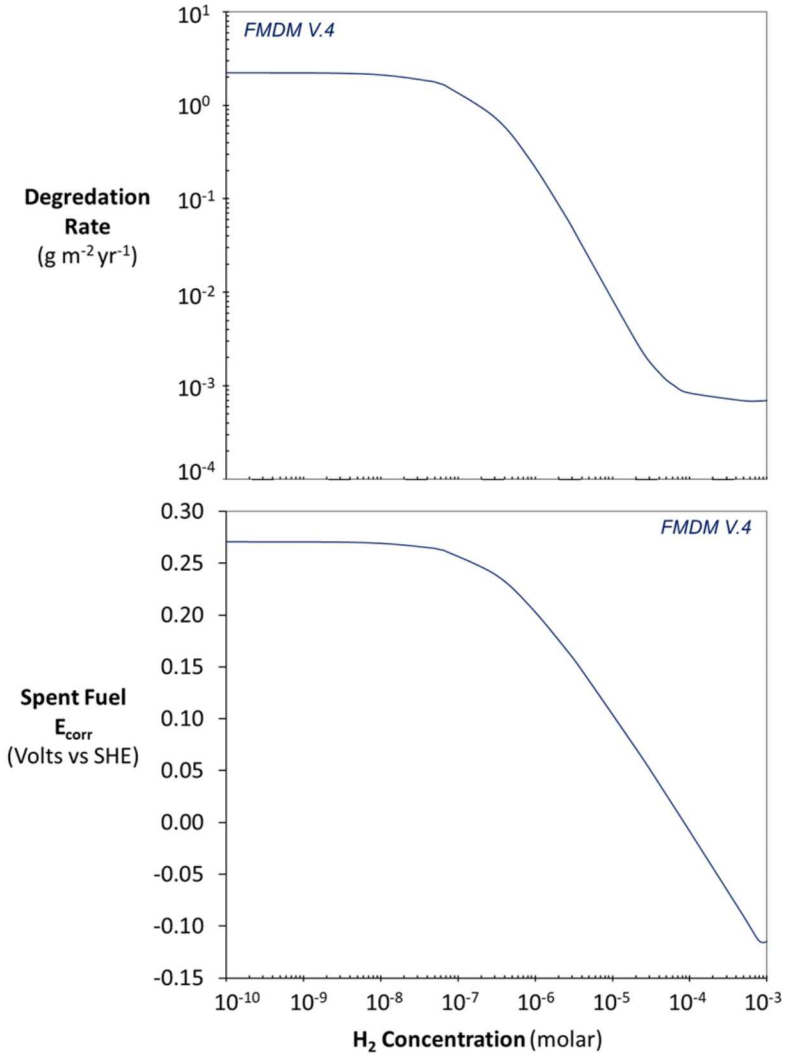


Figure 6. Results from version 4 of the FMD model showing the degradation rate and calculated Ecorr as functions of the H2 concentration at the spent fuel surface. For these runs the temperature was 25oC, the O2 concentration was 10-9 M and the H2O2 concentration was 10-6 M.

Figure 6 shows the degradation rate (top plot) and E_{corr} (bottom plot) calculated by the FMDM V.4 over a range of relevant dissolved concentrations of H_2 concentrations at the spent fuel surface. The degradation plot (top) shows an inflection around 10^{-7} M H_2 indicating that the oxidation of H_2 begins to counteract the oxidative dissolution of the fuel at sub micromolar concentrations. When the H_2 concentration increases to around 10^{-4} M, the oxidation of H_2 becomes the dominant anodic reaction at the fuel surface thus effectively shutting off oxidative dissolution. Under the conditions for this model run the threshold E_{corr} for effectively shutting down the oxidative dissolution of the fuel is around 0.0 volts vs. SHE. As shown in Figure 6, after oxidative dissolution is shut down by H_2 oxidation the fuel continues to degrade at a rate of approximately 10^{-3} g m^{-2} yr^{-1}, which is the chemical dissolution rate of the fuel [UO2(s) → UO_2(aq)]. This lower degradation rate value is consistent with experimental results under reducing conditions (Jerden et al., 2017a).

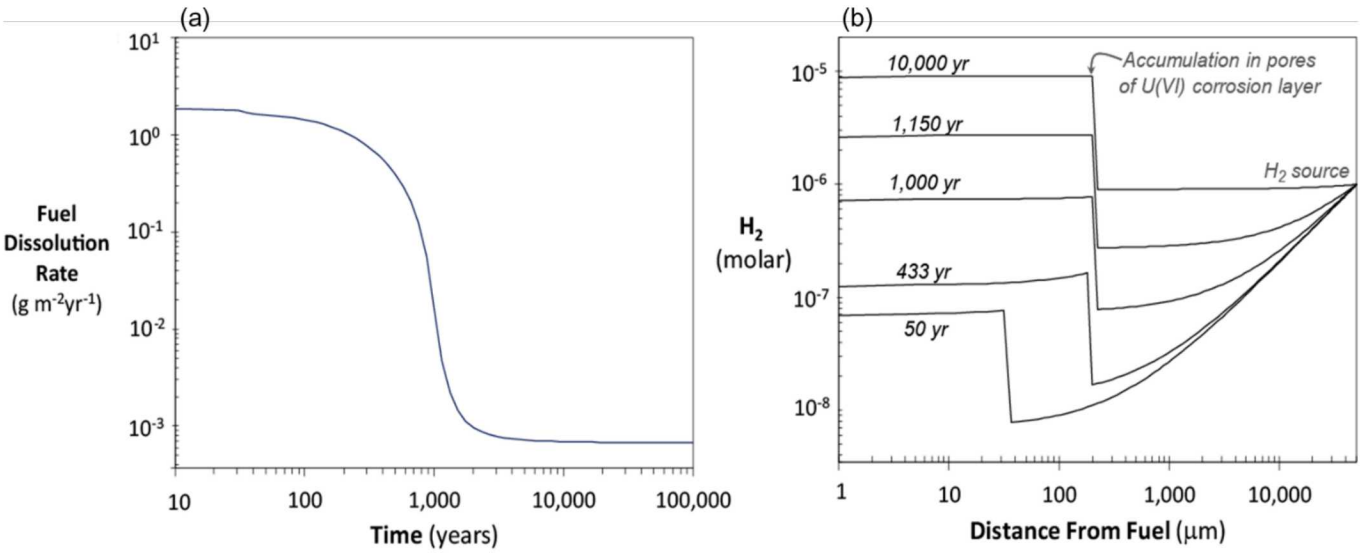


Figure 7. Model results using FMDM V.4 showing the fuel degradation rate as a function of time (a) and the H2 concentration as a function of distance from the fuel surface (b). The temperature for these model runs was 25oC, the O2 concentration was 10-9 M and the fuel burnup was 60 GWd/MTU.

Figure 7 shows the fuel degradation rate vs. time (a) and the H_2 concentration profiles at several times during a typical repository simulation. This example indicates the importance of the accumulation of H_2 near the fuel surface with time. This accumulation is accentuated by the presence of the porous U(VI) corrosion layer, which is modeled as a set of parallel tortuous pores that decrease species diffusion rates. In this example, a concentration of around $3x10^{-6}$ M H_2 is sufficient to counteract the oxidative dissolution of the fuel; however, this concentration is not achieved until around 1200 years. The H_2 source in this example is assumed to be a constant concentration of $1x10^{-6}$ M; however, in more realistic scenarios the H_2 source concentration will change depending on how changing repository conditions determine steel corrosion rates as a function of time. The addition of the steel corrosion module into the FMD model and the associated validation experiments will allow for the modeling of this more realistic scenario.

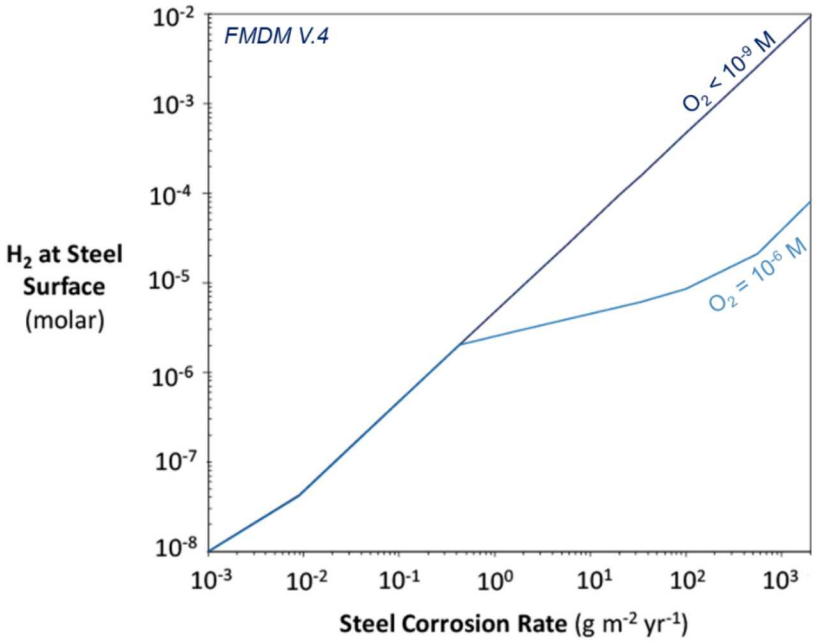


Figure 8. Model results using steel corrosion module of the FMDM V.4 showing the calculated H2 concentration at the fuel surface as a function of the steel corrosion rate. The temperature for these model runs was 25oC, the O2 concentration was 10-9 M and the O2 concentration is indicated on the plot.

Figure 8 shows the concentration of H_2 produced by steel corrosion calculated by the steel corrosion module of the FMDM V.4 for different starting O_2 concentrations. This plot indicates how changes in dissolved oxygen concentrations can significantly affect the amount of H_2 produced by steel corrosion. For example, for a steel corrosion rate of around 100 g m^{-2} yr^{-1} and nanomolar O_2 the H_2 concentration due to steel corrosion would be around $5x10^{-4}$ M vs. a H_2 concentration of around $9x10^{-6}$ for solutions containing micromolar O_2. As shown in Figures 6, a concentration of $5x10^{-4}$ M H_2 is more than enough to shut down the oxidative dissolution of the fuel, while concentrations around 10^{-5} M H_2 do not completely counteract oxidative fuel degradation for 60 GWd/MTU fuels that are less than 1000 years old. Figure 8 highlights the need for an accurate and experimentally validated steel corrosion model that will provide a way to account for different alloy corrosion rates (i.e. different H_2 source concentrations) under changing repository conditions.

3. Electrochemical Experiments to Parameterize the FMDM Steel Corrosion Module

3.1 Background

As discussed above, establishing accurate steel corrosion rates for relevant disposal conditions is essential for accurate spent fuel degradation and source term modeling because of the dominant effect of H_2 on the spent fuel dissolution rate (as shown in Figures 6 and 7 above). The half-cell reactions of particular interest for H_2 generation are as follows:

$Fe^0 \rightarrow Fe^{2+} + 2e^-$ (Reaction 1)

$2H_2O + 2e^- \rightarrow H_2 + 2OH^-$ (Reaction 2a)

$2H^+ + 2e^- \rightarrow H_2$ (Reaction 2b)

with the overall steel corrosion reactions

$Fe + 2H_2O \rightarrow H_2 + Fe^{2+} + 2OH^-$ (Reaction 3a)

$Fe + 2H^+ \rightarrow H_2 + Fe^{2+}$ (Reaction 3b)

Reactions 3b and 3a indicate the fundamental coupling between steel corrosion and H_2 generation in alkaline and acidic conditions (respectively). The oxidation of other steel constituents (e.g., Cr, Mo, Ni, and Mn) will contribute to the anodic current, but the oxidation of Fe will be dominant.

To provide context for the experimental plan, Figure 9, which is a simplified version of the reaction FMDM reaction scheme shown above in Figure 2 above, that highlights the key H_2 consuming and producing reactions and shows schematically the potential importance of Zircaloy cladding as a source of hydrogen. Carbon steels, stainless steels and Zircaloly will all be corroding simultaneously with the spent fuel, therefore, our experiments will include representative specimens of each of these alloy types.

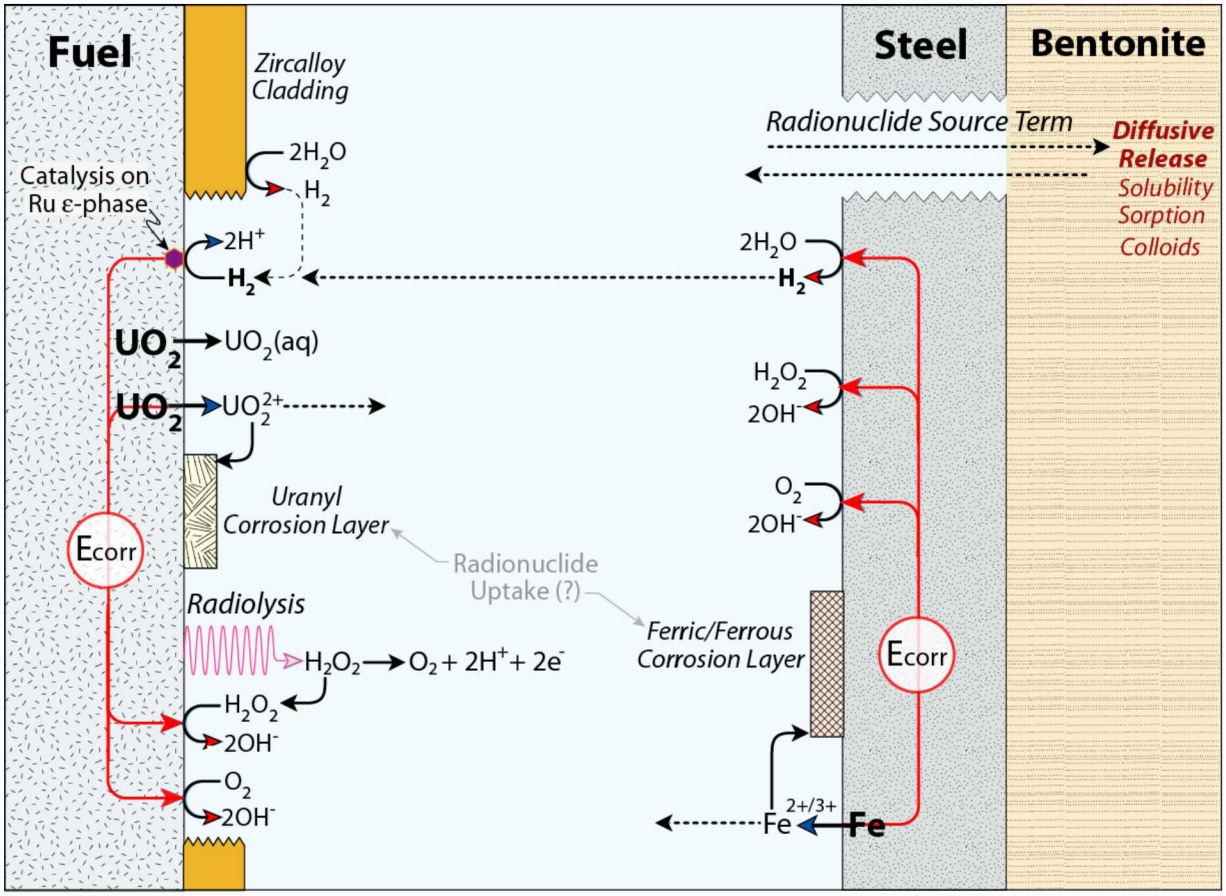


Figure 9. Schematic diagram of the FMD model reaction scheme highlighting the reactions that consume and produce H_2.

As discussed in Jerden et al., 2017(a), there is a wealth of literature on steel corrosion but much of the previous work was not done under conditions relevant for crystalline and argillite rock-type repositories. For example, Arthur has compiled corrosion rate data for a number of relevant alloys tested under a variety of conditions (Table 3); however, this compilation does not include the anoxic corrosion rates that that are more relevant to crystalline and argillite repository concepts. There is a significant amount of literature data on the corrosion of carbon steels, cast iron and forged steels (see reviews by Johnson and King, 2003 and King, 2007); however, much of these corrosion rate data are derived from batch style immersion tests that provide average cumulative rates rather than the instantaneous corrosion rates needed to represent the H_2 generation rates and to parameterize and validate the FMDM steel corrosion module.

Steel coupon immersion tests provide useful information on mineralogy and the evolution of the chemical system, but the Eh, pH and solution chemistry are not controlled and the surface conditions can change significantly over the test duration. Corrosion rates derived from immersion tests are based on cumulative mass loss measurements or corrosion layer thicknesses that do not indicate how the corrosion rate (and thus H_2 generation rate) varies with time or conditions (most importantly, with the solution Eh). Knowing these dependencies of the H_2 generation rate is essential for modeling spent fuel dissolution under evolving in-package chemical conditions.

Electrochemical tests can be used to quantify the effects of surface stabilization due to passivation and localized corrosion, such a pitting, that can only be qualitatively observed in coupon immersion tests. Furthermore, electrochemical methods can measure rates on the order of nanograms cm^{-2} d^{-1}. Thus, the use of electrochemical methods would provide reliable corrosion rates for durable EBS materials (including Zircaloy cladding) and provide dependencies on environmental conditions that could be used to predict the long-term generation of H_2 and attenuation of fuel degradation rates as the seepage water composition evolves.

To provide instantaneous corrosion rates under controlled redox conditions, we have initiated a set of electrochemical experiments focused on providing parameter values and validation data for the FMD model for a range of relevant alloys.

Table 3. Statistical summary of immersion-type corrosion test results compiled by Arthur, 2004 (adapted). The anaerobic carbon steel corrosion rates are from King, 2007.

Metal	Conditions	Corrosion Rate (g m^{-2} yr^{-1})				Standard Deviation
		Min	Max	Median	Mean	
Stainless Steel Types 302/304/304L	Dilute groundwater[1] (25°C to 100°C)	0.01	12.56	1.03	1.71	2.38
	Saltwater (26.7°C)	12.70	313.18	40.64	91.53	89.07
	Saltwater (90°C)	5.28	127.20	16.24	46.53	47.62
Stainless Steel Types 316/316L/AM-350	Dilute groundwater (29.5°C)	0.01	0.38	0.02	0.07	0.11
	Dilute groundwater (50°C to 100°C)	0.30	4.08	1.83	1.98	1.17
	Saltwater (26.7°C)	0.01	118.30	5.89	15.51	26.77
Neutronit (borated stainless steel)	Dilute groundwater (29.5°C)	0.01	0.09	0.02	0.03	0.03
	Dilute groundwater (50°C to 100°C)	0.20	2.64	1.62	1.65	0.70
	Saltwater (26.7°C)	14.48	233.76	59.04	88.48	81.52
Stainless Steel Type 304 Alloyed with 0.3% Boron	Dilute groundwater (~25°C)	24.40	97.52	36.56	48.80	30.88
	Dilute groundwater (boiling)	24.40	219.44	134.08	126.00	63.92
Stainless Steel Type 304 Alloyed with 1.5% Boron	Boiling Dilute groundwater	1292.32	2023.84	1694.72	1682.48	262.16
Carbon Steel	Dilute groundwater (60°C)	629.68	1045.60	815.60	821.68	98.96
	Dilute groundwater (90°C)	464.64	1040.16	616.40	649.12	121.04
	Concentrated groundwater (60°C)	402.00	833.60	502.16	544.64	113.36
	Concentrated groundwater (90°C)	59.12	176.48	99.36	102.24	30.16
	Anoxic DIW in bentonite (80°C)	31.6	87.5	NA	NA	NA
	Anoxic brine in bentonite (80°C)	50.3	161.3	NA	NA	NA

[1]Dilute groundwater: dilute simulated ground waters with compositions similar J13 well water, a dilute sodium carbonate groundwater from the Yucca Mountain Site (see Arthur et al., 2004 for composition); [2]Saltwater refers to sea water with ~17,000 ppm chloride; [3]Concentrated groundwater: simulated J13 well water concentrated 1000x by evaporation. NA: not applicable, no statistical analysis performed.

3.2 Method and Results

The electrochemical corrosion experiments being performed at Argonne employ the standard three electrode method as described by Bard and Faulkner, 2001. The three-electrode cell used for the Argonne tests consists of a 20 mL jacketed, borosilicate glass vessel with a saturated calomel reference electrode (SCE), a graphite counter electrode and a steel, Zircaloy or UO_2 working electrode. A typical electrochemical cell and working electrode is shown in Figure 10. For these scoping experiments, an aggressive 10 mM NaCl solution adjusted to pH 4 with sulfuric acid was used as the electrolyte.

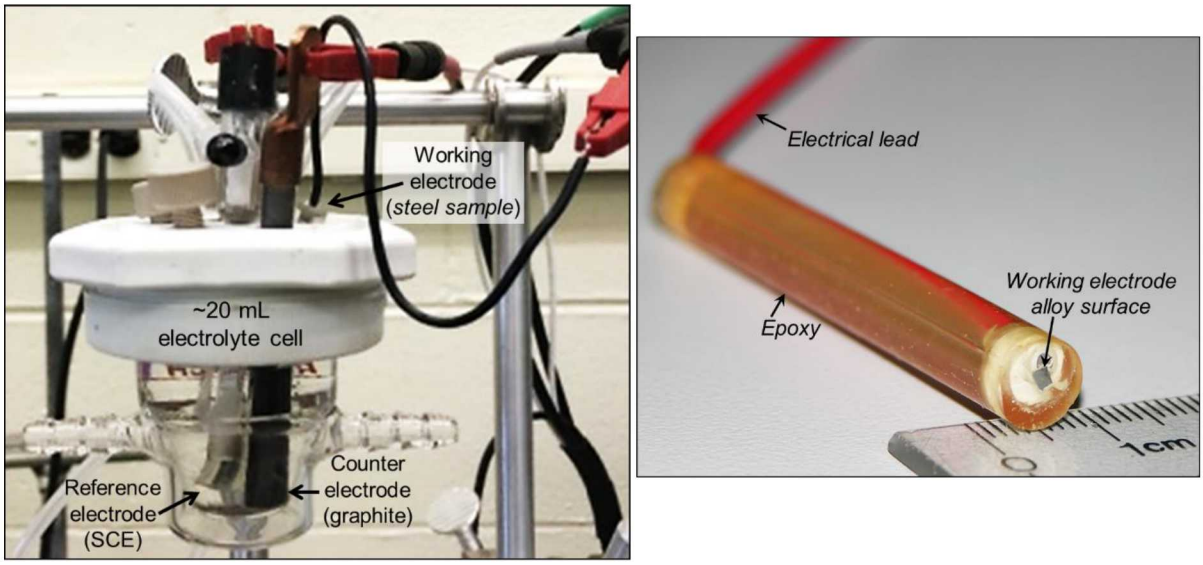


Figure 10. Three-electrode electrochemical cell used in Argonne electrochemical experiments (left) and an example alloy working electrode (right). The working electrode shown is made of Zircaloy-4, but the steel electrodes used for ongoing and future tests are the same size and mounted in the same way.

In the electrochemical tests, the electrolyte is used to impose chemical effects, including pH and Cl^- concentrations, and a potentiostat is used to impose a surface potential representing the solution Eh. The potentiostat can be used to impose a wide range of fixed potentials to efficiently determine the effect of the solution Eh on the steel corrosion and H_2 generation rate. In practice, a potentiodynamic scan is performed to measure E_{corr} for the polished surface in the test solution and identify regions of active and passive behavior to be studied in subsequent potentiostatic tests. The potentiodynamic scan indicates the propensity for active or passive corrosion, but the rapid scan rate does not allow stable passive layers to form. Potentiostatic tests are conducted to measure the corrosion currents as stable passive layers form or the constant currents are achieved with actively corroding metals.

Figure 11 (adapted from Jerden et al., 2017a) shows typical results for potentiodynamic (PD) scans (a) and potentiostatic (PS) measurements (b) in tests with the three main alloys of interest. These scoping tests were performed under aggressive corrosion conditions (pH 4 for steels and pH 1 for Zircaloy) to optimize the methodology. These types of PD and PS analyses will be performed under a range of relevant repository conditions as part of the ongoing FY18 and future FY19 electrochemical tests. The test matrix for these ongoing and planned experiments is shown in Table 5.

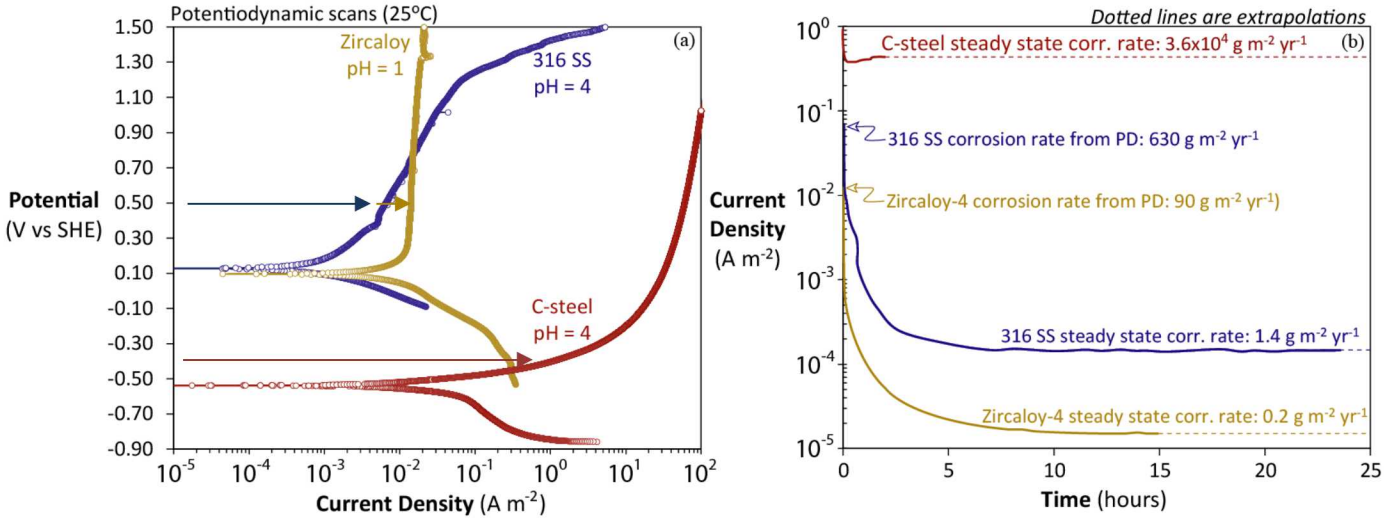


Figure 11. Example data from Jerden et al., 2017(a) showing they types of results obtained from electrochemical measurements: (a) potentiodynamic polarization and (b) potentiostatic corrosion of carbon steel at -0.4 V_{SHE} and pH = 4, 316L stainless steel at 0.5 V_{SHE} and pH = 4, and Zircaloy-4 at 0.5 V_{SHE} in pH 1 solution. The current densities measured in the PD scans are shown in (b) to illustrate the passive stabilization of 316 SS and Zircaloy-4 under these test conditions.

As shown in the scoping test data (Figure 11a) carbon steel, stainless steel and Zircaloy show significantly different corrosion behaviors (Jerden et al., 2017a). Carbon steel corrodes actively at very low potentials and does not passivate; while, stainless steel and Zircaloy-4 are noble at potentials below about -0.2 V and 316L passivates at moderate potentials, but corrodes actively above about 0.5 V. Zircaloy-4 passivates to high potentials in the absence of chloride (as shown), but passivation breaks down in the presence of even small amounts of chloride. As indicated by the arrows in Figure 11a, the potentiostatic tests (Figure 11b) were conducted at potentials above the E_{corr} values. The corrosion currents in the tests with Zircaloy-4 and 316L decrease as the surfaces are rapidly passivated in the pH 4 solution. Relative to the currents measured for the freshly polished clean surfaces in the potentiodynamic scans, the corrosion currents for Zircaloy-4 and 316L decrease about 1.5 and three orders of magnitude due to passivation, respectively. The initial corrosion rate of 316 SS is 630 g m^{-2} yr^{-1} (measured in the PD scan) but the steady state rate of the stabilized surface appropriate for calculating H_2 generation in the FMDM is only 1.4 g m^{-2} yr^{-1}. This rate is consistent with the 316 corrosion rates of 0.01 – 0.38 g m^{-2} yr^{-1} measured in dilute groundwater compiled by Arthur, 2004 (Table 3).

As pointed out in Jerden et al., 2017(a), the corrosion currents measured for the stabilized surfaces (Figure 11b) are appropriate for modeling the long-term H_2 generation rates in the FMD model. These passivated rates for Zircaloy-4 and 316L are readily measured electrochemically, but these are too low to have been measured by mass loss in coupon immersion tests. The corrosion behaviors and rates will be different under different environmental conditions, particularly for different Eh, pH, and Cl^- concentrations, and the differences must be taken into account in the FMD model. The electrochemical tests can provide the rate dependencies on these and other environmental variables.

Representative data from the solids characterization of corrosion phases produced during potentiostatic tests with 4320 carbon steel are shown in Figures 12 and 13. Figure 12 shows SEM micrographs of the freshly polished electrode surface (a) and (b) and the surfaces after potentiostatic corrosion at -0.45 V_{SCE} for different durations (c) and (d). The two distinct phases have different corrosion behaviors. The darker colored ferrite phase is the common body-centered cubic iron allotrope (α-iron) that corrodes preferentially relative to the lighter colored pearlite, which is a two-phased, lamellar structure consisting of alternating layers of ferrite and a corrosion resistant iron carbide phase (Fe_3C). characterizing the steel microstructure is essential to understanding the corrosion behavior.

The 4320-alloy produced enough oxide corrosion products under the aggressive corrosion conditions (pH 4, potentiostatic holds at 0.1 and -0.45 V_{SCE}) for powder XRD analysis to be performed, and the results are shown in Figure 13. The major mineral phases identified in the corrosion layer were the ferric oxy-hydroxides maghemite (γ-Fe_2O_3) and lepidocrocite [γ-FeO(OH)]. For this experiment, ferric corrosion phases were favored over ferrous phases due to the presence of O_2 in the electrolyte solution. Future tests will focus on lower potentials and lower dissolved O_2 concentrations that are more representative of the reducing conditions anticipated to prevail within crystalline and argillite rock type repositories. A controlled atmosphere glovebox has been constructed to provide a low-oxygen environment for the electrochemical tests.

Most electrochemical tests will not generate enough corrosion phases for phase identification by powder XRD; therefore, electron diffraction by TEM may be used to characterize corroded alloys for selected tests. The TEM samples will be prepared using Argonne's FEI Strata 400 focused ion beam, field emission microscope with an AutoProb 200 sample extraction system (FIB). Specimens will be provided to collaborators within the SFWST campaign.

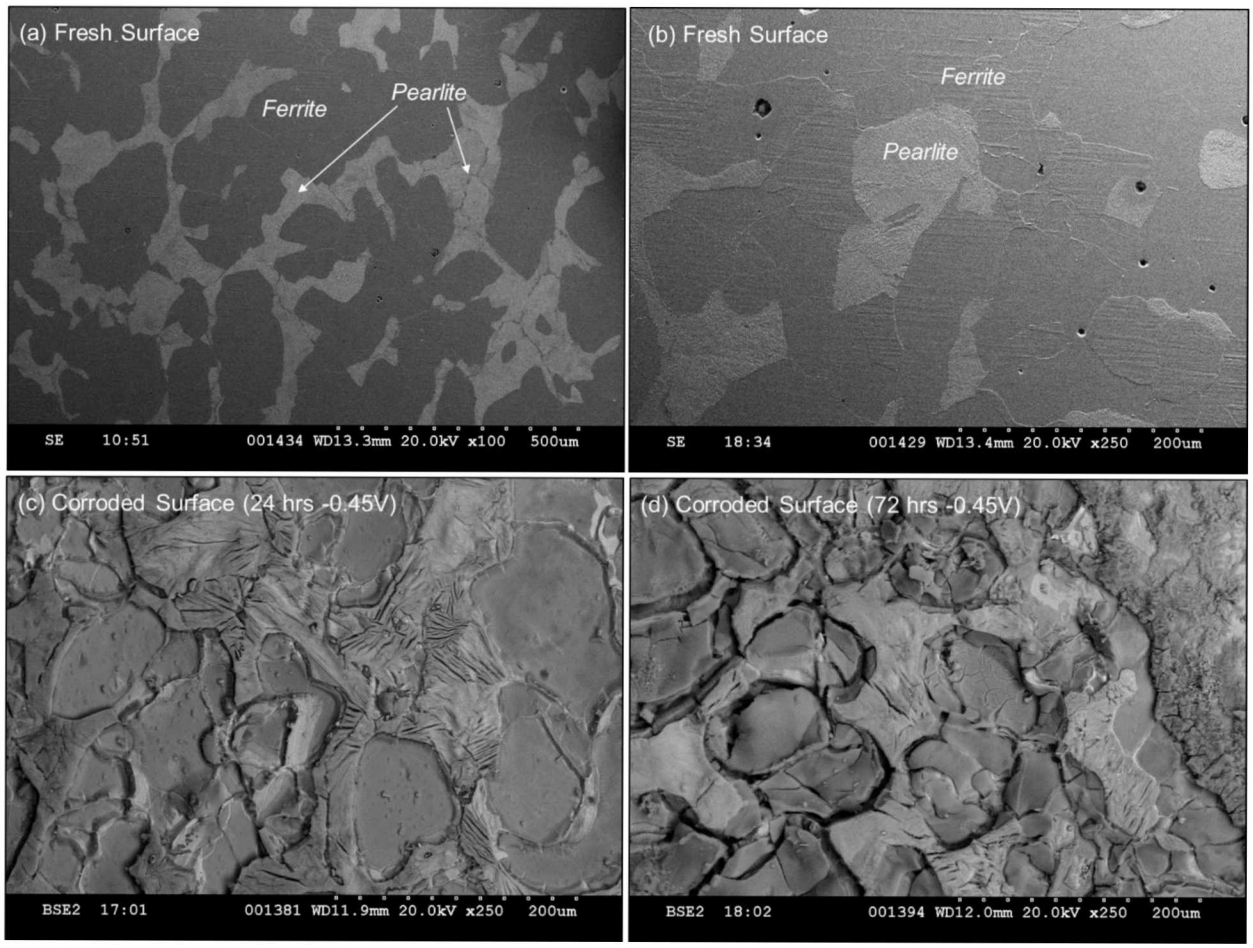


Figure 12. SEM micrographs of the polished unreacted 4320 steel electrodes (a) and (b) and the same electrode after 24 hours (c) and 72 hours (d) under potentiostatic conditions at 0.45 VSCE and pH 4 [Gattu et. al. 2018, NACE].

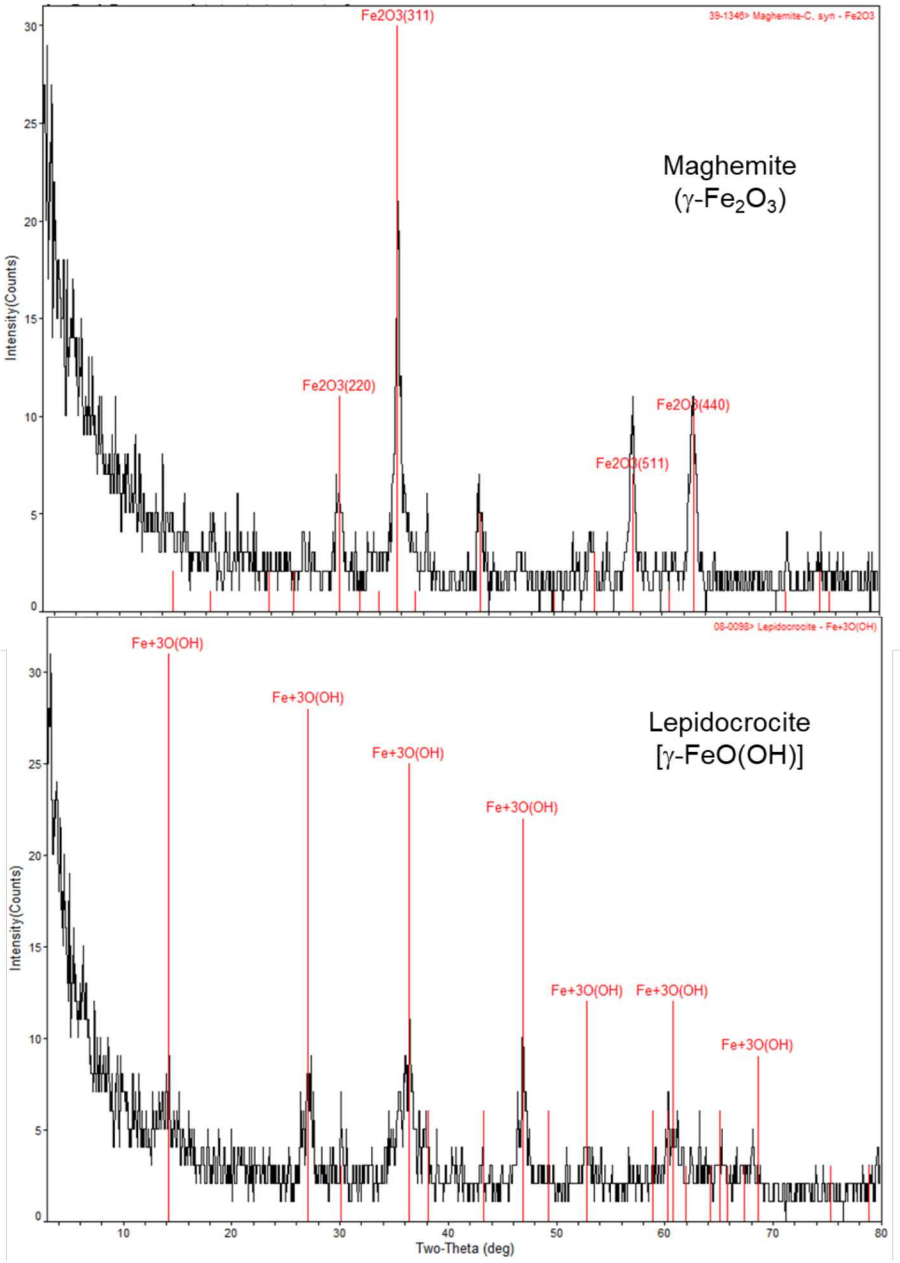


Figure 13. X-ray diffraction scans of oxide corrosion phases from the potentiostatic tests on 4320 carbon steel. The top diagram was for the -0.45 volts hold and the bottom diagram was for the 0.1 volts hold.

The test matrix shown in Table 5 calls for experiments to be performed in both sodium chloride and sodium sulfate solutions of varying concentrations to quantify the effect these anions have on steel and Zircaloy corrosion over a range of repository relevant Eh and pH conditions. The experimental concentrations for chloride and sulfate and other chemical variables such as pH and ionic strength are based on the chemical analyses of the bentonite pore waters presented in Fernandez et al., 2001 (Table 4).

As shown in Table 5, some experiments will be performed in the presence of a UO_2 (or lanthanide doped UO_2) electrode to provide a continuous source of uranium as the UO_2 dissolves at a rate established by the solution chemistry and measured electrochemically. These tests involving the simultaneous corrosion of the alloy and UO_2 will produce samples that can be used to determine if the dissolved uranium is incorporated into steel corrosion phases. Detailed analytical electron microscopy will be required to both identify the corrosion phases present and to determine their uranium content and disposition. A range of different types of steel corrosion phases can be produced using the electrochemical approach described above as some tests will involve relatively oxidizing potentiostatic holds while others will be held at reducing conditions just above the alloy's corrosion potential in low O_2 environments.

Each electrochemical experiment will generally involve the following sequence of tests:

- potentiodynamic scans to determine E_{corr} of alloy under conditions of interest,
- potentiostatic holds over a range of relevant redox conditions,
- standard electrical impedance spectroscopy to characterize the properties of passivating oxide layers,
- detailed microscopy (reflected light, SEM/EDS) to characterize alloy microstructures before and after corrosion tests.

The results from these tests will provide the following information:

- corrosion rates for stabilized surfaces under controlled environmental conditions,
- electrical properties of the passivated surfaces to provide confidence in their long-term stability,
- analytical expressions for key dependencies (Eh, pH, T, chloride concentration) to formulate rate laws for the corrosion of different materials required to calculate H_2 generation rates in the FMD model.
- corrosion products for further analyses

Table 4. Bentonite pore water chemistry from FEBEX bentonite water extraction tests (adapted from Fernandez et al., 2001).

Measured Values	**Surface:Volume**		
	4.2:1	3.8:1	3.3:1
pH	7.49	7.29	7.38
Species *(mg/L)*			
Cl^-	2200	3600	4000
SO_4^{2-}	603	1100	1260
Br^-	4.9	4.9	9.1
HCO_3^-	67	131	133
SiO_2(aq)	10.9	14.4	N.D.
Al^{3+}	0.34	N.D.	0.12
Ca^{2+}	295	450	510
Mg^{2+}	385	410	390
Na^+	800	1725	2100
K^+	7.5	54	15
Sr^{2+}	6.2	6.9	7.5

N.D.: Not Determined

Table 5. Test matrix for electrochemical experiments. Experiments will determine corrosion rates and mechanisms using standard potentiodynamic polarization, potentiostatic holds and electrical impedance spectroscopy techniques.

Solution Variables	2000 mg/L Cl^- No UO_2			4000 mg/L Cl^- No UO_2			2000 mg/L Cl^- UO_2 Pellet at OC			4000 mg/L Cl^- UO_2 Pellet at OC		
pH	4	7	10	4	7	10	4	7	10	4	7	10
316L SS	FY18	FY18	FY18	FY18	FY18	FY18	FY19	FY19	FY19	FY19	FY19	FY19
304L SS	Future work	Future work	Future work	Future work	Future work	Future work	Future work	Future work	Future work	Future work	Future work	Future work
Carbon Steel (4320)	FY18	FY18	FY18	FY18	FY18	FY18	FY19	FY19	FY19	FY19	FY19	FY19
Borated SS (Neutronit)	Future work	Future work	Future work	Future work	Future work	Future work	Future work	Future work	Future work	Future work	Future work	Future work
Zircaloy-4	FY18	FY18	FY18	FY18	FY18	FY18	NA	NA	NA	NA	NA	NA
Solution Variables	600 mg/L SO_4^{2-} No UO_2			1300 mg/L SO_4^{2-} No UO_2			600 mg/L SO_4^{2-} UO_2 Pellet at OC			1300 mg/L SO_4^{2-} UO_2 Pellet at OC		
pH	4	7	10	4	7	10	4	7	10	4	7	10
316L SS	Future work	Future work	Future work	Future work	Future work	Future work	Future work	Future work	Future work	Future work	Future work	Future work
304L SS	Future work	Future work	Future work	Future work	Future work	Future work	Future work	Future work	Future work	Future work	Future work	Future work
Carbon Steel (4320)	Future work	Future work	Future work	Future work	Future work	Future work	Future work	Future work	Future work	Future work	Future work	Future work
Borated SS (Neutronit)	Future work	Future work	Future work	Future work	Future work	Future work	Future work	Future work	Future work	Future work	Future work	Future work
Zircaloy-4	Future work	Future work	Future work	Future work	Future work	Future work	Future work	Future work	Future work	Future work	Future work	Future work

NA (not applicable) tests with UO2 and Zircaloy will not be performed.

Starting solution composition will from the middle column (3.8:1) shown in Table 1.

All tests to be performed at ambient temperature (will be measured and recorded for each test).

OC: Open Circuit.

4. Conclusions and Future Work

The accomplishments and conclusions of this study are summarized as follows:

- The parameter database for the FMD model was updated based on comparisons between model results and existing spent fuel and UO_2 dissolution rate data.

- Results from sensitivity runs with the new model version (FMDM V.4) reiterate the need for experimental data to parameterize and validate the steel corrosion module added to the FMD model as discussed in Jerden et al., 2017(a) and Jerden et al., 2017(b). Electrochemical tests are in progress to support implementation of an improved steel passivation model in the FMD model by providing data sets with which the model can be calibrated for metals that will be present in the repository engineered barrier system (EBS) and key environmental variables.

- Results from scoping experiments demonstrated a straightforward electrochemical method that provides the electrokinetic information needed for model parameterization and validation.

- Model simulations using the FMDM V.4 agree with previous FMD model results showing that the presence of metals that corrode at different rates can extend the time over which H_2 generation will attenuate the fuel degradation rate. The materials used in the EBS can be selected to benefit the long-term performance of disposed fuel based on their measured corrosion behaviors and impacts on fuel durability as quantified by the FMDM calculations.

Model runs performed for this report demonstrate a number of important information gaps that need to be addressed by experimental work and in further model developments. These information gaps, which were also noted in Jerden et al., 2017(b), are as follows:

- Electrochemical corrosion experiments are needed to quantify the dependencies of spent fuel and steel corrosion rates on environmental variables under carefully controlled conditions. Most importantly, the dependencies of the steel corrosion rates on Eh, pH and the attenuating effect of passivation must be known to calibrate and validate the FMD model. Electrochemically determined corrosion rates are appropriate for calibrating the H_2 generation rates calculated with the FMD steel corrosion module because they quantify the electron transfer rate in the reduction reaction that generates the H_2. Examples of those electrochemical tests are summarized in this report.

- Experimental and modeling studies investigating the corrosion rates of different alloys that may go into the waste package design and waste form degradation are needed. Understanding the corrosion behavior of a variety of relevant engineering materials would provide important insights as to the types of steel that could be used to optimize the long-term performance of the waste package and canister materials. For example, using a combination of actively corroding and passive metals having a range of corrosion rates could be utilized to ensure H_2 would be generated throughout most of the regulated service

life. The steel corrosion model developed to quantify H_2 generation from metal surfaces within a breached waste package can also be used to model the corrosion kinetics of external surfaces contacted by bentonite pore water and possibly to model container breaching.

- Electrochemical tests quantifying the kinetic parameters for individual reactions at the in-package solution – spent fuel interface are needed (e.g., see Table 2 above). Based on the use of robust canisters, it is likely that the majority of the spent fuel in a repository will not be contacted by groundwater until canisters begin to fail more than 1000 years after repository closure. More studies are needed to determine the effects of fuel aging on fuel dissolution rates by measuring dissolution rates of actinide oxide materials that simulate "aged" ~1000 year old fuel in the presence of H_2. Such materials can be represented by doping UO_2 with fission product oxides and actinides. Electrochemical tests to measure the dissolution rates of materials representing aged fuel alone and in the presence of corroding steel will provide the dataset required for reliable model validation to add confidence to the rate predictions.

- Modeling studies that build on our successful model integration efforts are needed. These investigations should focus on the chemical evolution of the in-package solution in contact with degrading spent fuel following the breach of the waste package and Zircaloy cladding. This is particularly important just after a breach due to acid-producing reactions that occur when radiolytic oxidants from the fuel contact reducing groundwaters, as demonstrated in Jerden et al., 2017(b).

5. References

Arthur, S., Aqueous Corrosion Rates for Waste Package Materials, ANL-DSD-MD-000001 REV 01, October 2004, DOC.20041012.0003

Bard, A., Faulkner, L., "Electrochemical methods: Fundamentals and Applications", John Wiley and Sons, Inc., 2001

Broczkowski, M.E., Noël, J.J., Shoesmith, D.W., The inhibiting effects of hydrogen on the corrosion of uranium dioxide under nuclear waste disposal conditions, *Journal of Nuclear Materials,* 346, 16–23, 2005

Buck E., Jerden, J., Ebert, W., Wittman, R., "Coupling the Mixed Potential and Radiolysis Models for Used Fuel Degradation," FCRD-UFD-2013-000290, 2013.

Gattu, V.K., Ebert, W.L., Tehrani, N., and Indacochea, J.E. (2018). "Electrochemical Measurements of Steel Corrosion for Modeling H_2 Generation." *Corrosion 2018*, May 11-14, 2018, Phoenix, AZ. Paper No. 11370.

Jerden J. Frey K. Ebert W., "A Multiphase Interfacial Model for the Dissolution of Spent Nuclear Fuel, *Journal of Nuclear Materials*, 462, 135–146, 2015.

Jerden, J., Frey, K., Ebert, W., "Spent Fuel Matrix Degradation and Canister Corrosion: Quantifying the Effect of Hydrogen", Report for Spent Fuel and Waste Science and Technology Project, Report #: SFWD-SFWST-2017-000039, February 28, 2017(a)

Jerden, J., Gattu, V. K., Ebert, W., "Progress Report on Development of the Spent Fuel Degradation and Waste Package Degradation Models and Model Integration", Report for Spent Fuel and Waste Science and Technology Project, Report #: SFWD-SFWST-2017-000091, August 14, 2017(b)

King F. and Kolar M., "An Improved C-Steel Corrosion Model For the Mixed-Potential Model for Used Fuel Dissolution (MPM Version 1.4)," Ontario Hydro, Nuclear Waste Management Division Report No: 06619-REP-01300-l0027-R00, 2001.

King F. and Kolar M., "Validation of the Mixed-Potential Model for Used Fuel Dissolution Against Experimental Data" Ontario Hydro, Nuclear Waste Management Division Report No. 06819-REP-01200-10077-R00, 2002.

King F. and Kolar M., "The Mixed-Potential Model for UO2 Dissolution MPM Versions V1.3 and V1.4," Ontario Hydro, Nuclear Waste Management Division Report No. 06819-REP-01200-10104 R00, 2003.

King, F., "Overview of a Carbon Steel Container Corrosion Model for a Deep Geological Repository in Sedimentary Rock," Nuclear Waste Management Organization Report TR-2007-01, March 2007, 71 p.

Ollila, K., "Dissolution of Unirradiated UO_2 and UO_2 Doped with ^{233}U in Low- and High-Ionic-Strength NaCl Under Anoxic and Reducing Conditions," Posiva Working Report 2008-50, 2008.

Radulescu, G., "Repository Science/Criticality Analysis," Oak Ridge National Laboratory, Reactor and Nuclear Systems Division Report: FTOR11UF0334, ORNL/LTR-2011, Oak Ridge National Laboratory, Oak Ridge, TN., 2011.

Röllin S., Spahiu K., Eklunda U., "Determination of Dissolution Rates of Spent Fuel in Carbonate Solutions Under Different Redox Conditions with a Flow-through Experiment," *Journal of Nuclear Materials*, vol. 297, pp. 231–243, 2001.

Shoesmith, D.W. and F. King. 1998. A mixed-potential model for the prediction of the effects of α-radiolysis, precipitation and redox processes on the dissolution of used nuclear fuel. Ontario Hydro, Nuclear Waste Management Division Report 06819-REP-01200-0038-R00. Toronto, Ontario.

Shoesmith, D., "The Role of Dissolved Hydrogen on the Corrosion/Dissolution of Spent Nuclear Fuel," Nuclear Waste Management Organization, Toronto, Ontario, Canada, TR-2008-19, November 2008.

Wang Y. et al., "Used Fuel Disposal in Crystalline Rocks: Status and FY14 Progress," FCRD-UFD-2014-000060, SAND2014, Sandia National Laboratories, Albuquerque, NM., 2014.

Appendices

Appendix A
Methods and mineral characterization

Experimental Setup

The bentonite used in this experimental work was mined from a reducing horizon in Colony, Wyoming. The bentonite was pulverized and sieved to < 3 mm and used with a free moisture content of ~15.5 wt. %. The groundwater solution was prepared using reagent grade materials dissolved in double deionized water. NaOH and HCl were added to adjust the initial solution pH. This solution was then filtered through a 0.45 μm filter and sparged with He before each experiment. The salt solution was added at 9:1 water:bentonite ratio. Initial components for wall rock experiments have been summarized in Table 2 of text.

A second series of experiments were performed to examine the bentonite system with host rock inclusion. Host-rock experiments focused on Opalinus Clay from the Swiss Underground Research Laboratory located at Mont Terri. The core was collected from BFE-A10 drill core (interval from 11 to 12 m and interval from 33 to 34 m from the borehole head). A portion of the Opalinus Clay was crushed and sieved with 10 mesh (~2 mm). Opalinus Clay to be used in experiments was reconstituted at 80 wt. % -10 mesh and 20 wt. % +10 mesh. Synthetic groundwater was chosen to replicate the groundwater composition that represents Opalinus Clay pore water (Table 2 of text, Pearson et al., 2003). The salt solution was added at 9:1 water: rock ratio.

The redox conditions for each system were buffered using a 1:1 mixture (by mass) of Fe3O4 and Fe° added at 0.07 wt. % of the bentonite mass. Approximately 7 wt. % (of total solids mass) 304 stainless steel (NIST SRM 101g), 316 stainless steel (NIST SRM 160b), and low-carbon steel (provided by Sandia National Laboratory) were added to the experiments to mimic the presence of a waste canister.

Reactants were loaded into a flexible gold and fixed into a 500 mL Gasket Confined Closure reactor (Seyfried et al., 1987). Experiments were pressurized to 150 - 160 bar and were heated isothermally at 300°C (cement reaction at 200°C) for 6-8 weeks. Reaction liquids were extracted during the experiments and analyzed to investigate the aqueous geochemical evolution in relationship to mineralogical alterations. The sampled reaction liquids were split three-ways producing aliquots for unfiltered anion, unfiltered cation, and filtered (0.45 μm syringe filter) cation determination. All aliquots were stored in a refrigerator at 1°C until analysis.

The steel corrosion experiment was conducted in a cold seal reaction vessel. The reactants (Opalinus Clay, 316 SS, LCS, Opalinus Clay brine, and solid buffers) were loaded into a gold capsule. The water/rock ratio was 2:1. The run was pressurized to 150 bar and heated isothermally at 150°C for 8 weeks.

Mineral Characterization

Chesapeake Energy Laboratory QXRD

X-ray diffraction (XRD) analyses of experimental materials determined mineral compositions. Each sample was ground with 20 wt. % corundum (Al_2O_3) for quantitative XRD analysis of the bulk rock (Chung, 1974). XRD measurements were conducted with a Siemens D500 diffractometer using Cu-Kα radiation. Data were collected from 2 to 70 °2θ with a 0.02 º2θ step-size and count times of 8 to 12 seconds per step. To better analyze the non-clay and clay fractions, the < 2 μm particles were separated via sedimentation in DI H_2O. An aliquot of the < 2 μm suspension was dropped on a zero-background quartz plate and dried. This oriented mount was X-rayed from 2 to 40 °2θ at 8 to 12 s per step. The oriented mount was then saturated with ethylene

glycol in a 60°C oven for 24 hours and XRD analysis was repeated. A portion of the > 2 μm particles was ground with a mortar/pestle, deposited on a zero-background quartz plate, and X-rayed under the same parameters as the bulk powder material. The remaining > 2 μm portion was used for electron microscopy. Mineral identification and unit-cell parameters analysis was performed using Jade© 9.5 X-ray data evaluation program with ICDD PDF-4 database. Quantitative phase analysis (QXRD) was performed using FULLPAT (Chipera and Bish, 2002). Illite-smectite composition of higher-ordered (R1-3) illite-smectites were modeled via ClayStrat+ (developed by Hongji Yuan and David Bish). Expandable component abundances for the disordered illite-smectites were calculated via the Δ°2Θ method (Środoń, 1980; Eberl et al., 1993; Moore and Reynolds, 1997). A regression from calculated data were used to calculate the % expandable (%Exp) component in each untreated and reacted bentonite. The equations are:

$$\%Exp = 973.76 - 323.45\Delta + 38.43\Delta^2 - 1.62\Delta^3$$

(Eberl et al., 1993, Eq. 3, R^2=0.99)

with Δ corresponding to Δ°2Θ between the 002 and 003 peak positions for the oriented, ethylene glycol saturated samples.

University Texas-Austin Geoscience Laboratory QXRD

Samples were milled to a fine powder in a tungsten carbide ring mill. Approximately 0.2 g of 0.3 μm corundum (Buehler) was added to a 1 g aliquot of each sample. The corundum and sample mixtures were homogenized by dry milling in an alumina mortar and pestle. A thin layer of petroleum jelly was applied to a one-inch round glass slide. Homogenized mixtures of corundum and sample were loaded onto glass slides such to form a thin layer of sample across the entirety of the glass slide. Samples were then loaded into the X-ray diffractometer (XRD) for analysis.

XRD Instrument Type and Scan Conditions

All XRD measurements were made at the University of Texas at Austin using a Bruker D8 Advance. The instrument is equipped with a Cu source and a LynxEye detector. The following optically configuration was used for all scans: 1.0 mm divergence slit at the source and a 3.0 mm slit, an anti-scatter tube, a Ni filter for Kb Cu radiation, and a 2.5° axial soller slit at the detector. The source was run at 45 kV and 40 mA for all scans. All samples were scanned between 4° and 70° 2Θ with a stepsize of 0.01° and a counting time of 1 s per step. Samples were rotated during acquisition to maximize random orientation of phases. Total run time for each sample was two hours.

Scan Processing: QXRD

Post-acquisition processing and quantitative XRD (QXRD) were performed using Bruker's DIFFRAC^{plus}Basic Evaluation Package (EVA v.15). EVA was used for background subtraction, $K\alpha_2$ stripping, scan smoothing, and 2Θ displacement. The reference intensity ratio (RIR) method was used for QXRD. The RIR method uses the most intense peak of corundum as a reference intensity to calculate weight fractions of other phases in a sample. Preferred orientation of phases results in poor-quality QXRD results. Rotation of samples during measurement and the method for loading samples in XRD holders minimized preferred orientation. QXRD results for most samples yielded approximately 18 wt.% corundum, which closely matches the amount of corundum added to the sample.

SEM analyses

Analytical electron microscopy was performed using a FEI™ Inspect F scanning electron microscope (SEM). All samples were Au/Pd-coated prior to SEM analysis. Imaging with the SEM was performed using a 5.0 kV accelerating voltage and 1.5 spot size. Energy dispersive X-ray spectroscopy (EDX) was performed at 30 kV and a 3.0 spot size.

Aqueous Geochemical Analyses

Major cations and trace metals were analyzed via inductively coupled plasma-optical emission spectrometry (Perkin Elmer Optima 2100 DV) and inductively coupled plasma-mass spectrometry (Elan 6100) utilizing EPA methods 200.7 and 200.8. Ultra-high purity nitric acid was used in sample and calibration preparation prior to sample analysis. Internal standards (Sc, Ge, Bi, and In) were added to samples and standards to correct for matrix effects. Standard Reference Material (SRM) 1643e Trace Elements in Water was used to check the accuracy of the multi-element calibrations. Inorganic anion samples were analyzed by ion chromatography (IC) following EPA method 300 on a Dionex DX-600 system. Aqueous geochemical results are presented in Appendix B.

Appendix B
Water Chemistry Samples EBS-14 to EBS-23
(Element Concentrations in ppm)

EBS-14 UNFILTERED

Lab ID	Sample Date	Al	B	Ba	Br	Ca	Cl	Cr	F	Fe	K	Li	Mg	Mn	Na	NO_3	PO_4	Si	SiO_2	SO_4	Sr	Ti	Zn	TDS	Cation	Anion	Balance
		ppm	ppm	ppm	ppm	ppm	ppm	ppm	ppm	ppm	ppm	ppm	ppm	ppm	ppm	ppm	ppm	ppm	ppm	ppm	ppm	ppm	ppm	ppm	ppm	ppm	
EBS14-00 UF	11/27/2013	<0.05	0.10	<0.05		426.33	6470.00	<0.05		<0.5	225.42	<0.05	194.27	<0.05	3846.10			1.08	2.32	988.32	0.16	<0.1	<0.05	12153	208	201	0.02
EBS14-01 UF	11/27/2013	<0.05	5.25	0.18		317.50	6484.00	<0.05		<0.5	173.57	2.37	8.16	0.09	3831.33			84.48	180.79	<1	2.46	<0.1	0.06	11006	188	181	0.02
EBS14-02 UF	12/6/2013	<0.05	5.68	0.17		495.68	6538.00	<0.05		<0.5	106.26	5.82	0.87	0.17	3570.56			77.97	166.86	<1	1.53	<0.1	0.08	10892	184	183	0.00
EBS14-03 UF	12/18/2013	<0.05	6.42	0.16		563.85	6497.00	<0.05		<0.5	231.58	11.95	1.21	0.23	3970.85			63.01	134.83	<1	2.28	<0.1	0.09	11420	208	181	0.07
EBS14-04 UF	1/6/2014	<0.05	6.69	0.28		546.31	6518.00	<0.05		<0.5	202.22	7.46	0.88	0.29	3472.80			56.01	119.85	<1	2.06	<0.1	0.09	10877	184	182	0.01
EBS14-05 UF	1/8/2014	1.32	6.41	0.22		1024.10	6630.39	<0.05		<0.5	164.06	6.04	<0.5	<0.05	3272.60			28.19	60.33	965.38	4.33	<0.1	0.81	12136	197	205	-0.02

EBS-14 FILTERED

Lab ID	Sample Date	Al	B	Ba	Br	Ca	Cl	Cr	F	Fe	K	Li	Mg	Mn	Na	NO_3	PO_4	Si	SiO_2	SO_4	Sr	Ti	Zn	TDS	Cation	Anion	Balance
		ppm	ppm	ppm	ppm	ppm	ppm	ppm	ppm	ppm	ppm	ppm	ppm	ppm	ppm	ppm	ppm	ppm	ppm	ppm	ppm	ppm	ppm	ppm	ppm	ppm	
EBS14-00 UF	11/27/2013	<0.05	0.22	<0.05		441.14	--	<0.05		<0.5	223.44	<0.05	193.25	<0.05	3781.04			0.51	1.08	--	0.17	<0.1	<0.05	4640	207	0	1.00
EBS14-01 UF	11/27/2013	<0.05	5.07	0.21		318.73	--	<0.05		<0.5	176.14	2.41	8.18	0.09	3835.18			36.27	77.61	--	2.47	<0.1	0.11	4426	188	0	1.00
EBS14-02 UF	12/6/2013	<0.05	6.48	0.12		507.28	--	<0.05		<0.5	105.55	5.71	1.07	0.16	3581.00			40.68	87.05	--	1.54	<0.1	0.06	4296	185	0	1.00
EBS14-03 UF	12/18/2013	<0.05	6.10	0.23		573.26	--	<0.05		<0.5	224.62	11.12	1.27	0.22	4056.12			50.56	108.20	--	2.39	<0.1	0.08	4984	213	0	1.00
EBS14-04 UF	1/6/2014	<0.05	5.51	0.29		590.49	--	<0.05		<0.5	334.21	13.32	1.30	0.24	4065.48			46.53	99.56	--	2.81	<0.1	0.15	5113	217	0	1.00
EBS14-05 UF	1/8/2014	1.28	6.90	0.27		1083.92	--	<0.05		<0.5	171.96	6.32	<0.5	<0.05	3370.66			26.65	57.03	--	4.49	<0.1	0.58	4703	206	0	1.00

EBS-15 UNFILTERED

Lab ID	Sample Date	Al	B	Ba	Br	Ca	Cl	Cr	F	Fe	K	Li	Mg	Mn	Na	NO_3	PO_4	Si	SiO_2	SO_4	Sr	Ti	Zn	TDS	Cation	Anion	Balance
		ppm	ppm	ppm	ppm	ppm	ppm	ppm	ppm	ppm	ppm	ppm	ppm	ppm	ppm	ppm	ppm	ppm	ppm	ppm	ppm	ppm	ppm	ppm	ppm	ppm	
EBS1500 UF	3/13/2014	<0.05	0.40	<0.05		431.23	7159.09	<0.05		<0.5	214.91	<0.05	187.89	<0.05	3702.44			<0.5	<1	1168.57	0.15	<0.1	0.58	12865	201	223	-0.05
EBS1501 UF	4/10/2014	0.61	4.09	0.16		47.80	3434.72	<0.05		<0.5	64.11	0.64	<0.5	<0.05	1912.15			98.14	210.02	26.28	0.23	<0.1	0.48	5701	89	97	-0.04
EBS1502 UF	4/17/2014	0.66	4.00	0.23		53.77	3002.23	<0.05		<0.5	61.98	0.91	<0.5	<0.05	1656.21			78.80	168.64	18.82	0.27	<0.1	0.47	4968	78	85	-0.04
EBS1503 UF	4/24/2014	0.55	3.48	0.31		56.78	2818.92	<0.05		<0.5	61.09	0.70	<0.5	<0.05	1534.58			48.67	104.15	19.48	0.27	<0.1	0.53	4601	72	80	-0.05
EBS1505 UF	5/1/2014	0.44	5.36	0.50		76.77	4800.87	<0.05		<0.5	91.62	1.48	<0.5	<0.05	2246.19			36.11	77.27	21.74	0.42	<0.1	0.79	7323	104	135	-0.13
EBS1506 UF	5/8/2014	0.35	4.74	0.38		70.72	3725.19	<0.05		<0.5	81.90	1.24	<0.5	<0.05	1922.19			53.90	115.35	22.54	0.35	<0.1	0.66	5946	90	105	-0.08
EBS1507 UF	5/14/2014	0.22	5.05	0.37		438.57	1231.00	<0.05		4.04	78.69	1.48	1.19	<0.05	2079.30			293.26	627.58	4108.00	1.47	<0.1	1.01	8578	121	119	0.01

EBS-15 FILTERED

Lab ID	Sample Date	Al	B	Ba	Br	Ca	Cl	Cr	F	Fe	K	Li	Mg	Mn	Na	NO_3	PO_4	Si	SiO_2	SO_4	Sr	Ti	Zn	TDS	Cation	Anion	Balance
		ppm	ppm	ppm	ppm	ppm	ppm	ppm	ppm	ppm	ppm	ppm	ppm	ppm	ppm	ppm	ppm	ppm	ppm	ppm	ppm	ppm	ppm	ppm	ppm	ppm	
EBS1500 F	3/13/2014	<0.05	<0.1	<0.05		431.65	--	<0.05		<0.5	214.73	<0.05	185.98	<0.05	3742.47			7.62	16.30	--	0.15	<0.1	0.83	4592	204	0	1.00
EBS1501 F	4/10/2014	0.32	3.91	0.17		46.20	--	<0.05		<0.5	62.26	0.60	<0.5	<0.05	1847.16			36.44	77.98	--	0.23	<0.1	0.26	2039	85	0	1.00
EBS1502 F	4/17/2014	0.69	3.66	0.25		52.04	--	<0.05		<0.5	60.91	0.70	<0.5	<0.05	1625.45			88.50	189.38	--	0.25	<0.1	0.54	1934	77	0	1.00
EBS1503 F	4/24/2014	0.50	3.39	0.30		56.21	--	<0.05		<0.5	60.20	0.68	<0.5	<0.05	1513.70			74.93	160.36	--	0.26	<0.1	0.53	1796	72	0	1.00
EBS1505 F	5/1/2014	0.27	5.13	0.53		76.72	--	<0.05		<0.5	90.26	1.44	<0.5	<0.05	2205.95			37.63	80.52	--	0.41	<0.1	0.83	2462	103	0	1.00
EBS1506 F	5/8/2014	0.28	4.75	0.40		71.99	--	<0.05		<0.5	83.35	1.25	<0.5	<0.05	1962.22			65.96	141.15	--	0.36	<0.1	0.38	2266	93	0	1.00
EBS1507 F	5/14/2014	<0.05	5.00	0.27		435.05	--	<0.05		3.42	78.42	1.48	0.87	<0.05	2052.90			281.36	602.11	--	1.44	<0.1	0.45	3181	120	0	1.00

EBS-17 UNFILTERED

Lab ID	Sample Date	Al	B	Ba	Br	Ca	Cl	Cr	F	Fe	K	Li	Mg	Mn	Na	NO_3	PO_4	Si	SiO_2	SO_4	Sr	Ti	Zn	TDS	Cation	Anion	Balance
		ppm	ppm	ppm	ppm	ppm	ppm	ppm	ppm	ppm	ppm	ppm	ppm	ppm	ppm	ppm	ppm	ppm	ppm	ppm	ppm	ppm	ppm	ppm	ppm	ppm	
EBS17 00 UF	6/27/2014	<0.05	<0.1	<0.05		409.76	7117.83	<0.05		<0.5	220.42	<0.05	185.63	<0.05	3812.21			<0.5	<1	1169.14	0.12	<0.1	<0.05	12915	205	222	-0.04
EBS17 01 UF	7/16/2014	0.52	6.10	0.51		34.31	7134.86	<0.05		<0.5	171.81	<0.05	<0.5	<0.05	3996.96			45.16	96.64	27.51	0.39	<0.1	<0.05	11470	179	200	-0.05
EBS17 02 UF	7/31/2014	0.41	6.80	0.50		128.77	6981.99	<0.05		<0.5	135.25	<0.05	<0.5	0.17	3750.13			39.24	83.97	10.32	0.85	<0.1	<0.05	11099	172	195	-0.06
EBS17 03 UF	8/7/2014	0.51	6.82	0.62		139.96	6738.79	<0.05		0.24	140.91	<0.05	<0.5	0.28	3581.20			55.53	118.84	11.13	0.94	<0.1	0.08	10740	166	189	-0.06
EBS17 04 UF	8/14/2014	0.44	6.36	0.75		136.40	6860.33	<0.05		0.34	134.29	<0.05	<0.5	0.38	3346.94			36.76	78.66	8.55	0.93	<0.1	0.24	10575	155	192	-0.11
EBS17 05 UF	8/21/2014	0.43	6.20	0.86		142.94	6494.33	<0.05		0.45	143.52	<0.05	<0.5	0.47	3428.02			42.24	90.40	8.41	0.98	<0.1	0.50	10318	159	182	-0.07
EBS17 06 UF	8/26/2014	0.34	6.64	0.72		144.06	6396.69	<0.05		0.39	139.83	<0.05	<0.5	0.46	3272.94			41.74	89.33	10.66	0.97	<0.1	0.43	10063	153	179	-0.08
EBS17 07 UF	8/27/2014	0.13	4.78	0.38		554.68	4719.48	<0.05		3.03	97.57	<0.05	1.02	0.54	2506.66			56.60	121.11	1219.84	2.20	<0.1	0.22	9232	140	157	-0.06

EBS-17 FILTERED

Lab ID	Sample Date	Al	B	Ba	Br	Ca	Cl	Cr	F	Fe	K	Li	Mg	Mn	Na	NO_3	PO_4	Si	SiO_2	SO_4	Sr	Ti	Zn	TDS	Cation	Anion	Balance
		ppm	ppm	ppm	ppm	ppm	ppm	ppm	ppm	ppm	ppm	ppm	ppm	ppm	ppm	ppm	ppm	ppm	ppm	ppm	ppm	ppm	ppm	ppm	ppm	ppm	
EBS17 00 F	6/27/2014	<0.05	<0.1	<0.05		419.59	--	<0.05		<0.5	227.86	<0.05	191.77	<0.05	3833.78			<0.5	<1	--	0.12	<0.1	<0.05	4673	208	0	1.00
EBS17 01 F	7/16/2014	0.47	6.18	0.50		34.05	--	<0.05		<0.5	169.56	<0.05	<0.5	0.05	3987.31			46.66	99.84	--	0.39	<0.1	<0.05	4298	180	0	1.00
EBS17 02 F	7/31/2014	0.70	7.51	0.49		131.93	--	<0.05		0.22	137.93	<0.05	<0.5	0.18	3781.08			37.41	80.05	--	0.89	<0.1	0.15	4141	175	0	1.00
EBS17 03 F	8/7/2014	0.48	6.84	0.65		141.40	--	<0.05		0.28	141.38	<0.05	<0.5	0.29	3614.29			37.28	79.78	--	0.94	<0.1	0.21	3987	168	0	1.00
EBS17 04 F	8/14/2014	0.34	6.55	0.78		142.36	--	<0.05		0.36	140.93	<0.05	<0.5	0.39	3481.94			35.84	76.71	--	0.97	<0.1	0.22	3852	163	0	1.00
EBS17 05 F	8/21/2014	0.37	7.53	0.73		157.35	--	<0.05		0.35	150.24	<0.05	<0.5	0.48	3519.35			45.14	96.60	--	1.06	<0.1	0.32	3934	165	0	1.00
EBS17 06 F	8/26/2014	0.27	6.58	0.77		147.62	--	<0.05		0.35	141.98	<0.05	<0.5	0.47	3337.10			44.14	94.47	--	0.99	<0.1	0.31	3731	157	0	1.00
EBS17 07 F	8/27/2014	<0.05	4.68	0.33		543.03	--	<0.05		0.83	95.10	<0.05	0.71	0.53	2450.51			54.04	115.64	--	2.12	<0.1	0.20	3214	137	0	1.00

EBS-18 UNFILTERED

Lab ID	Sample Date	Al	B	Ba	Br	Ca	Cl	Cr	F	Fe	K	Li	Mg	Mn	Na	NO_3	PO_4	Si	SiO_2	SO_4	Sr	Ti	Zn	TDS	Cation	Anion	Balance
		ppm	ppm	ppm	ppm	ppm	ppm	ppm	ppm	ppm	ppm	ppm	ppm	ppm	ppm	ppm	ppm	ppm	ppm	ppm	ppm	ppm	ppm	ppm	ppm	ppm	
EBS 18 UF	1/20/2016	1.83	3.60	0.19		16.54	3760.60	<0.02		<0.2	75.29	1.55	<0.2	0.03	2164.70			83.84	179.42	16.95	0.19	<0.04	0.24	6221	99	106	-0.03
EBS 18-0 UF	1/28/2016	0.17	4.73	0.35		27.82	4544.00	<0.02		<0.2	97.06	0.68	9.70	0.06	2608.67			102.56	219.49	57.60	0.20	<0.04	0.30	7571	120	129	-0.03
EBS-18-2-4 UF	2/4/2016	<0.02	3.10	0.13	0.17	13.93	2684.26	<0.02	3.17	<0.2	65.54	1.61	0.21	0.04	1568.32	0.15	<0.1	195.87	419.16	27.89	0.14	<0.04	<0.02	4788	75	76	-0.01
EBS-18-2-16 UF	2/16/2016	<0.02	0.71	0.11	<0.1	289.88	1376.74	<0.02	0.41	7.12	20.28	1.08	1.90	0.31	917.72	0.12	<0.1	103.71	221.94	956.52	1.72	<0.04	<0.02	3797	58	59	0.00
EBS-18-POST RUN UF	2/17/2016	<0.02	0.57	0.13	0.13	309.37	1435.15	<0.02	1.42	2.38	23.84	1.26	5.60	0.31	999.07	0.41	<0.1	79.61	170.36	1054.10	1.79	<0.04	<0.02	4006	62	62	0.00
EBS-18 RXN VESSEL	2/17/2016	<0.02	<0.04	0.02	<0.1	22.01	860.15	<0.02	0.15	21.44	17.32	0.34	0.03	0.38	511.01	0.14	<0.1	70.32	150.48	44.79	0.10	<0.04	<0.02	1628	27	25	0.03

EBS-18 FILTERED

Lab ID	Sample Date	Al	B	Ba	Br	Ca	Cl	Cr	F	Fe	K	Li	Mg	Mn	Na	NO_3	PO_4	Si	SiO_2	SO_4	Sr	Ti	Zn	TDS	Cation	Anion	Balance
		ppm	ppm	ppm	ppm	ppm	ppm	ppm	ppm	ppm	ppm	ppm	ppm	ppm	ppm	ppm	ppm	ppm	ppm	ppm	ppm	ppm	ppm	ppm	ppm	ppm	
EBS 18 F	1/20/2016	1.12	3.25	0.18		17.11	--	<0.02		<0.2	77.51	1.53	<0.2	0.02	2108.95			98.79	211.40	--	0.18	<0.04	0.19	2421	97	0	1.00
EBS 18-0 F	1/28/2016	0.13	3.91	0.36		29.46	--	0.02		<0.2	96.28	0.69	9.83	0.06	2571.74			215.40	460.96	--	0.20	<0.04	0.24	3174	122	0	1.00
EBS-18-2-4 F	2/4/2016	<0.02	2.65	0.12	--	13.79	--	<0.02	--	<0.2	62.25	1.48	<0.2	<0.02	1558.74	--	--	75.35	161.25	--	0.12	<0.04	<0.02	1800	72	0	1.00
EBS-18-2-16 F	2/16/2016	<0.02	0.82	0.11	--	284.28	--	<0.02	--	7.61	20.27	1.09	1.61	0.31	907.39	--	--	116.80	249.96	--	1.70	<0.04	<0.02	1475	58	0	1.00
EBS-18-POST RUN F	2/17/2016	<0.02	0.70	0.13	--	308.42	--	<0.02	--	1.83	23.80	1.27	5.40	0.32	1027.98	--	--	90.45	193.57	--	1.76	<0.04	<0.02	1565	64	0	1.00

EBS-19 UNFILTERED

Lab ID	Sample Date	Al	B	Ba	Br	Ca	Cl	Cr	F	Fe	K	Li	Mg	Mn	Na	NO_3	PO_4	Si	SiO_2	SO_4	Sr	Ti	Zn	TDS	Cation	Anion	Balance
		ppm	ppm	ppm	ppm	ppm	ppm	ppm	ppm	ppm	ppm	ppm	ppm	ppm	ppm	ppm	ppm	ppm	ppm	ppm	ppm	ppm	ppm	ppm	ppm	ppm	
EBS-19-1 UF	6/16/2016	1.25	23.08	0.82	0.82	204.04	7199.49	0.05	1.62	1.95	273.99	7.06	0.69	0.42	7676.34	0.11	0.08	116.54	249.39	25.39	1.33	<0.04	0.18	15668	350	202	0.27
EBS-19-2 UF	6/23/2016	0.09	16.24	0.98	0.59	176.19	6785.74	<0.02	1.60	<0.2	213.81	5.71	0.95	0.60	5479.48	0.45	0.03	83.28	178.23	16.64	1.20	<0.04	0.07	12879	252	190	0.14
EBS-19-3 UF	6/30/2016	0.09	14.92	1.02	0.89	174.97	6511.60	<0.02	1.91	<0.2	204.39	5.44	0.98	0.75	4971.16	0.32	0.21	83.92	179.59	20.84	1.15	<0.04	<0.02	12090	230	183	0.12
EBS-19-4 UF	7/7/2016	0.08	14.05	1.03	0.79	174.95	6616.72	<0.02	1.71	<0.2	199.97	5.30	1.13	0.93	4767.93	0.29	0.05	76.18	163.03	21.88	1.13	<0.04	0.03	11971	221	186	0.09
EBS-19-5 UF	7/14/2016	<0.02	22.09	1.65	0.86	283.00	6592.06	<0.02	1.51	0.25	326.21	8.57	1.98	1.70	7320.03	0.04	0.14	229.25	490.58	16.45	1.82	<0.04	0.03	15069	343	185	0.30
EBS-19-6 UF	7/15/2016	385.33	21.01	0.90	0.79	1508.52	6952.22	0.02	0.52	37.35	134.35	9.68	251.59	7.23	7100.95	0.22	<0.1	352.34	754.02	2384.34	6.35	0.08	0.12	19556	455	242	0.31

EBS-19 FILTERED

Lab ID	Sample Date	Al	B	Ba	Br	Ca	Cl	Cr	F	Fe	K	Li	Mg	Mn	Na	NO_3	PO_4	Si	SiO_2	SO_4	Sr	Ti	Zn	TDS	Cation	Anion	Balance
		ppm	ppm	ppm	ppm	ppm	ppm	ppm	ppm	ppm	ppm	ppm	ppm	ppm	ppm	ppm	ppm	ppm	ppm	ppm	ppm	ppm	ppm	ppm	ppm	ppm	
EBS-19-1 F	6/16/2016	0.57	17.30	0.74		162.77		<0.02		0.48	213.25	5.57	0.79	0.40	6002.33			78.23	167.42		1.03	<0.04	0.09	6573	276	1	0.99
EBS-19-2 F	6/23/2016	0.17	10.18	0.64		117.70		<0.02		<0.2	137.60	3.66	0.74	0.43	3600.00			54.46	116.54		0.74	<0.04	<0.02	3988	167	0	0.99
EBS-19-3 F	6/30/2016	0.41	14.28	0.96		173.16		<0.02		<0.2	194.37	5.19	0.99	0.78	4850.35			79.59	170.32		1.07	<0.04	<0.02	5412	226	1	0.99
EBS-19-4 F	7/7/2016	<0.02	16.01	1.13		202.17		<0.02		<0.2	229.66	6.07	1.29	1.09	5491.53			85.22	182.37		1.25	<0.04	0.04	6133	256	1	0.99
EBS-19-5 F	7/14/2016	0.26	17.86	1.34		227.02		<0.02		<0.2	257.80	6.87	1.68	1.37	5982.56			103.74	222.00		1.41	<0.04	<0.02	6720	280	1	0.99
EBS-19-6 F	7/15/2016	<0.02	17.89	0.90		1223.70		<0.02		13.94	109.23	8.40	9.39	3.14	6195.51			247.20	529.01		4.97	<0.04	0.02	8116	340	1	1.00

EBS-20 UNFILTERED

Lab ID	Sample Date	Al	B	Ba	Br	Ca	Cl	Cr	F	Fe	K	Li	Mg	Mn	Na	NO_3	Si	SiO_2	SO_4	Sr	Zn	TDS	Cation	Anion	Balance
		ppm	ppm	ppm	ppm	ppm	ppm	ppm	ppm	ppm	ppm	ppm	ppm	ppm	ppm	ppm	ppm	ppm	ppm	ppm	ppm	ppm	ppm	ppm	
EBS-20 Start	9/6/2016	<0.016	<0.203	<0.011	0.24	388.54	7233.70	<0.003	0.08	0.02	228.92	0.01	178.84	<0.003	3705.09	5.43	<0.278	<0.59492	1096.77	0.14	<0.052	12838	199	224	-0.06
EBS-20-1 UF	9/8/2016	<0.016	8.62	0.90	0.68	67.78	7679.15	<0.003	0.85	0.09	158.54	1.07	11.31	0.11	3817.63	15.42	41.36	88.52	32.82	0.62	<0.052	11884	174	215	-0.11
EBS-20-2 UF	9/22/2016	<0.032	10.04	0.58	0.37	88.84	7120.70	0.01	1.55	0.07	158.59	3.16	1.15	0.15	4465.79	2.85	37.57	80.40	16.63	0.69	0.17	11952	202	199	0.01
EBS-20-3 UF	10/6/2016	<0.016	8.83	0.65	0.89	88.00	14401.96	<0.003	1.46	0.12	139.82	2.60	0.69	0.22	3323.40	219.21	43.66	93.44	18.34	0.63	<0.052	18300	151	404	-0.46
EBS-20-4 UF	10/20/2016	<0.032	15.94	1.20	0.76	147.34	6013.24	<0.006	1.37	0.28	256.04	5.02	1.48	0.48	6295.94	2.60	105.14	225.01	9.91	1.19	0.29	12978	288	168	0.26
EBS-20-5 UF	11/3/2016	0.12	6.75	0.58	0.25	71.79	5516.05	0.01	2.27	0.11	131.70	2.70	0.82	0.32	2915.69	2.74	39.10	83.68	9.49	0.60	<0.208	8746	134	155	-0.07
EBS-20-6 UF	11/17/2016	<0.016	7.59	0.71	0.81	82.54	5777.60	0.01	2.14	0.16	156.69	3.03	0.85	0.37	3242.46	2.02	50.56	108.21	9.74	0.66	0.12	9396	150	162	-0.04
EBS-20-7 UF	12/1/2016	0.15	6.42	0.60	1.34	69.27	4338.48	0.01	1.90	0.28	133.59	2.54	0.72	0.32	2683.70	2.30	63.03	134.88	10.59	0.58	0.13	7388	125	122	0.01
EBS-20-8 UF	12/15/2016	0.25	6.21	0.60	0.32	63.75	5002.75	0.01	1.85	0.36	126.32	2.34	0.64	0.31	2531.71	3.04	65.55	140.29	9.89	0.54	0.05	7891	118	141	-0.09
EBS-20-9 UF	1/5/2017	<0.016	5.96	0.63	0.20	64.28	4861.78	0.01	1.72	0.18	127.92	2.37	0.64	0.30	2465.47	1.42	54.12	115.81	8.47	0.55	0.08	7658	115	137	-0.09
EBS-20-10 UF	1/19/2017	0.02	5.74	0.66	0.80	64.26	5933.85	0.01	2.17	0.16	128.50	2.35	0.61	0.31	2411.16	2.58	61.06	130.68	10.42	0.56	0.08	8695	112	167	-0.19
EBS-20-11 UF	2/2/2017	0.05	5.57	0.69	0.12	65.62	4731.67	0.01	1.61	0.32	130.62	2.40	0.65	0.26	2418.17	2.89	84.55	180.93	9.39	0.58	0.10	7552	114	133	-0.08
EBS-20-12 UF	2/16/2017	0.15	5.53	0.80	0.66	64.81	4634.58	0.01	1.47	0.33	128.25	2.35	0.53	0.32	2357.02	4.70	103.86	222.25	8.96	0.60	0.10	7433	111	130	-0.08

* In order to fit EBS-20 UF on page, empty columns (PO_4 and Ti) were not included.

EBS-20 FILTERED

Lab ID	Sample Date	Al	B	Ba	Br	Ca	Cl	Cr	F	Fe	K	Li	Mg	Mn	Na	NO_3	PO_4	Si	SiO_2	SO_4	Sr	Ti	Zn	TDS	Cation	Anion	Balance
		ppm	ppm	ppm	ppm	ppm	ppm	ppm	ppm	ppm	ppm	ppm	ppm	ppm	ppm	ppm	ppm	ppm	ppm	ppm	ppm	ppm	ppm	ppm	ppm	ppm	
EBS-20-1 F	9/8/2016	<0.016	8.51	0.95		96.55		0.00		0.28	160.49	1.06	10.32	0.09	3663.34			48.04	102.80		0.52		0.07	4045	170	0	1.00
EBS-20-2 F	9/22/2016	<0.016	9.00	0.56		76.55		<0.003		0.08	135.91	2.61	0.56	0.12	3685.98			45.66	97.72		0.57		0.08	4010	169	0	1.00
EBS-20-3 F	10/6/2016	0.12	8.42	0.63		81.69		<0.003		0.33	126.96	2.27	0.64	0.20	3014.62			52.48	112.31		0.58		0.07	3349	140	0	0.99
EBS-20-4 F	10/20/2016	0.07	15.26	1.15		150.43		<0.006		0.39	251.48	4.91	1.43	0.47	6134.54			103.45	221.39		1.13		0.25	6783	282	1	1.00
EBS-20-5 F	11/3/2016																										
EBS-20-6 F	11/17/2016	0.02	6.65	0.61		69.74		0.01		0.26	130.62	2.50	0.71	0.31	2777.05			51.01	109.17		0.56		<0.052	3098	129	0	1.00
EBS-20-7 F	12/1/2016	0.10	8.74	0.81		95.77		0.01		0.28	185.69	3.50	1.00	0.44	3725.12			62.32	133.36		0.80		0.13	4156	173	0	1.00
EBS-20-8 F	12/15/2016	0.14	7.07	0.69		74.54		0.01		0.33	145.50	2.70	0.75	0.35	2904.15			62.63	134.02		0.62		0.07	3271	135	0	1.00
EBS-20-9 F	1/5/2017	0.10	6.01	0.63		64.79		0.01		0.28	125.29	2.37	0.65	0.31	2448.48			66.55	142.41		0.55		0.07	2792	115	0	1.00
EBS-20-10 F	1/19/2017	0.11	5.64	0.66		64.94		0.01		0.24	128.89	2.39	0.61	0.31	2419.66			88.56	189.51		0.56		0.08	2814	114	0	1.00
EBS-20-11 F	2/2/2017	0.04	5.39	0.70		65.04		0.01		0.31	127.76	2.36	0.64	0.26	2385.36			85.26	182.46		0.58		0.11	2771	113	0	1.00
EBS-20-12 F	2/16/2017	0.09	5.80	0.77		66.27		0.01		0.51	130.79	2.34	0.66	0.33	2374.58			95.43	204.22		0.59		0.11	2787	112	0	1.00

EBS-21 UNFILTERED

Lab ID	Sample Date	Al	B	Ba	Br	Ca	Cl	Cr	F	Fe	K	Li	Mg	Mn	Na	NO_3	PO_4	Si	SiO_2	SO_4	Sr	Ti	Zn	TDS	Cation	Anion	Balance
		ppm	ppm	ppm	ppm	ppm	ppm	ppm	ppm	ppm	ppm	ppm	ppm	ppm	ppm	ppm	ppm	ppm	ppm	ppm	ppm	ppm	ppm	ppm	ppm	ppm	
EBS-21 Starting Solution	1/4/2017	6.62		<2.2	1.92	348.58	46884.48	<0.6	0.05	<3.6	<112.2	<1.2	159.60	<0.6	22792.91	0.82		<55.6	<118.984	1200.36	<0.08			71395	950	1251	-0.14
EBS-21-1 UF	1/12/2017	6.57		3.49	1.83	447.35	47951.11	<0.6	0.72	<3.6	131.85	<1.2	66.20	0.79	21403.15	2.26		<55.6	<118.984	664.35	6.51			70686	895	1270	-0.17
EBS-21-2 UF	1/19/2017	3.57		5.90	2.29	752.94	46268.36	<0.6	0.74	4.34	288.12	2.03	64.92	2.10	29748.25	0.92		<55.6	<118.984	638.12	12.34			77795	1241	1216	0.01
EBS-21-3 UF	1/26/2017	<3.2		5.61	2.03	569.60	45110.26	<0.6	0.50	4.59	118.65	1.90	27.39	1.33	22347.95	1.28		<55.6	<118.984	470.68	9.89			68672	938	1194	-0.12
EBS-21-4 UF	2/2/2017	5.32		7.18	2.42	578.16	47752.38	<0.6	0.70	10.67	175.81	2.39	19.24	1.50	20880.99	1.48		<55.6	<118.984	497.43	9.99			69946	879	1262	-0.18
EBS-21-5 UF	2/9/2017	6.85		5.83	2.16	615.35	46875.66	<0.6	0.80	8.17	114.44	2.28	12.83	1.62	21491.40	1.17		<55.6	<118.984	494.48	10.50			69644	904	1239	-0.16
EBS-21-6 UF	2/16/2017	3.84		9.33	2.38	642.07	44433.15	0.85	0.74	10.83	123.79	2.39	10.27	1.73	22189.20	1.39		<55.6	<118.984	499.52	10.99			67942	935	1178	-0.11
EBS-21-7 UF	2/23/2017	<3.2		8.33	1.64	626.99	44191.30	<0.6	0.65	10.76	113.79	1.84	5.81	1.77	20829.41	1.26		55.94	119.70	352.20	10.40			66276	881	1171	-0.14
EBS-21-8 UF	2/28/2017	<3.2		8.99	1.82	894.80	45055.54	<0.6	0.50	12.76	117.07	2.81	7.80	3.34	22230.50	0.74		77.38	165.59	929.73	12.31			69444	948	1200	-0.12

EBS-21 FILTERED

Lab ID	Sample Date	Al	B	Ba	Br	Ca	Cl	Cr	F	Fe	K	Li	Mg	Mn	Na	NO_3	PO_4	Si	SiO_2	SO_4	Sr	Ti	Zn	TDS	Cation	Anion	Balance
		ppm	ppm	ppm	ppm	ppm	ppm	ppm	ppm	ppm	ppm	ppm	ppm	ppm	ppm	ppm	ppm	ppm	ppm	ppm	ppm	ppm	ppm	ppm	ppm	ppm	
EBS-21-1 F	1/12/2017	<3.2		8.38		472.09		<0.6		19.75	128.33	2.38	71.36	1.42	22032.65			<55.6	<118.984		6.82			22743	970	0	1.00
EBS-21-2 F	1/19/2017	4.80		4.40		519.32		<0.6		4.82	123.51	1.25	41.66	1.07	21999.14			<55.6	<118.984		8.77			22709	968	0	1.00
EBS-21-3 F	1/26/2017	<3.2		4.91		558.84		<0.6		5.99	120.25	1.56	26.48	1.23	21890.05			<55.6	<118.984		9.71			22619	964	0	1.00
EBS-21-4 F	2/2/2017	<3.2		5.26		561.39		<0.6		8.57	113.31	1.49	16.62	1.27	20664.12			<55.6	<118.984		9.72			21382	912	0	1.00
EBS-21-5 F	2/9/2017	<3.2		7.13		610.68		<0.6		8.67	<112.2	2.10	13.16	1.48	21179.87			<55.6	<118.984		10.36			21833	933	0	1.00
EBS-21-6 F	2/16/2017	3.62		6.44		626.38		<0.6		8.99	114.96	1.84	8.72	1.57	21153.16			<55.6	<118.984		10.51			21936	936	0	1.00
EBS-21-7 F	2/23/2017	<3.2		9.07		635.76		<0.6		10.30	<112.2	2.31	6.67	1.65	21519.97			<55.6	<118.984		10.66			22196	948	0	1.00
EBS-21-8 F	2/28/2017	4.65		8.61		858.01		0.75		11.75	162.95	2.55	9.20	3.17	21510.09			60.91	130.35		12.12			22714	965	0	1.00
EBS-21-1 F	1/12/2017	<3.2		8.38		472.09		<0.6		19.75	128.33	2.38	71.36	1.42	22032.65			<55.6	<118.984		6.82			22743	970	0	1.00

EBS-22 UNFILTERED

Lab ID	Sample Date	Al	B	Ba	Br	Ca	Cl	Cr	F	Fe	K	Li	Mg	Mn	Na	NO_3	PO_4	Si	SiO_2	SO_4	Sr	Ti	Zn	TDS	Cation	Anion	Balance
		ppm	ppm	ppm	ppm	ppm	ppm	ppm	ppm	ppm	ppm	ppm	ppm	ppm	ppm	ppm	ppm	ppm	ppm	ppm	ppm	ppm	ppm	ppm	ppm	ppm	
EBS-22-1 UF	3/23/2017	<0.032	2.77	0.47	<0.2	111.95	2640.35	<0.006	<0.2	0.16	189.97	0.32	76.26	0.17	3949.83	0.34	0.00	78.16	167.27	124.02	0.89	<0.004	0.15	7265	189	77	0.42
EBS-22-2 UF	3/30/2017	<0.032	5.10	0.65	<0.2	127.57	2640.77	0.03	<0.2	0.16	178.79	0.74	31.55	0.19	4062.35	0.71	0.00	135.36	289.67	84.78	1.51	<0.004	<0.104	7425	192	76	0.43
EBS-22-3 UF	4/6/2017	<0.032	5.68	0.79	<0.2	149.97	2445.43	<0.006	<0.2	0.16	181.42	0.92	15.49	0.18	4176.27	1.34	0.00	174.66	373.78	67.30	1.99	<0.004	<0.104	7421	198	70	0.48
EBS-22-4 UF	4/13/2017	<0.032	5.61	0.83	0.22	159.85	2522.03	<0.006	<0.2	0.19	174.71	0.92	9.20	0.17	4034.93	<0.2	0.00	173.99	372.33	65.34	2.19	<0.004	<0.104	7349	192	72	0.45
EBS-22-5 UF	4/20/2017	<0.032	5.25	0.84	<0.2	152.84	2493.38	<0.006	<0.2	0.18	162.92	0.88	6.51	0.17	3816.92	0.47	0.00	130.89	280.11	62.01	2.19	<0.004	<0.104	6985	181	71	0.43
EBS-22-6 UF	4/27/2017	<0.032	5.30	0.86	<0.2	156.84	2212.83	<0.006	<0.2	0.20	167.63	0.89	5.60	0.15	3845.50	0.55	0.00	145.46	311.28	52.60	2.28	<0.004	<0.104	6763	182	63	0.48
EBS-22-7 UF	5/4/2017	<0.032	5.68	0.91	<0.2	157.34	2534.18	<0.006	<0.2	0.19	170.17	0.92	5.09	0.19	3891.59	0.37	0.00	148.88	318.60	59.33	2.40	<0.004	<0.104	7147	185	72	0.44
EBS-22-8 UF	5/11/2017	<0.032	5.39	0.95	<0.2	156.71	2599.04	0.01	<0.2	0.15	170.10	0.91	4.77	0.19	3940.39	1.38	0.00	149.50	319.93	60.67	2.47	<0.004	0.21	7263	187	74	0.43
EBS-22-F UF	5/18/2017	0.92	5.41	0.79	<0.2	463.48	3414.32	0.01	<0.2	1.81	166.66	0.93	9.62	0.65	3941.75	0.75	0.00	168.64	360.89	455.38	3.97	<0.004	0.19	8828	203	105	0.32

EBS-22 FILTERED

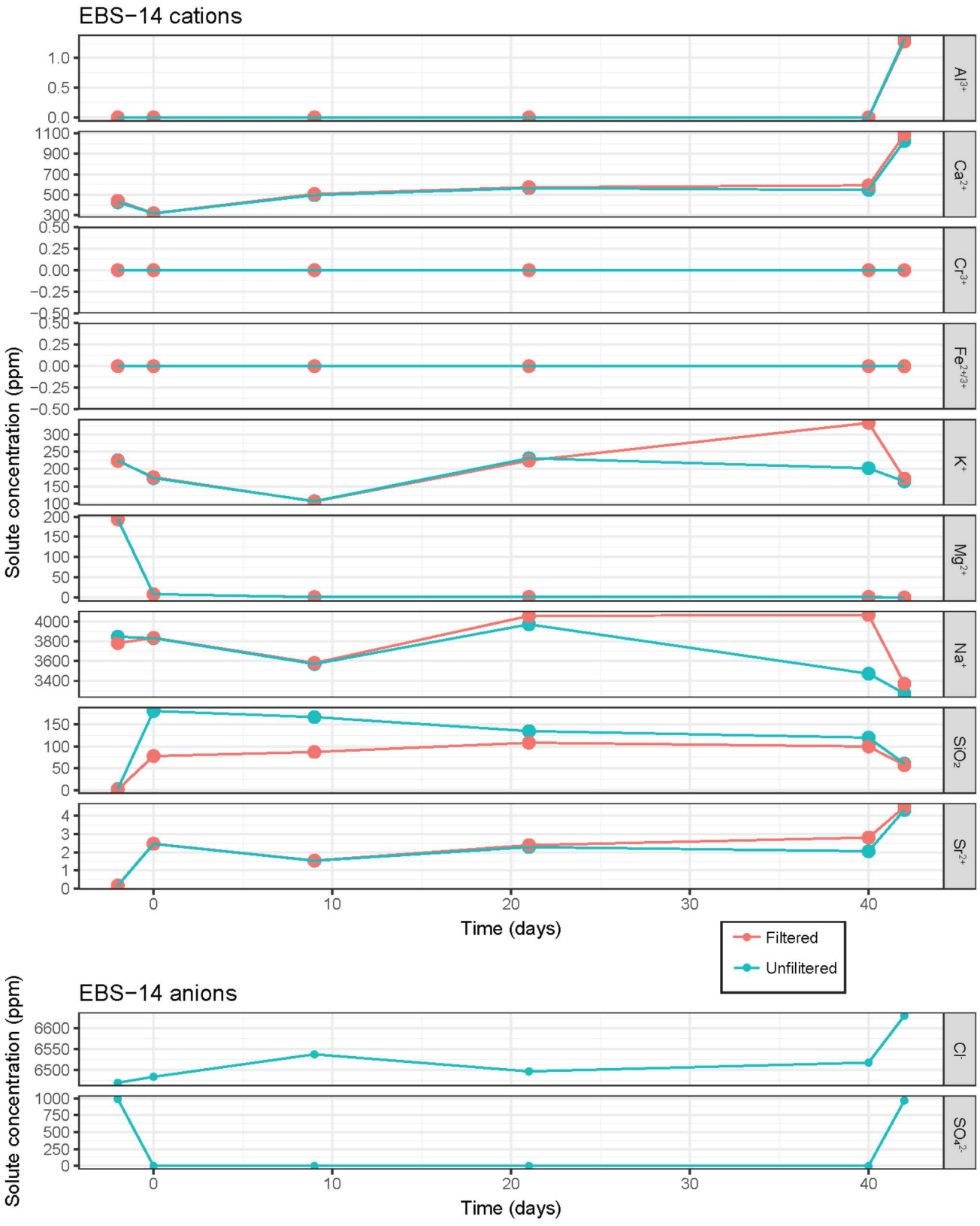
Lab ID	Sample Date	Al	B	Ba	Br	Ca	Cl	Cr	F	Fe	K	Li	Mg	Mn	Na	NO_3	PO_4	Si	SiO_2	SO_4	Sr	Ti	Zn	TDS	Cation	Anion	Balance
		ppm	ppm	ppm	ppm	ppm	ppm	ppm	ppm	ppm	ppm	ppm	ppm	ppm	ppm	ppm	ppm	ppm	ppm	ppm	ppm	ppm	ppm	ppm	ppm	ppm	
EBS-22-1 F	3/23/2017	<0.032	2.59	0.48		101.83		0.01		0.14	185.06	0.32	74.17	0.16	3817.64			78.50	168.00		0.86	<0.004	0.20	4351	183	0	1.00
EBS-22-2 F	3/30/2017	<0.03392	5.82	0.73		128.21		0.01		0.24	193.35	0.81	33.26	0.20	4343.44			119.70	256.16		1.65	<0.00424	0.27	4964	205	0	1.00
EBS-22-3 F	4/6/2017	<0.03392	4.66	0.68		147.45		<0.00636		0.08	183.61	0.89	14.96	0.17	3895.75			53.92	115.39		1.77	<0.00424	0.19	4366	183	0	1.00
EBS-22-4 F	4/13/2017	<0.03392	5.39	0.86		150.32		0.01		0.10	173.51	0.91	9.27	0.17	4035.89			51.44	110.09		2.15	<0.00424	0.16	4489	189	0	1.00
EBS-22-5 F	4/20/2017	<0.03392	6.22	1.00		172.89		0.01		0.12	194.79	1.04	7.62	0.20	4506.72			64.43	137.87		2.58	<0.00424	0.15	5031	211	0	1.00
EBS-22-6 F	4/27/2017	<0.03392	5.63	0.94		159.59		<0.00636		0.13	177.40	0.95	5.63	0.18	4064.14			54.10	115.77		2.42	<0.00424	0.20	4533	190	0	1.00
EBS-22-7 F	5/4/2017	<0.03392	5.98	1.04		174.63		0.01		0.13	189.24	0.99	5.78	0.21	4290.33			70.37	150.59		2.61	<0.00424	0.50	4822	202	0	1.00
EBS-22-8 F	5/11/2017	<0.03392	7.03	1.21		200.69		0.02		0.19	214.02	1.22	6.01	0.25	4865.11			188.30	402.95		3.06	<0.00424	0.28	5702	231	0	1.00
EBS-22-F F	5/18/2017	<0.03392	5.60	0.81		466.34		0.01		1.17	169.78	0.95	9.22	0.65	4021.31			67.74	144.95		4.01	<0.00424	0.28	4825	204	0	1.00

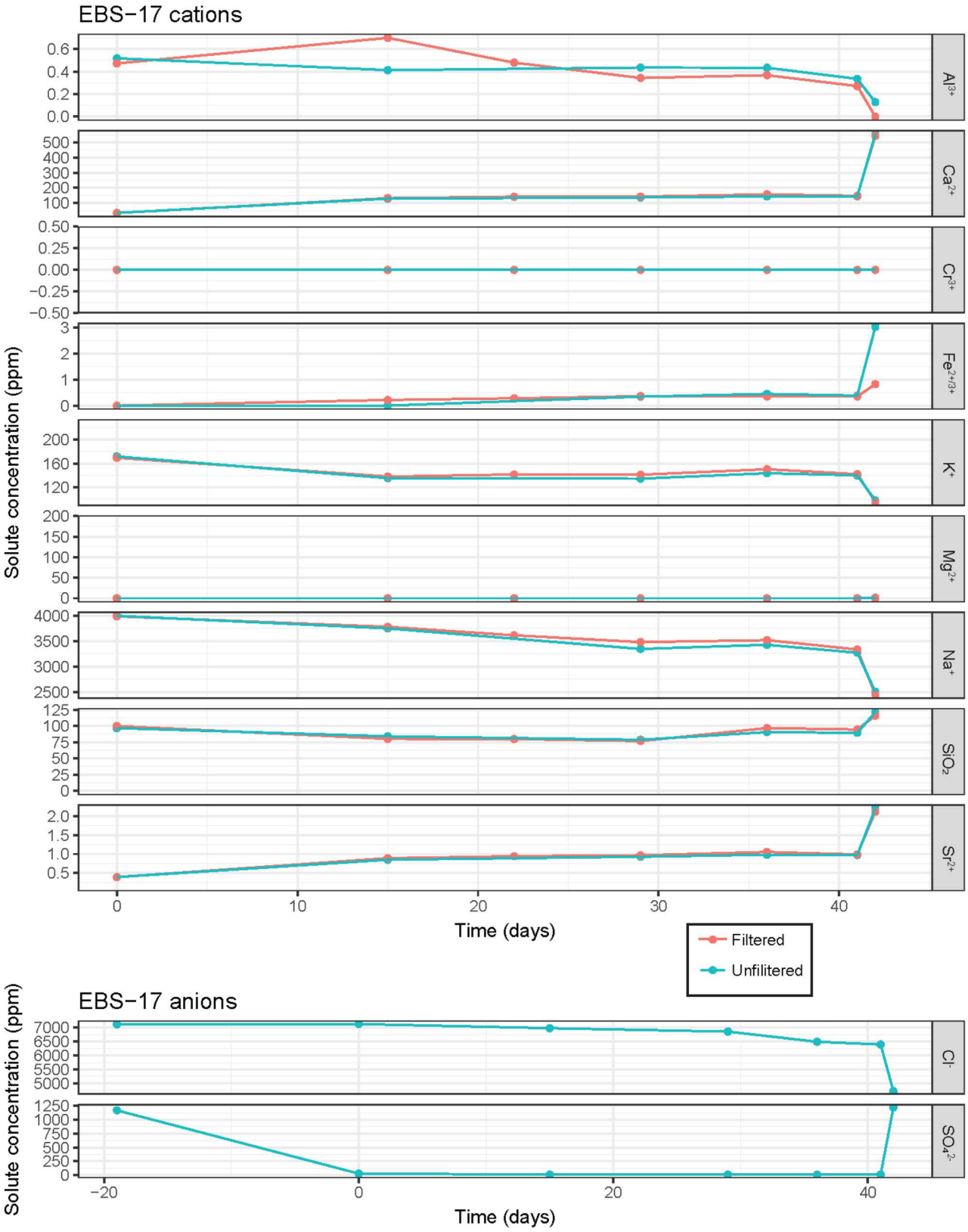
EBS-23 UNFILTERED

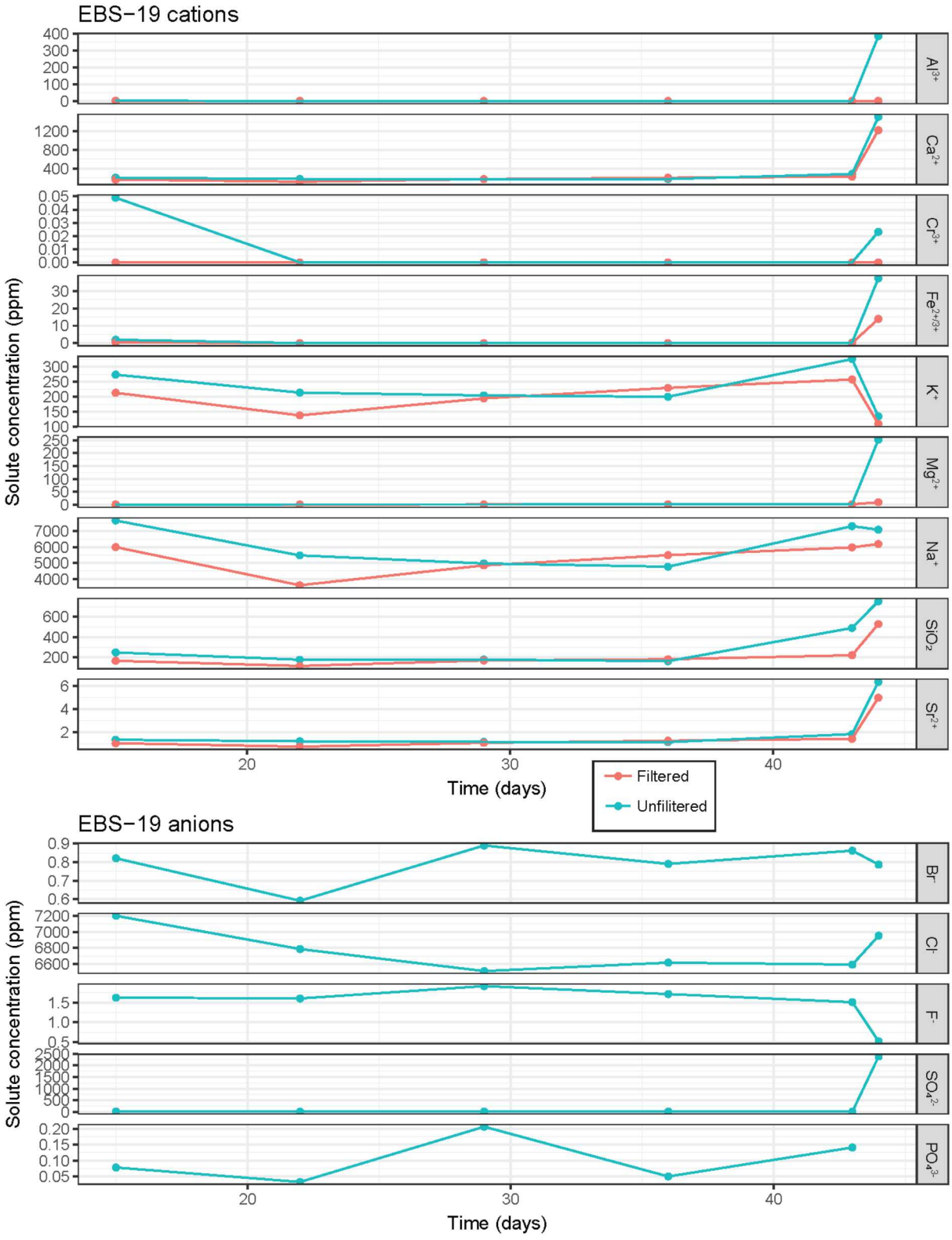
Lab ID	Sample Date	Al	B	Ba	Br	Ca	Cl	Cr	F	Fe	K	Li	Mg	Mn	Na	NO_3	PO_4	Si	SiO_2	SO_4	Sr	Ti	Zn	TDS	Cation	Anion	Balance
		ppm	ppm	ppm	ppm	ppm	ppm	ppm	ppm	ppm	ppm	ppm	ppm	ppm	ppm	ppm	ppm	ppm	ppm	ppm	ppm	ppm	ppm	ppm	ppm	ppm	
EBS-23-1 UF	3/22/2018	0.19	<2.03	0.41	0.33	105.02	3897.19	<0.03	0.29	<0.18	104.28	0.24	<0.1	<0.03	1951.46	0.79	<0.1	30.79	65.89	100.87	0.53	<0.02	<0.52	6227	93	111	-0.09
EBS-23-1 UF (rerun)	3/22/2018	0.41	<2.03	<0.11	0.33	112.64	3897.19	<0.03	0.29	<0.18	114.72	0.31	0.80	<0.03	1968.58	0.79	<0.1	31.04	66.42	100.87	0.55	<0.02	<0.52	6264	95	111	-0.08
EBS-23-2 UF	3/29/2018	0.54	<2.03	0.37	0.64	120.72	4249.60	<0.03	0.27	<0.18	100.20	0.34	<0.1	<0.03	2053.47	1.23	<0.1	36.04	77.12	103.28	0.65	<0.02	<0.52	6708	98	121	-0.10
EBS-23-3 UF	4/5/2018	0.17	<2.03	0.15	0.56	110.66	3029.12	<0.03	0.28	<0.18	74.37	0.43	0.13	<0.03	1568.50	0.79	<0.1	35.00	74.89	85.12	0.56	<0.02	<0.52	4946	76	87	-0.06
EBS-23-4 UF	4/12/2018	<0.16	<2.03	0.34	0.49	144.40	2854.58	<0.03	0.41	0.21	81.18	0.50	<0.1	<0.03	1730.95	0.67	<0.1	46.19	98.85	68.63	0.67	<0.02	<0.52	4982	85	82	0.02
EBS-23-5 UF	4/19/2018	0.32	<2.03	0.39	0.29	130.65	1568.73	<0.03	0.51	0.19	64.82	0.50	<0.1	<0.03	1300.11	0.72	<0.1	47.00	100.57	45.06	0.53	<0.02	<0.52	3213	66	45	0.19
EBS-23-6 UF	4/26/2018	<0.16	<2.03	0.39	0.44	108.63	2449.86	<0.03	0.64	0.26	45.74	0.45	0.77	1.06	888.26	0.59	<0.1	35.91	76.85	57.92	0.40	<0.02	8.09	3640	46	70	-0.20
EBS-23-7 UF	5/3/2018	0.18	<2.03	0.19	0.56	101.00	3154.84	<0.03	0.41	0.19	35.10	0.42	<0.1	<0.03	791.08	0.37	<0.1	44.36	94.92	63.29	0.33	<0.02	<0.52	4243	41	90	-0.37
EBS-23-8 UF	5/10/2018	<0.16	<2.03	0.17	0.32	141.60	3818.39	<0.03	0.50	0.23	46.91	0.49	<0.1	<0.03	1009.65	0.26	<0.1	50.52	108.12	65.02	0.42	<0.02	<0.52	5192	53	109	-0.34
EBS-23-9 UF	5/11/2018	<0.16	2.18	0.20	0.42	673.73	5172.97	<0.03	0.43	0.31	113.40	0.96	<0.1	<0.03	2557.81	0.10	<0.1	62.12	132.94	734.01	1.72	<0.02	<0.52	9391	148	160	-0.04

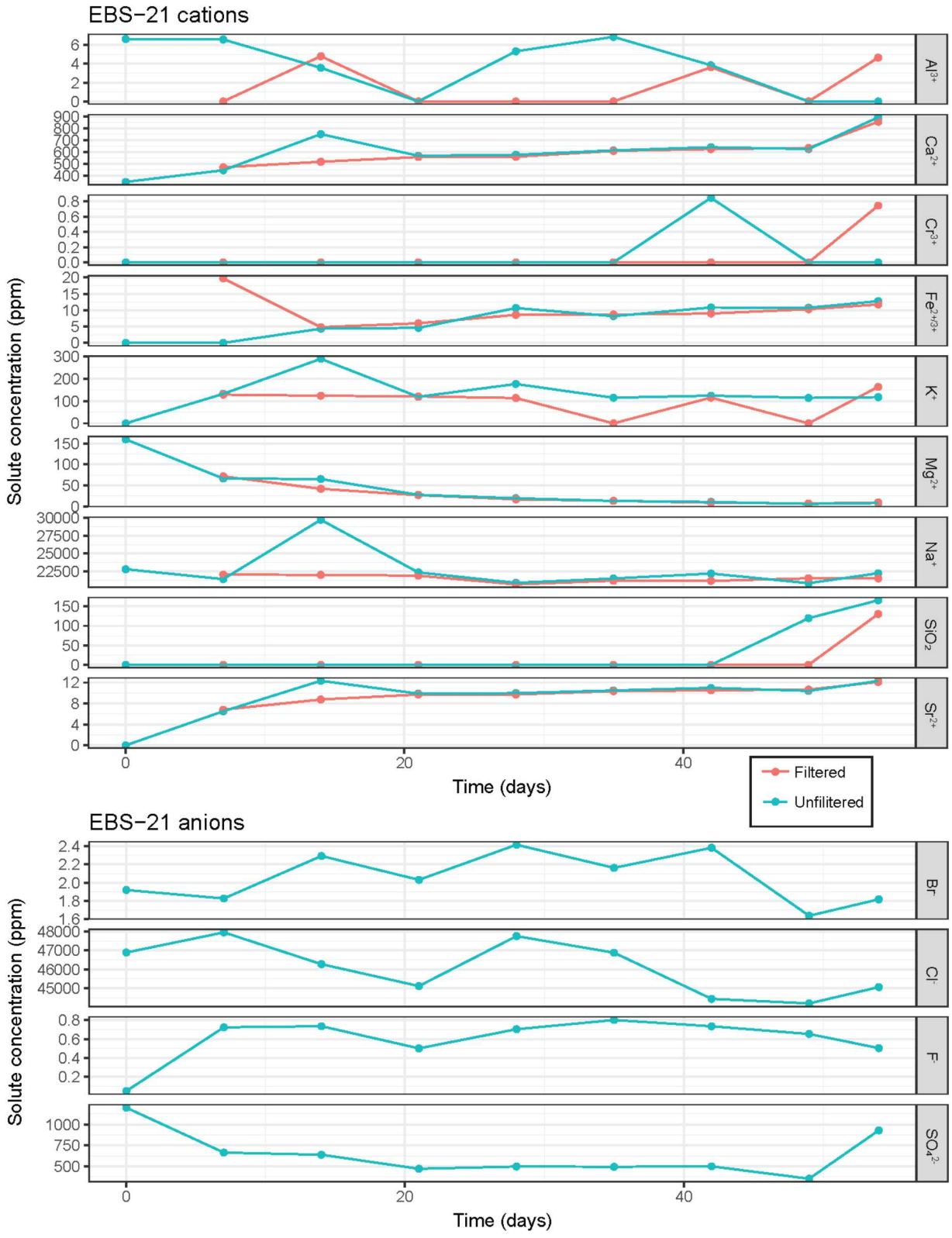
EBS-23 FILTERED

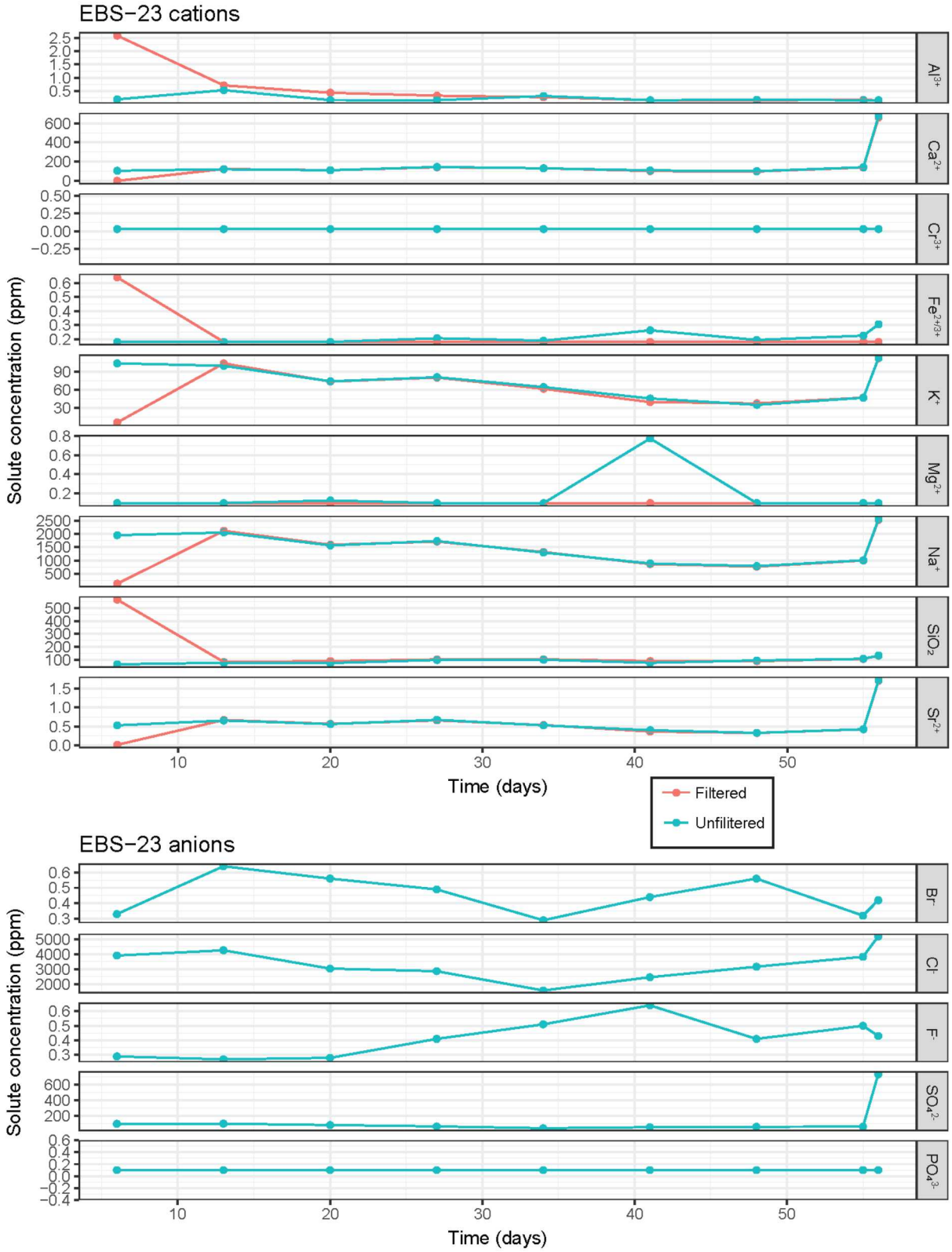
Lab ID	Sample Date	Al	B	Ba	Br	Ca	Cl	Cr	F	Fe	K	Li	Mg	Mn	Na	NO_3	PO_4	Si	SiO_2	SO_4	Sr	Ti	Zn	TDS	Cation	Anion	Balance
		ppm	ppm	ppm	ppm	ppm	ppm	ppm	ppm	ppm	ppm	ppm	ppm	ppm	ppm	ppm	ppm	ppm	ppm	ppm	ppm	ppm	ppm	ppm	ppm	ppm	
EBS-23-1 F	3/22/2018	2.58	2.27	<0.11		<0.45		<0.03		0.64	<5.61	<0.06	<0.1	<0.03	131.19			264.20	565.39		0.01	<0.02	<0.52	702	13	0	0.98
EBS-23-1 F (rerun)	3/22/2018	2.98	<2.03	<0.11		1.52		<0.03		0.50	<5.61	0.08	<0.1	<0.03	149.12			273.74	585.80		0.01	<0.02	<0.52	740	14	0	1.00
EBS-23-2 F	3/29/2018	0.72	<2.03	0.30		123.26		<0.03		<0.18	104.26	0.38	<0.1	<0.03	2114.05			38.97	83.40		0.67	<0.02	<0.52	2427	102	0	1.00
EBS-23-3 F	4/5/2018	0.44	<2.03	0.23		110.74		<0.03		<0.18	73.98	0.42	<0.1	<0.03	1593.41			42.04	89.97		0.57	<0.02	<0.52	1870	78	0	1.00
EBS-23-4 F	4/12/2018	0.33	<2.03	0.21		141.70		<0.03		<0.18	80.53	0.50	<0.1	<0.03	1710.55			48.11	102.95		0.66	<0.02	<0.52	2037	85	0	1.00
EBS-23-5 F	4/19/2018	0.27	<2.03	0.14		131.50		<0.03		<0.18	61.87	0.47	<0.1	<0.03	1318.94			48.63	104.08		0.53	<0.02	<0.52	1618	67	0	1.00
EBS-23-6 F	4/26/2018	<0.16	<2.03	0.20		101.32		<0.03		<0.18	39.71	0.39	<0.1	<0.03	865.24			42.37	90.67		0.36	<0.02	<0.52	1098	45	0	1.00
EBS-23-7 F	5/3/2018	<0.16	<2.03	<0.11		97.75		<0.03		<0.18	37.55	0.42	<0.1	<0.03	769.90			41.82	89.50		0.33	<0.02	<0.52	995	40	0	1.00
EBS-23-8 F	5/10/2018	0.17	<2.03	0.13		138.94		<0.03		<0.18	47.12	0.50	<0.1	<0.03	1001.69			50.21	107.46		0.42	<0.02	<0.52	1296	53	0	1.00
EBS-23-9 F	5/11/2018	<0.16	2.07	0.12		658.93		<0.03		<0.18	113.02	0.94	<0.1	<0.03	2525.67			61.51	131.63		1.70	<0.02	<0.52	3434	147	0	1.00

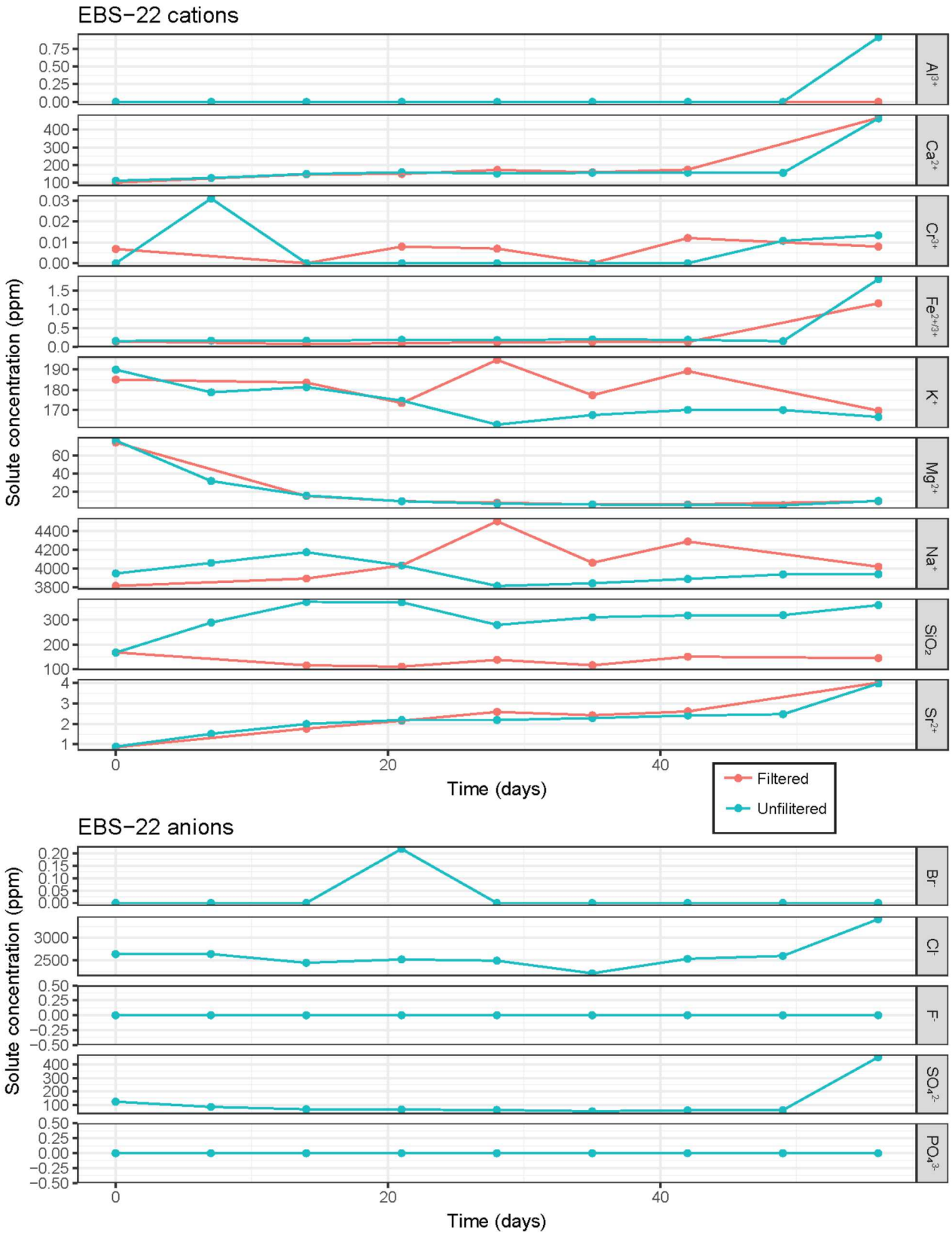

EBS−14 cations
Solute concentration (ppm)
Al3+
Ca2+
Cr3+
Fe2+/3+
K+
Mg2+
Na+
SiO2
Sr2+
Time (days)
Filtered
Unfilitered
EBS−14 anions
Cl-
SO4 2-
Time (days)


EBS−17 cations
Solute concentration (ppm)
Al3+
Ca2+
Cr3+
Fe2+/3+
K+
Mg2+
Na+
SiO2
Sr2+
Time (days)
Filtered
Unfilitered
EBS−17 anions
Solute concentration (ppm)
Cl-
SO4 2-
Time (days)


EBS−19 cations
Solute concentration (ppm)
Al3+
Ca2+
Cr3+
Fe2+/3+
K+
Mg2+
Na+
SiO2
Sr2+
Time (days)
Filtered
Unfilitered
EBS−19 anions
Solute concentration (ppm)
Br-
Cl-
F-
SO4 2-
PO4 3-
Time (days)


EBS−21 cations
Solute concentration (ppm)
Al3+
Ca2+
Cr3+
Fe2+/3+
K+
Mg2+
Na+
SiO2
Sr2+
Time (days)
Filtered
Unfilitered
EBS−21 anions
Solute concentration (ppm)
Br
Cl
F
SO4 2-
Time (days)


EBS−23 cations
Solute concentration (ppm)
Al3+
Ca2+
Cr3+
Fe2+/3+
K+
Mg2+
Na+
SiO2
Sr2+
Time (days)
Filtered
Unfilitered
EBS−23 anions
Solute concentration (ppm)
Br-
Cl-
F-
SO42-
PO43-
Time (days)


EBS−22 cations
Solute concentration (ppm)
Al3+
Ca2+
Cr3+
Fe2+/3+
K+
Mg2+
Na+
SiO2
Sr2+
Time (days)
Filtered
Unfilitered
EBS−22 anions
Solute concentration (ppm)
Br-
Cl-
F-
SO4 2-
PO4 3-
Time (days)

Appendix C
X-Ray Powder Diffraction Data: EBS-14 to EBS-23

Table C-1. Quantitative X-Ray Diffraction (QXRD) analyses of the buffer clay (Wyoming Bentonite) the wall rock (Opalinus Clay) and product results of experiments EBS-14 to EBS-23. Values are in weight percent. ***b.d.l.*** *= below detection limit,* * represents data set was normalized to 100.0, (+) represents material detectable but below 0.5 wt. %.

	Wyoming Bentonite	Switzerland Opalinus Clay	EBS-14 Opalinus Clay	EBS-15 Opal - 316 SS	EBS-17 Opal - Cu	EBS-18 Opalinus Clay	EBS-19 Opal -304 SS (1)	EBS-19 Opal -304 SS (2)	EBS-20 Opal -316 SS	EBS-21 Opal - 316LS SS	EBS-22	EBS-23	EBS-23 Cement
	4 weeks 125 - 300°C	6 weeks 300°C				3 weeks 300°C	6 weeks 300°C		6 months 300°C	8 weeks 200°C			
Analcime/ Wairakite	b.d.l.		5.5	1.3	3.0	0.5	0.4	0.4	1.4			8.57	52.92
Clinoptilolite	12.0			15.0	11.7	17.8	17.1	14.8	8.2	9.6	0.1		
Erionite-Ca												4.35	4.34
Smectite	66.4	24.1	39.8	51.6	63.8	62.8	54.0	56.7	41.4	53.6	2.4	13.53	
Kaolinite	b.d.l.	16.9	1.8	0.2							14.4		
Dickite												3.14	
Plagioclase	8.3	3	3.5	11.8	11.3	6.7	10.6	9.8	14.3	4.8	1.5		
Anorthite												58.82	
K-Feldspar	b.d.l.	5.9	4.3	2.3	3.1	0.1	2.7	1.3	0.8	1.9	0.6		
Biotite	2.8	7.4	11.9	9.7	2.0								
Muscovite						7.2	9.4	8.5	5.1	1.9	0.7		
Illite									20.9	18.3	50.0		
Chlorite	b.d.l.	9.1	11.1	1.3	1.1	0.6	0.4	0.4	0.4	0.4	3.5		
Calcite	5.5	16.4	9.4						0.1	1.3	13.6		34.06
Monohydrocalcite													6.78
Dolomite	+	0.7											
Quartz	0.9	13.8	8.4	5.5	3.3	3.9	4.9	7.2	4.9	3.0	9.4	8.09	1.90
Cristobalite/Opal-C	1.8					0.1			0.6	0.4			
Gypsum			0.5	0.3	0.1	0.4	0.2	0.5	0.3	0.2			
Halite							0.3	0.4	0.1	3.8	0.3		
Pyrite	0.4	1.1	0.7	+	0.2	+	+	+	+	+	+	+	+
Magnetite			3.1	1.1	0.5				1.4	0.6	3.6	3.50	
Siderite	1.8	0.1											
Total	**100.0***	**98.5**	**100.0**	**100.1**	**100.1**	**100.1**	**100.0**	**100.0**	**99.9**	**99.8**	**100.1**	**100.0**	**100.0**

Table C-2. Quantitative X-Ray Diffraction (QXRD) analyses of product results of the FEBEX experiments. Values are in weight percent. ***b.d.l.*** = *below detection limit,* (+) represents material detectable but below 0.5 wt. %.

	Starting Material	**Wall Rock**	**Inner Ring**			**Middle Ring**			**Outer Ring**		
	FEBEX	**BG-C-49-1 Granite**	**BM-C-49-1**	**BM-C-49-2**	**BM-C-49-3**	**B-C-49-8**	**B-C-49-10**	**B-C-49-12**	**B-C-49-7**	**B-C-49-9**	**B-C-49-11**
Quartz	26.73	44.02	12.03	9.19	9.98	12.49	10.89	12.03	12.75	7.07	9.31
Orthoclase	6.51	30.84	---	---	---	---	---	---	---	---	2.06
Albite	8.28	25.14	12.97	19.01	15.85	17.43	11.14	13.86	17.03	18.23	18.38
Smectite	58.62	---	75.00	71.93	74.06	70.08	77.85	74.11	70.22	74.82	70.37
Total	**100.14**	**100.00**	**100.00**	**100.13**	**99.89**	**100.00**	**99.88**	**100.00**	**100.00**	**100.12**	**100.12**

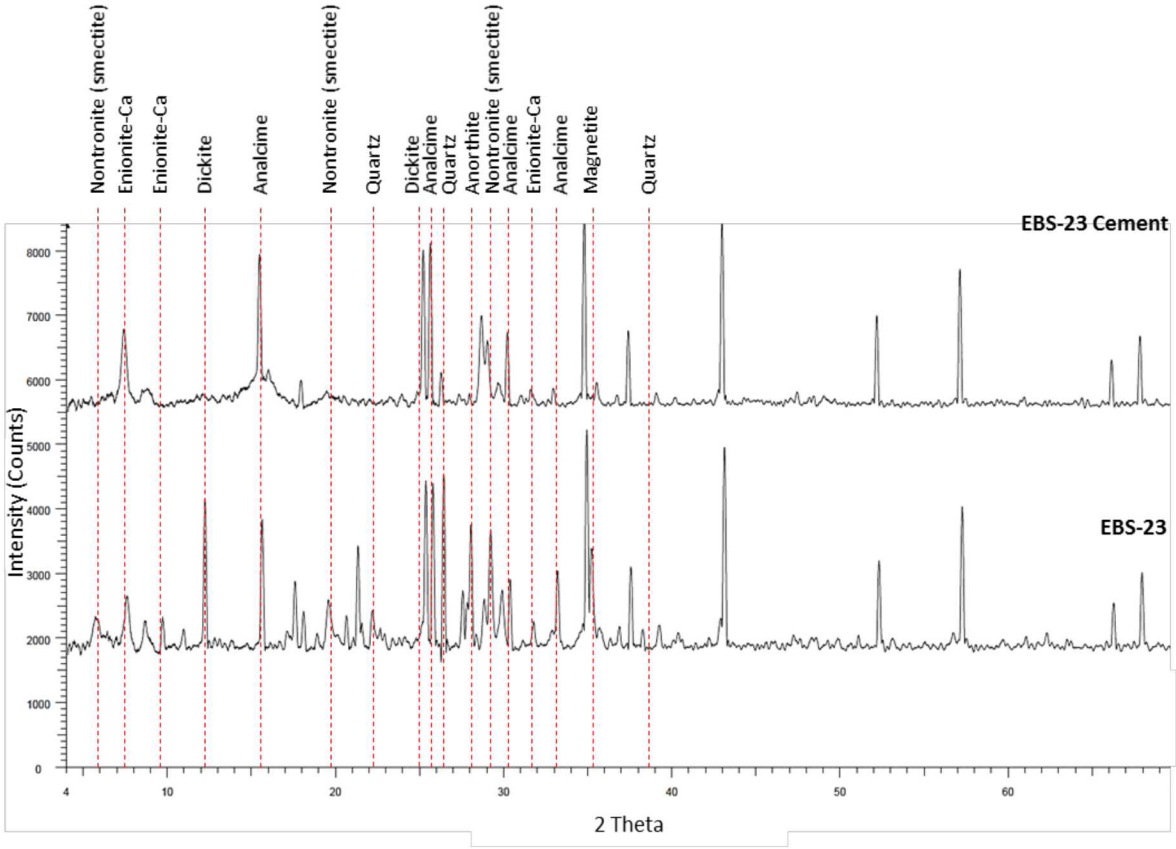


Figure C-1. XRD pattern for EBS-23 and the EBS-23 cement. The peaks are labeled to their corresponding minerals and unmarked peaks belong to the corundum standard.

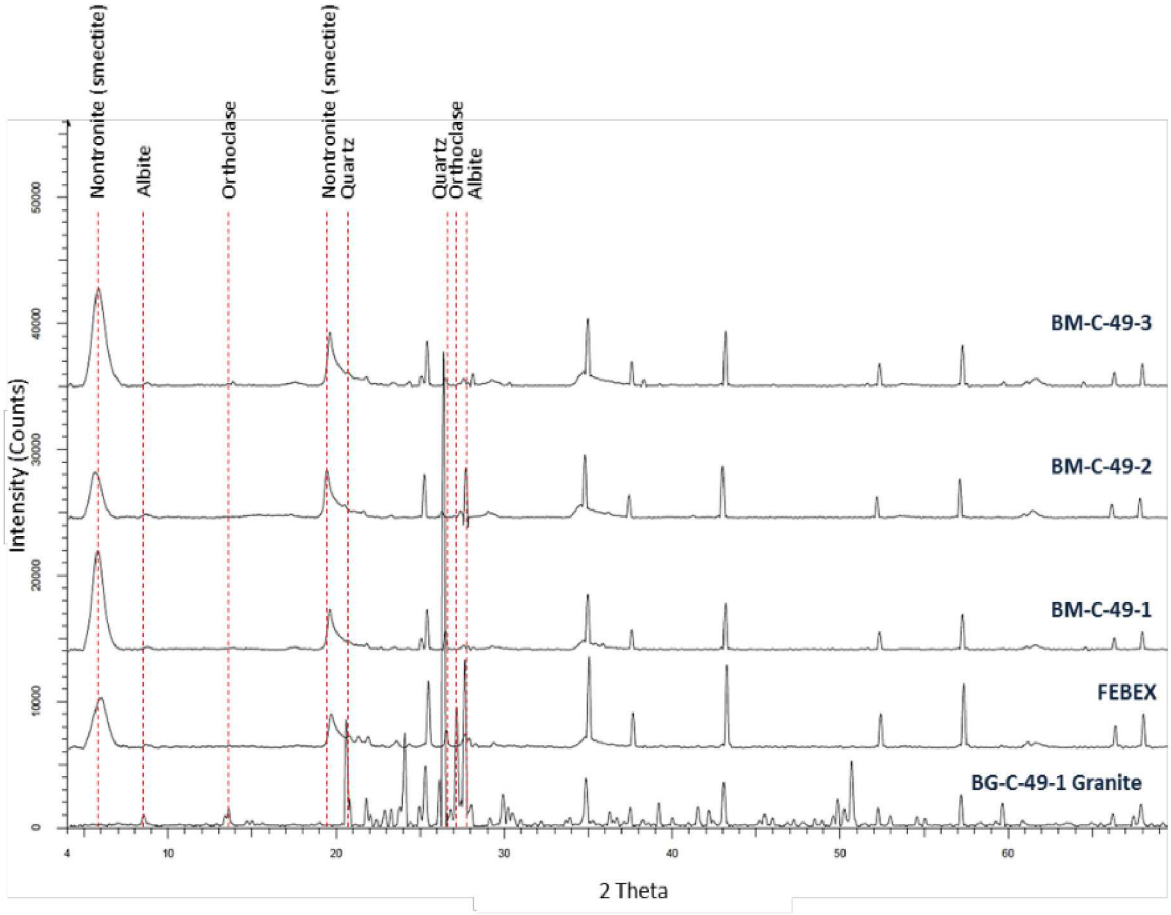


Figure C-2. XRD pattern from the FEBEX experiment including the FEBEX starting material, the granitic host rock and the inner ring bentonite samples. The peaks are labeled to their corresponding minerals and unmarked peaks belong to the corundum standard.

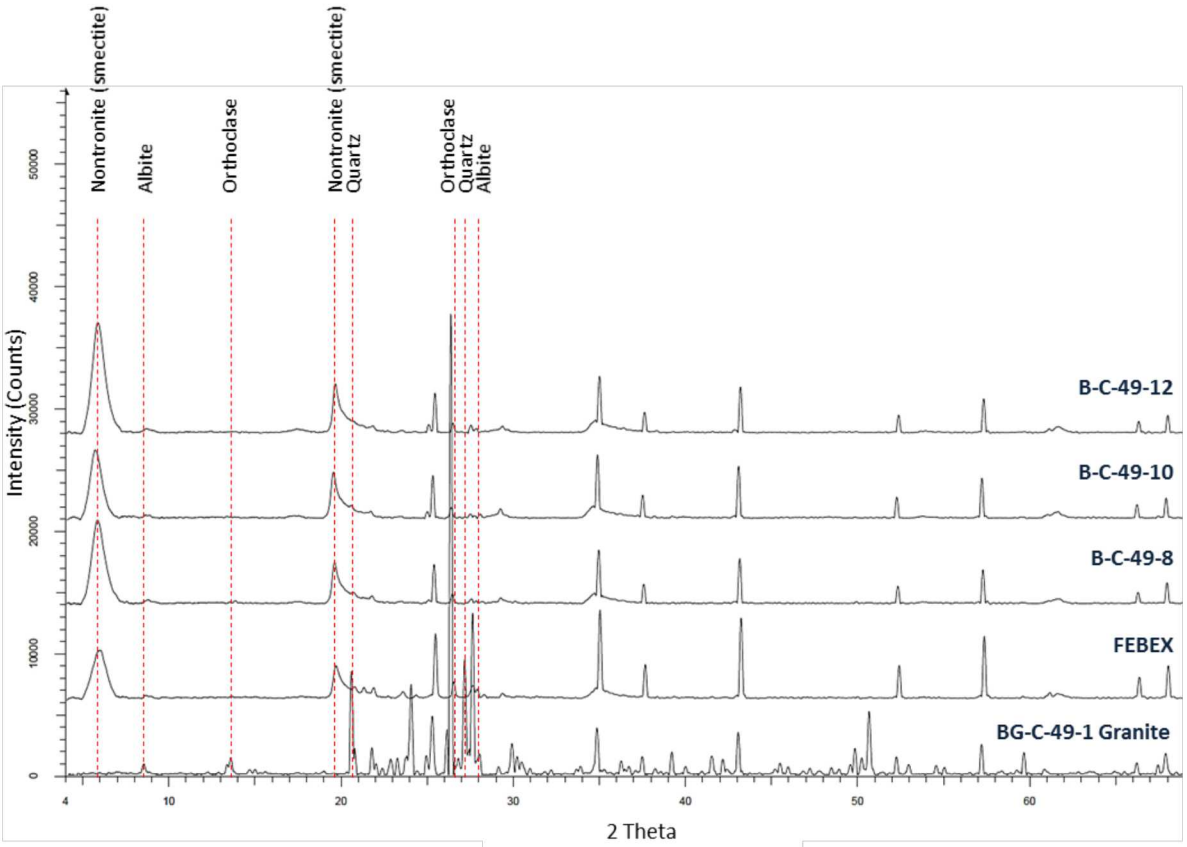


Figure C-3. XRD pattern from the FEBEX experiment including the FEBEX starting material, the granitic host rock and the middle ring bentonite samples. The peaks are labeled to their corresponding minerals and unmarked peaks belong to the corundum standard.

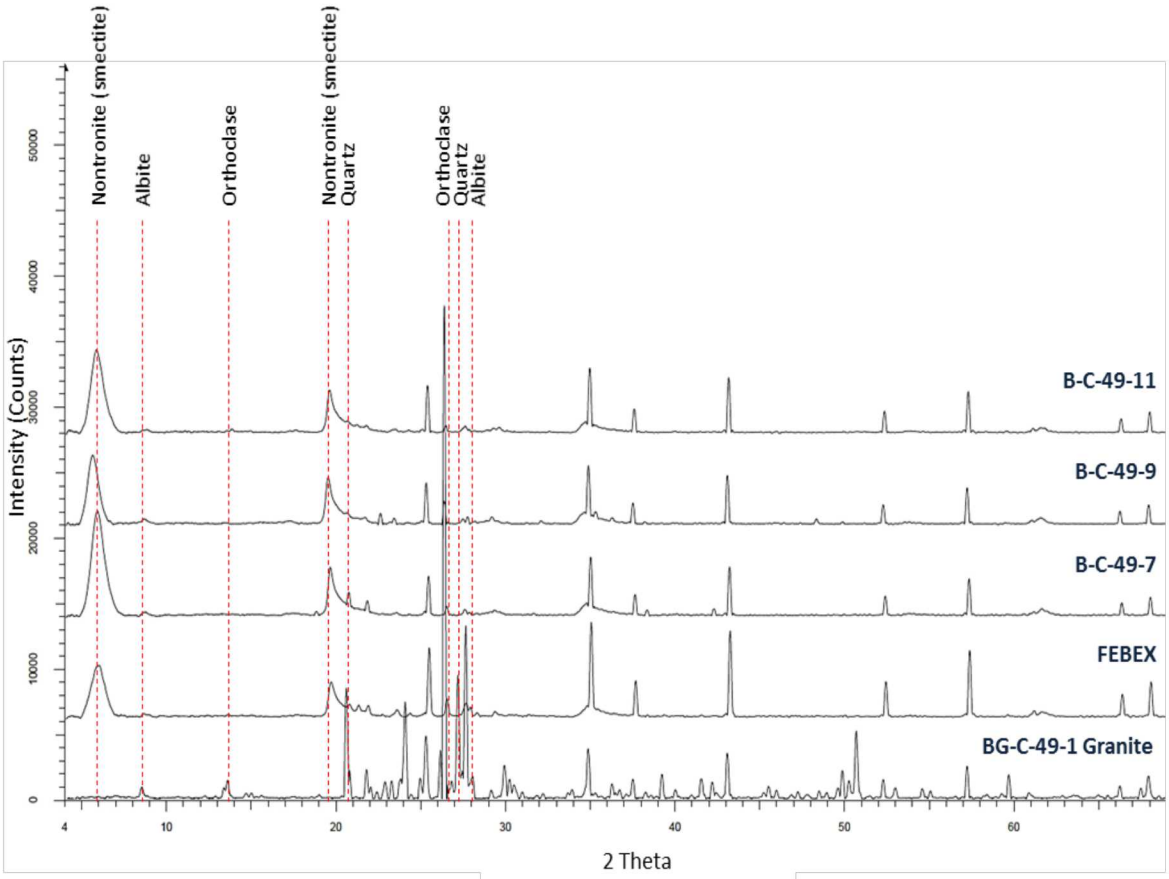


Figure C-4. XRD pattern from the FEBEX experiment including the FEBEX starting material, the granitic host rock and the outer ring bentonite samples. The peaks are labeled to their corresponding minerals and unmarked peaks belong to the corundum standard.

Appendix D
Electron Microprobe data

Electron Microprobe analyses

Electron microprobe (EMP) analyses were performed at the University of Oklahoma using a Cameca SX50 electron microprobe equipped with five wavelength-dispersive spectrometers and PGT PRISM 2000 energy-dispersive X-ray detector. Petrographic characterization was performed by backscattered electron imaging coupled with energy-dispersive X-ray analysis, using beam conditions of 20 kV acceleration and 20 nA sample current. Quantitative analysis was performed by wavelength-dispersive spectrometry using 20 kV accelerating voltage, 20 nA beam current, and 2 µm spot size. Matrix corrections employed the PAP algorithm (Pouchou and Pichoir, 1985), with oxygen content calculated by stoichiometry. Counting times were 30 seconds on peak for all elements, yielding minimum levels of detection (calculated at 3-σ above mean background) in the range of 0.01 to 0.03 wt. % of the oxides for all components except F (0.16 wt. %). All standards for elements in the silicates were analyzed using 30 second count times on peak, using K-alpha emissions. The standards and oxide detection limits, along with analytical data, are presented here in Appendix D.

Electron Microprobe Standards and Detection Limits

EMP standards and oxide detection limits for silicate analyses

Element	Standard Material	Minimum Detection Limit[a]
Mg	Synthetic Phlogopite	0.02
F	Synthetic Phlogopite	0.11
Na	Albite (Amelia, NC, U.S.A, Rutherford Mine)	0.02
Al	Labradorite (Chihuahua, Mexico)	0.02
Si	Labradorite (Chihuahua, Mexico)	0.02
Ca	Labradorite (Chihuahua, Mexico)	0.01
Cl	Tugtupite (Greenland)	0.01
K	Adularia (St. Gotthard, Switzerland)	0.01
Ti	Titanite glass (Penn State)	0.02
Cr	Synthetic Magnesio-chromite	0.04
Mn	Rhodonite (unknown locality)	0.02
Fe	Augite (unknown locality)	0.02
Ni	Synthetic Liebenbergite	0.06
Zn	Gahnite	0.05

[a] Minimum Detection Limit (MDL) values for oxides of respective elements

EBS-15		WEIGHT PERCENT													
SAMPLE	Pt#	SiO_2	TiO_2	Al_2O_3	Cr_2O_3	FeO	NiO	MnO	MgO	CaO	Na_2O	K_2O	Cl	F	TOTAL
ANALCIME															
EB15-Anl	1	65.29	0	19.9	0.01	0.54	0	0.01	0.12	3.57	4.15	0.01	0.01	0	93.61
EB15-Anl	2	65.79	0.03	20.34	0	0.23	0.01	0.01	0.06	3.91	4.4	0.04	0.01	0	94.82
EB15-Anl	3	65.92	0.01	20.75	0	0.19	0.02	0.02	0.04	4.2	3.39	0.03	0	0.08	94.69
EB15-Anl	4	66.44	0.01	19.63	0	0.48	0.02	0.02	0.13	3.53	3.41	0.03	0.03	0.07	93.78
EB15-Anl	5	66.29	0.01	20.25	0	0.41	0.02	0.02	0.11	3.71	3.5	0.02	0.02	0	94.37
EB15-Anl	6	66.21	0.04	19.43	0.01	0.42	0	0.03	0.09	3.83	2.9	0.01	0.02	0	92.99
EB15-Anl	7	65.54	0.01	20.23	0	0.55	0	0.02	0.17	3.45	3.39	0.05	0.02	0	93.45
EB15-Anl	8	65.61	0	19.52	0	0.3	0.02	0.02	0.05	4.05	3.67	0.03	0.01	0.08	93.36
EB15-Anl	9	65.92	0.04	19.15	0	0.35	0	0.01	0.13	3.57	4.36	0.02	0.02	0.02	93.6
EB15-Anl	10	66.11	0.01	19.05	0	0.19	0.01	0.01	0.04	3.66	3.89	0.06	0.02	0	93.05
EB15-Anl	11	65.82	0.02	19.36	0.03	0.34	0.01	0	0.11	3.78	3.77	0.02	0.01	0.11	93.39
EB15-Anl	12	66.19	0.01	19.23	0.01	0.25	0.01	0	0.09	3.95	3.79	0.01	0.02	0	93.55
EB15-Anl	13	65.73	0	20.06	0	0.24	0	0.02	0.06	3.72	4.37	0.08	0.03	0	94.34
AVERAGE		**65.91**	**0.01**	**19.76**	**0.01**	**0.34**	**0.01**	**0.01**	**0.09**	**3.76**	**3.77**	**0.03**	**0.02**	**0.03**	**93.77**
Std. Dev.		**0.33**	**0.01**	**0.53**	**0.01**	**0.13**	**0.01**	**0.01**	**0.04**	**0.22**	**0.46**	**0.02**	**0.01**	**0.04**	**0.6**
6 oxygen atoms per formula unit (sum excludes F & Cl)															
		Si	**Ti**	**Al**	**Cr**	**Fe**	**Ni**	**Mn**	**Mg**	**Ca**	**Na**	**K**	**Cl**	**F**	**SUM**
EB15-Anl	1	2.25	0	0.81	0	0.02	0	0.01	0	0.13	0.28	0	0	0	3.49
EB15-Anl	2	2.24	0	0.82	0	0.01	0	0	0	0.14	0.29	0	0	0	3.5
EB15-Anl	3	2.24	0	0.83	0	0.01	0	0	0	0.15	0.22	0	0	0.01	3.46
EB15-Anl	4	2.28	0	0.79	0	0.01	0	0.01	0	0.13	0.23	0	0	0.01	3.45
EB15-Anl	5	2.26	0	0.81	0	0.01	0	0.01	0	0.14	0.23	0	0	0	3.45

EB15-Anl	6	2.28	0	0.79	0	0.01	0	0	0	0.14	0.19	0	0	0	3.42
EB15-Anl	7	2.25	0	0.82	0	0.02	0	0.01	0	0.13	0.23	0	0	0	3.45
EB15-Anl	8	2.26	0	0.79	0	0.01	0	0	0	0.15	0.25	0	0	0.01	3.47
EB15-Anl	9	2.27	0	0.78	0	0.01	0	0.01	0	0.13	0.29	0	0	0	3.49
EB15-Anl	10	2.28	0	0.77	0	0.01	0	0	0	0.14	0.26	0	0	0	3.46
EB15-Anl	11	2.27	0	0.79	0	0.01	0	0.01	0	0.14	0.25	0	0	0.01	3.47
EB15-Anl	12	2.27	0	0.78	0	0.01	0	0	0	0.15	0.25	0	0	0	3.46
EB15-Anl	13	2.25	0	0.81	0	0.01	0	0	0	0.14	0.29	0	0	0	3.5
AVERAGE		**2.26**	**0**	**0.8**	**0**	**0.01**	**0**	**0**	**0**	**0.14**	**0.25**	**0**	**0**	**0**	**3.47**
Std. Dev.		**0.01**	**0**	**0.02**	**0**	**0**	**0**	**0**	**0**	**0.01**	**0.03**	**0**	**0**	**0**	**0.02**
SAMPLE	**Pt#**	**SiO2**	**TiO2**	**Al2O3**	**Cr2O3**	**FeO**	**NiO**	**MnO**	**MgO**	**CaO**	**Na2O**	**K2O**	**Cl**	**F**	**TOTAL**
PLAGIOCLASE															
EB15-Plg	1	59.6	0.01	25.86	0	0.2	0	0	0	7.22	7	0.73	0.01	0	100.63
EB15-Plg	2	59.55	0	26.03	0	0.18	0	0.02	0.01	7.3	6.88	0.72	0	0.04	100.71
EB15-Plg	3	61.96	0.03	23.89	0	0.26	0	0	0	5.48	7.94	0.86	0	0.14	100.52
AVERAGE		**60.37**	**0.01**	**25.26**	**0**	**0.21**	**0**	**0.01**	**0**	**6.67**	**7.27**	**0.77**	**0**	**0.06**	**100.62**
Std. Dev.		**1.38**	**0.01**	**1.19**	**0**	**0.04**	**0**	**0.01**	**0**	**1.03**	**0.58**	**0.08**	**0**	**0.07**	**0.1**
8 oxygen atoms per formula unit (sum excludes F & Cl)															
		Si	**Ti**	**Al**	**Cr**	**Fe**	**Ni**	**Mn**	**Mg**	**Ca**	**Na**	**K**	**Cl**	**F**	**SUM**
EB15-Plg	1	2.65	0	1.35	0	0.01	0	0	0	0.34	0.6	0.04	0	0	5
EB15-Plg	2	2.64	0	1.36	0	0.01	0	0	0	0.35	0.59	0.04	0	0.01	4.99
EB15-Plg	3	2.75	0	1.25	0	0.01	0	0	0	0.26	0.68	0.05	0	0.02	5
AVERAGE		**2.68**	**0**	**1.32**	**0**	**0.01**	**0**	**0**	**0**	**0.32**	**0.63**	**0.04**	**0**	**0.01**	**5**
Std. Dev.		**0.06**	**0**	**0.06**	**0**	**0**	**0**	**0**	**0**	**0.05**	**0.05**	**0**	**0**	**0.01**	**0**

SAMPLE	Pt#	SiO_2	TiO_2	Al_2O_3	Cr_2O_3	FeO	NiO	MnO	MgO	CaO	Na_2O	K_2O	Cl	F	TOTAL
SANIDINE															
EB15-San	1	66.4	0.01	19.14	0.01	0.12	0	0.01	0	0.15	3.45	11.7	0	0	100.97
EB15-San	2	64.91	0.01	19	0	0.11	0.02	0	0	0.19	2.47	12.71	0	0	99.43
EB15-San	3	64.8	0	18.7	0.01	0.24	0	0	0	0.18	2.49	12.78	0	0.01	99.21
AVERAGE		**65.37**	**0**	**18.95**	**0.01**	**0.16**	**0.01**	**0**	**0**	**0.17**	**2.81**	**12.4**	**0**	**0**	**99.87**
Std. Dev.		**0.89**	**0**	**0.22**	**0.01**	**0.07**	**0.01**	**0.01**	**0**	**0.02**	**0.56**	**0.6**	**0**	**0.01**	**0.96**
8 oxygen atoms per formula unit (sum excludes F & Cl)															
		Si	**Ti**	**Al**	**Cr**	**Fe**	**Ni**	**Mn**	**Mg**	**Ca**	**Na**	**K**	**Cl**	**F**	**SUM**
EB15-San	1	2.99	0	1.02	0	0	0	0	0	0.01	0.3	0.67	0	0	4.99
EB15-San	2	2.98	0	1.03	0	0	0	0	0	0.01	0.22	0.74	0	0	4.99
EB15-San	3	2.99	0	1.02	0	0.01	0	0	0	0.01	0.22	0.75	0	0	4.99
AVERAGE		**2.99**	**0**	**1.02**	**0**	**0.01**	**0**	**0**	**0**	**0.01**	**0.25**	**0.72**	**0**	**0**	**4.99**
Std. Dev.		**0**	**0**	**0.01**	**0**	**0**	**0**	**0**	**0**	**0**	**0.05**	**0.04**	**0**	**0**	**0**
SAMPLE	**Pt#**	**SiO_2**	**TiO_2**	**Al_2O_3**	**Cr_2O_3**	**FeO**	**NiO**	**MnO**	**MgO**	**CaO**	**Na_2O**	**K_2O**	**Cl**	**F**	**TOTAL**
BIOTITE															
EB15-Bt	1	34.71	4.08	13.27	0.02	25.6	0	0.27	7.4	0.02	0.29	8.53	0.23	0.44	94.66
EB15-Bt	2	35.06	4.13	13.56	0.01	25.48	0	0.28	7.51	0.02	0.32	8.56	0.24	0.31	95.39
EB15-Bt	3	35.07	3.7	13.48	0	26.87	0.02	0.41	6.88	0.04	0.29	8.54	0.29	0.82	96.08
AVERAGE		**34.94**	**3.97**	**13.44**	**0.01**	**25.99**	**0.01**	**0.32**	**7.26**	**0.03**	**0.3**	**8.54**	**0.25**	**0.53**	**95.38**
Std. Dev.		**0.21**	**0.24**	**0.15**	**0.01**	**0.77**	**0.01**	**0.08**	**0.34**	**0.01**	**0.02**	**0.01**	**0.03**	**0.27**	**0.71**
11 oxygen atoms per formula unit (sum excludes F & Cl)															
		Si	**Ti**	**Al**	**Cr**	**Fe**	**Ni**	**Mn**	**Mg**	**Ca**	**Na**	**K**	**Cl**	**F**	**SUM**
EB15-Bt	1	2.74	0.24	1.24	0.001	1.69	0.00	0.02	0.87	0.002	0.04	0.86	0.03	0.11	7.71

EB15-Bt	2	2.75	0.24	1.25	0.001	1.67	0.00	0.02	0.88	0.002	0.05	0.86	0.03	0.08	7.72
EB15-Bt	3	2.73	0.22	1.23	0.000	1.75	0.00	0.03	0.80	0.003	0.04	0.85	0.04	0.20	7.64
AVERAGE		**2.74**	**0.23**	**1.24**	**0.001**	**1.70**	**0.00**	**0.02**	**0.85**	**0.002**	**0.05**	**0.85**	**0.03**	**0.13**	**7.69**
Std. Dev.		**0.01**	**0.01**	**0.01**	**0.001**	**0.03**	**0.00**	**0.00**	**0.04**	**0.001**	**0.00**	**0.01**	**0.00**	**0.05**	**0.03**
SAMPLE	**Pt#**	**SiO_2**	**TiO_2**	**Al_2O_3**	**Cr_2O_3**	**FeO**	**NiO**	**MnO**	**MgO**	**CaO**	**Na_2O**	**K_2O**	**Cl**	**F**	**TOTAL**
STILPNOMELANE															
EB15-Mantle	1	33.93	0	14	0	31.8	0	0.12	2.21	6.12	0.05	0.02	0.36	0.07	88.68
EB15-Mantle	2	34.28	0.02	13.21	0	31.49	0	0.11	2.5	6.63	0.12	0.01	0.33	0.08	88.79
EB15-Mantle	3	29.55	0	16.05	0	36.29	0	0.21	3.07	2.8	0.01	0.01	0.26	0	88.26
AVERAGE		**32.59**	**0.01**	**14.42**	**0**	**33.19**	**0**	**0.15**	**2.59**	**5.18**	**0.06**	**0.01**	**0.32**	**0.05**	**88.58**
Std. Dev.		**2.64**	**0.01**	**1.47**	**0**	**2.69**	**0**	**0.06**	**0.44**	**2.08**	**0.06**	**0**	**0.05**	**0.04**	**0.28**
28 oxygen atoms per formula unit (sum excludes F & Cl)															
		Si	**Ti**	**Al**	**Cr**	**Fe**	**Ni**	**Mn**	**Mg**	**Ca**	**Na**	**K**	**Cl**	**F**	**SUM**
EB15-Mantle	1	8.035	0	3.908	0	6.298	0.024	0.78	0	1.552	0.022	0.005	0.144	0.055	20.62
EB15-Mantle	2	8.11	0.004	3.684	0.001	6.231	0.022	0.88	0	1.68	0.054	0.004	0.134	0.06	20.67
EB15-Mantle	3	7.306	0	4.677	0	7.504	0.044	1.132	0	0.742	0.003	0.003	0.109	0	21.41
AVERAGE		**7.817**	**0.001**	**4.09**	**0**	**6.677**	**0.03**	**0.931**	**0**	**1.325**	**0.026**	**0.004**	**0.129**	**0.039**	**20.9**
Std. Dev.		**0.444**	**0.002**	**0.521**	**0**	**0.716**	**0.012**	**0.181**	**0**	**0.509**	**0.026**	**0.001**	**0.018**	**0.034**	**0.44**
SAMPLE	**Pt#**	**SiO_2**	**TiO_2**	**Al_2O_3**	**Cr_2O_3**	**FeO**	**NiO**	**MnO**	**MgO**	**CaO**	**Na_2O**	**K_2O**	**Cl**	**F**	**TOTAL**
CHLORITE															
EB15M-Chl	1	34.62	0.07	13.35	0.15	19.01	0.29	0.16	2.4	1.72	0.43	0.14	0.3	0	72.62
EB15M-Chl	2	44.45	0.06	14.53	0.15	15.09	0.2	0.12	2.23	1.7	0.85	0.41	0.28	0.12	80.18
EB15M-Chl	3	37.17	0.04	14.3	0.32	23.07	0.33	0.16	3.86	2.08	1.11	0.17	0.13	0	82.76

EB15M-Chl	4	35.05	0.01	13.26	0.7	29.37	0.21	0.21	3.79	1.29	2.78	0.04	0.04	0.09	86.83
EB15M-Chl	5	34.2	0	13.02	0.64	28.92	0.21	0.2	3.85	1.23	3.59	0.04	0.02	0	85.93
EB15M-Chl	6	29.92	0.07	12.4	0.45	17.86	0.34	0.15	2.99	1.72	0.47	0.05	0.32	0.06	66.83
EB15M-Chl	7	33.08	0.02	14.24	0.76	29.22	0.27	0.2	3.85	1.49	1.94	0.12	0.01	0.12	85.36
EB15M-Chl	8	32.38	0.08	14.1	0.48	20.64	0.62	0.2	3.12	1.96	0.69	0.06	0.19	0	74.54
EB15M-Chl	9	27.61	0.02	11.05	0.1	18.6	0.47	0.17	1.87	1.46	1.16	0.07	0.29	0.01	62.89
AVERAGE		**34.27**	**0.04**	**13.36**	**0.42**	**22.42**	**0.33**	**0.17**	**3.11**	**1.63**	**1.45**	**0.12**	**0.18**	**0.05**	**77.55**
Std. Dev.		**4.48**	**0.03**	**1.05**	**0.24**	**5.18**	**0.13**	**0.03**	**0.74**	**0.27**	**1.04**	**0.11**	**0.12**	**0.05**	**8.26**
11 oxygen atoms per formula unit (sum excludes F & Cl)															
		Si	**Ti**	**Al**	**Cr**	**Fe**	**Ni**	**Mn**	**Mg**	**Ca**	**Na**	**K**	**Cl**	**F**	**SUM**
EB15M-Chl	1	3.29	0.00	1.49	0.01	1.51	0.02	0.01	0.34	0.18	0.08	0.02	0.05	0.00	6.95
EB15M-Chl	2	3.63	0.00	1.40	0.01	1.03	0.01	0.01	0.27	0.15	0.13	0.04	0.04	0.03	6.69
EB15M-Chl	3	3.17	0.00	1.44	0.02	1.64	0.02	0.01	0.49	0.19	0.18	0.02	0.02	0.00	7.18
EB15M-Chl	4	2.98	0.00	1.33	0.05	2.09	0.01	0.02	0.48	0.12	0.46	0.00	0.01	0.02	7.53
EB15M-Chl	5	2.96	0.00	1.33	0.04	2.09	0.01	0.01	0.50	0.11	0.60	0.00	0.00	0.00	7.66
EB15M-Chl	6	3.13	0.01	1.53	0.04	1.56	0.03	0.01	0.47	0.19	0.10	0.01	0.06	0.02	7.06
EB15M-Chl	7	2.87	0.00	1.46	0.05	2.12	0.02	0.01	0.50	0.14	0.33	0.01	0.00	0.03	7.51
EB15M-Chl	8	3.07	0.01	1.57	0.04	1.64	0.05	0.02	0.44	0.20	0.13	0.01	0.03	0.00	7.16
EB15M-Chl	9	3.13	0.00	1.48	0.01	1.76	0.04	0.02	0.32	0.18	0.25	0.01	0.06	0.00	7.20
AVERAGE		**3.13**	**0.00**	**1.45**	**0.03**	**1.72**	**0.02**	**0.01**	**0.42**	**0.16**	**0.25**	**0.01**	**0.03**	**0.01**	**7.22**
Std. Dev.		**0.21**	**0.00**	**0.08**	**0.02**	**0.33**	**0.01**	**0.00**	**0.08**	**0.03**	**0.17**	**0.01**	**0.02**	**0.01**	**0.29**

EBS-17		WEIGHT PERCENT													
SAMPLE	Pt#	SiO_2	TiO_2	Al_2O_3	Cr_2O_3	FeO	NiO	MnO	MgO	CaO	Na_2O	K_2O	Cl	F	TOTAL
ANALCIME															
EB17-Anl	1	64.82	0.03	20.36	0	0.2	0.01	0.01	0.03	4.05	4.12	0.02	0.01	0	93.67
EB17-Anl	2	64.74	0.03	21	0	0.7	0	0.02	0.22	4.07	4.14	0.03	0.04	0.12	95.11
EB17-Anl	3	65.07	0.01	20.95	0	0.4	0.02	0	0.12	3.94	4.41	0.02	0.02	0.07	95.02
EB17-Anl	4	65.62	0.01	19.4	0	0.51	0.01	0	0.14	4.21	3.63	0.07	0.01	0	93.62
EB17-Anl	5	65.84	0	19.86	0	0.24	0.02	0.01	0.06	4.04	4.17	0.02	0.01	0	94.3
EB17-Anl	6	65.64	0.03	19.87	0	0.16	0	0	0.04	4.18	4.17	0.02	0.02	0.06	94.2
EB17-Anl	7	65.17	0.01	19.69	0	0.17	0.02	0.01	0.04	4.38	3.74	0.03	0.01	0	93.29
EB17-Anl	8	65.64	0.01	19.86	0	0.16	0	0.01	0.04	4.01	3.88	0.04	0.01	0	93.66
EB17-Anl	9	65.73	0	19.72	0.01	0.13	0.02	0	0.04	4.16	4.28	0.03	0.01	0	94.12
EB17-Anl	10	66.49	0.03	19.89	0	0.27	0	0.01	0.09	3.76	4.3	0.04	0	0.04	94.94
AVERAGE		**65.47**	**0.01**	**20.06**	**0**	**0.29**	**0.01**	**0.01**	**0.08**	**4.08**	**4.09**	**0.03**	**0.01**	**0.03**	**94.19**
Std. Dev.		**0.53**	**0.01**	**0.54**	**0**	**0.19**	**0.01**	**0.01**	**0.06**	**0.17**	**0.25**	**0.02**	**0.01**	**0.04**	**0.65**
6 oxygen atoms per formula unit (sum excludes F & Cl)															
		Si	Ti	Al	Cr	Fe	Ni	Mn	Mg	Ca	Na	K	Cl	F	SUM
EB17-Anl	1	2.23	0	0.83	0	0.01	0	0	0	0.15	0.28	0	0	0	3.49
EB17-Anl	2	2.21	0	0.85	0	0.02	0	0.01	0	0.15	0.27	0	0	0.01	3.51
EB17-Anl	3	2.22	0	0.84	0	0.01	0	0.01	0	0.14	0.29	0	0	0.01	3.51
EB17-Anl	4	2.26	0	0.79	0	0.01	0	0.01	0	0.16	0.24	0	0	0	3.47
EB17-Anl	5	2.25	0	0.8	0	0.01	0	0	0	0.15	0.28	0	0	0	3.49
EB17-Anl	6	2.25	0	0.8	0	0	0	0	0	0.15	0.28	0	0	0.01	3.49
EB17-Anl	7	2.25	0	0.8	0	0	0	0	0	0.16	0.25	0	0	0	3.47
EB17-Anl	8	2.25	0	0.8	0	0	0	0	0	0.15	0.26	0	0	0	3.47

EB17-Anl	9	2.25	0	0.8	0	0	0	0	0	0.15	0.28	0	0	0	3.49
EB17-Anl	10	2.26	0	0.8	0	0.01	0	0	0	0.14	0.28	0	0	0	3.49
AVERAGE		**2.24**	**0**	**0.81**	**0**	**0.01**	**0**	**0**	**0**	**0.15**	**0.27**	**0**	**0**	**0**	**3.49**
Std. Dev.		**0.02**	**0**	**0.02**	**0**	**0.01**	**0**	**0**	**0**	**0.01**	**0.02**	**0**	**0**	**0**	**0.01**
SAMPLE	**Pt#**	**SiO_2**	**TiO_2**	**Al_2O_3**	**Cr_2O_3**	**FeO**	**NiO**	**MnO**	**MgO**	**CaO**	**Na_2O**	**K_2O**	**Cl**	**F**	**TOTAL**
PLAGIOCLASE															
EB17-Plg	1	63.37	0.03	23.41	0.01	0.21	0	0	0	4.44	8.44	0.95	0	0.02	100.88
EB17-Plg	2	61.48	0.01	24.62	0.01	0.29	0.01	0.02	0	6.08	7.63	0.81	0	0	100.95
EB17-Plg	3	61.73	0.03	24.1	0.01	0.4	0	0	0	5.39	7.73	0.98	0	0.07	100.43
AVERAGE		**62.19**	**0.02**	**24.04**	**0.01**	**0.3**	**0**	**0.01**	**0**	**5.3**	**7.93**	**0.91**	**0**	**0.03**	**100.75**
Std. Dev.		**1.02**	**0.01**	**0.61**	**0**	**0.09**	**0**	**0.01**	**0**	**0.82**	**0.44**	**0.09**	**0**	**0.04**	**0.28**
8 oxygen atoms per formula unit (sum excludes F & Cl)															
		Si	**Ti**	**Al**	**Cr**	**Fe**	**Ni**	**Mn**	**Mg**	**Ca**	**Na**	**K**	**Cl**	**F**	**SUM**
EB17-Plg	1	2.79	0	1.21	0	0.01	0	0	0	0.21	0.72	0.05	0	0	4.99
EB17-Plg	2	2.71	0	1.28	0	0.01	0	0	0	0.29	0.65	0.05	0	0	4.99
EB17-Plg	3	2.74	0	1.26	0	0.01	0	0	0	0.26	0.66	0.06	0	0.01	4.99
AVERAGE		**2.75**	**0**	**1.25**	**0**	**0.01**	**0**	**0**	**0**	**0.25**	**0.68**	**0.05**	**0**	**0**	**4.99**
Std. Dev.		**0.04**	**0**	**0.03**	**0**	**0**	**0**	**0**	**0**	**0.04**	**0.04**	**0.01**	**0**	**0.01**	**0**
SAMPLE	**Pt#**	**SiO_2**	**TiO_2**	**Al_2O_3**	**Cr_2O_3**	**FeO**	**NiO**	**MnO**	**MgO**	**CaO**	**Na_2O**	**K_2O**	**Cl**	**F**	**TOTAL**
SANIDINE															
EB17-San	1	65.51	0.01	18.83	0	0.19	0	0	0	0.18	3.46	11.49	0.01	0	99.69
EB17-San	2	65.12	0	18.66	0	0.13	0	0.02	0	0.17	3.43	11.5	0	0	99.03
AVERAGE		**65.32**	**0.01**	**18.74**	**0**	**0.16**	**0**	**0.01**	**0**	**0.18**	**3.45**	**11.49**	**0.01**	**0**	**99.36**

Std. Dev.		**0.27**	**0.01**	**0.12**	**0**	**0.05**	**0**	**0.01**	**0**	**0.01**	**0.02**	**0.01**	**0.01**	**0**	**0.47**
8 oxygen atoms per formula unit (sum excludes F & Cl)															
		Si	**Ti**	**Al**	**Cr**	**Fe**	**Ni**	**Mn**	**Mg**	**Ca**	**Na**	**K**	**Cl**	**F**	**SUM**
EB17-San	1	2.99	0	1.01	0	0.01	0	0	0	0.01	0.31	0.67	0	0	4.99
EB17-San	2	2.99	0	1.01	0	0	0	0	0	0.01	0.31	0.67	0	0	4.99
AVERAGE		**2.99**	**0**	**1.01**	**0**	**0.01**	**0**	**0**	**0**	**0.01**	**0.31**	**0.67**	**0**	**0**	**4.99**
Std. Dev.		**0**	**0**	**0**	**0**	**0**	**0**	**0**	**0**	**0**	**0**	**0**	**0**	**0**	**0**
SAMPLE	**Pt#**	**SiO_2**	**TiO_2**	**Al_2O_3**	**Cr_2O_3**	**FeO**	**NiO**	**MnO**	**MgO**	**CaO**	**Na_2O**	**K_2O**	**Cl**	**F**	**TOTAL**
BIOTITE															
EB17-Bt	1	34.46	4.62	13.3	0.01	26.89	0	0.24	7.23	0.03	0.31	8.51	0.22	0.78	96.3
EB17-Bt	2	34.87	4.88	13.05	0	27.36	0	0.21	6.2	0.03	0.33	8.49	0.3	0.57	96.03
AVERAGE		**34.66**	**4.75**	**13.17**	**0.01**	**27.12**	**0**	**0.23**	**6.72**	**0.03**	**0.32**	**8.5**	**0.26**	**0.67**	**96.17**
Std. Dev.		**0.29**	**0.18**	**0.17**	**0.01**	**0.33**	**0**	**0.02**	**0.72**	**0**	**0.02**	**0.01**	**0.05**	**0.15**	**0.19**
11 oxygen atoms per formula unit (sum excludes F & Cl)															
		Si	**Ti**	**Al**	**Cr**	**Fe**	**Ni**	**Mn**	**Mg**	**Ca**	**Na**	**K**	**Cl**	**F**	**SUM**
EB17-Bt	1	2.68	0.27	1.22	0.00	1.75	0.00	0.02	0.84	0.00	0.05	0.84	0.03	0.19	7.66
EB17-Bt	2	2.73	0.29	1.20	0.00	1.79	0.00	0.01	0.72	0.00	0.05	0.85	0.04	0.14	7.65
AVERAGE		**2.70**	**0.28**	**1.21**	**0.00**	**1.77**	**0.00**	**0.01**	**0.78**	**0.00**	**0.05**	**0.85**	**0.03**	**0.17**	**7.65**
Std. Dev.		**0.03**	**0.01**	**0.01**	**0.00**	**0.02**	**0.00**	**0.00**	**0.06**	**0.00**	**0.00**	**0.00**	**0.01**	**0.03**	**0.01**

EBS-18		WEIGHT PERCENT													
SAMPLE	Pt#	SiO_2	TiO_2	Al_2O_3	Cr_2O_3	FeO	NiO	MnO	MgO	CaO	Na_2O	K_2O	Cl	F	TOTAL
ANALCIME															
EB18-Anl	1	67.08	0.03	20.9	0	0.66	0	0	0.16	3.91	1.1	0.03	0.02	0.23	94.12
EB18-Anl	2	62.99	0.02	20.17	0	0.8	0.01	0	0.17	3.98	2.22	0.06	0.03	0.06	90.5
EB18-Anl	4	64.68	0.09	20.56	0	0.33	0.01	0.02	0.07	4.65	1.67	0.19	0.01	0	92.29
EB18-Anl	5	62.4	0.03	19.92	0	0.33	0	0.01	0.04	4.92	0.62	0.21	0.02	0	88.51
AVERAGE		**64.29**	**0.04**	**20.39**	**0**	**0.53**	**0**	**0.01**	**0.11**	**4.37**	**1.4**	**0.12**	**0.02**	**0.07**	**91.35**
Std. Dev.		**2.1**	**0.03**	**0.43**	**0**	**0.24**	**0.01**	**0.01**	**0.07**	**0.5**	**0.7**	**0.09**	**0.01**	**0.11**	**2.41**
6 oxygen atoms per formula unit (sum excludes F & Cl)															
		Si	Ti	Al	Cr	Fe	Ni	Mn	Mg	Ca	Na	K	Cl	F	SUM
EB18-Anl	1	2.271	0.001	0.834	0	0.019	0	0	0.008	0.142	0.072	0.001	0.001	0.024	3.348
EB18-Anl	2	2.236	0	0.844	0	0.024	0	0	0.009	0.151	0.153	0.003	0.002	0.007	3.42
EB18-Anl	4	2.244	0.002	0.841	0	0.01	0	0.001	0.003	0.173	0.112	0.009	0.001	0	3.394
EB18-Anl	5	2.25	0.001	0.847	0	0.01	0	0	0.002	0.19	0.043	0.01	0.001	0	3.352
AVERAGE		**2.25**	**0.001**	**0.841**	**0**	**0.015**	**0**	**0**	**0.006**	**0.164**	**0.095**	**0.006**	**0.001**	**0.008**	**3.379**
Std. Dev.		**0.02**	**0**	**0.01**	**0**	**0.01**	**0**	**0**	**0**	**0.02**	**0.05**	**0**	**0**	**0.01**	**0.03**
SAMPLE	Pt#	SiO_2	TiO_2	Al_2O_3	Cr_2O_3	FeO	NiO	MnO	MgO	CaO	Na_2O	K_2O	Cl	F	TOTAL
CLINOPTILOLITE															
EB18-Clinop	1	58.65	0.02	21.06	0.02	0.99	0	0.01	0.39	4.48	3.16	0.23	0.02	0	89.03
EB18-Clinop	2	60.56	0.03	22.7	0	0.5	0	0.01	0.58	5.68	2.71	1.36	0.01	0.07	94.21
EB18-Clinop	3	59.96	0.2	20.98	0.03	2.13	0	0.03	0.77	4.15	2.07	0.55	0.04	0.04	90.95
EB18-Clinop	4	72.82	0.29	15.08	0.02	1.84	0	0.04	0.66	2.17	1.35	0.95	0.05	0.11	95.37
EB18-Clinop	5	57.26	0.21	21.26	0.01	4.54	0.02	0.05	1.75	2.98	1.58	1.13	0.08	0	90.87

AVERAGE		**61.85**	**0.15**	**20.22**	**0.01**	**2**	**0**	**0.03**	**0.83**	**3.89**	**2.17**	**0.84**	**0.04**	**0.04**	**92.09**
Std. Dev.		**6.26**	**0.12**	**2.95**	**0.01**	**1.56**	**0.01**	**0.02**	**0.53**	**1.36**	**0.76**	**0.45**	**0.03**	**0.05**	**2.62**
18 oxygen atoms per formula unit (sum excludes F & Cl)															
		Si	**Ti**	**Al**	**Cr**	**Fe**	**Ni**	**Mn**	**Mg**	**Ca**	**Na**	**K**	**Cl**	**F**	**SUM**
EB18-Clinop	1	6.437	0.001	2.724	0.002	0.09	0	0.001	0.065	0.526	0.673	0.032	0.004	0	10.552
EB18-Clinop	2	6.332	0.002	2.797	0	0.043	0	0.001	0.091	0.636	0.549	0.182	0.002	0.024	10.633
EB18-Clinop	3	6.459	0.016	2.663	0.002	0.192	0	0.003	0.124	0.479	0.433	0.076	0.007	0.014	10.447
EB18-Clinop	4	7.3	0.022	1.782	0.001	0.155	0	0.003	0.098	0.233	0.262	0.121	0.009	0.034	9.978
EB18-Clinop	5	6.272	0.017	2.744	0.001	0.416	0.001	0.005	0.286	0.35	0.335	0.158	0.015	0	10.585
AVERAGE		**6.56**	**0.012**	**2.542**	**0.001**	**0.179**	**0**	**0.003**	**0.133**	**0.445**	**0.45**	**0.114**	**0.008**	**0.014**	**10.439**
Std. Dev.		**0.42**	**0.01**	**0.43**	**0**	**0.14**	**0**	**0**	**0.09**	**0.16**	**0.16**	**0.06**	**0.01**	**0.01**	**0.27**
SAMPLE	**Pt#**	**SiO_2**	**TiO_2**	**Al_2O_3**	**Cr_2O_3**	**FeO**	**NiO**	**MnO**	**MgO**	**CaO**	**Na_2O**	**K_2O**	**Cl**	**F**	**TOTAL**
STILPNOMELANE															
EB18-Stilp	1	34.47	0.04	15.25	0	31.11	0	0.08	2.12	2.33	0.61	0.01	0.21	0	86.22
EB18-Stilp	2	35.44	0.02	14.4	0	33.8	0	0.12	2.1	2.6	0.08	0.01	0.2	0.01	88.79
EB18-Stilp	3	34.63	0.03	14.16	0.01	32.71	0.01	0.1	1.95	2.68	0.43	0.01	0.26	0.05	87.03
EB18-Stilp	4	36.03	0.03	14.87	0	31.76	0	0.11	2.32	1.94	0.28	0.02	0.11	0	87.47
EB18-Stilp	5	36.59	0.03	14.22	0.01	31.48	0	0.11	2.31	1.89	0.32	0.01	0.27	0	87.24
AVERAGE		**35.43**	**0.03**	**14.58**	**0.01**	**32.17**	**0**	**0.1**	**2.16**	**2.29**	**0.34**	**0.01**	**0.21**	**0.01**	**87.35**
Std. Dev.		**0.9**	**0.01**	**0.47**	**0.01**	**1.09**	**0**	**0.01**	**0.16**	**0.37**	**0.19**	**0.01**	**0.07**	**0.02**	**0.93**
28 oxygen atoms per formula unit (sum excludes F & Cl)															
		Si	**Ti**	**Al**	**Cr**	**Fe**	**Ni**	**Mn**	**Mg**	**Ca**	**Na**	**K**	**Cl**	**F**	**SUM**
EB18-Stilp	1	7.50	0.01	3.91	0.00	5.66	0.00	0.01	0.69	0.54	0.26	0.00	0.08	0.00	5.33
EB18-Stilp	2	7.57	0.00	3.62	0.00	6.04	0.00	0.02	0.67	0.59	0.03	0.00	0.07	0.01	5.32

EB18-Stilp	3	7.54	0.00	3.63	0.00	5.96	0.00	0.02	0.63	0.63	0.18	0.00	0.10	0.03	5.34
EB18-Stilp	4	7.70	0.00	3.74	0.00	5.67	0.00	0.02	0.74	0.44	0.12	0.01	0.04	0.00	5.28
EB18-Stilp	5	7.82	0.00	3.58	0.00	5.63	0.00	0.02	0.74	0.43	0.13	0.00	0.10	0.00	5.26
AVERAGE		**7.63**	**0.00**	**3.70**	**0.00**	**5.79**	**0.00**	**0.02**	**0.69**	**0.53**	**0.14**	**0.00**	**0.08**	**0.01**	**5.30**
Std. Dev.		**0.12**	**0.00**	**0.12**	**0.00**	**0.17**	**0.00**	**0.00**	**0.04**	**0.08**	**0.07**	**0.00**	**0.02**	**0.01**	**0.03**
SAMPLE	**Pt#**	**SiO_2**	**TiO_2**	**Al_2O_3**	**Cr_2O_3**	**FeO**	**NiO**	**MnO**	**MgO**	**CaO**	**Na_2O**	**K_2O**	**Cl**	**F**	**TOTAL**
GOETHITE															
EB18-Alt-1	1	1.03	0	0.24	0.67	70.38	0.53	0.78	0	0.03	0.09	0	6.66	0	80.41
EB18-Alt-2	1	0.51	0.01	0.69	0.35	77.51	0.09	0.81	0.06	0.21	2.72	0.07	0.07	0	83.09
EB18-Alt-2	2	8.28	0.01	2.61	0.61	64.35	0.44	0.32	0.38	2.11	1.2	0.08	0.17	0	80.56
EB18-Alt-3	1	8.35	0.01	2.72	0.67	68.62	0.5	0.55	0.59	3.35	0.92	0.09	0.13	0.06	86.54
EB18-Alt-4	4	5.08	0.03	0.84	0.41	62.09	0.56	0.38	0.15	7.95	0.37	0.01	0.14	0	78
AVERAGE		**4.65**	**0.01**	**1.42**	**0.54**	**68.59**	**0.43**	**0.57**	**0.24**	**2.73**	**1.06**	**0.05**	**1.43**	**0.01**	**81.72**
Std. Dev.		**3.78**	**0.01**	**1.16**	**0.15**	**5.98**	**0.19**	**0.23**	**0.25**	**3.23**	**1.02**	**0.04**	**2.92**	**0.03**	**3.24**
22 oxygen atoms per formula unit (sum excludes F & Cl)															
		Si	**Ti**	**Al**	**Cr**	**Fe**	**Ni**	**Mn**	**Mg**	**Ca**	**Na**	**K**	**Cl**	**F**	**SUM**
EB18-Alt-1	1	0.357	0	0.099	0.184	20.442	0.149	0.231	0	0.009	0.063	0	3.919	0	21.534
EB18-Alt-2	1	0.156	0.003	0.253	0.086	20.017	0.023	0.212	0.026	0.069	1.626	0.028	0.036	0	22.499
EB18-Alt-2	2	2.265	0.002	0.841	0.133	14.727	0.097	0.074	0.156	0.619	0.637	0.027	0.079	0	19.578
EB18-Alt-3	1	2.136	0.002	0.82	0.135	14.684	0.103	0.118	0.226	0.919	0.456	0.028	0.056	0.046	19.626
EB18-Alt-4	4	1.51	0.006	0.294	0.096	15.445	0.134	0.095	0.068	2.534	0.211	0.004	0.071	0	20.396
AVERAGE		**1.285**	**0.003**	**0.461**	**0.127**	**17.063**	**0.101**	**0.146**	**0.095**	**0.83**	**0.599**	**0.017**	**0.832**	**0.009**	**20.727**
Std. Dev.		**0.98**	**0**	**0.35**	**0.04**	**2.91**	**0.05**	**0.07**	**0.09**	**1.03**	**0.62**	**0.01**	**1.73**	**0.02**	**1.27**

SAMPLE	Pt#	SiO_2	TiO_2	Al_2O_3	Cr_2O_3	FeO	NiO	MnO	MgO	CaO	Na_2O	K_2O	Cl	F	TOTAL
Fe-SAPONITE															
EB18-Alt-1	2	29.55	0.03	13.18	0.27	44.29	0.02	0.16	1.61	0.05	0.16	0.02	0.33	0.06	89.74
EB18-Alt-1	3	29.13	0.05	12.46	0.17	42.98	0.03	0.23	1.5	0.06	0.2	0.03	0.06	0.03	86.95
EB18-Alt-2	3	22.66	0.04	10.52	0.13	50.31	0.03	0.52	1.26	1.63	1.08	0.08	0.28	0.01	88.55
EB18-Alt-2	4	24.77	0.02	12.14	0	47.06	0.01	0.33	1.35	0.32	0.38	0.07	0.16	0	86.62
EB18-Alt-4	2	30.95	0.01	13.67	0.04	37.48	0.02	0.22	2.53	0.69	0.02	0.02	0.13	0.02	85.79
EB18-Alt-6	3	20.59	0	10.68	0.03	51.95	0.02	0.4	1.73	1.15	0.43	0.09	0.07	0	87.14
EB18-Alt-6	4	27.24	0.05	9.58	0	35.68	0.03	0.28	1.13	0.94	0.37	0.13	0.6	0.01	76.03
AVERAGE		**26.41**	**0.03**	**11.75**	**0.09**	**44.25**	**0.02**	**0.31**	**1.59**	**0.69**	**0.38**	**0.06**	**0.23**	**0.02**	**85.83**
Std. Dev.		**3.57**	**0.02**	**1.40**	**0.09**	**5.67**	**0.01**	**0.11**	**0.43**	**0.55**	**0.32**	**0.04**	**0.18**	**0.02**	**4.18**
12 oxygen atoms per formula unit (sum excludes F & Cl)															
		Si	**Ti**	**Al**	**Cr**	**Fe**	**Ni**	**Mn**	**Mg**	**Ca**	**Na**	**K**	**Cl**	**F**	**SUM**
EB18-Alt-1	2	2.88	0.00	1.51	0.02	3.60	0.00	0.01	0.23	0.01	0.03	0.00	0.05	0.02	**8.30**
EB18-Alt-1	3	2.93	0.00	1.48	0.01	3.61	0.00	0.02	0.22	0.01	0.04	0.00	0.01	0.01	**8.33**
EB18-Alt-2	3	2.43	0.00	1.33	0.01	4.51	0.00	0.05	0.20	0.19	0.22	0.01	0.05	0.00	**8.96**
EB18-Alt-2	4	2.61	0.00	1.51	0.00	4.15	0.00	0.03	0.21	0.04	0.08	0.01	0.03	0.00	**8.64**
EB18-Alt-4	2	3.03	0.00	1.58	0.00	3.07	0.00	0.02	0.37	0.07	0.00	0.00	0.02	0.01	**8.15**
EB18-Alt-6	3	2.28	0.00	1.39	0.00	4.81	0.00	0.04	0.29	0.14	0.09	0.01	0.01	0.00	**9.06**
EB18-Alt-6	4	3.09	0.00	1.28	0.00	3.39	0.00	0.03	0.19	0.11	0.08	0.02	0.12	0.00	**8.20**
AVERAGE		**2.75**	**0.00**	**1.44**	**0.01**	**3.88**	**0.00**	**0.03**	**0.25**	**0.08**	**0.08**	**0.01**	**0.04**	**0.01**	**8.52**
Std. Dev.		**0.29**	**0.00**	**0.10**	**0.01**	**0.58**	**0.00**	**0.01**	**0.06**	**0.06**	**0.07**	**0.01**	**0.03**	**0.01**	**0.34**

SAMPLE	Pt#	SiO_2	TiO_2	Al_2O_3	Cr_2O_3	FeO	NiO	MnO	MgO	CaO	Na_2O	K_2O	Cl	F	TOTAL
CHLORITE															
EB18-Alt-5	2	49.89	0.16	14.91	0.04	20.43	0.01	0.16	2.25	0.51	0.27	1.53	0.23	0.03	90.41
EB18-Alt-5	3	42.21	0.63	22.2	0	16.2	0	0.15	2.84	0.47	0.14	3.47	0.13	0.17	88.63
AVERAGE		**46.05**	**0.395**	**18.555**	**0.02**	**18.315**	**0.005**	**0.155**	**2.545**	**0.49**	**0.205**	**2.5**	**0.18**	**0.1**	**89.52**
Std. Dev.		**3.84**	**0.235**	**3.645**	**0.02**	**2.115**	**0.005**	**0.005**	**0.295**	**0.02**	**0.065**	**0.97**	**0.05**	**0.07**	**0.89**
11 oxygen atoms per formula unit (sum excludes F & Cl)															
		Si	**Ti**	**Al**	**Cr**	**Fe**	**Ni**	**Mn**	**Mg**	**Ca**	**Na**	**K**	**Cl**	**F**	**SUM**
EB18-Alt-5	2	3.68	0.01	1.29	0.00	1.26	0.00	0.01	0.25	0.04	0.04	0.14	0.03	0.01	6.72
EB18-Alt-5	3	3.18	0.04	1.97	0.00	1.02	0.00	0.01	0.32	0.04	0.02	0.33	0.02	0.04	6.92
AVERAGE		**3.43**	**0.02**	**1.63**	**0.00**	**1.14**	**0.00**	**0.01**	**0.28**	**0.04**	**0.03**	**0.24**	**0.02**	**0.02**	**6.82**
Std. Dev.		**0.25**	**0.01**	**0.34**	**0.00**	**0.12**	**0.00**	**0.00**	**0.04**	**0.00**	**0.01**	**0.09**	**0.01**	**0.02**	**0.10**

EBS-19		WEIGHT PERCENT													
SAMPLE	Pt#	SiO_2	TiO_2	Al_2O_3	Cr_2O_3	FeO	NiO	MnO	MgO	CaO	Na_2O	K_2O	Cl	F	TOTAL
ANALCIME															
EBS-19 Anl-1	2	64.85	0.01	19.08	0.03	0.17	0	0	0.02	3.72	2.49	0.04	0.04	0	90.47
EBS-19 Anl-1	3	63.43	0.01	19.06	0	0.19	0	0	0.02	3.83	2.76	0.03	0.02	0.06	89.37
EBS-19 Anl-1	4	66.14	0.02	19.31	0	0.34	0.01	0	0.12	3.38	2.68	0.01	0.07	0.03	92.09
EBS-19 Anl-1	5	64.72	0.01	19.08	0	0.4	0.01	0	0.06	3.3	2.39	0.04	0.35	0.01	90.36
EBS-19 Anl-1	6	65.64	0.02	19.4	0.02	0.37	0	0	0.04	3.55	2.47	0.02	0.03	0	91.57
EBS-19 Anl-1	7	62.94	0.01	20.57	0.01	0.28	0.01	0.01	0.08	3.87	2.12	0.04	0.23	0.1	90.17
EBS-19 Anl-1	8	63.99	0	19.46	0	0.25	0	0.02	0.05	3.42	2.1	0.03	0.08	0.07	89.41
EBS-19 Anl-2	1	61.55	0	20.15	0	0.25	0	0.01	0.06	3.63	2.23	0.02	0.05	0.02	87.96
EBS-19 Anl-2	2	63.24	0.01	20.1	0.01	0.22	0	0	0.07	3.63	1.58	0.02	0.06	0	88.94
EBS-19 Anl-2	3	66.78	0	19.72	0	0.3	0	0.01	0.1	3.48	2.86	0.05	0.21	0	93.52
EBS-19 Anl-2	4	66.07	0	20.75	0	0.35	0	0.02	0.09	3.33	3.18	0.03	0.17	0.08	93.99
EBS-19 Anl-2	5	65.24	0	19.71	0.01	0.2	0.01	0	0.04	3.5	2.17	0.05	0.18	0.02	91.12
EBS-19 Anl-2	6	66.66	0.02	20.25	0	0.21	0.01	0	0.06	3.77	2.01	0.01	0.07	0.07	93.07
EBS-19 Anl-1	1	68.65	0.02	21.03	0.01	0.17	0	0.03	0.08	3.33	1.4	0.08	0.05	0	94.84
EBS-19 Anl-2	1	68.62	0.01	21.08	0	0.3	0.01	0	0.16	3.3	2.43	0.03	0.03	0.03	96.02
EBS-19 Anl-3	1	65.84	0.01	21.08	0	0.28	0	0.01	0.09	3.5	1.66	0.09	0.05	0	92.63
EBS-19-Anl-4	1	65.48	0.01	20.57	0.17	0.7	0.08	0.03	0.15	3.4	1.82	0.06	0.05	0	92.52
EBS-19 Anl-5	1	65.43	0.01	19.94	0	0.36	0	0.04	0.14	3.09	2.42	0.05	0.06	0	91.54
EBS-19 Anl-6	1	67.47	0.01	20.57	0.01	0.24	0	0.02	0.07	3.75	2.78	0.06	0.02	0	95
EBS-19 Anl-7	1	66.94	0.06	20.44	0	0.35	0	0.03	0.26	3.41	2.27	0.3	0.25	0.06	94.38
EBS-19 Anl-8	1	68.99	0	21.43	0	0.48	0	0.01	0.2	3.14	2.79	0.12	0.12	0.1	97.37
EBS-19 Anl-0	1	68.72	0.02	22.2	0	0.47	0	0.02	0.18	3.15	1.63	0.04	0.13	0	96.56

EBS-19 Anl-11	1	64.56	0.01	20.35	0	0.3	0	0	0.1	3.16	1.15	0.04	0.07	0	89.76
EBS-19 Anl-12	1	66.28	0.03	20.01	0	0.41	0	0.01	0.14	2.95	2.46	0.04	0.14	0.04	92.49
EBS-19 Anl-13	1	63.13	0.26	20.92	0	0.99	0.02	0.01	0.39	3.59	2.66	0.67	0.12	0.02	92.78
AVERAGE		**65.66**	**0.02**	**20.24**	**0**	**0.33**	**0**	**0.01**	**0.11**	**3.45**	**2.28**	**0.08**	**0.11**	**0.03**	**92.31**
Std. Dev.		**1.97**	**0.05**	**0.8**	**0.01**	**0.16**	**0.01**	**0.01**	**0.08**	**0.24**	**0.49**	**0.14**	**0.08**	**0.03**	**2.49**
6 oxygen atoms per formula unit (sum excludes F & Cl)															
		Si	**Ti**	**Al**	**Cr**	**Fe**	**Ni**	**Mn**	**Mg**	**Ca**	**Na**	**K**	**Cl**	**F**	**SUM**
EBS-19 Anl-1	2	2.288	0	0.793	0.001	0.005	0	0	0.001	0.141	0.17	0.002	0.002	0.001	3.401
EBS-19 Anl-1	3	2.271	0	0.804	0	0.006	0	0	0.001	0.147	0.192	0.002	0.001	0.007	3.423
EBS-19 Anl-1	4	2.292	0.001	0.789	0	0.01	0	0	0.006	0.125	0.18	0.001	0.004	0.003	3.403
EBS-19 Anl-1	5	2.291	0	0.796	0	0.012	0	0	0.003	0.125	0.164	0.002	0.021	0.002	3.394
EBS-19 Anl-1	6	2.287	0.001	0.797	0	0.011	0	0	0.002	0.133	0.167	0.001	0.002	0	3.398
EBS-19 Anl-1	7	2.236	0	0.861	0	0.008	0	0	0.004	0.147	0.146	0.002	0.014	0.011	3.407
EBS-19 Anl-1	8	2.28	0	0.817	0	0.007	0	0.001	0.002	0.131	0.145	0.002	0.005	0.008	3.385
EBS-19 Anl-2	1	2.237	0	0.863	0	0.008	0	0	0.003	0.142	0.157	0.001	0.003	0.002	3.41
EBS-19 Anl-2	2	2.262	0	0.847	0	0.006	0	0	0.004	0.139	0.11	0.001	0.004	0	3.369
EBS-19 Anl-2	3	2.285	0	0.795	0	0.009	0	0	0.005	0.128	0.19	0.002	0.012	0	3.414
EBS-19 Anl-2	4	2.253	0	0.834	0	0.01	0	0.001	0.004	0.122	0.21	0.001	0.01	0.009	3.436
EBS-19 Anl-2	5	2.283	0	0.813	0	0.006	0	0	0.002	0.131	0.148	0.002	0.011	0.002	3.385
EBS-19 Anl-2	6	2.28	0	0.816	0	0.006	0	0	0.003	0.138	0.133	0.001	0.004	0.007	3.378
EBS-19 Anl-1	1	3.055	0.001	1.103	0	0.006	0	0.001	0.005	0.159	0.121	0.004	0.004	0	4.455
EBS-19 Anl-2	1	3.034	0	1.099	0	0.011	0	0	0.011	0.157	0.208	0.002	0.002	0.005	4.522
EBS-19 Anl-3	1	2.26	0	0.853	0	0.008	0	0	0.005	0.129	0.111	0.004	0.003	0.001	3.37
EBS-19-Anl-4	1	2.259	0	0.837	0.005	0.02	0.002	0.001	0.008	0.126	0.122	0.003	0.003	0	3.382
EBS-19 Anl-5	1	2.278	0	0.818	0	0.01	0	0.001	0.007	0.115	0.163	0.002	0.004	0	3.396

EBS-19 Anl-6	1	2.269	0	0.815	0	0.007	0	0.001	0.003	0.135	0.181	0.002	0.001	0	3.415
EBS-19 Anl-7	1	2.271	0.001	0.817	0	0.01	0	0.001	0.013	0.124	0.149	0.013	0.014	0.006	3.4
EBS-19 Anl-8	1	2.266	0	0.829	0	0.013	0	0	0.01	0.11	0.177	0.005	0.007	0.01	3.411
EBS-19 Anl-0	1	2.261	0	0.861	0	0.013	0	0.001	0.009	0.111	0.104	0.002	0.007	0	3.361
EBS-19 Anl-11	1	2.278	0	0.846	0	0.009	0	0	0.005	0.12	0.079	0.002	0.004	0	3.339
EBS-19 Anl-12	1	2.284	0.001	0.813	0	0.012	0	0	0.007	0.109	0.165	0.002	0.008	0.004	3.392
EBS-19 Anl-13	1	2.203	0.007	0.86	0	0.029	0.001	0	0.02	0.134	0.18	0.03	0.007	0.003	3.465
AVERAGE		**2.33**	**0.00**	**0.85**	**0.00**	**0.01**	**0.00**	**0.00**	**0.01**	**0.13**	**0.15**	**0.00**	**0.01**	**0.00**	**3.48**
Std. Dev.		**0.21**	**0.00**	**0.08**	**0.00**	**0.01**	**0.00**	**0.00**	**0.00**	**0.01**	**0.03**	**0.01**	**0.00**	**0.00**	**0.30**
SAMPLE	**Pt#**	**SiO_2**	**TiO_2**	**Al_2O_3**	**Cr_2O_3**	**FeO**	**NiO**	**MnO**	**MgO**	**CaO**	**Na_2O**	**K_2O**	**Cl**	**F**	**TOTAL**
STEEL ALTERATION (CHLORITE)															
EBS-19 Steel -6	1	37.03	0.06	17.4	0.89	23.09	0.91	0.36	3.59	2.96	0.78	0.12	0.11	0.12	87.32
EBS-19 Steel -6	2	42.08	0.08	14.88	0.94	16.65	0.6	0.28	2.93	2.41	0.52	0.21	0.08	0.05	81.69
EBS-19 Steel -6	3	36.63	0.03	16.4	1.03	24.75	0.84	0.31	3.85	3.22	0.97	0.09	0.1	0.05	88.23
EBS-19 Steel -7	3	28.34	0	10.08	8.79	24.06	0.91	0.33	3.17	4.32	2.42	0.04	0.28	0.07	82.75
AVERAGE		**36.02**	**0.04**	**14.69**	**2.91**	**22.14**	**0.82**	**0.32**	**3.39**	**3.23**	**1.17**	**0.12**	**0.14**	**0.07**	**85.00**
Std. Dev.		**4.93**	**0.03**	**2.81**	**3.39**	**3.22**	**0.13**	**0.03**	**0.36**	**0.70**	**0.74**	**0.06**	**0.08**	**0.03**	**2.82**
11 oxygen atoms per formula unit (sum excludes F & Cl)															
		Si	**Ti**	**Al**	**Cr**	**Fe**	**Ni**	**Mn**	**Mg**	**Ca**	**Na**	**K**	**Cl**	**F**	**SUM**
EBS-19 Steel -6	1	3.002	0.004	1.662	0.057	1.566	0.059	0.025	0.434	0.257	0.123	0.013	0.016	0.03	7.202
EBS-19 Steel -6	2	3.456	0.005	1.44	0.061	1.143	0.04	0.02	0.359	0.212	0.083	0.022	0.011	0.013	6.842
EBS-19 Steel -6	3	2.977	0.002	1.571	0.066	1.682	0.055	0.022	0.467	0.28	0.154	0.009	0.014	0.013	7.284
EBS-19 Steel -7	3	2.646	0	1.11	0.649	1.879	0.069	0.026	0.441	0.432	0.439	0.005	0.044	0.02	7.696
AVERAGE		**3.02**	**0.00**	**1.45**	**0.21**	**1.57**	**0.06**	**0.02**	**0.43**	**0.30**	**0.20**	**0.01**	**0.02**	**0.02**	**7.26**
Std. Dev.		**0.29**	**0.00**	**0.21**	**0.25**	**0.27**	**0.01**	**0.00**	**0.04**	**0.08**	**0.14**	**0.01**	**0.01**	**0.01**	**0.30**

EBS-20		WEIGHT PERCENT													
SAMPLE	Pt#	SiO_2	TiO_2	Al_2O_3	Cr_2O_3	FeO	NiO	MnO	MgO	CaO	Na_2O	K_2O	Cl	F	TOTAL
ANALCIME															
EBS-20 Anl-1	1	66.87	0	19.17	0.01	0.27	0	0	0.09	3.65	2.54	0.03	0.04	0.04	92.7
EBS-20 Anl-1	2	64.49	0.01	19.44	0.01	0.23	0	0.02	0.08	3.71	1.91	0.03	0.12	0.02	90.06
EBS-20 Anl-1	3	66.43	0.13	18.69	0	0.2	0.02	0.01	0.06	3.66	1.47	0.03	0.02	0.01	90.75
EBS-20 Anl-1	4	66.66	0	19.01	0	0.32	0.01	0.03	0.11	3.5	2.24	0.02	0.06	0.07	91.96
EBS-20 Anl-1	5	63.72	0	19.17	0	0.3	0	0	0.08	3.77	2.07	0.03	0.01	0.04	89.16
EBS-20 Anl-1	6	66.84	0	18.36	0	0.24	0.02	0	0.06	3.49	1.8	0.02	0.01	0	90.84
EBS-20 Anl-1	7	64.7	0	18.84	0.01	0.24	0	0.01	0.07	3.55	2.34	0.01	0.03	0.02	89.8
EBS-20 Anl-1	8	64.9	0.02	19.27	0	0.36	0	0.03	0.13	3.53	2.49	0.01	0.02	0.02	90.76
EBS-20 Anl-1	9	63.32	0.01	17.91	0.01	0.27	0	0.03	0.08	3.57	2.34	0.03	0.09	0	87.66
EBS-20 Anl-1	10	64.71	0.01	17.82	0	0.23	0	0.02	0.05	3.52	2.29	0.03	0.05	0.06	88.74
EBS-20 Anl-1	11	65.57	0.01	17.63	0	0.27	0	0	0.1	3.32	2.45	0.04	0.07	0.09	89.48
AVERAGE		**65.29**	**0.02**	**18.66**	**0**	**0.27**	**0.01**	**0.01**	**0.08**	**3.57**	**2.18**	**0.03**	**0.05**	**0.03**	**90.17**
Std. Dev.		**1.2**	**0.04**	**0.61**	**0**	**0.04**	**0.01**	**0.01**	**0.02**	**0.12**	**0.32**	**0.01**	**0.03**	**0.03**	**1.37**
6 oxygen atoms per formula unit (sum excludes F & Cl)															
		Si	Ti	Al	Cr	Fe	Ni	Mn	Mg	Ca	Na	K	Cl	F	SUM
EBS-20 Anl-1	1	2.3	0	0.777	0	0.008	0	0	0.005	0.135	0.17	0.002	0.002	0.004	3.397
EBS-20 Anl-1	2	2.282	0	0.811	0	0.007	0	0.001	0.004	0.141	0.131	0.001	0.007	0.003	3.379
EBS-20 Anl-1	3	2.32	0.004	0.769	0	0.006	0.001	0	0.003	0.137	0.1	0.001	0.001	0.002	3.342
EBS-20 Anl-1	4	2.308	0	0.776	0	0.009	0	0.001	0.006	0.13	0.15	0.001	0.003	0.008	3.38
EBS-20 Anl-1	5	2.279	0	0.808	0	0.009	0	0	0.004	0.145	0.144	0.001	0.001	0.004	3.39
EBS-20 Anl-1	6	2.332	0	0.755	0	0.007	0.001	0	0.003	0.13	0.122	0.001	0.001	0	3.351
EBS-20 Anl-1	7	2.296	0	0.788	0	0.007	0	0	0.004	0.135	0.161	0	0.002	0.002	3.391

EBS-20 Anl-1	8	2.282	0	0.799	0	0.011	0	0.001	0.007	0.133	0.17	0	0.001	0.002	3.403
EBS-20 Anl-1	9	2.305	0	0.768	0	0.008	0	0.001	0.004	0.139	0.165	0.002	0.005	0	3.393
EBS-20 Anl-1	10	2.322	0	0.753	0	0.007	0	0.001	0.003	0.135	0.159	0.001	0.003	0.007	3.382
EBS-20 Anl-1	11	2.333	0	0.739	0	0.008	0	0	0.005	0.127	0.169	0.002	0.004	0.01	3.383
AVERAGE		**2.305**	**0**	**0.777**	**0**	**0.008**	**0**	**0**	**0.004**	**0.135**	**0.149**	**0.001**	**0.003**	**0.004**	**3.381**
Std. Dev.		**0.019**	**0.001**	**0.022**	**0**	**0.001**	**0**	**0**	**0.001**	**0.005**	**0.022**	**0**	**0.002**	**0.003**	**0.018**

EBS-21		**WEIGHT PERCENT**													
SAMPLE	**Pt#**	**SiO_2**	**TiO_2**	**Al_2O_3**	**Cr_2O_3**	**FeO**	**NiO**	**MnO**	**MgO**	**CaO**	**Na_2O**	**K_2O**	**Cl**	**F**	**TOTAL**
GLASS															
EBS-21 Gl-1	1	64.12	0.01	8.66	0.02	0.11	0	0	0.05	0.9	5.25	0.1	0	0.02	79.21
EBS-21 Gl-2	1	58.46	0.01	12.06	0.01	0.11	0	0	0.08	0.86	4.89	0.05	0.01	0	76.55
EBS-21 Gl-2	2	62.63	0	11.65	0.01	0.11	0.02	0	0.06	1.04	3.58	0.05	0	0.06	79.14
EBS-21 Gl-3	1	62.76	0.01	12.3	0	0.42	0	0.02	0.14	0.64	4.2	0.11	0.02	0.01	80.6
EBS-21 Gl-3	2	65.01	0.01	11.51	0	0.22	0.01	0	0.07	0.64	4.89	0.13	0	0	82.49
AVERAGE		**62.6**	**0.01**	**11.24**	**0.01**	**0.19**	**0.01**	**0**	**0.08**	**0.81**	**4.56**	**0.09**	**0.01**	**0.02**	**79.6**
Std. Dev.		**2.25**	**0**	**1.32**	**0.01**	**0.12**	**0.01**	**0.01**	**0.03**	**0.16**	**0.6**	**0.03**	**0.01**	**0.02**	**1.95**
8 oxygen atoms per formula unit (sum excludes F & Cl)															
		Si	**Ti**	**Al**	**Cr**	**Fe**	**Ni**	**Mn**	**Mg**	**Ca**	**Na**	**K**	**Cl**	**F**	**SUM**
EBS-21 Gl-1	1	3.423	0	0.545	0.001	0.005	0	0	0.004	0.051	0.543	0.007	0	0.004	4.579
EBS-21 Gl-2	1	3.244	0	0.789	0	0.005	0	0	0.007	0.051	0.526	0.003	0.001	0.001	4.626
EBS-21 Gl-2	2	3.325	0	0.729	0	0.005	0.001	0	0.005	0.059	0.368	0.003	0	0.011	4.496
EBS-21 Gl-3	1	3.289	0	0.759	0	0.018	0	0.001	0.011	0.036	0.426	0.007	0.002	0.002	4.548
EBS-21 Gl-3	2	3.33	0	0.695	0	0.009	0	0	0.006	0.035	0.485	0.009	0	0	4.569

AVERAGE		**3.322**	**0**	**0.703**	**0**	**0.008**	**0**	**0**	**0.006**	**0.046**	**0.47**	**0.006**	**0.001**	**0.003**	**4.564**
Std. Dev.		**0.06**	**0**	**0.09**	**0**	**0.01**	**0**	**0**	**0**	**0.01**	**0.06**	**0**	**0**	**0**	**0.04**
SAMPLE	**Pt#**	**SiO_2**	**TiO_2**	**Al_2O_3**	**Cr_2O_3**	**FeO**	**NiO**	**MnO**	**MgO**	**CaO**	**Na_2O**	**K_2O**	**Cl**	**F**	**TOTAL**
GLASS															
EBS-21 shard-1	1	65.38	0	13.19	0.06	0.65	0.03	0.01	0.09	0.66	1.47	3.9	0.01	0	85.45
EBS-21 shard-1	2	70.5	0.01	14.12	0.07	0.36	0	0	0.06	0.65	2.09	4.95	0.02	0	92.85
EBS-21 shard-3	1	66	0	11.55	0.38	0.32	0.03	0.01	0.08	1.32	0.91	0.29	0.2	0	81.08
EBS-21 shard-3	2	74.37	0.01	13.29	0.04	0.13	0.03	0	0.1	1.19	1.61	0.23	0.24	0.01	91.25
AVERAGE		**69.06**	**0.01**	**13.04**	**0.14**	**0.36**	**0.02**	**0.01**	**0.08**	**0.95**	**1.52**	**2.34**	**0.12**	**0**	**87.66**
Std. Dev.		**3.65**	**0.01**	**0.93**	**0.14**	**0.19**	**0.01**	**0**	**0.01**	**0.3**	**0.42**	**2.12**	**0.1**	**0.01**	**4.69**
8 oxygen atoms per formula unit (sum excludes F & Cl)															
		Si	**Ti**	**Al**	**Cr**	**Fe**	**Ni**	**Mn**	**Mg**	**Ca**	**Na**	**K**	**Cl**	**F**	**SUM**
EBS-21 shard-1	1	3.28	0	0.78	0.002	0.027	0.001	0	0.006	0.036	0.143	0.25	0.001	0	4.526
EBS-21 shard-1	2	3.273	0.001	0.773	0.002	0.014	0	0	0.004	0.032	0.189	0.293	0.001	0	4.58
EBS-21 shard-3	1	3.39	0	0.699	0.015	0.014	0.001	0	0.006	0.072	0.09	0.019	0.017	0.001	4.308
EBS-21 shard-3	2	3.389	0	0.714	0.001	0.005	0.001	0	0.007	0.058	0.142	0.013	0.019	0.002	4.331
AVERAGE		**3.33**	**0**	**0.74**	**0.01**	**0.01**	**0**	**0**	**0.01**	**0.05**	**0.14**	**0.14**	**0.01**	**0**	**4.44**
Std. Dev.		**0.06**	**0**	**0.04**	**0.01**	**0.01**	**0**	**0**	**0**	**0.02**	**0.03**	**0.13**	**0.01**	**0**	**0.12**

EBS-22		WEIGHT PERCENT													
SAMPLE	Pt#	SiO_2	TiO_2	Al_2O_3	Cr_2O_3	FeO	NiO	MnO	MgO	CaO	Na_2O	K_2O	Cl	F	TOTAL
ANALCIME (??)															
EBS-22 Anl-1	1	45.25	2.26	26.13	0.02	9.24	0.01	0.05	2.52	1.92	0.52	3.19	0.09	0.13	91.18
6 oxygen atoms per formula unit (sum excludes F & Cl)															
		Si	Ti	Al	Cr	Fe	Ni	Mn	Mg	Ca	Na	K	Cl	F	SUM
EBS-22 Anl-1	1	1.738	0.065	1.183	0	0.297	0	0.001	0.144	0.079	0.039	0.156	0.006	0.016	3.703
SAMPLE	Pt#	SiO_2	TiO_2	Al_2O_3	Cr_2O_3	FeO	NiO	MnO	MgO	CaO	Na_2O	K_2O	Cl	F	TOTAL
CHLORITE															
EBS-22-Steel-1-Chl	1	26.32	0.05	0.81	0.79	45.02	0.63	0.5	0.36	1.87	2.06	0.29	0.67	0	79.49
EBS-22-Steel-1-Chl	1	26.32	0.05	0.81	0.79	45.02	0.63	0.5	0.36	1.87	2.06	0.29	0.67	0	79.49
EBS-22-Steel-1-Chl	2	29.24	0.03	0.93	0.78	42.82	0.64	0.48	0.55	2.78	2.16	0.4	0.51	0.01	81.48
EBS-22-Steel-1-Chl	3	30.14	0.02	1.27	0.71	41.87	0.65	0.29	0.58	1.43	3.09	0.91	0.1	0	81.27
EBS-22-Steel-2-Chl	1	19.66	0.01	1.05	0.44	54.51	0.32	0.48	0.48	1.36	1.39	0.29	1.62	0	81.63
EBS-22-Steel-2-Chl	2	22.59	0	0.5	0.53	52.53	0.43	0.42	0.14	0.18	1.05	0.34	1.38	0	80.12
EBS-22-Steel-2-Chl	3	25.31	0.04	0.35	0.59	53.58	0.35	0.53	0.33	0.18	1.36	0.23	1.52	0	84.4
EBS-22-Steel-3-Chl	1	31.12	0.01	0.13	0.71	45.9	0.66	0.28	0.29	0.54	3.82	0.23	0.61	0	84.42
EBS-22-Steel-4-Chl	1	31.3	0	0.71	0.85	36.8	0.7	0.21	1.18	1.76	3.06	0.79	0.16	0	77.77
EBS-22-Steel-4-Chl	2	25.8	0.02	0.17	0.68	44.23	0.52	0.21	0.34	1.87	2.86	0.57	0.11	0	77.56
EBS-22-Steel-5-Chl	2	24.84	0.03	0.17	0.75	50.75	0.63	0.29	0.23	0.42	1.57	0.24	0.33	0	80.24
EBS-22-Steel-6-Chl	1	20.9	0.01	0.13	0.61	55.07	0.47	0.31	0.08	0.1	1.2	0.14	1.87	0	80.92
EBS-22-Steel-6-Chl	3	22.72	0	0.15	0.73	50.45	0.59	0.28	0.12	0.3	2	0.24	0.62	0	78.24
AVERAGE		**25.87**	**0.02**	**0.55**	**0.69**	**47.58**	**0.56**	**0.37**	**0.39**	**1.13**	**2.13**	**0.38**	**0.78**	**0.00**	**80.54**
Std. Dev.		**3.64**	**0.02**	**0.38**	**0.11**	**5.42**	**0.12**	**0.11**	**0.27**	**0.85**	**0.82**	**0.22**	**0.59**	**0.00**	**2.09**

11 oxygen atoms per formula unit (sum excludes F & Cl)															
		Si	**Ti**	**Al**	**Cr**	**Fe**	**Ni**	**Mn**	**Mg**	**Ca**	**Na**	**K**	**Cl**	**F**	**SUM**
EBS-22-Steel-1-Chl	1	2.91	0.00	0.11	0.07	4.16	0.06	0.05	0.06	0.22	0.44	0.04	0.13	0.00	10.45
EBS-22-Steel-1-Chl	1	2.91	0.00	0.11	0.07	4.16	0.06	0.05	0.06	0.22	0.44	0.04	0.13	0.00	10.27
EBS-22-Steel-1-Chl	2	3.07	0.00	0.11	0.06	3.76	0.05	0.04	0.09	0.31	0.44	0.05	0.09	0.00	10.33
EBS-22-Steel-1-Chl	3	3.15	0.00	0.16	0.06	3.66	0.05	0.03	0.09	0.16	0.63	0.12	0.02	0.00	11.11
EBS-22-Steel-2-Chl	1	2.29	0.00	0.14	0.04	5.31	0.03	0.05	0.08	0.17	0.31	0.04	0.32	0.00	10.71
EBS-22-Steel-2-Chl	2	2.61	0.00	0.07	0.05	5.07	0.04	0.04	0.02	0.02	0.23	0.05	0.27	0.00	10.59
EBS-22-Steel-2-Chl	3	2.72	0.00	0.04	0.05	4.82	0.03	0.05	0.05	0.02	0.28	0.03	0.28	0.00	10.40
EBS-22-Steel-3-Chl	1	3.16	0.00	0.02	0.06	3.90	0.05	0.02	0.04	0.06	0.75	0.03	0.10	0.00	10.14
EBS-22-Steel-4-Chl	1	3.32	0.00	0.09	0.07	3.26	0.06	0.02	0.19	0.20	0.63	0.11	0.03	0.00	10.65
EBS-22-Steel-4-Chl	2	2.95	0.00	0.02	0.06	4.23	0.05	0.02	0.06	0.23	0.63	0.08	0.02	0.00	10.58
EBS-22-Steel-5-Chl	2	2.81	0.00	0.02	0.07	4.81	0.06	0.03	0.04	0.05	0.34	0.03	0.06	0.00	10.93
EBS-22-Steel-6-Chl	1	2.44	0.00	0.02	0.06	5.38	0.04	0.03	0.01	0.01	0.27	0.02	0.37	0.00	11.88
EBS-22-Steel-6-Chl	3	2.68	0.00	0.02	0.07	4.98	0.06	0.03	0.02	0.04	0.46	0.04	0.12	0.00	11.54
AVERAGE		**2.85**	**0.00**	**0.07**	**0.06**	**4.42**	**0.05**	**0.03**	**0.06**	**0.13**	**0.45**	**0.05**	**0.15**	**0.00**	**10.74**
Std. Dev.		**0.28**	**0.00**	**0.05**	**0.01**	**0.66**	**0.01**	**0.01**	**0.04**	**0.10**	**0.16**	**0.03**	**0.11**	**0.00**	**0.49**

Random points	**Pt #**	**SiO_2**	**TiO_2**	**Al_2O_3**	**Cr_2O_3**	**FeO**	**NiO**	**MnO**	**MgO**	**CaO**	**Na_2O**	**K_2O**	**Cl**	**F**	**TOTAL**
EBS-22-A1-calcite	1	0.06	0.00	0.00	0.00	1.05	0.00	0.20	1.02	50.89	0.02	0.06	0.01	0.24	53.30
EBS-22-A2-Anl?	2	0.19	0.02	0.07	0.00	3.58	0.00	0.27	1.23	51.14	0.03	0.14	0.02	0.06	56.69
EBS-22-A4 stilp?	5	12.95	0.01	0.00	0.00	40.02	0.02	0.09	0.09	0.10	0.75	0.07	0.24	0.01	54.35
EBS-22-A6 kfs?	7	65.03	0.01	19.19	0.00	0.26	0.00	0.00	0.00	0.01	0.43	15.93	0.00	0.00	100.87

	Pt #	Si	Ti	Al	Cr	Fe	Ni	Mn	Mg	Ca	Na	K	Cl	F	Sum
EBS-22-A1 calcite	1	0.02	0.00	0.00	0.00	0.27	0.00	0.05	0.48	17.14	0.01	0.02	0.00	0.24	18.00
EBS-22-A2-Anl?	2	0.02	0.00	0.01	0.00	0.30	0.00	0.02	0.18	5.43	0.01	0.02	0.00	0.02	5.99
EBS-22-A4 stilp?	5	6.00	0.00	0.00	0.00	15.49	0.01	0.03	0.06	0.05	0.67	0.04	0.19	0.02	22.36
EBS-22-A6 kfs?	7	2.98	0.00	1.04	0.00	0.01	0.00	0.00	0.00	0.00	0.04	0.93	0.00	0.00	4.99
Clay Matrix	**Pt #**	**SiO2**	**TiO2**	**Al2O3**	**Cr2O3**	**FeO**	**NiO**	**MnO**	**MgO**	**CaO**	**Na2O**	**K2O**	**Cl**	**F**	**TOTAL**
EBS-22-A6 clay	8	49.53	0.15	27.77	0.25	3.95	0.00	0.06	2.96	0.53	0.10	8.27	0.15	0.26	93.72
EBS-22-A7 clay	9	47.16	0.48	31.44	0.03	1.77	0.00	0.01	1.96	0.11	0.29	10.30	0.01	0.14	93.55
EBS-22-A3 clay	3	47.93	0.54	33.01	0.00	2.40	0.02	0.01	1.69	0.05	0.24	10.39	0.03	0.16	96.30
EBS-22-A3 clay	4	48.56	0.12	26.68	0.01	6.14	0.02	0.02	2.50	0.04	0.04	10.58	0.02	0.07	94.73
EBS-22-A5 clay	6	49.06	0.79	29.46	0.02	5.51	0.00	0.02	1.81	0.64	0.72	6.34	0.06	0.09	94.42
AVERAGE		**48.45**	**0.42**	**29.67**	**0.06**	**3.95**	**0.01**	**0.02**	**2.18**	**0.27**	**0.28**	**9.18**	**0.05**	**0.14**	**94.54**
Std. Dev.		**0.93**	**0.28**	**2.59**	**0.10**	**1.90**	**0.01**	**0.02**	**0.54**	**0.29**	**0.27**	**1.84**	**0.06**	**0.07**	**1.10**
		11 oxygen atoms per formula unit (sum excludes F & Cl)													
	Pt #	**Si**	**Ti**	**Al**	**Cr**	**Fe**	**Ni**	**Mn**	**Mg**	**Ca**	**Na**	**K**	**Cl**	**F**	**Sum**
EBS-22-A6 clay	8	3.36	0.01	2.22	0.01	0.22	0.00	0.00	0.30	0.04	0.01	0.71	0.02	0.06	6.89
EBS-22-A7 clay	9	3.20	0.02	2.52	0.00	0.10	0.00	0.00	0.20	0.01	0.04	0.89	0.00	0.03	6.98
EBS-22-A3 clay	3	3.17	0.03	2.57	0.00	0.13	0.00	0.00	0.17	0.00	0.03	0.88	0.00	0.03	6.97
EBS-22-A3 clay	4	3.33	0.01	2.16	0.00	0.35	0.00	0.00	0.26	0.00	0.01	0.93	0.00	0.02	7.05
EBS-22-A5 clay	6	3.29	0.04	2.33	0.00	0.31	0.00	0.00	0.18	0.05	0.09	0.54	0.01	0.02	6.83
AVERAGE		**3.27**	**0.02**	**2.36**	**0.00**	**0.22**	**0.00**	**0.00**	**0.22**	**0.02**	**0.04**	**0.79**	**0.01**	**0.03**	**6.94**
Std. Dev.		**0.08**	**0.01**	**0.18**	**0.01**	**0.11**	**0.00**	**0.00**	**0.06**	**0.02**	**0.03**	**0.16**	**0.01**	**0.02**	**0.09**

EBS-23	WEIGHT PERCENT														
Analcime in matrix	**Pt #**	**SiO_2**	**TiO_2**	**Al_2O_3**	**Cr_2O_3**	**FeO**	**NiO**	**MnO**	**MgO**	**CaO**	**Na_2O**	**K_2O**	**Cl**	**F**	**TOTAL**
EBS-23-A1 Anl-m	1	58.72	0.01	23.59	0.00	0.07	0.00	0.02	0.00	3.44	5.11	0.01	0.00	0.00	90.98
EBS-23-A1 Anl-m	2	58.52	0.01	23.14	0.00	0.04	0.02	0.00	0.00	3.39	6.64	0.02	0.01	0.00	91.79
EBS-23-A1 Anl-m	3	60.31	0.01	23.25	0.00	0.05	0.00	0.00	0.01	3.20	6.61	0.02	0.01	0.00	93.47
EBS-23-A1 Anl-m	4	56.92	0.01	22.26	0.00	0.10	0.01	0.02	0.06	5.87	4.96	0.02	0.02	0.00	90.25
EBS-23-A3Anl-rim-m	12	56.31	0.02	22.98	0.00	0.07	0.00	0.01	0.01	4.22	5.82	0.02	0.02	0.00	89.49
EBS-23-A3Anl-core-m	13	59.62	0.02	23.37	0.00	0.07	0.00	0.00	0.00	3.60	5.21	0.03	0.02	0.03	91.93
EBS-23-A3 Anl-m	14	60.43	0.00	22.46	0.00	0.05	0.02	0.01	0.00	3.11	6.49	0.04	0.01	0.07	92.62
EBS-23-A5 Anl-m	22	58.15	0.15	19.96	0.00	0.57	0.00	0.03	0.03	6.71	3.49	0.03	0.04	0.12	89.15
EBS-23-A6Anl-rim-m	24	61.82	0.00	23.19	0.00	0.05	0.00	0.00	0.00	3.22	4.56	0.01	0.01	0.03	92.87
EBS-23-A6Anl-core-m	25	59.40	0.02	21.54	0.00	0.18	0.00	0.00	0.03	7.16	3.47	0.05	0.07	0.04	91.92
EBS-23-A7 Anl-m	28	54.56	0.01	23.89	0.00	0.09	0.00	0.02	0.03	5.27	4.99	0.02	0.01	0.00	88.89
EBS-23-A7 Anl-m	29	58.02	0.00	23.95	0.00	0.05	0.00	0.00	0.01	3.96	5.84	0.02	0.01	0.02	91.86
AVERAGE		**58.56**	**0.02**	**22.80**	**0.00**	**0.12**	**0.00**	**0.01**	**0.02**	**4.43**	**5.27**	**0.03**	**0.02**	**0.03**	**91.27**
Std. Dev.		**1.98**	**0.04**	**1.13**	**0.00**	**0.15**	**0.01**	**0.01**	**0.02**	**1.45**	**1.08**	**0.01**	**0.02**	**0.04**	**1.51**
		6 oxygen atoms per formula unit (sum excludes F & Cl)													
	Pt #	**Si**	**Ti**	**Al**	**Cr**	**Fe**	**Ni**	**Mn**	**Mg**	**Ca**	**Na**	**K**	**Cl**	**F**	**Sum**
EBS-23-A1 Anl-m	1	2.10	0.00	0.99	0.00	0.00	0.00	0.00	0.00	0.13	0.35	0.00	0.00	0.00	3.58
EBS-23-A1 Anl-m	2	2.09	0.00	0.97	0.00	0.00	0.00	0.00	0.00	0.13	0.46	0.00	0.00	0.00	3.65
EBS-23-A1 Anl-m	3	2.11	0.00	0.96	0.00	0.00	0.00	0.00	0.00	0.12	0.45	0.00	0.00	0.00	3.64
EBS-23-A1 Anl-m	4	2.08	0.00	0.96	0.00	0.00	0.00	0.00	0.00	0.23	0.35	0.00	0.00	0.00	3.62
EBS-23-A3Anl-rim-m	12	2.07	0.00	0.99	0.00	0.00	0.00	0.00	0.00	0.17	0.41	0.00	0.00	0.00	3.64
EBS-23-A3Anl-core-m	13	2.11	0.00	0.97	0.00	0.00	0.00	0.00	0.00	0.14	0.36	0.00	0.00	0.00	3.58

EBS-23-A3 Anl-m	14	2.13	0.00	0.93	0.00	0.00	0.00	0.00	0.00	0.12	0.44	0.00	0.00	0.01	3.63
EBS-23-A5 Anl-m	22	2.14	0.00	0.87	0.00	0.02	0.00	0.00	0.00	0.26	0.25	0.00	0.00	0.01	3.55
EBS-23-A6Anl-rim-m	24	2.15	0.00	0.95	0.00	0.00	0.00	0.00	0.00	0.12	0.31	0.00	0.00	0.00	3.53
EBS-23-A6Anl-core-m	25	2.12	0.00	0.91	0.00	0.01	0.00	0.00	0.00	0.27	0.24	0.00	0.00	0.00	3.55
EBS-23-A7 Anl-m	28	2.69	0.00	1.39	0.00	0.00	0.00	0.00	0.00	0.28	0.48	0.00	0.00	0.00	4.85
EBS-23-A7 Anl-m	29	2.76	0.00	1.34	0.00	0.00	0.00	0.00	0.00	0.20	0.54	0.00	0.00	0.00	4.84
AVERAGE		**2.21**	**0.00**	**1.02**	**0.00**	**0.00**	**0.00**	**0.00**	**0.00**	**0.18**	**0.39**	**0.00**	**0.00**	**0.00**	**3.81**
Std. Dev.		**0.24**	**0.00**	**0.17**	**0.00**	**0.00**	**0.00**	**0.00**	**0.00**	**0.07**	**0.09**	**0.00**	**0.00**	**0.00**	**0.49**
Analcime coating Opalinus Clay	**Pt #**	**SiO_2**	**TiO_2**	**Al_2O_3**	**Cr_2O_3**	**FeO**	**NiO**	**MnO**	**MgO**	**CaO**	**Na_2O**	**K_2O**	**Cl**	**F**	**TOTAL**
EBS-23-A2 Anl-c	7	60.42	0.01	23.11	0.00	0.11	0.00	0.01	0.00	2.91	6.73	0.04	0.01	0.00	93.36
EBS-23-A2 Anl-c	8	60.34	0.01	22.16	0.02	0.11	0.00	0.01	0.01	2.95	7.03	0.04	0.01	0.04	92.68
EBS-23-A2 Anl-c	9	59.04	0.00	21.79	0.01	0.08	0.00	0.02	0.00	2.94	6.89	0.04	0.04	0.00	90.85
EBS-23-A3 Anl-c/m	10	58.10	0.01	22.29	0.00	0.05	0.00	0.02	0.00	3.13	6.09	0.03	0.01	0.01	89.73
EBS-23-A4 Anl-c	19	60.51	0.01	23.92	0.00	0.09	0.01	0.01	0.00	3.16	5.11	0.03	0.01	0.05	92.84
EBS-23-A5 Anl-c	20	61.99	0.02	23.09	0.00	0.10	0.00	0.01	0.00	2.63	4.97	0.04	0.01	0.03	92.85
EBS-23-A5 Anl-c	21	61.81	0.02	22.11	0.00	0.13	0.00	0.02	0.00	2.89	4.93	0.04	0.01	0.02	91.96
AVERAGE		**60.31**	**0.01**	**22.64**	**0.00**	**0.10**	**0.00**	**0.01**	**0.00**	**2.94**	**5.96**	**0.04**	**0.01**	**0.02**	**92.04**
Std. Dev.		**1.39**	**0.01**	**0.75**	**0.01**	**0.03**	**0.00**	**0.01**	**0.00**	**0.17**	**0.95**	**0.01**	**0.01**	**0.02**	**1.30**
		6 oxygen atoms per formula unit (sum excludes F & Cl)													
	Pt #	**Si**	**Ti**	**Al**	**Cr**	**Fe**	**Ni**	**Mn**	**Mg**	**Ca**	**Na**	**K**	**Cl**	**F**	**Sum**
EBS-23-A2 Anl-c	7	2.11	0.00	0.95	0.00	0.00	0.00	0.00	0.00	0.11	0.46	0.00	0.00	0.00	3.64
EBS-23-A2 Anl-c	8	2.13	0.00	0.92	0.00	0.00	0.00	0.00	0.00	0.11	0.48	0.00	0.00	0.00	3.65
EBS-23-A2 Anl-c	9	2.13	0.00	0.93	0.00	0.00	0.00	0.00	0.00	0.11	0.48	0.00	0.00	0.00	3.65
EBS-23-A3 Anl-c	10	2.11	0.00	0.96	0.00	0.00	0.00	0.00	0.00	0.12	0.43	0.00	0.00	0.00	3.62

EBS-23-A4 Anl-c	19	2.11	0.00	0.98	0.00	0.00	0.00	0.00	0.00	0.12	0.35	0.00	0.00	0.01	3.57
EBS-23-A5 Anl-c	20	2.16	0.00	0.95	0.00	0.00	0.00	0.00	0.00	0.10	0.33	0.00	0.00	0.00	3.54
EBS-23-A5 Anl-c	21	2.17	0.00	0.92	0.00	0.00	0.00	0.00	0.00	0.11	0.34	0.00	0.00	0.00	3.54
AVERAGE		**2.13**	**0.00**	**0.94**	**0.00**	**0.00**	**0.00**	**0.00**	**0.00**	**0.11**	**0.41**	**0.00**	**0.00**	**0.00**	**3.60**
Std. Dev.		**0.02**	**0.00**	**0.02**	**0.00**	**0.00**	**0.00**	**0.00**	**0.00**	**0.01**	**0.07**	**0.00**	**0.00**	**0.00**	**0.05**
Unknown hydrous phase (chabazite)	**Pt #**	**SiO_2**	**TiO_2**	**Al_2O_3**	**Cr_2O_3**	**FeO**	**NiO**	**MnO**	**MgO**	**CaO**	**Na_2O**	**K_2O**	**Cl**	**F**	**TOTAL**
EBS-23-A3-chaz	11	45.89	0.00	21.24	0.00	0.05	0.00	0.00	0.00	6.43	8.01	0.18	0.02	0.01	81.82
EBS-23-A3-chaz	15	45.47	0.00	20.70	0.00	0.03	0.00	0.00	0.00	7.63	6.42	0.13	0.02	0.02	80.41
AVERAGE		**45.68**	**0.00**	**20.97**	**0.00**	**0.04**	**0.00**	**0.00**	**0.00**	**7.03**	**7.22**	**0.16**	**0.02**	**0.01**	**81.12**
Std. Dev.		**0.30**	**0.00**	**0.38**	**0.00**	**0.01**	**0.00**	**0.00**	**0.00**	**0.85**	**1.12**	**0.04**	**0.00**	**0.01**	**1.00**
		12 oxygen atoms per formula unit (sum excludes F & Cl)													
	Pt #	**Si**	**Ti**	**Al**	**Cr**	**Fe**	**Ni**	**Mn**	**Mg**	**Ca**	**Na**	**K**	**Cl**	**F**	**Sum**
EBS-23-A3-chaz	11	3.82	0.00	2.08	0.00	0.00	0.00	0.00	0.00	0.57	1.29	0.02	0.00	0.00	7.79
EBS-23-A3-chaz	15	3.84	0.00	2.06	0.00	0.00	0.00	0.00	0.00	0.69	1.05	0.01	0.00	0.01	7.66
AVERAGE		**3.83**	**0.00**	**2.07**	**0.00**	**0.00**	**0.00**	**0.00**	**0.00**	**0.63**	**1.17**	**0.02**	**0.00**	**0.00**	**7.72**
Std. Dev.		**0.01**	**0.00**	**0.02**	**0.00**	**0.00**	**0.00**	**0.00**	**0.00**	**0.08**	**0.17**	**0.00**	**0.00**	**0.00**	**0.10**
K-Feldspar	**Pt #**	**SiO_2**	**TiO_2**	**Al_2O_3**	**Cr_2O_3**	**FeO**	**NiO**	**MnO**	**MgO**	**CaO**	**Na_2O**	**K_2O**	**Cl**	**F**	**TOTAL**
EBS-23-A3-kfs	17	65.07	0.00	18.53	0.01	0.08	0.00	0.01	0.00	0.14	3.23	11.87	0.01	0.03	98.93
EBS-23-A7-kfs	27	63.31	0.01	17.88	0.00	0.09	0.00	0.01	0.01	0.23	3.18	11.38	0.00	0.04	96.09
AVERAGE		**64.19**	**0.01**	**18.20**	**0.00**	**0.09**	**0.00**	**0.01**	**0.01**	**0.18**	**3.20**	**11.62**	**0.01**	**0.04**	**97.51**
Std. Dev.		**1.24**	**0.00**	**0.46**	**0.00**	**0.00**	**0.00**	**0.00**	**0.00**	**0.07**	**0.03**	**0.35**	**0.00**	**0.01**	**2.01**
		8 oxygen atoms per formula unit (sum excludes F & Cl)													
	Pt #	**Si**	**Ti**	**Al**	**Cr**	**Fe**	**Ni**	**Mn**	**Mg**	**Ca**	**Na**	**K**	**Cl**	**F**	**Sum**

EBS-23-A3-kfs	17	2.99	0.00	1.00	0.00	0.00	0.00	0.00	0.00	0.01	0.29	0.70	0.00	0.00	5.00
EBS-23-A7-kfs	27	3.00	0.00	1.00	0.00	0.00	0.00	0.00	0.00	0.01	0.29	0.69	0.00	0.01	4.99
AVERAGE		**3.00**	**0.00**	**1.00**	**0.00**	**0.00**	**0.00**	**0.00**	**0.00**	**0.01**	**0.29**	**0.69**	**0.00**	**0.01**	**4.99**
Std. Dev.		**0.00**	**0.00**	**0.00**	**0.00**	**0.00**	**0.00**	**0.00**	**0.00**	**0.00**	**0.00**	**0.01**	**0.00**	**0.00**	**0.00**
Shard	**Pt #**	**SiO_2**	**TiO_2**	**Al_2O_3**	**Cr_2O_3**	**FeO**	**NiO**	**MnO**	**MgO**	**CaO**	**Na_2O**	**K_2O**	**Cl**	**F**	**TOTAL**
EBS-23-A4-shard	18	57.27	0.00	11.90	0.01	0.20	0.01	0.00	0.02	4.99	0.84	0.43	0.05	0.00	75.73
		18 oxygen atoms per formula unit (sum excludes F & Cl)													
	Pt #	**Si**	**Ti**	**Al**	**Cr**	**Fe**	**Ni**	**Mn**	**Mg**	**Ca**	**Na**	**K**	**Cl**	**F**	**Sum**
EBS-23-A4-shard	18	7.24	0.00	1.77	0.00	0.02	0.00	0.00	0.00	0.68	0.21	0.07	0.01	0.00	10.00
Plagioclase	**Pt #**	**SiO_2**	**TiO_2**	**Al_2O_3**	**Cr_2O_3**	**FeO**	**NiO**	**MnO**	**MgO**	**CaO**	**Na_2O**	**K_2O**	**Cl**	**F**	**TOTAL**
EBS-23-A5-plag	23	65.46	0.01	22.62	0.01	0.22	0.00	0.00	0.00	3.87	8.03	1.02	0.01	0.06	101.24
EBS-23-A6-plag	26	60.08	0.00	25.65	0.00	0.16	0.00	0.01	0.01	7.24	6.85	0.63	0.01	0.00	100.64
AVERAGE		**62.77**	**0.00**	**24.13**	**0.00**	**0.19**	**0.00**	**0.01**	**0.00**	**5.55**	**7.44**	**0.82**	**0.01**	**0.03**	**100.94**
Std. Dev.		**3.80**	**0.00**	**2.14**	**0.01**	**0.04**	**0.00**	**0.01**	**0.01**	**2.39**	**0.83**	**0.28**	**0.00**	**0.04**	**0.43**
		8 oxygen atoms per formula unit (sum excludes F & Cl)													
	Pt #	**Si**	**Ti**	**Al**	**Cr**	**Fe**	**Ni**	**Mn**	**Mg**	**Ca**	**Na**	**K**	**Cl**	**F**	**Sum**
EBS-23-A5-plag	23	2.85	0.00	1.16	0.00	0.01	0.00	0.00	0.00	0.18	0.68	0.06	0.00	0.01	4.94
EBS-23-A6-plag	26	2.66	0.00	1.34	0.00	0.01	0.00	0.00	0.00	0.34	0.59	0.04	0.00	0.00	4.98
AVERAGE		**2.76**	**0.00**	**1.25**	**0.00**	**0.01**	**0.00**	**0.00**	**0.00**	**0.26**	**0.63**	**0.05**	**0.00**	**0.00**	**4.96**
Std. Dev.		**0.13**	**0.00**	**0.13**	**0.00**	**0.00**	**0.00**	**0.00**	**0.00**	**0.12**	**0.06**	**0.02**	**0.00**	**0.01**	**0.03**

BM-C-49-1	**WEIGHT PERCENT**

SAMPLE	Pt #	SiO_2	TiO_2	Al_2O_3	Cr_2O_3	FeO	NiO	MnO	MgO	CaO	Na_2O	K_2O	Cl	F	TOTAL
Plagioclase															
BM-C-49-1Area1plag	1	57.86	0.01	27.81	0.00	0.21	0.00	0.01	0.01	8.94	5.97	0.45	0.00	0.01	101.26
BM-C-49-1Area3plag	6	57.72	0.01	26.27	0.01	0.18	0.00	0.00	0.00	8.25	6.48	0.33	0.00	0.00	99.27
BM-C-49-1Area2	17	58.30	0.01	27.04	0.00	0.18	0.00	0.02	0.00	8.44	6.08	0.57	0.00	0.06	100.64
AVERAGE		**57.96**	**0.01**	**27.04**	**0.00**	**0.19**	**0.00**	**0.01**	**0.00**	**8.54**	**6.17**	**0.45**	**0.00**	**0.02**	**100.39**
Std.Dev.		**0.30**	**0.00**	**0.77**	**0.01**	**0.01**	**0.00**	**0.01**	**0.00**	**0.36**	**0.27**	**0.12**	**0.00**	**0.03**	**1.02**
		8 oxygen atoms per formula unit (sum excludes F & Cl)													
	Pt #	**Si**	**Ti**	**Al**	**Cr**	**Fe**	**Ni**	**Mn**	**Mg**	**Ca**	**Na**	**K**	**Cl**	**F**	**Sum**
BM-C-49-1Area1plag	1	2.56	0.00	1.45	0.00	0.01	0.00	0.00	0.00	0.42	0.51	0.03	0.00	0.00	4.98
BM-C-49-1Area3plag	6	2.60	0.00	1.40	0.00	0.01	0.00	0.00	0.00	0.40	0.57	0.02	0.00	0.00	4.99
BM-C-49-1Area2	17	2.59	0.00	1.42	0.00	0.01	0.00	0.00	0.00	0.40	0.52	0.03	0.00	0.01	4.98
AVERAGE		**2.59**	**0.00**	**1.42**	**0.00**	**0.01**	**0.00**	**0.00**	**0.00**	**0.41**	**0.53**	**0.03**	**0.00**	**0.00**	**4.98**
Std.Dev.		**0.02**	**0.00**	**0.03**	**0.00**	**0.00**	**0.00**	**0.00**	**0.00**	**0.01**	**0.03**	**0.01**	**0.00**	**0.00**	**0.01**
	Pt #	**SiO_2**	**TiO_2**	**Al_2O_3**	**Cr_2O_3**	**FeO**	**NiO**	**MnO**	**MgO**	**CaO**	**Na_2O**	**K_2O**	**Cl**	**F**	**TOTAL**
Smectite															
BM-C-49-1Area1smectite	2	55.47	0.22	20.90	0.00	6.97	0.00	0.03	4.95	1.45	0.51	2.38	0.45	0.10	93.33
BM-C-49-1Area1smectite	3	55.77	0.11	19.76	0.00	1.99	0.01	0.00	5.74	1.64	0.47	0.32	0.57	0.26	86.39
BM-C-49-1Area3smectite	10	49.50	0.28	18.96	0.01	4.10	0.03	0.02	4.70	1.72	0.40	0.64	0.60	0.22	80.94
BM-C-49-1Area2smectite	16	48.82	0.13	20.04	0.00	2.44	0.00	0.05	5.06	1.61	0.38	0.32	0.62	0.18	79.47
BM-C-49-1Area3smectite	12	48.91	0.10	20.24	0.00	3.04	0.00	0.01	4.35	1.68	0.38	0.46	0.90	0.17	80.08
BM-C-49-1Area3smectite	13	54.41	0.28	19.51	0.01	8.33	0.00	0.01	4.96	1.63	0.40	1.38	0.90	0.21	91.81
AVERAGE		**52.14**	**0.19**	**19.90**	**0.00**	**4.48**	**0.01**	**0.02**	**4.96**	**1.62**	**0.42**	**0.92**	**0.67**	**0.19**	**85.33**
Std.Dev.		**3.40**	**0.08**	**0.66**	**0.00**	**2.59**	**0.01**	**0.02**	**0.46**	**0.09**	**0.06**	**0.82**	**0.19**	**0.06**	**6.13**
		12 oxygen atoms per formula unit (sum excludes F & Cl)													

	Pt #	Si	Ti	Al	Cr	Fe	Ni	Mn	Mg	Ca	Na	K	Cl	F	Sum
BM-C-49-1Area1smectite	2	4.03	0.01	1.79	0.00	0.42	0.00	0.00	0.54	0.11	0.07	0.22	0.06	0.02	7.21
BM-C-49-1Area1smectite	3	4.20	0.01	1.75	0.00	0.13	0.00	0.00	0.65	0.13	0.07	0.03	0.07	0.06	6.97
BM-C-49-1Area3smectite	10	4.07	0.02	1.84	0.00	0.28	0.00	0.00	0.58	0.15	0.06	0.07	0.08	0.06	7.06
BM-C-49-1Area2smectite	16	4.04	0.01	1.95	0.00	0.17	0.00	0.00	0.62	0.14	0.06	0.03	0.09	0.05	7.03
BM-C-49-1Area3smectite	12	4.04	0.01	1.97	0.00	0.21	0.00	0.00	0.54	0.15	0.06	0.05	0.13	0.04	7.02
BM-C-49-1Area3smectite	13	4.05	0.02	1.71	0.00	0.52	0.00	0.00	0.55	0.13	0.06	0.13	0.11	0.05	7.17
AVERAGE		**4.07**	**0.01**	**1.84**	**0.00**	**0.29**	**0.00**	**0.00**	**0.58**	**0.14**	**0.06**	**0.09**	**0.09**	**0.05**	**7.08**
Std.Dev.		**0.06**	**0.00**	**0.11**	**0.00**	**0.15**	**0.00**	**0.00**	**0.05**	**0.01**	**0.01**	**0.07**	**0.03**	**0.01**	**0.09**
Sericite/K-Feldspar?	**Pt #**	**SiO_2**	**TiO_2**	**Al_2O_3**	**Cr_2O_3**	**FeO**	**NiO**	**MnO**	**MgO**	**CaO**	**Na_2O**	**K_2O**	**Cl**	**F**	**TOTAL**
BM-C-49-1Area1sericite?	4	65.47	0.01	19.15	0.00	0.08	0.01	0.00	0.01	0.00	0.06	16.58	0.00	0.00	101.36
BM-C-49-1Area1sericite?	5	63.02	0.00	18.91	0.00	0.09	0.02	0.02	0.01	0.33	0.18	16.00	0.00	0.00	98.58
BM-C-49-1Area3sericite?	11	65.82	0.00	18.96	0.00	0.14	0.01	0.02	0.00	0.01	0.05	16.16	0.00	0.00	101.18
BM-C-49-1Area2sericite	18	65.50	0.00	18.43	0.00	0.04	0.01	0.00	0.00	0.00	0.07	15.89	0.00	0.00	99.95
BM-C-49-1Area2sericite	19	65.06	0.00	18.67	0.00	0.02	0.00	0.00	0.00	0.00	0.08	16.18	0.00	0.00	100.03
AVERAGE		**64.97**	**0.00**	**18.82**	**0.00**	**0.07**	**0.01**	**0.01**	**0.00**	**0.07**	**0.09**	**16.16**	**0.00**	**0.00**	**100.22**
Std.Dev.		**1.13**	**0.00**	**0.28**	**0.00**	**0.05**	**0.01**	**0.01**	**0.00**	**0.15**	**0.05**	**0.26**	**0.00**	**0.00**	**1.12**
		8 oxygen atoms per formula unit (sum excludes F & Cl)													
	Pt #	**Si**	**Ti**	**Al**	**Cr**	**Fe**	**Ni**	**Mn**	**Mg**	**Ca**	**Na**	**K**	**Cl**	**F**	**Sum**
BM-C-49-1Area1sericite?	4	2.98	0.00	1.03	0.00	0.00	0.00	0.00	0.00	0.00	0.01	0.96	0.00	0.00	4.99
BM-C-49-1Area1sericite?	5	2.96	0.00	1.05	0.00	0.00	0.00	0.00	0.00	0.02	0.02	0.96	0.00	0.00	5.00
BM-C-49-1Area3sericite?	11	3.00	0.00	1.02	0.00	0.01	0.00	0.00	0.00	0.00	0.00	0.94	0.00	0.00	4.97
BM-C-49-1Area2sericite	18	3.01	0.00	0.99	0.00	0.00	0.00	0.00	0.00	0.00	0.01	0.92	0.00	0.00	4.93
BM-C-49-1Area2sericite	19	3.01	0.00	1.00	0.00	0.00	0.00	0.00	0.00	0.00	0.01	0.94	0.00	0.00	4.96

AVERAGE		**2.99**	**0.00**	**1.02**	**0.00**	**0.00**	**0.00**	**0.00**	**0.00**	**0.00**	**0.01**	**0.94**	**0.00**	**0.00**	**4.97**
Std.Dev.		**0.02**	**0.00**	**0.02**	**0.00**	**0.00**	**0.00**	**0.00**	**0.00**	**0.01**	**0.00**	**0.02**	**0.00**	**0.00**	**0.03**
K-Feldspar	**Pt #**	**SiO_2**	**TiO_2**	**Al_2O_3**	**Cr_2O_3**	**FeO**	**NiO**	**MnO**	**MgO**	**CaO**	**Na_2O**	**K_2O**	**Cl**	**F**	**TOTAL**
BM-C-49-1Area3kfs	7	65.83	0.00	18.53	0.00	0.03	0.00	0.03	0.01	0.03	0.07	16.40	0.00	0.01	100.92
BM-C-49-1Area3kfs	8	65.76	0.00	18.55	0.00	0.03	0.03	0.01	0.00	0.00	0.05	16.35	0.00	0.00	100.79
AVERAGE		**65.80**	**0.00**	**18.54**	**0.00**	**0.03**	**0.01**	**0.02**	**0.01**	**0.02**	**0.06**	**16.38**	**0.00**	**0.00**	**100.85**
Std.Dev.		**0.05**	**0.00**	**0.02**	**0.00**	**0.01**	**0.02**	**0.01**	**0.01**	**0.01**	**0.02**	**0.04**	**0.00**	**0.01**	**0.09**
		8 oxygen atoms per formula unit (sum excludes F & Cl)													
	Pt #	**Si**	**Ti**	**Al**	**Cr**	**Fe**	**Ni**	**Mn**	**Mg**	**Ca**	**Na**	**K**	**Cl**	**F**	**Sum**
BM-C-49-1Area3kfs	7	3.01	0.00	1.00	0.00	0.00	0.00	0.00	0.00	0.00	0.01	0.96	0.00	0.00	4.97
BM-C-49-1Area3kfs	8	3.01	0.00	1.00	0.00	0.00	0.00	0.00	0.00	0.00	0.00	0.95	0.00	0.00	4.97
AVERAGE		**3.01**	**0.00**	**1.00**	**0.00**	**0.00**	**0.00**	**0.00**	**0.00**	**0.00**	**0.01**	**0.96**	**0.00**	**0.00**	**4.97**
Std.Dev.		**0.00**	**0.00**	**0.00**	**0.00**	**0.00**	**0.00**	**0.00**	**0.00**	**0.00**	**0.00**	**0.00**	**0.00**	**0.00**	**0.00**

BC-49-9	WEIGHT PERCENT													
Plagioclase	**Pt #**	**SiO_2**	**TiO_2**	**Al_2O_3**	**Cr_2O_3**	**FeO**	**NiO**	**MnO**	**MgO**	**CaO**	**Na_2O**	**K_2O**	**Cl**	**F**	**TOTAL**
BC-49-9Area1plag	1	54.00	0.01	30.45	0.00	0.21	0.00	0.01	0.02	11.14	4.68	0.19	0.00	0.03	100.71
BC-49-9Area1plag	2	57.40	0.00	27.86	0.01	0.18	0.01	0.00	0.00	8.60	5.98	0.55	0.00	0.00	100.61
BC-49-9Area2plag	7	55.58	0.01	25.17	0.00	0.19	0.00	0.00	0.00	8.63	6.09	0.35	0.00	0.00	96.02
BC-49-9Area3plag	9	61.08	0.00	23.21	0.00	0.05	0.00	0.01	0.01	5.03	7.88	0.81	0.00	0.01	98.09
BC-49-9Area3plag	10	55.52	0.00	27.07	0.00	0.19	0.00	0.00	0.00	9.27	5.80	0.46	0.00	0.00	98.31
AVERAGE		**56.72**	**0.00**	**26.75**	**0.00**	**0.16**	**0.00**	**0.00**	**0.01**	**8.54**	**6.09**	**0.47**	**0.00**	**0.01**	**98.75**
Std.Dev.		**2.72**	**0.01**	**2.74**	**0.00**	**0.06**	**0.00**	**0.00**	**0.01**	**2.21**	**1.15**	**0.23**	**0.00**	**0.01**	**1.96**
		8 oxygen atoms per formula unit (sum excludes F & Cl)													
	Pt #	**Si**	**Ti**	**Al**	**Cr**	**Fe**	**Ni**	**Mn**	**Mg**	**Ca**	**Na**	**K**	**Cl**	**F**	**Sum**
BC-49-9Area1plag	1	2.42	0.00	1.61	0.00	0.01	0.00	0.00	0.00	0.53	0.41	0.01	0.00	0.00	4.99
BC-49-9Area1plag	2	2.56	0.00	1.46	0.00	0.01	0.00	0.00	0.00	0.41	0.52	0.03	0.00	0.00	4.99
BC-49-9Area2plag	7	2.60	0.00	1.39	0.00	0.01	0.00	0.00	0.00	0.43	0.55	0.02	0.00	0.00	5.00
BC-49-9Area3plag	9	2.76	0.00	1.24	0.00	0.00	0.00	0.00	0.00	0.24	0.69	0.05	0.00	0.00	4.99
BC-49-9Area3plag	10	2.54	0.00	1.46	0.00	0.01	0.00	0.00	0.00	0.45	0.51	0.03	0.00	0.00	5.00
AVERAGE		**2.58**	**0.00**	**1.43**	**0.00**	**0.01**	**0.00**	**0.00**	**0.00**	**0.42**	**0.54**	**0.03**	**0.00**	**0.00**	**4.99**
Std.Dev.		**0.12**	**0.00**	**0.13**	**0.00**	**0.00**	**0.00**	**0.00**	**0.00**	**0.11**	**0.10**	**0.01**	**0.00**	**0.00**	**0.01**
Smectite	**Pt #**	**SiO_2**	**TiO_2**	**Al_2O3**	**Cr_2O_3**	**FeO**	**NiO**	**MnO**	**MgO**	**CaO**	**Na_2O**	**K_2O**	**Cl**	**F**	**TOTAL**
BC-49-9Area1smectite	4	58.69	0.16	24.04	0.01	3.31	0.00	0.00	4.91	1.52	0.93	0.53	0.02	0.29	94.12
BC-49-9Area4smectite	13	60.18	0.22	20.63	0.00	5.68	0.01	0.00	5.34	1.27	1.06	1.78	0.02	0.13	96.19
BC-49-9Area2smectite	8	59.46	0.13	21.22	0.00	2.83	0.00	0.02	5.74	1.45	1.02	0.33	0.02	0.30	92.21
BC-49-9Area3smectite	11	63.58	0.14	19.80	0.00	2.35	0.00	0.01	6.76	1.39	1.10	0.20	0.02	0.34	95.36

BC-49-9Area6smectite	16	60.25	0.13	19.89	0.00	3.22	0.02	0.04	5.46	1.19	0.72	0.80	0.01	0.34	91.74
AVERAGE		**60.43**	**0.16**	**21.12**	**0.00**	**3.48**	**0.01**	**0.01**	**5.64**	**1.36**	**0.97**	**0.73**	**0.02**	**0.28**	**93.93**
Std.Dev.		**1.87**	**0.04**	**1.73**	**0.00**	**1.29**	**0.01**	**0.02**	**0.69**	**0.13**	**0.15**	**0.63**	**0.01**	**0.09**	**1.93**
		12 oxygen atoms per formula unit (sum excludes F & Cl)													
	Pt #	**Si**	**Ti**	**Al**	**Cr**	**Fe**	**Ni**	**Mn**	**Mg**	**Ca**	**Na**	**K**	**Cl**	**F**	**Sum**
BC-49-9Area1smectite	4	4.07	0.01	1.96	0.00	0.19	0.00	0.00	0.51	0.11	0.13	0.05	0.00	0.06	7.03
BC-49-9Area4smectite	13	4.16	0.01	1.68	0.00	0.33	0.00	0.00	0.55	0.09	0.14	0.16	0.00	0.03	7.13
BC-49-9Area2smectite	8	4.19	0.01	1.76	0.00	0.17	0.00	0.00	0.60	0.11	0.14	0.03	0.00	0.07	7.01
BC-49-9Area3smectite	11	4.31	0.01	1.58	0.00	0.13	0.00	0.00	0.68	0.10	0.14	0.02	0.00	0.07	6.98
BC-49-9Area6smectite	16	4.27	0.01	1.66	0.00	0.19	0.00	0.00	0.58	0.09	0.10	0.07	0.00	0.08	6.98
AVERAGE		**4.20**	**0.01**	**1.73**	**0.00**	**0.20**	**0.00**	**0.00**	**0.58**	**0.10**	**0.13**	**0.06**	**0.00**	**0.06**	**7.02**
Std.Dev.		**0.09**	**0.00**	**0.15**	**0.00**	**0.07**	**0.00**	**0.00**	**0.07**	**0.01**	**0.02**	**0.06**	**0.00**	**0.02**	**0.06**
K-Feldspar	**Pt #**	**SiO_2**	**TiO_2**	**Al_2O_3**	**Cr_2O_3**	**FeO**	**NiO**	**MnO**	**MgO**	**CaO**	**Na_2O**	**K_2O**	**Cl**	**F**	**TOTAL**
BC-49-9Area4kfs	12	64.64	0.00	19.02	0.00	0.06	0.02	0.02	0.09	0.07	0.07	15.90	0.00	0.00	99.90
BC-49-9Area1kfs	3	64.65	0.00	18.91	0.00	0.01	0.00	0.00	0.00	0.00	0.04	16.47	0.00	0.03	100.08
BC-49-9Area5kfs	14	63.69	0.01	19.21	0.01	0.11	0.00	0.00	0.01	1.52	2.31	12.02	0.00	0.00	98.88
BC-49-9Area6kfs	15	64.91	0.01	19.90	0.00	0.21	0.00	0.00	0.00	2.24	3.17	9.24	0.00	0.01	99.68
AVERAGE		**64.47**	**0.00**	**19.26**	**0.00**	**0.10**	**0.00**	**0.01**	**0.03**	**0.96**	**1.40**	**13.41**	**0.00**	**0.01**	**99.63**
Std.Dev.		**0.53**	**0.01**	**0.45**	**0.00**	**0.08**	**0.01**	**0.01**	**0.05**	**1.11**	**1.59**	**3.41**	**0.00**	**0.02**	**0.53**
		8 oxygen atoms per formula unit (sum excludes F & Cl)													
	Pt #	**Si**	**Ti**	**Al**	**Cr**	**Fe**	**Ni**	**Mn**	**Mg**	**Ca**	**Na**	**K**	**Cl**	**F**	**Sum**
BC-49-9Area4kfs	12	2.98	0.00	1.03	0.00	0.00	0.00	0.00	0.01	0.00	0.01	0.94	0.00	0.00	4.97
BC-49-9Area1kfs	3	2.98	0.00	1.03	0.00	0.00	0.00	0.00	0.00	0.00	0.00	0.97	0.00	0.00	4.99
BC-49-9Area5kfs	14	2.95	0.00	1.05	0.00	0.00	0.00	0.00	0.00	0.08	0.21	0.71	0.00	0.00	4.99

BC-49-9Area6kfs	15	2.94	0.00	1.06	0.00	0.01	0.00	0.00	0.00	0.11	0.28	0.53	0.00	0.00	4.93
AVERAGE		**2.96**	**0.00**	**1.04**	**0.00**	**0.00**	**0.00**	**0.00**	**0.00**	**0.05**	**0.12**	**0.79**	**0.00**	**0.00**	**4.97**
Std.Dev.		**0.02**	**0.00**	**0.02**	**0.00**	**0.00**	**0.00**	**0.00**	**0.00**	**0.05**	**0.14**	**0.20**	**0.00**	**0.00**	**0.03**

BC-49-10	**WEIGHT PERCENT**														
Plagioclase	**Pt #**	**SiO_2**	**TiO_2**	**Al_2O_3**	**Cr_2O_3**	**FeO**	**NiO**	**MnO**	**MgO**	**CaO**	**Na_2O**	**K_2O**	**Cl**	**F**	**TOTAL**
BM-C-49-10Area1plag	1	56.00	0.00	26.24	0.00	0.21	0.01	0.00	0.01	8.08	6.22	0.56	0.00	0.00	97.34
BC-49-10Area2plag	3	54.92	0.00	26.84	0.01	0.19	0.00	0.01	0.01	8.41	5.74	0.46	0.00	0.00	96.58
BC-49-10Area3plagcore	9	54.13	0.01	29.28	0.00	0.18	0.00	0.00	0.01	10.29	5.15	0.24	0.00	0.00	99.29
BC-49-10Area4plag	11	58.11	0.00	24.52	0.00	0.16	0.00	0.00	0.01	6.97	6.69	0.68	0.00	0.00	97.15
BC-49-10Area5plag	17	58.55	0.00	25.23	0.00	0.07	0.00	0.01	0.00	6.57	7.43	0.21	0.00	0.00	98.07
AVERAGE		**56.34**	**0.00**	**26.42**	**0.00**	**0.16**	**0.00**	**0.00**	**0.01**	**8.06**	**6.25**	**0.43**	**0.00**	**0.00**	**97.68**
Std.Dev.		**1.94**	**0.00**	**1.83**	**0.00**	**0.06**	**0.01**	**0.00**	**0.00**	**1.46**	**0.87**	**0.20**	**0.00**	**0.00**	**1.04**
		8 oxygen atoms per formula unit (sum excludes F & Cl)													
	Pt #	**Si**	**Ti**	**Al**	**Cr**	**Fe**	**Ni**	**Mn**	**Mg**	**Ca**	**Na**	**K**	**Cl**	**F**	**Sum**
BM-C-49-10Area1plag	1	2.58	0.00	1.42	0.00	0.01	0.00	0.00	0.00	0.40	0.56	0.03	0.00	0.00	5.00
BC-49-10Area2plag	3	2.55	0.00	1.47	0.00	0.01	0.00	0.00	0.00	0.42	0.52	0.03	0.00	0.00	4.99
BC-49-10Area3plagcore	9	2.46	0.00	1.57	0.00	0.01	0.00	0.00	0.00	0.50	0.45	0.01	0.00	0.00	5.00
BC-49-10Area4plag	11	2.74	0.00	1.21	0.00	0.01	0.00	0.00	0.00	0.85	0.53	0.02	0.00	0.00	5.36
BC-49-10Area5plag	17	2.66	0.00	1.35	0.00	0.00	0.00	0.00	0.00	0.32	0.65	0.01	0.00	0.00	5.00
AVERAGE		**2.60**	**0.00**	**1.40**	**0.00**	**0.01**	**0.00**	**0.00**	**0.00**	**0.50**	**0.54**	**0.02**	**0.00**	**0.00**	**5.07**
Std.Dev.		**0.11**	**0.00**	**0.13**	**0.00**	**0.00**	**0.00**	**0.00**	**0.00**	**0.21**	**0.07**	**0.01**	**0.00**	**0.00**	**0.16**
Smectite	**Pt #**	**SiO_2**	**TiO_2**	**Al_2O3**	**Cr_2O_3**	**FeO**	**NiO**	**MnO**	**MgO**	**CaO**	**Na_2O**	**K_2O**	**Cl**	**F**	**TOTAL**

BC-49-10Area2smectite	4	61.88	0.10	19.64	0.01	2.87	0.00	0.02	6.24	1.14	1.09	0.30	0.03	0.25	93.32
BC-49-10Area2smectite	6	58.25	0.12	18.51	0.00	2.33	0.00	0.02	6.16	1.17	0.87	0.18	0.03	0.33	87.65
BC-49-10Area3outersmectiterim	7	54.18	0.26	21.24	0.01	5.06	0.01	0.03	4.28	1.12	0.82	3.04	0.02	0.17	90.05
BM-C-49-10Area1smectite	2	59.09	0.10	19.35	0.00	2.65	0.00	0.03	6.37	1.28	1.06	0.18	0.01	0.45	90.12
BC-49-10Area3smectite	10	53.67	0.11	20.71	0.00	2.25	0.01	0.04	5.24	1.35	0.72	0.19	0.02	0.23	84.31
BC-49-10Area5smectite	12	52.16	0.13	24.17	0.00	2.81	0.02	0.01	3.87	1.45	0.67	0.42	0.03	0.11	85.74
BC-49-10Area5smectite	13	56.30	0.11	23.36	0.00	2.40	0.00	0.02	4.23	1.59	0.65	0.30	0.03	0.22	89.00
AVERAGE		**56.51**	**0.13**	**21.00**	**0.00**	**2.91**	**0.01**	**0.02**	**5.20**	**1.30**	**0.84**	**0.66**	**0.03**	**0.25**	**88.60**
Std.Dev.		**3.44**	**0.06**	**2.10**	**0.00**	**0.98**	**0.01**	**0.01**	**1.08**	**0.18**	**0.18**	**1.05**	**0.01**	**0.11**	**3.01**
		12 oxygen atoms per formula unit (sum excludes F & Cl)													
	Pt #	**Si**	**Ti**	**Al**	**Cr**	**Fe**	**Ni**	**Mn**	**Mg**	**Ca**	**Na**	**K**	**Cl**	**F**	**Sum**
BC-49-10Area2smectite	4	4.30	0.01	1.61	0.00	0.17	0.00	0.00	0.65	0.08	0.15	0.03	0.00	0.05	6.98
BC-49-10Area2smectite	6	4.29	0.01	1.61	0.00	0.14	0.00	0.00	0.68	0.09	0.12	0.02	0.00	0.08	6.97
BC-49-10Area3outersmectiterim	7	4.04	0.01	1.87	0.00	0.32	0.00	0.00	0.48	0.09	0.12	0.29	0.00	0.04	7.21
BM-C-49-10Area1smectite	2	4.25	0.01	1.64	0.00	0.16	0.00	0.00	0.68	0.10	0.15	0.02	0.00	0.10	7.00
BC-49-10Area3smectite	10	4.13	0.01	1.88	0.00	0.14	0.00	0.00	0.60	0.11	0.11	0.02	0.00	0.06	6.99
BC-49-10Area5smectite	12	3.97	0.01	2.17	0.00	0.18	0.00	0.00	0.44	0.12	0.10	0.04	0.00	0.03	7.01
BC-49-10Area5smectite	13	4.10	0.01	2.00	0.00	0.15	0.00	0.00	0.46	0.12	0.09	0.03	0.00	0.05	6.96
AVERAGE		**4.15**	**0.01**	**1.82**	**0.00**	**0.18**	**0.00**	**0.00**	**0.57**	**0.10**	**0.12**	**0.06**	**0.00**	**0.06**	**7.02**
Std.Dev.		**0.13**	**0.00**	**0.22**	**0.00**	**0.06**	**0.00**	**0.00**	**0.11**	**0.02**	**0.02**	**0.10**	**0.00**	**0.02**	**0.09**
K-Feldspar	**Pt #**	**SiO_2**	**TiO_2**	**Al_2O_3**	**Cr_2O_3**	**FeO**	**NiO**	**MnO**	**MgO**	**CaO**	**Na_2O**	**K_2O**	**Cl**	**F**	**TOTAL**
BC-49-10Area3kfsrim	8	65.32	0.00	19.57	0.00	0.00	0.00	0.00	0.00	0.02	0.21	15.37	0.00	0.00	100.49
BC-49-10Area5kfs?	14	60.61	0.02	17.30	0.00	0.08	0.00	0.01	0.00	0.42	2.67	11.32	0.00	0.00	92.43
BC-49-10Area5kfs?	15	62.55	0.01	18.64	0.00	0.09	0.02	0.01	0.00	0.06	0.74	14.65	0.00	0.00	96.77

BC-49-10Area5kfs	18	65.90	0.00	18.24	0.00	0.03	0.01	0.00	0.00	0.00	0.05	14.50	0.00	0.01	98.72
AVERAGE		**63.59**	**0.01**	**18.44**	**0.00**	**0.05**	**0.01**	**0.00**	**0.00**	**0.12**	**0.92**	**13.96**	**0.00**	**0.00**	**97.10**
Std.Dev.		**2.47**	**0.01**	**0.94**	**0.00**	**0.04**	**0.01**	**0.00**	**0.00**	**0.20**	**1.20**	**1.80**	**0.00**	**0.01**	**3.47**
		8 oxygen atoms per formula unit (sum excludes F & Cl)													
	Pt #	**Si**	**Ti**	**Al**	**Cr**	**Fe**	**Ni**	**Mn**	**Mg**	**Ca**	**Na**	**K**	**Cl**	**F**	**Sum**
BC-49-10Area3kfsrim	8	2.99	0.00	1.03	0.00	0.00	0.00	0.00	0.00	0.00	0.02	0.88	0.00	0.00	4.92
BC-49-10Area5kfs?	14	2.99	0.00	1.01	0.00	0.00	0.00	0.00	0.00	0.02	0.26	0.71	0.00	0.00	4.99
BC-49-10Area5kfs?	15	2.97	0.00	1.04	0.00	0.00	0.00	0.00	0.00	0.00	0.07	0.89	0.00	0.00	4.98
BC-49-10Area5kfs	18	3.04	0.00	0.99	0.00	0.00	0.00	0.00	0.00	0.00	0.00	0.85	0.00	0.00	4.89
AVERAGE		**3.00**	**0.00**	**1.02**	**0.00**	**0.00**	**0.00**	**0.00**	**0.00**	**0.01**	**0.09**	**0.83**	**0.00**	**0.00**	**4.95**
Std.Dev.		**0.03**	**0.00**	**0.02**	**0.00**	**0.00**	**0.00**	**0.00**	**0.00**	**0.01**	**0.12**	**0.08**	**0.00**	**0.00**	**0.05**
Sericite?	**Pt #**	**SiO_2**	**TiO_2**	**Al_2O_3**	**Cr_2O_3**	**FeO**	**NiO**	**MnO**	**MgO**	**CaO**	**Na_2O**	**K_2O**	**Cl**	**F**	**TOTAL**
BC-49-10Area5sericite?	16	74.74	0.17	11.63	0.01	1.79	0.00	0.05	0.01	1.23	1.48	1.76	0.36	0.15	93.25
	Pt #	**Si**	**Ti**	**Al**	**Cr**	**Fe**	**Ni**	**Mn**	**Mg**	**Ca**	**Na**	**K**	**Cl**	**F**	**Sum**
BC-49-10Area5sericite?	16	3.40	0.01	0.62	0.00	0.07	0.00	0.00	0.00	0.06	0.13	0.10	0.03	0.02	4.40

Appendix E
XRF and XRD Data (FEBEX SAMPLES)

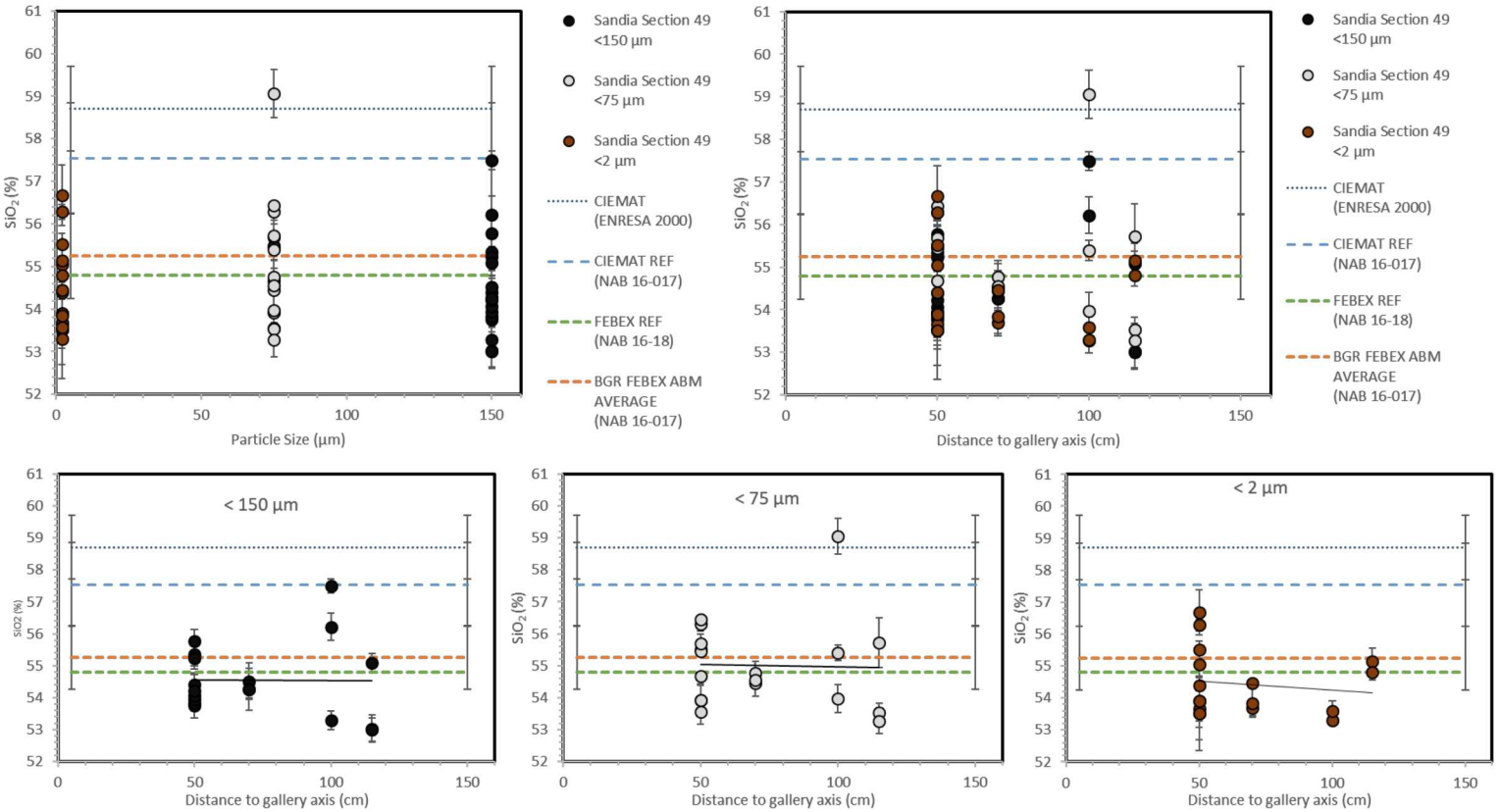


Figure E-1. Bulk bentonite XRF analyses of SiO_2 content for Section 49 samples as a function of distance from the gallery axis and particle size. Filled symbols denote analyses conducted in this study for size fractions of <150, <75, and <2 microns. Horizontal dashed-lines delineate the range of FEBEX bentonite compositions including reference values by different groups (Villar et al. 2017).

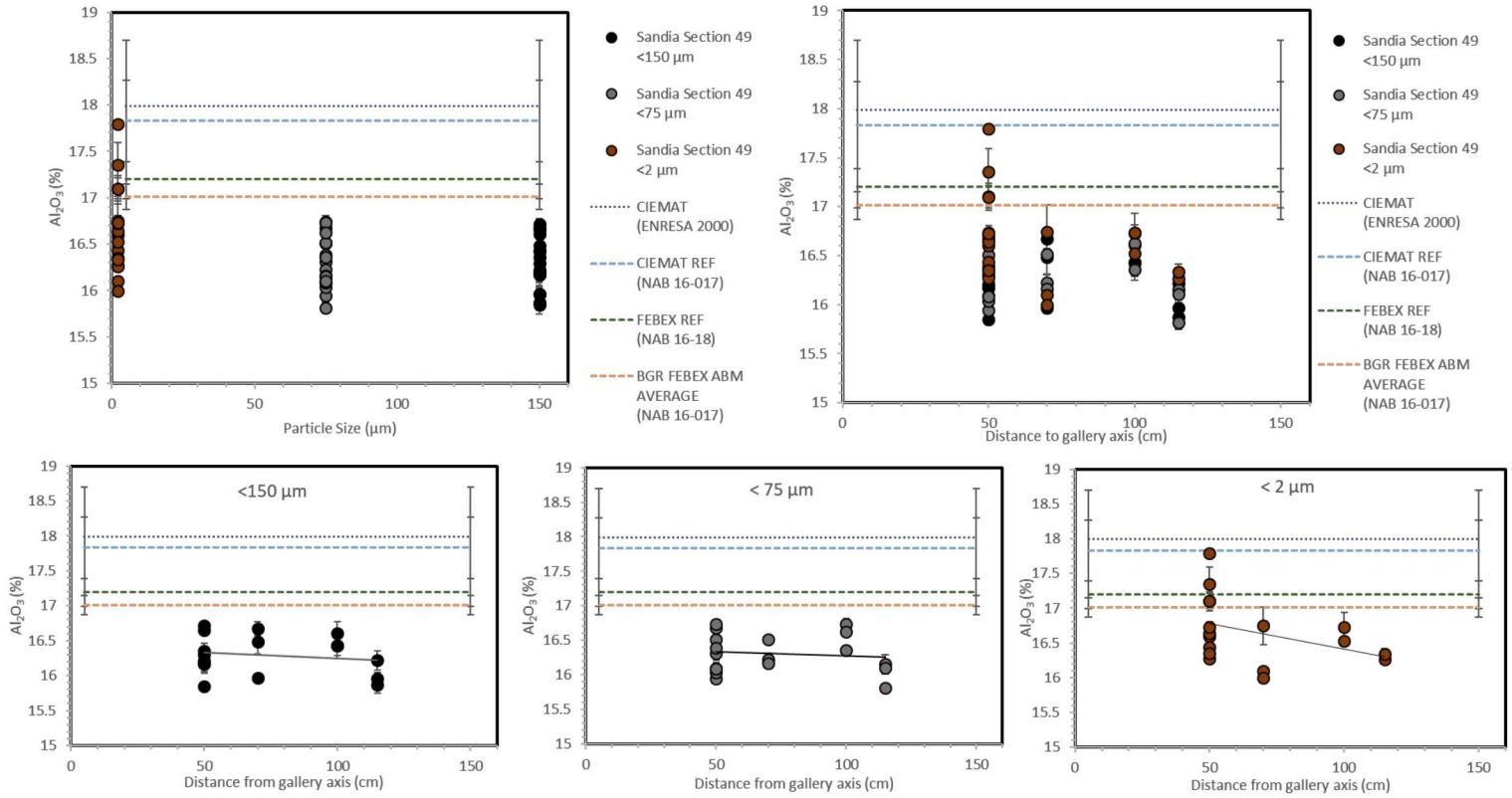


Figure E-2. Bulk bentonite XRF analyses of Al_2O_3 content for Section 49 samples as a function of distance from the gallery axis and particle size. Filled symbols denote analyses conducted in this study for size fractions of <150, <75, and <2 microns. Horizontal dashed-lines delineate the range of FEBEX bentonite compositions including reference values by different groups (Villar et al. 2017).

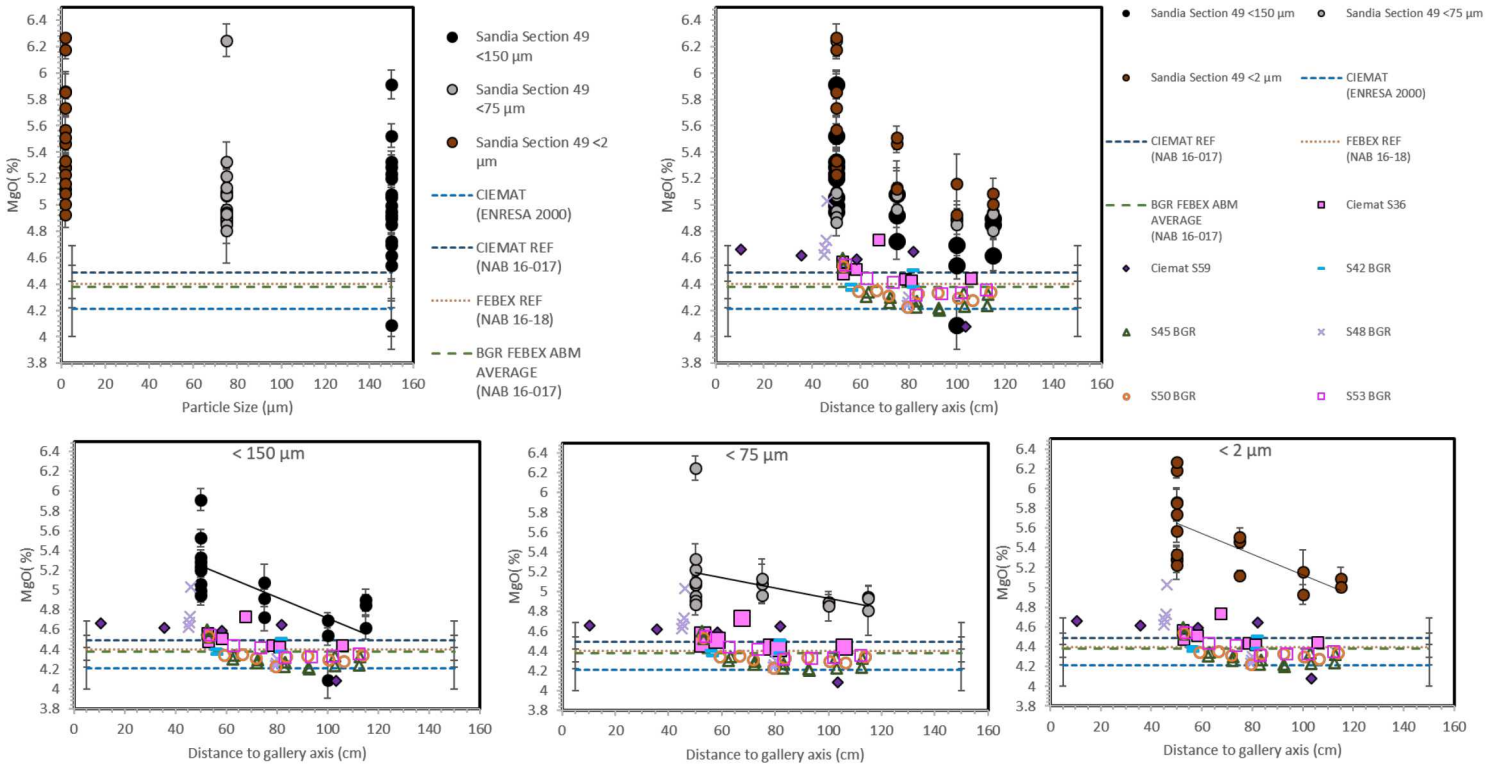


Figure E-3. Bulk bentonite XRF analyses of MgO contents for Section 49 samples as a function of distance from the gallery axis and particle size. Filled circles denote analyses conducted in this study for size fractions of <150, <75, and <2 microns. Horizontal dashed-lines delineate the range of FEBEX bentonite compositions including reference values by different groups (Villar et al. 2017).

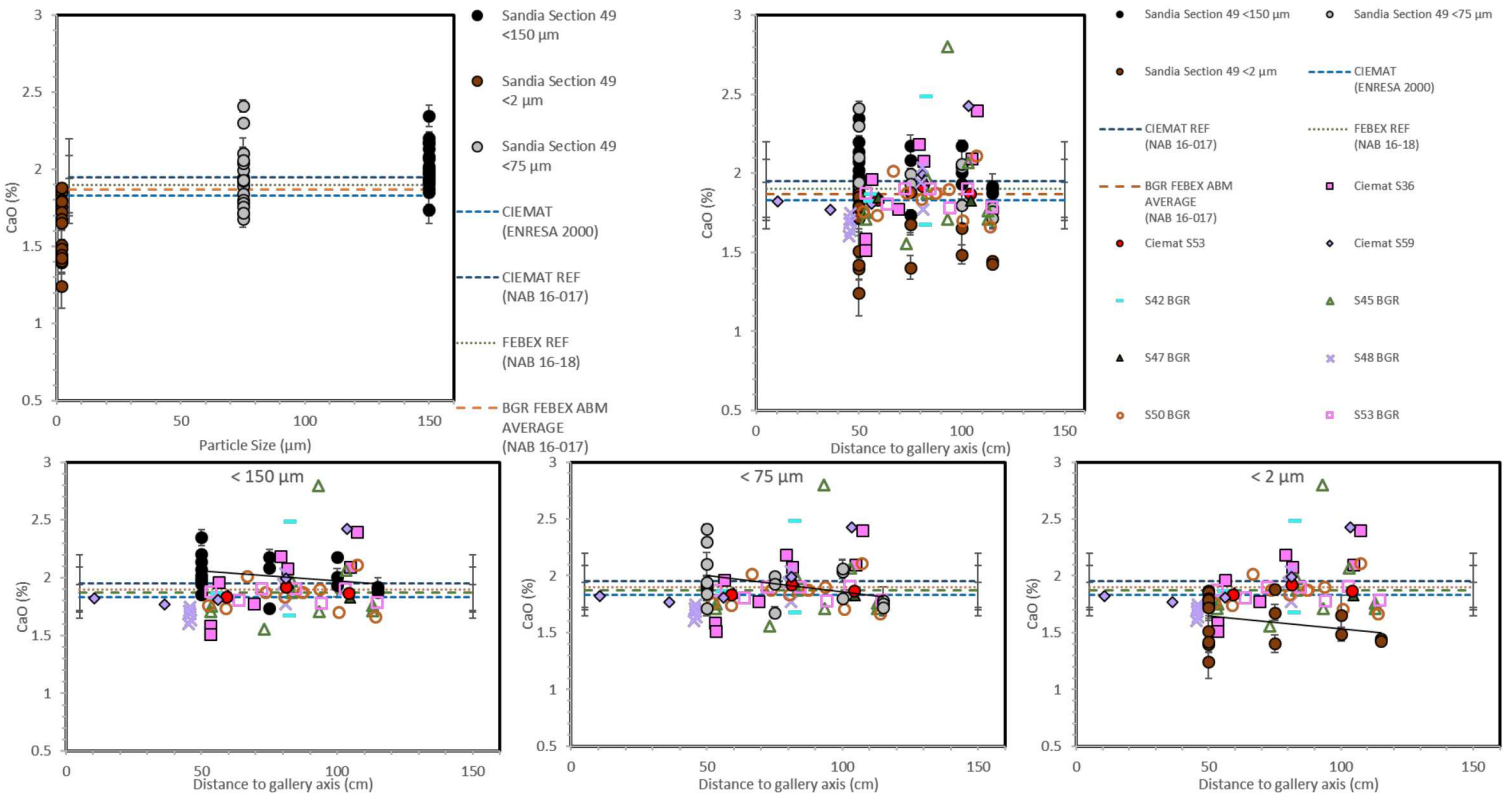


Figure E-4. Bulk bentonite XRF analyses of CaO contents for Section 49 samples as a function of distance from the gallery axis and particle size. Filled circles denote analyses conducted in this study for size fractions of <150, <75, and <2 microns. Horizontal dashed-lines delineate the range of FEBEX bentonite compositions including reference values by different groups (Villar et al. 2017).

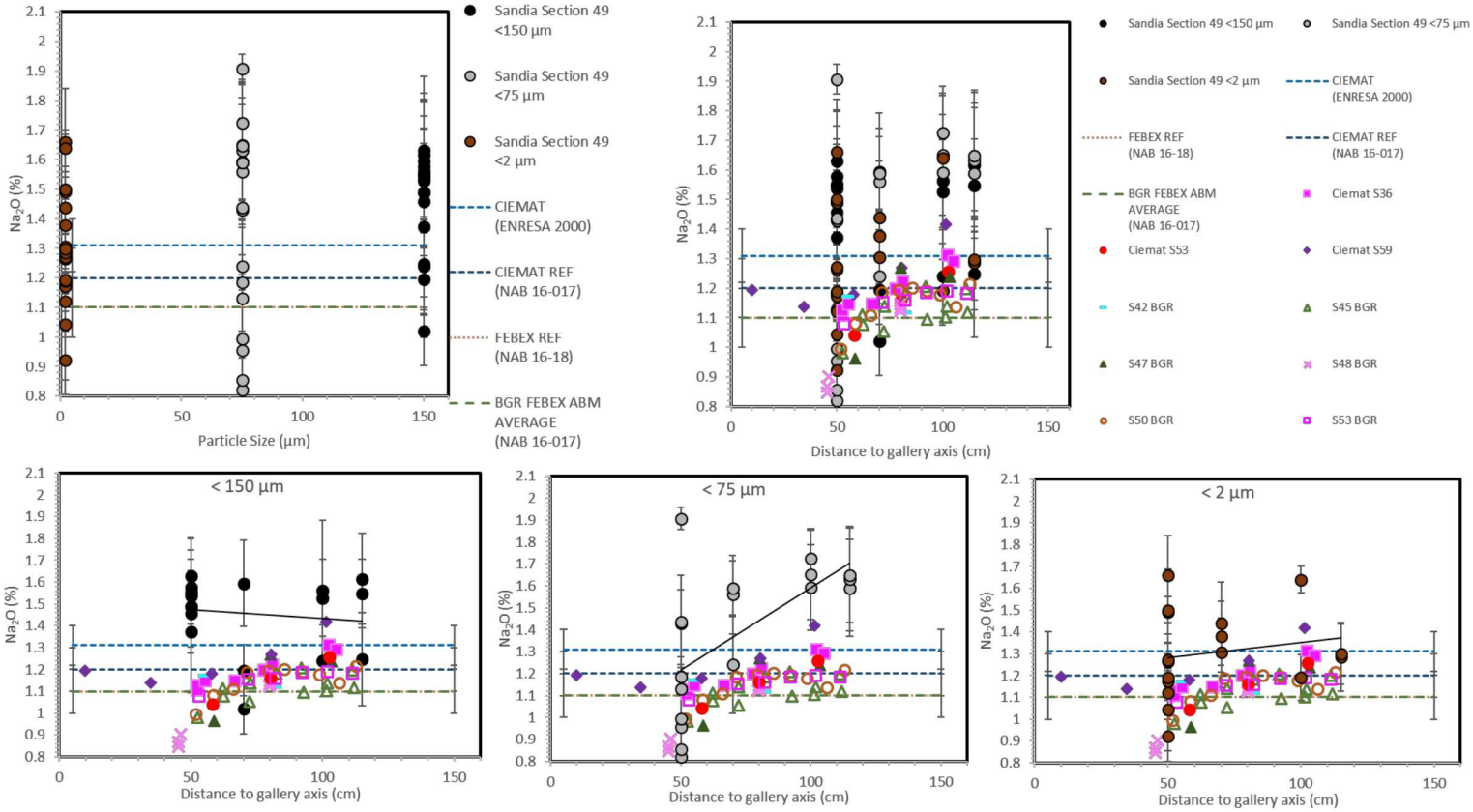


Figure E-5. Bulk bentonite XRF analyses of Na_2O contents for Section 49 samples as a function of distance from the gallery axis and particle size. Filled circles denote analyses conducted in this study for size fractions of <150, <75, and <2 microns. Horizontal dashed-lines delineate the range of FEBEX bentonite compositions including reference values by different groups (Villar et al. 2017).

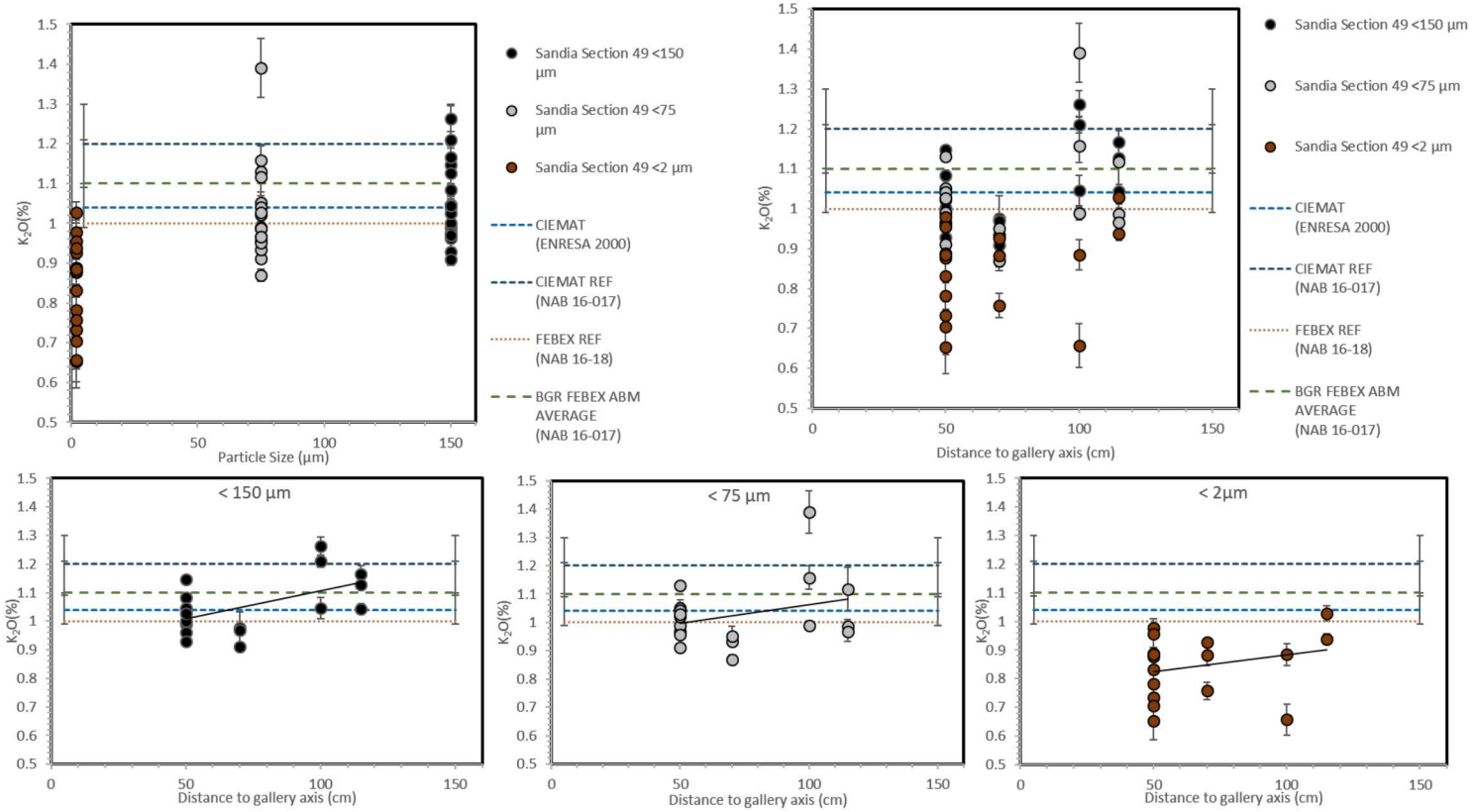


Figure E-6. Bulk bentonite XRF analyses of K_2O contents for Section 49 samples as a function of distance from the gallery axis and particle size. Filled circles denote analyses conducted in this study for size fractions of <150, <75, and <2 microns. Horizontal dashed-lines delineate the range of FEBEX bentonite compositions including reference values by different groups (Villar et al. 2017).

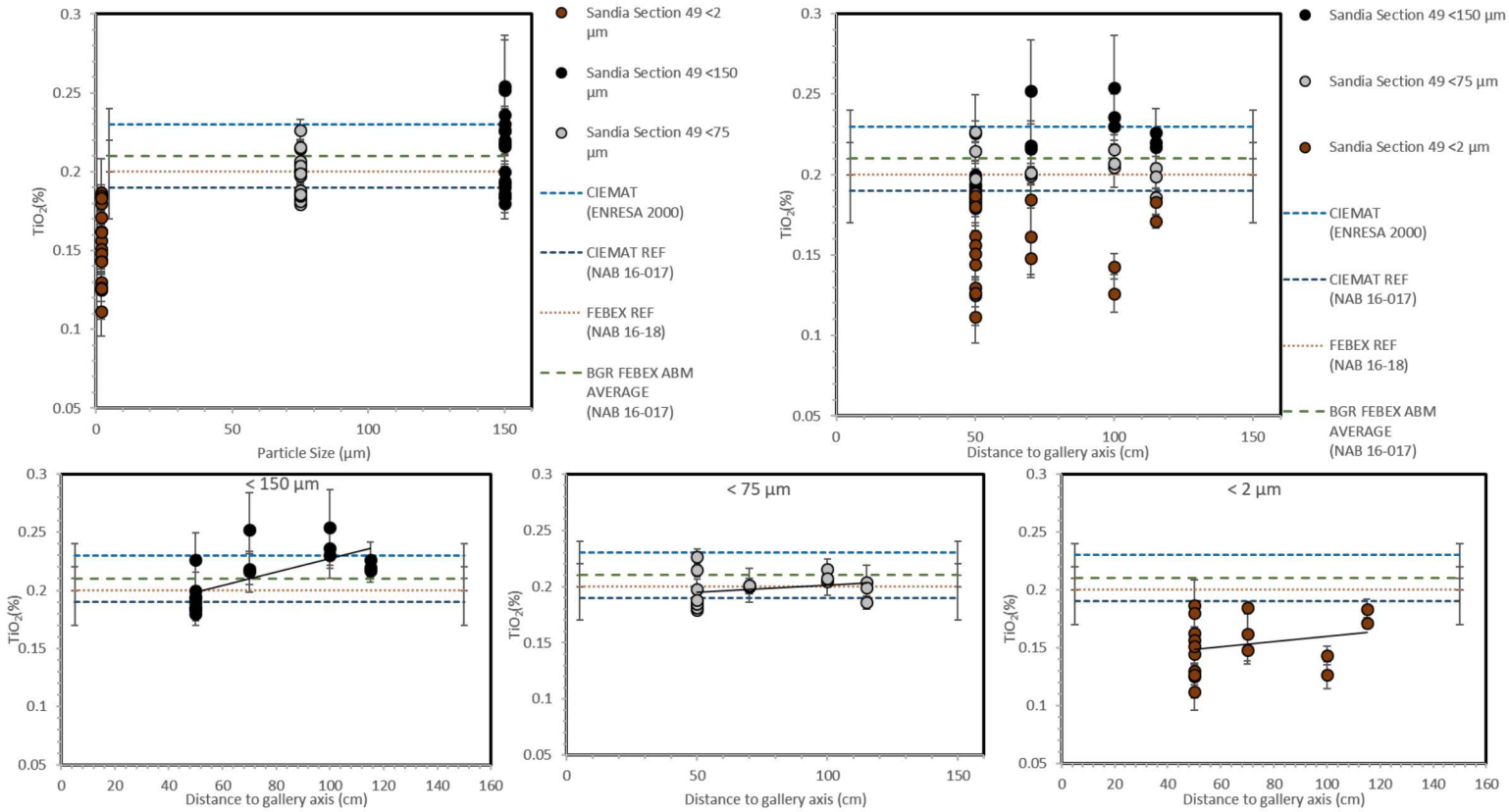


Figure E-7. Bulk bentonite XRF analyses of Ti_2O contents for Section 49 samples as a function of distance from the gallery axis and particle size. Filled circles denote analyses conducted in this study for size fractions of <150, <75, and <2 microns. Horizontal dashed-lines delineate the range of FEBEX bentonite compositions including reference values by different groups (Villar et al. 2017).

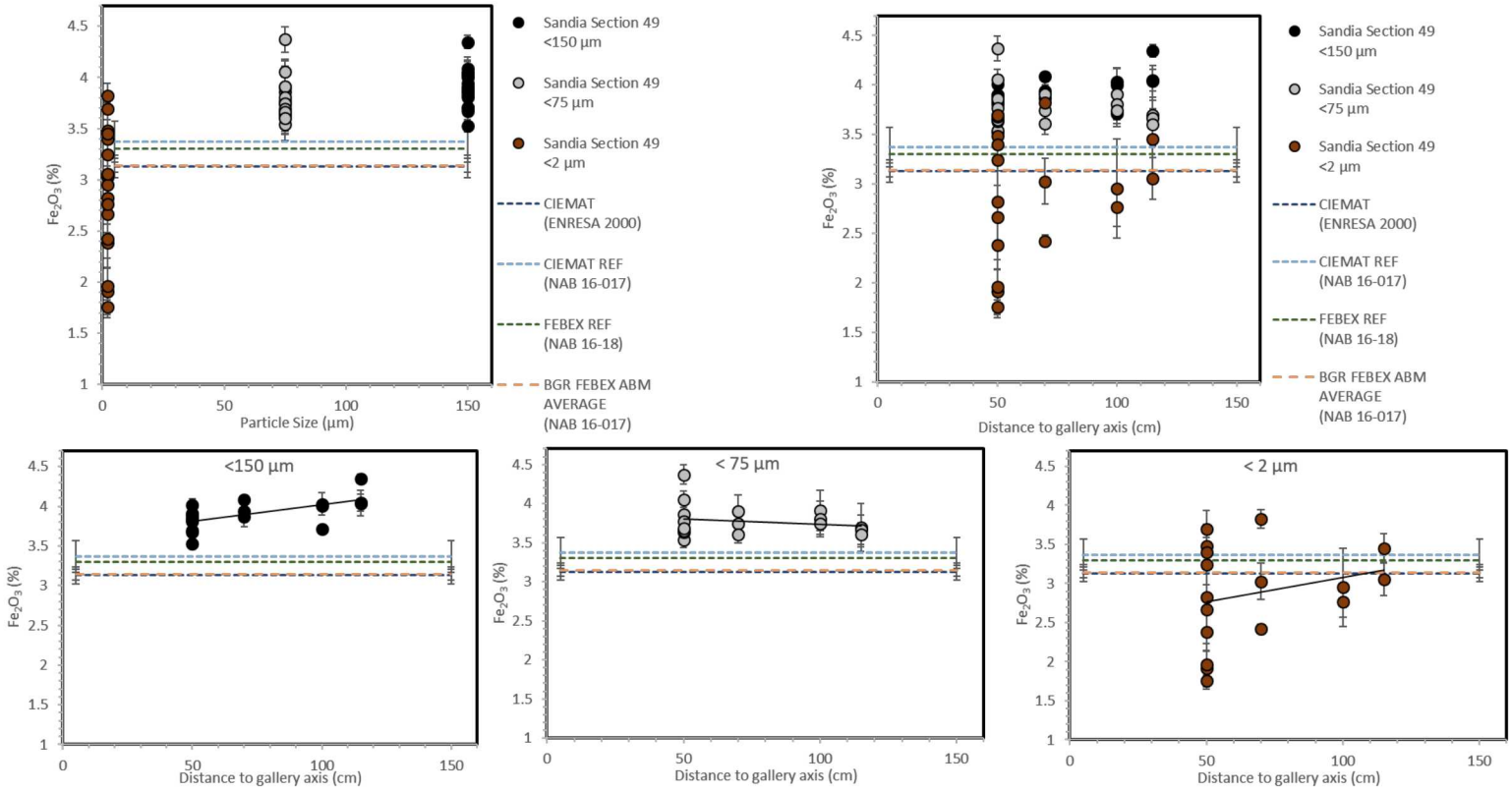


Figure E-8. Bulk bentonite XRF analyses of Fe_2O_3 contents for Section 49 samples as a function of distance from the gallery axis and particle size. Filled circles denote analyses conducted in this study for size fractions of <150, <75, and <2 microns. Horizontal dashed-lines delineate the range of FEBEX bentonite compositions including reference values by different groups (Villar et al. 2017).

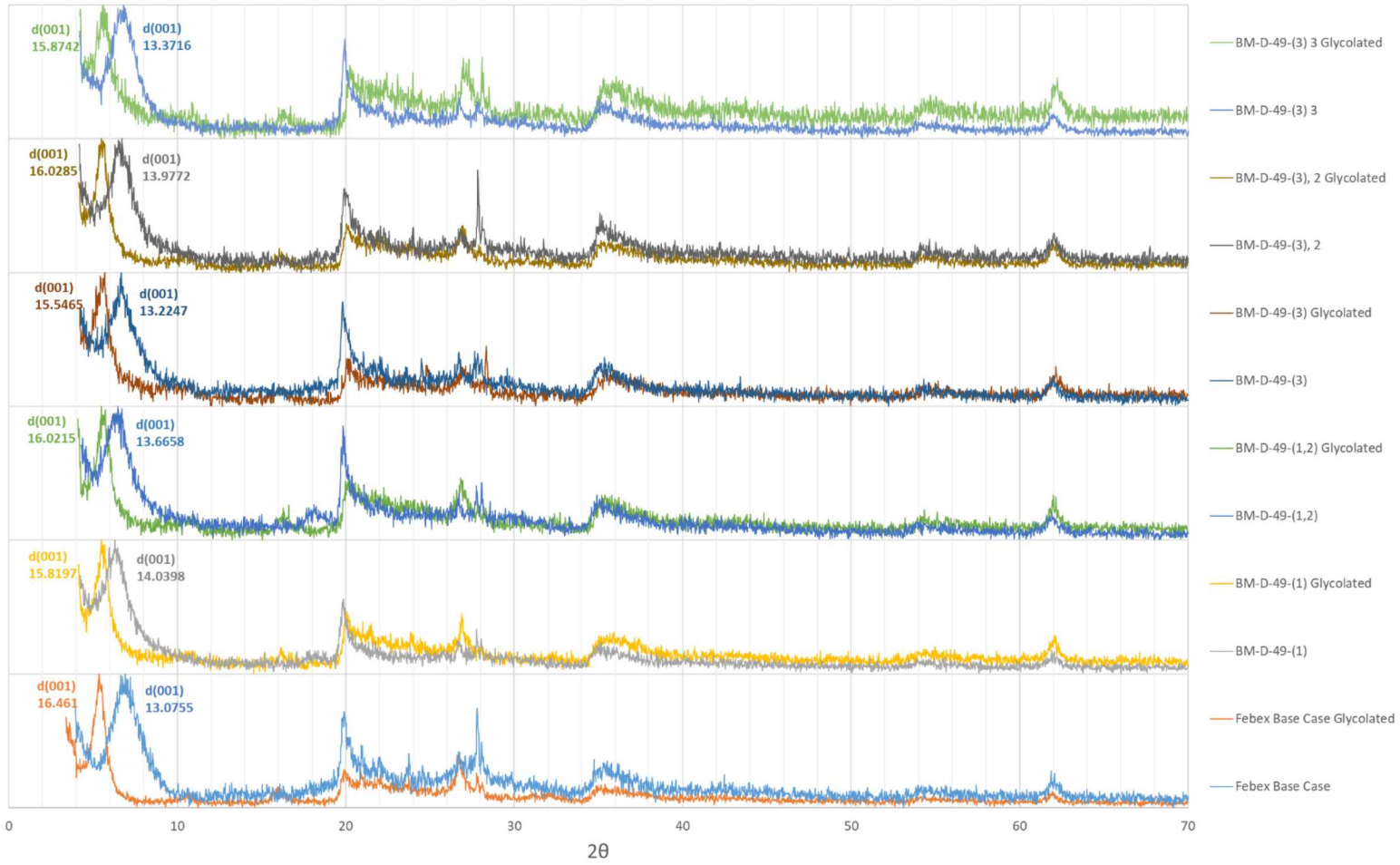


Figure E-9. XRD spectra (air-dried and glycolated) for various positions of BM-D-49 samples in the same blocks along with d-spacings (see schematic Fig. 3 for sample locations). XRD spectrum of FEBEX base case or reference material is shown at the bottom for comparison. These samples are closest to the heater.

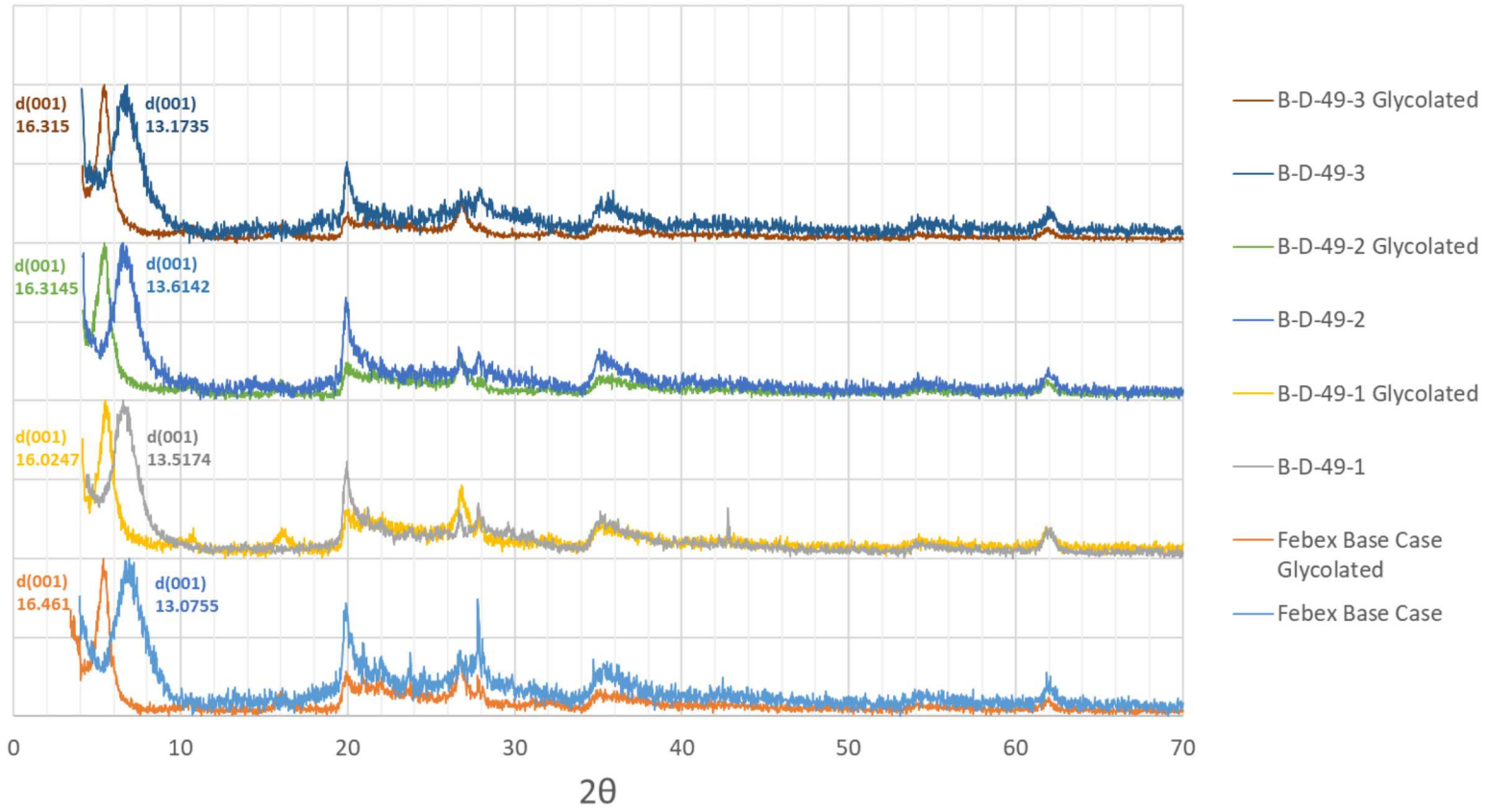


Figure E-10. XRD spectra (air-dried and glycolated) for various positions of B-D-49 samples in the same blocks along with d-spacings (see schematic Fig. 3 for sample locations). XRD spectrum of FEBEX base case or reference material is shown at the bottom for comparison.

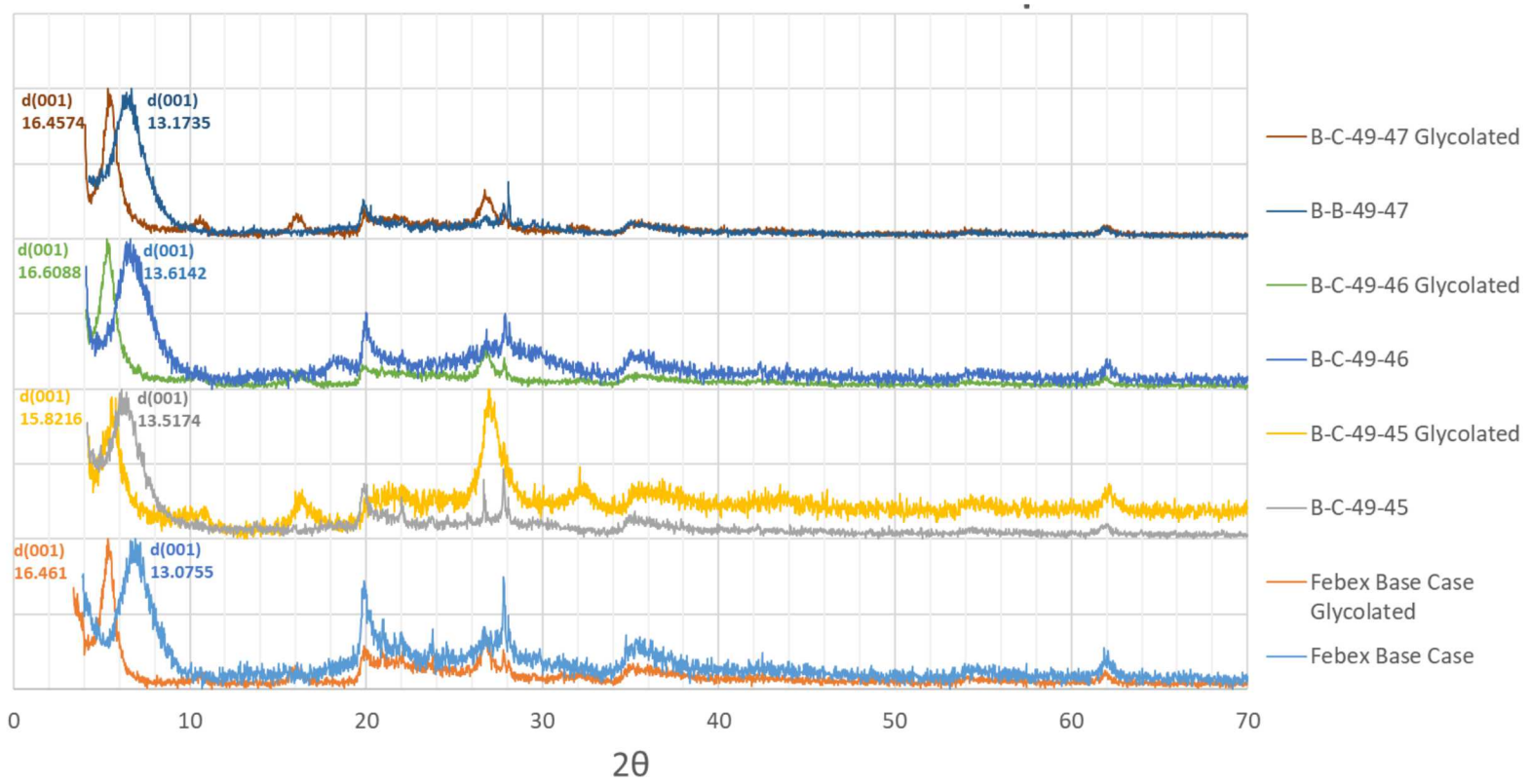


Figure E-11. XRD spectra (air-dried and glycolated) for various positions of B-C-49 samples in the same blocks along with d-spacings (see schematic Fig. 3 for sample locations). XRD spectrum of FEBEX base case or reference material is shown at the bottom for comparison.



Figure E-12. XRD spectra (air-dried and glycolated) for various positions of BG-C-49 samples in the same blocks along with d-spacings (see schematic Fig. 3 for sample locations). XRD spectrum of FEBEX base case or reference material is shown at the bottom for comparison. These are the most distal bentonite samples from the heater surface.

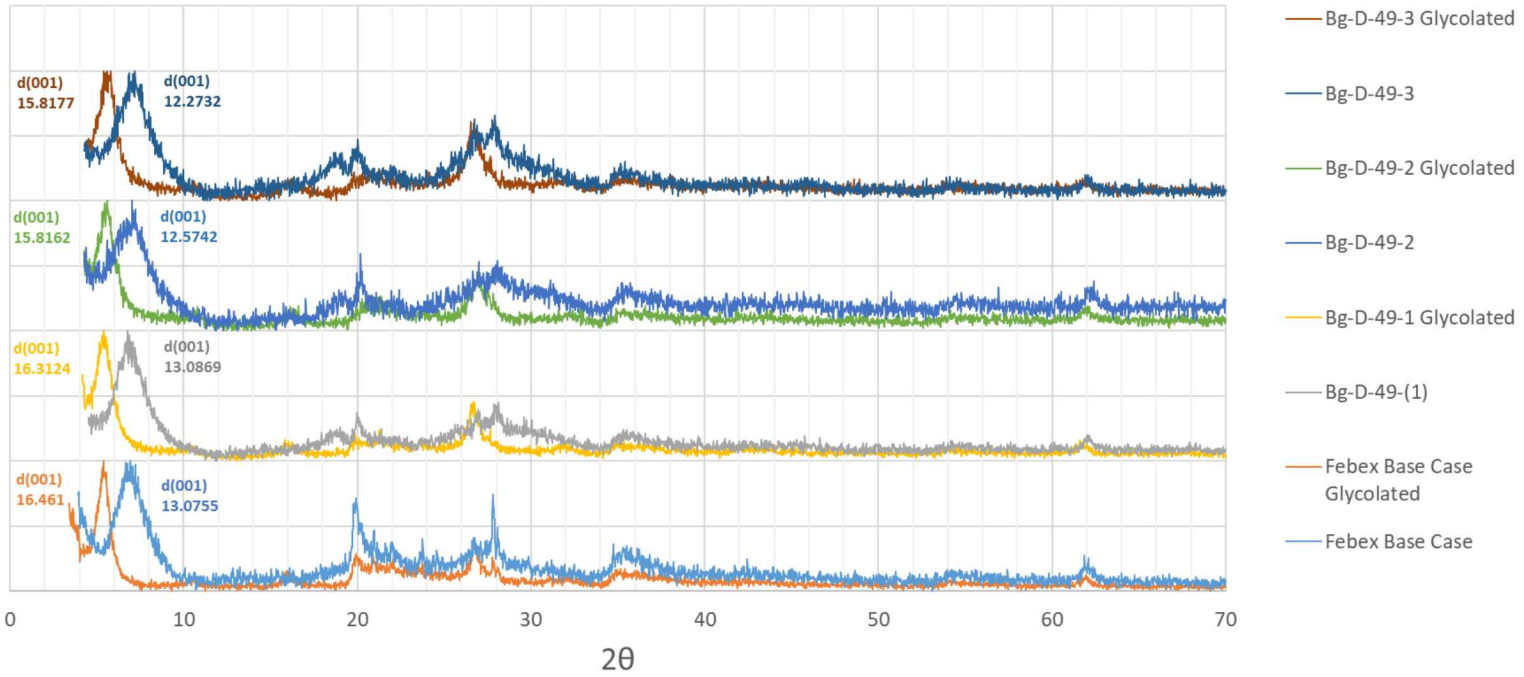


Figure E-13. XRD spectra (air-dried and glycolated) for various positions of BG-D-49 samples in the same blocks along with d-spacings (see schematic Fig. 3 for sample locations). XRD spectrum of FEBEX base case or reference material is shown at the bottom for comparison. These are the most distal bentonite samples from the heater surface.

Appendix F
SEM Images (EBS-14 to EBS-23) and (FEBEX SAMPLES)

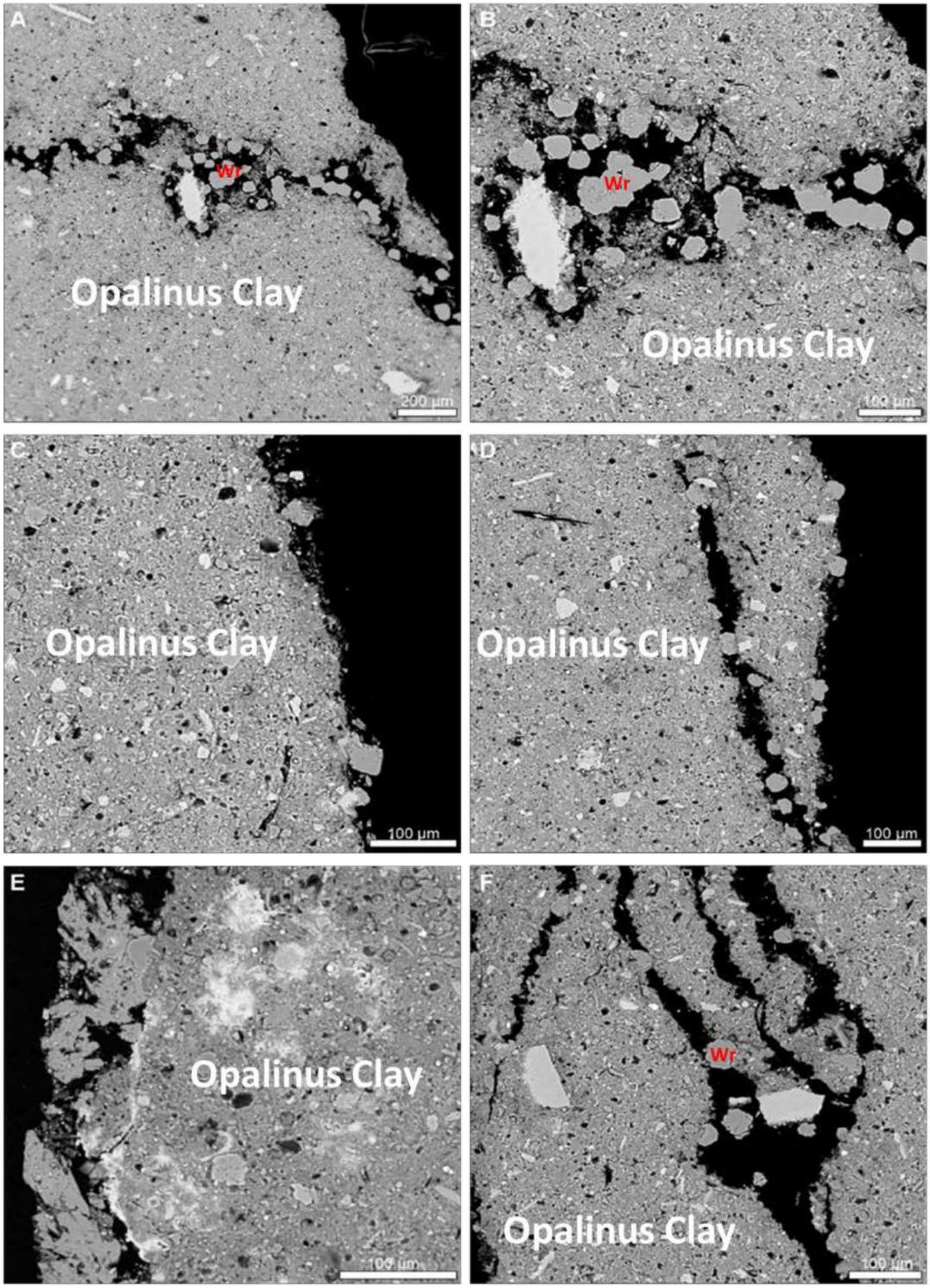


Figure F-1. EBS-14. Backscattered electron images of thin section. Opalinus Clay cracks filled with large wairakite (wr) crystals in voids [**A, B, C, D, F**]. Within Opalinus Clay matrix itself, wairakite crystals occur less frequently [**C, E**].

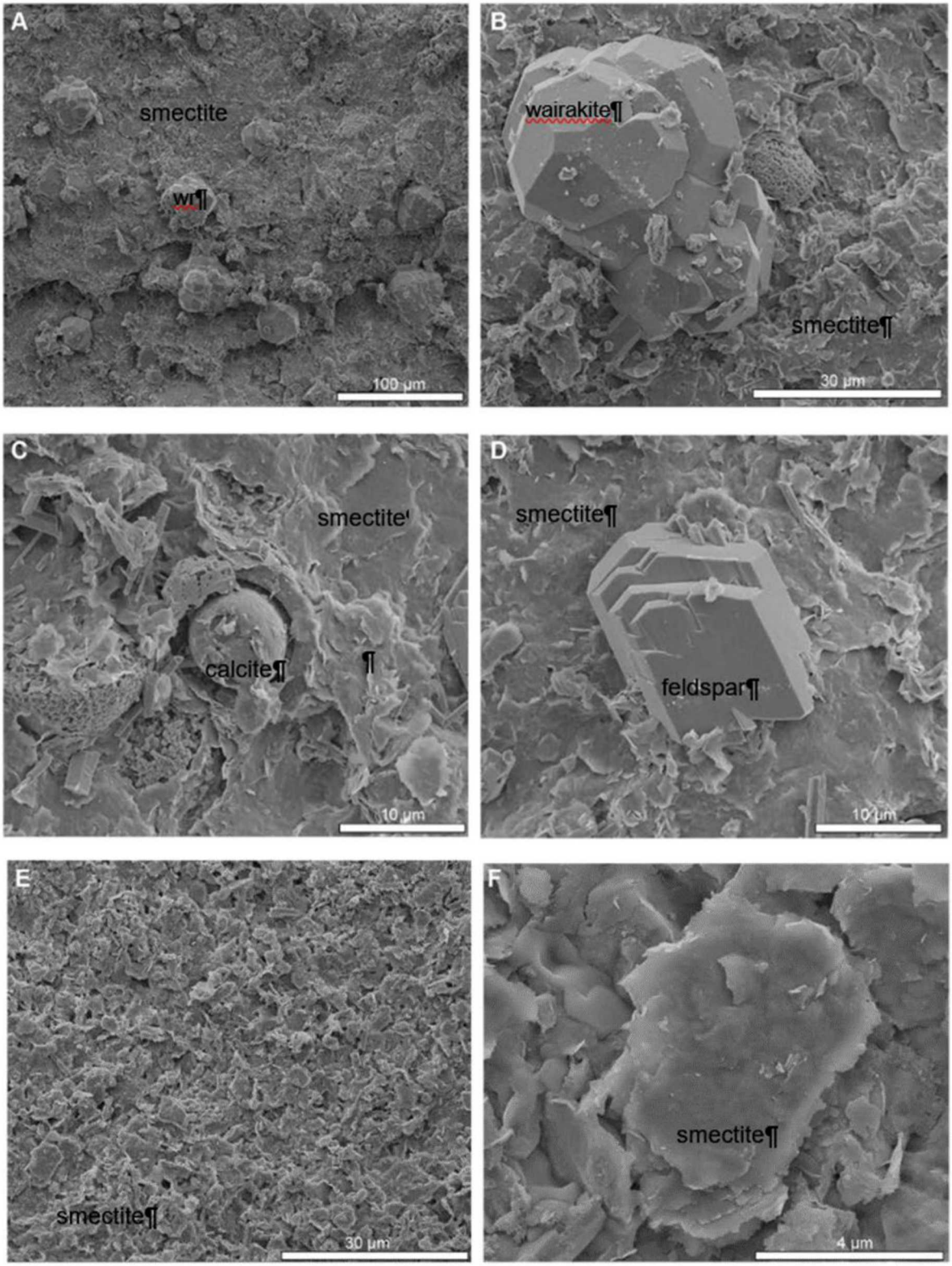


Figure F-2. EBS-14. SEM images of smectite matrix with wairakite crystals [**A, B**] or smectite matrix alone [**E**]. Sphere of calcite [**C**] feldspar crystal [**D**] and corroded smectite [**F**].

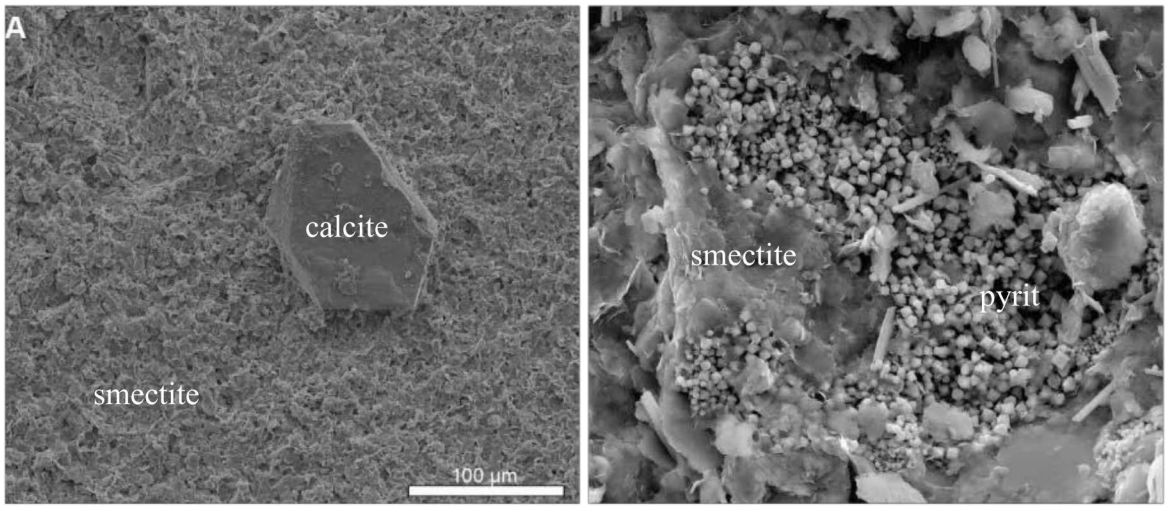


Figure F-3. EBS-14. SEM images of a carbonate imbedded in a smectite matrix [**A**] and framboidal pyrite [**B**].

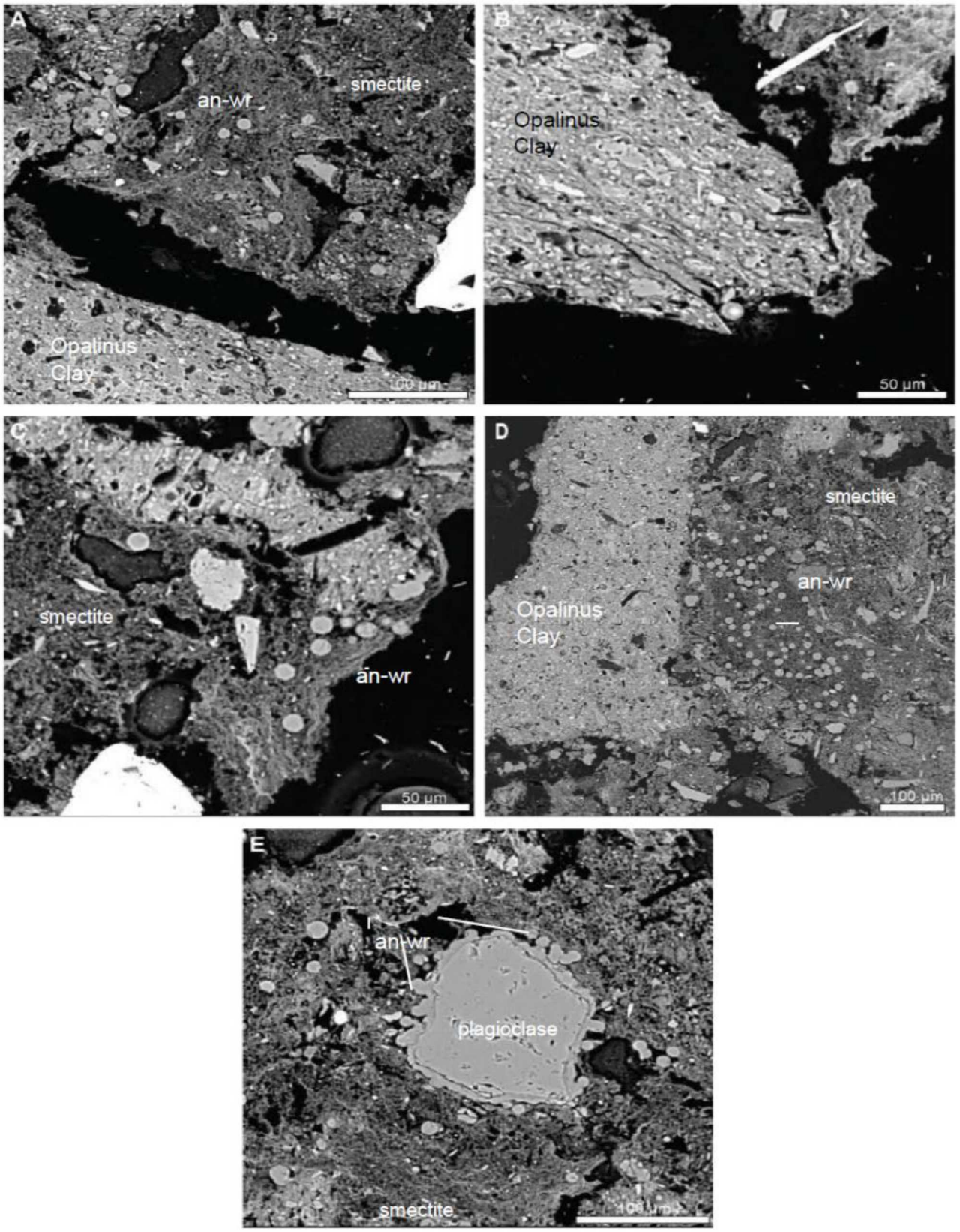


Figure F-4. EBS-15. Electron Microprobe backscattered images of Opalinus Clay with analcime- wairakite (an-wr) [**A, B, C**] Opalinus Clay on the left and bentonite on the right with analcime [**D**]. Analcime mantling plagioclase [**E**].

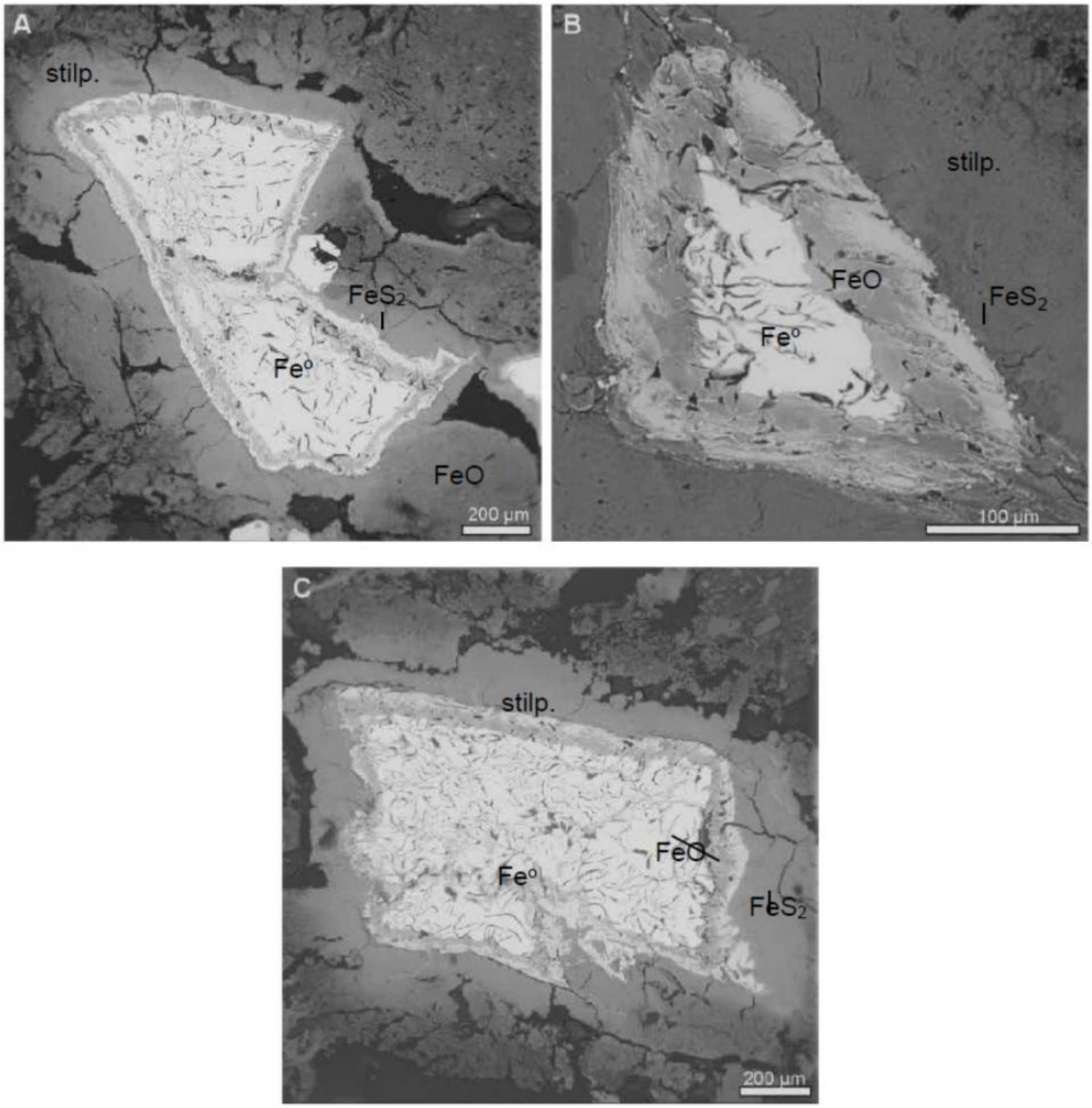


Figure F-5. EBS-15. Electron microprobe backscattered images of native iron grain with zoning and outward alteration from Fe-oxide, Fe-sulfide, stilpnomelane [**A, B, C**].

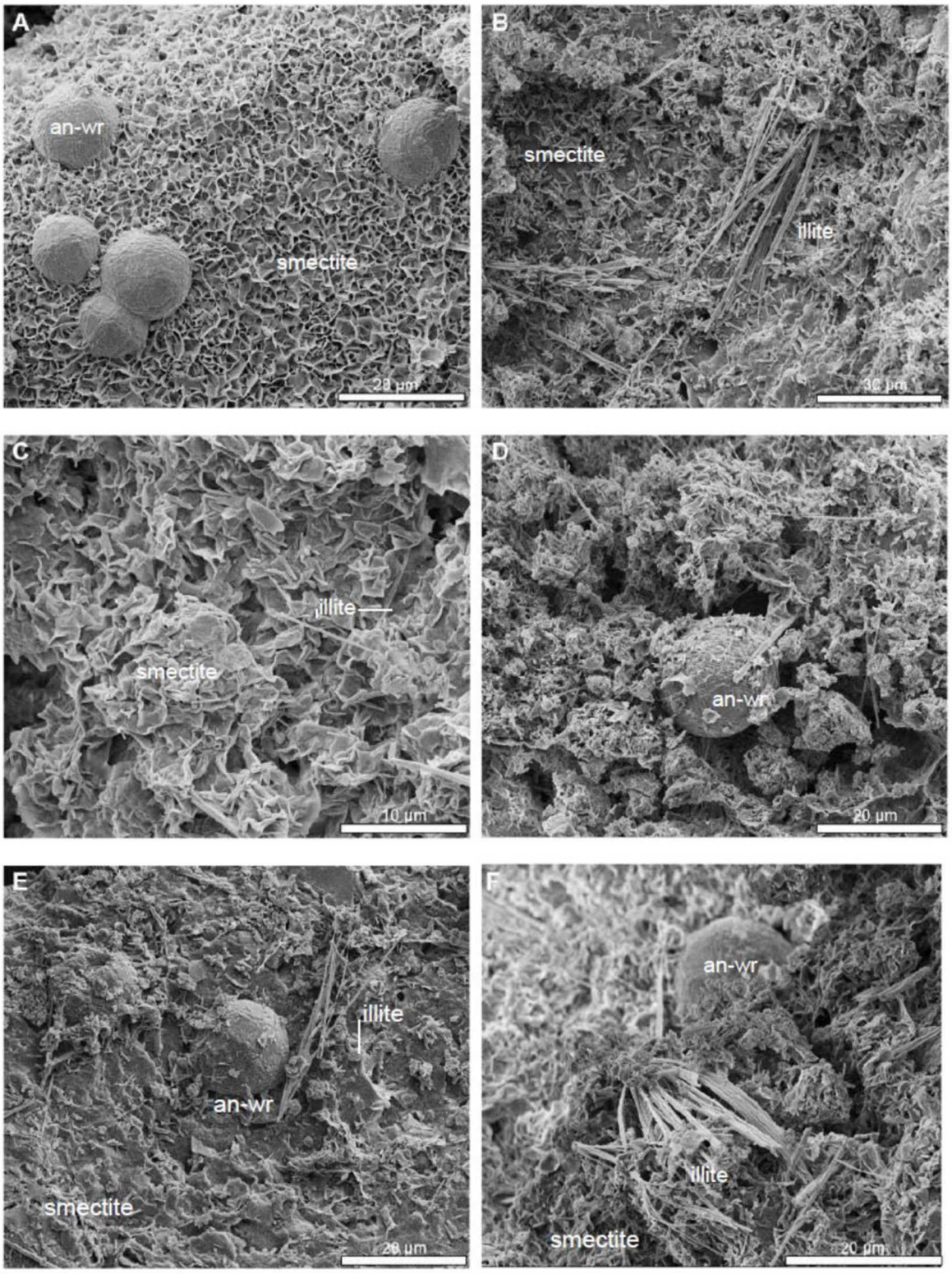


Figure F-6. EBS-15. SEM images of smectite matrix with analcime-wairakite crystals [**A**] illite growth [**B, F**]. Foliated bentonite with some minor illite [**C**]. Analcime-wairakite solid solution crystal with smectite and illite [**D, E**].

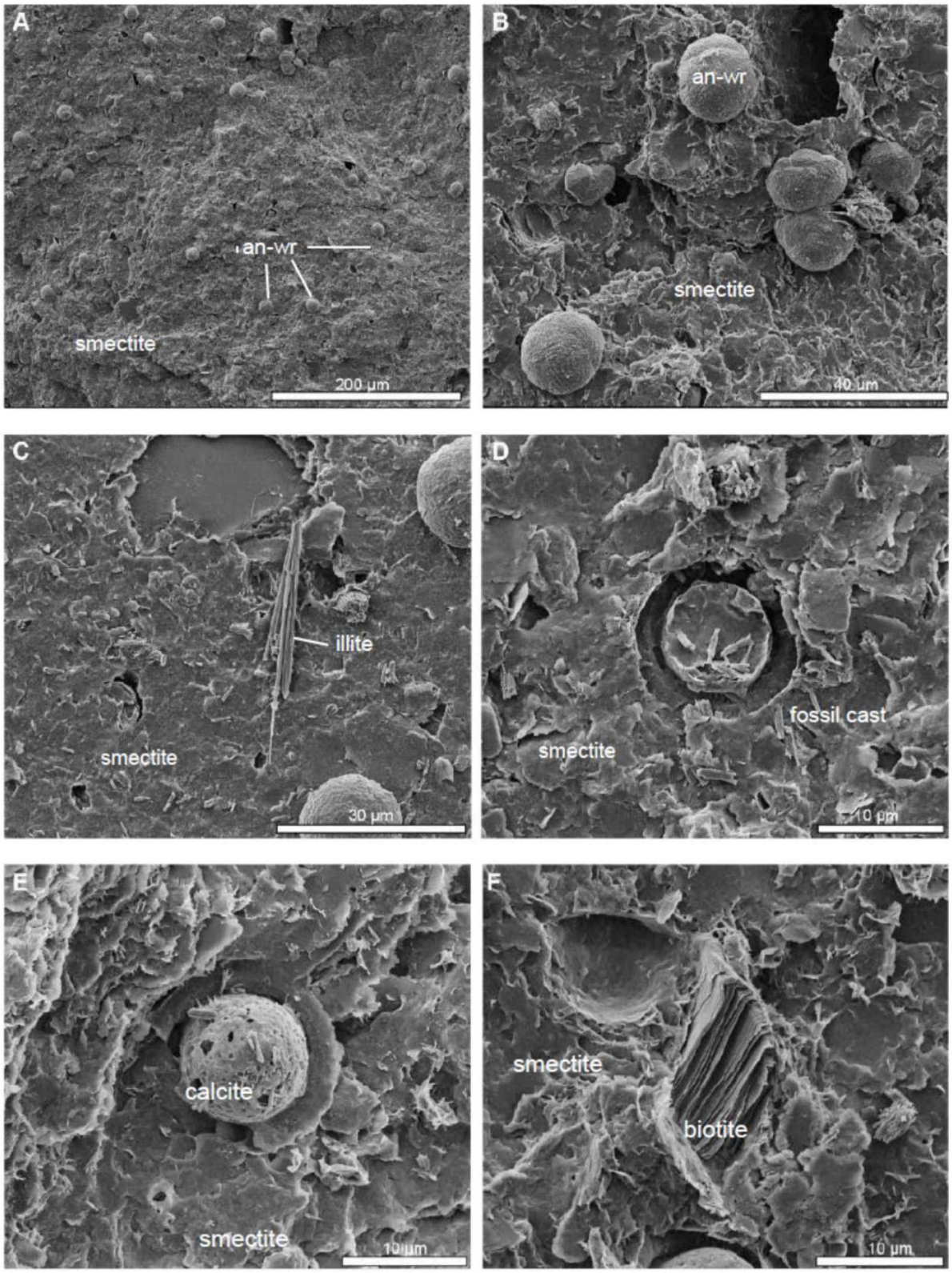


Figure F-7. EBS-15. SEM images of smectite matrix with analcime-wairakite crystals [**A**]. Analcime wairakite solid solution crystals [**B**]. Possible illite [**C**] fossil cast [**D**]. Calcite ball [**E**]. Biotite [**F**].

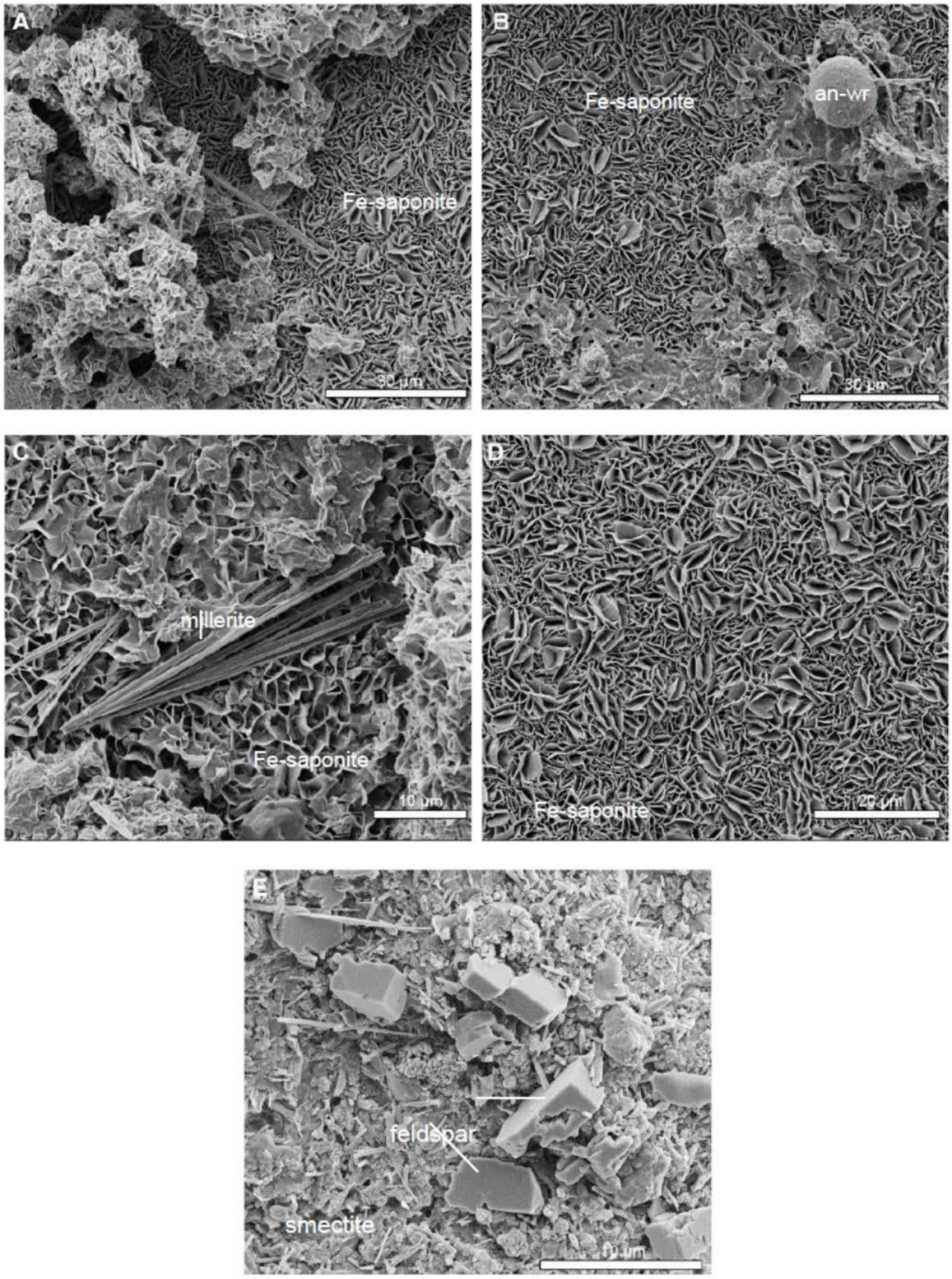


Figure F-8. EBS-15. SEM images of unknown fibrous material on saponite [**A**]. Saponite and analcime-wairakite crystals on 316 SS [**B**]. Fibrous millerite on saponite [**C**]. Saponite mat [**D**]. SEM image of unknown crystal growth (possibly feldspar) suspended in smectite [**E**].

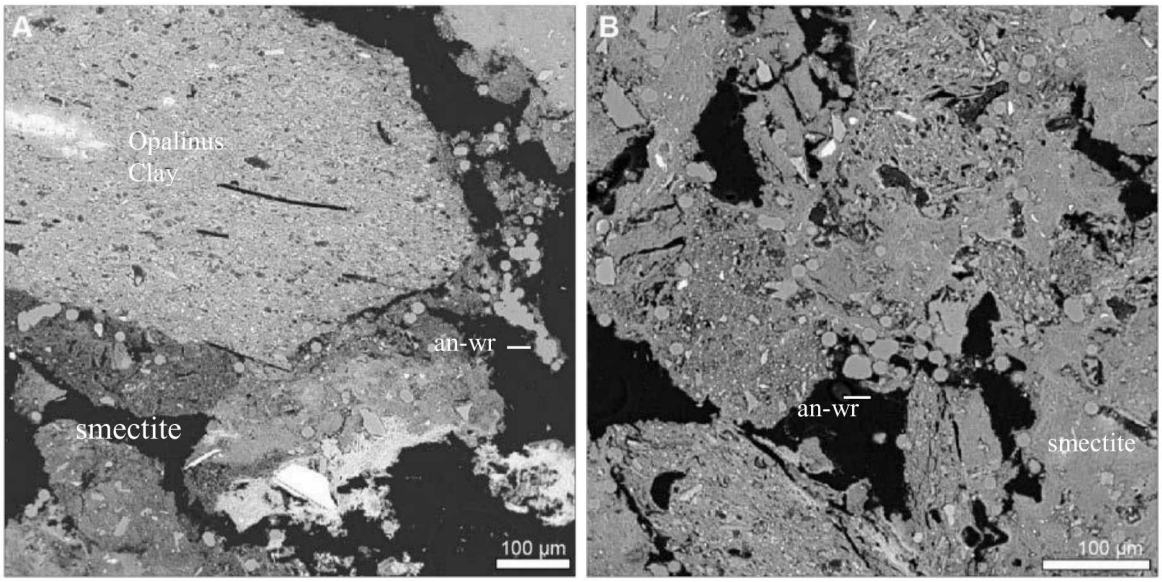


Figure F-9. EBS-17. Electron microprobe images of thin section Opalinus Clay with analcime-wairakite crystals [**A, B**].

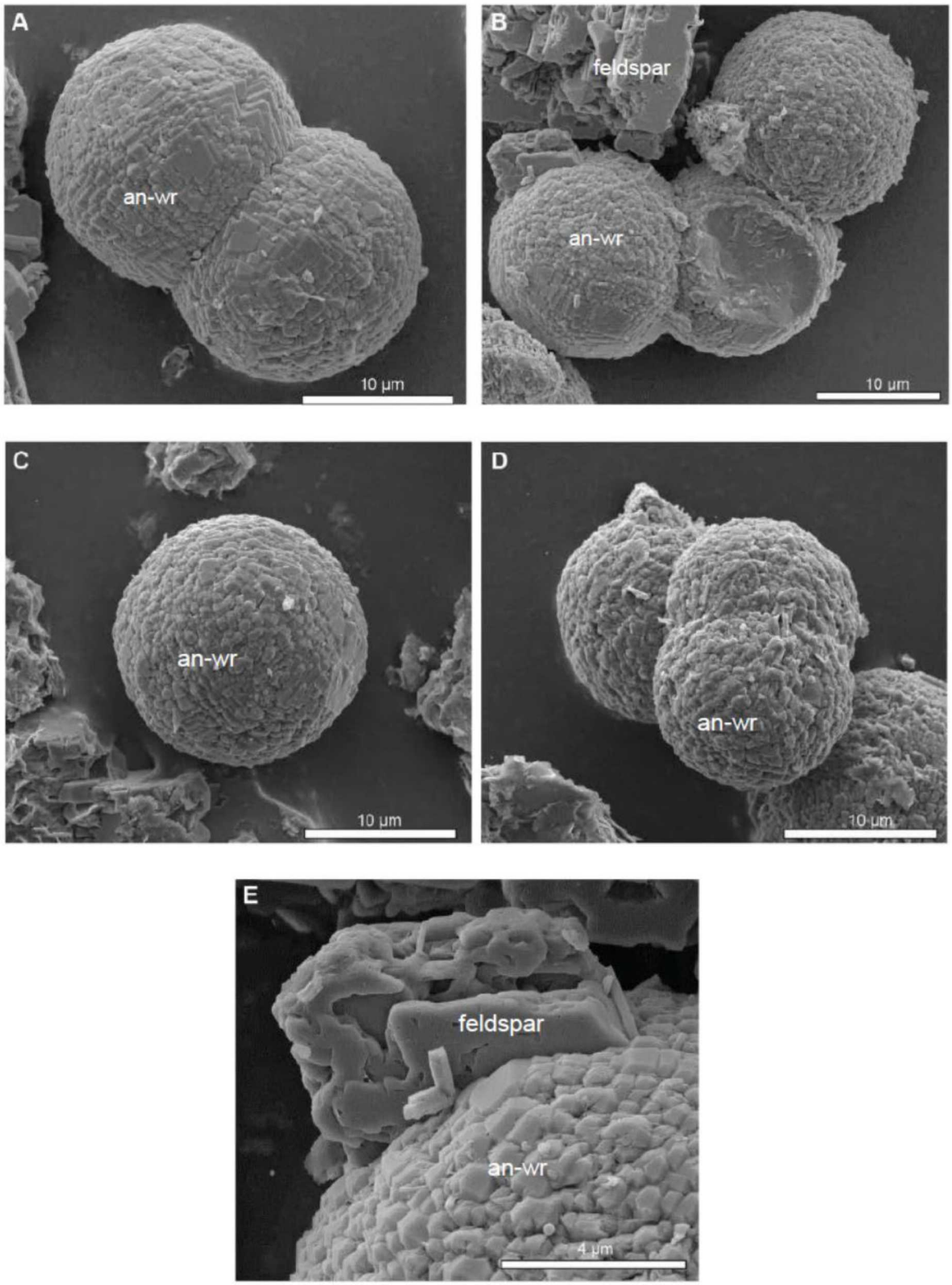


Figure F-10. EBS-17. SEM images of analcime-wairakite solid solution crystals [**A, B, C, D**]. Feldspar dissolution in contact with analcime-wairakite crystal [**E**].

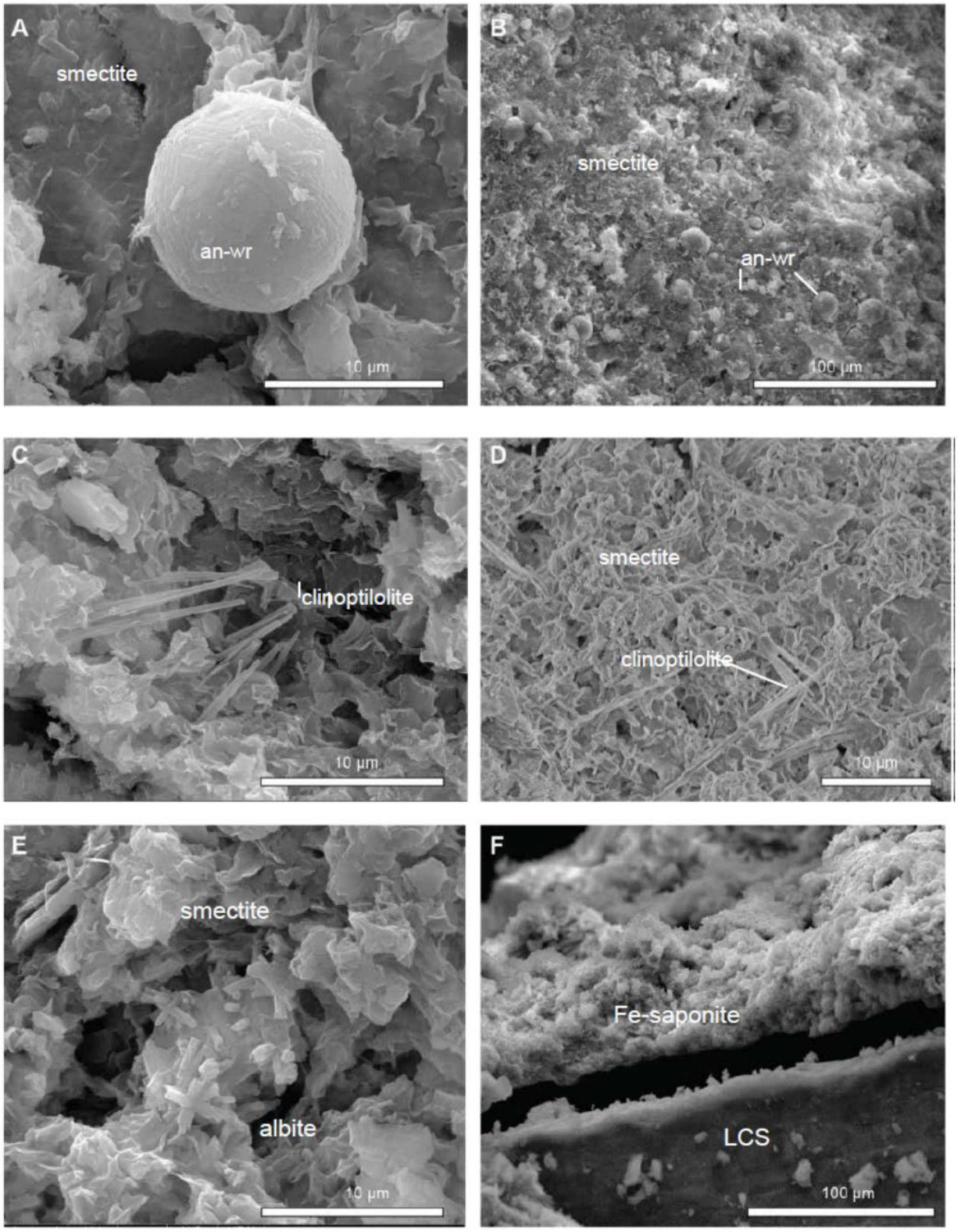


Figure F-11. EBS-18. SEM images of analcime-wairakite zeolite in smectite matrix [**A, B**]. Acicular [**C**] and fibrous [**D**] clinoptilolite in smectite. Radial authigenic plagioclase growth [**E**]. Fe-saponite (fine-grained material above black zone) grown on low carbon steel (lower grey mass) [**F**].

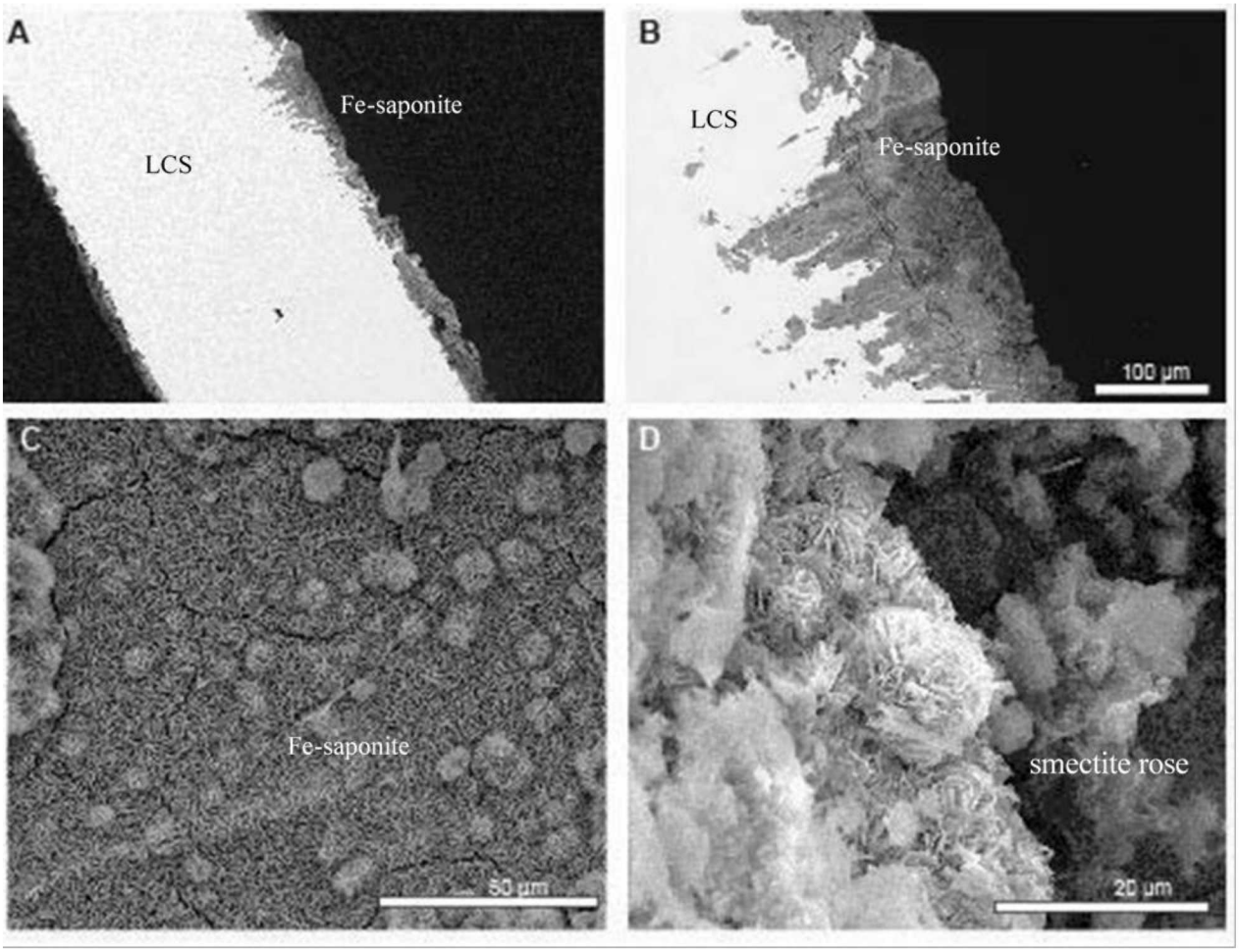


Figure F-12. EBS-18. Electron microprobe backscattered image of thin sections showing low carbon steel corrosion (LCS) [**A, B**]. SEM images of Fe-saponite crystal growth perpendicular to low carbon steel [**C**] and secondary smectite rose [**D**].

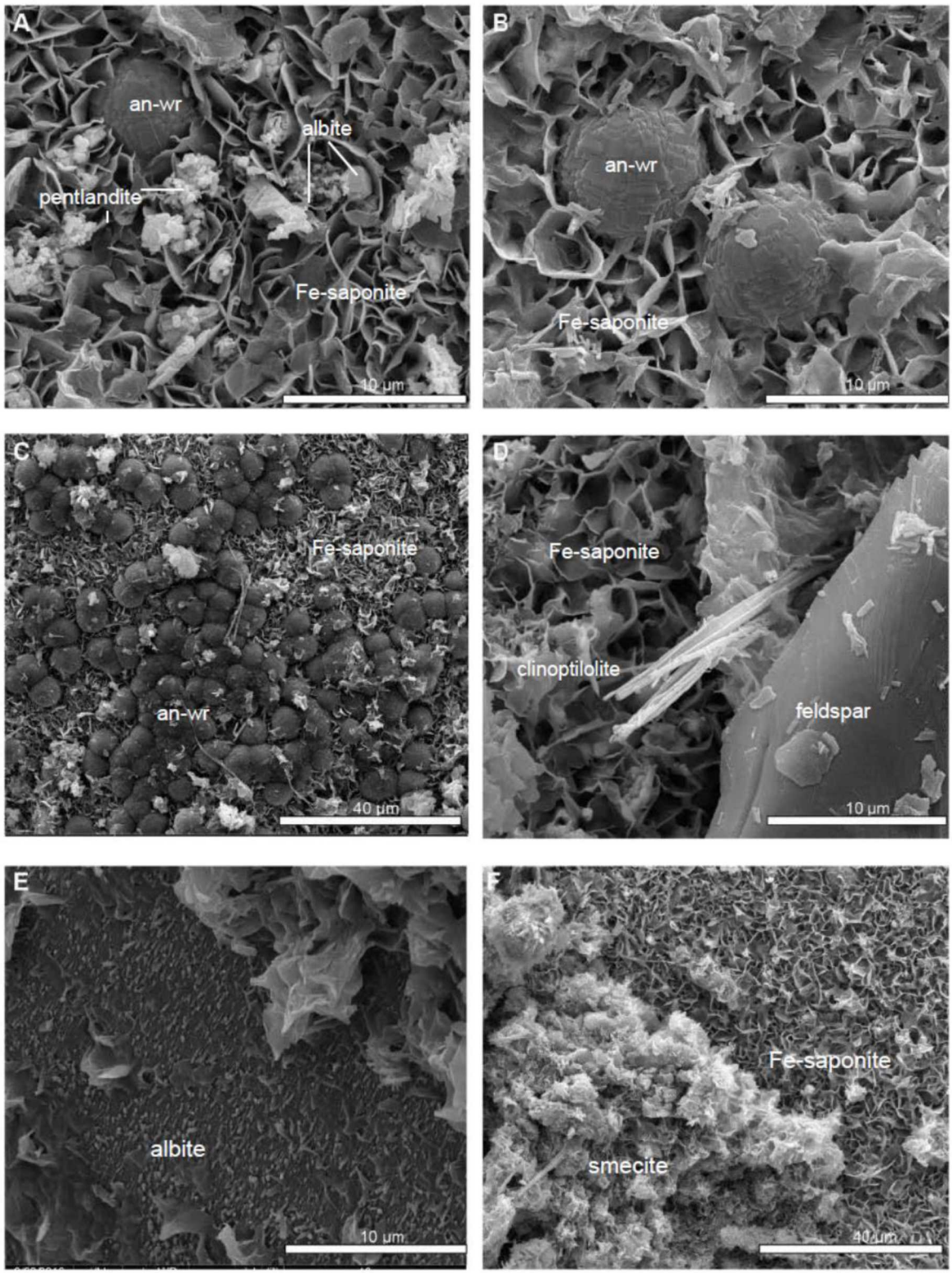


Figure F-13. EBS-19. SEM images of Fe-saponite, analcime-wairakite, with minor smectite, albite, and pentlandite crystals [**A**]. Analcime-wairakite embedded in Fe-saponite [**B, C**]. In [**C**] most likely the zeolite cluster replaced glass lapilli. Acicular clinoptilolite next to resorbing K- feldspar phenocryst [**D**]. Secondary albite growth on plagioclase phenocryst [**E**] Smectite overlying Fe-saponite [**F**].

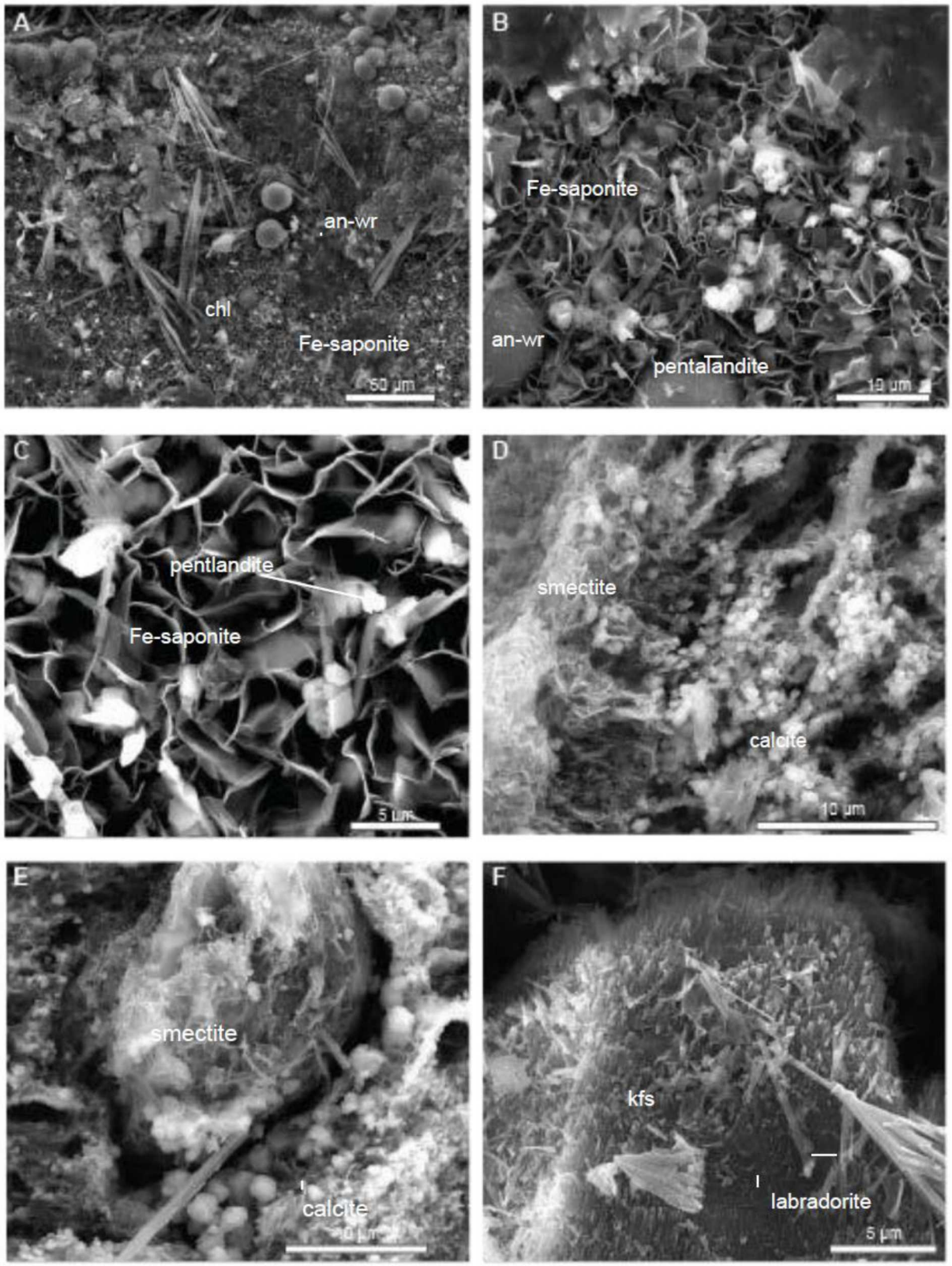


Figure F-14. EBS-20. SEM images of chlorite sprays with analcime-wairakite solid solution zeolite [**A, B**]. Analcime-wairakite solid solution zeolite surrounded by Fe-saponite, with late stage pentlandite (white crystals) [**B**]. Close up of late stage pentlandite (white crystals) on Fe- saponite [**C**]. Possible calcite spheres in smectite [**D, E**]. Feldspar sprays (likely Labradorite), with background K-feldspar dissolution texture [**F**].

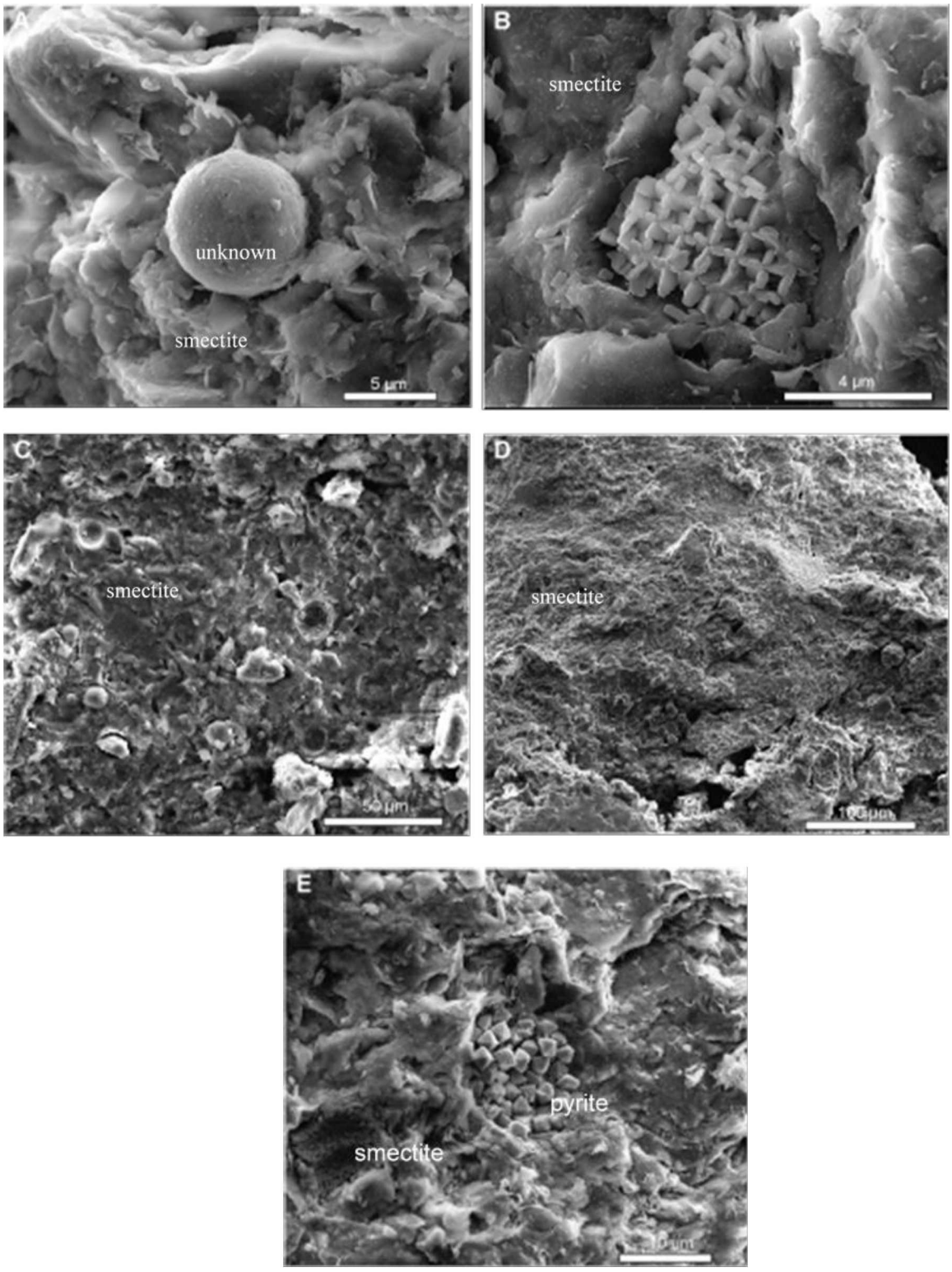


Figure F-15. EBS-21. SEM images of unknown Al-silicate in smectite matrix [**A, B**]. Examples of smectite matrix [**C, D**] and framboidal pyrite [**E**].

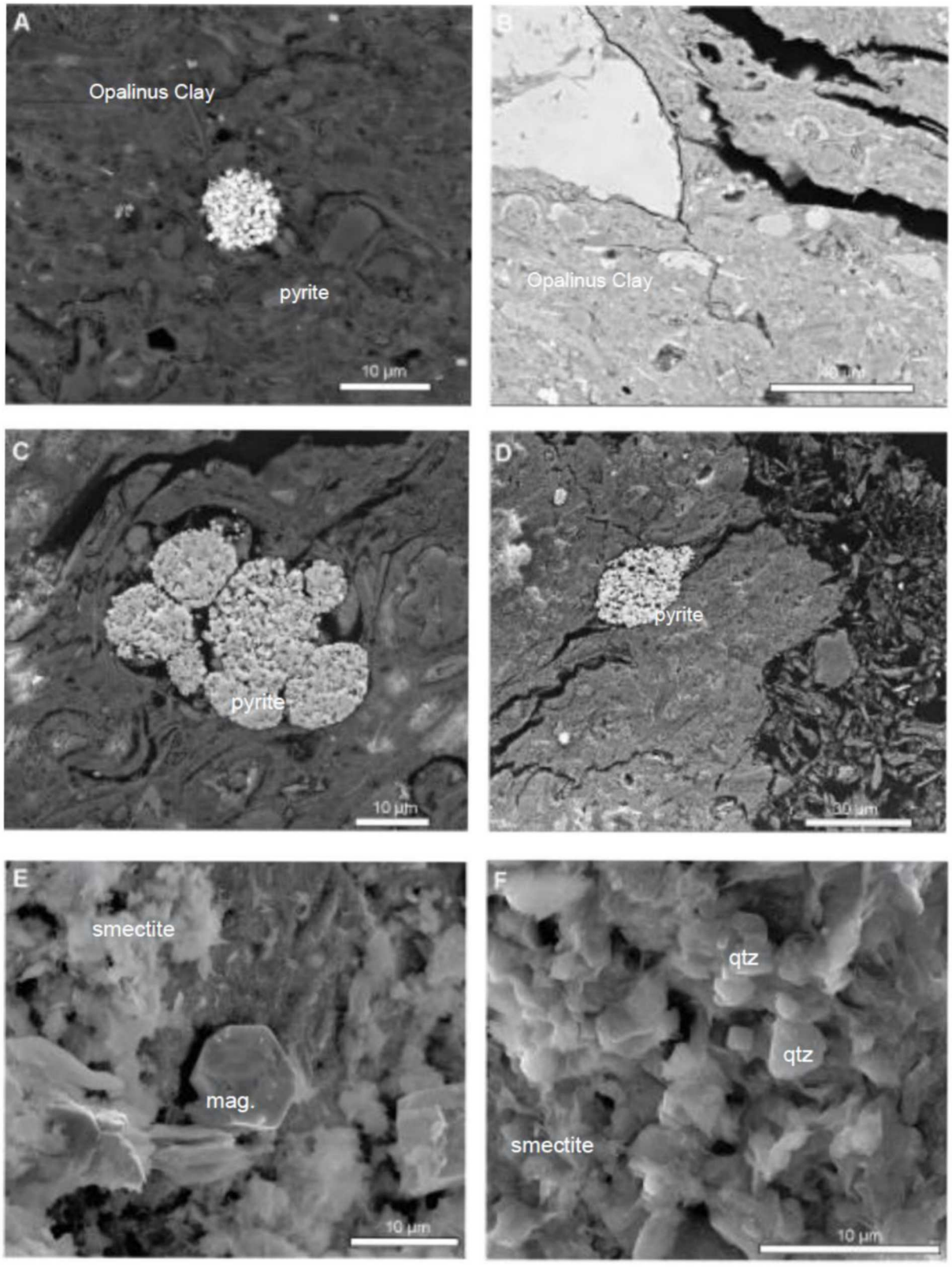


Figure F-16. EBS-22. Electron Microprobe backscattered images of framboidal pyrite [**A**] and Opalinus Clay fragments [**B, D**] with replacement of fossil casts lined with calcite [**B**] and carbonate crystal clusters [**C**]. Magnetite crystal (solid buffer material) [**E**] and authigenic quartz in center of image [**F**].

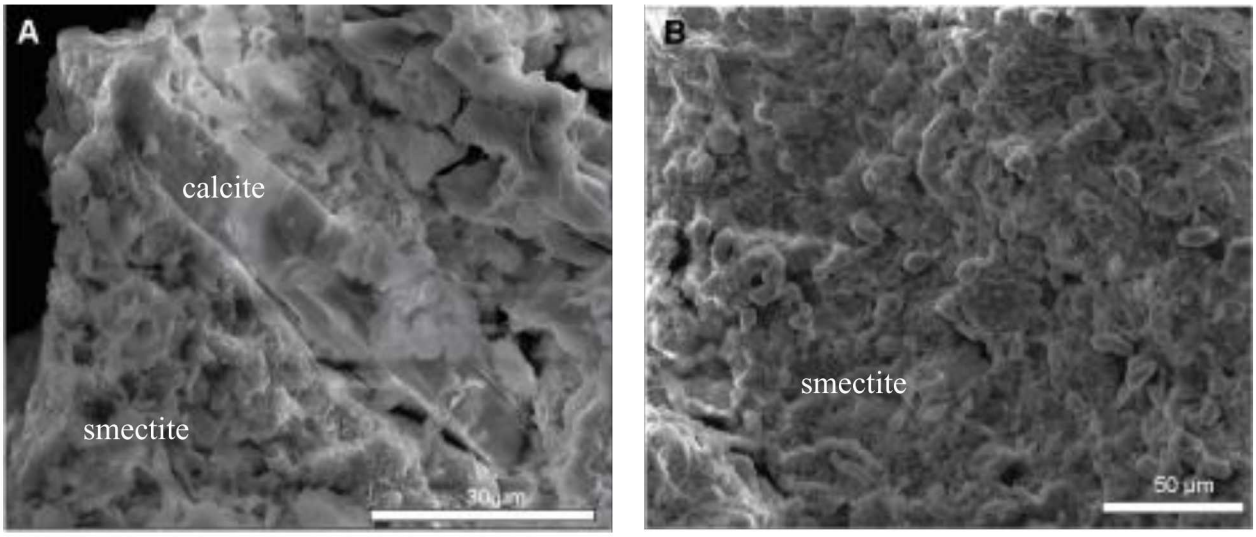


Figure F-17. EBS-22. Electron Microprobe backscattered images of secondary calcite on smectite [**A**] and authigenic gypsum lath [**B**].

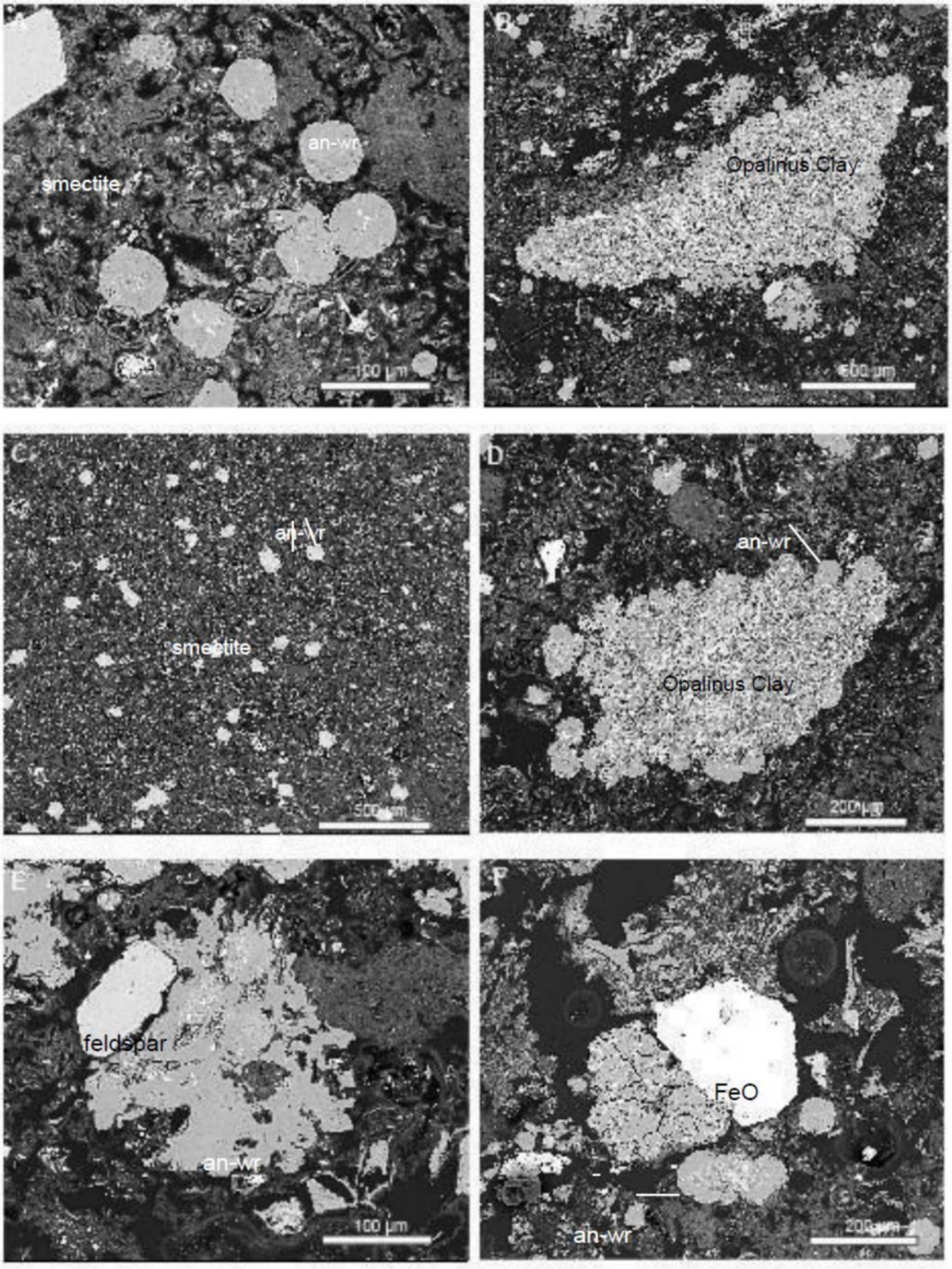


Figure F-18. EBS-23. Electron Microprobe backscattered images of analcime-wairakite solid solution crystals [**A, B, C**]. Note analcime-wairakite solid solution rims Opalinus Clay fragment [**B**]. wairakite crystals mantling Opalinus Clay fragment [**D**]. Feldspar crystal adjacent to analcime-wairakite solid solution crystals replacing pumice lapilli [**E**]. Bright Fe- oxide crystal next to a wairakite-rich analcime zeolite [**F**].

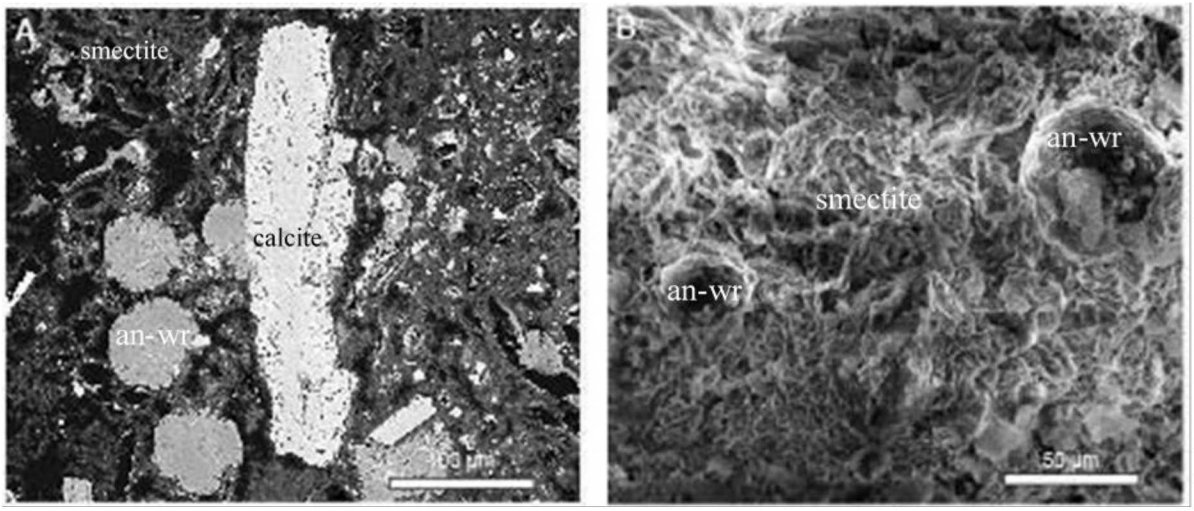


Figure F-19. EBS-23. Electron Microprobe backscattered image of calcite crystal surrounded by analcime-wairakite crystals. Zeolite crystals to left of calcite crystal and analcime-rich, while zeolite abutting calcite is wairakite-rich [**A**]. analcime-wairakite solid solution crystals residing in smectite matrix [**B**].

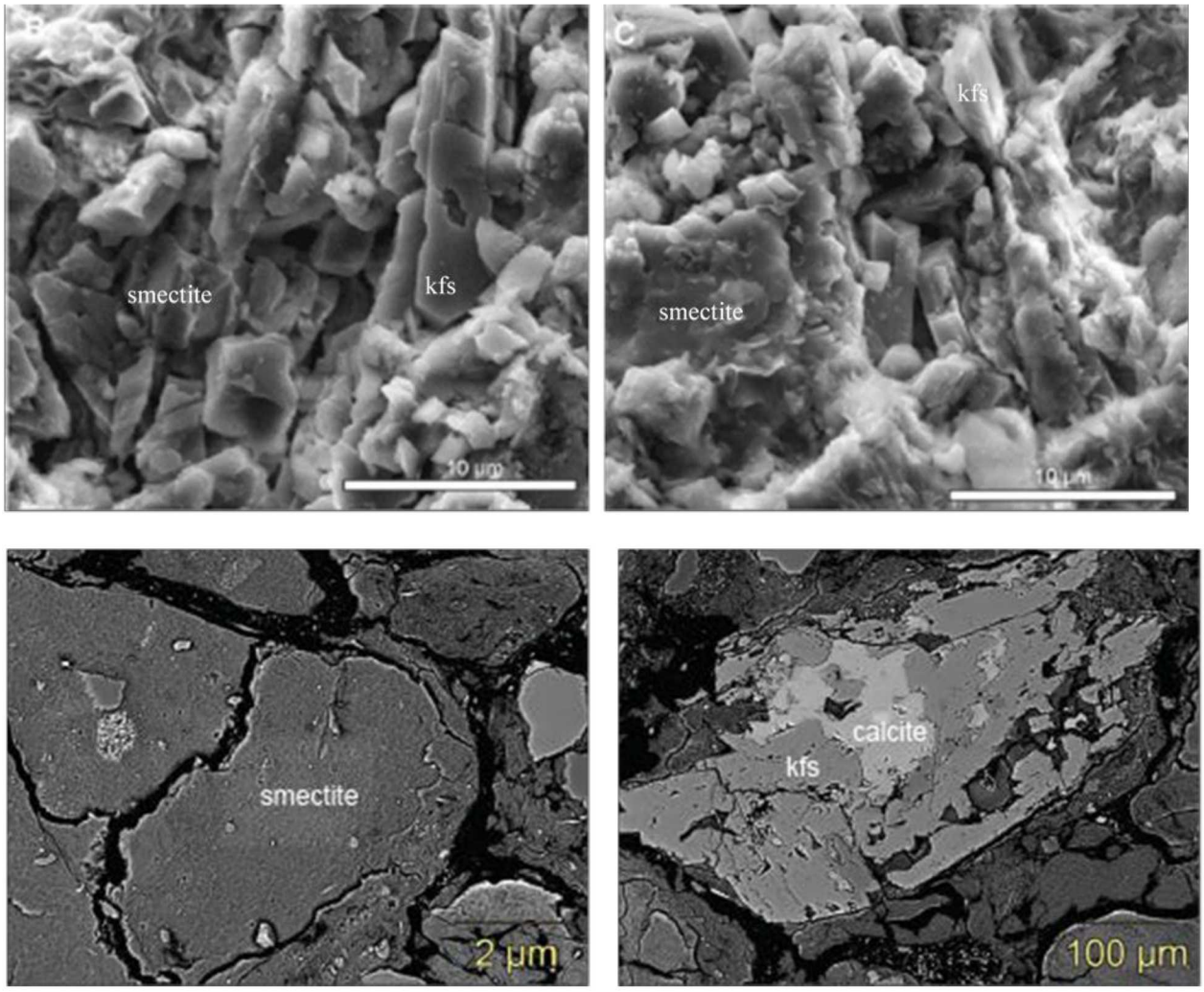


Figure F-20. FEBEX BM-C-49-1. [A, B] Electron microprobe secondary electron (SE) images of potassium feldspar/smectite mix. [C, D] Electron microprobe backscattered electron (BSE) images collected during microprobe analyses. [C] Smectite textures and morphology. [D] Intergrowth of K- feldspar (kfs) and calcite rimmed by smectite.

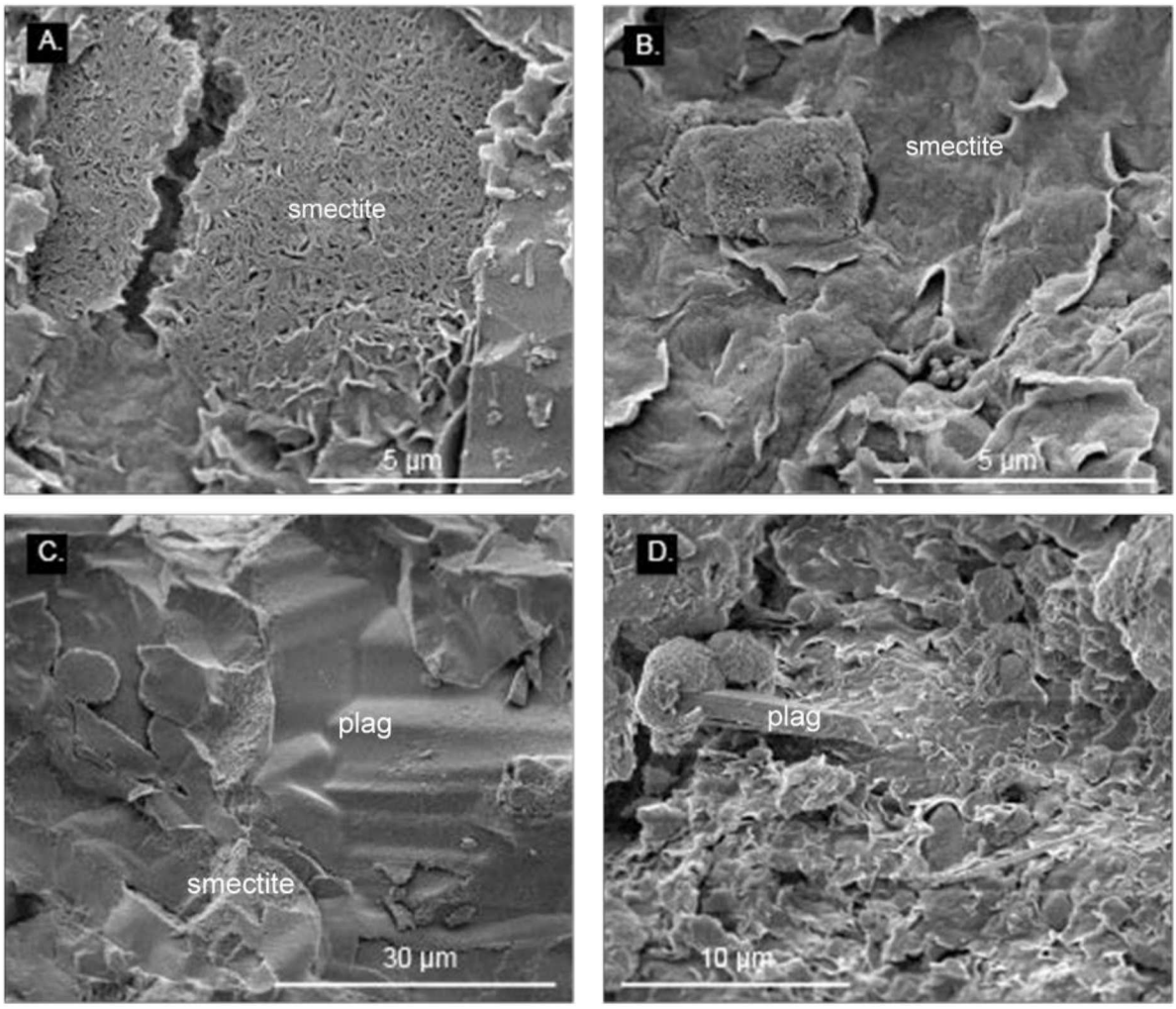


Figure F-21. FEBEX BM-C-49-3. [A, B, C, D] Electron microprobe secondary electron (SE) images depicting clay textures. [C, D] Intergrowth of plagioclase feldspar with clay.

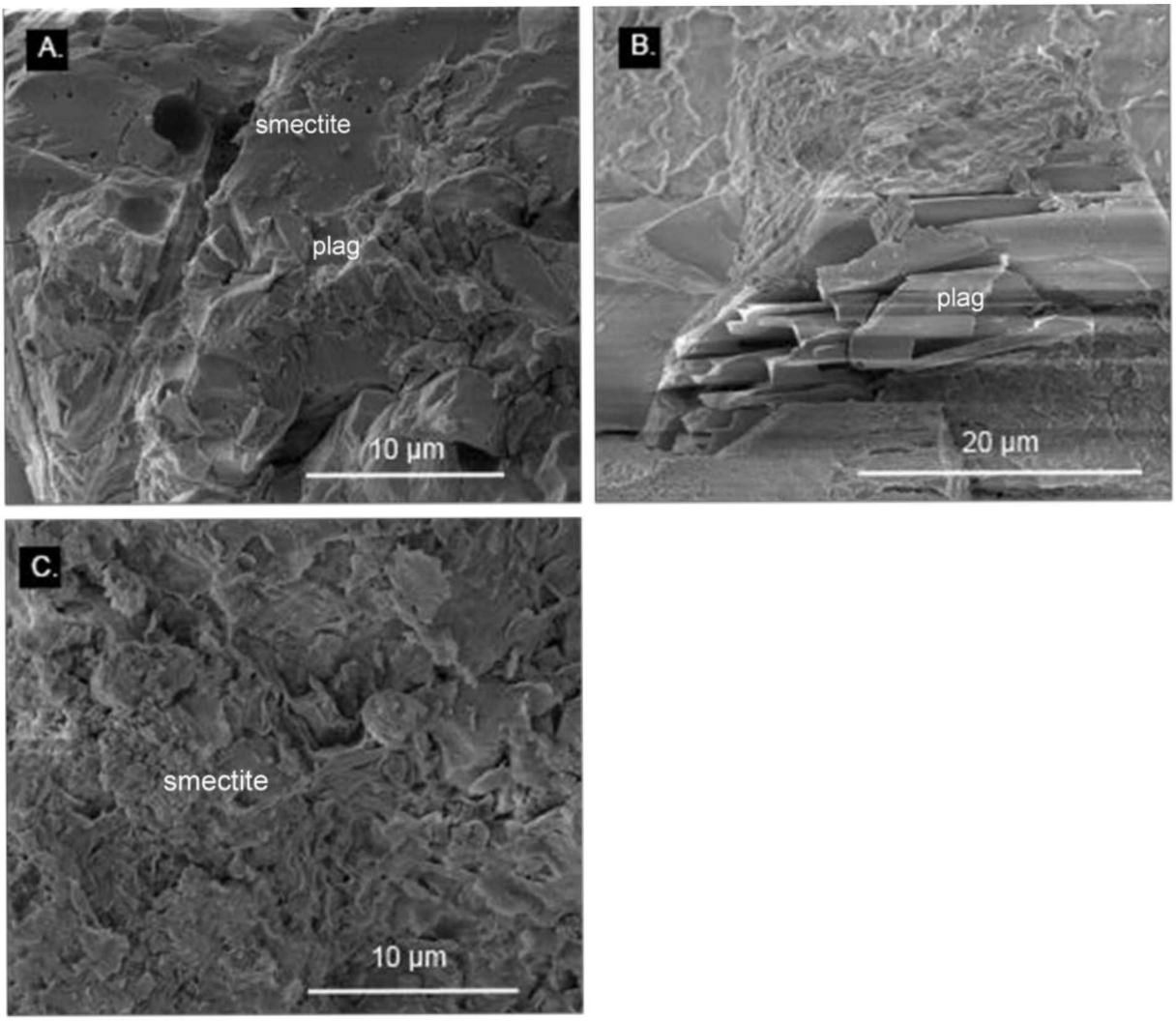


Figure F-22. FEBEX B-C-49-8. [A, B, C] Electron microprobe secondary electron (SE) images depicting clay textures and authigenic plagioclase [A, B].

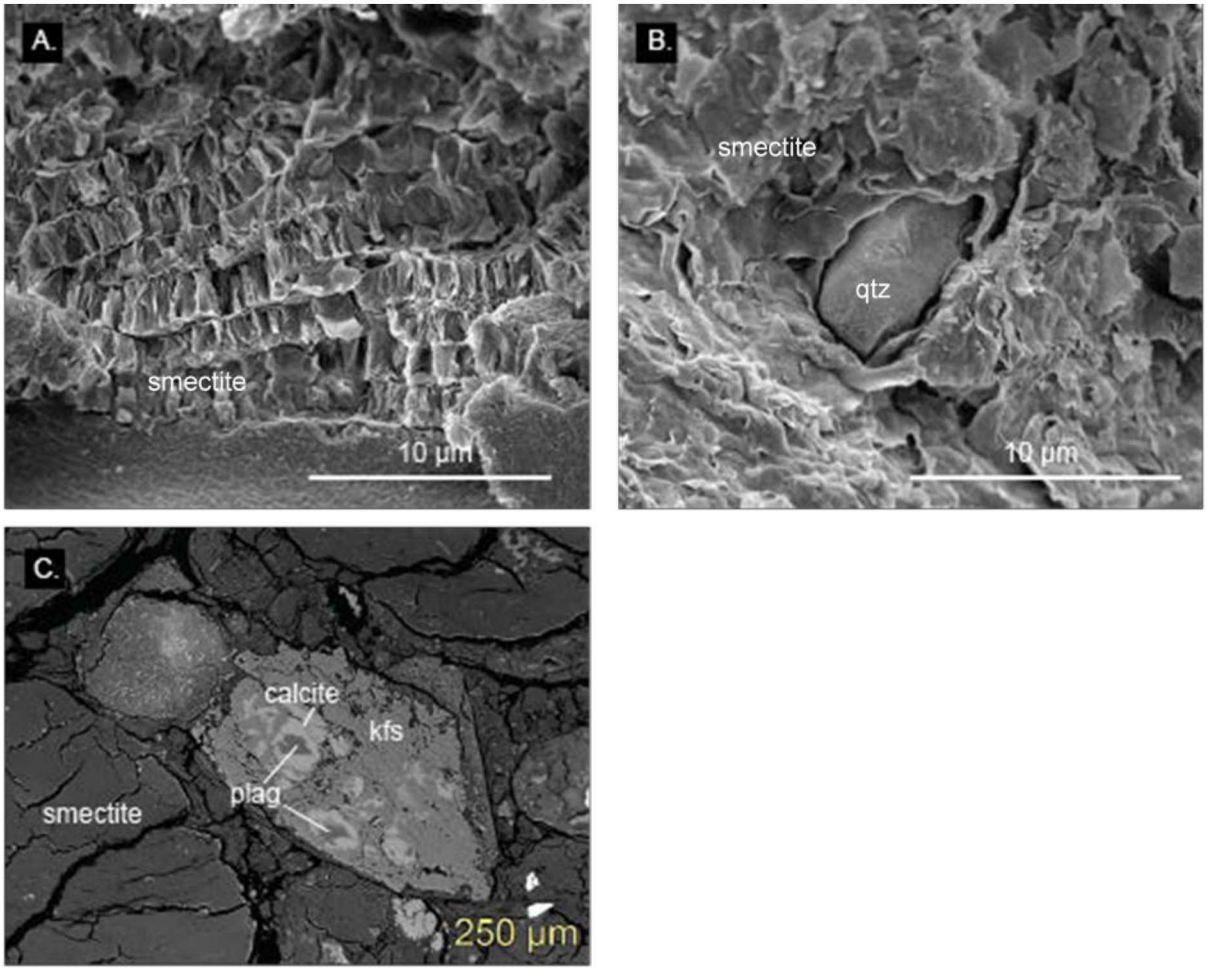


Figure F-23. FEBEX B-C-49-10. [A, B] Electron microprobe secondary electron (SE) images depicting clay textures. [C] Intergrowth of plagioclase, calcite, and K-feldspar in a smectite matrix.

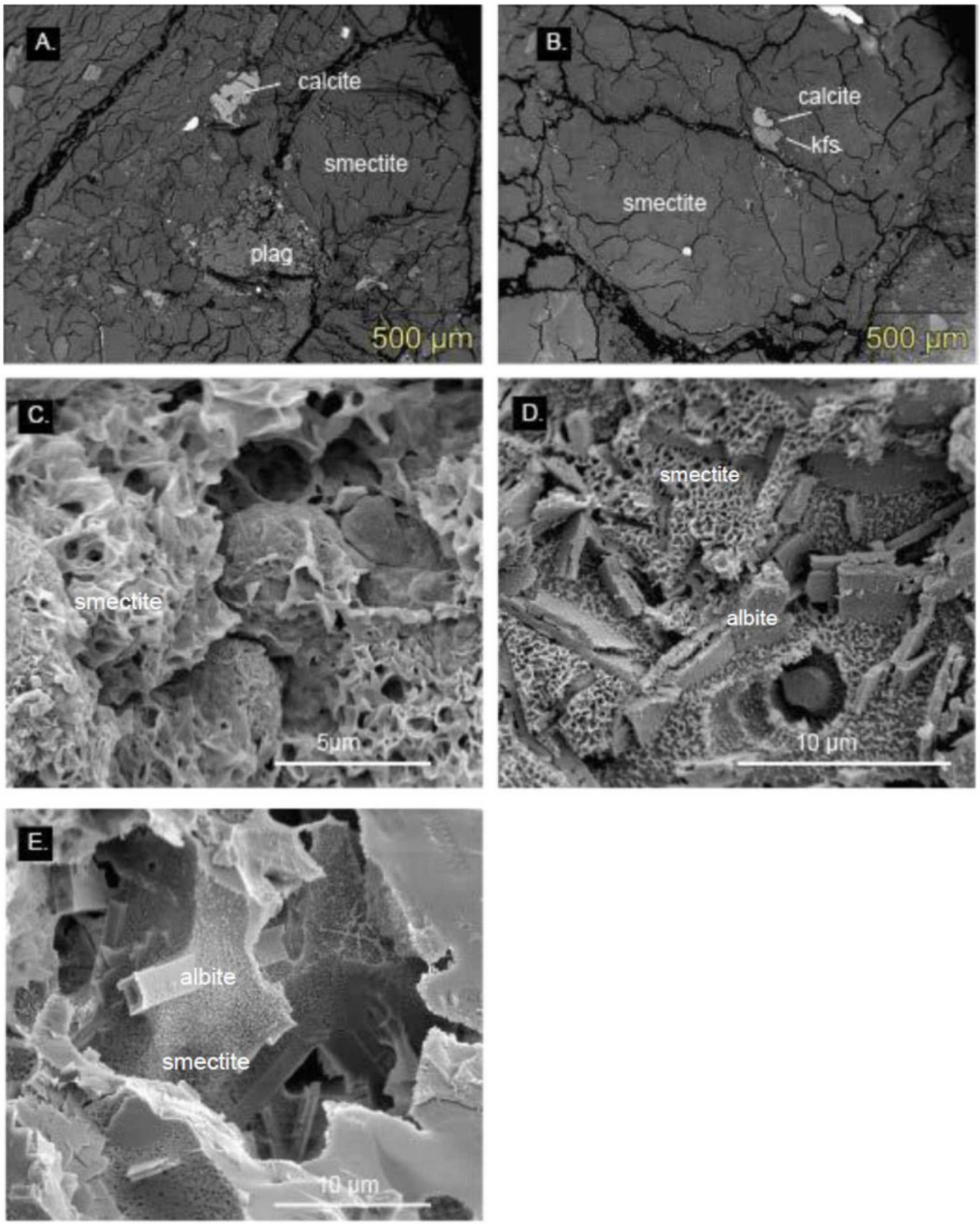


Figure F-24. FEBEX B-C-49-9. [A, B] Electron microprobe BSE images. [C, D, E] SE images of clay matrix and authigenic blocky, elongate feldspar crystals [D, E].

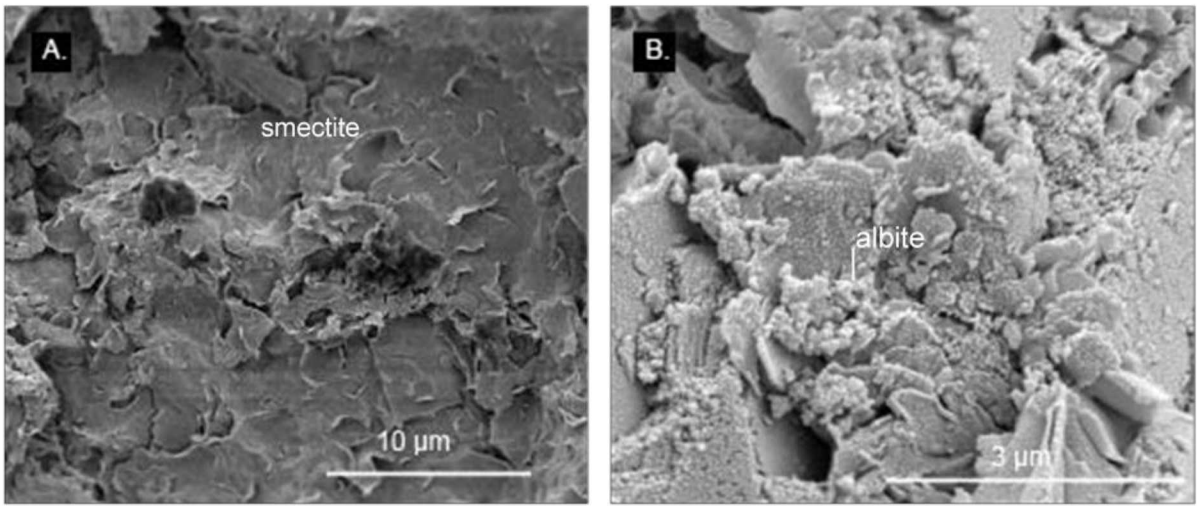


Figure F-25. FEBEX B-C-49-11. [A, B] Electron microprobe BSE images. [A] Clay texture. [B] Authigenic albite growth.